AD-A119 315 DAVID W TAYLOR NAVAL SHIP RESEARCH AND DEVELOPMENT CE--ETC F/G 20/4
FIRST INTERNATIONAL CONFERENCE ON NUMERICAL SHIP HYDRODYNAMICS --ETC(U)
1975 J W SCHOT, N SALVESEN

UNCLASSIFIED NL

1 of 8
AD A
119315

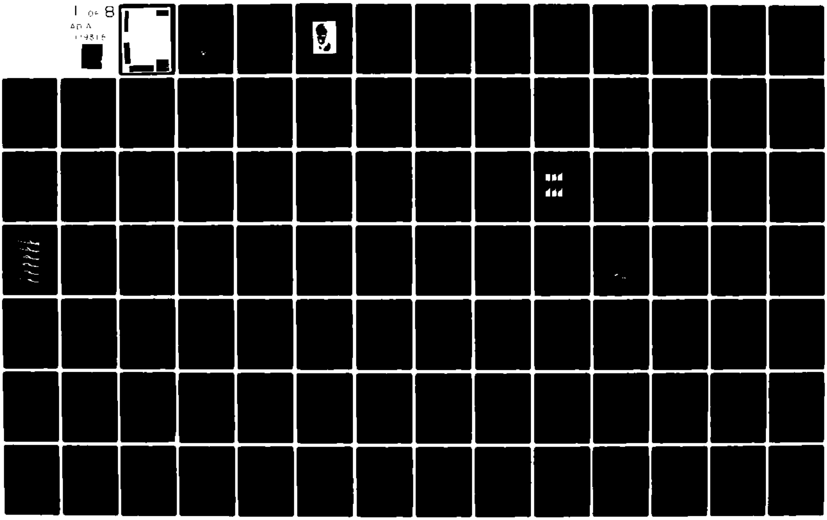

First International Conference on Numerical Ship Hydrodynamics

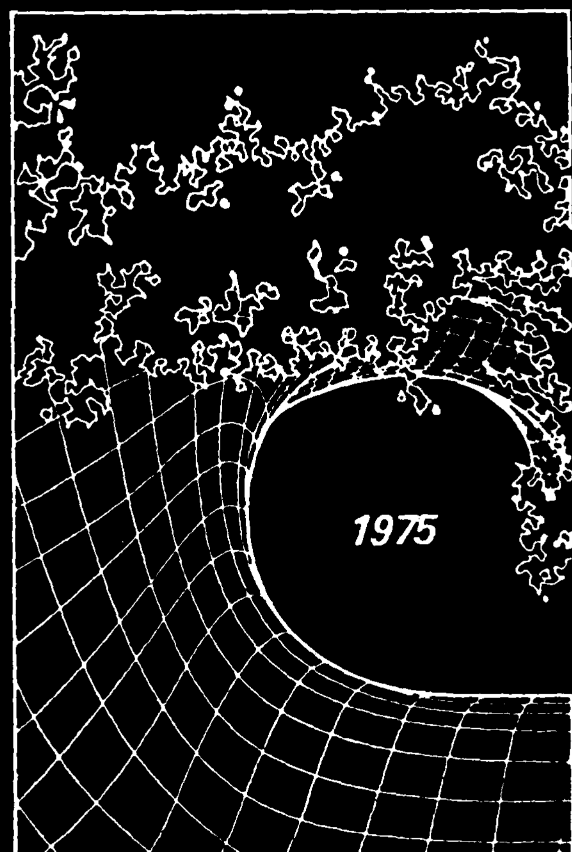

Proceedings

FIRST INTERNATIONAL CONFERENCE
ON
NUMERICAL SHIP HYDRODYNAMICS

Edited by

Joanna W. Schot

and

Nils Salvesen

Sponsored by

David W. Taylor Naval Ship Research and Development Center

With the Support of the

Office of Naval Research

20 – 22 October 1975

David W. Taylor Naval Ship Research and Development Center
Bethesda, Maryland 20084
United States of America

Statements and opinions contained herein are those of the authors and are not to be construed as official or reflecting the views of the Navy Department or of the naval service at large.

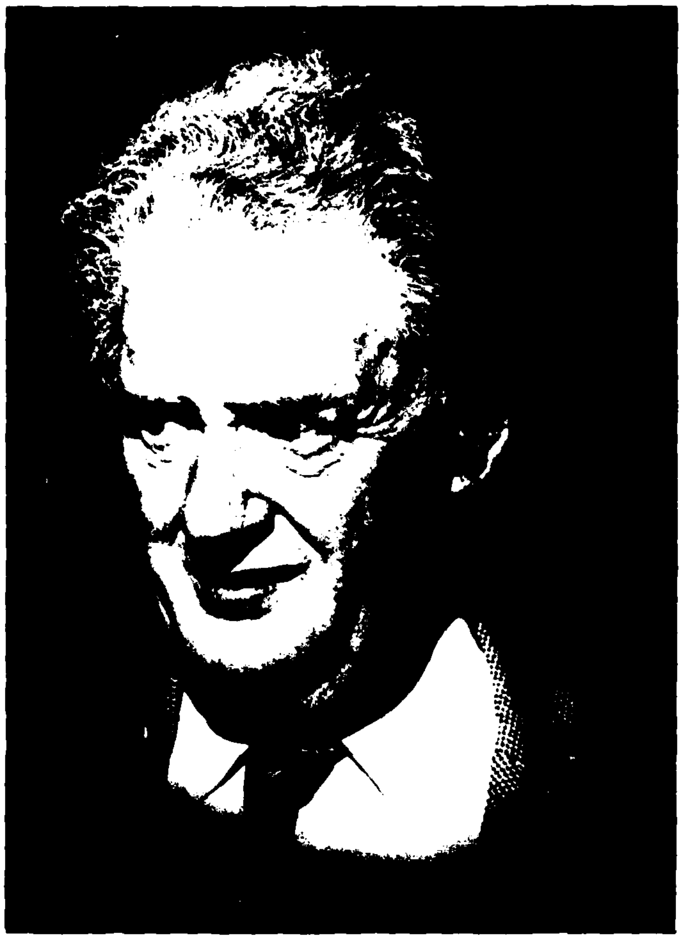

Dedicated to the Memory of

Professor Reinier Timman (1917 – 1975)
Delft University of Technology

DEDICATION

It is sad that Reinier Timman's keynote address which opened the First International Conference on Numerical Ship Hydrodynamics was to become his last formal presentation. It is fortunate that this Conference gave his colleagues from all over the world a last opportunity to express their esteem for him and his contribution to ship hydrodynamics.

Shortly after his return to Delft, twenty days after the conference opening, Reinier Timman died suddenly on 9 November 1975 at the age of 58. He will long be remembered as an innovative mathematician and philosopher with a wide range of interests. His impact upon the development of theoretical and numerical hydrodynamics is due not only to his own work, but to his unique ability to inspire and encourage others.

We in the United States, and particularly those of us at the David W. Taylor Naval Ship Research and Development Center, were fortunate to benefit from Reinier's frequent visits. During each of his visits, he spent endless hours helping us to formulate and solve our technical problems. On two particular occasions, Spring 1962 and Spring 1972, he presented lecture series on hydrofoil theory, control theory, and gravity-wave theory.

It is with deep admiration and respect that we dedicate these Proceedings to Reinier Timman's memory and to his wife Anneke and their four children, Ton, Yolande, Jan, and Reinier. The memory of his character and spirit will be a continuous inspiration to all of us.

A

PREFACE

The First International Conference on Numerical Ship Hydrodynamics was held in Gaithersburg, Maryland on 20-22 October 1975 at the National Bureau of Standards. The Conference was sponsored and organized by the David W. Taylor Naval Ship Research and Development Center (DTNSRDC) with support from the Office of Naval Research.

The need for a concentrated and multidisciplinary research effort in numerical ship hydrodynamics has been recognized for some time. In 1973 recommendations were prepared by DTNSRDC for advancing the capability within the U.S. Navy in numerical naval hydrodynamics. The Office of Naval Research sponsored a Workshop held at the National Academy of Sciences in May 1974 to assess the status of numerical hydrodynamics and to identify areas of needed research. At that Workshop Dr. W.E. Cummins described several basic ship hydrodynamics problems which had not been adequately solved by traditional methods but which could be attacked by numerical techniques. One of the conclusions reached at the Workshop was that a "persistent long range effort" will be required for the "successful application of numerical hydrodynamics to practically important hydrodynamic problems." Recognizing this need, DTNSRDC established a Numerical Naval Hydrodynamics Program in the summer of 1974 to accelerate the use of advanced numerical methods in ship hydrodynamics research. To promote wider communication among experts in ship hydrodynamics and numerical mathematics, an international conference was planned.

The purpose of this First International Conference was to present new results in the field of numerical ship hydrodynamics and to call attention to new computer techniques that can be used to attack problems in the areas of free surface flows, cavity flows, and viscous/boundary layer flows. These Proceedings contain both the invited and contributed papers presented at the Conference and reflect the diversity of numerical approaches being developed by researchers from different disciplines.

The success of this Conference was due to the enthusiasm and hard work of many dedicated people. To each of the members of the Organizing Committee special recognition is due. The outstanding cooperation of the National Bureau of Standards Conference Manager, Mrs. Sarah Torrance, is gratefully acknowledged. There are several other individuals whose contributions deserve explicit mention: Mr. Gene Gleissner consistently supported this Conference from its early inception; Dr. Alan Powell, who presented the Opening Remarks at the Conference, has been a strong supporter of Numerical Ship Hydrodynamics research; Dr. Hans J. Lugt did much to establish the environment which made this Conference possible; Mr. Ron Schmidt and his staff in the Technical Services Division worked creatively and efficiently in preparing all the publications associated with the Conference. Finally, the editors wish to thank the session chairmen for their excellent contribution to the program, the authors for their cooperation in preparing their manuscripts, and Mrs. Janet Dean for her editorial assistance.

ORGANIZING COMMITTEE

Chairman: J.W. Schot

Co-Chairman: N. Salvesen

Paper Selection

R.B. Chapman	H.J. Oser (NBS)
H.J. Haussling	N. Salvesen
H.J. Lugt	J.W. Schot
J.H. McCarthy	

Technical and Administrative Support

A.H. Centineo	K.W. Stabenau
J.S. Dean	S. Wybraniec
B. Schultz	G.R. Yarnall

CONTENTS

NUMERICAL METHODS IN SHIP HYDRODYNAMICS

R. Timman

Dept. of Mathematics, University of Technology
Delft, The Netherlands

1. Introduction

In ship hydrodynamics there are many problems to which numerical methods have been applied, e.g., the evaluation of measurements of wave resistance and the numerical calculation of analytical formulae, such as the Kelvin source potential. The topic of this meeting, however, is more ambitious.

In other branches of hydrodynamics and aerodynamics, numerical methods have obtained a more decisive position. For the determination of the effects of tidewaves in channels or estuaries, numerical calculation is a feasible alternative to investigation by model-scale experiments. Both methods have advantages and disadvantages and a combination can be very useful. In the design of supersonic airplanes, the calculation of the flow field plays, in combination with suitable experiments, a dominant role. Modern transonic wing sections are designed by advanced numerical methods.

Often, advantage is taken of the particular geometry (relatively thin wings), so that many methods refer to an integral equation (lifting surface theory) approach; for the airplane body, results are also obtained. For supersonic wings similar numerical procedures are used and for the transonic range, special methods (in particular in the two-dimensional case) have been developed. The question arises: can a similar setup be achieved for ships?

In place of the difficulties arising from compressibility effects, we have in ship hydrodynamics the free surface, origin of ship waves and wave resistance, and also the dominant factor in the study of the motion of ships at sea. If the free boundary condition can be applied in a linearized approximation, analytical formulae can be widely applied, such as in thin or slender ship theory. However, the limitations of the approximations readily become apparent.

A second serious simplification of the theory is the absence of viscosity. The frictional component of ship resistance can only be obtained by empirical methods and extrapolation procedures. The structure of the wake behind the hull, which is of dominant importance for the prediction of propeller behaviour can only be determined by measurements, which are

mostly performed at model scale. Theoretical information on this wake could follow from calculations of the turbulent boundary layer around a ship hull. A second problem, which belongs to the subject of numerical methods in ship hydrodynamics is the calculation of the pressure distribution on propellers, which is coupled to cavitation effects on the blades. Here, also, much remains to be done.

2. Potential Flow Around a Ship Hull by Integral Equations

2.1 Infinite fluid

The simplest problem in the collection is the problem of potential flow around a ship hull in an infinite fluid. In principle there are two methods to solve this problem.

For simplicity we consider a double body, such that the free boundary condition is replaced by a symmetry condition. Introducing rectangular coordinates x, y, z with the z-axis vertical, the symmetry plane is the xy plane. If only irrotional flow is considered, there exists a velocity potential, ϕ, which, for an incompressible fluid, satisfies the Laplace equation

$$\phi_{xx} + \phi_{yy} + \phi_{zz} = 0$$

For a moving ship the boundary condition at the ship hull is given by

$$\underline{n} \cdot \nabla\phi = \underline{n} \cdot \underline{v}$$

where $\underline{n}$ is the unit normal vector to the ship surface and $\underline{v}$ is the velocity at a point of the ship hull under consideration. At infinity, the fluid is assumed to be at rest with respect to a coordinate system fixed in space.

Because of the symmetry of the double body the condition at the xy-plane can take different forms, according to the motion of the ship. For a steady translational motion (in the x^+ direction) we see that the boundary conditions are such that

$$\frac{\partial\phi}{\partial z}(x, y, z) = -\frac{\partial\phi}{\partial z}(x, y, -z)$$

which gives for ϕ the relation,

$$\phi(x, y, z) = \phi(x, y, -z), \quad \frac{\partial\phi}{\partial z} = 0 \text{ for } z = 0.$$

Also of interest is the motion of ships about a steady equilibrium position (oscillations). Then the symmetry depends on the mode of oscillation. For heave and pitch motions ϕ turns out to be an odd function of z; for the other modes such as sway and yaw, ϕ is an even function of z.

In all cases we have to solve the Laplace equation for a half space with boundary conditions on the ship hull, which specify the normal derivative of the velocity potential. By application of Green's theorem, we can derive an integral equation for the value of the velocity potential on the hull. Assuming the integrals over a lower half sphere with infinite radius to vanish, we have for a point $P(x,y,z)$, in the lower half space, R_L,

$$4\pi\,\phi_P = \iint_{\text{hull}} \left\{ \phi \frac{\partial}{\partial n} \frac{1}{r_p} - \frac{\partial \phi}{\partial n} \cdot \frac{1}{r_p} \right\} dS + \iint_{\text{xy-plane}} \left(\phi \frac{\partial}{\partial n} \frac{1}{r_p} - \frac{\partial \phi}{\partial n} \cdot \frac{1}{r_p} \right) dS,$$

where $r_p\,(x,y,z)$ is the distance from a point on the surface of integration to the point $P(x,y,z) \epsilon R_L$, and n is the unit normal vector to the surface. For the image point P′ of P in the upper half space, R_U, we have

$$0 = \iint_{\text{hull}} \left(\phi \frac{\partial}{\partial n} \frac{1}{r_{p'}} - \frac{\partial \phi}{\partial n} \frac{1}{r_{p'}} \right) dS + \iint_{\text{xy-plane}} \left(\phi \frac{\partial}{\partial n} \frac{1}{r_{p'}} - \frac{\partial \phi}{\partial n} \frac{1}{r_{p'}} \right) dS.$$

On the xy-plane $(z = 0)$, $r_P\,(x,y,0) = r_{P'}\,(x,y,0)$. If ϕ is an odd function of z, then $\phi(x,y,0) = 0$ and $\partial/\partial n$ is continuous at $z = 0$. If ϕ is an even function of z, then $\left.\frac{\partial \phi}{\partial n}\right|_{z=0} = 0$ and ϕ is continuous at $z = 0$. In either case we have

$$4\pi\,\phi_P = \iint_{\text{hull}} \left\{ \phi \frac{\partial}{\partial n} \cdot \left(\frac{1}{r_P} + \frac{1}{r_{P'}} \right) - \frac{\partial \phi}{\partial n} \left(\frac{1}{r_P} + \frac{1}{r_{P'}} \right) \right\} dS.$$

Letting P approach a point on the ship hull, we obtain an integral equation for ϕ, the value of ϕ_P on the hull; since $\frac{\partial \phi}{\partial n}$ is known on the hull, the second integral can be evaluated. Usually a simpler equation is obtained by inserting beforehand an unknown source distribution, μ, on the hull, such that

$$\phi_P = \iint_{\text{hull}} \mu \left\{ \frac{1}{r_P} \pm \frac{1}{r_{P'}} \right\} dS.$$

An expression for $\frac{\partial \phi}{\partial n}$ is then derived and equated to the known value of $\frac{\partial \phi}{\partial n}$ on the hull. This is the basis for the famous method of Hess and Smith, wherein the hull surface is approximated by a set of panels, with the source density constant on each panel. Working out the integrals, a linear set of equations for the values of μ is obtained which can be solved by standard computer programs.

2.2 Free surface

The method, sketched above, can be extended to include the case of the linearized free-surface condition. This gives a representation of the surface waves from a ship. For steady motion in the x-direction, with velocity u, the linearized free-surface condition is given by

$$u^2 \phi_{xx} + g\phi_z = 0, \text{ on } z = 0.$$

For unsteady small-amplitude motions about a rest position

$$\phi_{tt} + g\phi_z = 0, \text{ on } z = 0.$$

Instead of the kernels $\frac{1}{r_P} \pm \frac{1}{r_{P'}}$ we obtain kernels for each of these cases by Fourier-transform methods. For a steady motion in infinitely deep water, the kernel is given by

$$\frac{1}{r_P} - \frac{1}{r_{P'}} + \frac{4g}{u^2\pi} \int_0^{\pi/2} d\theta \oint_0^{\infty} \frac{e^{-k(2+z_P)} \cos[k(x-x_P)\cos\theta] \cos[k(y-y_P)\sin\theta]}{k\cos^2\theta - g/u^2}\, dk -$$

$$-4\frac{g}{u^2} \int_0^{\pi/2} e^{-g/u^2(2+z_P)\sec^2\theta} \left[\sin\frac{g}{u^2}(x-x_P)\sec\theta\right] \cos\left[\frac{g}{u^2}(y-y_P)\sin\theta\sec^2\theta\right] \sec^2\theta\, d\theta,$$

with a similar expression for the unsteady case.

The expressions can be manipulated, but always have the form of the infinite fluid kernel with an additional term, consisting of a double integral over an oscillating integrand, which has to be evaluated numerically. Consequently the numerical work for this case is appreciable. Moreover the linearized free-surface boundary condition for a blunt ship in steady forward motion certainly is not consistent with the bluntness. Up to now satisfactory analytical results for the bow wave problem have not been obtained.

It should be remarked that the integral equation method cannot be used for the non-linear free surface condition. Here, the unknown elevation of the free surface is a part of the solution.

3. Potential Flow Round a Ship Hull by Finite Differences or Finite Elements

3.1 Finite differences

An alternative to the integral equation methods is the solution of the corresponding Neumann problem for the ship by finite difference methods. Here again, the infinite fluid problems gives the least difficulties. Many methods are available, beginning with relaxation methods for the Laplace equation. The problem is the size of the region, which surrounds

the ship as well as the determination of the various mesh sizes. Also, as is always the case with finite-difference methods, the fitting of the hull surface requires special care. For an infinite fluid the calculations can be done by standard methods. The linearized free-surface boundary condition requires a device at the boundaries of the region, since the waves do not die out at infinity. Hence, it is not possible to insert the condition $\phi = 0$ at large distances from the ship.

Use can be made of analytical asymptotic expressions for the wave form at a large distance from the ship. In the two-dimensional case of an oscillating ship this is easily worked out. The phase difference between the ship's motion and the asymptotic expression follows from the solution of the difference scheme. Another possibility is to use a numerical radiation condition at the outer boundary of the region.

Similar procedures should be developed for three-dimensional nets. The nonlinear free-surface boundary condition requires special treatment; in particular, with a fine mesh, the moving surface may cause difficulty.

3.2 An alternative to a finite difference method is a finite element method

Here the elements of the net do not have to be squares, but can have a geometry which is more or less arbitrary. The standard derivation of the finite element method rests on the construction of a functional over the field, which must be minimized. For an infinite fluid (double body) this functional is simply the Dirichlet integral for the region. The boundary conditions are taken account of by suitable additions to the functional. For the linearized free-surface condition a similar set-up can be used. Here a functional can be constructed, but at the outer boundaries a radiation condition must be introduced.

It should be remarked, that for the finite element method it is not necessary to construct a functional, which has to be minimized; the necessary formulae can also be obtained by orthogonalization.

In the first place we construct a quadratic functional of the potential ϕ, i.e. the Dirichlet integral

$$D = \iiint_V (\nabla\phi)^2 \, dV + \iint_S \tilde{L}\phi \, dS,$$

where the second term takes account of the boundary conditions. If we expand ϕ in a series of orthogonal functions, ϕ_n, we have

$$\int \phi_m \cdot \phi_n \, dV = 0, \; n \neq m$$

$$\phi = \sum_{n=0}^{\infty} a_n \phi_n .$$

If we take a finite approximating sum,

$$\phi \sim \sum_{n=1}^{N} a_n \phi_n ,$$

we construct an approximation for D

$$D_N = \iiint \left(\sum_{n=1}^{N} a_n \nabla \phi_n \right)^2 dV + \sum_{n=1}^{N} a_n \iint \widetilde{L} \phi_n \, dS$$

$$= \sum_{m=1}^{N} \left[\sum_{n=1}^{N} (A_{mn} a_m a_n) + b_m a_m \right] ,$$

which gives rise to a quadratic function in a_n. Minimizing gives a linear set of equations

$$\sum_{n=1}^{N} A_{mn} a_n = b_m$$

where the b_m follow from the boundary conditions. This is the Ritz principle. In the finite element method, the expansion functions are obtained by dividing the region into elements and defining $\phi_n = 0$ outside element n. Inside of the element, the function ϕ_n is chosen such that the solution will not show discontinuities at the dividing surfaces.

The Galerkin method is slightly different. For a linear equation,

$$L\phi = 0$$

with linear boundary condition, $\widetilde{L}\phi = 0$, we can choose the set ϕ_n such that

$$\sum_{n=0}^{N} a_n \widetilde{L} \phi_n = 0.$$

The Galerkin method now replaces the equation $L\phi = 0$ by the set of equations

$$\sum_{n=0}^{N} a_n \iiint \phi_m L \phi_n \, dV = 0, \; m = 0, \ldots . N.$$

If the functional exists and the equation $L\phi = 0$ is the Euler-Lagrange equation of the corresponding variational problem, we can, by partial integration, transform the above volume integral in to an integral over the volume, plus an integral over the bounding surface; the result is equivalent to the right hand side of the Dirichlet integral discussed previously. Here, also, the non-linear free-surface boundary condition requires discussion.

Two possibilities are open, fixed elements where the boundary moves, inside the element, or a Lagrangian approach. For the ship hull a complete three-dimensional calculation is very laborious. A quasi-two dimensional method is now being worked upon in Delft (C. Korving). Instead of working out three-dimensional finite elements, a set of planes is introduced and ϕ is written as a function of one coordinate, which determines the planes and two other coordinates in the plane. The dependence on the first coordinate is introduced by a set of splines with coefficients, which are functions of the other coordinates. For a ship the planes are taken to be planes through the axis of the ship. In this scheme,

$$\phi = \sum \phi_n(x,y)\,\mathcal{L}_n(\sigma),$$

where σ is the angle which determines the planes and $\mathcal{L}_n(\sigma)$ are spline polynomials. The minimization of the total functional gives rise to minima for the separate $\phi_n(x,y)$. One obtains a system of coupled two-dimensional problems each of which is solved by plane finite elements. Results are available for an ellipsoid in infinite fluid with a rigid wall condition $\partial\phi/\partial z = 0$ at the free surface. Each two-dimensional problem refers to an ellipse and for the rigid wall condition very little computer effort is needed. For the next stage, satisfying linearized free-surface conditions, the asymptotic behavior at the outer boundary must first be worked out; these calculations are now in progress.

4. Propeller Theory

A few remarks are made on propeller theory. In recent years the lifting surface theory of propellers has become a tool in design. It is based on the integral equation method and numerical methods of solution are available.

A problem, however, which is not adequately worked out, is the calculation of the cavity region on a propeller cavitating in a non-uniform wake field. Here, unsteady lifting surface theory is necessary. Although programs for harmonic inputs are available, these do not suffice to calculate the cavities. Also extensions to heavily loaded and shrouded propellers should be developed.

5. Boundary Layer Flow Around a Ship Hull

As a final subject of this talk the boundary layer round a ship hull presents itself as a challenge for numerical treatment.

Although the boundary layer is a viscous phenomenon and viscous flow is described by the equations of Navier-Stokes, numerical solutions of these equations are of no use for the calculation of the viscous layer along the ship. It is impossible to calculate boundary layer phenomena by pure numerical methods, because the flow is turbulent. Nevertheless a discussion of this problem has a place in a paper on numerical methods in ship hydrodynamics.

Basic for the calculation of boundary layer flows are the momentum equations. For laminar flows, boundary-layer equations give a satisfactory approximation in most cases. The calculation method for turbulent boundary layers can be considered as a generalization. For boundary-layer calculations the potential flow must be known in advance; depending on the results of the boundary-layer calculations the potential-flow pressure distribution may have to be modified.

One way of working with the boundary layer equations is to introduce a set of curvilinear coordinates with the streamlines of the potential flow at the surface and a set of orthogonal trajectories as coordinates. If we denote the components of the flow velocity in the boundary layer by u and v, and the outer velocity by U, we have the displacement thicknesses vector

$$\delta_1 = \int_0^\delta \left(1 - \frac{u}{U}\right) dz, \; \delta_2 = \int_0^\delta \frac{v}{U}\, dz,$$

where δ is the boundary layer thickness. The momentum thickness is a tensor defined by,

$$\theta_{11} = \int_0^\delta \frac{u}{U}\left(1 - \frac{u}{U}\right) dz, \; \theta_{12} = \int_0^\delta \frac{uv}{U^2}\, dz, \; \theta_{21} = \delta_2 - \theta_{12}, \; \theta_{22} = \int_0^\delta \frac{v^2}{U^2}\, dz.$$

From the momentum theorem a set of equations for these quantities can be devised, which contain the shearing stress at the wall and the pressure gradient of the outer flow.

For laminar boundary layers we can, in this concept, represent the velocity profiles $\frac{u}{U}$ and $\frac{v}{U}$ as functions of suitable shape parameters, which depend on the coordinates. The art of the problem formulation then leads to two free parameters, which are determined by the set of momentum equations in the streamline and cross-flow directions. The shearing stress at the wall is directly expressible as a function of the parameters. For turbulent boundary layers a similar procedure can, in principle, be followed. Instead of devising the relations between the parameters and the pressure gradient and shearing stress from the theory,

suitable experiments have to be performed. In both cases a set of partial differential equations along the ship hull can be obtained. The solution of these equations is a numerical problem.

Boundary conditions arise at the free surface. The forward stagnation point of the flow is a singular point at which special care must be taken. To obtain a solution is a formidable problem, requiring theoretical and numerical skill and good supporting experimental data for turbulent boundary layers. The calculation should also give information on turbulent separation. If the ship hull has sharp edges, it is obvious that there separation will occur. The behavior after separation is a subject, that needs a totally different approach, which is not considered here.

NUMERICAL SOLUTION OF NAVAL FREE-SURFACE HYDRODYNAMICS PROBLEMS

C. von Kerczek

David W. Taylor Naval Ship Research and Development Center
Bethesda, Maryland 20084 U.S.A.

ABSTRACT

A review of numerical techniques for solving the partial differential equations of free-surface hydrodynamics problems is given. The results of their application to solve such problems are discussed and compared, as far as possible. The main problems that are discussed fall into the following categories: sloshing in containers; free waves; oscillating bodies; accelerated and uniform motion of bodies. It is found that a variety of numerical techniques have been developed, each of which provides good approximate solutions of problems in one or two of the above classes. However only one or two methods have been developed that can be used for problems in all of the above classes.

1. Introduction

As a prelude to this conference on numerical ship hydrodynamics, we discuss in this paper the status of numerical methods for the solution of free-surface problems. We mainly consider numerical solutions of field problems (i.e., direct numerical solutions of the partial differential equations) rather than numerical solution of the corresponding integral equations. Since our ultimate goal is to deal with free-surface problems at ship scales, we consider the water to be incompressible, homogeneous, inviscid and without surface tension.

In this review we first discuss mathematical formulations of the general free-surface problem with which we are concerned. Then we describe some elementary numerical methods for obtaining approximate solution of such problems. These numerical methods are presented only to illustrate method; they may not actually be efficacious. Many, if not most, of the currently used numerical methods are extensively modified and refined versions of the basic methods which are presented here. However, a description of the basic methods does provide an overview of the type of calculations that have been attempted.

We discuss various implementations of numerical methods to solve problems in the following four categories:

A. Sloshing in containers

B. Free waves

C. Oscillating bodies in or near the free surface

D. Uniform and accelerated motion near a free surface

Groups A and B overlap. For group A problems we mainly emphasize nonpathological motions of the free surface and for group B problems we are concerned mainly with the generation, propagation, and runup of waves in tanks or channels.* The problems of group C are mainly concerned with the forced oscillation of a body in the free surface or the response of a floating body when waves, generated far away from the body, impinge on it. The problems of group D are mainly wave resistance problems. We discuss the approach of an acceleration problem to a steady state and some turning problems.

While we can not discuss all of the intricacies and difficulties that are encountered in any one particular numerical method, we will discuss briefly the two primary difficulties in the numerical simulation of free-surface ship hydrodynamics. These two difficulties are the stability of the numerical time integration procedure of the free-surface equations (or, analogously, the method of generating the unknown free-surface boundary in steady flow

*The scale of motion in group A is generally of the container dimensions, whereas for group B the scale of motion is much smaller than the container dimensions.

problems) and the closure of the algebraic equations that approximate the partial differential equations when infinite fluid domains are truncated to finite ones.

2. General Formulation

We consider a region of inviscid, incompressible and homogeneous water whose motion is irrotational. The fluid region may be finite or infinite in spatial extent and its motion may be produced by several alternative (or simultaneous) means. These may be: (i) forced motion of rigid boundaries located a finite distance from the origin, (ii) forced pressure variations on the free surface, (iii) deviation of the fluid from its equilibrium position,* (iv) forced motion of boundaries located at infinity (i.e., free-wave problems). In some cases we study a secondary motion, superimposed on a given basic motion, which is produced by rigid freely-floating or stationary boundaries. The motion of primary interest is called the disturbance and the agent producing this motion is called the disturber.

In a reference frame labeled with the cartesian coordinates (x, y, z), the body of water occupies the region R(t) and has the boundary $\partial R(t)$ where t denotes time. We assume that the gravitational force is directed along the negative y-axis so that its potential is $G = -gy$. We let $(\vec{i}, \vec{j}, \vec{k})$ be a triple of unit vectors in the (x, y, z) directions respectively.

Let the free surface be described by an equation of the form

$$\eta(x, z, t) - y = K$$

or parametrically as

$$\vec{r}(x, z, t) = x(t)\vec{i} + \eta(t)\vec{j} + z(t)\vec{k}$$

where K is a constant. (Henceforth, we simply denote any constant by the letter K.). Let $\vec{V}_B(t)$ be the velocity of a point on the boundary of R(t) and $\vec{N}(t)$ the inward normal vector to the boundary at this point. We denote by $p_a(x, z, t)$ a specified pressure variation on the free surface $y = \eta$ and from now on we denote the free surface by $\mathcal{S}$, and other boundaries by ∂R.

The main formulations of this problem are well-known and we follow Lamb (1945) in their statements. We give here the formulations of the direct, or "primitive", form of the problem (i.e., in terms of the momentum equations) and the potential-flow form of the problem which results from constraining the motion to be irrotational. The primitive and potential forms of the free-surface flow problem are given in the Eulerian and Lagrangian variables as follows:

*The water has a stationary equilibrium position for fixed boundaries and stationary free-surface pressure distributions.

(i) Eulerian primitive problem;

$$\left.\begin{aligned} \frac{\partial \vec{V}}{\partial t} + \vec{V}\cdot\nabla\vec{V} + \nabla\left(\frac{P}{\rho} - G\right) = 0 \\ \nabla\cdot\vec{V} = 0 \end{aligned}\right\} \text{ in } R \qquad (2.1\text{ a, b})$$

where

$$\nabla \equiv \vec{i}\,\frac{\partial}{\partial x} + \vec{j}\,\frac{\partial}{\partial y} + \vec{k}\,\frac{\partial}{\partial z}$$

$$\vec{N}(t)\cdot\vec{V}(t) = \vec{N}(t)\cdot\vec{V}_B(t) \quad \text{on } \partial R \qquad (2.2)$$

$$\left.\begin{aligned} P = p_a(x, z, t) \\ \frac{d\vec{r}}{dt} = \vec{V}(r, t) \end{aligned}\right\} \text{ on } \mathcal{S} \qquad (2.3\text{ a, b})$$

(ii) Eulerian Potential problem;

$$\left.\begin{aligned} \vec{V} = \nabla\Phi \\ \nabla^2\Phi = 0 \end{aligned}\right\} \text{ in } R \qquad (2.4)$$

$$\vec{N}(t)\cdot\nabla\Phi = \vec{N}(t)\cdot\vec{V}_B(t) \quad \text{on } \partial R \qquad (2.5)$$

$$\left.\begin{aligned} \frac{\partial\Phi}{\partial t} + \frac{1}{2}\vec{V}\cdot\vec{V} + \frac{p_a(x, z, t)}{\rho} + g\eta = K \\ \frac{\partial\eta}{\partial t} + \vec{V}\cdot\nabla(\eta - y) = 0 \end{aligned}\right\} \text{ on } \mathcal{S} \qquad (2.6\text{ a, b})$$

(iii) Lagrangian Primitive problem;

$$\left.\begin{aligned} \frac{\partial\vec{R}}{\partial t} = \vec{V} \\ \left(\frac{\partial\vec{V}}{\partial t} - \nabla_{\mathcal{L}}G\right)\cdot\nabla_{\mathcal{L}}\vec{R} + \frac{1}{\rho}\nabla_{\mathcal{L}}P = 0 \\ \frac{\partial}{\partial t}(\rho J) = 0 \end{aligned}\right\} \text{ in } R \qquad (2.7\text{ a, b})$$

where

$$J \equiv \frac{\partial(X, Y, Z)}{\partial(a, b, c)} \qquad \text{(Jacobian)}$$

$$\vec{R} \equiv (X(a, b, c, t),\ Y,\ Z),\ \vec{R}(a, b, c, o) = (a, b, c)$$

$$\nabla_{\mathcal{L}} \equiv \vec{i}\,\frac{\partial}{\partial a} + \vec{j}\,\frac{\partial}{\partial b} + \vec{k}\,\frac{\partial}{\partial c}$$

$$\vec{N}(t)\cdot\vec{V}(t) = \vec{N}(t)\cdot\vec{V}_B(t) \qquad \text{for } \vec{R}\epsilon\partial R \qquad (2.8)$$

$$\left.\begin{aligned}\frac{\partial^2 X}{\partial t^2}\frac{\partial X}{\partial a}+\left(\frac{\partial^2 Y}{\partial t^2}+g\right)\frac{\partial Y}{\partial a}+\frac{\partial^2 Z}{\partial t^2}\frac{\partial Z}{\partial a}&=-\frac{1}{\rho}\frac{\partial p_a}{\partial a}\\ \frac{\partial^2 X}{\partial t^2}\frac{\partial X}{\partial c}+\left(\frac{\partial^2 Y}{\partial t^2}+g\right)\frac{\partial Y}{\partial c}+\frac{\partial^2 Z}{\partial t^2}\frac{\partial Z}{\partial c}&=-\frac{1}{\rho}\frac{\partial p_a}{\partial c}\end{aligned}\right\}\text{ on } \mathcal{S}(b=K) \qquad (2.9\text{ a, b})$$

(iv) Lagrangian Potential Problem;

$$\left.\begin{aligned}\frac{\partial \vec{R}}{\partial t}&=\vec{V}\\ \nabla_{\mathcal{L}}\times\left(\frac{\partial \vec{V}}{\partial t}\cdot\nabla_{\mathcal{L}}\vec{R}\right)&=0\\ \frac{\partial}{\partial t}(\rho J)&=0\end{aligned}\right\}\text{ in R} \qquad (2.10\text{ a, b})$$

$$\vec{N}(t)\cdot\vec{V}(t)=\vec{N}(t)\cdot\vec{V}_B(t) \qquad \text{for } \vec{R}\epsilon\partial R \qquad (2.11)$$

$$\left.\begin{aligned}\frac{\partial^2 X}{\partial t^2}\frac{\partial X}{\partial a}+\left(\frac{\partial^2 Y}{\partial t^2}+g\right)\frac{\partial Y}{\partial a}+\frac{\partial^2 Z}{\partial t^2}\frac{\partial Z}{\partial a}&=-\frac{1}{\rho}\frac{\partial p_a}{\partial a}\\ \frac{\partial^2 X}{\partial t^2}\frac{\partial X}{\partial c}+\left(\frac{\partial^2 Y}{\partial t^2}+g\right)\frac{\partial Y}{\partial c}+\frac{\partial^2 Z}{\partial t^2}\frac{\partial Z}{\partial c}&=-\frac{1}{\rho}\frac{\partial p_a}{\partial c}\end{aligned}\right\}\text{ on } \mathcal{S}(b=K) \qquad (2.12\text{ a, b})$$

In each of the above formulations, it is understood that suitable initial conditions are provided. Also, if any freely-floating bodies are present, the governing equations of the fluid motion are coupled, through the boundary conditions, to suitable dynamical equations of motion of the body.

The general nonlinear problems formulated above are very difficult to analyze. For this reason, certain approximations are usually made to simplify them. The main approximatio usually considered, which is the one we shall refer to as "the linearized problem" is given below in terms of the potential problem in Eulerian variables:

(i) Unsteady and time-periodic flows; the linearized free-surface conditions on $\mathcal{S}$ are given by

$$\left.\begin{aligned}\frac{\partial \Phi}{\partial t}+\frac{p_a(x,z,t)}{\rho}+g\eta&=K\\ \frac{\partial \eta}{\partial t}-\vec{V}\cdot\vec{j}&=0\end{aligned}\right\}\text{ on } y=0 \qquad (2.13\text{ a, b})$$

(ii) Steady flow with speed $V=-U\vec{i}$ far upstream and $\Phi=-Ux+\varphi$; the linearized free-surface conditions on $\mathcal{S}$ are given by

$$
\left.\begin{aligned}
\frac{\partial^2\varphi}{\partial x^2} + \frac{g}{U^2}\frac{\partial\varphi}{\partial y} &= \frac{p_a(x,z)}{\rho U} \\
\eta &= \frac{U}{g}\frac{\partial\varphi}{\partial x} - \frac{p_a(x,z)}{\rho g}
\end{aligned}\right\} \text{on } y = 0 \qquad (2.14\text{ a, b})
$$

Problems with boundaries at infinity lead to different mathematical requirements in their formulation depending on whether or not they are transient or steady state. We consider motions that are periodic as steady state motions. The transient formulations have been given above (2.1 - 2.13). The steady state formulations differ in that intial conditions must, naturally, be dropped. Moreover, boundedness at infinity (in space) is not sufficient to insure uniqueness. One must, in addition, specify that if the disturber is finitely placed (i.e., the disturber can be enclosed in a bounded subdomain of the fluid), then the disturbance radiates outwards towards infinity, i.e., the flux of disburbance energy is away from the disturber.

It is not always obvious what the condition of outward radiation ought to be. If one can determine all the eigenfunctions of a particular problem or class of problems with no disturber present, then one can construct a "filter" which removes all those disturbances which do not either manifest outward flow of energy or decay spatially. A prototype problem illustrating this principal is the linear problem of the symmetric forced oscillation of the free surface in a homogeneous constant-depth liquid extending horizontally to infinity. This problem is discussed by Stoker (1957).

A somewhat different situation is illustrated by the steady flow past a stationary body. This type of problem is unsymmetrical upstream and downstream. The unique solution is obtained by requiring that the disturbance of the uniform motion of the stream vanishes very far upstream. In the linearized version of this problem, a sufficient condition to insure uniqueness is that the flow is uniform with an undisturbed free surface far upstream. This is in fact the radiation condition for this problem and no statement about the downstream flow (except that it is bounded) need be made.

Infinite boundaries present special difficulties in numerical solution of steady state problems. The domains must be truncated at finite length and the effect on the fluid motion of the discarded part of the domain must be accounted for. The transient problems seem to be more amenable (at least conceptually) to numerical solution because of the necessity of truncating the infinite flow domain. Transient problems are well-posed on infinite domains by simply requiring boundedness at infinity. These problems lead, at least in principal, to the correct steady state limit (if it exists) by letting $t \to \infty$ (cf. Stoker, 1957). If the motion of the fluid is caused by a finitely placed disturber, then discernible fluid motion at

infinity is felt only after an infinite interval of time. Thus, one may consider only a finite fluid domain R_B (but one large enough to completely contain the motion generating boundaries) and be assured that the approximate solution in R_B is essentially the same for some time interval $[0,T]$ as the restriction on R_B of the exact solution. If R_B is large enough one might then obtain an approximate "local" steady state after some time $T^* < T$ if T is large enough. By a "local" steady state it is meant that there exists a sub-domain $R_S \subset R_B$, where R_S completely contains the disturber and in which the motion is steady for $T^* < t < T$. However, it may be the case in many problems involving a free surface that T and T^* as well as R_B are too large for practical calculations. Hence, it is of some value to develop numerical methods for steady state problems in unbounded domains. In such methods the truncation of the numerical domain and the method used to simulate the effect of the discarded part of the fluid domain on the remaining part can play a crucial role in the calculations. Because there is no known rational closure method for nonlinear steady-state problems, it would seem that the only mathematically-justified approach to a steady state problem is through an initial value problem. However, certain ad-hoc closure conditions have been used with some apparent success in numerical simulations of steady nonlinear problems (cf. von Kerczek and Salvesen, 1974). These are based on the idea that what happens far downstream of the disturbance does not have an appreciable affect near the disturbance as long as mass flux out of the region is preserved. For some linear-theory problems one can make use of known analytic information. For example, if the radiation conditions or the eigenfunctions of the problem are known when no disturber is present, these can be used to provide truncation boundary conditions. In some cases, it may even be advantageous to use the known Green function of the problem to provide truncation boundary conditions while close to the disturber the problem is solved numerically.

3. Numerical Methods

In this chapter we present some numerical approximations of the potential and primitive formulations in Eulerian variables of a sample problem. We also briefly describe similar numerical simulations of the Lagrangian formulations. We have already mentioned that the numerical methods described here are mainly for the purpose of illustration.

The sample problem selected is the two-dimensional motion of fluid in a partially-filled rectangular container. The motion takes place in the x, y plane and is initiated, say, by displacing the free surface from its equilibrium position.

Consider first the potential problem in Eulerian variables. Probably the best known numerical approximation is the finite difference method (cf. Forsythe and Wasow, 1960). In this method the flow field is overlaid by a regular grid as shown in Figure 1. The spatial discretization is supposed, here, to be uniform with spacing h and time is discretized with spacing Δt. Spatial and temporal discretization need not be uniform but these are assumed to be uniform here for simplicity. The approximate velocity potential is sought at each node of the grid. Each node of the grid is denoted by its coordinates (x_i, y_j), the kth time step is $t_k = k\Delta t$ and the points at which the free surface is cut by vertical grid lines are denoted by η_i. Then the discrete values of Φ and η are defined by

$$\Phi_{ij}^k \equiv \Phi(x_i, y_j, t_k)$$

$$\eta_i^k \equiv \eta(x_i, t_k)$$

Henceforth Φ_{ij}^k and η_i^k also will denote the approximate values of Φ and η obtained from the finite difference problem.

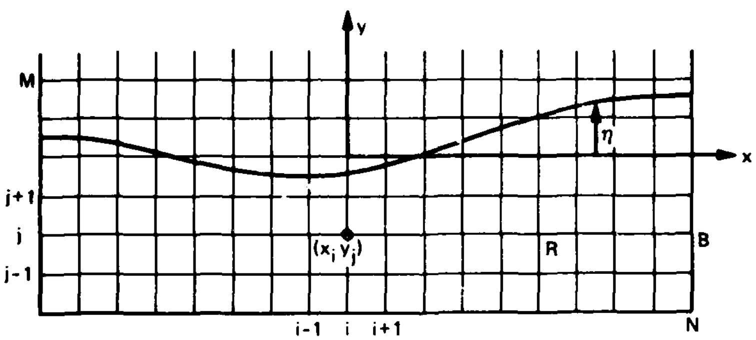

Figure 1 – Finite Difference Grid for the Eulerian Potential Problem

Both the Eulerian and Lagrangian formulations of the sample flow problem consist of two parts; the part governing the time evolution of the flow and the second part relating to the kinematical constraint on the entire flow which must at all times be satisfied. The idea behind all numerical methods is to use the evolution part of the problem to extrapolate forward in time the values of certain variables from the initial conditions and then to determine the rest of the dependent variables in such a way that the kinematical constraint is satisfied in the entire field.

In the Eulerian potential problem, time evolution is governed by the free-surface condition whereas the interior kinematical constraint (incompressibility and irrotationality) is enforced by satisfaction of Laplace's equation. Thus, in a finite difference approximation, using the grid described above, one can approximate first and second derivatives on the uniform part of the grid by central difference formulae (cf. Forsythe and Wasow, 1960). One obtains in this way the five-point differencing approximation

$$4\,\Phi^k_{ij} - \Phi^k_{i+1,j} - \Phi^k_{i-1,j} - \Phi^k_{i,j+1} - \Phi^k_{i,j-1} = 0 \tag{3.1}$$

for $\nabla^2\Phi = 0$ at interior nodes surrounded by equal length grid segments. Next to the free surface at nodes surrounded by unequal length grid segments one obtains the more general five-point differencing approximation

$$\Phi^k_{ij} - a^k_{ij}\,\Phi^k_{i+1,j} - b^k_{ij}\,\Phi^k_{i-1,j} - c^k_{ij}\,\Phi^k_{i,j+1} - d^k_{ij}\,\Phi^k_{i,j-1} = 0 \tag{3.2}$$

where the coefficients a^k_{ij}, b^k_{ij}, c^k_{ij}, d^k_{ij} depend on the lengths of the grid segments surrounding node ij. Since these lengths depend on the instantaneous location of the free surface, the coefficients depend on time and hence the superscript k. On a stationary inpenetrable straight boundary such as B, one can approximate the boundary condition $\left.\frac{\partial\Phi}{\partial x}\right|_{x\epsilon B} = 0$ by a central difference formula such as

$$\left.\frac{\partial\Phi}{\partial x}\right|_{N,j} \approx \frac{\Phi^k_{N+1,j} - \Phi^k_{N-1,j}}{2h} \tag{3.3}$$

The undefined value of $\Phi^k_{N+1,j}$ which lies outside the domain is eliminated by combining (3.3) with (3.1) evaluated at the point i = N,j. This yields the boundary equation at i = N,j

$$\Phi^k_{N,j} - \frac{1}{4}\left(2\Phi^k_{N-1,j} + \Phi^k_{N,j+1} + \Phi^k_{N,j-1}\right) = 0 \tag{3.4}$$

Similar equations can be derived for the other rigid boundaries.

The free surface equations (2.6 a, b) are used to advance the solution in time by approximating the time derivatives by the simple linear formulae

$$\left(\frac{\partial\Phi}{\partial t}\right)_i \approx \frac{\Phi^{k+1}_i - \Phi^k_i}{\Delta t} \tag{3.5a}$$

$$\left(\frac{\partial\eta}{\partial t}\right)_i \approx \frac{\eta^{k+1}_i - \eta^k_i}{\Delta t} \tag{3.5b}$$

where the single subscript i is used to denote a quantity defined on the free surface η. The approximation (3.5) can be considered to hold for any value of $t\epsilon\,[t_k, t_{k+1}]$. Thus, the free-surface equations (2.6) are approximated by

$$\Phi_i^{k+1} = \Phi_i^k + \Delta t \left(- \frac{1}{2} \vec{V} \cdot \vec{V} - g\eta - \frac{p_a}{\rho} \right)_i^{k,k+1} \tag{3.6a}$$

$$\eta_i^{k+1} = \eta_i^k + \Delta t \left(- \vec{V} \cdot \nabla(\eta - y) \right)_i^{k,k+1} \tag{3.6b}$$

The double superscript notation in (3.6) denotes that the quantity in parenthesis may be evaluated at any value of $t \epsilon [t_k, t_{k+1}]$ (or may even be certain averages of the quantity for various values of $t \leqslant t_{k+1}$). The two most elementary, and most widely used, approximations of the terms in parenthesis in (3.6), which also illustrate the two basic types of numerical integration methods of differential equations, are as follows: The explicit method in which the evaluation of the terms in parenthesis in (3.6) is made at $t = t_k$, and the fully implicit method in which these terms are evaluated at $t = t_{k+1}$. We note that evaluation of the spatial derivatives of Φ and η required in (3.6) is done by numerical finite differences. We do not dwell on this item, but only note that these approximations can be made in a variety of ways (cf. Forsythe and Wasow, 1960). It must, however, be recognized that this approximation can be crucial to the success of the entire numerical simulation and we do not dismiss this item lightly.

The relative advantages and disadvantages of explicit versus implicit time integration methods are as follows:

Explicit	Implicit
1) Requires simple evaluation of functions at each time step.	1) Requires solution of a system of algebraic equations at each time step.
2) Numerically stable only for severely restricted time steps Δt (in above problem $\Delta t < Kh$).	2) For linear problems there is no restriction on Δt for stability. For nonlinear problems, necessity of iterative solution of algebraic equations imposes a Δt restriction for convergence.

As yet no numerical or theoretical evidence has been presented to establish a clear-cut advantage of explicit over implicit methods or vice versa in nonlinear problems. In fact, the explicit method is used most often for such problems merely because of simplicity. In linear problems, there is a clear theoretical and practical advantage in using the implicit method. We will see later, when considering various specific implementations, that maintaining the stability of the numerical integration of the free-surface equations is still a major problem.

The numerical schemes for advancing the solution one time step, from t_k to t_{k+1}, follows:

(1) Explicit method: (3.6a) is used to obtain Φ_i^{k+1}; (3.1), (3.2) and (3.4) are used to obtain Φ_{ij}^{k+1} throughout the field and then (3.6b) is used to advance the free surface to η_i^{k+1}.

(2) Implicit method: Equations (3.6) together with (3.1), (3.2) and (3.4) are a coupled system of nonlinear algebraic equations which must be solved by iteration. One possible, and popular, method is the predictor-corrector method in which tentative values of Φ_{ij}^{k+1}, Φ_i^{k+1} and η_i^{k+1} are obtained by the explicit method. These are used in the terms in parenthesis in (3.6) to obtain new tentative values of Φ_{ij}^{k+1} and η_i^{k+1}. Iteration of this procedure some desired number of times completes one implicit integration step.

Before turning to brief descriptions of other numerical methods, we note that there are two main characteristic numerical errors (besides those of spatial resolution) inherent in each numerical method. These errors are directly related to the truncation errors of the numerical approximation of various derivatives and how these truncation errors combine when the numerical approximation formulas are combined according to the governing equations. These errors are called numerical viscosity errors and dispersion errors. Numerical viscosity denotes an inadvertant artificial damping of the motion with time (say, for instance, a loss of energy in a system that is supposed to be conservative). Dispersion errors pertain to the propagation of various wave modes at the wrong wave speed. As mentioned above, these errors are attributed to the combination of spatial and temporal numerical approximations made. The cause of these characteristic errors can be analyzed for many approximation methods (see, for instance, Roache, 1973). Sometimes, using a numerical method that has a certain amount of numerical viscosity is useful to overcome a tendency towards instability of the time integration.

An alternative class of numerical methods is generally known as spectral methods. These are based on the idea of the expansion of the dependent variables in a suitable complete set of functions. The unknown coefficients of this expansion are determined by satisfying a certain functional (for instance, minimization of the total mechanical energy of the flow) that is equivalent in a certain sense to solving the partial differential equations. The two most prominant methods in this category are the finite element method and Galerkin's method. The finite element method can be considered to be a form of Galerkin's method which is based on a special class of expansion functions. A very brief description of a Galerkin's method follows:

Consider our sample problem and the following sets of functions.

$$S_1 = \left\{ f_n(x,y) \;\middle|\; f_n \epsilon C^2_{x,y} \text{ in R, are complete and satisfy condition (2.5) on } \partial R \right\}$$

$$S_2 = \left\{ g_m(x) \;\middle|\; g_m \epsilon C^1_x \text{ on } \mathcal{J} \text{ and are complete} \right\}$$

$$T_1 = \left\{ h_n(x,y) \;\middle|\; h_n \text{ are linearly independent} \right\}$$

$$T_2 = \left\{ e_m(x) \;\middle|\; e_m \text{ are linearly independent} \right\}$$

In the Galerkin method, one approximates Φ and η by

$$\Phi(x,y,t) = \sum_{n=1}^{N} a_n(t) f_n(x,y) \tag{3.7a}$$

$$\eta(x,t) = \sum_{m=1}^{M} b_m(t) g_m(x) \tag{3.7b}$$

and equations for $\{a_n\}$ and $\{b_m\}$ are obtained by demanding that

$$\iint_R h_i \, \nabla^2 \Phi = 0 \tag{3.8a}$$

$$\int_{\mathcal{J}} e_j \mathcal{B}(\Phi, \eta) = 0 \tag{3.8b}$$

for $i = 1, \ldots, I$ and $j = 1, \ldots, J$ such that $I + J = N$ and where $\mathcal{B}$ denotes the dynamic free-surface condition (2.6a) on $\mathcal{J}$. One also demands that

$$\int_{\mathcal{J}} \left(\frac{\partial \eta}{\partial t} + V \cdot \nabla(\eta - y) \right) e_j = 0 \tag{3.9}$$

for $j = 1, \ldots, M$.

Condition (3.8) yields a coupled system of algebraic and nonlinear ordinary differential equations for the coefficients $\{a_n(t)\}$ and (3.9) results in a set of nonlinear ordinary differential equations for the coefficients $\{b_m\}$. These equations are very complex and must be integrated numerically.

For the sample problem, a very convenient choice for S_1 is the set

$$\left\{ f_n(x,y) = \cosh \frac{(2n+1)(y+D)\pi}{2L} \sin \frac{(2n+1)\pi x}{2L} \right\} \tag{3.10}$$

where 2L is the width of the container and D is the depth of undisturbed fluid in the container. This set of functions satisfies the Laplace equation in R and the boundary conditions on ∂R so that (3.8) reduces to the line integral over $\mathcal{J}$ and involves only the

dynamic free surface condition evaluated on $\mathcal{J}$. The resulting nonlinear ordinary differential equations involve the coefficients $\{b_n\}$ as well as $\{a_n\}$ because the expansion (3.7b) must be substituted for y in (3.10).

Note that using the set (3.10) for S_1 and appropriate trigonometric functions for S_2 and T_2 in the linearized problem leads to the exact solution for $N \to \infty$.

The major disadvantage of this type of Galerkin method is its practical restriction to simple boundary shapes (unless a finite element method is used). A second major problem encountered with implementation of Galerkin's method, is maintaining numerical stability in the time integration.

We leave aside description of the finite element method since some of its ideas are contained in the above discussion and details are readily available (see for instance, Strang and Fix, 1973) and extensively expounded in some later papers of this conference.

The Eulerian primitive formulation can be simulated numerically in several ways similar to that for the potential formulation. We briefly describe a certain finite difference approximation of the primitive equations. This approximation is the basis of the very extensively used and successful MAC (Marker And Cell) method (see, for instance, Harlow and Amsden, 1971).

In this method a staggered finite difference mesh as shown in Figure 2 is used.

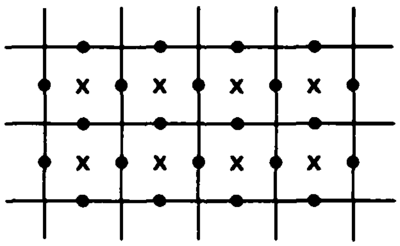

Figure 2 — Staggered Finite Difference Mesh of the MAC Method

The pressure p is evaluated at the points denoted by crosses and labeled by integers i, j ($p(x_i, y_j) = p_{ij}$) and the velocity $\overline{V}$ is evaluated at the dots which are labeled as i + 1/2, j on the vertical segments and i, j + 1/2 on the horizontal segments. The horizontal component of $\overline{V}$, u, is defined only at the i + 1/2, j points and the vertical component v, only at the i, j + 1/2 points. A complete derivation and tabulation of the finite difference formulae that approximate the momentum and continuity equations (2.1 a, b) can be found in Harlow and Amsden (1971). It suffices to state here that spatial derivatives are approximated by central differences throughout giving $O(h^2)$ accuracy. Whenever a finite difference approximation requires the value of a variable where it is not defined in the discrete problem, then this

value is obtained by averaging the two nearest values. For instance

$$u_{ij} \equiv \frac{1}{2}(u_{i-1/2,j} + u_{i+1/2,j})$$

This approximation preserves the $O(h^2)$ accuracy of the finite differencing.

The basic MAC procedure is as follows: First-order differencing of the time derivatives in the momentum equations (2.1a) (similar to that of (3.5)) is used for the explicit advancement in time. This approximation results in the equations

$$u^{k+1}_{i+1/2,j} = u^k_{i+1/2,j} + \Delta t\left(-\vec{V}\cdot\nabla\vec{V} - \nabla\left(\frac{p}{\rho} - G\right)\right)^k_{i+1/2,j}$$
$$v^{k+1}_{i,j+1/2} = v^k_{i,j+1/2} + \Delta t\left(-\vec{V}\cdot\nabla\vec{V} - \nabla\left(\frac{p}{\rho} - G\right)\right)^k_{i,j+1/2} \qquad (3.11\ a, b)$$

Continuity is maintained by solving the Poisson equation

$$\nabla^2 p = -\nabla\cdot(\vec{V}\cdot\nabla\vec{V}) \qquad (3.12)$$

for pressure p by using the standard five-point difference formula (cf. Forsythe and Wasow, 1960).

$$p^k_{ij} - \frac{1}{4}(p^k_{i+1,j} + p^k_{i-1,j} + p^k_{i,j+1} + p^k_{i,j-1}) = -(\nabla\cdot(\vec{V}\cdot\nabla\vec{V}))^k_{ij} \qquad (3.13)$$

(We note that (3.13) requires some correction terms in actual numerical calculations in order to accurately maintain zero flow divergence.) The boundary conditions are not elaborated here (but see Harlow and Amsden, 1971) except to note that the free surface is advanced in time using the Lagrangian kinematic free-surface condition (2.3b) in an explicit manner similar to (3.11).

Finite difference approximations of the Lagrangian formulations follow closely the spirit of such approximations of the Eulerian formulations. In the Lagrangian formulations, a rectangular grid divides the region R in the independent variable space, (a, b, c). The dependent variables $\vec{R}$ and $\vec{V}$ are defined at each nodal point of this grid. This results in the flow field being divided, at each instant, into an irregular grid in the Eulerian coordinates. For example at time step k, the coordinates R_{ij} are given by

$$\vec{R}_{ij} = (X(a_i, b_j, t_k), Y(a_i, b_j, t_k))$$
$$= (X^k_{ij}, Y^k_{ij})$$

so that the square cell (a_i, b_j), (a_{i+1}, b_j), (a_{i+1}, b_{j+1}), (a_i, b_{j+1}) in the (a, b) reference plane has the physical coordinates shown in Figure 3.

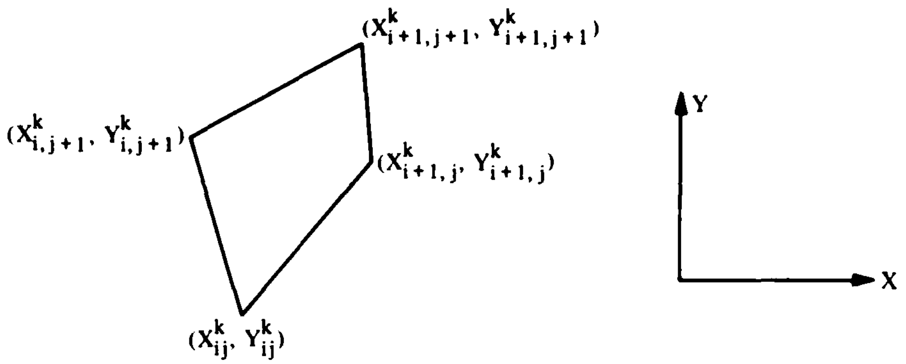

Figure 3 – Lagrangian Finite Difference Cell

The numerical simulation follows the recipe:

(i) The coordinates are advanced implicitly or explicitly using first-order time differencing of

$$\frac{\partial \vec{R}}{\partial t} = \vec{V}$$

(ii) The velocities are updated by either (a) maintaining cell area (continuity) and cell circulation (irrotationality) using finite difference approximations of these quantities on the Lagrangian cell of Figure 3, or by (b) updating the velocity according to the Lagrangian momentum equation, approximating the time derivative by first-order finite difference formulae, and obtaining the pressure p by maintaining cell continuity similar to the MAC method.

An example implementing the finite difference approximation of the Lagrangian potential problem for the two-dimensional flow in a container is given by Brennen and Whitney (1970).

4. Examples of Numerical Simulation of Free-Surface Problems

In this chapter we discuss some problems which have been numerically simulated by some form of one of the methods discussed in Chapter 3. We consider first solutions of problems of water sloshing in a container. Although the solutions of such problems have direct applications, our main interest is in the testing of the numerical methods in problems involving either gentle, though nonlinear, free-surface motions or violent motions that ultimately lead to disintegration of the free surface.

Our second category of problems, whose numerical simulation is considered, is that of free waves. These are of interest because one always expects that "free waves" are present far from a disturber and form a part of our main problem of moving bodies near or in the

free surface. Thus, accurate solutions of free-wave problems can aid in checking solutions of body-wave problems. Free-wave problems are also of interest in other applications and are of great concern in tank testing where waves are generated at one end by a wavemaker and propogate to the other end of the tank.

The last two categories, oscillating bodies and uniform and accelerated motion of bodies along the free surface, need little explanation because these contain precisely those problems whose numerical simulation is the subject of this conference.

Each of these groups of problems is discussed in one of the following sections. We begin each section with a table of the relevant papers and listing of the problem simulated and the numerical method used.

A. Sloshing in Containers

Table 1 contains the relevant references which report on numerical simulation of two nonlinear sloshing problems. The first is the Taylor instability problem in which a container with an open top and partly filled with water is suddenly accelerated downwards with an acceleration exceeding that of gravity. The other problem is that in which the water in a stationary upright container is given some initial motion or displacement away from equilibrium and water subsequently sloshes around in the container.

TABLE 1
Sloshing

Authors	Problems	Method
Moore and Perko (1965)	Axisymmetric Sloshing and Taylor Instability	Galerkin
Perko (1965)	Nonaxisymmetric Sloshing and Taylor Instability	Galerkin
Easton and Catton (1972)	Axisymmetric Sloshing	Galerkin
Harlow and Welch (1966)	2D Taylor Instability	MAC
Hirt, Cook and Butler (1970)	2D Taylor Instability	MAC - Lagrangian Mesh

The first three papers listed in Table 1 describe the use of a Galerkin method similar to the one described in Chapter 3. The expansion functions used are the axisymmetric analogues of the set (3.10) which satisfy Laplace's equation in the fluid domain and the container boundary conditions. The time integration in the first two papers is essentially the fully implicit method that we described in Chapter 3, applied in a predictor-corrector fashion.

The main purpose of simulating the Taylor problem is that it poses a severe test of a numerical method. In the Taylor problem, the fluid leaves the container in the form of a spike along one wall (the container width is chosen to be half the characteristic wave length of the critical mode that is initially excited). A void, or bubble, sinks into the container on the other side. Taylor (1950) studied the initial fluid motion by a linear theory and also experimentally. The late time motion of the bubble and spike has also been studied, using various approximations, by others. Comparison of the numerical results of Moore and Perko (1965), Perko (1969) and Harlow and Welch (1966) with other studies shows good agreement over the relevant range of the parameters. This gives confidence in the reliability of the numerical simulations and gives some indication of their capability in simulating rather large free-surface motions.

Figure 4 shows the free surface contours at various times in the Taylor problem. The sequence of pictures at the left is from Harlow and Welch (1966) (starting at upper left and ending at lower right). The figure on the right is from Moore and Perko (1965). The curves represent the free surface contours at various times beginning with the small segment in the lower right corner. Although the configuration of Harlow and Welch is planar, whereas that of Moore and Perko is axisymmetric, one might expect the spike shape to be similar. Note that the spike is indeed very similar at certain advanced time steps. It seems to have a fairly sharp tip and then bulge outward and narrow down before spreading to the downward traveling void. This agreement in detail between entirely different types of numerical simulations gives some confidence in the methods. The very late time behavior of the spike in the results of Moore and Perko (1965) shows that the spike sharpens and then becomes looped (breaks ?). This is very similar to the behavior of waves running up a sloping beach as calculated by a second-order perturbation method and shown in Stoker (1957, p. 366).

The aim of the work of Easton and Catton (1972) is the testing of several numerical time-integration methods. All the methods tested are similar to the explicit and implicit methods described in Chapter 3. One of these methods is, in fact, the explicit and implicit method used in predictor-corrector form as described in Chapter 3. It was found by Easton and Catton that all the methods that they considered, except the predictor-corrector method of Chapter 3, are at least slightly unstable. The exceptional method is stable, but has considerable numerical viscosity.

Hirt, Cooke and Butler (1970) combine the Eulerian and Lagrangian descriptions in a method that uses Lagrangian coordinates for tracking the fluid motion, but solves the Eulerian momentum equations on this grid in a manner similar to MAC. This has the advantage of providing an easy description of the free surface but also the disadvantage

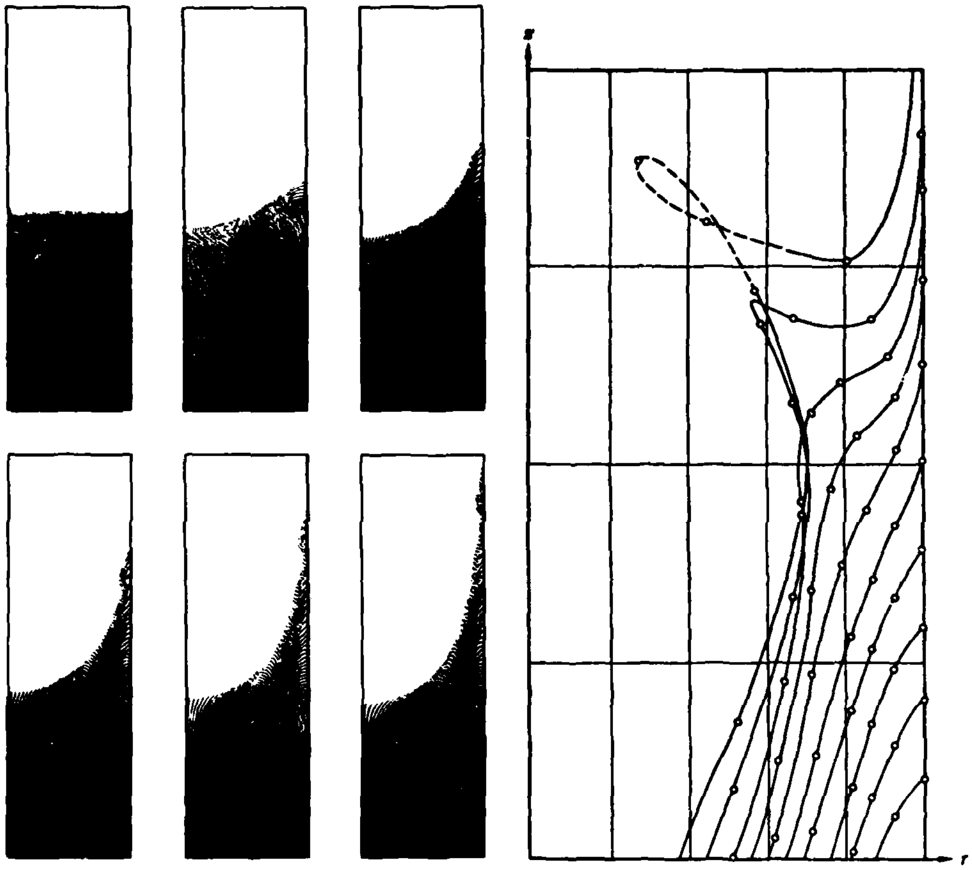

2D Taylor Instability at various times

Axisymmetric Taylor instability at various times

Figure 4 – Numerical Simulation of Taylor Instability

of a grossly distorted finite-difference mesh when the fluid is highly strained, as in the Taylor problem, which causes severe loss in accuracy of the finite difference equations.

One finds in these works that both the Galerkin and MAC methods do a good job of simulating violent motions of confined pieces of fluid. For gentle motions, say longtime periodic simulations, both the Galerkin and MAC methods exhibit either numerical instability of the integration of the free-surface equations or severe loss of accuracy in predicting the free surface profile. The original MAC method utilizes a crude approximation at the free surface. The pseudo-Lagrangian method of Hirt, Cooke and Butler (1970) overcomes to some extent the inaccuracy problem at the free surface.

B. Free Waves

Only two-dimensional free waves are considered; these are progressive and solitary waves. Table 2 gives the relevant references in which numerical solutions of nonlinear free wave problems are obtained.

TABLE 2
Free Waves

Authors	Problems	Method
Thomas (1968, 1975)	2D Progressive Waves	Numerical Solution of Nonlinear Integral Equation
Schwartz (1974)	2D Progressive Waves	High Order Perturbation Series
Southwell and Vaisey (1948)	2D Progressive Waves	Finite Difference and Free-Surface Guessing
Chan (1974)	2D Solitary Waves	Inverse Potential Problem and Finite Difference
Street, Chan and Fromm (1970)	2D Time Harmonic Pressure on Free Surface and Solitary Waves	SUMMAC Initial Value Problem
Brennen and Whitney (1970)	2D Wave Generated by Tank Boundary Motion	Lagrangian Finite Difference Initial Value Problem
Chan (1975)	2D Waves in Tank	Lagrangian Finite Difference Initial Value Problem
Multer (1973)	2D Waves in Tank Generated by Wavemaker	Galerkin's Method

The work of Thomas (1968, 1975) and Schwartz (1974) is not in the category of numerical solution we are considering here, but we include them because a relatively complete characterization of the relationship between the wave height (trough-to-peak) A, wave length λ, and phase velocity c for progressive waves is given. This is very useful for checking other numerical simulations. Figure 5, taken from Thomas (1975) gives this relationship.

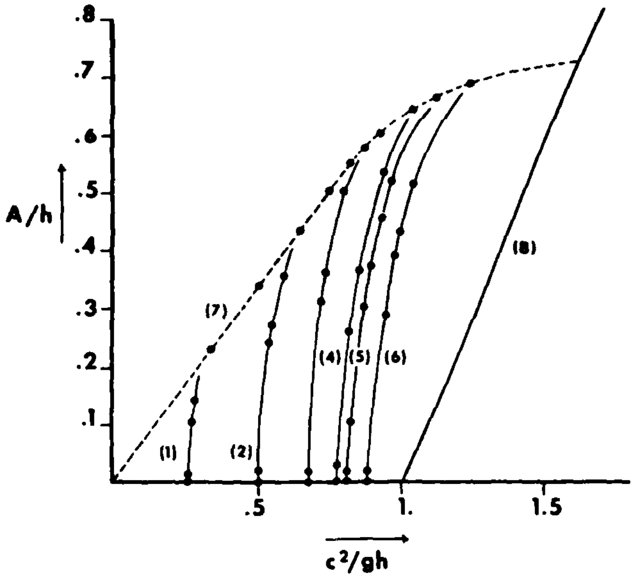

Figure 5 – The Graphs of A/h Versus c^2/gh for Six Different Constant Values of h/λ and of the Limiting Case of A/h Versus c^2/gh for the Highest Wave

In this figure h is the static equilibrium depth of the stream and g is gravity. Curves (1)-(6) are for h/λ = 0.6, 0.3, 0.2, 0.15, 0.13655, and 0.10632, respectively. Curve (7) is the envelope of maximum obtainable values of A/h and (8) is a fourth-order approximation of this relationship for the solitary wave. A direct numerical solution of the solitary wave problem is given by Chan (1974) (the fourth item in Table 2). Chan (1974) gives the "exact" graph of A/h versus c^2/gh for the solitary wave.

The work of Southwell and Vaisey (1948), though inconclusive, represents the first direct attempt to solve wave problems by a finite difference method. Their method of systematically modifying free surface shape until the dynamic free-surface condition is satisfied at all free surface nodes has been recast for high-speed computer calculations and used with success by von Kerczek and Salvesen (1974) and Salvesen and von Kerczek (1975).

Street, Chan and Fromm (1970) (see also Chan and Street, 1970) present a modified MAC method (SUMMAC) which implements an accurate interpolation scheme at the free surface so that wave motion can be accurately simulated (a deficiency of the original MAC method). The power of the SUMMAC method to simulate free surface wave motion is illustrated in Figure 6, taken from Chan and Street (1970). Chan and Street simulate the propogation of a solitary wave, of height H_0 on water of depth d, without the wave present,

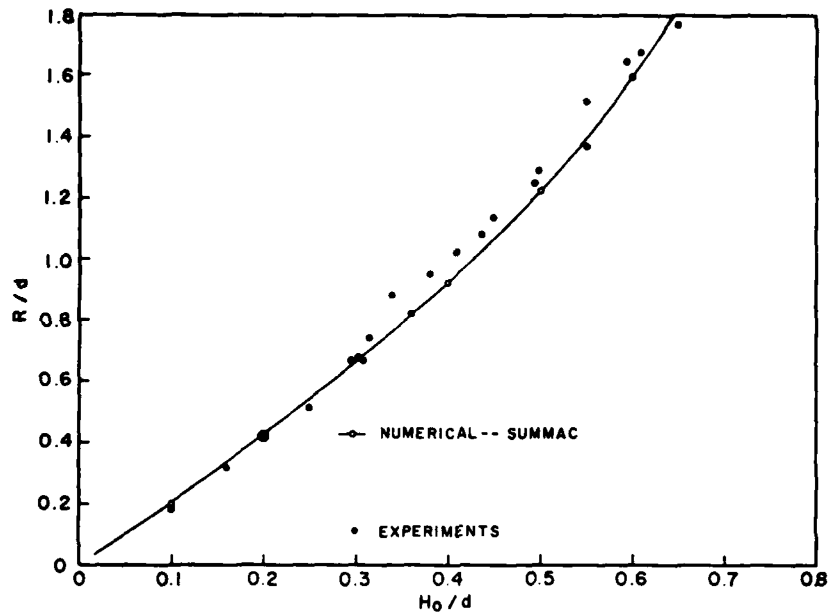

(a)

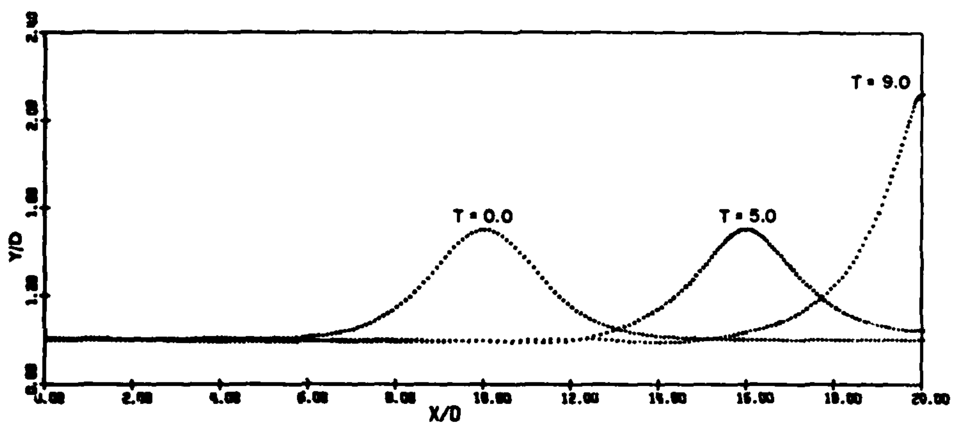

(b)

Figure 6 – Runup and Reflection of a Solitary Wave from a Vertical Wall

against a vertical wall and its reflection away from it. Figure (6a) shows the calculated ratio of R/d, where R is the maximum height the wave attains when it runs up the wall, versus H_0/d compared to experimental values. A time history of wave runup and reflection is shown in Figure (6b). Chan and Street claim that at some later time, the wave regains the position and "exactly" the same shape it had at T = 0. This is a very fine test of the numerical method in that the process of running up the wall and reflection from it involves large fluid and free surface distortions.

Brennen and Whitney (1970) and Chan (1975) simulate, by finite differences, the Lagrangian potential problem. The methods are similar, with Chan's (1975) method incorporating several refinements to overcome difficulties experienced by Brennen and Whitney (1970). The main problem of Lagrangian finite difference methods on a rectangular grid is that the physical grid (Figure 3) undergoes severe distortion in regions of large strain of the fluid. This causes the finite-difference approximations of the formulas for the preservation of cell area and circulation, which are written in terms of the physical cells such as in Figure 3, to lose accuracy. Chan (1975) overcomes this difficulty by a procedure of redefining cells every so often in the course of a calculation. The Lagrangian methods seem suited for simulating free-surface flows in confined simply-connected domains, but are more complex for problems of flow past obstacles.

Multer (1973) considers the problem of the wavemaker at one end of a long tank. His Galerkin method is very similar to the one described in Chapter 3 (and to that of Moore and Perko, 1965). He compares his results with experiment and shows good agreement between his computed and experimental waves. As mentioned previously, these Galerkin methods do not seem to be suitable for problems with complicated boundaries.

The methods of Chan, Street and Fromm (1970) and of Chan (1975) are of particular interest here since they are very general and hold promise for other applications. The results produced by these methods for the problems tested seem very accurate and reliable. We mention here that the MAC method has been used for a great variety of transient free surface flows. Many examples are given by Harlow and Amsden (1971). Of particular interest here is the runup and breaking of a wave on a sloping beach which is shown in Figure 7 taken from this reference.

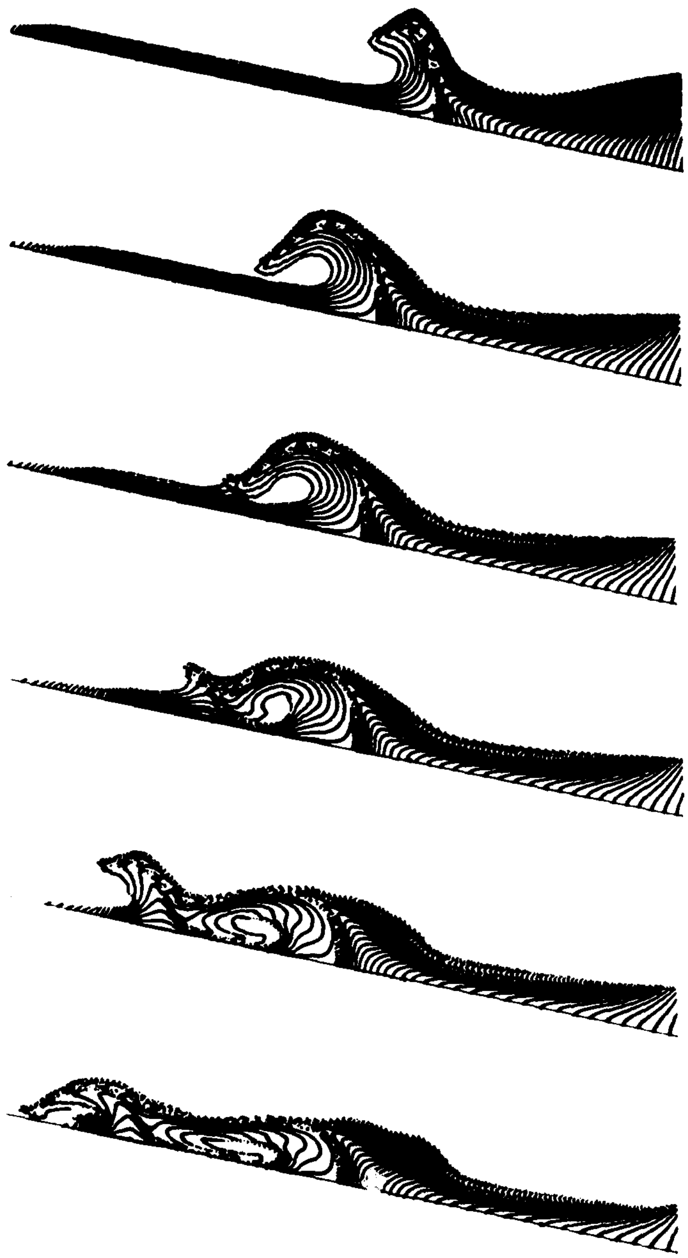

Figure 7 – MAC Calculation of a Wave Breaking
on a Sloping Beach

C. Oscillating Bodies

The problem of the flow due to an oscillating body near a free surface is central to the understanding of ship motion in a seaway. Much is known about the linearized version of this problem (cf. Wehausen, 1971), but little is known about the exact nonlinear problem. When the water is infinitely deep or has a horizontal bottom, the Green function satisfying the linear free-surface condition and the proper radiation conditions is known. Thus, these problems admit convenient integral-equation formulations. The role of direct numerical methods for solving the partial differential equation is mainly in problems where the Green function is not known, i.e., the nonlinear problem or linear problems with a locally non-horizontal bottom. In two-dimensional problems direct numerical methods may even require less computer time, but this does not seem likely for three-dimensional problems.

There have been few attempts at the direct numerical simulation of oscillating body problems at this time. Table 3 lists these examples. Note that three of the references report only on the linear problem and there is only one attempt of numerical simulation of a nonlinear problem.

TABLE 3
Oscillating Bodies

Authors	Problems	Method
Bai (1975)	2D Linear Diffraction Problem	Finite Element and Radiation Conditions
Chen and Mei (1974)	Quasi-3D, Linear Diffraction Problem	Finite Element and Eigenfunction Expansion
Bai and Yeung (1974)	2 and 3D, Linear Forced Oscillation and Diffraction	Finite Element and Eigenfunction Expansion, and Integral Equation
Chan and Hirt (1974)	2D Linear and Nonlinear Forced Oscillation, IVP	Lagrangian Finite Difference and Finite Difference Potential Problem

Of main interest in the work of Bai (1975), Chen and Mei (1974) and Bai and Yeung (1974) is the method used to truncate the numerical domain. In these problems the radiation conditions and far-field eigenfunctions are known. Bai (1975) and Bai and Yeung (1974) use the radiation conditions at a suitable distance from the disturber to provide conditions on the truncation boundary. Bai and Yeung (1974) also use eigenfunction expansion to match with the interior numerical solution at the truncation boundary. This technique is also used by

Chen and Mei (1974). Matching of the interior numerical solution with an exterior eigenfunction expansion at the truncation boundary is very efficient (computationally) because this matching can be carried out as close to the disturber as the local bottom irregularities allow (the matching must take place in the region where the bottom is horizontal). This method is called a "localized finite element method" by Bai and Yeung (1974).

The diffraction problem treated by Chen and Mei (1974) consists of an island with vertical sides sitting on the horizontal bottom and piercing the free surface. This allows explicit integration of the equations of motion in the vertical direction, leaving only a two-dimensional problem in the horizontal plane.

Bai and Yeung (1974) also present a novel integral equation method which uses simple sources that satisfy no boundary conditions of the problem. These sources are distributed on all the boundaries and result in an integral equation over a much larger surface than the one required if the Kelvin wave-source potential is used, but the kernel of the integral equation is much easier to evaluate. The numerical implementation of this integral equation method compares favorably, in execution time requirements on a computer, with the localized finite element method for the two-dimensional problems considered. Bai and Yeung also use this integral-equation method to solve some three-dimensional problems. It seems that this method may be superior to the finite element (or finite difference) method for three-dimensional problems.

These works indicate that well-formulated two-dimensional linear-theory problems can be solved very accurately and efficiently by the finite-element method and presumably also finite-difference methods. The infinite flow domain can be truncated in the numerical simulation with known analytical information providing truncation boundary conditions. Presumably similar procedures can be applied in some three-dimensional problems. The main difficulty seems to be in computing cost.

Chan and Hirt (1974) consider the initial value problem (I.V.P.) for a cylinder oscillating in a free-surface. They carry out computations using the Lagrangian finite-difference method of Chan (1975) and a method, based on the finite-difference potential problem in Eulerian form as discussed in Chapter 3. Their results are rather meager and show only that the numerical simulations yield results that seem to be correct. A significant finding is that a local steady state is reached very quickly. For example, the vertical force on the heaving cylinder becomes periodic in time within half a period of oscillation after the sudden start. The free-surface motion near the cylinder is periodic in time well within two periods of cylinder oscillation. Thus, using the I.V.P. approach to attain steady-state conditions may, in certain cases, be competitive with numerical simulations of steady-state problems. At present, this seems to be the only mathematically-rigorous way to simulate nonlinear problems.

E. Uniform and Accelerated Motion Near a Free Surface

The problem of the steady motion of a body parallel to and near the free surface is very fundamental and much studied (cf. Wehausen, 1974). Several linear theories of approximation have been developed for water of uniform or infinite depth but none are adequate for describing the flow accurately close to the body and none seem to give more than just a rough estimate of the wave resistance. These linear theories, e.g., thin ship, slender ship, flat ship (cf. Wehausen, 1973) involve not only the linearization of the free-surface conditions but also some kind of simplification of the body boundary condition. The exact nonlinear problem is analytically intractable.

Even with linear free-surface boundary conditions, the problem is so difficult that the body boundary condition is also simplified in order to obtain approximate solutions. This is done for two reasons, the first is, of course, to be able to obtain analytical solutions; the second reason is because, when the body is near the free surface, it must be either thin or slender or flat or geometrically restricted in some way so that it produces only small free-surface disturbances, allowing the free-surface linearization.

The lack of agreement between linear theories and experimental results (see, for instance, Wehausen, 1974, for comparison of wave resistance by thin ship theory and experiment) has prompted the search for different linear theories, higher order theories and possibly the direct numerical solution of the exact nonlinear problem. An example of a different linear theory is one in which the body boundary condition is satisfied exactly but the free-surface conditions are linearized. Such problems are very difficult to solve and direct numerical attacks on them are just now getting underway. One can also develop perturbation methods in which one of the above linear theories is only the first term. However, their evaluation meets with some vexing questions concerning the effects of the front and rear ends of the body and it is an extremely difficult numerical task just as when computing, numerically, solutions of linear theory problems.

We consider here the direct numerical solution of the linear-theory problem, in which the body boundary condition is satisfied exactly, and the exact nonlinear problem. We also consider some unsteady motion problems and, a problem that is solved by a mixture of approximations that yield simpler nonlinear problems which are solved numerically.

One of the first difficulties, in solving steady-flow problems that must be overcome is the problem of truncating the flow field in the numerical approximation. This is more difficult in the steady-flow problem because radiation conditions are either unavailable or insufficient (in a numerical sense). For example, in two-dimensional linear problems all one has as a radiation condition is that the water is undisturbed far upstream. An approach for

linear two-dimensional problems is to use the fact that the asymptotic form of the far downstream wave (i.e., its sinusoidal and has known wavelength) is known. Thus, the numerical solution can be matched to this wave at the downstream truncation boundary. Unfortunately, such a method of closure does not work in three-dimensions because the flow far downstream is not periodic, but a superposition of many wave components in many different directions. A third method of closure of the numerical approximation of the linear problem is to use the complete (known for uniform depth problems) set of eigenfunctions to match the numerical solution with an eigenfunction expansion at the truncation boundary. This method is the one developed in Bai and Yeung (1974) and Chen and Mei (1974) in the context of finite element methods and called the localized finite-element method. It can also be used in connection with the finite-difference method. Another alternative is to combine the method of source distribution on the body using the Green function which satisfies the linear free surface condition with a numerical method for solving the field equations. The source distribution on the body is used only for providing the closure condition for the numerical problem. The strength of the source distribution on the body is proportional to the normal derivative of the (perturbation) potential there and provides, through Green's theorem, a relationship between the values of the potential at the truncation boundary and the body. This method avoids the difficult calculation of the source potential (i.e., the Green function of the problem) close to the body by placing the numerical closure boundary just far enough away where the source potential is easy to calculate.

Thus we see that there are several possible ways to overcome the domain truncation problem of the numerical approximation of the steady-flow linear theory problem. Few of these have been investigated by numerical experimentation so that no definitive statements on their effectiveness can be made. No mathematically-rigorous method to close the numerical truncation of the infinite field of the nonlinear problem is known.

Table 4 lists the examples of numerical simulation of problems in this category.

Oddly, the first one of these steady flow problems to be solved numerically is an exact nonlinear problem. Southwell and Vaisey (1948) considered the two-dimensional problem of an infinitely-wide planing flat plate. In this problem, one must be specially careful about uniqueness. Several possibilities occur depending on the far upstream and far downstream mean depths and mean velocities assumed. One must carefully specify enough conditions at upstream and downstream boundaries to either allow or not allow the formation of waves. Southwell and Vaisey (1948) specify only the mass flux and depth far upstream and obtain contradictory results from two sets of computations.

TABLE 4
Uniform and Accelerated Motion Near a Free Surface

Authors	Problems	Method
Southwell and Vaisey (1948)	2D Steady Planing Plate	Finite Difference Free-Surface Guessing
von Kerczek and Salvesen (1974-75)	2D Steady Submerged Vortex and Free-Surface Pressure Distribution	Finite-Difference Free-Surface Guessing and Perturbation Theory
Tu (1971)	2D Steady, Linear Submerged Vortex	Finite Element
Chapman (1975)	3D Steady Surface-Piercing Strut	Approximate Theory and 2D Finite Difference
Haussling and Van Eseltine (1974)	2D Free-Surface Pressure Distribution, Linear and Nonlinear IVP	Galerkin and Finite Difference
Haussling and Van Eseltine (1975)	3D Free-Surface Pressure Distribution, Linear IVP	Galerkin
Nichols and Hirt (1973)	3D Nonlinear Obstruction IVP	MAC

Southwell and Vaisey's (1948) method is an iteration procedure which starts with an assumed free-surface shape, solves Laplace's equation in the resulting domain by finite differences and adjusts the free surface based on the error in the dynamic free-surface condition. They also used this method to investigate the problem of free waves on a finite-depth channel. Von Kerczek and Salvesen (1974) describe a highly refined computerized method based on the same ideas. They use this method to study the wave resistance of a two-dimensional obstruction in a uniform flow.

One of the major conceptual problems in the work of von Kerczek and Salvesen (1974) is the truncation of the domain far downstream of the obstruction. As mentioned above, no mathematically-rigorous scheme is known for truncating the domain and expecting the resulting solutions to be accurate approximations of the exact ones. The method used is based on the ad hoc idea that all one really seems to need in a steady flow is a condition that at least preserves mass flux out of the region. Whatever disturbance exists at the downstream boundary it has only limited upstream influence so as long as it is applied far enough downstream; the numerical solution near the disturber ought to be an accurate approximation (within the inherent accuracy of the finite-difference grid size) of the exact one. We will discuss the Salvesen, von Kerczek work in some detail because it provides the only numerical

solutions to the exact nonlinear steady free-surface/body problem.

Preliminary results reported by von Kerczek and Salvesen (1974) for moderate strength obstructions (a submerged vortex and a free-surface pressure distribution) are compared with analytical solutions of the linearized and second-order theory problems. Agreement is fairly good in the range considered. In subsequent work by Salvesen and von Kerczek (1975), the disturber is a submerged vortex and numerical solutions are compared in detail with third-order perturbation theory solutions. Certain nonlinear effects stand out for larger values of circulation. (In this investigation the stream depth, D, submergence depth of the vortex, b, and free-stream velocity, U, are fixed while the circulation, τ, is varied to obtain variations in downstream wave height.) The third-order theory, for deep water, predicts a shortening of wave lengths with increasing wave height. This nonlinear effect is obtained by the numerical solution as shown in Figure 8. The numerical results for wave length are larger than the third-order perturbation theory because the former are for finite depth whereas the latter is for infinite depth. The depth Froude number of the numerical results is 0.572 which is a value barely on the verge of what can be considered very deep water. It is shown in Salvesen and von Kerczek (1975) that for shallower depth cases, the wavelength increases with vortex circulation for fixed Froude number. A comparison of the wave resistance and free-surface elevations with those predicted by first, second and third-order theory reveals excellent agreement with third order theory for positive circulation of strength large enough to produce waves that are very close to the steepest ones obtained before breaking in certain experiments. For negative circulation, the comparison with third-order theory reveals rather poor agreement at larger values of circulation. Figure 9 shows the wave resistance comparison.

The waves behind a submerged vortex in a shallow-stream are shown in Figure 10 (the flow is from right to left and the depth Froude number is 0.69). Note that the wavelength increases with increasing circulation. The inset table in Figure 10 gives the height of the wave peaks, η_{max}, the height of the troughs, η_{min}, the mean depth of the fluid beneath the wave, D_{mean}, and the phase velocity, c, of the wave which is not the same as the speed U far upstream. Interpolating the wave length λ, based on c and a depth d defined by $cd \equiv UD$ using Thomas' (1975) Figure 5 given in part B of this chapter, yields results in good agreement with the values of λ given in the table.

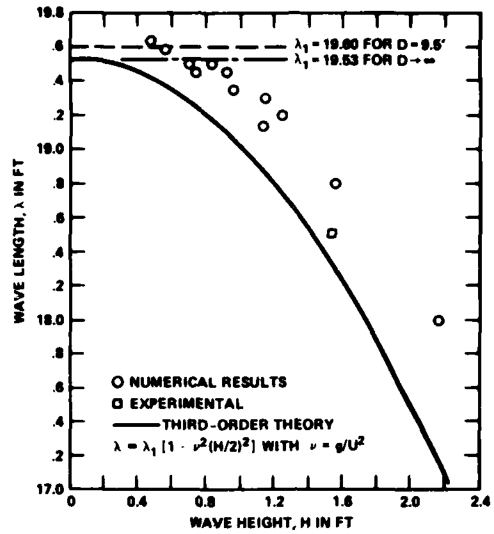

Figure 8 – The Nonlinear Relationship Between Wave Length and Wave Height Far Downstream of the Disturbance

(The depth is 9.5 ft for the numerical, infinite for the analytical, and several times the wave length for the experimental results.)

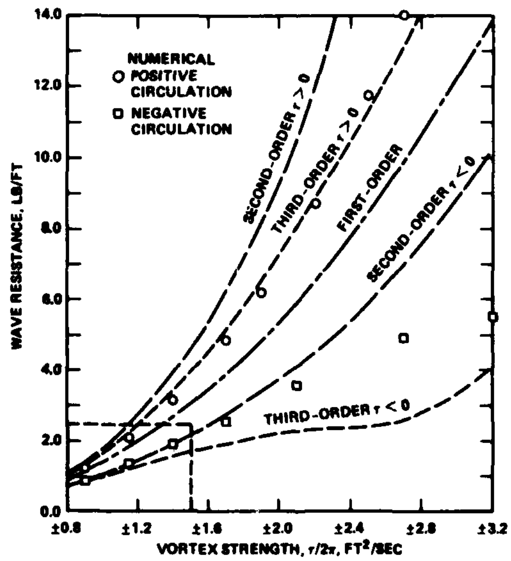

Figure 9

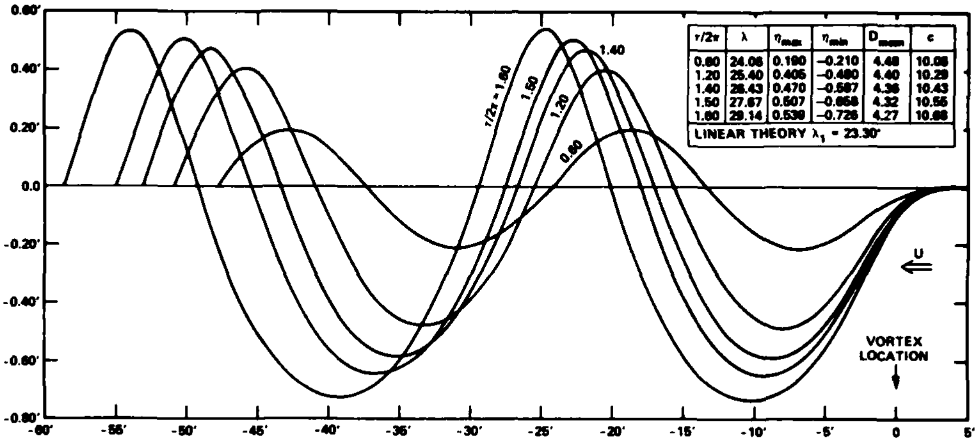

Figure 10 – Wave Elevations Computed by Numerical Method for Submerged Vortex (b = 3.5 ft) in Uniform Stream (U = 10 ft/sec) with Finite Depth (D = 4.5 ft)

The only other attempts to solve steady flow problems are those of Tu (1971) and Chapman (1975). Tu (1971) solves, using a finite element method, the linear-theory problem for a submerged two-dimensional vortex in a finite-depth stream. He uses as a closure scheme, for the truncation of the numerical domain, the condition that the free-surface elevation and slope is zero at some finite distance upstream. Tu shows only one numerical result which is in fair agreement with the known solution. The discrepancies are probably due to the very short domain used in the numerical problem so that the upstream boundary conditions are not applied far enough upstream.

Chapman (1975) develops a new theory for high-speed motion of slender bodies in the free surface. The main idea behind the theory is that not only is longitudinal variation of flow quantities very small compared to lateral variations, as in standard slender body theory, but the upstream influence of these variations are completely negligible. Thus, the problem is reduced to an unsteady problem, which is like a parabolic or boundary-layer problem, in which the longitudinal coordinate behaves like a time coordinate. Thus the exact flow problem reduces to a two-dimensional unsteady flow problem with a body either expanding or moving in the transverse plane. One cannot study wave resistance with such an approximation but it does give estimates of some local flow quantities particularly those associated with side forces. The two-dimensional free-surface problems that must be solved are very similar to the problems of waves generated in a container by boundary motion. Chapman used an implicit finite difference method similar to the one described in Chapter 3.

He obtains good agreement for computed and measured side forces on a yawed vertical plate.

Attempts to compute numerical solutions of unsteady problems are described by Haussling and Van Eseltine (1974 - 1975) and Nichols and Hirt (1973).

Haussling and Van Eseltine (1974) study the hydrodynamics of an accelerating two-dimensional pressure distribution on the free surface using a Galerkin method similar to the one described in Chapter 3, for both the linear and nonlinear problems. The motion takes place in a long, but finite, container and the pressure distribution is suddenly accelerated to a constant speed. While it is not possible to achieve a precise local steady state, the computed wave resistance and wavelengths of the second and third waves in the linear formulation, have nearly the same values as given by steady linear theory.

As described in Chapter 3, the nonlinear problem is very complicated and requires considerably more computer time. For this reason Haussling and Van Eseltine consider a much smaller container, thus requiring fewer terms in the Galerkin expansion. The penalty for this is that a local steady state can barely be reached. For small values of pressure amplitude, the nonlinear results are fairly close to the linear results. While the first couple of downstream waves can barely be considered to have reached steady state, the expected higher peaks, shallower troughs and shorter wavelengths are computed for the nonlinear formulation. Quantitative comparisons cannot be made because of the uncertainties of transient effects. For larger pressure amplitudes, the method encounters a numerical instability just as the generated waves approach the limiting wave slope for steady-state free waves. Small modifications to reduce the instability of the numerical calculations, for instance by using upstream differencing, enabled the calculation to proceed further in time. The upstream differencing induces an artificial viscosity effect causing a damping of the waves downstream of the disturbance. The effect of this artificial viscosity on the flow near the disturbance is not completely known but may be negligible. Much more numerical experimentation is needed to enable one to draw definitive conclusions.

Haussling and Van Eseltine (1975) extended their Galerkin method to linear theory three-dimensional flows and consider the motion of a rectangular pressure distribution on a circular course. The motion takes place in a rectangular box and is only considered for a time interval in which no waves reflect from the walls. The time interval is long enough for the motion to be nearly steady state and resistance, side force and yawing moment are calculated. While comparison with other calculations, theory or experiment are not given, earlier solutions of the linear problem indicate that no unusual difficulties are present. Thus, one can consider the results of Haussling and Van Eseltine (1975) to be accurate and reliable.

Nichols and Hirt (1973) make a bold attempt to calculate the nonlinear three-dimensional flow past a surface-piercing body. They use a slightly modified version of the MAC method for three-dimensional flows. The flow takes place in a finite-depth rectangular channel and the body is simply a square post on the bottom which extends through the free surface. The channel is truncated a relatively short distance upstream and downstream and the mesh is relatively crude. The attempt here is truly of an experimental nature just to get some idea of what happens. The upstream boundary condition is a set inflow velocity and the downstream boundary conditon requires zero velocity gradient and zero shear stress. Nichols and Hirt state that this downstream condition, which seems to amount to simply parallel flow out of the region (i.e., no waves there), has little upstream effect though no numerical evidence is presented. The flow is started from rest and the numerical time integration is explicit. They find that integrating the kinematic free-surface condition in this way is unstable, so they add to it a correction which is proportional to the horizontal Laplacian of the free-surface elevation. This correction is a numerical damping term whose coefficient is chosen to just balance the instability.

It is very difficult to assess the accuracy and reliability of the numerical solution obtained. Figure 11 is one of their results at some time after an impulsive start. On this meager basis, one can say though that the method has promise and should be investigated further. Needless to say, such calculations are not cheap. One of the major difficulties with the method is that accurate solutions would require a mesh refinement. Explicit time differencing requires for stability that the time step is decreased proportionately to the spatial grid scale (the square of the spatial grid scale if viscosity is not zero). It is easy to see that enormous amounts of computer time are needed for adequate resolution.

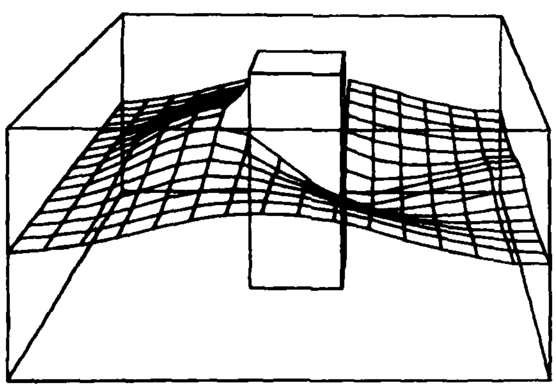

Figure 11 – Perspective View of the Surface Configuration Resulting from Flow Past a Rectangular Post (Flow is from left to right)

5. Summary

Most of the simulations discussed in Chapter 4 are for two-dimensional problems. Very few attempts at numerically simulating three-dimensional problems have been made. The work of Haussling and Van Eseltine (1975) and Nichols and Hirt (1973) appear to be the only exceptions.

It can be seen from the previous chapters that most of the methods described in Chapter 3 can be used successfully as the basis of a numerical simulation procedure in at least one of the classes of problems that we considered. Only the Galerkin and MAC methods have been used for problems in several of these classes. However, the Galerkin method is difficult to apply in cases of complicated geometry. Thus, its usefulness for problems involving ship hulls piercing the free surface seems limited. The MAC method (and its later development, SUMMAC) is general enough to be used in any of the classes of problems mentioned, and in fact, has been.

Numerical methods based on Lagrangian formulations seem ideal when free surfaces are present. However, little clear advantage over Eulerian formulations is obvious because of the introduction of special difficulties, most notably the finite-difference grid distortions in highly strained motions. While Chan (1975) has largely overcome this difficulty and others associated with Lagrangian methods, his method is complicated, computationally expensive, and still may not be suitable for some body-flow problems.

It is rather surprising that numerical simulations based on the Eulerian finite-difference potential problem have not been used more often. It seems that ultimately the two methods that are most suited for numerically simulating free-surface ship hydrodynamics problems are MAC and the finite difference (or finite element) approximation of the Eulerian potential problem. One advantage in using the finite difference (or finite element) approximation of the Eulerian potential problem over the MAC method is that there is only one dependent variable, the potential Φ (we do not count the free-surface elevation η since it requires little storage and calculation compared to Φ) in either two or three dimensions, whereas in the MAC method, there are three dependent variables in two-dimensional problems and four in three-dimensional ones. This larger number of dependent variables complicates storage problems and in three dimensions, becomes critical for present-day computer hardware. A disadvantage in the potential problem is the requirement of numerical differentiation to obtain the velocities. In either of the above methods, the major computational work at each step is the solution of a Poisson (or Laplace) equation for one dependent variable so that if a machine with unlimited core storage were available, then the two methods ought to be comparable at least in computer execution time. At present, however, it seems

that more simulations based on the finite difference (or finite element) approximation of the Eulerian potential problem should be pursued.

We find that all the numerical simulations of linear problems were fairly successful. For the steady-state problems considered, there is enough analytical information available so that an infinite domain can be replaced by a finite domain with suitable conditions imposed on the truncation boundary to help assure accurate approximation of the exact solution. The main question to be answered here is which, if any, of the numerical methods can be used in three-dimensional steady-state problems with reasonable efficiency. This is a matter that cannot be answered yet, but methods such as the localized finite-element (or a similar localized finite-difference) method seems to hold promise for this task. However, the integral equation methods, either ones based on the Kelvin wave sources (cf. Wehausen, 1974) or the simple sources (cf. Bai and Yeung, 1974) may ultimately be the most efficient methods for three-dimensional problems. In this competition for the most efficient method to numerically simulate linear, three-dimensional steady-state problems, one must also consider I.V.P. approaches. A significant finding of Chan and Hirt (1974) and Hausling and Van Eseltine (1974 - 75) is that for such problems a local steady state is rapidly attained after a sudden start. We should mention that a time-dependent Green function approach (cf. Wehausen, 1971) has not been thoroughly investigated as yet.

Finally we mention that it seems that the only practical way to simulate nonlinear free-surface problems is through an I.V.P. approach. Although the method of von Kerczek and Salvesen (1974 - 75) seems to do well for steady two-dimensional problems, the extension to three-dimensional problems seems almost hopeless. However, their downstream closure condition, which amounts to just extrapolating the streamlines downstream, may be useful for other steady nonlinear problems.

Acknowledgement

I wish to express my thanks to Mr. Justin McCarthy for his support and encouragement of my work. Whatever merit this paper may have is to a large degree, brought out by his understanding and editorial skill.

This work was begun at the University of Maryland and completed at the David W. Taylor Naval Ship Research and Development Center. The work has been supported by the Numerical Naval Hydrodynamics Program which is jointly sponsored by the Office of Naval Research, the Naval Sea Systems Command and the David W. Taylor Naval Ship Research and Development Center.

REFERENCES

Bai, K.J. and R.W. Yeung (1974), "**Numerical Solutions to Free-Surface Flow Problems,**" 10th ONR Symposium on Naval Hydrodynamics, Cambridge, Mass.

Bai, K.J. (1975), "**Diffraction of Oblique Waves by an Infinite Cylinder,**" J. Fluid Mechanics, 63, 513.

Brennen, C. and A.K. Whitney (1970), "**Unsteady Free-Surface Flows: Solutions Employing the Lagrangian Description of the Motion,**" 8th ONR Symposium on Naval Hydrodynamics, Pasadena, Calif., 117.

Chan, R. K.-C. and R.L. Street (1970), "**A Computer Study of Finite-Amplitude Water Waves,**" J. Comp. Phys., 6, 68.

Chan, R. K.-C. (1974), "**A Discretized Solution for the Solitary Wave,**" J. Comp. Phys., 16, 32.

Chan, R. K.-C. and C.W. Hirt (1974), "**Two-Dimensional Calculations of the Motion of Floating Bodies,**" 10th ONR Symposium on Naval Hydrodynamics, Cambridge, Mass.

Chan, R. K.-C. (1975), "**A Generalized Arbitrary Lagrangian-Eulerian Method for Incompressible Flows with Sharp Interfaces,**" J. Comp. Phys., 17, 311.

Chapman, R.B. (1975), "**Free-Surface Effects for Yawed Surface-Piercing Plates,**" to be published in J. Ship Research.

Chen, H.S. and C.C. Mei (1974), "**Oscillations and Wave Forces in a Man-Made Harbor in the Open Sea,**" 10th ONR Symposium on Naval Hydrodynamics, Cambridge, Mass.

Easton, C.R. and I. Catton (1972), "**Initial Value Techniques in Free-Surface Hydrodynamics,**" J. Comp. Phys., 9, 424.

Forsythe, G.E. and W.R. Wasow (1960), "**Finite-Difference Methods for Partial Differential Equations,**" John Wiley and Sons, Inc., New York.

Harlow, F.H. and A.A. Amsden (1971), "**Fluid Dynamics,**" Report LA-4700, Los Alamos Scientific Laboratory, Los Alamos, New Mexico.

Harlow, F.H. and J.E. Welch (1966), "**Numerical Study of Large Amplitude Free-Surface Motions,**" Phys. Fluids, 9, 842.

Haussling, H.J. and R.T. Van Eseltine (1974), "**A Combined Spectral Finite-Difference Method for Linear and Nonlinear Water Wave Problems,**" David W. Taylor Naval Ship Research and Development Center Report 4580, Bethesda, Md.

Haussling, H.J. and R.T. Van Eseltine (1975), "**Unsteady Air-Cushion Vehicle Hydrodynamics Using Fourier Series,**" to be published in J. Ship Research.

Hirt, C.W., J.L. Cook, and L.D. Butler (1970), "**A Lagrangian Method for Calculating the Dynamics of an Incompressible Fluid with Free Surfaces,**" J. Comp. Phys., 5, 103.

Lamb, H. (1945), "**Hydrodynamics,**" Dover Publications, New York.

Moore, R.E. and L.M. Perko (1965), "**Inviscid Fluid Flow in an Accelerating Cylindrical Container**," J. Fluid Mechs., 22, 305.

Multer, R.H. (1973), "**Exact Nonlinear Model of Wave Generator**," J. Hydraulics Div., ASCE, 99, 31.

Nichols, B D. and C.W. Hirt (1973), "**Calculating Three-Dimensional Free-Surface Flows in the Vicinity of Submerged and Exposed Structures**," J. Comp. Phys., 12, 234.

Perko, L.M. (1969), "**Large-Amplitude Motions of a Liquid-Vapour Interface in an Accelerating Container**," J. Fluid Mechanics, 35, 77.

Roache, P.J. (1972), "**Computational Fluid Dynamics**," Hermosa Publishers, Albuquerque, New Mexico.

Salvesen, N. and C. von Kerczek (1975), "**Comparison of Numerical and Perturbation Solutions of Two-Dimensional Nonlinear Water-Wave Problems**," to be published in J. Ship Research.

Schwartz, L.W. (1974), "**Computer Extension and Analytic Continuation of Stokes' Expansion for Gravity Waves**," J. Fluid Mechs., 62, 553.

Southwell, R.V. and G. Vaisey (1948), "**Relaxation Methods Applied to Engineering Problems. XII. Fluid Motions Characterized by Free Streamlines**," Philosophical Transactions of the Royal Society of London, Series A, 240, 117.

Stoker, J.J. (1957), "**Water Waves**," Interscience Publishers, Inc., New York.

Street, R.L., R. K.-C. Chan, and J.E. Fromm (1970), "**Two Methods for the Computation of the Motion of Long Water Waves - A Review and Applications**," 8th ONR Symposium on Naval Hydrodynamics, Pasadena, Calif., 147.

Taylor G.I. (1950), "**The Instability of Liquid Surfaces in a Direction Perpendicular to Their Plane. I**," Proc. Roy. Soc., A201, 192.

Thomas, J.W. (1968), "**Irrotational Gravity Waves of Finite Height: A Numerical Study**," Mathematika, 15, 139.

Thomas, J.W. (1975), "**A Numerical Study of the Relationship Between the Dimensionless Parameters in the Problem of Periodic Waves of Permanent Type in a Liquid of Finite Depth**," Q. Appl. Math., 22, 403.

von Kerczek, C.H. and N. Salvesen (1974), "**Numerical Solutions of Two-Dimensional Nonlinear Wave Problems**," 10th ONR Symposium on Naval Hydrodynamics, Cambridge, Mass.

Wehausen, J.V. (1971), "**The Motion of Floating Bodies**," Annual Review of Fluid Mechanics, 3, 237.

Wehausen, J.V. (1973), "**The Wave Resistance of Ships**," Advances in Applied Mechanics, 13, 93.

FINITE ELEMENT ANALYSIS OF SURFACE WAVE PROBLEMS BY A METHOD OF SUPERPOSITION

Hideyuki Seto

Hiroshima Technical Institute, Mitsubishi Heavy Industries, Ltd., Kannonshin-machi, Hiroshima 733

Yoshiyuki Yamamoto

Department of Naval Architecture, University of Tokyo
Bunkyo-ku, Tokyo 113 Japan

ABSTRACT

A numerical method for solving wave propagation problems is proposed herein, and is applied to water waves. It is based on the linearity of the governing equations, and solutions are obtained in the form of a sum of analytical and numerical solutions. The finite element method is an efficient tool to obtain this numerical solution and is used in the method presented here. The finite element equations derived have symmetric coefficient matrices and can easily be solved with the help of general purpose programs for structural analysis. Several authors have proposed finite element formulations for similar problems, and Bai and Yeung's approach can be regarded as a special instance of the present method.

1. INTRODUCTION

Numerical techniques for solving linear water wave problems have been developed by many authors, and as for the finite element method, Chenault [1] and Bai [2] proposed their schemes. They overcame a difficulty resulting from the radiation condition at infinity by applying this condition at a fictitious boundary according to the suggestion of Zienkiewicz and Newton [3]. Newton, Chenault and Smith [4] applied Chenault's scheme to ship hydrodynamics. In the case of shallow water waves,

Berkhoff [5] proposed a matching technique of far- and near-field solutions on a fictitious surface; the near-field solutions are obtained by the finite element method, and the far-field ones as solutions caused by pulsating sources distributed on the fictitious surface. Chen and Mei [6] developed a similar formulation on the concept of the hybrid method by using eigenfunctions as the far-field solutions. Bai and Yeung [7] improved Bai's original formulation by using a scheme similar to Chen and Mei's, and succeeded to reduce the domain to be analyzed with the aid of eigenfunctions obtained by the wave maker theory. This improved formulation, however, has a weakness; with the increase of depth of water, this method becomes impractical, because the far-field solution includes an integral expression at the limit.

In this paper, the authors propose a finite element technique taking advantage of the linearity of the governing equations and the physical considerations on the asymptotic behavior of solutions at infinity. The same technique has been applied successfully to static problems in solid mechanics [8, 9], and is called the method of superposition. It is based on the assumption that a solution is expressed in the form of a sum of analytical and numerical solutions: The analytical solution is defined throughout the water field and satisfies the radiation condition at infinity, but it may not satisfy the condition on the surface of the body under consideration. The numerical solution is obtained only within a fictitious surface so that the resulting velocity potential satisfies the condition on the surface of the body and the condition of continuity on the fictitious surface. The analytical solution used is desirable to approximate the rigorous solution, and at least it should be a good approximation in the outer water field beyond the fictitious surface; the better the analytical solution is, the more accurate the resulting solution becomes and the smaller the domain to be analyzed. In general, such an analytical solution can be

obtained by assuming pulsating singularities chosen properly on the physical basis, and it can be determined even in the case of oscillating ships with forward velocity. The present method can be applied to various kinds of steady wave problems including seismic waves and electromagnetic waves, if a proper analytical solution is obtained. For obtaining numerical solutions, the finite element method is an efficient and convenient tool, and any other numerical method can be used for the same purpose. The concept of the method of superposition is somewhat similar to that of the matched asymptotic expansion method [10, 11], but this method has no restrictions on frequencies and ship shapes.

The theoretical foundation of the present method is developed on the basis of the variational principle of hybrid type. Equations to be solved are given as a set of linear equations with real symmetric matrices, and can be solved with the aid of general purpose programs for structural analysis.

In this paper, only radiation problems will be illustrated, but diffraction problems can also be treated in the same way.

2. MATHEMATICAL FORMULATION

Consider a water field Ω with the free surface S_F as shown in Fig. 1.* A floating or immersed body is in contact with water on the surface S_H. Introduce a reference coordinate system such that S_F is given by $z = 0$, and the body is located near the origin. The depth of water, h, may be finite or infinite, and the bottom of finite depth, S_B, is given by $z = -h$. Let ϕ be the velocity potential. Then water flows caused by harmonic motion of the surface is governed by the following equations:

$$\Delta\phi = 0 \qquad \text{in} \quad \Omega \tag{1}$$

$$g\frac{\partial \phi}{\partial z} - \omega^2\phi = 0 \qquad \text{on} \quad z = 0 \tag{2}$$

*Figures are at the end of the paper.

$$\frac{\partial\phi}{\partial n}\begin{cases} = 0 & \text{on} \quad z = -h \quad \text{if} \quad h < \infty \qquad (3a) \\ \to 0 & \text{as} \quad z \to -\infty \quad \text{otherwise} \qquad (3b) \end{cases}$$

$$\frac{\partial\phi}{\partial n} = v_n \qquad \text{on} \quad S_H \tag{4}$$

Here, ω is the angular frequency of harmonic motion, g is gravitational acceleration, n is the outward unit normal vector from the water field on its boundary, and v_n is the normal velocity prescribed on S_H . In order to determine the solution uniquely, it is necessary to impose the so-called radiation condition that the water flow behaves as an outgoing progressive wave at infinity. In the following, a velocity potential ϕ satisfying Eqs. (1), (2) and (3) will be called a wave function.

By introducing a fictitious surface S_R , the water field Ω can be divided into Ω^I and Ω^{II}, which are the inner and outer domain with respect to S_R , respectively. The condition of continuity on S_R is given by

$$\frac{\partial\phi^I}{\partial n^I} = -\frac{\partial\phi^{II}}{\partial n^{II}}, \qquad \phi^I = \phi^{II} \qquad \text{on} \quad S_R \tag{5, 6}$$

where the indeces I and II correspond to the quantities defined in Ω^I or Ω^{II}, respectively. A velocity potential ϕ satisfying Eqs. (1) and (2) together with Eq. (3) in Ω^{II} will be called an auxiliary function. In most cases, auxiliary functions can be obtained with the aid of velocity potentials caused by pulsating sources. In case of infinite water depth, a velocity potential due to a pulsating source with strength $\cos(\omega t - \alpha)$ is given in the following form;

in the two-dimensional case,

$$G = [\log(r_2/r_2{}^*) - 2\int_\zeta^\infty \frac{k\cos k(z+\zeta) + K\sin k(z+\zeta)}{k^2 + K^2} \cdot\exp(-k|x-\xi|)\,dk]\cos(\omega t - \alpha)$$

$$+ 2\pi\exp[K(z+\zeta)]\sin[-K|x-\xi| + \omega t - \alpha] \tag{7}$$

in the three-dimensional case

$$G = [\frac{1}{r} + \frac{1}{r^*} + \frac{4K}{\pi}\int_0^\infty \frac{k \sin k(z+\zeta) - K \cos k(z+\zeta)}{k^2 + K^2}$$

$$\cdot K_o(k\varpi)\, dk] \cos(\omega t - \alpha)$$

$$+ 2\pi K \exp[K(z+\zeta)][J_o(K\varpi) \sin(\omega t - \alpha)$$

$$- Y_o(K\varpi) \cos(\omega t - \alpha)] \qquad (8)$$

where

$$\left.\begin{array}{l} r_2 \\ r_2{}^* \end{array}\right\} = [(x-\xi)^2 + (z \mp \zeta)^2]^{1/2}, \quad \left.\begin{array}{l} r \\ r^* \end{array}\right\} = [\varpi^2 + (z \mp \zeta)^2]^{1/2} \qquad (9)$$

$$\varpi = [(x-\xi)^2 + (y-\eta)^2]^{1/2}, \quad K = \frac{\omega^2}{g}$$

In Eqs. (7) and (8), (ξ, η) and (ξ, η, ζ) indicate the coordinates of the source. Eq. (7) is given by Kim [12] in a form convenient for numerical computation. In case of constant finite water depth, similar expressions are given in Eqs. (13.34) and (13.18) of Reference 13.

According to the potential theory, the velocity potential under consideration is given in the form

$$\phi = \frac{1}{2\pi}\int_{S_H} (\frac{\partial\phi}{\partial n} - \phi\frac{\partial}{\partial n})\, G\, dS \qquad (10)$$

This suggests that auxiliary functions effective for the present purpose can be obtained by using G and its derivatives.

3. METHOD OF SUPERPOSITION

The solution of the problem can be obtained according to the following procedure:

1° Choose the auxiliary function which is given as a linear combination of a number of auxiliary functions ϕ_{aj}, (j = 1 -- N, N = 2m), and assume the solution as a sum of the auxiliary function and the residual solution ϕ_r. That is,

$$\phi = \phi_a + \phi_r, \qquad \phi_a = \sum_{j=1}^{N} c_j \phi_{aj} \qquad (11, 12)$$

where c_j, (j = 1 -- N), are unknown coefficients.

2° Introduce a fictitious boundary S_R so that ϕ_a is a

good approximation of the solution in Ω^{II}. It can be assumed, therefore, that the residual solution ϕ_r vanishes in Ω^{II} and satisfies Eqs. (1), (2) and (3) and the conditions

$$\frac{\partial \phi_r}{\partial n} = v_n - \sum_{j=1}^{N} c_j \frac{\partial \phi_{aj}}{\partial n} \qquad \text{on } S_H \tag{13}$$

$$\frac{\partial \phi_r}{\partial n} = 0 \quad , \quad \phi_r = 0 \qquad \text{on } S_R \tag{14,15}$$

3° Determine the solution ϕ_o numerically in Ω^I such that it satisfies Eqs. (1), (2), (3) and (14), and determine the solutions ϕ_{rj}, (j = 1--N), numerically in Ω^I such that they satisfy Eqs. (1), (2) and (14) and the condition

$$\frac{\partial \phi_{rj}}{\partial n} = - \frac{\partial \phi_{aj}}{\partial n} \qquad \text{on } S_H \text{ and } S_B \tag{16}$$

Then the residual solution is given in the form

$$\phi_r = \phi_o + \sum_{j=1}^{N} c_j \phi_{rj} \tag{17}$$

4° Reduce the condition given by Eq. (15) into N individual conditions. It can be done by the collocation method with or without the method of least squares or by the variational method of hybrid type. If the collocation points P_k, (k = 1--m), are chosen on S_R properly, the condition given by Eq. (15) is given in the form

$$\phi_o + \sum_{j=1}^{N} c_j \phi_{rj} = 0 \quad \text{at } P_k \quad (k = 1 -- m) \tag{18}$$

The unknown coefficients c_j, (j = 1--N), can be determined by the resulting N independent conditions (cf. Sec. 6).

5° The solution ϕ in Ω^I is given by

$$\phi = \phi_o + \sum_{j=1}^{N} c_j (\phi_{aj} + \phi_{rj}) \tag{19}$$

The condition of continuity of tangential derivative of ϕ on S_R is naturally satisfied in the average sense.

An alternative scheme can be developed for directly determining ϕ in Ω^I. The wave function ϕ satisfies Eqs. (1), (2), (3) and (4) and the conditions

$$\frac{\partial \phi}{\partial n} = \sum_{j=1}^{N} c_j \frac{\partial \phi_{aj}}{\partial n} , \quad \phi = \sum_{j=1}^{N} c_j \phi_{aj} \quad \text{on } S_R \tag{20, 21}$$

Determine the wave function ϕ_o for the original scheme, and the wave functions ϕ_{ej}, (j = 1--N), by Eqs. (1), (2) and (3) and the conditions

$$\frac{\partial \phi_{ej}}{\partial n} = 0 \quad \text{on } S_H \tag{22}$$

$$\frac{\partial \phi_{ej}}{\partial n} = \frac{\partial \phi_{aj}}{\partial n} \quad \text{on } S_R \tag{23}$$

Then the velocity potential ϕ in Ω^I is given in the form

$$\phi = \phi_o + \sum_{j=1}^{N} c_j \phi_{ej} \tag{24}$$

where c_j, (j = 1--N), are determined by the N conditions reduced from Eq. (21), such as

$$\phi_o + \sum_{j=1}^{N} c_j \phi_{ej} = \sum_{j=1}^{N} c_j \phi_{aj}, \text{ at } P_k, (k = 1 \text{ -- } m) \tag{25}$$

for the collocation method.

The second scheme is effective even if singular points or discontinuities of the auxiliary function used exist in the water field Ω^I. In case of finite depth of water, this scheme is identical with Bai and Yeung's if the condition given by Eq. (21) is reduced by the Galerkin method based on the variational principle of hybrid type.

It should be noticed that both of the schemes described above can be modified by exchanging the roles of Eqs. (14) and (15).

4. EXAMPLE -- WAVE MAKER PROBLEM

Characteristics of the solution obtained by the present method will be investigated by a simple two-dimensional example called the wave maker problem. Consider the water field ($x > 0$, $-h < z < 0$) shown in Fig. 2. The wave maker S_H is given by $x = 0$. Let the fictitious surface be

$x = \ell$. Then the domain to be analyzed is given by $(0 < x < \ell, -h < z < 0)$, and solutions satisfying Eqs. (1), (2), (3), and (14) can be obtained analytically in the form

$$\phi = a_o \cos(\omega t - \alpha_o) \cosh \kappa_o(z+h) \cos \kappa_o(x-\ell) + \sum_{k=1}^{\infty} a_k \cos(\omega t - \alpha_k) \cos \kappa_k(z+h) \cosh \kappa_k(x-\ell) \tag{26}$$

where

$$\kappa_o \tanh \kappa_o h = \omega^2/g \;, \quad \kappa_k \tan \kappa_k h = -\omega^2/g \tag{27, 28}$$

Here the constants a_k and α_k are determined by the condition on S_H with the aid of orthogonality of $\cosh \kappa_o(z+h)$ and $\cos \kappa_k(z+h)$. The eigenvalues ω_k of the domain Ω^I can be obtained by introducing the condition given by Eq. (14), and it follows that

$$a_k = 0, \; (k = 1, 2, \ldots) \quad \text{and} \quad a_o \sin \kappa_o \ell = 0$$

Then the eigenvalues are determined by Eq. (27) and the condition

$$\sin \kappa_o \ell = 0 \tag{29}$$

It can easily be confirmed from Eq. (27) that

$$(k - 1/2)\pi < \kappa_k h < k\pi \tag{30}$$

This means that the second term in the right hand side of Eq. (26) can be roughly approximated by assuming S_F as a fixed boundary and becomes insignificant on S_R if

$$\kappa_1 \ell \gtrsim 5 \quad \text{or} \quad \ell/h \gtrsim 3 \tag{31}$$

The fictitious surface S_R should be chosen in general so that this relation holds. If only the upper part of the wave maker of depth d moves, the domain to be analyzed can be reduced so that

$$\ell/d \gtrsim 3$$

When the normal velocity on S_H is given by

$$v_n = [V_o \cosh \kappa_o(z+h) + \sum_{k=1}^{\infty} V_k \cos \kappa_k(z+h)] \sin \omega t \tag{32}$$

the exact solution is given by

$$\phi = (V_o/\kappa_o) \cosh \kappa_o(z + h) \cos (\kappa_o x - \omega t)$$

$$- \sum_{k=1}^{\infty} (V_k/\kappa_k) \cos \kappa_k(z + h) \exp (-\kappa_k x) \sin \omega t \qquad (33)$$

When the auxiliary function ϕ_{a1} is given by

$$\phi_{a1} = \cosh \kappa_o(z + h) \cos (\kappa_o x - \omega t + \alpha_1) \qquad (34)$$

The solutions ϕ_o and ϕ_{r1} can easily be obtained with the help of Eq. (26) as

$$\phi_o = [(V_o/\kappa_o) \cosh \kappa_o(z + h) \cos \kappa_o(x - \ell)/\sin \kappa_o\ell$$

$$- \sum_{k=1}^{\infty} (V_k/\kappa_k) \cos \kappa_k(z + h) \cosh \kappa_k(x - \ell)/\sinh \kappa_k\ell] \sin \omega t \qquad (35)$$

$$\phi_{r1} = -[\cosh \kappa_o(z + h) \cos \kappa_o(x - \ell)/\sin \kappa_o\ell]\sin \omega t \qquad (36)$$

Let the collocation point P_1 on S_R be $(\ell, 0)$. It then follows that

$$\alpha_1 = 0$$

$$c_1 = V_o/\kappa_o - (\sin \kappa_o\ell/\cosh \kappa_o h) \sum_{k=1}^{\infty} (V_k/\kappa_k)(\cos \kappa_k h/\sinh \kappa_k\ell) \qquad (37)$$

Now the approximate solution ϕ^* obtained by the present method is given by

$$\phi^* = c_1 \cosh \kappa_o(z + h) \cos (\kappa_o x - \omega t)$$

$$- [\sum_{k=1}^{\infty} (V_k/\kappa_k) \cos \kappa_k(z + h) \cosh \kappa_k(x - \ell)/\sinh \kappa_k\ell]\sin \omega t$$

$$0 < x < \ell, \; -h < z < 0 \qquad (38)$$

By comparing the approximate solution ϕ^* with the exact one, it can be observed that ϕ^* gives sufficient accuracy under the condition given by Eq. (31); that is,

$$\left.\begin{aligned} &|c_1 - V_o/\kappa_o| < \sum_{k=1}^{\infty} |V_k/\kappa_k| \; 4 \exp (-\kappa_o h - \kappa_1\ell) \\ &|\cosh \kappa_k(x - \ell)/\sinh \kappa_k\ell - \exp (-\kappa_k x)| < \exp (-1.5\ell/h) \end{aligned}\right\} \qquad (39)$$

As can be seen from Eq. (37), the present method gives the exact radiating part of solution if $\sin \kappa_o\ell = 0$; however, it is not the case in actual computation because rounding errors

in ϕ_o and ϕ_{r1} may become significant in this case.

5. VARIATIONAL PRINCIPLE

The validity of the method of superposition can be shown by the variational approach for flow problems. The following variational principle is based on a similar model to hybrid displacement model II for solid mechanics [14], and holds for a radiation problem in case of finite depth of water:

$$\begin{aligned}
&\Gamma[\phi^I, \phi^{II}, \phi^R, \lambda^I, \lambda^{II}] \\
&= \frac{1}{2}\int_{\Omega^I} (\nabla\phi^I)^2 d\Omega^I - \frac{\omega^2}{2g}\int_{S_F \wedge \partial\Omega^I} (\phi^I)^2 dS - \int_{S_H} v_n \phi^I dS \\
&\quad - \int_{S_R} [\lambda^I(\phi^I - \phi^R) + \lambda^{II}(\phi^{II} - \phi^R)] dS + \frac{1}{2}\int_{S_R \wedge S_B \wedge \partial\Omega^{II}} \phi^{II} \frac{\partial\phi^{II}}{\partial n^{II}} dS \\
&\quad - \frac{1}{2}\int_{\Omega^{II}} \phi^{II} \Delta\phi^{II} d\Omega^{II} + \frac{1}{2}\int_{S_F \wedge \partial\Omega^{II}} \phi^{II} [\frac{\partial\phi^{II}}{\partial z} - \frac{\omega^2}{g}\phi^{II}] dS \\
&= \text{stationary} \qquad (40)
\end{aligned}$$

where λ^I , λ^{II} and ϕ^R are the Lagrange multipliers defined on S_R , and ϕ^{II} satisfies the radiation condition at infinity. It can easily be shown that this variational principle is equivalent to the boundary value problem defined by Eqs.(1) --(4) together with the radiation condition. Introducing Eqs. (19) and (12) for ϕ^I and ϕ^{II} in Eq. (40) and manipulating the resulting relations leads to the condition

$$\int_{S_R} \frac{\partial\phi_{ak}}{\partial n} (\phi_o + \sum_{j=1}^{N} c_j \phi_{rj}) dS = 0 \;, \quad (k = 1, \ldots, N) \qquad (41)$$

This Galerkin-type condition is equivalent to Bai and Yeung's, and is also equivalent to the condition given by Eq. (18) if the collocation points P_k's are chosen properly. In general, significant terms of $\frac{\partial\phi_{aj}}{\partial n}$ on S_R decrease rapidly with the increase of $|z|$, and it suggests that the collocation points for Eq. (18) should be chosen near the free surface S_F .

6. FINITE ELEMENT FORMULATION AND COMPUTATIONAL ASPECTS

The solutions ϕ_o and ϕ_{rj} or ϕ_{ej} can easily be determined in Ω^I by the finite element method formulated on the basis of the variational principle

$$\frac{1}{2}\int_{\Omega^I}(\nabla\phi)^2 d\Omega^I - \frac{\omega^2}{2g}\int_{S_F\cap\partial\Omega^I}\phi^2 dS - \int_{S_H\cup S_B\cap\partial\Omega^I} v_n^*\phi dS = \text{stationary} \tag{42}$$

where v_n^* is the normal velocity defined on S_H and S_B appropriately. Then the finite element equations can be obtained in the form

$$\begin{aligned}([K] - \frac{\omega^2}{g}[M])[\phi_o^c,\phi_o^s,\phi_{r1}^c,\phi_{r1}^s,\phi_{r2}^c,\ldots]\\ = [b_o^c,b_o^s,b_{r1}^c,b_{r1}^s,b_{r2}^c,\ldots]\end{aligned} \tag{43}$$

where

$$\begin{aligned}[\phi_o^c,\phi_o^s,\phi_{r1}^c,\ldots] &= [\{\phi_o^c\},\{\phi_o^s\},\{\phi_{r1}^c\},\ldots]\\ [b_o^c,b_o^s,b_{r1}^c,\ldots] &= [\{b_o^c\},\{b_o^s\},\{b_{r1}^c\},\ldots]\end{aligned} \tag{44}$$

$\{\phi_o^c\}$ etc. being the vectors of nodal values of the cosine or sine components of ϕ and b such that

$$\begin{aligned}\phi &= \phi^c \cos\omega t + \phi^s \sin\omega t\\ b &= b^c \cos\omega t + b^s \sin\omega t\end{aligned} \tag{45}$$

Here $[K]$ and $[M]$ are positive or non-negative definite matrices, and b is related to v_n^* .

Eq. (43) can be uniquely solved, unless ω is any of the eigenvalues defined by

$$([K] - \frac{\omega^2}{g}[M])\{\phi\} = \{0\} \tag{46}$$

Eq.(43) cannot be solved numerically in case where ω is nearly equal to one of the eigenvalues.

Let $\{\phi^o\}$ be the vector consisting of the nodal values of ϕ at the collocation points, and let $\{\phi^\dagger\}$ be the vector consisting of the rest. Eq. (43) can then be rewritten as

$$\left(\begin{bmatrix}K^{oo} & K^{o\dagger}\\ K^{\dagger o} & K^{\dagger\dagger}\end{bmatrix} - \frac{\omega^2}{g}\begin{bmatrix}M^{oo} & M^{o\dagger}\\ M^{\dagger o} & M^{\dagger\dagger}\end{bmatrix}\right)\begin{bmatrix}\phi_o^{oc} & \phi_o^{os} & \phi_{r1}^{oc} & \phi_{r1}^{os} & \cdots\\ \phi_o^{\dagger c} & \phi_o^{\dagger s} & \phi_{r1}^{\dagger c} & \phi_{r1}^{\dagger s} & \cdots\end{bmatrix}$$

$$= \begin{bmatrix} b_o^{oc} & b_o^{os} & b_{r1}^{oc} & b_{r1}^{os} & \cdots \\ b_o^{c} & b_o^{s} & b_{r1}^{c} & b_{r1}^{s} & \cdots \end{bmatrix} \tag{47}$$

In general, $\{\phi^\dagger\}$ can be eliminated from Eq. (47). Combining the resulting equation with Eq. (17) leads to the condition equivalent to Eq. (18) such that

$$[b_o^{oc} + \sum_{j=1}^{N} c_j\, b_{rj}^{oc}\,,\; b_o^{os} + \sum_{j=1}^{N} c_j\, b_{rj}^{os}] - [K^{o\dagger} - \frac{\omega^2}{g}M^{o\dagger}][K^{\dagger\dagger} - \frac{\omega^2}{g}M^{\dagger\dagger}]^{-1}$$
$$[b_o^{\dagger c} + \sum_{j=1}^{N} c_j\, b_{rj}^{\dagger c}\,,\; b_o^{\dagger s} + \sum_{j=1}^{N} c_j\, b_{rj}^{\dagger s}] = [0,0] \tag{48}$$

This is effective even if ω is an eigenvalue. After determining c_j, $\{\phi^o\}$ and $\{\phi^\dagger\}$ can be completely obtained by Eq. (47). In reality, this difficulty can be avoided by calculating the results for several values of ω near the desired one; the results to be obtained are estimated by interpolating or extrapolating the resulting ones.

In the present scheme, $\phi_r = \phi_o + \Sigma c_j \phi_{rj}$ is to be obtained, and therefore, the size of finite elements should be determined by considering the flow due to ϕ_r. That is, mesh size should be chosen by taking account of geometry of the body and bottom. In the case of the second scheme, however, mesh subdivision depends upon both the geometry and the wave length.

In general three-dimensional cases, collocation points should be chosen on the fictitious surface, by taking account of the mode of auxiliary functions. Number of collocation points may be more than one half of that of unknown coefficients in ϕ_a; in this case, the number of independent conditions can be reduced by the method of least square.

Instead of the finite element method, the integral equation can be used for obtaining the solution. In the two-dimensional case, the velocity potential is expressed in the form

$$\phi(P) = \int_{\partial\Omega^I} m(Q) \log r_2(P, Q)\, dS_Q \tag{49}$$

where $P = (x, y)$, $Q = (\xi, \eta)$, and $r_2(P, Q)$ is the dis-

tance between P and Q . The source distribution can be determined by the integral equation [cf. Reference 7]

$$\pi m(P) + \int_{\partial\Omega^I} m(Q) \frac{\partial}{\partial n_Q} \log r_2(P, Q)\, dS_Q$$

$$= \begin{cases} \dfrac{\omega^2}{g} \displaystyle\int_{S_F} m(Q) \log r_2(P, Q)\, dS_Q & \text{on } S_F \wedge \partial\Omega^I \\ v_n^* & \text{on } S_H \vee S_B \wedge \partial\Omega^I \end{cases} \tag{50}$$

A difficulty caused by existence of bilge keels can be settled by properly subdividing Ω^I .

7. SOME NUMERICAL RESULTS

Pressure distributions on a semi-immersed circular cylinder (Fig. 3) heaving in infinitely deep water are calculated with mesh subdivision shown in Fig. 4. The shape functions are linear or bi-linear in each element. The velocity potential G given by Eq. (7) with $(\xi, \eta) = (0, 0)$ is used as the auxiliary function. For the heaving motion $A \cos \omega t$, the pressure distributions calculated

$$p = \rho g A (P^c \cos \omega t + P^s \sin \omega t) \tag{51}$$

are shown in Fig. 3. Here, ρ is water density, and P^c and P^s correspond to the added mass of water and the damping force, respectively. The results show good agreement with Porter's analytical solutions [15] and Bai's numerical ones. In the same figure are also shown the numerical results by the integral equation method.

In the case of cylindrical bodies of Lewis form $(B/T = 2)$, the added mass M and the damping force N are calculated by the present method for heaving and swaying motions in infinitely deep water, and the results are compared with Tasai's analytical results [16] in Figs. 5 and 6; they show good agreement. According to Tasai's notation,

$$M = \begin{cases} C_A \frac{1}{2}\rho\pi \left(\frac{B}{2}\right)^2 , \; C_A = K_4 C_o & \text{for heaving motion} \\ C_A \frac{1}{2}\rho\pi \; T^2 & \text{for swaying motion} \end{cases} \tag{52}$$

$$N = \rho\omega \frac{\bar{A}^2}{K^2} \tag{53}$$

where T , B , σ , and $\bar{A}$ are draft, breadth, the sectional area coefficient, and the asymptotic wave height ratio, and C_o is given by

$$C_o = [(1 + a_1)^2 + 3a_3{}^2]/(1 + a_1 + a_3) \tag{54}$$

a_1 and a_3 being the parameters of Lewis form.

Consider a semi-circular cylinder with two bilge keels as shown in Fig. 7. The added mass coefficient C_A and the asymptotic wave height ratio $\bar{A}$ for heaving motion are calculated, and the results are shown in Fig. 7. It shows that the added mass coefficients increase with the depth of bilge keel, d, while the wave height ratios remain unchange.

Consider a catamaran with two semi-circular cylinders. Numerical results for the added mass and the asymptotic wave height ratio are compared with Ohkusu's analytical solutions [17] in Figs. 8 and 9, which show fairly good agreement.

As a three dimensional example, hydrodynamic force acting on a semi-immersed sphere in heaving motion is calculated, and the results are compared with Havelock's ones [18] in Fig. 10. The upward force due to heaving motion $A \cos \omega t$ is given by

$$\frac{2}{3}\pi a^3 \rho \omega^2 A(f^c \cos \omega t + f^s \sin \omega t) \tag{55}$$

where a is the radius of the sphere, and f^c and f^s correspond to the added mass and the damping force, respectively. For numerical calculations, the velocity potential G given by Eq. (8) with $(\xi, \eta) = (0, 0)$ is used as the auxiliary function.

8. CONCLUSION

In the present paper a combination of analytical and finite element methods are used to solve water wave radiation problems. The technique is applied to simple examples which show good agreement with analytical solutions obtained by previous authors. This approach can also be applied to diffraction problems where

the normal velocity on the surface of the body and on the bottom is set equal to the incident wave.

This method can be applied widely to wave propagation problems if governing equations are linear and the radiating waves are given analytically; water waves caused by oscillating bodies with forward velocity and problems of seismic waves can easily be solved by the present method.

It should be noted that the present method of satisfying the radiation condition can be used in conjunction with other kinds of numerical methods, such as finite difference and integral equation methods.

REFERENCES

1. W. Chenault, II, Motion of a Ship at the Free Surface, M.S. Thesis, Naval Postgraduate School, Monterey, Calif., 1970.
2. K. J. Bai, A Variational Method in Potential Flows with a Free Surface, Univ. of California, Berkeley, College of Engng., Rep. No. NA 72-2, 1972.
3. O. C. Zienkiewicz and R. E. Newton, "Coupled Vibrations of a Structure Submerged in a Compressible Fluid," Proc. of Symp. on Finite Element Techniques, Stuttgart, 1969, 359-379.
4. R. E. Newton, D. W. Chenault, II, and D. A. Smith, Jr., "Finite Element Solution for Added Mass and Damping," Finite Element Methods in Flow Problems, Univ. of Alabama in Huntsville Press, 1974, 159-170.
5. J. C. W. Berkhoff, "Computation of Wave Propagation by Means of the F. E. M.," ibid. 289-293.
6. H. S. Chen and C. C. Mei, "Oscillations and Wave Forces in a Man-Made Harbor in the Open Sea," 10th Symp. on Naval Hydrodynamics, 1974.
7. K. J. Bai and R. W. Yeung, "Numerical Solutions to Free-Surface Flow Problems," ibid.
8. Y. Yamamoto, "Finite Element Approaches with the Aid of Analytical Solutions," Recent Advances on Matrix Methods of Structural Analysis and Design, Univ. of Alabama Press, 1971, 85-103.
9. Y. Yamamoto and N. Tokuda, "Determination of Stress Intensity Factors in Cracked Plates by the Finite Element Method," Int. J. for Numer. Meth. in Engng., 6, 3, 1973,

427-439.

10. T. F. Ogilvie and E. O. Tuck, A Rational Strip Theory of Ship Motions: Part I, Univ. of Michigan, Dept. of Naval Architecture and Marine Engng., Report No. 013, 1979.

11. O. Faltinsen, "Wave Forces on a Restrained Ship in Head-Sea Waves," 9th Symp. on Naval Hydrodynamics, 1972.

12. W. D. Kim, "On the Harmonic Oscillations of a Rigid Body on a Free Surface," J. Fluid Mech., 21, 3, 1965, 427-451.

13. J. V. Wehausen and E. V. Laiton, "Surface Waves," Handbuch der Physik, 9, Springer, 1960, 446-778.

14. P. Tong, "New Displacement Hybrid Finite Element Methods for Solid Continua," Int. J. for Numer. Meth. in Engng., 2, 1970, 73-83.

15. W. R. Porter, Pressure Distributions, Added Mass, and Damping Coefficients for Cylinders Oscillating in a Free Surface," Univ. of Calif., Berkeley, Inst. of Engng. Research Report, Series 82, Issue 16, 1960.

16. F. Tasai, "On the Damping Force and Added Mass of Ship's Heaving and Pitching," J. of Soc. of Naval Architects of Japan, 105, 1959, 47-56.

17. M. Ohkusu, "On the Motion of Multihull Ship in Waves," J. of Soc. of Naval Architects of West Japan, 40, 1970, 19-47.

18. T. H. Havelock, "Waves due to a Floating Sphere Making Periodic Heaving Oscillations," Proc. of Royal Soc. of London, Ser. A, 231, 1955, 1-7; The Collected Papers of Sir Thomas Havelock on Hydrodynamics, Office of Naval Research, ONR/ACR-103, 1963, 602-608.

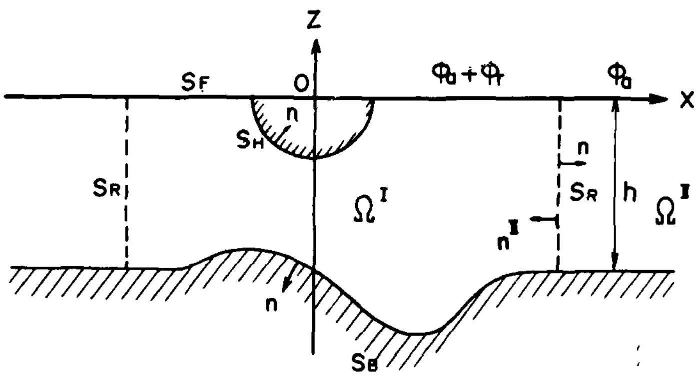

Fig. 1 Two-dimensional water field

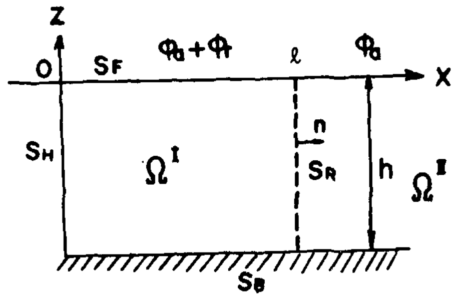

Fig. 2 Wave maker problem

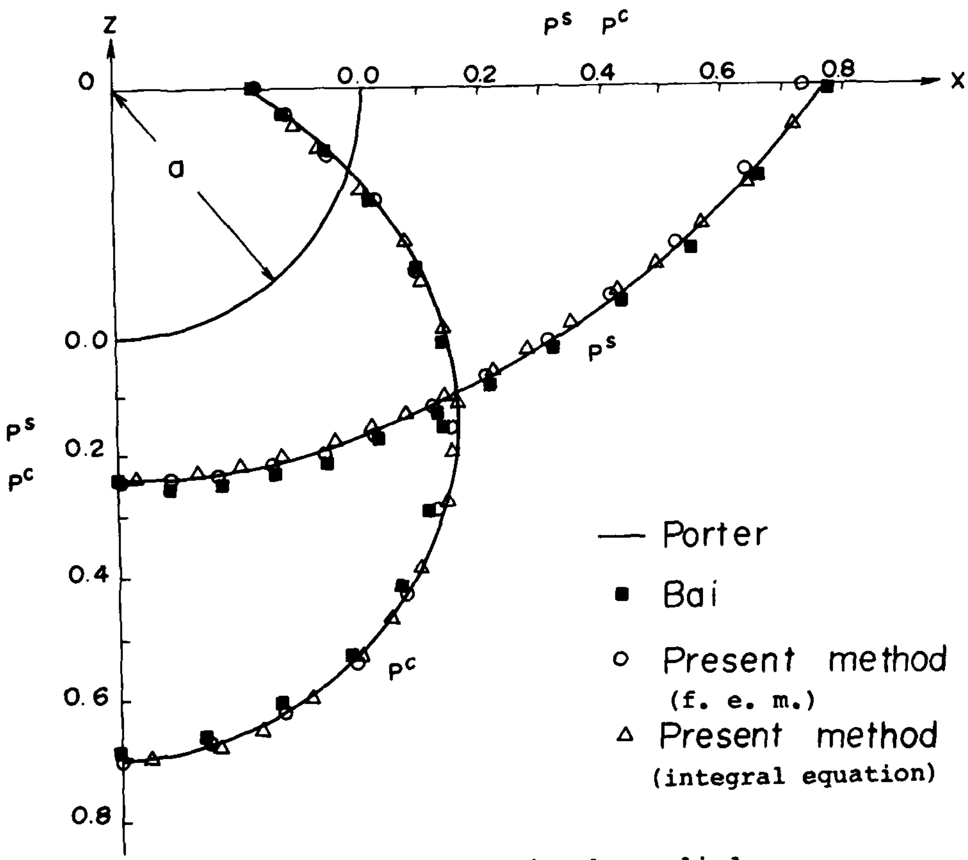

Fig. 3 Pressure on a circular cylinder
in heaving motion (K a = 1.0)

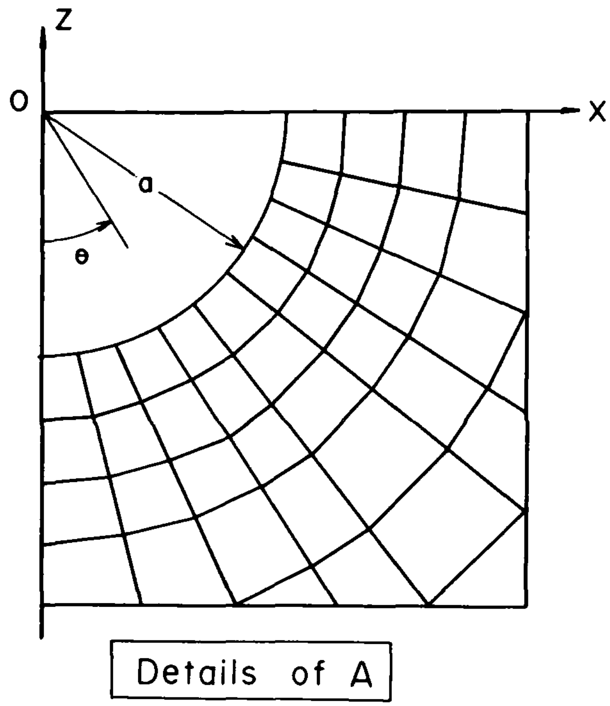

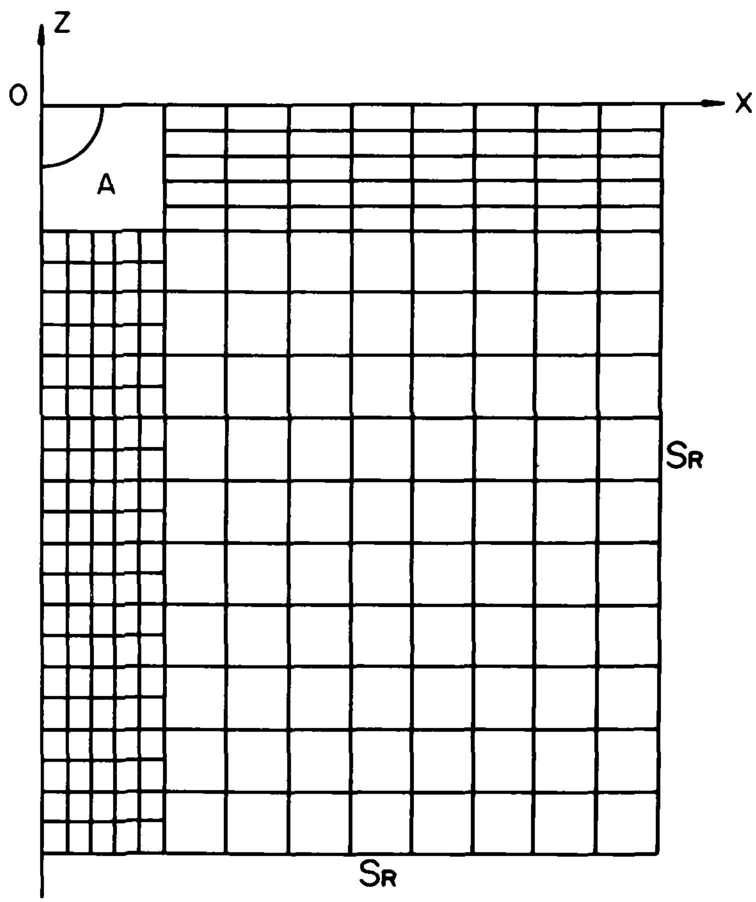

$v_n = -A\omega \cos\theta \sin\omega t$

Fig. 4 Mesh subdivision

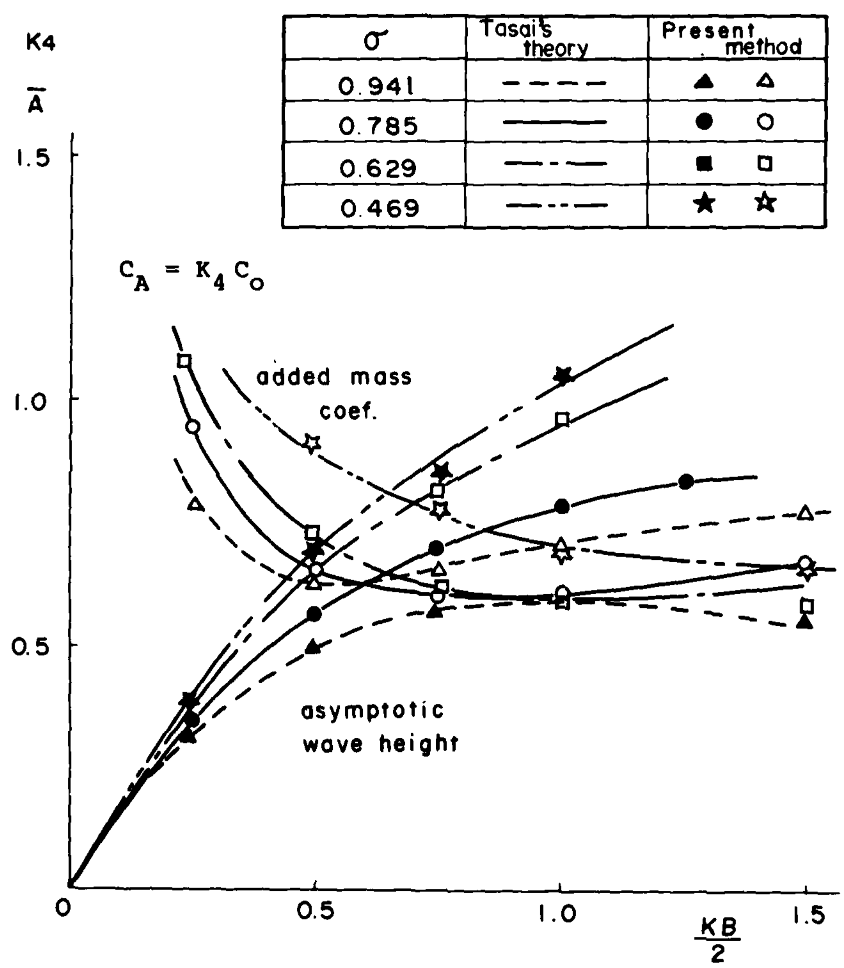

Fig. 5 Added mass coefficient and asymptotic wave height ratio of Lewis form cylinders due to heaving motion (B/T = 2)

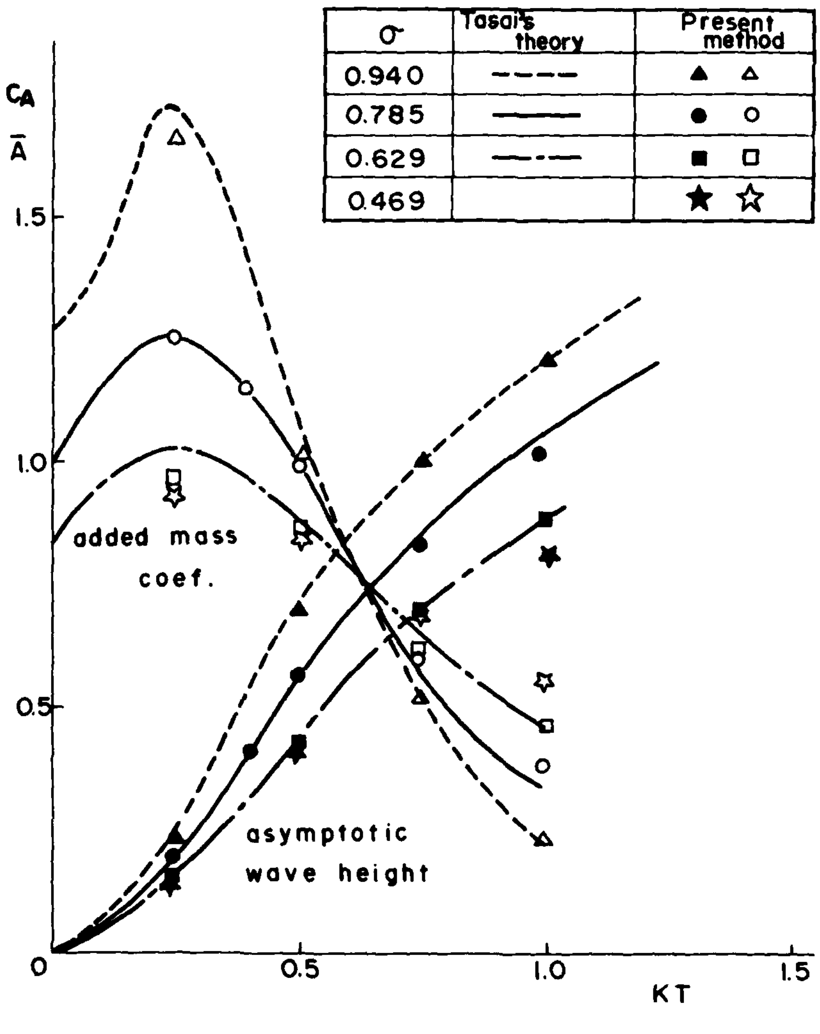

Fig. 6 Added mass coefficient and asymptotic wave height ratio of Lewis form cylinders due to swaying motion (B/T = 2)

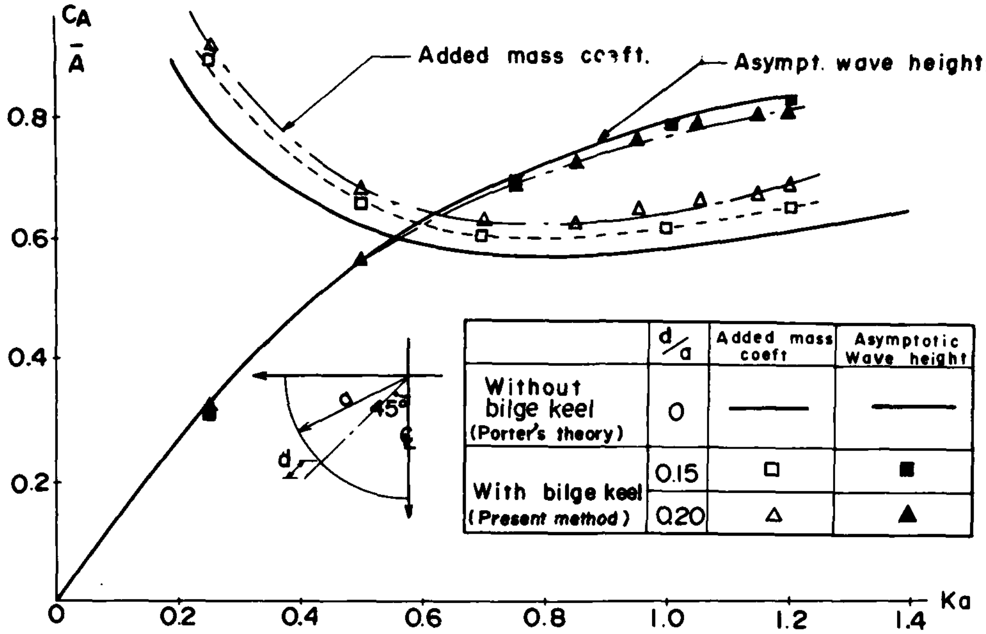

	d/a	Added mass coeft	Asymptotic Wave height
Without bilge keel (Porter's theory)	0	———	———
With bilge keel (Present method)	0.15	□	■
	0.20	△	▲

Fig. 7 Added mass coefficient and asymptotic wave height ratio for heaving circular cylinders with or without bilge keels (B/T = 2, σ = 0.785)

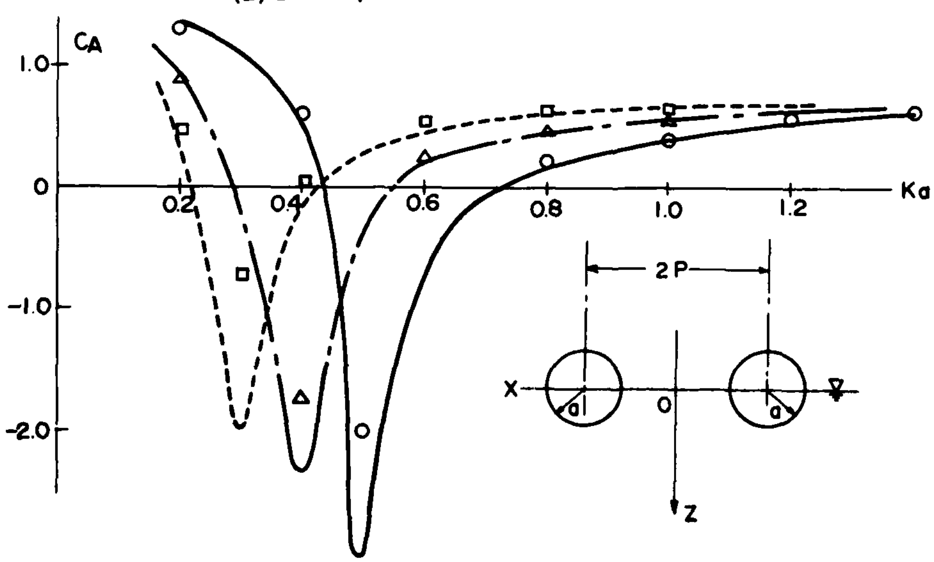

Fig. 8 Added mass coefficient for a pair of heaving circular cylinders

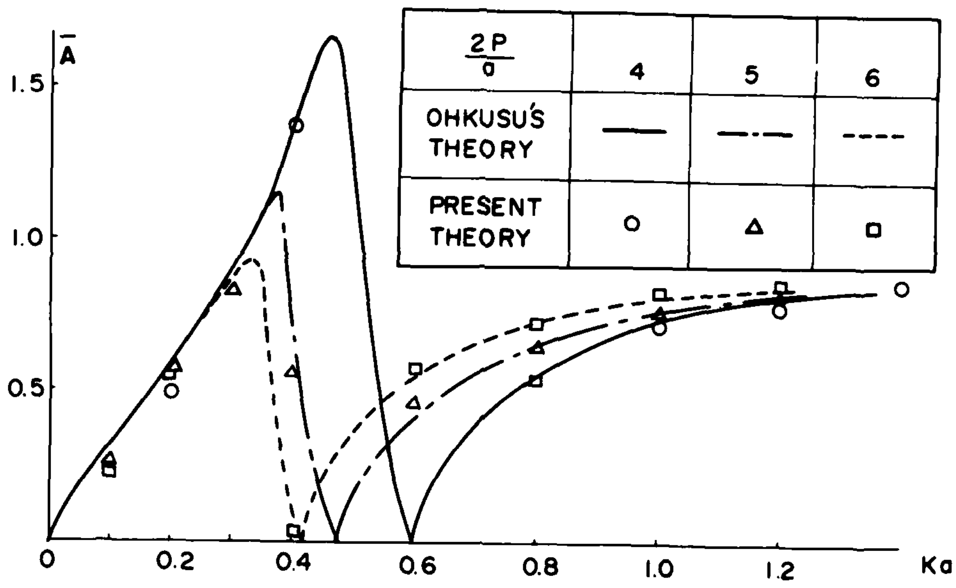

Fig. 9 Aymptotic wave height ratio for a pair of heaving circular cylinders

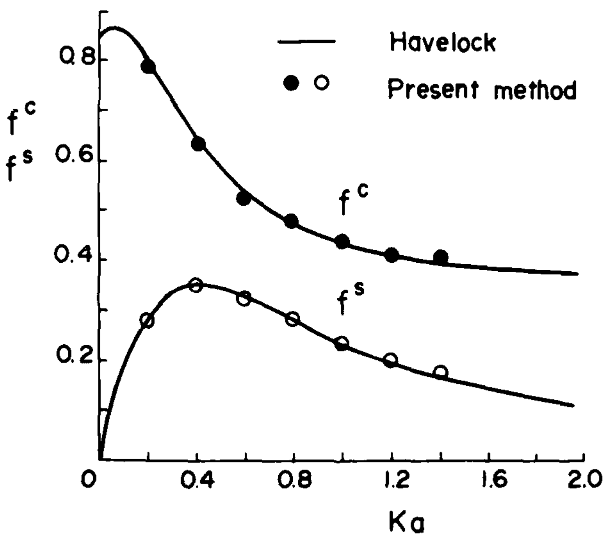

Fig. 10 Added mass coefficient and damping parameter for a heaving semi-immersed sphere

FREE-SURFACE LINEAR WATER-WAVE PROBLEMS BY THE FINITE ELEMENT METHOD

D. C. Tolefson
Deepsea Ventures, Gloucester Point, Va. 23062 U.S.A.
L. Boichot
Sun Shipbuilding, Chester, Pa. 19013 U.S.A.

ABSTRACT

A numerical procedure based on the finite element method for the solution of three-dimensional free-surface linear water-wave problems is presented. Both the time harmonic and time-independent cases are considered. Numerical results of some two-dimensional examples are presented and compare favorably with existing theoretical solutions. The details necessary to conduct three-dimensional analyses are discussed. Conclusions of the study are that the procedure has promise as a working tool for practical ship hydrodynamic investigations such as wave making resistance and ship motions.

1. Introduction

Analytical results for ship hydrodynamic problems such as wavemaking resistance, added resistance due to waves, and ship motions are virtually nonexistent except for cases where fairly restrictive assumptions regarding the body geometry are made. For example, practically all purely theoretical analyses require assumptions as to the thinness or slenderness of the ship or object under investigation. The work

reported in {1}*, for instance, is an example of some of the most current progress in ship wavemaking characteristics and the slenderness assumption is required in order to obtain results. In ship motion problems additional assumptions over and above the slenderness or thinness assumptions are also made. These usually concern the frequency of wave-encounter and the dimensionality of the flow, i.e. the flow is assumed to occur in transverse planes. The purpose of this paper is to present a method of analysis, using numerical procedures, which disposes of these restrictions. Specifically, general three-dimensional flow about an object of arbitrary size and shape is permitted as long as the flow disturbances are not too great to create large waves which would violate the linearized free-surface condition.

Examples validating the theoretical basis of the present method are given by means of two-dimensional cases with known solutions. Three-dimensional examples have not been completed yet, and, thus the economic and practical viability for actual ship forms can only be estimated at this time.

Previous work of other investigators bearing on the hydrodynamics of actual ship forms has been reported in the literature. All of these bear heavily on numerical methods, as does the present method. Perhaps the work of Adee {2} and that of Gadd {3} are representative of the state-of-the-art. In {2}, theoretical wave-making resistance of a series 60, Block 70 ship form is calculated by means of a brute-force numerical quadrature evaluation of Havelock or Kelvin integrals. In {3}, application of Guilloton's method for calculating wavemaking resistance is demonstrated and compared to experimental data with favorable results. The latter procedure is made practical by computer usage and it

*Numbers in brackets refer to references listed at the back.

appears to be attractive in cost since some computer runs can be accomplished for less than $200 {4}. The advantage that the present method may have over the above alternatives is that this method, in all its essential aspects, can be applied with about equal ease to either steady or time-harmonic problems. For example, once the geometry of a ship hull is input, both its wavemaking characteristics and its response to waves can be calculated automatically from the same basic information within one computer program.

Finite element applications in water wave problems have also been given in the literature. For example, references {5} and {6} use the finite element method in time-harmonic problems involving forced-motion and diffraction of waves. To the best of our knowledge steady problems characterized by an object moving on or near the free surface of a fluid have not been treated by the finite element method. The apparent reason for this is that previous finite element investigations have been based on variational formulations which have not, as far as is known, been discovered for the steady problem. This obstacle is obviated herein by using the process of weighted residuals to develop the ground work of the theory. Once the problem is so formulated, the finite element concept is subsequently introduced to find solutions.

2. Governing Equations

The mathematical analysis which will be employed requires that the fluid domain be terminated at some finite distance away from the object of interest in order to limit the number of calculations. An imaginary surface in the form of a vertical cylinder enclosing the object will suffice at this stage of the development. Some statement consistent with the physics of the problem at hand must be made, of course, concerning the fluid behavior along this surface. As it is more convenient to do this at latter stages of the

development the following will concentrate on the other remaining aspects of the derivation.

Consider Cartesian axes (x,y,z) fixed in space with the origin on the undisturbed free-surface of the fluid. The y-direction is positive in the direction opposite to gravity.

For an ideal fluid undergoing irrotational motion the linearized governing equations are

$$\nabla^2 \Phi (x,y,z,t) = 0 \qquad \text{in the fluid} \quad (1)$$

$$\Phi_{tt}(x,o,z,t) + g\Phi_y(x,o,z,t) = 0 \qquad \text{on the free surface} \quad (2)$$

$$\Phi_n = V_n \qquad \text{on the solid boundaries} \quad (3)$$

where Φ is the velocity potential whose positive gradient gives the velocity vector. V_n is the normal velocity of the solid boundaries. A subscript x,y,z,t or n on Φ indicates partial differentiation with respect to that subscript. n denotes the outward normal direction. The equation of the free-surface elevation, η is

$$\eta = -\frac{1}{g} \Phi_t \ (x,o,z,t) \qquad (4)$$

For the case of an object translating at constant speed c through a previously undisturbed fluid, the motion becomes steady in a reference frame moving with the object. Then, in this frame, equations (1) - (4) become

$$\nabla^2 \Phi(x,y,z) = 0 \qquad (5)$$

$$\Phi_y(x,o,z) + \frac{c^2}{g} \Phi_{xx}(x,o,z) = 0 \qquad (6)$$

$$\Phi_n = 0 \qquad (7)$$

$$\eta = \frac{c}{g} \Phi_x \ (x,o,z) \qquad (8)$$

These equations assume that the object is moving along the x-axis in the positive direction.

In the case of time-harmonic fluid motion, such as that which results from forced harmonic motion of a solid object,

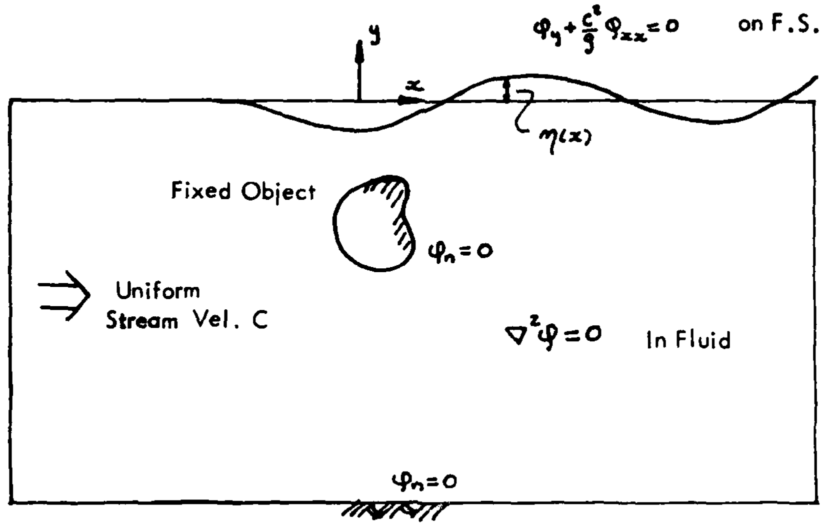

(a) STEADY CASE

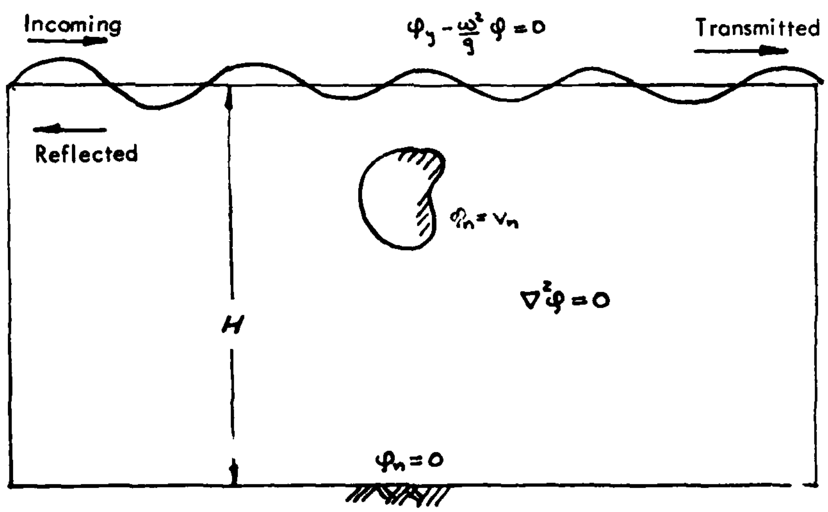

(b) HARMONIC CASE

FIGURE 1. SCHEMATIC AND DEFINITIONS

for example, the time element can be factored out of the problem. This is done easily by introducing complex-variable methods. In this case let

$$\Phi = \mathbf{Re}\{\phi(x,y,z)e^{i\omega t}\} \tag{9}$$

where $\phi(x,y,z)$ is complex, ω is the frequency of motion, i is the imaginary unit, and Re denotes the real part of a complex variable. With this substitution equations (1)-(4) become

$$\nabla^2\phi(x,y,z) = 0 \qquad \text{in the fluid} \tag{10}$$

$$\phi(x,o,z) - \frac{g}{\omega^2}\,\phi_y(x,o,z) = 0 \qquad \text{on the free-surface} \tag{11}$$

$$\phi_n = v_n \qquad \text{on solid boundaries} \tag{12}$$

$$\eta = \mathrm{Re}\{-\frac{i\omega}{g}\,\phi(x,o,z)e^{i\omega t}\} \tag{13}$$

where the normal velocity of the solid boundaries is $Vn = \mathrm{Re}\{v_n e^{i\omega t}\}$.

The formulation of the governing equations is complete with the exception of some statement concerning the fluid behavior at the imaginary control surface and, in addition, some comment on bottom effects. The ensuing development will eventually address these points.

3. Finite Element Formulation

A brief outline of the procedure will be given. See reference (7) for details, especially Chapter 3.

The fluid domain is divided into a grid of finite elements, see Figure (2) for instance. The elements are fixed in space i.e. they are non-material quantities through which the fluid moves. The intersections of the grid elements are referred to as node points. Within each element we approximate the potential as

$$\Phi(x,y,z) = \sum_{i=1}^{m} N_i(x,y,z)\;\Phi_i \tag{14}$$

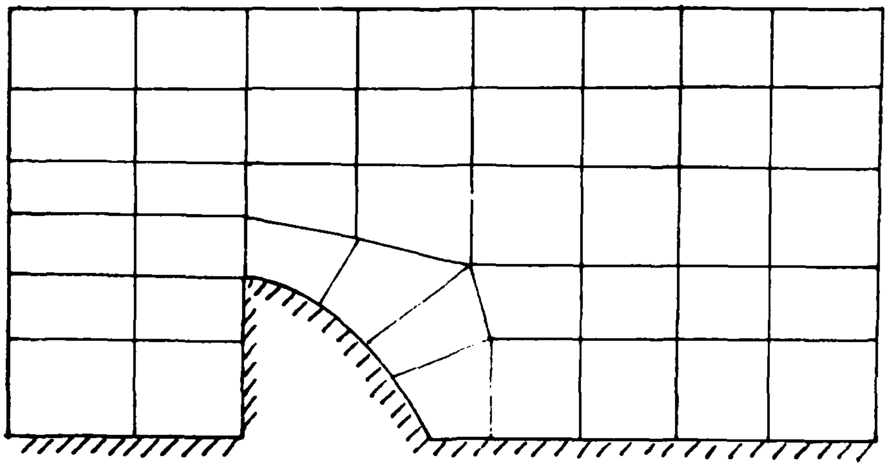

FIGURE 2 (a). SUBDIVISION OF FLUID INTO ELEMENTS

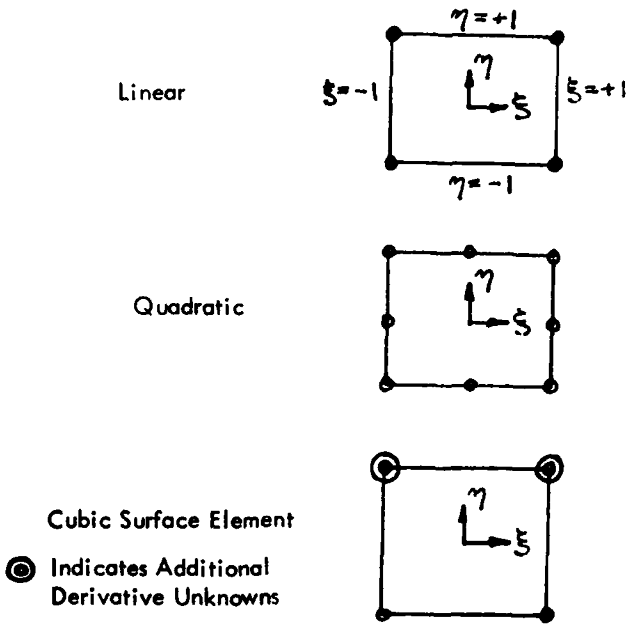

FIGURE 2 (b). ELEMENTS USED IN ANALYSIS

Φ_i are the nodal values of Φ, i is the node number, and m is the number of nodes per element. N_i are the shape functions which prescribe the (assumed) variation of Φ within the element. See the appendix for specific examples of these.

Using the process of weighted residuals with weighting function N_i, the equations to be formulated for each element are

$$\int_V N_i \{\Phi_{xx} + \Phi_{yy} + \Phi_{zz}\} \, dxdydz = 0 \tag{15}$$

over the element volume V. This integral means Laplace's equation is satisfied throughout the element in some mean sense. Integrating by parts we obtain

$$\int_V \{N_{ix}\Phi_x + N_{iy}\Phi_y + N_{iz}\Phi_z\} dxdydz - \int_S N_i\Phi_n dS = 0 \tag{16}$$

The second integral is over the boundary S of the element.

Substituting the finite element approximation (14) into the first integral of (16) yields equations of the type

$$k_{ij}\Phi_j - \int_S N_i\Phi_n \, dS = 0 \qquad \text{(sum on j, i=1,m)} \tag{17}$$

where the element "stiffness" is defined as

$$k_{ij} = \int_V \{N_{ix}N_{jx} + N_{iy}N_{jy} + N_{iz}N_{jz}\} \, dxdydz \tag{18}$$

When summing contributions from all the elements by the usual finite element procedure, the integral appearing explicitly in (17) does not contribute anything at the internal node points since the contribution from one element is cancelled by the adjacent element. Thus the integral term needs to be considered only at the external or surface nodes. For a finite depth fluid $\Phi_n = 0$ on the bottom and consequently the integral term vanishes here. Further, for an infinite depth region we can approximate Φ_n as zero at a

suitable depth below the free surface, dependent on the length of the surface waves. On a fixed object the integral vanishes since, here, $\Phi_n=0$ also. For objects undergoing specified motion $\Phi_n=v_n$ is known on the body and the integral can be evaluated. On the free-surface a different approach is required. First the normal derivative in the integral is replaced by the derivative with respect to y. This is justified in linear theory since all flow variables are evaluated on the mean position of the (flat) free-surface, y=0. Hence, for elements forming the free surface of the fluid, the substitution $\Phi_n=\Phi_y$ is made in (17).

For the harmonic case, in which ϕ is substituted for Φ in the previous development, $\phi_y= \frac{\omega^2}{g}\phi$ from (11). Using the interpolating function (14), the integral in (17) becomes a linear combination of the ϕ_i terms and it can be combined with k_{ij} to get (superscript h stands for harmonic)

$$k^h_{ij}\ \phi_j = 0 \qquad \text{(sum on } j,i = 1,m) \qquad (19)$$

In this case the stiffness for the "harmonic" surface element is

$$k^h_{ij} = \int_V \{N_{ix}N_{jx}+N_{iy}N_{jy}+N_{iz}N_{jz}\}\ dxdydz\ -\frac{\omega^2}{g}\int_S N_iN_j dS \quad (20)$$

The matrix of the k_{ij} terms is symmetric.

For the steady case $\Phi_y= -\frac{c^2}{g}\Phi_{xx}$ from (6). Using the interpolating function we get an expression for Φ_{xx} within an element, viz.

$$\Phi_{xx} = \sum_{i=1}^{m} N_{ixx}\ \Phi_i \qquad (21)$$

Substituting this into the boundary integral of (17) we arrive at (superscript s means steady case)

$$k^s_{ij}\ \Phi_j = 0 \qquad \text{(sum on } j,i = 1,m) \qquad (22)$$

where the stiffness for the steady case surface element is

$$k_{ij}^{s} = k_{ij} + \frac{c^2}{g} \int_S N_i \sum_{j=1}^{m} N_{jxx} dS \qquad (23)$$

The matrix of k_{ij} terms in this case is, in general, unsymmetric. However, in the special case where the functions, N_{ix}, are continuous across element boundaries the assembled stiffness matrix becomes symmetric. This can be seen by integrating by parts in (23). Further, this special continuity requirement is highly desirable for it is one of several conditions which ensure convergence with grid refinement.*

The remaining boundary conditions are those along the truncated boundaries. At this point our discussion will be limited to the two-dimensional case in order to simplify the presentation. The three-dimensional case will be outlined later.

4. Steady Case

We take the time-independent case first and consider the problem of an object fixed in a finite depth channel with constant and uniform flow velocity, c, upstream (see Figure 1a). This problem, of course, is equivalent to the case where the object is translating through the fluid at constant speed c and the frame of reference is attached to the body.

The condition of uniform flow upstream of the body is

$$\Phi = cx \qquad (x = -\infty) \qquad (24)$$

and therefore, for later reference,

$$\Phi_x = c \qquad (x = -\infty) \qquad (25)$$

* See Reference (7), page 35, for a discussion of these conditions.

As x approaches $+\infty$, we require the fluid motion to take the form of a non-progressing free-wave on a running stream. In this case we have (where H is the depth of the stream)

$$\Phi = A \cosh k\ (y+H) \cos\ (kX+\delta) + cx + d \qquad (26)$$

where d accounts for stream blockage. It follows that

$$\Phi_x = -Ak \cosh k(y+H) \sin\ (kX+\delta) + c \qquad (27)$$

A, δ and d are unknown constants and k must be a root of

$$\frac{gH}{c^2} \tanh kH - kH = 0 \qquad (28)$$

in order that Φ will satisfy the free-surface condition(6).

For the numerical solution we will truncate the fluid domain with vertical boundaries far enough removed from the source of the disturbance *so that the infinity conditions* can be applied there with negligible error. It appears, based upon a few test cases, that this distance need not be much more than one wavelength downstream of the disturbance and less than one wavelength upstream for the range of parameters used in this example.

On the upstream boundary we choose to prescribe $\Phi=cx$. In this case certain of the equations (17) are not used, namely the ones corresponding to nodes which lie along this boundary. On the downstream boundary we prescribe Φ_n. It is equal to Φ_x which we know from (27) in terms of A and δ. Substituting this into (17) and using some elementary trigonometric formulae gives the integral term in the form

$$\int_S N_i \Phi_n dS = (A \cos\ \delta)\ D_i + (A \sin\ \delta)E_i + F_i \qquad (29)$$

D_i, E_i, F_i, are the known results of integrations along the sides of the elements which lie on the boundary. These terms

are transposed to the right hand side of (17).

The finite element assembly of the elements results in a master set of equations of the form,

$$[k]\{\Phi\} = \{\alpha\} + A\cos\delta\{\beta\} + A\sin\delta\{\gamma\} \tag{30}$$

where the curly brackets indicate column matrixes, $[k]$ is the matrix of the assembled element stiffnesses, $\{\Phi\}$ contains unknown nodal values of the potential and $\{\alpha\}$, $\{\beta\}$, $\{\gamma\}$, all have only known elements. Appending to this set of equations condition (25) evaluated at an arbitrary node along $x = -\infty$ and (26) at two nodes at $x = +\infty$, yields a system of (N+3) equations in the unknowns ϕ_i (say, N, in number), $A\cos\delta$, $A\sin\delta$ and d. In order to take advantage of the banded* and symmetric nature of $[k]$ the actual solution consists of solving (30) repeatedly, each time with a different right-hand side, ignoring the factors $A\cos\delta$ and $B\sin\delta$. We get

$$\{\Phi\} = \{\Phi_I\} + A\cos\delta\{\Phi_{II}\} + A\sin\delta\{\Phi_{III}\} \tag{31}$$

where $k\{\Phi_I\} = \{\alpha\}$ and so forth. Except for the two unknowns, $A\cos\delta$ and $A\sin\delta$, (31) represents the desired solution. Selecting two arbitrary nodal points on the downstream boundary we apply (31) and equate it to (26), yielding two equations in unknowns $A\cos\delta$, $A\sin\delta$ and d. Similarly, on the upstream boundary the x-derivative of Φ is formed using (31). This is equated to (25), thereby yielding the required third equation. Thus the solution in its essentials is complete. Physical quantities such as pressure and velocity can be found by differentiating (14) and applying appropriate formulaes.

5. Time-Harmonic Case

We have the following development typifying problem solutions for the time-harmonic case. Referring to Figure (1-b)

* Judicious node numbering in most cases gives a narrow bandwidth.

there is a progressive wave incoming from the left which, upon meeting the fixed object, sets up both a reflected and transmitted wave disturbance, each with unknown amplitude and phase with respect to the original wave. Hence, the resultant velocity potential Φ to the far left is

$$\Phi = \text{Re}\ \{(\bar{\phi} + \phi_R)e^{i\omega t}\} \qquad (x = -\infty) \tag{32}$$

where the potential $\bar{\phi}$ of the incident wave (of assumed unit amplitude) is

$$\bar{\phi} = \frac{g}{\omega}\ \frac{\cosh k(y+H)}{\cosh kH}\ e^{-ikx} \tag{33}$$

and the potential ϕ_R of the reflected wave is

$$\phi_R = \frac{\rho g}{\omega}\ \frac{\cosh k\ (y+H)}{\cosh kH} e^{i(kX+\delta)} \tag{34}$$

ρ and δ are the unknown amplitude and phase angle of the reflected disturbance. Similarily, to the far right,

$$\Phi = \text{Re}\ \{(\bar{\phi} + \phi_T)e^{i\omega t}\} \qquad (x = +\infty\ ) \tag{35}$$

where

$$\phi_T = \frac{\tau g}{\omega}\ \frac{\cosh k(y+H)}{\cosh kH}\ e^{-i(kx-\varepsilon)} \tag{36}$$

in which τ and ε are the unknown amplitude and phase angle of the disturbance, ϕ_T, created by and transmitted across the barrier.

The final equations to be solved are given by (17) except that the potential function ϕ is composed of both real and imaginary parts, say ϕ_1 and ϕ_2. It is instructive to carry the details of the analysis slightly further so that the coupling between the left-and right-hand boundaries can be seen.

The equations for ϕ_1 and ϕ_2 reduce to

$$k^h_{ij}\ \phi_{1j} = b_{1i} \qquad \text{(sum on } j, i=1,m) \tag{37}$$

and

$$k_{ij}^{h}\ \phi_{2j} = b_{2i} \qquad \text{(sum on } j,i = 1,m) \qquad (38)$$

where $b_{1i} = b_{2i} = 0$ except for values of i corresponding to nodes lying along the boundaries at $x = \pm\infty$. The matrix coefficients k_{ij}^{h} for ϕ_1 and ϕ_2 are identical. These are given by (18) except for nodes on the free-surface in which case (20) applies. Right-hand side members b_{1i} are,

$$b_{1i} = \frac{gk}{\omega}\ \frac{\cosh k(y+H)}{\cosh kH}\ \{\int_{x=-\infty} N_i(-\frac{\partial}{\partial x})(\cos kx + (\rho \cos \delta) \cos kx$$

$$-(\rho \sin \delta) \sin k x)\, dy + \int_{x=+\infty} N_i(\frac{\partial}{\partial x})(\cos kx + (\tau \cos \varepsilon) \cos kx$$

$$+ (\tau \sin \varepsilon) \sin kx)dy\} \qquad (39)$$

with a similar lengthy expression for b_{2i}.

After the integrations in b_{1i} (and b_{2i}) are conducted and the final equations are assembled, (37) and (38) reduce to,

$$[k]\ \{\phi_1\} = \{d\} + \rho \cos \delta\{e\} + \rho \sin \delta\ \{f\}$$

$$+ \tau \cos \varepsilon\ \{g\} + \tau \sin \varepsilon\{h\} \qquad (40)$$

and

$$[k]\{\phi_2\} = \{d'\} + \rho \cos \delta\{e'\} + \rho \sin \delta\{f'\}$$

$$+ \tau \cos \varepsilon\ \{g'\} + \tau \sin \varepsilon\ \{h'\}, \qquad (41)$$

respectively. The matrix elements d, d', e, etc. are all known numerically. As in the steady case, the above equations are solved repeatedly, each time with a different right-

hand side. Thus,

$$\phi_1 = \phi_{1I} + \rho \cos \delta \, \phi_{1II} + \rho \sin \delta \, \phi_{1III}$$

$$+ \tau \cos \varepsilon \, \phi_{1IV} + \tau \sin \varepsilon \, \phi_{1V} \tag{42}$$

where ϕ_{1I} is the solution of

$$\{k\} \, \phi_{1I} = \{d\}, \tag{43}$$

ϕ_{1II} is the solution of

$$\{k\} \, \phi_{1II} = \{e\}, \text{ etc.} \tag{44}$$

and a similar expression applies to ϕ_2.

It now remains to determine the four groups of parameters $\rho \cos \delta$, $\rho \sin \delta$, $\tau \cos \varepsilon$, and $\tau \sin \varepsilon$. This is done by equating (42) and a similar expression for ϕ_2 to the real and imaginary parts, respectively, of the term $(\bar{\phi} + \phi_R)$ in (32) at an arbitrary node point along $x = -\infty$. This yields two equations. Repeating this operation at $x = +\infty$ but using the term $(\bar{\phi} + \phi_T)$ in (35) gives two more algebraic equations, thus, providing the necessary four equations to be solved simultaneously. In essence this completes the solution.

Transmission and reflection coefficients, wave forces and profiles, etc. are easily found by application of their corresponding expressions involving ϕ and the parameters $\rho \cos \delta$, etc. For instance, the reflection and transmission coefficients, R and T, respectively, are found directly from

$$R = \rho = \sqrt{(\rho \cos \delta)^2 + (\rho \sin \delta)^2}$$

and

$$T = \sqrt{1 + \tau^2 + 2\tau \cos \varepsilon}$$

6. Exa ie Problems

Examples for the harmonic problems and the accuracy attainable can be found in {5} and {8} where the method is similar. We show an additional result in Figure (3), a wave incident upon a vertical barrier. The incoming wave is moving from left to right. In this case eight node quadratic elements were used. See the appendix for the shape functions for the element. The grid pattern was composed of square elements of side 1 unit. The results compared to the analytical solution of Mei and Black {9} are indicated on the figure. It was found in problems of this type that the quadratic element required a grid size of at least eight elements per wave length for good accuracy.

For the time independent problem a few cases with simple geometry were chosen as demonstration problems. In all cases the finite element grid was composed entirely of square elements of side .5 units. The elements were linear elements except for the elements bounding the surface where a special surface element was used. This element has a Hermitian interpolation along the side representing the free surface (see Appendix and Section 3). The use of the derivative as a nodal unknown automatically ensures continuous first derivatives along the free-surface.

There are no theoretical solutions for these problems, however, Gazdar {10} presents a theoretical solution for a Rankine type body on the bottom of a running stream and a comparison of sorts can be made between the long rectangular block of our example and the long Rankine ovoid in {10}.

Figure (4) shows the wave profiles obtained for a .5x4 rectangular block fixed in an eight unit deep channel flowing from left to right. The parameter c^2/gH is equal to .239. The profiles show the effect of locating the object at different depths. Curve 1 is for the object fixed in the bottom and curve 2 for the object fixed at mid-depth. For clarity, the wave height η is plotted to a scale fives time greater than

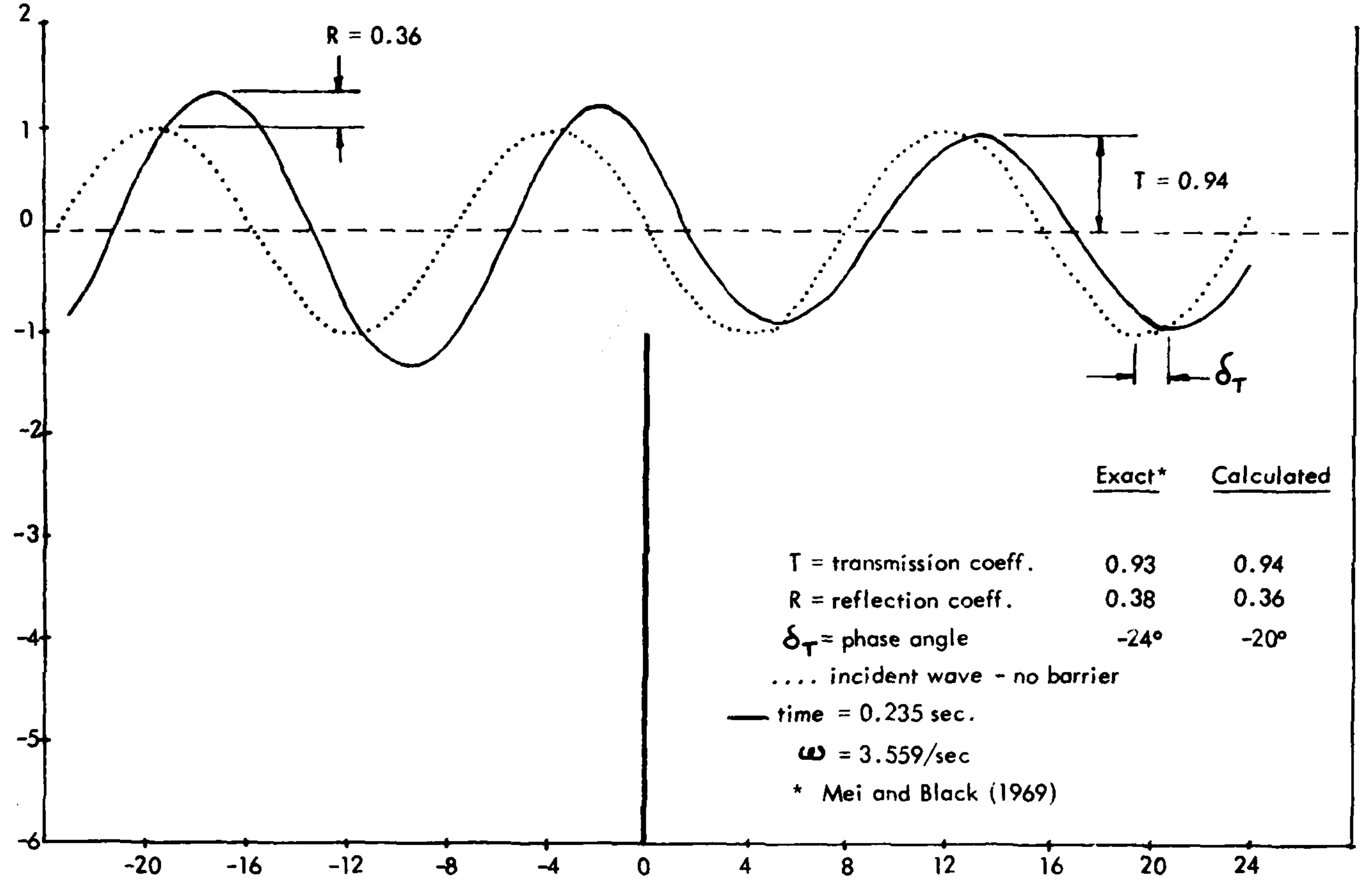

FIGURE 3. WAVE INCIDENT UPON THIN PLATE BARRIER

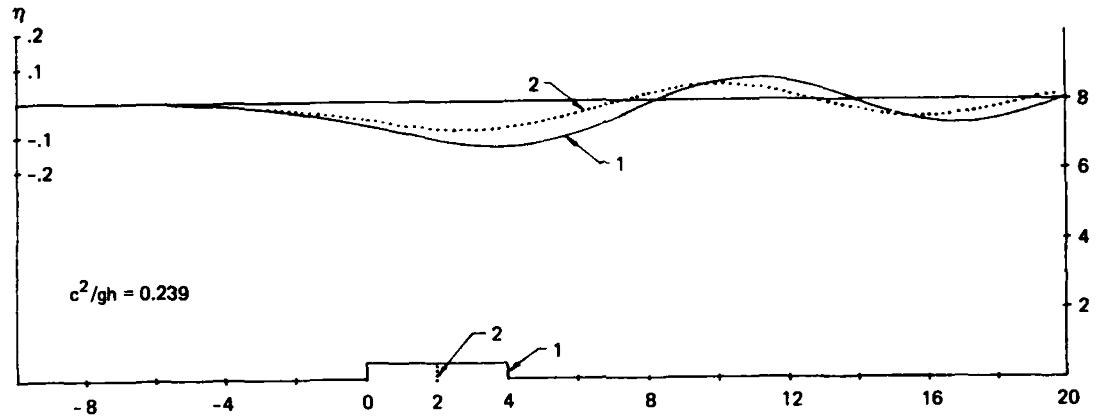

FIGURE 5. EFFECT OF LENGTH OF OBSTACLE

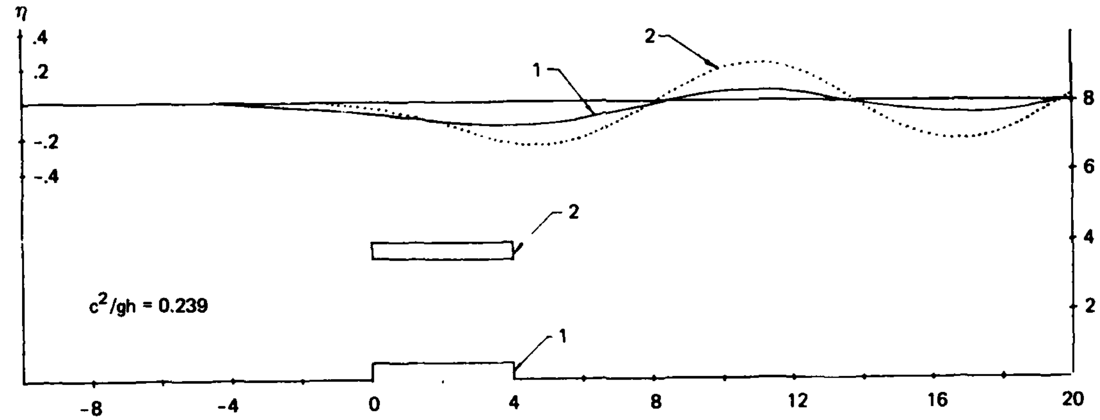

FIGURE 4. EFFECT OF SUBMERGENCE DEPTH OF OBSTACLE

the rest of the figure. The downstream wave height is .067. Gazdar's results for a long ovoid of around the same length and height is a wave height of .051 for very large x.

The effect of decreasing the length of a rectangular block fixed on the bottom of a channel is shown in Figure (5). The scale for the wave height is ten times greater than the rest of the figure. c^2/gH is again .239.

An interesting case is shown in Figure (6). It is again the same .5x4 block, but the stream velocity is lowered such that c^2/gH is .0635. Note again the increase in scale for η At this critical velocity there is no wave-like motion. This case of destructive interference is obtained in {10} when the wavelength of the free wave is equal to the distance between the source and sink of the Rankine ovoid. In our example the ratio of wave length to length of object is .8.

These examples illustrate the types of parametric studies that can be easily done with the finite element method. Automatic mesh generation was used. These problems involved the solving of around 1000 simultaneous linear equations. A Honeywell 6030 using single precision required less than a minute of cp time. Decreasing the mesh size indicated the original mesh size gave a convergent numerical solution.

7. Discussion and Conclusions

A method for the finite element solution of linear free-surface water-wave problems for both the steady and time-harmonic cases has been presented. It consists essentially in truncating the fluid domain at sections where the so-called infinity conditions can be applied, then adjusting the finite element solution to satisfy the infinity conditions for the potential and its normal derivative at the truncated boundaries.

Although only rectangular elements were used in the examples presented, triangular or curved elements needed to represent irregular shaped objects are obtainable in the literature.

AD-A119 315 DAVID W TAYLOR NAVAL SHIP RESEARCH AND DEVELOPMENT CE--ETC F/G 20/4
FIRST INTERNATIONAL CONFERENCE ON NUMERICAL SHIP HYDRODYNAMICS --ETC(U)
1975 J W SCHOT, N SALVESEN

UNCLASSIFIED NL

2 OF 8
AD A
119315

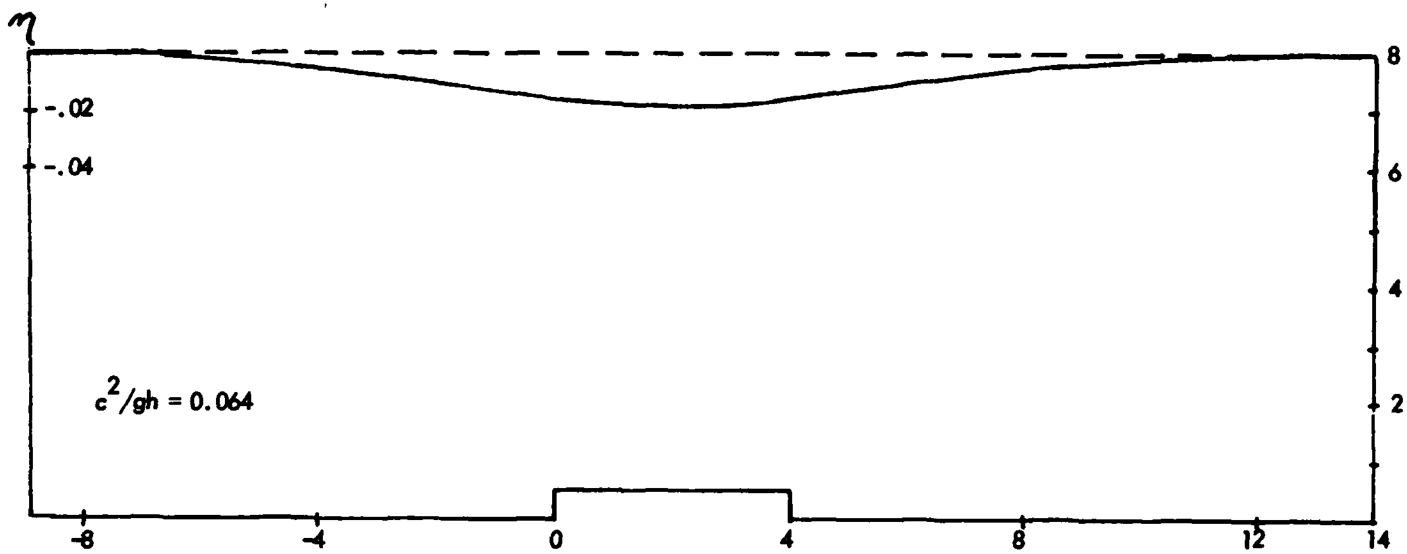

FIGURE 6. DESTRUCTIVE INTERFERENCE

The results for the harmonic problem are quantitatively correct. The results presented for the steady problems are qualitatively correct and agree reasonably with similar examples with analytic solutions. The applicability of the finite element method to steady free-surface flows has been demonstrated.

Three-dimensional problems are treated in identical fashion to the two-dimensional cases described above. Although the principles are identical, in actual practice, however, the effort will be many times as great. Two main reasons are behind this. First, the fluid region to be modeled is, in general, irregularly shaped and it fills three-dimensional space between the object and an imaginary control surface located somewhere in the vicinity of the far-field. Thus it is almost mandatory to have automatic means of generating elements. Because of the existence of computer codes primarily in structural analysis fields which do this, this barrier is practically removed. Even though, it must be born in mind that a system of equations numbering in the thousands will be required to be solved. But, again, existing structural analysis codes now do this routinely and efficiently.

The second reason concerns the far-field analytical expression for the velocity potential. Considering the steady case in three-dimensions it can be written most simply, perhaps, as {11},

$$\Phi = \int_0^{\pi/2} f(\theta) e^{k_o z \sec^2\theta} \cos(k_o X \sec\theta) \cos(k_o y \sin\theta \sec^2\theta) \cos\theta d\theta$$

where $f(\theta)$ is a wave amplitude function and $k_o = g/c^2$, g being the gravity constant. This equation is formulated by the superposition of plane waves advancing at angles θ with respect to X, the direction in which the object is traveling. By expanding $f(\theta)$ into a Fourier series Φ can be expressed in terms of the Fourier coefficients. This is analogous to (26)

in the previous development, but in this case it is apparent that the calculational effort is many times greater, due primarily to the highly oscillatory nature of the integrand. Fortunately, for sufficiently large distances from the object asymptotic approximations to ξ and its normal derivative can easily be developed by the method of stationary phase {12} which would considerably reduce the number of calculations. Using this idea, and a conveniently shaped fluid control surface such as a wedge, it would seem that three-dimensional hydrodynamic analyses are at hand.

8. Acknowledgement

This work was conducted while the authors were employed by Newport News Shipbuilding and Dry Dock Co. Their support is gratefully appreciated.

References

{1} Reed, Arthur, "Wavemaking; A Low-Speed Slender BodyTheory", Univ. of Michigan, Ph.D. Thesis (1975).

{2} Adee, Bruce H., "Calculation of the Streamlines About A Ship Assuming A Linearized Free-Surface Boundary Condition", Journal of Ship Research, Vol. 17, No. 3, September, 1973.

{3} Gadd, G. E., "Wave Resistance Calculations By Guilloton's Method", RINA Journal, 1973.

{4} Private Communication.

{5} Bai, K. J., "A Variational Method in Potential Flows With A Free-Surface", Univ. of California, Berkeley, Report No. NA-72-2, September, 1972.

{6} Chen, H. S., and Mei, C. C. "Oscillations and Wave Forces in A Man-Made Harbor In The Open Sea", 10th Symposium in Naval Hydrodynamics, 1974, Office of Naval Research.

{7} Zienkiewicz, D. C., "The Finite Element Method In Engineering Science", McGraw-Hill, New York, 1971.

{8} Bai, K. J., and Yeung, R. W., "Numerical Solutions To Free-Surface Flow Problems", Symposium in Naval Hydrodynamics, 1974, Office of Naval Research.

{9} Mei, C. C., and Black, J. L., "Scattering of Surface Waves By Rectangular Obstacles In Waters Of Finite Depth", Journal of Fluid Mechanics, Vol. 38 (1969), p. 499-511.

{10} Gazdar, A. S., "Generation of Waves of Small Amplitude by An Obstacle Placed On The Bottom Of A Running Stream", Journal of the Physical Society of Japan, Vol. 34, No. 2, February, 1973.

{11} Havelock, T. H., "The Calculation of Wave Resistance" from the Collected Papers of Sir Thomas Havelock on Hydrodynamics, p. 391 (1963).

{12} Stoker, J. J., Water Waves, The Mathematical Theory with Applications, Interscience Publishers, Inc., New York, (1957).

Appendix: Shape Functions For Elements

The interpolation or shape functions that were used in the the analysis are presented here. The elements used are the so called isoparametric elements. See Zienkiewicz {7} for further details such as the numerical integration techniques required. The shape functions are given in terms of local coordinates, ξ, η. ξ_i stands for the value of ξ at the i^{th} coordinate, i.e. either +1 or -1. Similarly for η_i. Refer to Figure (2).

Linear Element:

$$N_i = 1/4(1+\xi\xi_i)(1+\eta\eta_i) \qquad \text{Corner Nodes}$$

Quadratic:

$$N_i = 1/4(1+\xi\xi_i)(1+\eta\eta_i)(\xi\xi_i+\eta\eta_i-1) \qquad \text{Corner Nodes}$$

$$N_i = 1/2(1-\xi^2)(1+\eta\eta_i) \qquad \xi_i=0 \qquad \text{Midside Nodes}$$

$$N_i = 1/2(1-\eta^2)(1+\xi\xi_i) \qquad \eta_i=0 \qquad \text{Midside Nodes}$$

Cubic:

$$N_i = 1/4(1+\xi\xi_i)(1+\eta\eta_i) \qquad i = 1,2$$

$$N_i = 1/8(1+\xi\xi_i)^2(2-\xi\xi_i)(1+\eta\eta_i) \qquad i = 3,4$$

$$N_i = \frac{-a}{8}\,\xi_i(1+\xi\xi_i)^2(1-\xi\xi_i)(1+\eta\eta_i) \qquad i = 5,6$$

Here 1 and 2 refer to the corner nodes below the surface, 3 and 4 refer to the surface nodes and 5 and 6 refer to ϕ_x at the surface nodes. Recall $\phi = N_i\,\phi_i$. In this case $\phi_5 \equiv \phi_x$ evaluated at node point 3, and $\phi_6 \equiv \phi_x$ at point 4. a is the half-length of the element.

CALCULATIONS OF TWO-DIMENSIONAL SHIP WAVES BY A HYBRID ELEMENT METHOD BASED ON VARIATIONAL PRINCIPLES

H. S. Chen and C. C. Mei
Department of Civil Engineering
Massachusetts Institute of Technology
Cambridge, Massachusetts 02139 U.S.A.

ABSTRACT

By splitting the linearized two-dimensional ship wave problem into two fictitious problems (radiation of simple harmonic waves from the body and diffraction of simple harmonic waves by the body), one can use a hybrid element method (HEM) based on variational principles. Numerical examples are given for a circular cylinder in channels of different depths. Necessary modifications for sharp leading and trailing edges are discussed.

1. Introduction

Consider a cylinder submerged in an otherwise uniform flow with a free surface. When viscous and rotational effects are ignored, the linearized ship wave problem in two dimensions involves the solution of a velocity potential ϕ. Let the x-axis be in the mean free surface and the z-axis point vertically upwards. We denote by $U\,\vec{i}$ the velocity vector of the incoming uniform stream in the direction of the positive x-axis and define the velocity potential as the gradient of the disturbed velocity field

$$\vec{u} = U\,\vec{i} + \nabla\phi \tag{1.1}$$

Then ϕ must satisfy

$$\nabla^2\phi = \frac{\partial^2\phi}{\partial x^2} + \frac{\partial^2\phi}{\partial z^2} = 0 \tag{1.2}$$

and on the submerged body,

$$\frac{\partial\phi}{\partial n} = -\vec{U}\,\vec{i}\cdot\vec{n} \equiv V \qquad \text{on } B \tag{1.3}$$

where $\vec{n}$ is the unit normal pointing out of the fluid. If the body has a sharp trailing edge, Kutta condition must be added so that the velocity is finite at the edge. On the sea bottom which is assumed to be horizontal

$$\frac{\partial\phi}{\partial z} = 0 \qquad z = -h = \text{constant} \qquad \text{on } B_o \tag{1.4}$$

On the mean free surface $z = 0$, the dynamic condition of zero pressure gives

$$g\eta + U\phi_x = 0 \tag{1.5}$$

while the kinematic condition that the flow should be tangential to the free surface gives

$$U\eta_x = \phi_z \tag{1.6}$$

Eliminating η from (1.5) and (1.6) we get

$$\alpha\phi_{xx} + \phi_z = 0 \qquad \text{with } \alpha = U^2/g \tag{1.7}$$

To these one must add the radiation conditions at infinity. Far upstream there should be no velocity disturbance. Far downstream, there is also no velocity disturbance if the flow is supercritical, $F^2 = U^2/gh = \alpha/h > 1$; for a subcritical flow, however, waves must be present. The general mathematical statement of this condition is

$$\begin{aligned} &\phi \sim C_- && x \sim -\infty && && \\ &\phi \sim C_+ && x \sim +\infty && U^2/gh > 1 && \text{supercritical flow} \\ &\ \ \sim C_+ + \text{waves} && && U^2/gh < 1 && \text{subcritical flow} \end{aligned} \tag{1.8}$$

We remark that the difference $C = C_+ - C_-$ (and not C_+ or C_- individually) corresponds to the blockage constant discussed previously for flows without a free surface [1]. Although its physical significance is minor, C cannot be ignored in a mathematical analysis. This was first found when examining analytically the problem of a slender obstacle on the sea bed of depth h [2], for which the velocity potential can be written as an

exponential Fourier integral. In addition to the usual poles of the integrand which give the downstream wave for a subcritical flow there is also a simple pole at the origin. If the integration path is indented below this pole, we find

$$C_- = 0, \qquad C_+ = \frac{UA}{h - \alpha} \qquad x \sim +\infty \tag{1.9}$$

where A is the protruded area of the obstacle above the sea bed. Indentation above the origin or other interpretation of this singular integral will change the values of $C_\pm$ but not their difference. In the Appendix to [2], it is also found by considering mass conservation that for a non-slender submerged body

$$C = C_+ - C_- = [UA - \int_B (\phi_L \frac{\partial Z_L}{\partial x} - \phi_U \frac{\partial Z_U}{\partial x}) dx\ ]/(h - \alpha) \tag{1.10}$$

where $Z_L(x)$ ($Z_U(x)$) is the lower (upper) surface of the obstacle and $\phi_L \equiv \phi(x, -Z_L(x))$, etc. Since this pole is removable in the Fourier integral representation for η which is the usual object of interest, the blockage constant has not received due attention heretofore. Clearly C becomes insignificant as the depth h becomes large.

This problem can be solved by the semi-analytical method of singularity distribution, in which one first obtains an integral equation along the body, and then replaces it by discretizing the body surface to get a large system of algebraic equations. This method has been employed by Giesing and Smith [3] and others, all for infinite depth. We shall outline here a more direct numerical method [2] employing finite elements which are known to be versatile tools for complicated boundary geometry. In particular there are two special features of our method: (i) It is a hybrid method where finite elements are used only in a neighborhood close to the body, and infinite elements (called the super-elements) are used elsewhere. Polynomials are used in the finite elements as interpolation functions and infinite series of eigen functions are used in the super-elements. (ii) The boundary value problem is reformulated as a variational principle and the stationary integral involves only the interior and the boundaries of the region of finite elements.

The idea of the super-element was first used in elasticity where the neighborhood of a crack is a point of infinite stress; it was found that treating analytically the neighborhood of the crack instead of the usual finite element approximation enhances the numerical convergence significantly. We remark that there are ways which use super-elements but are not based on variational principles, e.g., the weighted residual method. However, the variational method is regarded by many to be more desirable, since for a given choice of the elements and the interpolation functions it ensures that first order errors in the approximations lead to a second order error in a global sense, or specifically, in the stationary functional. Furthermore a variational principle involves derivatives of lower order than the original differential equation, hence, the requirements on the smoothness of the interpolation functions need not be as stringent. Lastly for many problems of physical interest, a variational principle often leads to a set of algebraic equations with a symmetric coefficient matrix, which are theoretically better understood and computationally advantageous.

In water wave problems involving diffraction and radiation of time - harmonic waves, variational principles for hybrid element methods have been used recently by Chen and Mei [4] for two horizontal dimensions and Bai and Yeung [5] for one horizontal and one vertical dimension. The same technique can be straightforwardly applied to the supercritical flows $U^2/gh > 1$. However for subcritical flows the lack of symmetry in the radiation conditions at two infinities has so far defied our attempts for a direct variational principle. Fortunately by imitating a device of Drazin and Moore [6] to replace the steady flow problem by two fictitious problems: a radiation problem and a diffraction problem, this difficulty is circumvented. While details of this effort are described in [2] we shall outline the main points of the analytical basis and present further numerical results. Extension to bodies with sharp edges which was not discussed in [2], is also indicated here. An alternate proof of the variational principle is given in the Appendix.

2. Splitting into Two Fictitious Problems for Subcritical Flows

We introduce the decomposition

$$\phi = \phi^{(r)} + \phi^{(s)} \tag{2.1}$$

The part $\phi^{(r)}$ is to be governed by

$$\frac{\partial^2\phi^{(r)}}{\partial x^2} + \frac{\partial^2\phi^{(r)}}{\partial z^2} = 0 \qquad -H < z < 0 \tag{2.2}$$

$$\frac{\partial\phi^{(r)}}{\partial n} = V \qquad \text{on } B \tag{2.3}$$

$$\alpha\,\frac{\partial^2\phi^{(r)}}{\partial x^2} + \frac{\partial\phi^{(r)}}{\partial z} = 0 \qquad z = 0 \tag{2.4}$$

$$\begin{aligned}\phi^{(r)} &= B\,e^{-ikx}\cosh k(z+h) + C_-^{(r)} && x \sim -\infty\\ &= A\,e^{+ikx}\cosh k(z+h) + C_+^{(r)}. && x \sim +\infty\end{aligned} \tag{2.5}$$

When multiplied by the time factor e^{-it}, $\phi^{(r)}$ can be viewed as the potential due to the forced oscillation of the body. In particular (2.5) states that $\phi^{(r)}$ behaves as outgoing waves at $x \sim \pm\infty$. The part $\phi^{(d)}$ is also governed by (2.2) and (2.4), with the distinction that

$$\frac{\partial\phi^{(d)}}{\partial n} = 0 \qquad \text{on } B \tag{2.6}$$

$$\begin{aligned}\phi^{(d)} &\sim E(e^{-ikx} + Re^{ikx})\cosh k(z+h) + C_+^{(d)} && x \sim +\infty\\ &\sim E\,Te^{-ikx}\cosh k(z+h) + C_-^{(d)} && x \sim -\infty\end{aligned} \tag{2.7}$$

Now $\phi^{(d)}$ may be viewed as the spatial factor of the diffracted wave potential due to the same body with incident wave of amplitude E from $x \sim +\infty$. R and T are the reflection and transmission coefficients respectively. We are not aware of any physical problem which has (2.4) on the free surface, hence the two problems are fictitious.

The procedure is to solve for $\phi^{(r)}$, and $\phi^{(d)}$ with $E = 1$, using the hybrid element method. Then the upstream wave in the original problem is

eliminated by requiring that

$$E = - B/T . \tag{2.8}$$

Thus the composite potential satisfies all the conditions for ϕ. The blockage constant is simply

$$C = C_+^{(r)} + C_+^{(d)} - (C_-^{(r)} + C_-^{(d)}) \tag{2.9}$$

If the body has a sharp trailing edge we require that both $\phi^{(r)}$ and $\phi^{(d)}$ separately satisfy the Kutta condition. This is, of course, not a natural situation in *bona-fide* radiation and diffraction problems.

This splitting suggests that any computational method developed for the usual radiation or diffraction problem can be applied with only minor modifications. Our purpose is to apply finite elements.

3. Variational Principle for the Hybrid Method

We illustrate the case of radiation $\phi^{(r)}$ only; the corresponding variational principle for the diffraction problem is similar. For brevity the superscript $(\ )^{(r)}$ will be dropped. We divide the channel into three main regions by the vertical planes S_+ and S_-, which are on two sides of, and can be as close as possible to, the body, as sketched in Fig. 1.

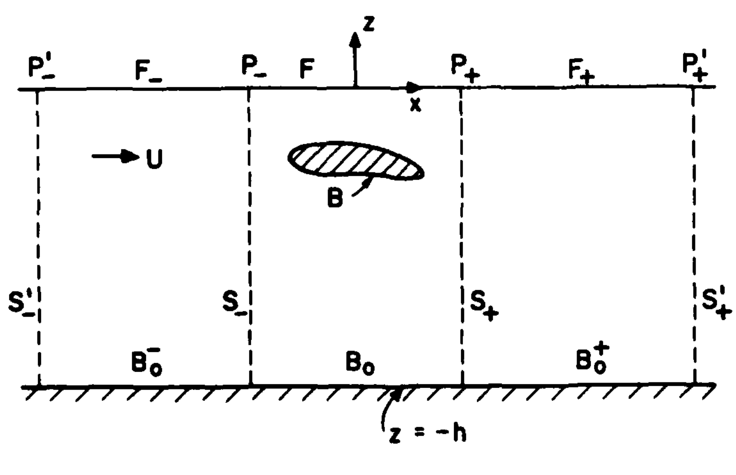

Figure 1 - Definition Sketch

The regions beyond $S_\pm$ are called the super elements where the depth is assumed to be constant. The conditions governing the potentials therein are

$$\nabla^2\phi^\pm = 0 \qquad \text{in } D_\pm \tag{3.1}$$

$$\alpha\phi^\pm_{xx} + \phi^\pm_z = 0 \qquad z = 0 \qquad \text{on } F_\pm \tag{3.2}$$

$$\phi^\pm_z = 0 \qquad z = -h \qquad \text{on } B^\pm_o \tag{3.3}$$

$$\phi^\pm_x \mp ik\phi^\pm = \mp ikC_\pm \qquad x \sim \pm\infty \qquad \text{on } S'_\pm \tag{3.4}$$

Within $D_\pm$ we use as the "interpolation functions" the following eigenfunction expansions. Each term in the series satisfies the above conditions exactly.

$$\phi^- = \sum_{n=0}^{\infty} A^-_n e^{-ik_n x} \cosh k_n(z + h) \tag{3.5}$$

$$\phi^+ = \sum_{n=0}^{\infty} A^+_n e^{ik_n x} \cosh k_n(z + h) \tag{3.6}$$

where $k_o = 0$, k_1 is the positive real root of

$$\alpha k = \tanh kh \tag{3.7}$$

and k_2, k_3 ... are the discrete positive imaginary roots of the same equation. Note that $A^-_o = C_-$ and $A^+_o = C_+$. The set of functions $\{\cosh k_m\}$ $m = 0, 1, 2, \ldots$ form an orthogonal set in the following sense

$$\int_{-h}^{0} \cosh k_n(z + h) \cosh k_m(z + h)dz - \alpha \cosh k_nh \cosh k_mh$$

$$\begin{aligned} &= \frac{1}{4k_n}(2k_nh - \sinh 2k_nh)\delta_{nm} && \text{if } n \text{ or } m \neq 0 \\ &= h - \alpha && \text{if } n = m = 0 \end{aligned} \tag{3.8}$$

Introducing Dirac's delta function $\delta(z)$, the left hand side of (3.8) can be written more compactly as

$$\int_{-h}^{0} [1 - \alpha\delta(z)] \cosh k_n(z + h) \cosh k_m(z + h)\, dz$$

Inside the region D, ϕ will be obtained approximately. It can be shown however that if ϕ is so chosen that it extremizes the following functional

$$J = \underbrace{\iint_D \frac{1}{2} (\nabla\phi)^2 dxdz}_{(i)} - \underbrace{\int_F \frac{\alpha}{2} (\phi_x)^2 dx}_{(ii)} - \underbrace{\oint_B V\phi\, ds}_{(iii)} \qquad (3.9)$$

$$+ \int_{S_+} [1 - \alpha\delta(z)] \left(\tfrac{1}{2} \phi^+ - \phi\right)\phi_x^+\, dz - \int_{S_-} [1 - \alpha\delta(z)]\left[\tfrac{1}{2} \phi^- - \phi\right]\phi_x^-\, dz$$

(iv) (v) (vi) (vii)

then the choice is equivalent to the solution which satisfies (2.2), (2.3) and (2.4) within the confines of $S_\pm$, and matches with the potentials in $D_\pm$:

$$\phi = \phi^\pm, \qquad \phi_x = \phi_x^\pm \qquad \text{on } S_\pm. \qquad (3.10,\ 11)$$

In otherwords, ϕ is the exact solution. A proof along the more conventional lines has been given in [2]; a shorter alternate proof is given in the Appendix.

It may be pointed out that using the representations (3.5) and (3.6), $C_\pm$ does not enter J at all because of the orthogonal property (3.8). The blockage constant can, however, be computed by using (1.10).

4. Modification for Sharp Edges

On a submerged hydrofoil there are one or two sharp edges. In particular at the leading edge the velocity is singular. At the trailing edge the velocity should be finite (Kutta condition). In the approach

of Giesing and Smith [3], two problems must be solved: one for the source distribution and one for the vorticity distribution on the hydrofoil. For an airfoil in an infinite fluid de Vries and Norrie [7] used finite elements (without super elements) and solved first for the potential without satisfying the Kutta condition, then solved a second problem for the stream function by assuming a circulation along an infinite contour. In both approaches, the total circulation is finally adjusted so that the composite solution satisfies the Kutta condition.

The idea of super elements is particularly suited here, which works for both the leading and the trailing edges. We introduce a small circle ∂D_E surrounding the leading edge. The fluid interior bounded by the edge, and by the circle is designated as D_E. For small D_E we assume that the edge can be approximated by a wedge. Using local polar coordinates (r,θ) with $\theta = 0$, θ_E denoting the two sides of the wedge, we require that the interpolation function within D_E satisfies exactly

$$\nabla^2\phi = 0 \qquad \text{in } D_E \tag{4.1}$$

and

$$\frac{\partial\phi}{\partial\theta} = 0 \qquad \theta = 0,\ \theta_E \tag{4.2}$$

It is readily shown that

$$\phi = \sum_{n=0}^{\infty} \ell_n r^{\beta_n} \cos \beta_n\theta \qquad \beta_n = n\pi/\theta_E \tag{4.3}$$

where ℓ_n are unknown coefficients. Note that ϕ is finite at the edge $(r = 0)$ but due to the term $n = 1$ above, the velocity

$$\frac{\partial\phi}{\partial r} \propto r^{(\beta_1 - 1)} = r^{(\frac{\pi}{\theta_E} - 1)}, \qquad r \sim 0 \tag{4.4}$$

is singular since $2\pi > \theta_E > \pi$.

Now to the functional J we must add the following line integral

$$\oint_{\partial D_E} (\tfrac{1}{2}\,\phi_E - \phi)\,\frac{\partial\phi_E}{\partial n}\,ds \tag{4.5}$$

The continuity of ϕ and $\partial\phi/\partial r$

$$\phi_E = \phi, \qquad \frac{\partial\phi_E}{\partial r} = \frac{\partial\phi}{\partial r} \tag{4.6}$$

become the natural boundary conditions.

Around the trailing edge the same is done with the exception that the term $n=1$ must be deleted from the series so that the Kutta condition is satisfied.

5. Numerical Example

Once the variational principle is found for ϕ (i.e., $\phi^{(r)}$ or $\phi^{(d)}$), the domain D is divided into discrete finite elements within each of which ϕ is approximated by an interpolation function. We have chosen the simplest three-node triangular elements so that the unknown parameters in the interpolation functions are just the unknown nodal values of the potential. After substitution integrals (i), (ii) and (iii) can be evaluated straightforwardly. Truncating the series of (3.5) and (3.6) after a finite number of terms, integrals (iv) and (vi) can also be evaluated. These integrals are all expressed in quadratic forms with symmetric stiffness matrices. Integral (v) becomes a bilinear form in the nodal potentials $\{\phi\}$ along S_+ and the coefficients $\{A^+\}$; it may be rearranged as follows

$$\frac{1}{2}\,\{\phi\}^T[K]\{A\} + \frac{1}{2}\,\{A\}^T[K]^T\{\phi\} \tag{5.1}$$

where [K] is a full rectangular matrix and { } is a column vector and the superscript T denotes the transpose. This arrangement ensures that the assembled global stiffness matrix is symmetric. Extremizing J with respect to each of the unknown parameters gives a set of linear algebraic equations which can be solved by Gaussian elimination. The element size should be much less than the wavelength and should be further reduced near the solid boundary where the local curvature is large. If the water depth is large, then the element size can be increased at great depth because of the expected exponential attenuation. The number of expansion coefficients M is decided by numerical convergence experiments.

Details of the computational aspects are fully reported in [2] where comprehensive checks with existing work can also be found.

In [2] the case for a circular cylinder in a sea of finite depth is studied for the effect of differing depths of submergence. In this paper we report the results for the same cylinder located at a fixed depth below the free surface, but for different sea depths. The choices of the geometry are made solely for illustrating the numerical technique and not for physical reality.

In particular, we let the center of the cylinder, of radius R, be at the level $z = -2R$. The water depths are taken to be $h = 4R$, $5R$, and $8R$. The calculated range of velocities is such that the Froude number based on the sea depth $F = U(gh)^{-1/2}$ is $0.2 < F < 2.0$. The choice of such a shallow submergence is made so as to provide comparison with earlier calculations for infinite sea depth, [1] and [3]. Violation of the linearized free surface condition is expected for certain range of F and will be discussed later. In Figures 2 and 3 are shown the total horizontal wave drag X and lift Y forces calculated from the total potential $\phi = \phi^{(r)} + \phi^{(d)}$ by integrating the pressure on the body

$$\binom{X}{Y} = -\frac{\rho}{2}\oint_B (2\,U\,\phi_x + \phi_x^2 + \phi_y^2)\binom{dy}{dx} \tag{5.2}$$

We note first that for supercritical flows, there is no wave far downstream hence the wave drag X vanishes. For subcritical flows the wave drag approaches a finite limit as the critical speed is reached from below, $F \to 1$. The vertical force is upward for low subscritical speeds but downward for high subcritical and supercritical speeds. There are finite discontinuities at the critical speed.

Fig. 4 plots the wave amplitudes far downstream for subcritical flows. Except for very low Froude numbers the amplitudes are very large; this is due to the bluntness of the cylinder and the shallow submergence. For a streamlined body or deep submergence, the amplitudes should reduce to within the realm of linearization. The singularity at $F = 1$ where the wavelength is infinite can only be remedied by a nonlinear analysis. The

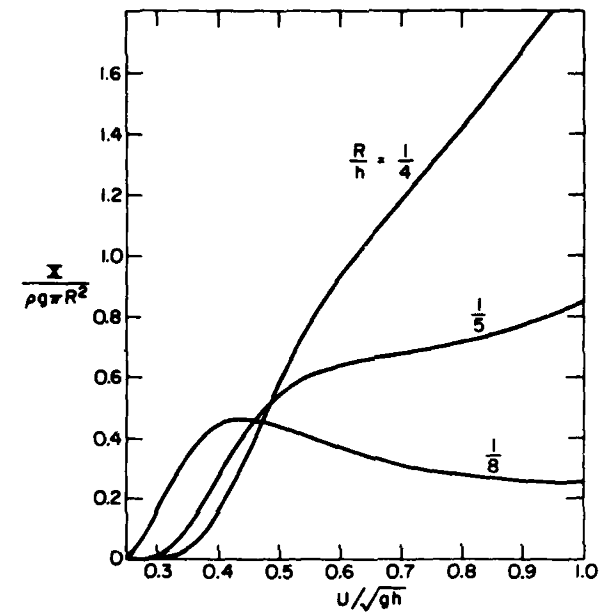

Figure 2 - Normalized Horizontal Wave Drag

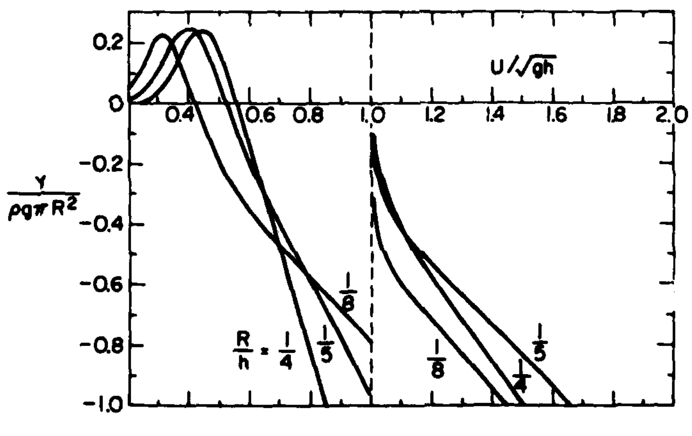

Figure 3 - Normalized Vertical Force

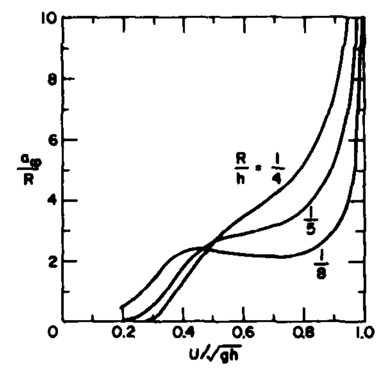

Figure 4 - Normalized Wave Amplitude Far Downstream

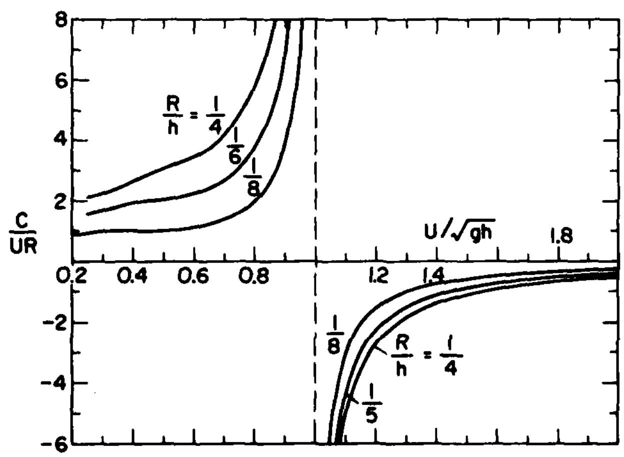

Figure 5 - Normalized Blockage Constant

reason that the wave drag X approaches a finite constant as $F \to 1$ is because $C_g/C \to 1$ as can be verified analytically from the example of a slender obstacle on the sea bed.

The blockage constant C is shown in Figure 5. As is true to the name it bears, the blockage constant is greater for larger R/h. Again there is a singularity at the critical speed.

In all these calculations, the super-element boundaries $S_{\pm}$ are only R/2 from the cylinder. Near the cylinder, three-node triangular elements are used, the size of which is less than one-tenth of the wavelength or of the cylinder radius, whichever is smaller. At great depth the element size can be somewhat relaxed. In the global stiffness matrix the bandwidth is roughly equal to the number of nodes on a vertical line (~ 20 in our calculations). The series (3.5) and (3.6) can be safely truncated after 15 terms. For one value of the Froude number the CPU time is about 10 sec on the IBM 370.

We have not worked out numerical examples involving sharp edges. The treatment of a sharp leading edge is similar to that given in [4] in a different context. Since the treatment of a sharp trailing edge is similar there is no reason to believe that the present method will not succeed.

ACKNOWLEDGEMENT

The authors wish to acknowledge the financial support of the National Science Foundation Grant GK 43866X, and of the Office of Naval Research, Contract NR-062-228.

REFERENCES

[1] Newman, J.N. "Lateral Motion of a Slender Body between two Parallel Walls", *J. Fluid Mech.*, Vol. 39, pp. 97-115 (1969).

[2] Mei, C.C. and Chen, H.S. "A Hybrid Element Method for the Linearized Theory of Steady Free-surface Flows", (to appear in *Num. Meth. Eng.*).

[3] Giesing, J.P. and Smith, A.M.O. "Potential Flow about Two-Dimensional Hydrofoils", *J. of Fluid Mech.*, Vol. 28, pp. 113-129 (1967).

[4] Chen, H.S. and Mei, C.C. "Oscillations and Wave Forces in a Man-Made Harbor in the Open Sea", *Proceedings of the 10th Symposium on Naval Hydrodynamics*, Office of Naval Research, June (1974).

[5] Bai, K.J. and Yeung, R.W. "Numerical Solutions to Free Surface Flow Problems", *Proceedings of the 10th Symposium on Naval Hydrodynamics*, Office of Naval Research, June (1974).

[6] Drazin, P.G. and Moore, D.W. "Steady Two-dimensional Flow of Fluid of Variable Density over an Obstacle", *J. Fluid Mech.*, Vol. 28, pp. 353-370 (1967).

[7] Havelock, T.H. "The Forces on a Circular Cylinder Submerged in a Uniform Stream", *Proceedings, Royal Society of London*, A. Vol. 157, pp. 526-534 (1936).

APPENDIX: THE STATIONARY FORM OF J, Eq. (3.9)

After the usual integration by parts, the first variation of J can be arranged as follows (with the obvious integration elements dxdz, dx, ds omitted).

$$\delta J = -\frac{1}{2}\int_D \delta\phi\, \nabla^2\phi + \int_F \delta\phi[\alpha\phi_{xx} + \phi_z] + \int_{S_+} \delta\phi(\phi_x - \phi_x^+) - \int_{S_+} (\phi^+ - \phi)\delta\phi_x^+$$

$$- \int_{S_-} \delta\phi(\phi_x - \phi_x^-) - \int_{S_-} (\phi^- - \phi)\delta\phi_x^-$$

$$+ \int_B \delta\phi\, (\frac{\partial\phi}{\partial n} - V) - \int_{B_o} \delta\phi\, \phi_z$$

$$+ \frac{1}{2}\int_{S_+} [1 - \alpha\delta(z)]\, (\delta\phi^+\, \phi_x^+ - \phi^+\, \delta\phi_x^+) - \frac{1}{2}\int_{S_-} [1 - \alpha\delta(z)][\delta\phi^-\, \phi_x^- - \phi^-\, \delta\phi_x^-] \tag{A.1}$$

If the last two integrals involving $\phi^\pm$ are identically zero, then for arbitrary $\delta\phi$ and $\delta\phi^\pm$ the vanishing of δJ implies, and is implied by, (2.2) as the Euler's equations and (2.3), (2.4), (3.10) and (3.11) as the natural boundary conditions. We now prove the first premise.

Recalling that ϕ^+ satisfies Laplace equation exactly, we have from Green's formula

$$0 = \int_{D_+} (\delta\phi^+\nabla^2\phi^+ - \phi^+\nabla^2\delta\phi^+) = \int_{F_+} (\delta\phi^+\phi_z^+ - \phi^+\, \delta\phi_z^+) - \int_{B_o^+}(\delta\phi^+\phi_z^+ - \phi^+\, \delta\phi_z^+)$$

$$+ (\int_{S_+^!} - \int_{S_+^!})(\delta\phi^+\, \phi_x^+ - \phi^+\, \delta\phi_x^+) \tag{A.2}$$

We now use the fact that ϕ_+ also satisfies (3.3) exactly, so that the integral along B_o^+ vanishes. Using (3.2), integrating by parts and invoking

(3.4) we obtain

$$\int_{P_+} = - ik \, [-\alpha(\delta\phi^+ C_+ - \phi^+ \delta C_+]_{P_+'} + \alpha[\delta\phi^+ \phi_x^+ - \phi^+ \delta\phi_x^+]_{P_+} \tag{A.3}$$

Again from the radiation condition, we have

$$\int_{S_+'} = - ik \int_{S_+'} (\delta\phi^+ C_+ - \phi^+ \delta C_+) \tag{A.4}$$

Substituting (A.3) and (A.4) into (A.2) we get

$$0 = - \int_{S_+} [1 - \alpha\delta(z)](\delta\phi^+ \phi_x^+ - \phi^+ \delta\phi_x^+) - ik \int_{S_+'} [1 - \alpha\delta(z)](\delta\phi^+ C_+ - \phi^+ \delta C_+) \tag{A.5}$$

Using the asymptotic expression for ϕ^+ (cf. (3.6)) it follows readily that

$$\int_{S_+'} [1 - \alpha\delta(z)]\phi^+(z) = C_+(h - \alpha) \tag{A.6}$$

whose first variation leads to the vanishing of the second integral in (A.5). Thus, the first integral in (A.5) also vanishes. By a similar argument, the integral along S_- is also zero, hence $\delta J = 0$.

Although this proof is shorter than the one given in [2] it sheds less light on how the stationary form is derived.

CAVITY FLOW AND NUMERICAL METHODS

T. Y. Wu

California Institute of Technology
Pasadena, California 91125 U.S.A.

ABSTRACT

Existing methods of calculating cavity flows will be first reviewed for the classical case of steady, plane potential flow past a two-dimensional body of arbitrary shape. The semi-analytical method of solution is based first on the conversion of the original boundary problem, expressed in terms of a known theoretical flow model, into a set of nonlinear functional equations of the Villat type, for which a number of numerical methods of solution will be discussed.

For more general cases of three-dimensional cavity flow problems, or when the effects of fluid compressibility, viscosity, gravity, and flow unsteadiness become significant, the value of direct numerical methods appears especially appealing. For the solution of these problems various singularity methods, finite-difference methods, and, more recently, finite-element methods have attracted considerable research effort directed towards their further development. Their quantitative evaluation will be discussed from the standpoint of their effectiveness in specific situations that may be problem-dependent.

1. Introduction

The free streamline theory has had quite a colorful history, starting over a century ago with the pioneering work of Helmholtz (1868) and Kirchhoff (1869). Its introduction had a great significance in the context of resolving the classical paradox of D'Alembert, and its development has been much stimulated by the increasing demand of engineering and physical applications, and by the need of more thorough knowledge essential to the studies of viscous wakes. The mathematical development of existence and uniqueness theory forms a chapter of brilliant achievement of its own. The

studies along these lines will continue to be of principal importance in hydromechanics and mathematics.

The general problem of cavity and wake flows, even when only the inviscid flow outside the boundary layer and the ensuing cavity-wake system is of interest, is nevertheless still considered as one of the most difficult of all because of its highly nonlinear nature (though in the recent past linear theory has been developed for thin or slender bodies at small incidences to flow). Only in the special case of steady, incompressible, plane flows can the powerful tool of function theory be fully utilized. In the three-dimensional case, only the flows with axisymmetry are simple enough to have received some theoretical development by resourceful applications of the surface-singularity method or certain parametric continuation in space dimensions. In these limited scopes the boundary-value problem in potential theory can be solved for several classes of simple body shapes, or can be reduced for curved bodies to certain types of functional equations that have permitted some notable success of early numerical effects.

Coming with the dawn of high-speed computers the prospects of solving more complex cavity and wake flow problems, including consideration of such effects as due to compressibility, gravity, surface tension, viscosity, etc. have become much enhanced. From the numerical standpoint, quantitative evaluation in any particular situation is to a large extent problem-dependent, on account of the great variety of problems that can arise. The optimum choice and necessary development of a numerical method may depend on (i) the space dimensions and geometrical domain in question, (ii) the differential equation and boundary conditions involved, (iii) any preliminary analysis that may be desired to simplify the problem, and perhaps also other factors. In the working level, numerical efforts have several aspects in their objectives regarding the calculation of unknown functions and functionals that may arise from the analysis, and the calculation of the unknown location of free boundaries. That the state of the art is not a simple straightforward matter is exemplified by the case that the theory of unsteady cavity flow still remains to date in its infancy.

It is therefore gratifying to observe the commencement of this series of International Conferences with especial reference to free-surface flows and related viscous flow problems. We may anticipate them to play a

significant role in helping push forward the frontier of ship hydromechanics and numerical mathematics. Personally, I feel most appreciative indeed of this privileged opportunity called by Mrs. Joanna Schot to take on this introductory talk on cavity flow and numerical methods. I would like first to discuss the classical case of steady plane cavity flows with its theoretical and experimental background and related numerical methods. For more complicated problems the value of finite-difference methods applied directly to the field equation and boundary conditions has been generally recognized. Finally, I hope to say a few words about the finite-element method that may be useful for cavity flow evaluations.

2. Inviscid cavity flow; the free streamsurface theory

The inviscid approximation for cavity and wake flows at high Reynolds numbers is based on the assumptions that the thin viscous layer adjacent to the body surface and cavity boundary may be neglected; the outer flow enveloping the body, cavity, and its ensuing wake is inviscid and irrotational; and the overall manifest of the far-wake trailing the cavity closure may be represented by a suitable theoretical model. Further, any intrinsic unsteady motion of the free shear layer and the viscous far-wake that can generally be attributed to certain types of flow instability, such as fully developed turbulence in the boundary layer or shear layer, rolling up and mixing of trailing vortices, etc. is not considered since only the mean steady flow is of primary interest unless the unsteady cavity flow is generated by time-dependent body motions and disturbances (of body scale) in the basic flow. For completeness, we state the theory including the last general case.

Under these assumptions, the flow has a velocity potential $\phi(\underline{x}, t)$, satisfying the Laplace equation

$$\Delta\phi = 0, \tag{1}$$

and the prescribed basic flow $U(\underline{x}, t) = \nabla\phi$ at upstream infinity. The classical boundary conditions are as follows.

(i) On a solid body, with its motion prescribed by $S(\underline{x}, t) = 0$,

$$S_t + (\nabla\phi) \cdot \nabla S = 0 \qquad \text{on} \quad S(\underline{x}, t) = 0. \tag{2}$$

(ii) On a free boundary, $F(\underline{x}, t) = 0$ say, the kinematic condition requires

$$F_t + (\nabla \phi) \cdot \nabla F = 0 \qquad \text{on } F(\underline{x}, t) = 0. \tag{3}$$

In addition, the classical dynamic condition assumes the pressure to be a constant, $p = p_c$ say, on $F(\underline{x}, t) = 0$. Hence Bernoulli's law (neglecting the effect of surface tension) gives

$$\frac{1}{\rho} p_c + \frac{\partial \varphi}{\partial t} + \frac{1}{2} (\nabla \varphi)^2 - \underline{g} \cdot \underline{x} = c(t) \quad \text{on } F(\underline{x}, t) = 0 \tag{4}$$

where ρ is the fluid density and $\underline{g}$ is the constant gravitational field, $c(t)$ being independent of $\underline{x}$. Unless for problems of special physical interest, p_c is assumed to be the minimum pressure of the entire flow.

(iii) A detachment line, at which the cavity surface of an inviscid flow leaves the body, may be either fixed if it is at a pointed corner of the body, or free if it is at a certain (unknown à priori) location of a smoothly curved body surface. The classical condition for the determination of the free-detachment position is the one due to Brillouin (1911) and Villat (1914), which requires the streamwise curvature of a free surface to be finite at free detachment. This is the Villat-Brillouin condition, originally introduced for steady plane flows and may be extended to the three-dimensional case. It is primarily based on the following mathematical argument concerning the local singular behavior of the free streamline. Either the streamline has a finite curvature at detachment if it detaches from a certain point D_f, say (see Fig. 1), on a given body of a continuous positive curvature at D_f (+ or − sign of curvature being adopted according as the body surface is convex or concave to flow), then the streamline curvature is continuous across D_f, or the free streamline has a positive infinite curvature if it detaches at D_f', a new detachment point upstream of D_f, but it would have to cut immediately into the body. On the other hand, another detachment point D_f'' downstream of D_f would result in a negative infinite curvature of the streamline at D_f'', thus violating the condition of p_c being the minimum pressure (see curve 3 for c_p in Fig. 1). The general validity of the Villat-Brillouin condition, as viewed both from comparison with experiment and from the boundary-layer calculation

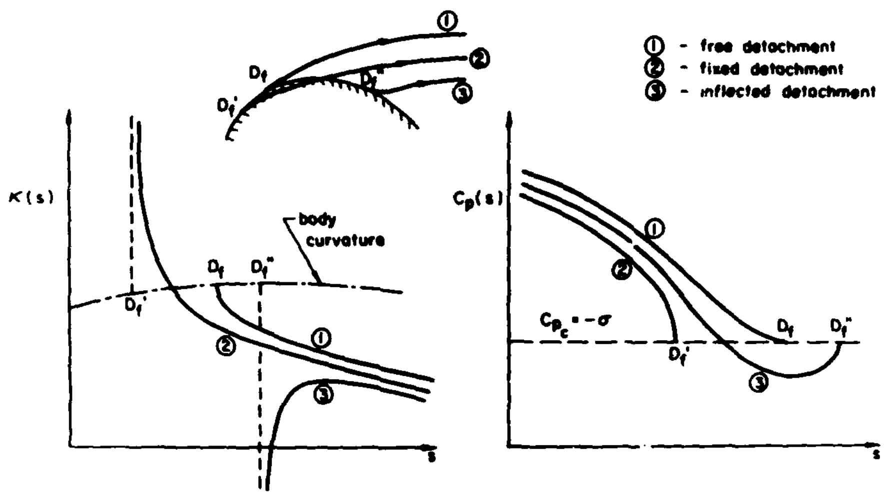

Fig. 1. A schematic drawing of the curvature κ and pressure coefficient C_p along a curved body surface and three detached streamlines, measured by arc length s.

based on the inviscid pressure distribution, is a most important issue in cavity flow theory and should require careful examination. We shall return to this point at a later stage.

For finite cavities and wakes, it is further necessary to introduce in the framework of potential theory a specific flow model for an adequate representation of the turbulent far-wake so as to admit the cavity under-pressure-coefficient (known as the cavitation number) or, equivalently, the cavity size (relative to body dimension) as a free parameter. In the present state of the art, application of cavity flow theory must require the specification, by experimental measurement, of the cavitation number,

$$\sigma = (p_\infty - p_c)/\tfrac{1}{2}\rho U^2 \tag{5}$$

where p_∞ is a reference pressure of the free stream, usually taken as the pressure at infinity if p_∞ is uniform. A far-reaching objective is to establish a valid relation between σ and some known flow parameter,

such as the Reynolds number based on the free stream velocity U and a characteristic body dimension ℓ, so that no experimental measurement will be routinely required in applying the theory. Though this aim has attracted considerable interest (see, e.g. Roshko & Fiszdon 1967), such a general relationship for bodies of arbitrary shape is still far beyond reach, and this most important problem remains to call for further challenging effort.

There are several cavity flow models in common use, all of which contain some sort of artifice in order to account for the momentum defect in the viscous wake, or, equivalently, the energy loss due to dissipation. (It should be noted that from the standpoint of potential flow, conservations of mass, momentum, and energy are related to each other in a unique manner.) Since their description is well-known (see e.g. Wu 1972), we need only remark on some of the most commonly used models with direct extension to curved bodies, which are shown in Fig. 2. Generalization to the three-dimensional case is immediate.

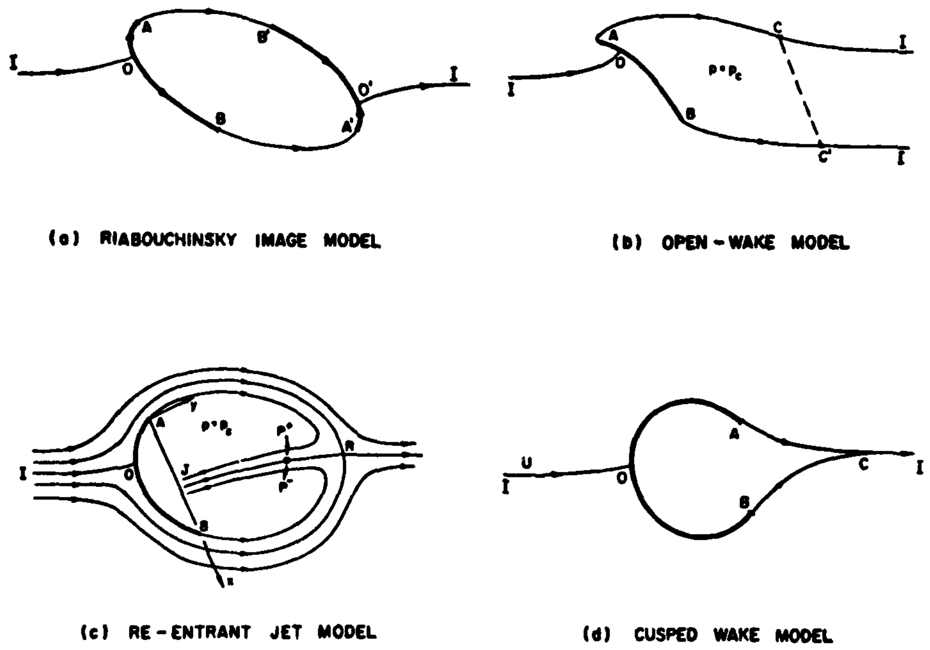

Fig. 2. Potential-flow models for arbitrary body with a finite cavity or wake bubble, referred to the physical plane.

1. The Riabouchinsky image model. — For lifting flows it is more appropriate to have the image body symmetric with respect to a central point rather than to a centerplane normal to the free stream, for in the latter case it would imply a nonzero circulation around the body-cavity system which lacks a physical basis.

2. Open-wake model. — The open strip (or duct) trailing the cavity (or near-wake) models the actual viscous far-wake of constant momentum thickness, whether the near-wake 'cavity' consists of a fluid of different or the same density as in the surrounding flow.

3. The reentrant-jet model. — The loss of mass carried away by the reentrant jet provides an alternative account for the removal of momentum and flow energy, even though the ensuing wake appears to have a 'negative' width.

4. Cusped-wake model. — This model may be useful for representing ventilated or pressurized cavities.

5. Single-spiral-vortex model. — It may be pointed out that this model, which was proposed by Tulin (1964), has a physical interpretation equivalent to placing two backward-facing point forces, one each at the points c and c' of the depicted open-wake model, causing a finite abrupt turn in direction of the free-streamsurface.

There are still other cavity flow models that can represent finite cavities. All of these models yield nearly the same hydrodynamic force on a given body when the cavity is sufficiently long, for they all reduce to the classical model of Helmholtz-Kirchhoff for infinite cavities as the cavitation number $\sigma \to 0$. Only in the case of thin bodies, especially when the cavity becomes rather short and when the flow is further constrained (such as by side walls) do they appreciably differ from each other. Including this range of high resolution between different flow models, Wu, Whitney, & Brennen (1971) have conducted a critical examination of the accuracy of the first three models mentioned above in predicting the pressure distribution on the body and the resultant force. As shown in Fig. 3 for a wedge of total vortex angle of 30°, with base width ℓ, situated symmetrically inside a straight water tunnel of spacing h, the prediction of the Riabouchinsky model is typically superior of the three investigated (the overestimate of the other two models, by about 10% in this case, is not shown). This particular result is of significance for it provides a

refined assessment of the theoretical models and may aid the choice of a flow model for theoretical and numerical calculations under various circumstances.

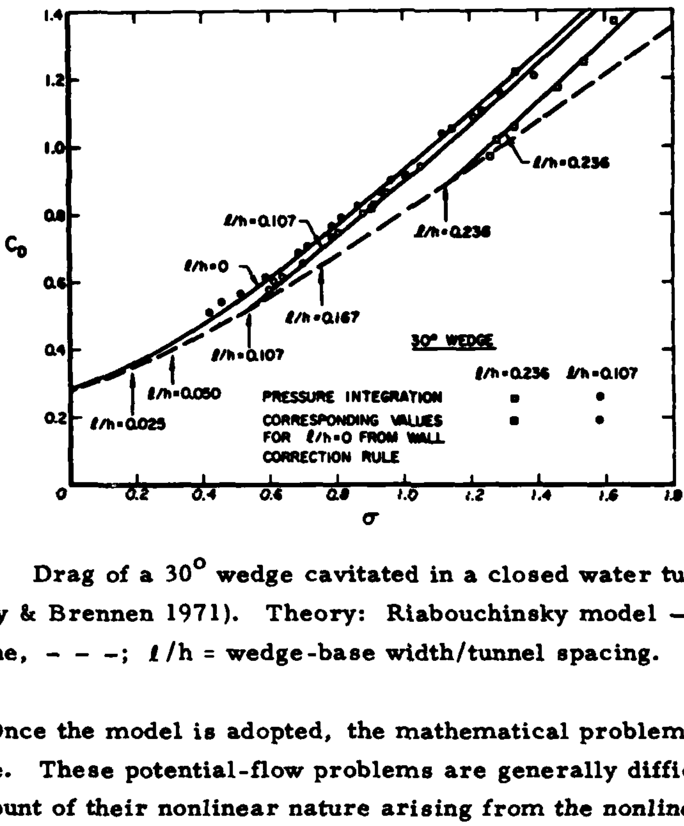

Fig. 3. Drag of a 30° wedge cavitated in a closed water tunnel (Wu, Whitney & Brennen 1971). Theory: Riabouchinsky model ——; choked-flow line, – – –; ℓ/h = wedge-base width/tunnel spacing.

Once the model is adopted, the mathematical problem becomes definite. These potential-flow problems are generally difficult to solve on account of their nonlinear nature arising from the nonlinear free-surface conditions and the unknown location of the free boundary. In the special case of steady, plane flows, however, the powerful technique of generalized conformal mapping and complex function theory can be effected to yield for curved bodies a set of functional equations of the Villat type. From these equations the exact solution is readily obtained for the simple case of an inclined flat plate (in unbounded flow), since the integrations are then elementary (see Wu 1962). Similarly, the problem for a polygonal body can be reduced to a nonlinear algebraic one (see e.g., Wu & Wang 1964a) which can also be resolved by standard, e.g. the Newton-Raphson method. These exact solutions are of fundamental value not only in their own rights, but also in such useful role as to provide effective initial

approximations for iterative calculations for curved bodies. In the general case of curved bodies of arbitrary shape we have seen in recent development several numerical methods demonstrating successful calculations of the exact solution in typical cases, which we are to discuss next. Before doing this we may also point out that the Villat functional equation further provides a powerful basis for studies of existence and uniqueness theory (we refer such discussions to the text by Birkhoff & Zarantonello (1957) and Gilbarg (1960)).

3. Steady plane flows; the Villat functional equation method

The general problem of primary interest is for a steady, incompressible, two-dimensional potential flow, in the physical plane $z = x+iy$, past a piece-wise continuously curved body, with its wetted boundary given parametrically by

$$x = x(s), \qquad y = y(s) \qquad (0 < s < S), \tag{6}$$

where s is the arc length along the body surface, running from point A to point B (see Fig. 2). This boundary-value problem is in general effectively expressed in terms of a parametric $\zeta = \xi + i\eta$ plane, so that the flow region is mapped conformally into the lower half of the ζ-plane, with the wetted body surface mapped onto $(-1 < \xi < 1,\ \eta = 0)$, the stagnation point at the origin $\zeta = 0$, and the cavity boundary onto $(|\xi| > 1,\ \eta = 0)$. The solution is first sought in the parametric form: $f = f(\zeta)$, $\omega = \omega(\zeta)$, where $f = \varphi + i\psi$ is the complex potential, $w = df/dz = u - iv$ the complex velocity, and

$$\omega = \log(q_c/w) = \tau + i\theta, \quad \tau = \log(q_c/|w|), \quad \theta = \tan^{-1}(v/u) \tag{7}$$

is the logarithmic hodograph with reference to the constant flow speed, q_c, on the cavity. Since the function analysis for different cavity-flow models is quite similar, it suffices to demonstrate the method specifically for the Riabouchinsky model, which is shown in Fig. 4. (For the solution in terms of other models, see Wu 1972).

Based on the Riabouchinsky model, the mapping $f = f(\zeta)$ can be directly written down, according to the generalized Schwarz-Christoffel theorem (see Gilbarg 1949), as

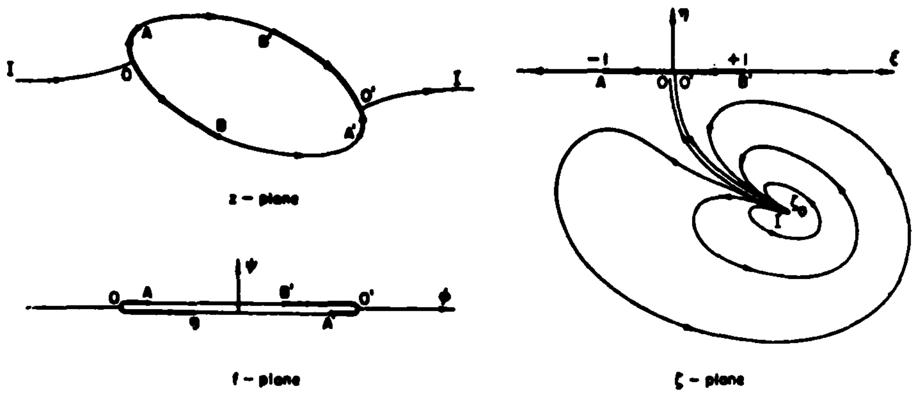

Fig. 4. Conformal mappings between the physical, complex potential and the parametric planes for the Riabouchinsky model.

$$df/d\zeta \;=\; A\zeta(\zeta - \zeta_o)^{-3/2}(\zeta - \bar{\zeta}_o)^{-3/2} \tag{8}$$

where A is a real constant, ζ_o corresponds to $f = \infty$, and $\bar{\zeta}_o$ is the complex conjugate of ζ_o. The boundary conditions for $\omega(\zeta) = \tau(\xi,\eta) + i\theta(\xi,\eta)$ are given by

$$\theta(\xi, 0^-) = \pi H(-\xi) + \hat{\beta}(s(\xi)) \qquad (-1 < \xi < 1), \tag{9}$$

$$\tau(\xi, 0^-) = 0 \qquad (|\xi| > 1), \tag{10}$$

where $H(-\xi)$ denotes the Heaviside step function, $\hat{\beta}(s) = \tan^{-1}[y'(s)/x'(s)]$, the primes denoting differentiation. The solution of this Riemann-Hilbert problem is readily obtained as

$$\omega(\zeta) = \omega_o(\zeta) + \omega_1(\zeta) \;, \tag{11}$$

$$\omega_o(\zeta) \;=\; \log\{[1 + i(\zeta^2 - 1)^{1/2}]/\zeta\} \;, \tag{12}$$

$$\omega_1(\zeta) = \frac{1}{i\pi}\int_{-1}^{1}\left(\frac{\zeta^2-1}{1-t^2}\right)^{1/2}\frac{\beta(t)dt}{t-\zeta}\,, \tag{13}$$

where $\beta(\xi) = \hat{\beta}(s(\xi))$, the function $(\zeta^2-1)^{1/2}$ is analytic in the cut (between -1 and 1) ζ-plane.

The physical plane is now given by the quadrature

$$z(\zeta) = \frac{1}{q_c}\int e^{\omega(\zeta)}\frac{df}{d\zeta}\,d\zeta\,. \tag{14}$$

The arc length $s(\xi)$ along the body surface (with a proper account of the branch cut) is

$$s(\xi) = \frac{A}{q_c}\int_{-1}^{\xi} e^{\Gamma(\xi)}\,\nu(\xi;\zeta_o)d\xi \qquad (-1 < \xi < 1), \tag{15}$$

where
$$\Gamma(\xi) = -\frac{1}{\pi}\int_{-1}^{1}\left(\frac{1-\xi^2}{1-t^2}\right)^{1/2}\frac{\beta(t)dt}{t-\xi}, \tag{16}$$

$$\nu(\xi;\zeta_o) = A^{-1}\exp\left[\omega_o(\xi - i0)\right](df/d\xi). \tag{17}$$

The integral in (16) assumes its Cauchy principal value. The total arc length is specified by

$$S = s(1). \tag{18}$$

Further, the velocity condition at $z = \infty$, or $\zeta = \zeta_o$, requires that

$$\omega(\zeta_o) = \log(q_c/U) + i\alpha = \frac{1}{2}\log(1+\sigma) + i\alpha, \tag{19}$$

where α is the incidence angle of the chord AB, and σ is the cavitation number. Finally, we state the Villat-Brillouin condition for free detachment, if it takes place, as

$$d\omega/d\zeta \to 0 \qquad \text{as } \zeta \to 1 \quad \text{and/or} \quad \zeta \to -1, \tag{20}$$

whichever (one end, both ends, or neither) is applicable.

Equations (15) and (19) may be symbolically written as

$$s(\xi)/\tilde{A} = \mathcal{L}_1[\hat{\beta}\,(s(\xi));\,\zeta_o] \qquad (-1 < \xi < 1, \tilde{A} = A/q_c) \quad (21)$$

$$(1+\sigma)^{1/2} e^{i\alpha} = \mathcal{L}_2[\hat{\beta}\,(s(\xi));\,\zeta_o]\,, \quad (22)$$

where $\mathcal{L}_1$ and $\mathcal{L}_2$ stand for the same (nonlinear) integral operators as given explicitly in (15) and (19). At this stage we note that for the so-called 'inverse problem', defined by prescribing the quantities

$$P' \,\{\beta(\xi);\, A/q_c,\, \zeta_o\} \qquad (-1 < \xi < 1), \quad (23)$$

the solution is completely determined by (15) - (19) provided $A > 0$, and $-\pi < \arg \zeta_o < 0$. On the other hand, for a physical, or direct problem, with the prescribed quantities

$$P\,\{\hat{\beta}(s);\, \alpha,\, \sigma,\, S\} \qquad (0 < s < S), \quad (24)$$

equations (21) and (22) form two coupled nonlinear functional equations which are of the Villat type. The operators $\mathcal{L}_1$ and $\mathcal{L}_2$ provide the functional transformations of $s(\xi)$ and ζ_o into the left-hand side members of (21) and (22), $s(\xi)$ and ζ_o being the fixed points of the transformation. There are several numerical methods especially developed for calculating the Villat equations (21) and (22), which we shall proceed to discuss.

3. 1. The discrete-curvature iteration method. — The first successful calculations of free surface flows past curved bodies were carried out by Brodetsky (1923) for the plane, unbounded, infinite-cavity flow past circular and elliptical arcs. His method is based on a trigonometric interpolation (in the Levi-Civita parametric plane) of the functional equations involving the curvature of the body surface (which can be derived from (21) by differentiation); this method was later extended by Birkhoff et al. (1953, 1954). We refer the details to the well-documentated literature (Birkhoff & Zarantonello 1957, Gilbarg 1960), leaving some general trends of thought to be presented in a later discussion (§ 3. 4) of a further modified method that can be applied to treat asymmetric curved barriers with a finite cavity formation.

3.2. The single-loop integral-iteration method. — Instead of dealing with the functional equation involving the curvature function, Wu & Wang (1964a) proposed to calculate directly the arc-length function $s(\xi)$, for the given parameters (24), from the functional equation (21) and (22) by the following 'single-loop' iterative scheme

$$s^{(n+1)}(\xi)/\tilde{A}^{(n+1)} = \mathcal{L}_1[\hat{\beta}(s^{(n)}(\xi));\ \zeta_o^{(n)}] \tag{25}$$

$$(1+\sigma)^{1/2}e^{i\alpha} = \mathcal{L}_2[\hat{\beta}(s^{(n)}(\xi));\ \zeta_o^{(n)},\ \zeta_o^{(n+1)}] \tag{26}$$

In (26), $\zeta_o^{(n+1)}$ may be suitably factored out for relatively simple and effective calculations so that both $s^{(n+1)}(\xi)$ and $\zeta_o^{(n+1)}$ can be computed simultaneously for each of $n = 1, 2, \ldots$. For instance, replacing $\omega_o(\zeta_o)$ by $\omega_o(\zeta_o^{(n+1)})$, and $\omega_1(\zeta_o)$ by $\omega_1(\zeta_o^{(n)})$ in (19) to obtain (26) is an adequate choice, according to our experience. This scheme of iteration by dealing directly with the arc-length function has an advantage (e.g. over the curvature functional equation) in the calculation of $\tilde{A}^{(n)}$, which is determined at each step by just setting $s^{(n)}(+1) = S$. If a different (such as the curvature) function is adopted for calculation, it may require an additional iterative equation for $\tilde{A}$.

For flows with fixed detachment the rate of convergence of this iteration scheme depends on the mean square of $\hat{\beta}(s)$ (of which $\tilde{A}$ is a monotone function), the values of α and σ, the initial approximate solution $s^{(o)}(\xi)$ and $\zeta_o^{(o)}$, and the size and distribution of integration intervals. Generally speaking, the rate of convergence becomes slower for smaller α and σ, especially for thin and highly curved bodies. The limiting case of $\sigma \to 0$ is best reached by extrapolation of the numerical results for positive small values of σ. Our own experience indicates that the rate of convergence is invariably enhanced by an averaged iteration, as suggested by Birkhoff et al. (1954), with a 'relaxation parameter' ϵ, such that

$$s_\epsilon^{(n)}(\xi) = \epsilon\, s^{(n)}(\xi) + (1-\epsilon)s^{(n-1)}(\xi) \qquad (0 \leqslant \epsilon < 1), \tag{27}$$

$$\zeta_{o\epsilon}^{(n)} = \epsilon\, \zeta_o^{(n)} + (1-\epsilon)\, \zeta_o^{(n-1)}, \tag{28}$$

with $s_\epsilon^{(n)}$, $\zeta_{0\epsilon}^{(n)}$ replacing $s^{(n)}$ and $\zeta_0^{(n)}$ in (25) and (26) in each iterative step. The optimum value of ϵ, by numerical experiment, was not always far from 0. 3. In this manner the method has exhibited convergence in all the cases tried. A typical example is for an inclined circular arc hydrofoil of 16° arc angle. For each prescribed α and σ, the computation (based on the open-wake model) was performed with 320 integration intervals and a relative error required of $s(\xi)$ and ζ_0 less than 10^{-4}, taking about 30 sec. on the older IBM 7090 computer. The corresponding result for the lift and drag coefficients, C_L and C_D, is shown in Fig. 5 together with the experimental data of Parkin's (1958).

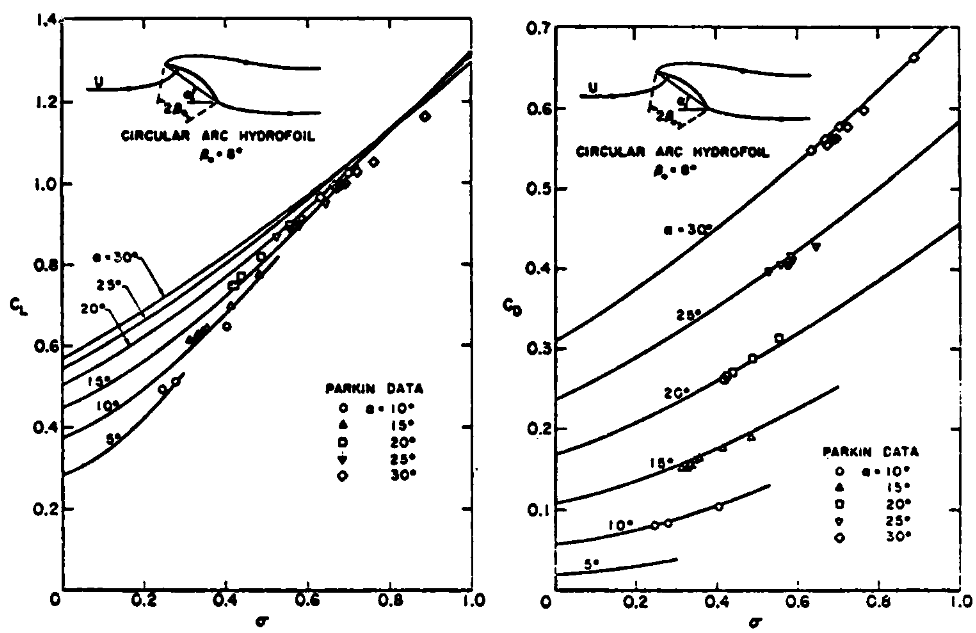

Fig. 5. Lift and drag coefficients of an inclined circular arc hydrofoil in cavity flow.

For the case of flows with free detachment of the cavity boundary, it is convenient to start from a fixed-detachment configuration and extend the wetted body surface outward, on one or both sides, until the free-detachment condition (20) is satisfied.

3.3. Double-loop integral-iteration method. — In executing the above single-loop iterative scheme, it was found that $s^{(n)}(\xi)$ generally converges considerably faster than $\zeta_o^{(n)}$, and, on the other hand, the computation of $s^{(n)}(\xi)$ from (25), which involves a double integration, requires much longer time than that of (26) for $\zeta_o^{(n)}$, which has only a single integration. This observation led Wu & Wang (1964b) to propose an approximate method of iterating $s^{(n)}(\xi)$ and $\zeta_o^{(n)}$ at different levels that has been further refined by Furuya (1975). The refined 'double-loop' iterative scheme may be expressed, in place of (25) and (26), as

$$s^{(n+1)}(\xi)/\hat{A}^{(n+1)} = \mathcal{L}_1[\hat{\beta}(s^{(n)}(\xi));\ \zeta_o^{(m)}] , \tag{29}$$

$$(1+\sigma)^{1/2}e^{i\alpha} = \mathcal{L}_2[\hat{\beta}(s^{(n)}(\xi));\ \zeta_o^{(m+1)}] . \tag{30}$$

In words, (29) provides the iteration on $s^{(n)}(\xi)$, in n, with all the explicit $\zeta_o^{(m)}$ kept fixed, and (30) is used for calculating $\zeta_o^{(m+1)}$ by keeping $s^{(n)}$ fixed. Since in the latter problem (30) becomes a set of two real nonlinear algebraic equations for two real unknowns, $\xi_o^{(m+1)}$ and $\eta_o^{(m+1)}$ (the real and imaginary parts of $\zeta_o^{(m+1)}$), they can be solved by Newton's iterative method or an accelerated iterative scheme (see in § 3.4). Thus, the iterative computations of $s^{(n)}(\xi)$ and $\zeta_o^{(m)}$ are separately executed around two different loops. These iterations must both converge if the corresponding single-loop scheme converges, since the process (29) implies the case of the given body at certain unspecified (α, σ), whereas (30) implies a certain unspecified body held at given (α, σ).

In fact, the rate of convergence of this scheme has been found much superior to the single-loop method in all the cases tested. For the same problem of 16^o circular arc, Wu & Wang (1964b) held $n = 1$, after using the flat-plate solution for $s^{(o)}$ and $\zeta_o^{(o)}$, iterated $\zeta_o^{(m)}$ until its relative error was less than 10^{-3}, and obtained C_L and C_D within the same accuracy, which is remarkably good, while the saving in machine time was as high as by 90% of that used in the single-loop calculation! The high efficiency of this method has made several complex problems tractable to Furuya (1975), who will discuss further aspects of the method later in this session.

3.4. <u>The parameter-iteration method.</u> — This method is proposed here as a further modification (and simplification) of the original Brodetsky (1924) method. First, we use the Chebyshev polynomial approximations to the shape function $\beta(\xi)$, of the form

$$\beta(\xi) = \sum_{n=1}^{N} a_n \cos n\chi + \frac{a_o}{2}, \quad (\xi = \cos\chi) \tag{31}$$

where all the coefficients a_n are real. Then, by (16),

$$\Gamma(\xi) = -\sum_{n=1}^{N} a_n \sin n\chi \tag{32}$$

Substitution of (32) in (15) expresses $s(\zeta)$ in terms of the discrete parameters a_n and ζ_o. Further, by the Fourier inversion,

$$\begin{aligned} a_n &= \frac{1}{\pi}\int_0^{\pi} \hat{\beta}\,(s(\xi))\cos n\chi\, d\chi \quad (n = 0, 1, 2, \ldots N) \\ &\equiv F_{n+1}(a_o, a_1, \ldots a_N, \xi_o\, \eta_o) \quad \text{say,} \end{aligned} \tag{33}$$

in which the last expression, in terms of a nonlinear function of the parameters a_n and $\zeta_o = \xi_o + i\eta_o$, results from substituting (15) and (32) for $s(\xi)$ in $\hat{\beta}(s(\xi))$ of the above integrand. Similarly, substituting (31) in (13), we may rearrange (19) and separate its real and imaginary parts to express the result in the form

$$\xi_o = F_{N+2}(a_n, \xi_o, \eta_o), \qquad \eta_o = F_{N+3}(a_n, \xi_o, \eta_o). \tag{34}$$

Equations (33) and (34) can be combined into a single equation in vector form

$$\underset{\sim}{b} = \underset{\sim}{F}(\underset{\sim}{b}), \tag{35}$$

where

$$\underset{\sim}{b} = (a_o, a_1, \ldots a_N, \xi_o, \eta_o) \equiv (b_1, b_2, \ldots b_{N+2}, b_{N+3}), \tag{36a}$$

$$\underset{\sim}{F} = (F_1, F_2, \ldots F_{N+3}). \tag{36b}$$

The original functional equations (21) and (22) are thus approximated by the nonlinear vector equation (35) of N+3 dimensions.

There are several numerical methods for solving (35) by iteration. One of these is Newton's method (see, e.g. Isaacson & Keller 1966, p. 113):

$$\underset{\sim}{b}^{(\nu+1)} = \underset{\sim}{b}^{(\nu)} - J^{-1}(\underset{\sim}{b}^{(\nu)})\,[\underset{\sim}{b}^{(\nu)} - \underset{\sim}{F}(\underset{\sim}{b}^{(\nu)})], \tag{37}$$

where $J^{-1}(\underset{\sim}{b})$ is the inverse of the square matrix

$$J(\underset{\sim}{b}) \equiv (\delta_{ij} - \partial F_i(\underset{\sim}{b})/\partial b_j), \tag{38}$$

δ_{ij} being the Kronecker delta symbol. Success of this method obviously requires that $J(\underset{\sim}{b})$ be nonsingular at the root of equation (35). When this is the case, the convergence of Newton's method is quadratic since $\underset{\sim}{F}(\underset{\sim}{b})$ is seen to be at least twice differentiable. Uniqueness of the solution, in the case of cavity problems, is perhaps implied by the uniqueness theory of the Villat equations (21) and (22), which has been extensively discussed in the literature.

Another applicable method is the 'accelerated iterative scheme' discussed by Isaacson & Keller (1966, p. 120):

$$b_j^{(\nu+1)} = \gamma_j^{(\nu)} F_j(\underset{\sim}{b}^{(\nu)}) + (1 - \gamma_j^{(\nu)})\, b_j^{(\nu)} \quad (j = 1, 2, \ldots N+3), \tag{39}$$

where $\gamma_j^{(\nu)}$ are the 'acceleration parameters', for which the optimum choice is

$$\gamma_j^{(\nu)} = 1/J_{jj}(b^{(\nu)}), \tag{40}$$

J_{jj} being the j-th diagonal element of the matrix J defined by (38). This procedure seems to be somewhat simpler than Newton's method, since at each λ-th step we need only evaluate the (N+3) partial derivatives, $\partial F_j/\partial b_j$, rather than the whole matrix J.

This parameter-iteration scheme has not yet been tried out, though it seems already very plausible. Whether it is more efficient than the double-loop integral-iteration scheme also remains to be examined.

4. Three-dimensional cavity flows

Primarily due to the great mathematical difficulties the development of three-dimensional cavity theory has been largely limited to the axisymmetric case. Before we proceed to discuss the direct numerical approach, it is in order to mention the following numerical methods that have proved to be useful for calculating axisymmetric cavity flows.

4.1. Trefftz's integral-equation method.

— Using Green's theorem for the axisymmetric velocity potential $\phi(x, r)$, Trefftz (1916) derived the following integral equation for ϕ:

$$\phi(s) = \int_{\Gamma_1+\Gamma_2} G(s,t)\phi(t)dt + f(s) \qquad (s \text{ on } \Gamma_1+\Gamma_2) \tag{41}$$

$$G(s,t) = r(t)\partial\Phi(s,t)/\partial n_t, \qquad \Phi(s,t) = (2/\pi r_1)K(k), \tag{42}$$

$$r_1^2 = (x_s - x_t)^2 + (r_s + r_t)^2, \qquad k^2 = 4r_s r_t/r_1^2, \tag{43}$$

where s and t denote the arc length along the body surface Γ_1 and cavity boundary Γ_2 in a meridian plane, (x_s, r_s), (x_t, r_t) denote the position vectors of any two points on $\Gamma_1+\Gamma_2$, $r(t) \equiv r_t$, $K(k)$ denotes the complete elliptical integral of the first kind, and $f(s)$ is a fixed function of s. The problem is to determine the shape of Γ_2, and hence implicitly the kernel $G(s,t)$, so that $\phi(s)$ satisfies (41) under the constant pressure condition $\partial\phi/\partial s = q_c$ on Γ_2. Thus by this method, calculations of the flow field in a three-dimensional space is reduced to that along the boundary of one dimension, much the same as the integral equation method for plane flows.

Trefftz computed $\phi(s)$ for a jet issuing from a circular orifice in a plane by an iterative scheme, finding the jet contracting coefficient $C_c = 0.61$. In the numerical calculations it has been noted that extreme refinement, near detachment in particular, is essential to accuracy.

4.2. Surface-singularity method.

— The method of distributing sources over the body and cavity surfaces has been applied to different problems

(Shiffman & Spencer 1951, Salamotov 1959). It has been extended by Struck (1970) to include non-axisymmetric source distributions for treating axisymmetric bodies at small incidences, with the cross-flow component linearized. The resulting integral equation, which is similar to Trefftz's equation, and the finite cavity shape were determined by iteration. At $\sigma = 0$ (infinite cavity) his drag coefficient of the disk (normal to flow) is $C_D(0) = 0.83$, and for the sphere, $C_D(0) = 0.31$, with the free-detachment at an arc angle $\theta_s = 57^o$ from the front stagnation point.

It is also possible to represent the axisymmetric body-cavity boundary by a surface distribution of vortex rings. This approach has been adopted by Hunt (1968) to obtain an integral equation for the Trefftz jet problem, which was solved numerically, with the jet boundary adjusted by trial and error until the surface velocity farthermost from the orifice was essentially constant (with the maximum error less than $\pm$ 0.015). Hunt noted that surface velocities were extremely sensitive to very small changes in shape and position of the free streamline, near the orifice in particular, which is typical in all free surface flows. For vanishingly small orifice-to-tank area ratio, his result for the contraction coefficient is $C_c = 0.578$.

4.3. Stream-function method — For axisymmetric flows in a space of $(\epsilon + 2) \geq 2$ dimensions, the stream function $\psi(x, r)$ satisfies the equation

$$\psi_{xx} + \psi_{rr} - \epsilon\,\psi_r/r = 0, \tag{44}$$

where r is the radial coordinate normal to the x-axis of symmetry. For an axisymmetric cavity flow in this space, $\psi(x, r;\epsilon)$ satisfies the condition $\psi = 0$ on the body surface Γ_1 (a line in the meridian plane) and $r^{-\epsilon}\ \partial\psi/\partial n = 1$ on a free boundary $\Gamma_2(\epsilon)$. For this class of problems Garabedian (1956) developed a new method in which $\psi(x, r;\epsilon)$ is assumed to be a regular function of ϵ in the half plane $\mathrm{Re}(\epsilon) > -1$ so that the solution may be continued, analytically in ϵ, to arbitrary dimensions. By expanding ψ about the corresponding plane flow $\psi_o(x, y) = \psi(x, r;0)$, where $y \equiv r$, in a power series in $\delta = \epsilon/(\epsilon+2)$ within the circle of convergence $|\delta| < 1$, the required solution in the physical case is then $\psi(x, r;1)$ corresponding to $\delta = 1/3$. With the aid of numerical computation and

extrapolation in the dimension parameter ϵ, Garabedian provided for the circular disk in infinite cavity flow the drag coefficient $C_D = 0.827$, and for the circular orifice jet the contraction coefficient $C_c = 0.579$.

5. Finite-difference methods

The relaxation or finite-difference approach was first used by Southwell and Vaisey (1946) to evaluate a number of free-surface flows, including the axisymmetric jet from an orifice, the cylinder and sphere with a cusped cavity, and a two-dimensional planing surface under gravity. In these calculations the 5-point formula was adopted for the finite difference approximation to the equation (44) (with $\epsilon = 1$) for the stream function. The principal difficulty, as also later experienced by other authors in computing all free-surface flows, is that the shape and asymptotic position of the free boundary must be adjusted, essentially by trial and error, in successive steps of computation. To achieve a uniformly small error it is usually necessary to refine the mesh size carefully in a neighborhood of the detachment point. By this method Southwell and Vaisey obtained for the jet problem a contraction coefficient of $C_c = 0.608$, which agrees with the result given by Trefftz and by Abul-Fetouh (1949) who also employed the finite-difference method, but is noticeably higher than the value of Garabedian's and Hunt's, who used different methods.

In respect to special handling of the free surface configuration, corner discontinuities, and the asymptotic flow field the contribution of Brennen (1969), who treated the axisymmetric finite-cavity flows past a circular disk and sphere by the finite-difference method, is noteworthy. In his theory the Raibouchinsky model is adopted for its advantageous symmetry, and the velocity potential ϕ and stream function ψ are taken as the independent variables so that the flow boundaries become known straight lines in the (ϕ, ψ) plane. Although the basic equation:

$$\partial^2(\log f)/\partial\phi^2 + \partial^2 f/\partial\psi^2 = 0, \tag{45}$$

where $f = r^2$ (the square of the radial variable), is now nonlinear, but it is of little disadvantage in numerical methods. Further, careful handling of the critical regions near the stagnation and detachment points was provided by imbedding series expansions of the local solution. An

asymptotic form of the solution was also applied on the upstream boundary. These aspects of careful preparation for the use of relaxation method should rule out several possible sources of error in the numerical result that may be speculated in other instances. Brennen applied the relaxation calculations to the basic equations in a quadrant of the flow bounded laterally by concentric cylinders of different sizes, the unbounded-flow case being reached by extrapolation, with the maximum error in f estimated to be less than 0.5 per cent. His disk drag coefficient at $\sigma = 0$ is $C_D = 0.826$, which is in agreement with Garabedian's 0.827. For the sphere with an infinite cavity, Brennen obtained a value of $C_D = 0.317$, and a free detachment at $\theta_s = 56^\circ$, which are in close agreement with Struck's results.

These consistent theoretical predictions, however, are at variance with the experimental observations. The measured sphere drag by Eisenberg & Pond (1948) and Hsu & Perry (1954), when extrapolated to $\sigma = 0$, has a mean of $C_D \simeq 0.25$, which is considerably smaller than the predicted value of 0.31. In addition, the measured separation position lies invariably downstream of the predicted free-detachment point. For instance, at $\sigma = 0.1$ and the Reynolds number 10^5, the experimental result is $\theta_s = 82^\circ$, versus the theoretical value of $\theta_s \simeq 58^\circ$. These evidences all indicate the importance of the viscous effect on the process of separation from curved bodies, and hence on the wake-pressure drag. They also raise the question whether some modification of the Villat-Brillouin condition for free detachment will be required for improving the accuracy of the inviscid theory.

In regard to the margin of confidence in the finite-difference and other related methods as we have discussed with special reference to free surface flows, we note that a uniform error bound is generally difficult to achieve, since small variation in the velocity and the shape of free boundary near a free or fixed detachment point may give rise to relatively large displacements of the free surface downstream. Further, we find in many cases a bent shape of the free streamline near a fixed detachment point, and the local theoretical prediction of a continuous slope of the free streamline is not borne out by the finite-difference method, even with increased refinement of the mesh size in that neighborhood. Finally, the question of the magnitude of truncation error in ...e

finite-difference technique still remains to be clarified. The difficulty of this problem is magnified by the need of trial-and-error procedures in these calculations.

Acknowledgment

This work was jointly sponsored by the Office of Naval Research and by the Naval Ship System Command General Hydrodynamics Research Program, under the administration of the Naval Ship Research and Development Center.

References

Abul-Fetouh, A. 1949 Characteristics of irrotational flow from axially symmetric orifices. Ph.D. Dissertation, Univ. of Iowa, Iowa.

Birkhoff, G., Goldstine, H. & Zarantonello, E. 1954 Rend. Seminar. Mat. Univ. Politec. Torino 13, 205-224.

Birkhoff, G., Young, D., & Zarantonello, E. 1953 Proc. Symp. Appl. Math. 4, 117-140.

Birkhoff, G. and Zarantonello, E. 1957 Jets, Wakes and Cavities. Academic Press, New York.

Brennen, C. 1969 A numerical solution of axisymmetric cavity flows. J. Fluid Mech. 37, 671-688.

Brillouin, M. 1911 Les surfaces de glissement de Helmholtz et la résistance des fluides. Ann. Chim. Phys. 23, 145-230.

Brodesky, S. 1923 Proc. Roy. Soc. London A, 102, 542-553.

Eisenberg, P. & Pond, H. C. 1948 Water tunnel investigations of steady state cavities. David Taylor Model Basin Rep. 668, Washington, D. C.

Furuya, O. 1975 Nonlinear calculation of arbitrarily shaped super-cavitating hydrofoils near a free surface. J. Fluid Mech. 68, 21-40.

Garabedian, P. 1956 The mathematical theory of three-dimensional cavities and jets. Bull. Amer. Math. Soc. 62, 219-235.

Gilbarg, D. 1960 Jets and Cavities. In Handbuch der Physik, vol. ix, 311-445, Springer-Verlag, Berlin.

Gilbarg, D. 1949 Proc. Nat. Acad. Sci. U.S.A., 35, 609-612.

Helmholtz, H. 1868 Uber diskontinuierliche Flüssigkeitsbewegungen Monatsber. Akad. Wiss. Berlin, 215-228; Wiss Abh. 1, 154, Vol V; ibid. Phil. Mag. (4) 36, 337.

Hsu, E-Y., & Perry, B. 1954 Water tunnel experiments on spheres in cavity flow. Calif. Inst. Technol. Rep. No. E-24.9.

Hunt, B.W. 1968 Numerical solution of an integral equation for flow from a circular orifice. J. Fluid Mech. 31, 361-377.

Isaacson, E. & Keller, H.B. 1966 Analysis of Numerical Methods. New York, Wiley.

Kirchhoff, G. 1869 Zur theorie freier Flüssigkeitsstrahlen. J. reine agnew. Math. 70, 289-298; Ges. Abh. 416.

Parkin, B.R. 1958 Experiments on circular-arc and flat-plate hydrofoils. J. Ship Res. 1, 34-56.

Roshko, A. & Fiszdon, W. 1967 On the persistence of transition in the near-wake. 60th Anniv. Volume for L.I. Sedov, USSR National Committee on Theor. and Appl. Mech.

Salamotov, D. 1959 J. Appl. Math. Mech. 23, 2.

Shiffman, M. and Spencer, D. 1951 The force of impact on a cone striking a water surface. Comm. Pure Appl. Math. 4, 379-417.

Southwell, R.V. and Vaisey, G 1946 Fluid motions characterized by free streamlines. Phil. Trans. 240, 117-161.

Struck, H.D. 1970 NASA TN D-5634.

Trefftz, E. 1916 Über die Kontraktion kreisformiger Flüssigkeitsstrahlen. Z. Math. Phys. 64, 34-61.

Tulin, M.P. 1964 Supercavitating flows - small perturbation theory. J. Ship Res. 7, 16-37.

Villat, H. 1914 Sur la validité des solutions de certains problemes d'hydrodynamique. J. de Math. (6) 10, 231-290.

Wu, T. Y. 1962 A wake model for free streamline flow theory, Part I. Fully and partially developed wake flows and cavity flows past an oblique flat plate. J. Fluid Mech. 13, 161-181.

Wu, T. Y. 1972 Cavity and wake flows. Ann. Rev. Fluid Mech. 4, 243-284.

Wu, T. Y. & Wang, D. P. 1964a A wake model for free-streamline flow theory, Part 2. Cavity flows past obstacles of arbitrary profile. J. Fluid Mech. 18, 65-93.

Wu, T. Y. & Wang, D. P. 1964b An approximate numerical scheme for the theory of cavity flows past obstacles of arbitrary profile. Trans. ASME, J. Basic Eng. 86D, 556-560.

Wu, T.Y., Whitney, A.K. & Brennen, C. 1971 Wall effects in cavity flows. J. Fluid Mech. 49, 223-256.

A VARIATIONAL PRINCIPLE ASSOCIATED WITH A LOCALIZED FINITE-ELEMENT TECHNIQUE FOR STEADY SHIP WAVE AND CAVITY PROBLEMS

B. Yim

David W. Taylor Naval Ship Research and Development Center
Bethesda, Maryland 20084 U.S.A.

ABSTRACT

Variational treatments of steady ship wave and cavity problems are formulated for numerical solution. In each problem, the Lagrangian is constructed and the equivalence of the variational formulation to the corresponding boundary value problem is proved. Certain computing aspects of the problems are discussed and a simple example of the formulation for a two-dimensional cavity flow is given.

To find the numerical solution for flow fields near a body, a localized finite-element technique is considered in a small domain near the body. The total flow field is divided into the inner field and the outer field with a common boundary surface between the two fields. The common boundary or interface may intersect the body. In the outer field, we use conventional linear solutions such as superposition of eigen solutions or Green's functions with unknown coefficients which are to be determined by the conditions at the interface. Variational principles are applied to formulate the Lagrangian which can be used to obtain the inner solution by a finite-element technique, and the coefficients for the outer solution.

1. Introduction

Since the advent of high-speed computers, many complicated hydrodynamic problems have been solved by the use of a finite difference scheme, finite-element technique, or the method of singularity distribution. However, most of these problems are still limited to either two-dimensional or axisymmetric flows, or simple versions of three-dimensional flows. Although computers are extremely fast, they are not fast enough or do not have adequate

storage capacity at present to deal with a vast number of elements in three dimensions. The benefits of these numerical schemes are in their practical applicability to arbitrary boundaries whereas the analytical representations of the boundary condition are extremely cumbersome or inaccurate. In order to benefit the most from numerical schemes, and yet apply them to a wider range of problems including the practical three-dimensional ones, we consider here the localized finite-element technique and the associated variational problems.

In many flow problems, linear analytical solutions are available. However, these linear solutions may not be accurate enough to be useful, especially near the bodies concerned. Sometimes the linear solutions have singularities at certain points on the bodies. Nevertheless, such solutions may still be very useful far from the body. To make use of this far field solution and to circumvent the difficulty near the body, we can apply the method of singular perturbation or the method of matched asymptotic expansion.[1*] Heretofore, this method has been applied only to simple problems with simple geometries. If numerical solutions for the inner expansion are matched to an analytical outer solution, the scope of applicability of the numerical scheme would become considerably wider, and more practical problems could be solved effectively. This scheme can be used not only for the case of singular perturbations but also when we want to consider the boundary condition on the body more accurately. The feasibility of such techniques has been demonstrated recently by the application of a finite-element technique in the inner field for sinusoidal wave problems.[2,3]

In the formulation of such a technique, variational principles can be utilized very effectively. An application of the variational principle to steady ship-wave problems was investigated by Bessho,[4] and his method has been used to obtain numerical solutions for several problems.[5] Variational treatment of cavity flows is an old problem.[6,7] In application of the variational principle, the main task is to find a functional, i.e., Lagrangian which has an extremum at the solution of the problem concerned, and to prove that the extremum of the functional is equivalent to the solution of the given boundary value problem.

In the present study, we divide the problem into an inner and an outer field. In the outer field, the solution can be obtained by superposition of eigen solutions or Green functions with unknown coefficients. If the linear outer solution is available, this can be used with a minor correction. In the inner field, we use the finite-element technique with the exact body boundary conditions. The solutions for the inner and outer fields satisfy the conditions at the interface which require the continuity of the solution and the normal derivative of the solution at the interface. The inner field may only be a small domain near

*See list of references at end of paper.

a three-dimensional body. Here, we formulate the Lagrangian which will lead to inner as well as outer solutions for steady ship wave and cavity problems.

It is well-known that existing linear ship wave theories give poor predictions of wave resistance. Thus, with a linear free-surface condition, an improved treatment of the ship boundary condition, even just at the forebody, is desireable. Although the Green function for ship waves is known, it is very difficult to evaluate this function numerically, using the normal method of singularity distribution. However, with the present method, the evaluation of the Green function is required only at convenient locations and at fewer points.

For either the cavity or ship wave problem, the Lagrangian is constructed and the equivalence with the corresponding boundary value problem is proven. The computing aspects of the problems are discussed and a simple example of the treatment for a two-dimensional cavity flow is shown.

2. Nonlinear Ship Wave Problem

An expression for hydrodynamic pressure has been shown[4,8] to be usable as a Lagrangian for free-surface flow problems when the equations of motion and boundary conditions in an inviscid and incompressible fluid are derived from a variational principle. Since Luke[8] has derived expressions for an unsteady two-dimensional flow problem, we will start with a similar derivation for a steady three-dimensional flow problem, followed by imbedding the numerical solution within the field of known analytical eigen solutions after the technique used by Bai and Yeung[2] or Chen and Mei.[3]

We consider a perturbation velocity potential $\varphi(x,y,z)$ defined in a fluid domain D, below $z = h(x,y)$, which may consist of a free surface S_F and a ship surface S_s. A right-handed Cartesian coordinate system $(O - x,y,z)$ is used. The perturbation velocity is $\bar{q} = -\nabla\varphi$. At infinity, the flow is considered to be uniform with velocity $\bar{U}$ in the x direction. Gravity g acts in the negative z direction. We consider a domain D enclosed by a mathematical surface S_J below $z = h(x,y)$. For the time being, we assume $\delta\varphi = 0$ and $\delta h = 0$ on S_J as in Luke's treatment. We construct a function J to have an extremum value at the solution of the free-surface boundary-value problem in D:

$$J = \iiint_D^{h} \left(\frac{1}{2}\nabla\varphi \cdot \nabla\varphi - \bar{U} \cdot \nabla\varphi\right) dz dx dy + \iint_{S_F} g \frac{h^2}{2} dx dy \tag{1}$$

where $\varphi(x,y,z)$ and $h(x,y)$ are allowed to vary over their domain of definition. We prove that minimization of the function J is indeed equivalent to formulating the free-surface boundary-value problem. By performing a variation on (1), applying the Green theorem

$$\frac{1}{2}\iiint_D \delta(\nabla\varphi\cdot\nabla\varphi)dzdxdy = -\iiint_D \delta\varphi\nabla^2\varphi\, dzdxdy - \iint_S \delta\varphi\varphi_n\, dS$$

and the Gauss theorem

$$\iiint_D \bar{U}\cdot\nabla\varphi\, dzdxdy = -\iint_S \bar{U}\cdot\bar{n}\,\varphi\, dS$$

and noting that the upper limit of the z-integration is a variable h we obtain

$$\delta J = \iint_{S_F}\left(\frac{1}{2}(\nabla\varphi)^2 - U\varphi_x + gz\right)_{z=h(x,y)}\delta h\, dxdy - \iiint_D \delta\varphi\nabla^2\varphi\, dzdxdy$$

$$-\iint_{S_s US_F}\delta\varphi(\varphi_n - \bar{U}\cdot\bar{n})\, dS \qquad (2)$$

where $\bar{n}$ is a normal vector on the surface directed into the interior of D. Since δh and $\delta\varphi$ are arbitrary, we obtain

$$\begin{aligned} \frac{1}{2}(\nabla\varphi)^2 - U\varphi_x + gz &= 0 && \text{on } S_F \\ \nabla^2\varphi &= 0 && \text{in D} \\ \varphi_n &= \bar{U}\cdot\bar{n} && \text{on } S_s US_F \end{aligned} \qquad (3)$$

These are exactly the equations associated with the inviscid incompressible flow past boundaries, including a free surface, in an otherwise infinite medium ($D\to\infty$), except that a radiation condition is missing. The condition $\delta\varphi = \delta h = 0$ at ∞ does not seem to be equivalent to a radiation condition since a ship wave has the particular quality that it decays very rapidly upstream of the ship, while it propagates in the wake, decaying slowly in three dimensions but not in two dimensions. If we know the asymptotic behavior of the solution, by choosing eigen solutions or the Green functions φ_i that satisfy the Laplace equation and the asymptotic behavior at infinity, we may substitute[4]

$$\varphi = \sum_{i=1}^{N} a_i\varphi_i$$

in equation (1) and obtain a_i by solving the simultaneous equations

$$\frac{\partial J}{\partial a_i} = 0$$

which assure that J is an extremum with respect to the coefficients a_i.

The number N may depend on selection of φ_i and the desired accuracy. For a nonlinear solution, we may use an iteration scheme starting with the first-order solution as is common in nonlinear problems.

Now, when we want to use the function J to obtain a numerical solution by the finite-element technique, we have two problems: (1) the domain D is too large, and (2) the radiation condition has to be satisfied. As we have seen previously, the eigen solution can be conveniently used to satisfy the latter problem. Thus, combining the finite-element technique and the eigen solutions may include the advantages of both approaches.

We divide the infinite domain into D_1 and D_2, and in the smaller domain D_1, we will apply the finite-element technique. In domain D_2, which includes infinity, we can find the far-field eigen solutions[9] or the analytical Green functions that satisfy the Laplace equation and the linear, free-surface boundary condition, including the radiation condition. For example, a far-field solution obtained from a Kelvin source distribution m on the ship surface can be used in D_2, where m is determined by a variational principle to be explained below. At the interface S_J between D_1 and D_2, the potentials, φ_1 and φ_2, in the two domains, should match. We consider that either S_J consists of planes S_{Jx} $(x = x_1, x_2)$, S_{Jy} $(y = y_1, y_2)$, and S_{Jz} $(z = z_1)$ so that D_1 is a rectangular box with a free-surface containing a ship or that S_J intersects the ship surface, S_s, leaving a part of the ship in D_1 and the other part in D_2. (See Figure 1).

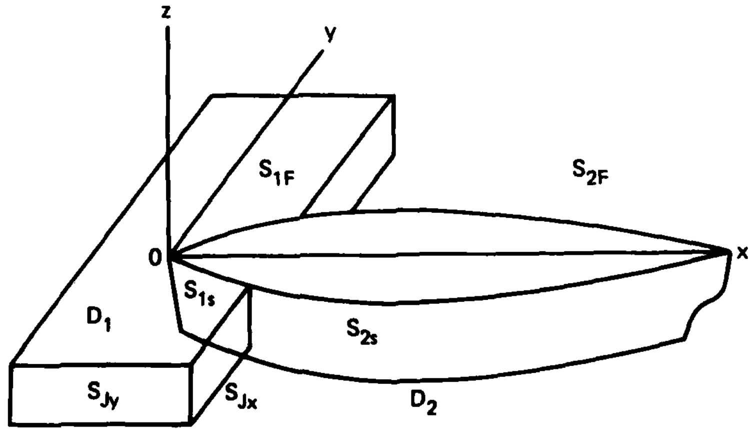

Figure 1 – Domains of Ship-Wave Problem

First, we would like to find a solution φ_1 satisfying the Laplace equation and the exact free-surface boundary condition in D_1, while the potential φ_2 in D_2 which is represented by

$$\varphi_2 = \sum_{i=1}^{N} m_i \varphi_{2i} \tag{4}$$

is known to satisfy the linear free-surface boundary condition,

$$\varphi_{2xx} + \frac{g}{U^2}\varphi_{2z} = 0 \qquad \text{on } S_F \cap D_2 \tag{5}$$

Nonlinear conditions to the value of φ_1 on $S_J \cap S_F$ are assumed to be negligible.

It follows from equations (1) through (5) that a Lagrangian which has an extremum for the ship-wave problem can be given by

$$J = \iiint_D \int_{z_1}^{h_1} \left(\frac{1}{2}\nabla\varphi_1\nabla\varphi_1 - \bar{U}\cdot\nabla\varphi_1 + gz\right) dzdxdy + \iint_{S_{2S}}^{\frac{U}{g}\varphi_{2x}(z=0)} \bar{U}\cdot\bar{n}_2\,\varphi_2\, dS$$

$$-\iint_{S_J}\int_{z_1}^{h_o}\left(\varphi_1 - \frac{1}{2}\varphi_2\right)\varphi_{2n}\, dS - \iint_{S_{Jx}}\int_{z_1}^{\frac{U}{g}\varphi_{2x}} \bar{U}\cdot\bar{n}_1\,\varphi_1\, dS$$

$$-\iint_{S_{2S}}^{h_o} \frac{1}{2}\varphi_{2n}\varphi_2\, dS - \frac{U^2}{g}\oint_{\substack{2F \\ (S_{Jx} \cup S_{2S}) \cap S_F}} (\varphi_2\varphi_{2x})\, dy \tag{6}$$

where $\bar{n}$ is directed into the interior of domain D; h_1 is the unknown wave height; h_o is a known function of x and y with the first approximation taken as zero; subscripts 1 and 2 refer to quantities belonging to D_1 and D_2, respectively, as in $S_{2S} \equiv S_s \cap D_2$; and the integral symbols $\iint_{S_{2S}}^{\frac{U}{g}\varphi_{2x}}$ indicate that the limit of S_{2S} integrals on the free surface is taken to be $z = U\varphi_{2x}/g$ at $z = 0$. The relation between the directions of the normal to the specified surface and the line integral enclosing the surface is the same as the relation between the direction of a vortex and the rotation of the vortex. We denote the line integral as $\oint_{1F}$ indicating that the line integral is enclosing the surface S_{1F} where the normal is already defined into the flow. When there could be an ambituity in the normal directions, we denote it as in $\oint_{J,2}$ where the surface is S_J and the normal direction is into D_2.

In taking the variation of J we use

$$\bar{n} = \pm (h_x, h_y, -1)/(h_x^2 + h_y^2 + 1)^{1/2}, \pm \Bigg\} \text{for} \Bigg\{ \begin{matrix} S_F \\ S_S \end{matrix}$$

$$dS = dxdy\,(h_x^2 + h_y^2 + 1)^{1/2}, \text{ and } \bar{n}_1 = -\bar{n}_2 .$$

Application of the Green and Gauss theorems as in equation (2) and neglect of higher-order terms in D_2 leads to

$$\delta J = \iint_{S_{1F}} \left[\frac{1}{2}(\nabla\varphi_1)^2 - U\varphi_{1x} + gz\right]_{z=h_1(x,y)} \delta h\,dxdy - \iiint_{D_1} \delta\varphi_1 \nabla^2\varphi_1\,dzdxdy$$

$$- \iint_{S_{1S} \cup S_{1F}} (\varphi_{1n} - \bar{U}\cdot\bar{n})\,\delta\varphi_1\,dS - \iint_{S_{2S}} (\varphi_{2n} - \bar{U}\cdot\bar{n})\,\delta\varphi_2\,dS - \iint_{S_J} (\varphi_{1n} + \varphi_{2n})\,\delta\varphi_1\,dS$$

$$- \iint_{S_J} (\varphi_1 - \varphi_2)\,\delta\varphi_{2n}\,dS - \frac{U^2}{g}\left[\oint_{\substack{1F \\ S_{Jx} \cap S_F}} \varphi_1\,\delta\varphi_{2x}\,dy - \oint_{\substack{2F \\ S_{2S} \cap S_F}} \varphi_2\,\delta\varphi_{2x}\,dy\right]$$

$$+ \frac{1}{2}\iint_{S_J \cup S_{2S}} (\delta\varphi_2\,\varphi_{2n} - \varphi_2\,\delta\varphi_{2n})\,dS - \frac{U^2}{2g}\oint_{\substack{2F \\ (S_{2S} \cup S_{Jx}) \cap S_F}} (\delta\varphi_2\,\varphi_{2x} + \varphi_2\,\delta\varphi_{2x})\,dy \tag{7}$$

From the identity

$$\iiint_{D_2} [\delta\varphi_2\,\nabla^2\varphi_2 - \varphi_2\,\nabla^2(\delta\varphi_2)]\,dzdxdy = \iint_{S_2} (\varphi_{2n}\,\delta\varphi_2 - \varphi_2\,\delta\varphi_{2n})\,dS = 0 \tag{8}$$

and from equation (5) and the condition that $\varphi_{2z} = -\varphi_{2n}$ on $z = 0$, we have

$$\iint_{S_J \cup S_{2S}} (\delta\varphi_2\,\varphi_{2n} - \varphi_2\,\delta\varphi_{2n})\,dS$$

$$= -\iint_{S_{2F}} (\delta\varphi_2\,\varphi_{2n} - \varphi_2\,\delta\varphi_{2n})\,dxdy = -\frac{U^2}{g}\iint_{S_{2F}} (\delta\varphi_2\,\varphi_{2xx} - \varphi_2\,\delta\varphi_{2xx})\,dxdy$$

$$= \frac{U^2}{g}\oint_{\substack{2F \\ (S_{Jx} \cup S_{2S}) \cap S_F}} (\delta\varphi_2\,\varphi_{2x} - \varphi_2\,\delta\varphi_{2x})\,dy \tag{9}$$

Equation (8) provides a reciprocity relation in S_2. However, equation (9) indicates that the reciprocity does not hold for the integrating domain $S_J \cup S_{2S}$. This fact makes construction of the Lagrangian difficult.

From equations (6) through (9), we obtain

$$\delta J = \iint_{S_{1F}} \left[\frac{1}{2}\nabla\varphi_1 \nabla\varphi_1 - U\varphi_{1x} + gz\right]_{z=h(x,y)} \delta h \, dxdy - \iiint_{D_1} \delta\varphi_1 \nabla^2\varphi_1 \, dzdxdy$$

$$- \iint_{S_S \cup S_F} (\varphi_n - \bar{U}\cdot\bar{n})\,\delta\varphi \, dS - \iint_{S_J} \delta\varphi_1 (\varphi_{1n} + \varphi_{2n})\, dS$$

$$- \iint_{S_J} (\varphi_1 - \varphi_2)\,\delta\varphi_{2n}\, dS + \frac{U^2}{g} \oint_{\substack{2F \\ S_{Jx}\cap S_F}} (\varphi_1 - \varphi_2)\,\delta\varphi_{2x}\, dy \tag{10}$$

Since δh, $\delta\varphi_1$, $\delta\varphi_2$, $\delta\varphi_{2x}$ and $\delta\varphi_{2n}$ are arbitrary, we obtain

$$\begin{aligned}
&\frac{1}{2}(\nabla\varphi_1)^2 - U\varphi_{1x} + gh = 0 && \text{on } S_{1F} \\
&\nabla^2\varphi_1 = 0 && \text{in } D_1 \\
&\varphi_n = \bar{U}\cdot\bar{n} && \text{on } S_s \cup S_F \\
&\varphi_{1n} = -\varphi_{2n},\ \varphi_1 = \varphi_2 && \text{on } S_J
\end{aligned} \tag{11}$$

These equations provide the nonlinear boundary value problem. For numerical computation by a finite-element scheme, we may use a simpler but equivalent form of the Lagrangian given in (6).

$$J = \iiint_{D_1} \int_{z_1}^{h_1(x,y)} \frac{1}{2}\nabla\varphi_1 \nabla\varphi_1 \, dzdxdy + \iint_{S_{1S}\cup S_{1F}} Uh_x\varphi_1 \, dxdy + \iint_{S_{1F}} \frac{gh^2}{2}\, dxdy$$

$$+ \iint_{S_{2S}} \int^{\frac{U}{g}\varphi_{2x}} \bar{U}\cdot\bar{n}\,\varphi_2 \, dzdx - \frac{1}{2}\iint_{S_{2S}} \int^{h_o} \varphi_{2n}\varphi_2 \, dS - \iint_{S_{Jx}} \int^{\frac{U}{g}\varphi_{2x}} \bar{U}\cdot\bar{n}\,\varphi_1 \, dzdx$$

$$- \iint_{S_J} \int_{z_1}^{h_o} \left(\varphi_1 - \frac{\varphi_2}{2}\right)\varphi_{2n}\, dS - \frac{U^2}{g} \oint_{\substack{2F \\ (S_{Jx}\cup S_{2S})\cap S_F}} (\varphi_2\varphi_{2x})\, dy \tag{12}$$

In order to numerically minimize J, we use an iteration scheme because of the nonlinear terms appearing in (12); for the first approximation, we use finite elements in a small region D_{11} beneath an initially assumed free surface, the surface $z = 0$. We assign φ_1 for each element point in D_{11} but allow $h(x,y)$ to be variable for points on $z = 0$ on S_{1F}:

$$\begin{aligned} \varphi_1 &= \Sigma N_i \varphi_{1i} \qquad \text{in } D_{11} \\ h &= \Sigma H_i h_i \qquad \text{on } S_{1F} \end{aligned} \tag{13}$$

where φ_{1i} and h_i denote values of φ_1 and h at the ith nodal point of finite elements in D_{11} and S_{1F}, respectively; N_i and H_i are the so-called shape functions[10] which are one at the ith nodal point and zero at the other points in D_{11} and S_{1F}, respectively. By taking

$$\frac{\partial J}{\partial \varphi_{1i}} = 0, \ \frac{\partial J}{\partial h_i} = 0, \ \frac{\partial J}{\partial m_i} = 0 \tag{14}$$

we will have a set of simultaneous equations to solve for φ_{1i}, h_i, and m_i. However, for the first iteration, we neglect all of the nonlinear terms. When we have obtained φ_{1i} in D_{11}, h_i in S_{F1} and m_i, we can use the values of h_i to create new finite elements and feed φ_{1i}, h_i, and m_i into the second-order terms for the second iteration which will also be a set of linear simultaneous equations. In the first linearization process, for the values of φ on the unknown free surface, we may use a Taylor expansion such as

$$\varphi_2(z) = \varphi_2(o) + \varphi_{2z}(o)z + \frac{1}{2}\varphi_{2zz}(o)z^2 + \ldots \tag{15}$$

When D_1 includes the whole ship, the S_{2S}-integration will disappear in equation (12).

3. Cavity Flow

For a high-speed cavitating flow with zero-gravity, using the same notation as previously given, the Lagrangian is given by

$$\begin{aligned} J = &\iiint_{D_1}^{h} \left(\frac{1}{2}\nabla\varphi_1 \cdot \nabla\varphi_1 - \overline{U}\cdot\nabla\varphi_1\right) dz\,dx\,dy + U^2 \iint_{S_c \cap (D_1 \cup D_2)} \frac{\sigma}{2} h\, dx\,dy + \frac{U}{2} \iint_{S_{2c}} \varphi_{2x} h\, dx\,dy \\ &- \iint_{S_J}^{h_o} \left(\varphi_1 - \frac{1}{2}\varphi_2\right)\varphi_{2n}\, dS + \frac{U}{2} \oint_{\substack{J,2 \\ S_J \cap (S_F \cup S_c)}} (\varphi_2 h)\, dy - \iint_{S_J}^{h} \overline{U}\cdot\bar{n}\varphi_1\, dS \end{aligned} \tag{16}$$

where the cavitation number σ is defined by

$$\sigma = (p_\infty - p_c)/\left(\frac{1}{2}\rho U^2\right) \tag{17}$$

with p_∞ the pressure at infinity and p_c the pressure in the cavity. In the domain D_2, the potential φ_2 is a superposition of either eigen functions or the Green functions which satisfy the Laplace equation and the condition at infinity; h is the z coordinate of surfaces S_s and S_F or the cavity surface, S_c, i.e.,

$$z = h(x, y) \tag{18}$$

The variational problem that extremizes equation (16) for variables φ_1, φ_2, and h, is equivalent to the following cavity flow problem.

A cavity flow due to a body surface S_s is enclosed by a domain D_1 which surrounds the body and all or a part of the cavity. In the domain D_2, which is outside of the domain D_1, a linearized boundary condition is assumed to hold, i.e.,

$$\begin{aligned} \nabla^2\varphi_2 &= 0 && \text{in } D_2 \\ \varphi_{2x} &= 0 && \text{on } S_{2F} \\ \varphi_{2n} &= \overline{U}\cdot\overline{n} = \pm\, Uh_{2x}/(h_{2x}^2 + h_{2y}^2 + 1)^{1/2} && \\ &\left.\pm\right\}\text{ for }\left\{\begin{matrix} S_{2F} \\ S_{2c} \end{matrix}\right. && \end{aligned} \tag{19}$$

and

$$\varphi_{2x} = -\frac{\sigma}{2}U \qquad \text{on } S_{2c}$$

where $z = h_2(x, y)$ is unknown.

However, in D_1, the nonlinear cavity boundary condition is satisfied, i.e.,

$$\begin{aligned} \nabla^2\varphi_1 &= 0 && \text{in } D_1 \\ \varphi_{1n} &= \overline{U}\cdot\overline{n} && \text{on } S_s \\ U\varphi_{1x} - \frac{1}{2}\nabla\varphi_1\nabla\varphi_1 &= 0 && \text{on } S_F \\ U\varphi_{1x} + \frac{\sigma}{2}U^2 - \frac{1}{2}\nabla\varphi_1\nabla\varphi_1 &= 0 && \text{on } S_c \end{aligned} \tag{20}$$

On the interface S_J

$$\varphi_1 = \varphi_2 \text{ and } \varphi_{1n} = -\varphi_{2n}$$

By an operation similar to that used to obtain equation (7), we have

$$
\begin{aligned}
\delta J = &-\iiint\limits_{D_1} \delta\varphi_1 \nabla^2 \varphi_1 \, dzdxdy - \iint\limits_{S_1} \delta\varphi_1 (\varphi_{1n} - \overline{U} \cdot \overline{n}) \, dS \\
&+ \iint\limits_{S_{1F}} \left(\frac{1}{2} \nabla\varphi_1 \nabla\varphi_1 - U \varphi_{1x}\right) \delta h \, dxdy + U^2 \iint\limits_{S_{2c}} \frac{\sigma}{2} \delta h \, dxdy \\
&- \iint\limits_{S_{1c}} \left(\frac{1}{2} \nabla\varphi_1 \nabla\varphi_1 - U^2 \frac{\sigma}{2} - U \varphi_{1x}\right) \delta h \, dxdy - \iint\limits_{S_J} \delta\varphi_{2n} (\varphi_1 - \varphi_2) \, dS \\
&- \iint\limits_{S_J} \delta\varphi_1 (\varphi_{1n} + \varphi_{2n}) \, dS + \frac{U}{2} \iint\limits_{S_{2c}} (\delta\varphi_{2x} h + \varphi_{2x} \delta h) \, dxdy \\
&- U \oint\limits_{\substack{J,2 \\ S_s \cap (S_F \;\; S_c)}} \varphi_1 \delta h \, dy + \frac{U}{2} \oint\limits_{\substack{J,2 \\ S_s \cap (S_F \cup S_c)}} (\varphi_2 \delta h + h \delta\varphi_2) \, dy \\
&+ \frac{1}{2} \iint\limits_{S_J} (\delta\varphi_2 \varphi_{2n} - \varphi_2 \delta\varphi_{2n}) \, dS
\end{aligned}
\tag{21}
$$

However, since

$$
\iint\limits_{S_J \cup S_{2c} \cup S_{2F}} (\delta\varphi_2 \varphi_{2n} - \varphi_2 \delta\varphi_{2n}) \, dS = 0,
$$

$$
\varphi_{2n} = \overline{U} \cdot \overline{n} = \pm U h_x / (h_x^2 + h_y^2 + 1)^{1/2}
$$

$$
\left.\pm\right\} \text{ for } \left\{\begin{matrix} S_{2F} \\ S_{2c} \end{matrix}\right. \tag{22}
$$

and

$$dS = (h_x{}^2 + h_y{}^2 + 1)^{1/2}\, dxdy\,,$$

we have

$$\iint_{S_J} (\delta\varphi_2\, \varphi_{2n} - \varphi_2\, \delta\varphi_{2n})\, dS = -\iint_{S_{2F} \cup S_{2c}} (\delta\varphi_2\, \varphi_{2n} - \varphi_2\, \delta\varphi_{2n})\, dS$$

$$= \mp U \iint_{S_{2F} \cup S_{2c}} (\delta\varphi_2\, h_x - \varphi_2\, \delta h_x)\, dxdy \qquad \left(\mp\right\} \text{ for } \left\{\begin{matrix} S_{2F} \\ S_{2c} \end{matrix}\right)$$

$$= U \oint_{\substack{2F,\,2c \\ (S_{2c} \cup S_{2F}) \cap S_J}} (\delta\varphi_2\, h - \varphi_2\, \delta h)\, dy + U \iint_{S_{2c}} (\varphi_{2x}\, \delta h - \partial\varphi_{2x}\, h)\, dxdy \tag{23}$$

where we have used the fact that

$$\varphi_{2x} = 0 \text{ and } \delta\varphi_{2x} = 0 \qquad \text{on } S_{2F}$$

Thus, we obtain

$$\delta J = -\iiint_{D_1} \delta\varphi_1\, \nabla^2 \varphi_1\, dzdxdy - \iint_{S_1} \delta\varphi_1\, (\varphi_{1n} - \overline{U} \cdot \overline{n})\, dS$$

$$+ \iint_{S_{1F}} \left(\frac{1}{2} \nabla\varphi_1\, \nabla\varphi_1 - U\varphi_{1x}\right) \delta h\, dxdy + \iint_{S_{2c}} \left(U^2 \frac{\sigma}{2} + U\varphi_{2x}\right) \delta h\, dxdy$$

$$- \iint_{S_{1c}} \left(\frac{1}{2} \nabla\varphi_1\, \nabla\varphi_1 - U^2 \frac{\sigma}{2} - U\varphi_{1x}\right) \delta h\, dxdy$$

$$- \iint_{S_J} \delta\varphi_1\, (\varphi_{1n} + \varphi_{2n})\, dS - \iint_{S_J} \delta\varphi_{2n}\, (\varphi_1 - \varphi_2)\, dS$$

$$+ U \oint_{\substack{J,2 \\ S_J \cap (S_F \cup S_c)}} (\varphi_2 - \varphi_1)\, \delta h\, dy \tag{24}$$

Since $\delta\varphi_1$, $\delta\varphi_{2n}$ and δh are arbitrary, we obtain the original boundary-value problems of equations (19) and (20).

Thus, equation (16) can be used as the Lagrangian for solution of cavity flow problems which have a finite-element numerical solution imbedded in domain D_1. For φ_2 we may use a potential for doublets distributed on a convenient surface inside the body and cavity.

When $\sigma = 0$, the normal variational formulation[6,7] for an infinite medium is not applicable because the first integral in J becomes infinite. However, when D_1 is a finite domain, this infinity does not appear. In this case, presetting the linear boundary conditions in D_2, i.e., $\sigma = 0$ and $\varphi_{2x} = 0$ on S_{2c}, we have

$$J = \iiint_{D_1} \left(\frac{1}{2} \nabla\varphi_1 \nabla\varphi_1 - \overline{U} \cdot \nabla\varphi\right) dzdxdy - \iint_{S_J} \overline{U} \cdot \overline{n} \varphi_1 \, dzdy$$

$$- \iint_{S_J} \left(\varphi_1 - \frac{1}{2} \varphi_2\right) \varphi_{2n} \, dS + \frac{U}{2} \int_{\substack{J,2 \\ S_J \cap (S_F \cup S_c)}} (\varphi_2 h) \, dy \tag{25}$$

where φ_2 is a superposition of eigen solutions which satisfy $\nabla^2 \varphi = 0$ and $\varphi_{2x} = 0$ on $S_F \cup S_{2c}$ plus additional conditions at infinity.

When S_J does not intersect the cavity, we have

$$J = \iiint_{D_1} \left(\frac{1}{2} \nabla\varphi_1 \nabla\varphi_1 - \overline{U} \cdot \nabla\varphi\right) dzdxdy$$

$$+ U^2 \iint_{S_c} \frac{\sigma}{2} h \, dxdy - \iint_{S_J} \left(\varphi_1 - \frac{1}{2} \varphi_2\right) \varphi_{2n} \, dS$$

$$- \iint_{S_J} \overline{U} \cdot \overline{n} \, \varphi_1 \, dzdy \tag{26}$$

If $D_2 \rightarrow 0$, the integrals on the interface, S_J, disappear. In that case, it has been shown[11] that

$$J = M + U^2 \frac{\sigma}{2} V$$

where M is the virtual mass and V is the cavity volume.

For a blunt-nosed supercavitating hydrofoil, the linearized flow field near the nose is singular. Therefore, application of the present method would be as useful as the method of matched asymptotic expansion.

4. Example

For a simple example, we consider the case of a symmetric two-dimensional cavity produced by a symmetric parabolic body at zero cavitation number. For this problem, some approximate solutions[12,13] and a solution by the method of matched asymptotic expansions[14] are available. A linear two-dimensional solution for the complex perturbation velocity is given by

$$w(z) = B/(2i\sqrt{z})$$

in the z plane, where the parabolic body is represented by

$$h = B\sqrt{x}$$

Thus, the linear complex velocity has a singularity at the origin and it is not appropriate for the computation of flow velocities and pressure near the origin and the drag of the foil. Considering a chord length equal to 1, we define the inner region D_1 by the region inside the circle, $r^2 \equiv x^2 + y^2 = 1$, $y > 0$ in $x \leqslant 0$, and $y \geqslant B\sqrt{x}$ in $x \geqslant 0$. (See Figure 2).

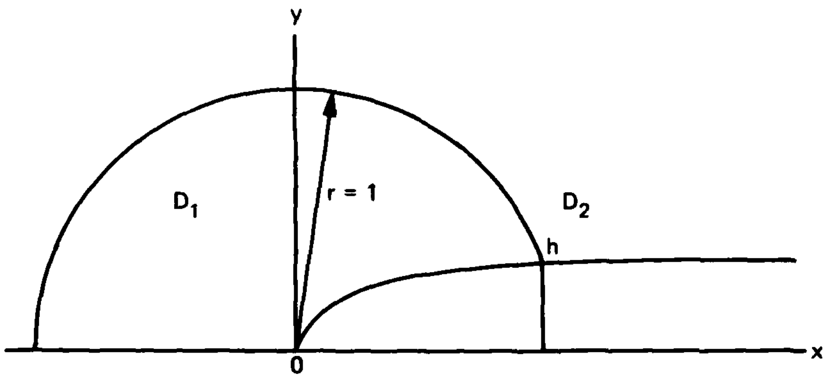

Figure 2 – Domains of Cavity Problem

For simplicity we consider an eigen solution with an unknown constant B_o in D_2

$$\varphi_2 = - B_o\sqrt{r}\,\sin\frac{\theta}{2}$$

with

$$\varphi_{2n} = -\frac{B_o}{2}\sin\frac{\theta}{2} \qquad \text{on } r = 1$$

From equation (25) we have for the Lagrangian

$$J = \iint_{D_1} \frac{1}{2} \nabla\varphi_1 \nabla\varphi_1 \, dxdy - U \int_{S_{1S}} h_x \varphi_1 \, dx$$

$$- \int_{S_J} \left(\varphi_1 - \frac{1}{2}\varphi_2\right) \varphi_{2n} \, dS + \frac{U}{2} \varphi_2 h(1)$$

or

$$J = \iint_{D_1} \frac{1}{2} \nabla\varphi_1 \nabla\varphi_1 \, dxdy - U \int_0^1 \frac{B}{2\sqrt{x}} \varphi_1 \, dx$$

$$+ \int_{\theta_1}^{\pi} \left(\varphi_1 + \frac{B_2}{2} \sin\frac{\theta}{2}\right) \frac{B_o}{2} \sin\frac{\theta}{2} \, d\theta$$

$$- BB_o \frac{U}{2} \sin\frac{\theta_1}{2}$$

where $\theta_1 = \tan^{-1} B$. Application of the finite-element technique to J will lead to the values of φ in D_1 and B_o.

5. Discussion and Concluding Remarks

Under the present formulation, the inner field D_1 will usually be small, and an approximate solution will be assumed known in the outer field. Thus, in the outer field, the additional Green functions or eigen solutions with unknown coefficients for matching may not need too many terms. Therefore, the number of simultaneous equations for the finite-element technique with matching condition should not be very large, and the solution should be readily obtained. Even, if the number of finite elements in D_1 is fairly large, the benefit of the narrow-banded matrix may be fully exploited although the band width may become large for several columns because of the matching conditions. All of the numerical procedures are well-developed in numerous structural applications of the finite-element technique.

The present analysis seems to be significant in extending the idea of matched asymptotic expansions to numerical solution by finite-element techniques. However, in the present method, there is no need for a separate analytical matching procedure.

It will be very interesting to see numerical results for many different problems using the present method. Nevertheless, before going into the numerical computation, it would be more interesting to determine the possibility of constructing simpler Lagrangians for a series

of problems, to inspect the matching behavior of inner and outer fields, and to compare the technique with other similar methods. The present work gives the formulation required for the numerical computation by a matched finite-element technique which, we believe, will have very wide application.

Acknowledgement

This work has been supported by the Numerical Naval Hydrodynamics Program at David W. Taylor Naval Ship Research and Development Center. This program is jointly sponsored by the Office of Naval Research, Naval Sea Systems Command, and DTNSRDC.

References

1. Van Dyke, M., "**Perturbation Methods in Fluid Mechanics,**" Academic Press, New York (1964).

2. Bai, K.J. and R. Yeung, "**Numerical Solutions of Free-Surface Flow Problems,**" 10th Symposium on Naval Hydrodynamics, Office of Naval Research (1974).

3. Chen, H.S. and C.C. Mei, "**Oscillations and Wave Forces in a Man-Made Harbor in the Open Sea,**" 10th Symposium on Naval Hydrodynamics, Office of Naval Research (1974).

4. Bessho, M., "**Variational Approaches to Steady Ship Wave Problems,**" Eighth Symposium on Naval Hydrodynamics, ARC-179, Office of Naval Research, pp. 547-572 (1970).

5. Sao, K., H. Maeda, and J.H. Hwang, "**On the Heaving Oscillation of a Circular Deck,**" Journal of the Society of Naval Architects of Japan, Vol. 130, pp. 121-131 (Dec 1971).

6. Gilbarg, D., "**Jets and Cavities,**" Encyclopedia of Physics, Vol. IX, Fluid Dynamics III, Springer-Verlag, Berlin, pp. 387-391 (1960).

7. Birkhoff, G. and E.H. Zarantonello, "**Jets, Wakes, and Cavities,**" Academic Press, Inc., New York, pp. 85-90 (1957).

8. Luke, J.C., "**A Variational Principle for a Fluid with a Free Surface,**" Journal of Fluid Mechanics, Vol. 27, Part 2, pp. 395-397 (1967).

9. Wehausen, J.V., "**The Wave Resistance of Ships**" in "**Advances in Applied Mechanics,**" Vol. 13, Academic Press, Inc., p. 110 (1973).

10. Zienkiewicz, O.Z., "**The Finite-Element Method in Engineering Science,**" McGraw-Hill, London (1971).

11. Garabedian, P. and D.C. Spencer, "**Extremal Methods in Cavitational Flow,**" Journal of Rational Mechanics, Analysis 1, pp. 359-409 (1952).

12. Tulin, M.P., "**Supercavitating Flow Past Foils and Struts, Cavitation in Hydrodynamics,**" NPL (Teddington, England) (1956).

13. Johnson, V.E., Jr. and T.A. Rasnick, "**The Drag Coefficient of Parabolic Bodies of Revolution Operating at Zero Cavitation Number and Zero Angle of Yaw,**" NASA TRR-86 (1961).

14. Furuya, O. and A. Acosta, "**A Note on the Calculation of Supercavitating Hydrofoils with Round Noses,**" Journal of Fluids Engineering, ASME, 95, pp. 222–238 (1973).

NUMERICAL PROCEDURES FOR THE SOLUTION OF TWO DIMENSIONAL SUPERCAVITATING FLOWS NEAR A FREE SURFACE

O. Furuya*

Tetra Tech, Inc.

Pasadena, California 91107 U.S.A.

ABSTRACT

A nonlinear exact free-streamline theory is used to solve the two-dimensional gravity-free potential flow around a supercavitating body near a free surface. Numerical difficulties arise with this type of theory due to the inherent nonlinearity of the theory itself. Apart from a few simple cases, such as flat plates, these difficulties pose a challenging numerical problem. The procedure used is to solve the problem in terms of the "mapped" complex potential plane. An interesting feature is that the relationship between physical plane and the potential plane emerges as part of the solution to our nonlinear development. In the present problem a system of four integral-algebraic equations is solved for four unknown solution parameters together with the functional relationship mentioned above. The technique employs a novel combination of Newton's method with a functional numerical iterative procedure and successfully obtains fast and stable convergent solutions. Emphasis of the paper will be placed upon this numerical scheme. Representative numerical computations are made for (i) flat-plate foils and (ii) circular arc foils having elliptic leading edges with and without flaps. The pressure distribution, force coefficients and free streamline shapes of the cavity are calculated. Typical execution times on an IBM 370-158 vary from 200 to 500 seconds. Some of the results are compared with the experimental data, showing excellent agreement. The present numerical technique has wide application to many hydrodynamic problems. Extensions of the technique to multiple bodies (such as cascades) and three-dimensional bodies have shown similar success.

---

* The fundamental part of this work was developed during the author's research fellowship at the California Institute of Technology.

1. Introduction

The problems of nonlinear free streamline theory such as cavity and wake flows with or without free surface (s) are classified as one category of mathematical problems from the standpoint of the type of equations to be solved. Since we have two different kinds of boundaries - one solid boundary and the other free streamline -, the problem is called "mixed-type" boundary value problem, usually leading to a set of integral equations. Levi-Civita (1907) first presented the mathematical formulation for the problem of a branched jet flow, using hodograph techniques. Although the formulation is made for any arbitrarily shaped bodies, the equations obtained can not be analytically solved except for a few cases of simple body configurations such as flat plates and symmetric wedges (see for example, the work by Larock and Street (1967)). The integral equations for general body cases do not have any closed form unlike the above simple configurations and thus the problem becomes completely unsolvable. More specifically, difficulties arise because the nonlinear streamline theory must use the complex potential plane instead of the physical plane. The inclination of the tangent to the wetted body surface in the integral equations is not known as a function of the potential a priori although it is specified in the geometric plane as part of the problem. The relationship between physical plane and the potential plane however emerges as part of the solution. For the flat plate case it is clearly seen that the body angle is independent of the coordinate system and thus no problem arises in evaluating the integrals.

Many attempts have been made to resolve this inherent implicitness of the theory. The first development was made by Brodetsky (1922) who represented the body angle by a power series in terms of potentials in solving the cavity flows about circular and elliptic cylinders. The application of his method is limited however, to symmetric flows around symmetric bodies. More recently, Larock and Street (1968) formulated the problem for more general cases by incorporating an advanced mathematical technique of mixed-type boundary value problems (see the paper of Larock and Street (1965) for more details of the mathematical treatment). They expressed the body angle in a piecewise linear parametric function of the

modified potential. Furthermore, Murai and Kinoe (1968) incorporated the leading edge curvature in their power series expansions. In all the above approaches in what is called an "inverse" method the unknown coefficients or parameters of power series are determined by collocation only at finite discrete points on the body so that the body profile obtained as the result of calculations are somewhat different from what is desired. This particularly becomes an undesirable point in solving the flow about foils having rounded-leading edges of specified radius.

The first direct method was introduced by Wu and Wang (1964) who used a numerical iterative procedure in the problem of two-dimensional cavity flows in an unbounded flow medium. Their formulation of the problem is similar to that of Brodetsky but using a new wake model for the cavity flow. For the case of infinite cavity flows they have two integral equations for two unknown solution parameters with a functional relation between the geometric plane and mapped plane unknown (see Wu and Wang's paper for detailed form of equations). In order to explain the numerical procedure, these equations are now written in the equivalent vector form:

$$\underline{f}(\underline{a}, \beta(\xi(x, \underline{a}), \underline{a}) = 0 \tag{1}$$

where $\underline{f}$ denotes the two nonlinear equations, $\underline{a}$ an unknown vector with two components representing solution parameters and β the local slope of the body. ξ is a coordinate in the transformed potential plane and x is that in the physical plane. Defining a new vector function $\underline{g}$

$$\underline{g}(\underline{a}, \beta(\xi(x, \underline{a}), \underline{a})) \equiv \underline{a} - \underline{f}\ , \tag{2}$$

the problem becomes equivalent to solving the iterative loop of the following form:

$$\underline{a}_{\nu+1} = \underline{g}(\underline{a}_{\nu}, \beta_{\nu}(\xi(x, \underline{a}), \underline{a}_{\nu}), \quad \nu = 0, 1, 2, \ldots, \tag{3}$$

where the subscript ν denotes the number of the functional iteration. If the starting values, $\underline{a}_o$ and $\beta_o(\xi(x, \underline{a}_o))$ are known, a new set of values of $\underline{a}_1$ can

be calculated without any difficulty since $\underline{g}$ is a known vector function as defined in (2). The procedure is carried on until the convergent solution is obtained. It seems reasonable to choose a flat plate solution as the very first starting values for $\underline{a}_o$ and β_o since that is the only case for which the analytical solution is obtained in the present problem. The choice of the starting angle of attack will be made depending on the foil profile to be solved, generally on a trial and error basis.

With this method used they obtained converged numerical solutions for the cases of flat-plate foils with flaps, cusped bodies and circular-arc foils all having sharp leading edges. Lurye (1966) applied the same method to the base-ventilated flow around the parabolic struts but experienced a numerical instability in obtaining converged solutions. Some improvement was made by Furuya (1973) on the same problem where a'weighted' iterative method was introduced to obtain convergent solutions. Figures 1(a) and (b) show examples of divergent and convergent solutions to the supercavitating flows around parabolic foils. AN and GAMOLD in the figures are the two solution parameters, representing a scaling parameter and a coordinate of the transformed plane corresponding to the point of infinity, respectively. The difference between convergence and divergence here stemmed from the difference in choice of the angles of attack of the starting solution; for the former $\beta_o = -\pi/4$ and for the latter $\beta_o = -\pi/5.1$ were used. This indicated that even the improved method is very sensitive to the initial solutions in obtaining a convergent solution.

In the present title problem we have four integral and algebraic equations for four solution parameters, instead of two and it may be therefore expected from the above experience that one may have even a greater numerical instability with the direct application of Wu and Wang's method. It is for this reason that the development of a new method for the numerical procedure was in order. In what follows, a short description of the formulation of the problem will be given (refer to Furuya (1975a) for detailed formulation), followed by a section explaining a new numerical method used for solving the equations obtained above.

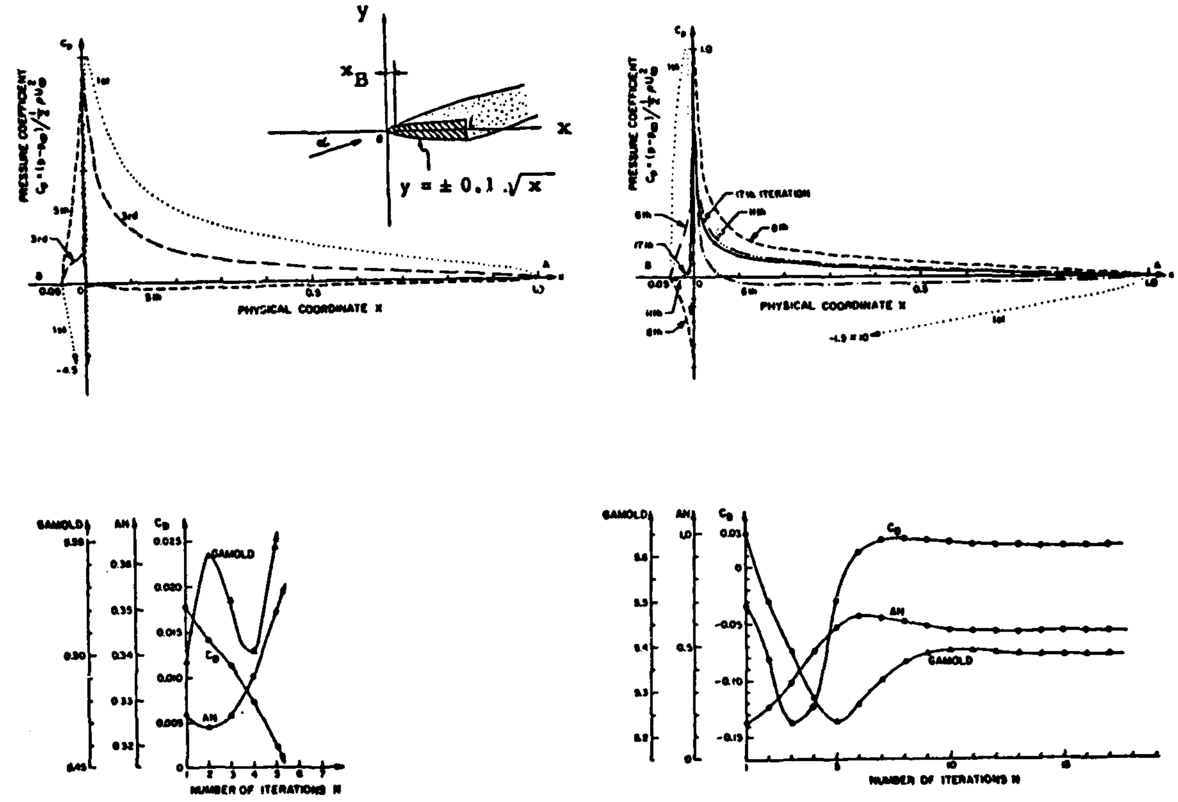

(a) (b)

FIGURE 1: Pressure Distributions and Key Solution Parameters to Show (a) Divergent and (b) Convergent Solutions for a Base-Ventilated Parabola of $y = \pm\ 0.1\sqrt{x}$ with a Separation Point $x_B = 0.05$ at $\alpha = 1°$ Using Wu and Wang's Method

2. Formulation of the Problem

Figure 2(a) shows a physical plane depicting a supercavitating flow around a foil under a free surface. With the assumption of a gravity-free potential flow, the whole flow field is mapped onto a complex potential plane $W=\phi+i\psi$ of Figure 2(b) in which highly turbulent flow regime after the cavity is represented by the double-spiral-vortex model of Tulin (1964). The potential plane W is once more mapped onto the upper half of $\zeta=\xi+i\eta$ plane by the mapping function;

$$W=-\frac{\psi_o}{\pi d}\left(\zeta+d\,\ln\frac{\zeta-d}{-d}\right). \tag{1}$$

Figure 2(c) shows the ζ-plane with all the boundary conditions given. The problem is now formulated in terms of a hodograph variable ω which is defined by:

$$dW/dz = qe^{-i\theta} = q_\infty e^{-i\omega} \tag{2}$$

$$\omega = \theta+i\tau, \quad \tau = \ln(q/q_\infty). \tag{3}$$

The solution satisfying the boundary conditions specified either in the real part or the imaginary part of ω in Figure 1(c) will be given by:

$$\begin{aligned}\omega(\zeta) = [(\zeta+1)(\zeta-b)]^{\frac{1}{2}}\Bigg\{&\frac{1}{2\pi i}\int_a^{-1}\frac{-i\ln(1+\sigma)}{[(\xi'+1)(\xi'-b)]^{\frac{1}{2}}}\frac{d\xi'}{\xi'-\zeta}\\
&+\frac{1}{2\pi i}\int_{-1}^{b}\frac{2\beta(\xi')}{i[(1+\xi')(b-\xi')]^{\frac{1}{2}}}\frac{d\xi'}{\xi'-\xi}+\frac{1}{2\pi i}\int_0^b\frac{2\pi}{i[(1+\xi')(b-\xi')]^{\frac{1}{2}}}\frac{d\xi'}{\xi'-\xi}\\
&+\frac{1}{2\pi i}\int_b^c\frac{i\ln(1+\sigma)}{[(\xi'+1)(\xi'-b)]^{\frac{1}{2}}}\frac{d\xi'}{\xi'-\xi}\Bigg\}\end{aligned} \tag{4}$$

where

$$\sigma=\frac{p_\infty-p_c}{\frac{1}{2}\rho q_\infty^2} \quad : \text{ cavitation number} \tag{5}$$

$$\beta = \tan^{-1}d\tilde{f}/dx\ , \quad y=\tilde{f}(x) \text{ body shape.} \tag{6}$$

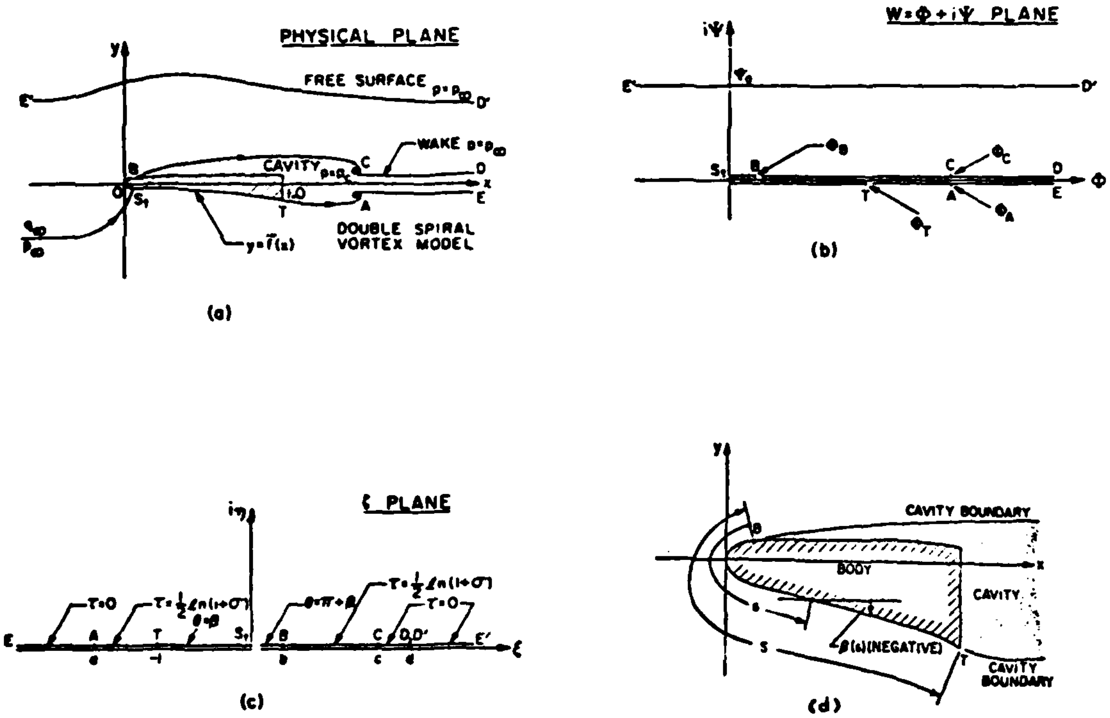

FIGURE 2: (a) Flow Configuration and (b) Potential Plane W (c) Transform Plane ζ and (d) Definition of s, S and β on the Body

We have four unknown parameters a, ...d in (1),...(4), requiring four boundary conditions to determine them uniquely;

(i) $\theta(\infty) = 0$

(ii) $\theta(d) = 0$

(iii) $\Phi_C - \Phi_A = \Gamma\ (\equiv C_L q_\infty/2)$ where Γ denotes the circulation and C_L is the lift coefficient.

(iv) Total wetted foil length ≡ S (see Figure 2(d) for the definition of S).

Each of those conditions provides one equation, totally four $f_1, \ldots f_4$ as shown below:

$$f_1 \equiv \frac{\ell n(1+\sigma)}{2\pi}\left\{\ell n \frac{-(b+1)}{2[(a+1)(a-b)]^{\frac{1}{2}}+(a+1)+(a-b)} + \ell n \frac{b+1}{2[(c+1)(c-b)]^{\frac{1}{2}}+(c+1)+(c-b)}\right\} \tag{7}$$

$$+ \frac{1}{\pi}\int_{-1}^{b} \frac{\beta(\xi')}{[(1+\xi')(b-\xi')]^{\frac{1}{2}}}\, d\xi' + \left(\frac{\pi}{2} - \sin^{-1}\frac{1-b}{1+b}\right) = 0$$

$$f_2 \equiv \frac{\ell n(1+\sigma)}{2\pi}\left\{\ell n \frac{(1+b)(a-d)}{2[(a+1)(a-b)(d+1)(d-b)]^{\frac{1}{2}}+(a+1)(d-b)+(a-b)(d+1)} + \ell n \frac{(1+b)(d-c)}{2[(c+1)(c-b)(d+1)(d-b)]^{\frac{1}{2}}+(c+1)(d-b)+(c-b)(d+1)}\right\} \tag{8}$$

$$- \frac{[(d+1)(d-b)]^{\frac{1}{2}}}{\pi}\int_{-1}^{b} \frac{\beta(\xi')}{[(1+\xi')(b-\xi')]^{\frac{1}{2}}}\,\frac{d\xi'}{\xi'-d} + \left(\frac{\pi}{2} + \sin^{-1}\frac{d(b-1)+2b}{d(b+1)}\right) = 0$$

$$f_3 \equiv \frac{\psi_0}{\pi d}\left\{\left(a + d\,\ln\frac{a-d}{-d}\right) - \left(c + d\,\ln\frac{c-d}{-d}\right) - \frac{C_L q_\infty}{2} = 0\right. \tag{9}$$

$$f_4 \equiv s(-1) - S = 0 \tag{10}$$

where

$$s(\xi) = -\frac{1}{q_\infty}\int_\xi^b h(\xi', a, b, c)\, k(\xi', d, \psi_0)\, d\xi' \tag{11}$$

$$\begin{aligned} h(\xi, a, b, c) &= \exp\left\{-\mathrm{Im}(\omega(\xi))\right\}, \quad -1 < \xi < b \\ &= \left[\exp\left\{-\frac{\ln(1+\sigma)}{2\pi}\left(\pi + \sin^{-1}\frac{(1+\xi)(a-b)+(\xi-b)(1+a)}{(\xi-a)(1+b)}\right.\right.\right. \\ &\quad \left. + \sin^{-1}\frac{(1+\xi)(c-b)+(\xi-b)(1+c)}{(c-\xi)(1+b)}\right) ; \frac{[(1+\xi)(b-\xi)]^{\frac{1}{2}}}{\pi} \\ &\quad \left.\left. \times \int_{-1}^{b} \frac{\beta(\xi')}{[(1+\xi')(b-\xi')]^{\frac{1}{2}}}\frac{d\xi'}{\xi'-\xi}\right\}\right] \frac{2[b(1+\xi)(b-\xi)]^{\frac{1}{2}}+\xi(b-1)+2b}{-\xi(1+b)}, \end{aligned} \tag{12}$$

$$k(\xi, d, \psi_0) = \frac{dW}{d\xi} = -\frac{\psi_0}{d\pi}\frac{\xi}{\xi - d}\ . \tag{13}$$

It is easily seen from these equations that if β is constant, such as in the case of a flat plate, the problem reduces from solving a set of integral equations to nonlinear algebraic equations. However, in more general cases, β is variable as a function of physical coordinate or arc length s and thus of ξ. Only one relation connecting these two planes is given by equation (11) and this can be solved provided that all parameters a...d and also $\beta(\xi)$ be known. It is this feature that poses a difficult non-

linear problem in this type of integral equation and thus the help of numerical technique is necessary.

3. Numerical Method

Instead of using a simple substitution method explained before, Newton's iterative method is introduced in solving the above equations. A new vector equation is now defined as follows:

$$\underline{g}(\underline{a}, \beta(\xi(x,\underline{a}),a)) \equiv \underline{a} - J^{-1} \cdot \underline{f}(\underline{a}, \beta(\xi(x,\underline{a}),\underline{a})) \tag{14}$$

where J^{-1} denotes the inverse of a matrix $J = \partial\underline{f}/\partial\underline{a} \equiv \left\{\partial f_i/\partial a_j\right\}$. Iterative procedure is now established by writing (14)

$$\underline{a}_\nu^{(n+1)} = \underline{g}(\underline{a}_\nu^{(n)}, \beta_\nu)$$

or

$$J(\underline{a}_\nu^{(n)}, \beta_\nu) \cdot (\underline{a}_\nu^{(n+1)} - \underline{a}_\nu^{(n)}) = -f(\underline{a}_\nu^{(n)}, \beta_\nu) \tag{15}$$

where the superscript (n) denotes the number of Newton's iteration whereas the subscript ν has the same meaning as before. The Newton's method, usually used to solve a system of nonlinear equations is superior to a simple substitution method of Equation (3). The speed of convergence of the method is of 'second - order', which provides a rapid convergence as well as improves the stability of convergence. Assuming β_0 and $\underline{a}_0^{(o)}$ in (15) as starting values, one can calculate the values of J and $\underline{f}$ without any difficulty since all the integrals having β in their kernels now become just numbers, then find $\underline{a}_0^{(1)}$. This procedure will be continued until a set of convergent solutions are obtained. (It is noted that this part of iteration is simply solving a set of nonlinear algebraic equations by using Newton's method). With converged solutions $\underline{a}_0^{(n+1)}$ and β_0 known, the relation between s and ξ is now given through Equation (11) and thus the actual body angle will be incorporated first time into the problem in the next iteration where $\nu = 1$. This procedure will be repeated until a convergent solution is obtained. The test of convergence is usually made on the

solution parameters in such a way that:

$$\|(\underline{a}_{\nu+1}-\underline{a}_{\nu})/\underline{a}_{\nu+}\| < \delta$$

where $\| \ \|$ denotes a vector norm and δ a desired value for accuracy. Other key factors such as the overall force coefficients C_L and C_D may be also used in the same way as above for the convergence test.

Once a complete solution to one problem is obtained by the above method, the results of such a solution are extremely useful in solving problems having physical parameters and body profile close and similar to the problem already solved. Such problems will be therefore continuously solved by changing physical parameters or body profiles slightly at a time with the previously obtained data always used in the subsequent computations. In this way the computation time is substantially saved and the convergence is always guaranteed.

Some of the partial derivatives in J are easily obtained in analytical forms but some must be numerically calculated by using a finite difference method. One of the numerical difficulties in the present computations is to calculate the Cauchy integral particularly at $\xi'=\xi$ in f_4. A usual practice to avoid this difficulty is to use a formula

$$\frac{[(1+\xi)(b-\xi)]^{\frac{1}{2}}}{\pi} \oint_{-1}^{b} \frac{\beta(\xi')}{[(1+\xi')(b-\xi')]^{\frac{1}{2}}} \frac{d\xi'}{\xi'-\xi} = \frac{[(1+\xi)(b-\xi)]^{\frac{1}{2}}}{\pi} \times$$

$$\int_{-1}^{b} \frac{\beta(\xi')-\beta(\xi)}{\xi'-\xi} \frac{d\xi'}{[(1+\xi')(b-\xi')]^{\frac{1}{2}}} + \frac{\beta(\xi)}{\pi} \ln \frac{b-\xi}{1+\xi}$$

with the fact in mind that this whole term vanishes at $\xi = b$ and -1.

The numerical integration in the computations presently made (some of the results being shown later) employed Simpson's rule with the step

size changed. The variable step size is particularly important in accurate numerical integrals for the cases of foils having relatively thin but rounded leading edge since β rapidly changes near the leading edge. In some of the computations made here the step size near the leading edge was ten times finer than the other part of the body.

4. Numerical Difficulty as $\psi_0 \to 0$ and $\sigma \to 0$ and Corresponding Numerical Method

No numerical difficulties have been experienced when the length of cavity becomes infinite, i.e, in the case of zero cavitation number. The problem reduced to two integral equations for two unknown parameters, the formula being shown in the paper of Furuya (1975a). However, for the cases of small but finite ψ_0 and σ, for example, $\psi_0 = 1$ with $\sigma = 0.05$ or $\psi_0 = 0.5$ with $\sigma = 0.1$ at $\alpha = 10°$ for a flat plate foil, some numerical difficulties arise in obtaining convergent solutions (see the report of Wang and Shen (1975) for more details). What will happen in these cases is that two coordinates, c and d, become too close to each other, even up to the tenth digits. This is far beyond the resolution of single precision operation of the computer and the iteration of the present method failed to converge. One could consider the use of double precision arithmetic in the calculations but this again would not guarantee convergence.

A simple modification has been presently made in numerical treatment of the four fundamental equations (8) - (11) instead of using the double precision. As soon as (d-c) becomes smaller than a number in the iterative procedure (10^{-5} was used in our computations), the term appearing as a group of (d-c) was considered to be a new parameter, say, e, and d appearing as independent of c, not as (d-c), is replaced by c with an assumption of negligibly small errors due to this. Therefore, the new equations are obtained by replacing a, b, c, e for a, b, c, d in Equations (7)-(11) as follows; $a \to a$, $b \to b$, $c \to c$, $d \to c$, $d-c \to e$. The partial derivatives in J must be changed accordingly. With this method used, we have successfully obtained convergent solutions without any difficulty for the case of $\psi_0 = 1$ and $\sigma = 0.034$ at $\alpha = 10°$ in which the value e itself has been found to be 10^{-16}. Although the cases of further small values of ψ_0 and σ have not

been tested, the combination of the above ψ_0 and σ is believed to be small enough to cover the practical range of the submergence and cavitation number.

5. Results

The numerical technique mentioned above was used to calculate several different types of supercavitating flows. First two examples in Figure 3 show mainly the numerical aspect of convergence. The body profiles of both cases are circular arc with elliptic noses of leading edge radius $R_o = 0.1\%$ chord. Only the difference between two cases is a flap of 3° at 20% of the trailing and the flow angle $\alpha = -1°$ for the case (b). For the first case (a) a flat plate solution was used as a starting point whereas a previously obtained solution, the configuration of which is close to the present one, was used for the case (b) (see β of the first iteration in Figure 3 (a)-3 and 3(b)-3). It is obviously seen from pressure distributions Cp, angle of the body $\beta(\xi)$, and four parameters in Figure 3(b)-2, -3 and -4 that much faster convergence was naturally obtained in the case of (b) than (a). In this calculation, the term $C_L q_\infty /2$ in Equation (9) was taken as zero as Larock and Street (1967) for simplicity so that the end points of cavity do not quite match in terms of the x-coordinate. (The example of using exactly the form of Equation (9) will be shown later). It took about 500 seconds on IBM 370-158 for the first case whereas only 200 seconds for the second case, saving substantial amounts of computer time.

Some of the calculated results are compared with experimental data to check the accuracy of the theory and of numerical methods used here. Figure 4 shows pressure distributions on flat plates at various angles of attack, submergence depths and cavitation numbers in comparison with the experimental results of Dawson and Bates (1962). In this comparison the definition of the submergence depth is different, for the theory ψ_0 being specified and for the experiment actual depth s/c being used (see Figure 4(a) for the reference point of s/c). For the cases of large submergences with small angles of attack, the present assumption using the same values of ψ_0 as s/c for comparison must be very accurate and this may be well applied to all three cases of Figure 4. The correlation is seen to be excellent

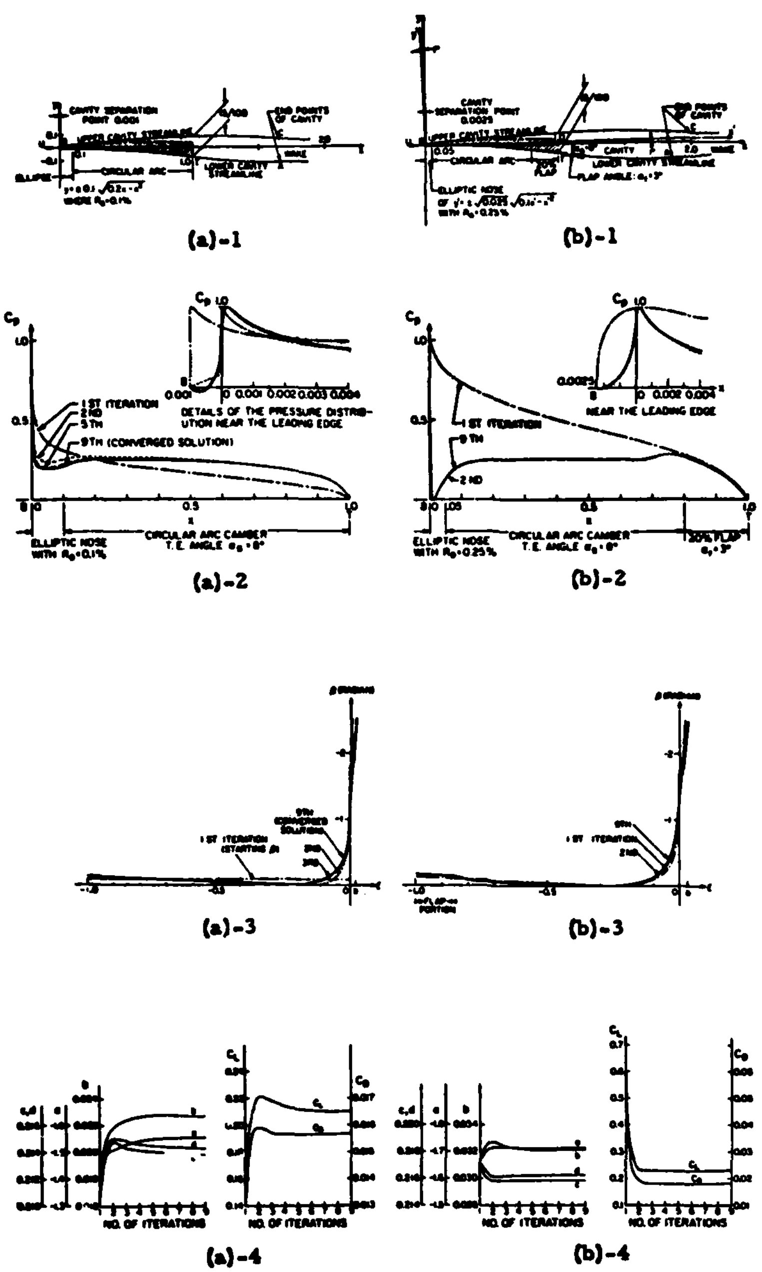

FIGURE 3: Example Computations of the Present Method on Supercavitating Circular Arc Foils Having Elliptic Leading Edges (a) with and (b) without a Flap at $\sigma = 0.1$ and $\psi_o = 1$; (a)-1,(b)-1 Foil Profiles and Calculated Free Streamlines; (a)-2, (b)-2 Pressure Distribution, (a)-3 and (b)-3 the Change of β as a Function of ξ and (a)-4 and (b)-4 Solution Parameters, all as Functions of Iteration Numbers

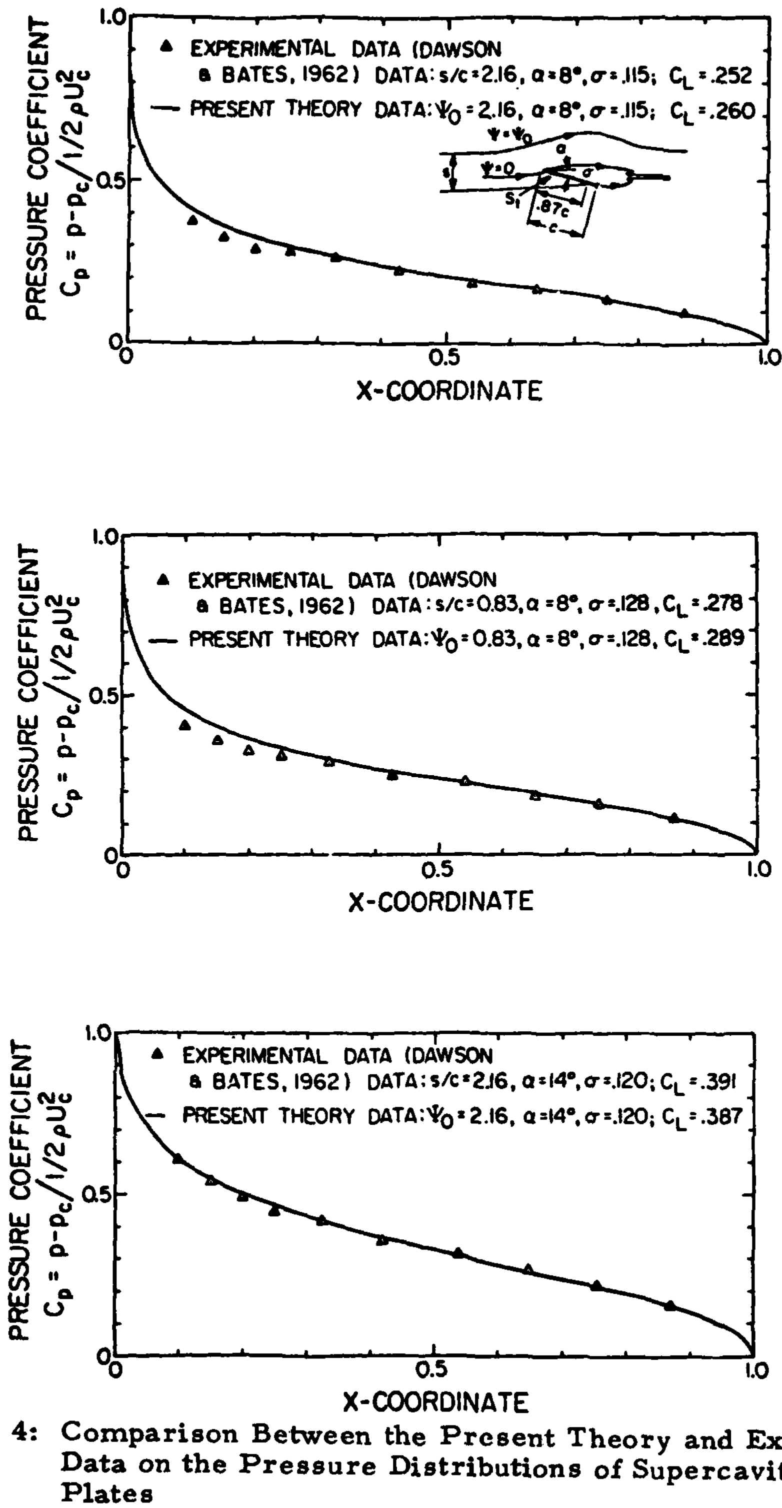

FIGURE 4: Comparison Between the Present Theory and Experimental Data on the Pressure Distributions of Supercavitating Flat Plates

for the pressure distributions and also for the lift coefficients.

Recently, an experimental study has been conducted at the Hydrodynamics Laboratory of the California Institute of Technology on supercavitating circular arc hydrofoils with and without flaps having elliptic leading edges (see Figure 5(b)). The design work was done by using the computer program developed there. One of the most critical factors in designing this type of hydrofoil is to ensure that cavity separation occurs at the design point and that the upper part of the body lies within the cavity boundary at the lowest possible angle of attack designated for experiments. The minimum envelope of the upper cavity boundary was calculated over the complete range of test parameters. The foil thickness was taken to be $85 \sim 95\%$ of this height at three points ($A \sim C$ in Figure 5(b)). Two of the lowest cavity boundaries are shown in Figure 5(b). These points were then connected by straight lines, the last line from A to the leading edge being drawn tangential to the leading edge circle of 0.25% chord radius. This creates a kink or discontinuity of curvature at the tangent point and in this way, at least theoretically, the cavity is expected to spring at this transition point. The experiment using the hydrofoil designed in this way has certainly supported the design criteria; at the design angle of attack $\alpha = 0^\circ$ and $\sigma = 0.2$ it was observed that the cavity certainly separated at the kink point and cleared all upper body boundary with absolutely no interference. In this computation, the exact form of Equation (9) was used and it is seen that the end points of the upper and lower cavity boundaries match each other in the x-coordinate. The lift coefficients measured in the experiment (see the report of Baker and Ward (1975) for more detailed results), with and without flaps at different angles of attack are compared in Figure 6 with the theory, showing good correlation up to large lift coefficients.

One of the difficulties in designing supercavitating foils arises from the fact that very small lift coefficient, i.e., small camber or angle of attack is necessary at high speeds such as 80 knots. The upper cavity boundary in such cases becomes very close to the foil allowing a limited foil thickness distribution for mechanical strength. The accurate calculation of the free streamlines is therefore a key factor in design

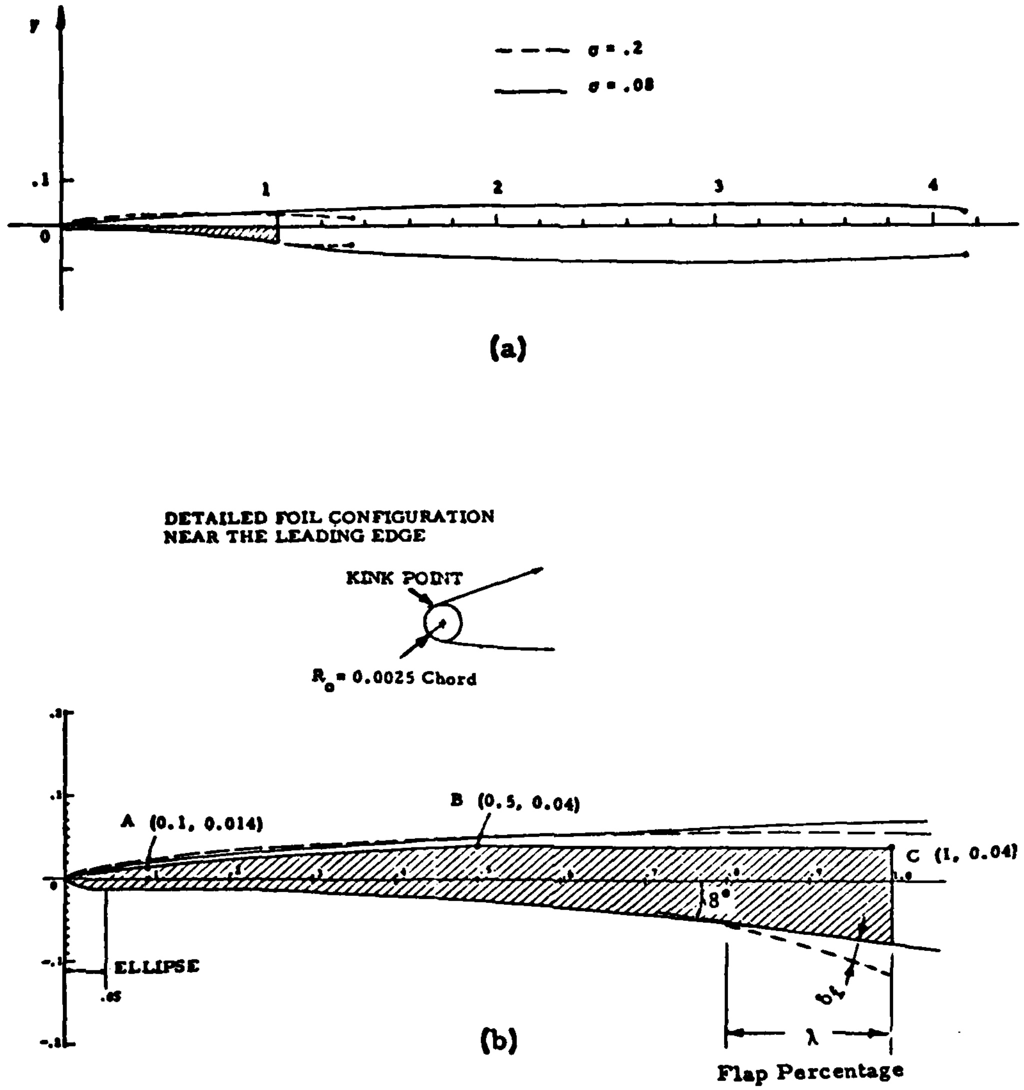

FIGURE 5: Calculated Cavity Shapes on the Circular Arc Foil Having Elliptic Leading Edge of $R_o = 0.25\%$ Chord at $\alpha = 0$ and $\sigma = 0.2$ and 0.08 with Cavity Separation Point at $R_o/2$; (a) Total Cavity Shapes and (b) Detailed Upper Cavity Shapes Near the Foil

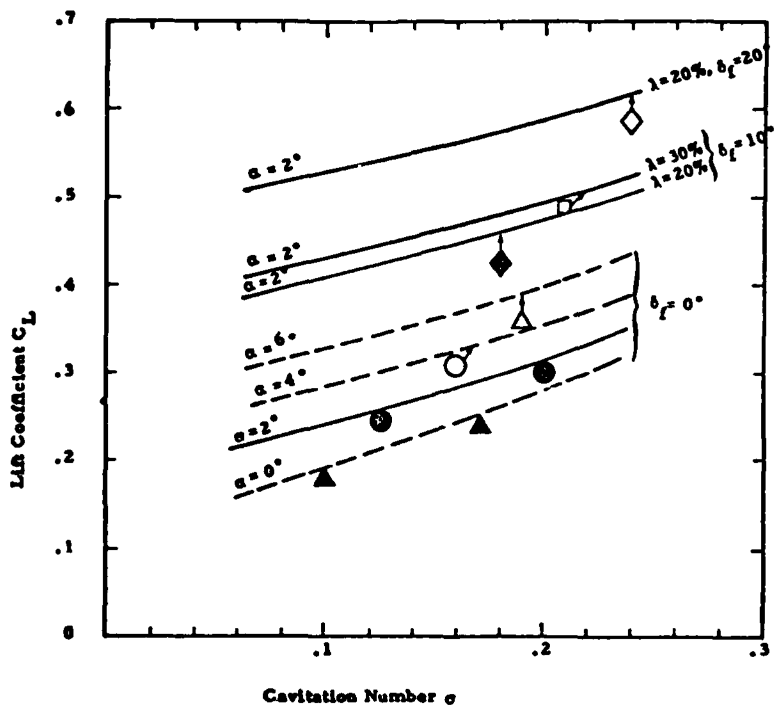

FIGURE 6: Comparison of Lift Coefficients Between the Theory (Lines) and Experiments (Points) of Barker and Ward (1975) on the Same Foils with and without Flaps as Depicted in Figure 5.

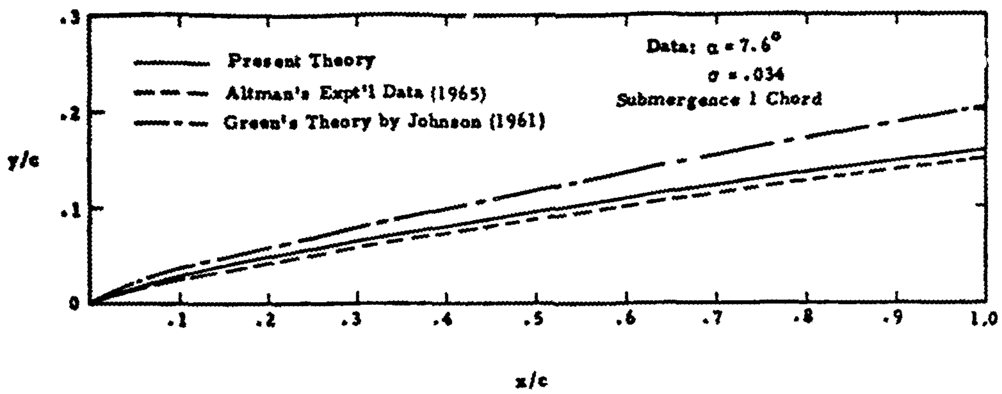

(a)

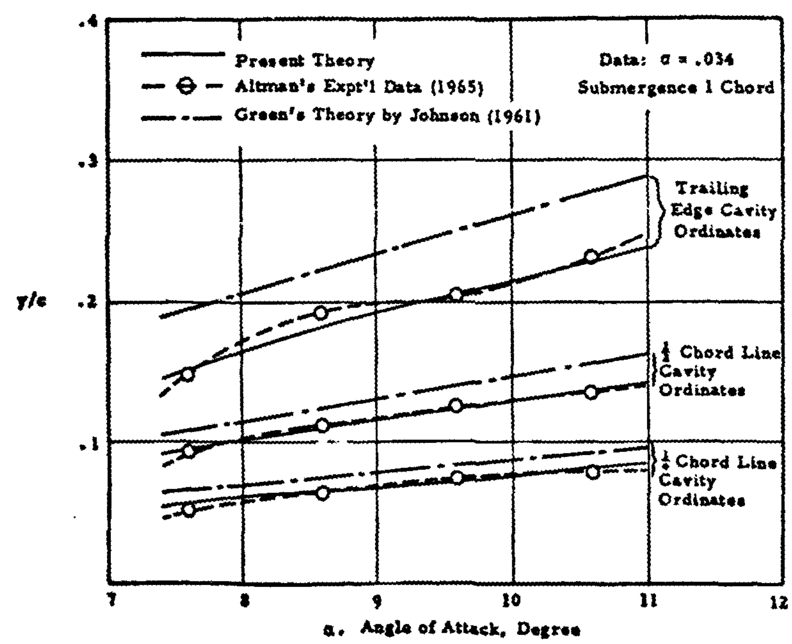

(b)

FIGURE 7: Comparison for the Location of the Upper Cavity Boundaries of Flat-Plate Foils Between the Present Theory and Experimental Data Where $\psi_o = 1$ is Used for the Theory; (a) The Ordinates of the Upper Cavity Boundary and (b) Those as a Function of Angle of Attack at Various Locations, the Theoretical Results of Green for $\sigma = 0$ Being Also Shown.

work. Presently, measured data on the upper cavity boundary by Altman (1965) are used for comparison. Figure 7(a) shows good correlation between the experimental data and the present prediction. Theoretical data obtained by Johnson (1961) using Green's (1936) theory is also shown in this figure. A large discrepancy is seen here, possibly due to the assumption of zero cavitation number. It must be mentioned that for this computation, numerical difficulties would have existed, due to the small cavitation number ($\sigma = 0.034$) if the regular method had been used. The new technique mentioned in Section 4 was used for this case and convergent solutions were obtained without any difficulty. In Figure 7(b) the coordinates of upper cavity boundaries at various locations are plotted over different angles of attack. It is again seen that the present nonlinear theory predicts the cavity boundaries very well.

6. Conclusion

A new technique incorporating Newton's method into iterative procedures in solving a nonlinear system of integral equations has been found very powerful in obtaining fast and convergent solutions. Some representative results of various supercavitating flows have been compared with experimental data, proving the accuracy and versatility of the nonlinear theory in combination with the present numerical method.

Essentially the same numerical procedure has been applied to the problems of supercavitating cascade (Furuya 1975b) and of finite aspect ratio supercavitating foils under a free surface (Furuya 1975c). Although these problems gave much more complicated equations, both having five algebraic-integral equations, convergent solutions with this present method used has been obtained in an equally straightforward way.

Acknowledgement

The author thanks Professor Acosta of the California Institute of Technology for many helpful suggestions and encouragement throughout this research work. Discussions with Drs. Y. Shen and D. P. Wang and Mr. E. Baker at the Naval Ship Research and Development Center were also helpful

and these are gratefully acknowledged. This work was supported by the Naval Ship Systems Command General Hydrodynamics Research Program, technically administered by the Naval Ship Research and Development Center under Contract N00014-75-C-0430 and partly by Tetra Tech, Inc.

References

Altman, R.J., 1965 Measurement of Cavity Shapes Above Ventilated Hydrofoils . Hydronautics Tech. Rep. 457-1.

Brodetsky, S. 1922 Discontinuous Fluid Motion Past Circular and Elliptic Cylinders . Proc. Roy. Soc. A102, 542-553.

Barker, S. & Ward, T. 1975 Experiments on a Cavitating Hydrofoil Fitted with Flaps in Two and Three Dimensional Flow . California Inst. Tech. Graduate Aero. Lab. Galcit Rep. HSWT-1120.

Dawson, T.E. & Bates, E.R. 1962 An Experimental Investigation of a Fully Cavitating Two Dimensional Flat-Plate Hydrofoil Near a Free Surface . California Inst. Tech. Rep. E-118.12.

Furuya, O. 1973 Numerical Computations of Supercavitating Hydrofoils of Parabolic Shape with Wu and Wang's Exact Method . California Inst. Tech. Rep. E-79A.15.

Furuya, O. 1975a Nonlinear Calculation of Arbitrarily Shaped Supercavitating Hydrofoils Near a Free Surface. J. Fluid Mech. 68, 1, 21-40.

Furuya, O. 1975b Exact Supercavitating Cascade Theory . ASME Proceedings at the Symposium on Cavity Flows, Minnesota.

Furuya, O. 1975c Three Dimensional Theory on Supercavitating Hydrofoils Near a Free Surface . J. Fluid Mech. in press.

Green, A. 1936 Notes on the Gliding of a Plate on the Surface of a Stream . Proc. Cambridge Phil. Soc. Vol. Part 2.

Johnson, V. 1961 Theoretical and Experimental Investigations of Supercavitating Hydrofoils Operating Near the Free Water Surface . NASA Tech. Rep. R-93.

Larock, B. & Street, R. 1965 A Riemann-Hilbert Problem for Nonlinear, Fully Cavitating Flow, J. Ship Res. 9, 170-178.

Larock, B. & Street, R. 1967 Nonlinear Solution for a Fully Cavitating Hydrofoil Beneath a Free Surface . J. Ship Res. 11, 131-140.

Larock B. & Street R. 1968 Cambered Bodies in Cavitating Flow - a Nonlinear Analysis and Design Procedure, J. Ship Res. 12, 1-13.

Levi-Civita, T. 1907 Scie . leggi di resistenzia. R.C. cir. mat., Palerno, 18, 1-37.

Lurye, J. 1966 Numerical Aspects of Wu's Method for Cavitated Flow as Applied to Sections Having Rounded Noses. Rep., Melville, N.Y., TRG-156-SR-3.

Murai, H. & Kineo, T 1968 Theoretical Research on Blunt-Nosed Hydrofoil in Fully Cavitating Flow. Rep. Inst. High Speed Mech., Japan, No. 20.

Wang, D. & Shen Y. 1975 A Validation Study of the Mixed Foil Concept for High Speed Hydrofoils. Penn.State Univ. Rep. ARL TM-75-171.

Wu, T.Y. & Wang, D.P. 1964 A Wake Model for Free-Streamline Flow Theory. Part 2. Cavity Flows Past Obstacles of Arbitrary Profile, J.Fluid Mech. 18, 65-93.

CALCULATION OF INCOMPRESSIBLE UNDERWATER BUBBLE PHENOMENA BY THE MARKER AND CELL METHOD

Michael J. Vander Vorst and Andrew H. Van Tuyl
Naval Surface Weapons Center, White Oak Laboratory
Silver Spring, Maryland 20910 U.S.A.

ABSTRACT

The motion of an axisymmetric underwater explosion bubble in an incompressible inviscid fluid is calculated by a marker and cell computer code. Calculations are presented for the case of the explosion bubble produced by detonation of a 354 pound charge of TNT at a depth of 81 feet. These calculations show known features of the motion, such as the bubble jet and the toroidal shape at the first minimum. Good agreement is found between calculated and experimental bubble shapes. Refinements have been made to earlier versions of the code in order to reduce the effect of an instability found at the beginning of the bubble's contraction phase. They include the "irregular star" finite difference technique and extension of the velocity field by an extrapolation normal to fluid surfaces.

I. INTRODUCTION

1. The Marker and Cell Method

In this paper we present the numerical solution by the marker and cell method of the unsteady, inviscid, incompressible flow following an underwater explosion. The Marker and Cell (MAC) method, originally developed by Harlow and coworkers [1-4] has been widely used and refined to calculate unsteady, incompressible fluid flows with free surfaces and solid boundaries [5-15]. The MAC method is characterized as a finite difference solution of the incompressible equations of motion in the primitive variables of velocity and pressure. The velocity is differenced explicitly in both time and space, while the pressure is obtained as the solution of a Poisson equation. The unique feature of this method is that free surfaces are represented by massless marker particles. These particles divide the underlying rectangular Eulerian mesh into empty and full regions, so that the computation is only carried out in those cells which contain the fluid.

Since its inception, many refinements have been made to the MAC method. Those improvements which are applicable to the solution of the underwater explosion problem have been incorporated into this version, MACBUB, of the MAC method. The origin of MACBUB was Pritchett's [5,6] MACYL code for computing the motion of an underwater steam bubble formed by a nuclear explosion. Pritchett utilized Harlow's basic methodology in a cylindrical coordinate system instead of two-dimensional Cartesian coordinates. In addition he allowed for up to two free surfaces, one for the air and one for the bubble, and he introduced an unevenly spaced mesh.

From MACYL the code evolved with the use of some of the simplifications in the methodology from SMAC [7]. A significant increase in accuracy was achieved by incorporating Chan and Street's [10,11] irregular star technique to enforce the free surface pressure boundary condition. As did Chan and Street, we found that better results were obtained by extending the velocity field across free surfaces than by arbitrarily assigning these velocities in partially filled cells so that the difference equation for conservation of mass is satisfied as if the cells were full. However, instead of restricting the extrapolation to a vertical or horizontal direction, we extrapolate in a direction normal to the surface. In addition, to insure that the finite difference equations for the pressure are first order under general uneven mesh spacing, we have modified the locations of the dependent variables with respect to the finite difference cells. The positions of the dependent variables still remain identical to Harlow's original formulation when the mesh is equally spaced; that is, velocities are defined on cell sides and the pressure at cell centers.

Our numerical calculations of the bubble motion described in the last section were made by an older program in which the set of finite difference approximations to the convective term of the momentum equation were not fully first order. Hence the effect of changing the positions of the dependent variables is not established by these calculations. However, the results of using the irregular star technique and velocity extrapolation at the free surfaces are clearly shown.

2. The Underwater Explosion Bubble

The present paper is concerned with the calculation of underwater explosion bubbles produced by charges of explosives. The aim of such

calculations is to relate the size and nature of the explosive charge and the depth of explosion to the subsequent motion of the explosion bubble, the resulting velocity and pressure fields, and the free surface motion.

In such an underwater explosion, there is a time interval at the beginning during which compressibility of the water is important, and a much longer subsequent motion in which the water can be assumed incompressible. The present calculations are concerned only with the latter part of the flow and start from initial conditions which must be obtained either empirically or from other calculations. The compressible flow at the beginning can be calculated by methods such as that described by Sternberg and Walker [16]. This compressible flow contains a strong spherical shock moving radially outward, and a series of rarefactions and weak shocks within the explosion bubble.

The bubble begins to expand immediately after disappearance of the shock, and when no boundaries are nearby, the subsequent motion consists of a number of oscillations together with an upward migration due to buoyancy. Shortly before each minimum, when the migration velocity becomes large, a jet forms at the bottom of the bubble. When the depth is not too large, this jet strikes the top of the bubble and causes it to become temporarily toroidal in shape. A fraction of the original energy is lost at each minimum, and this loss can be taken into account approximately by use of results due to Snay [17].

In the present report, as shown in Figure 1, the fluid outside the bubble is assumed to be bounded by a cylindrical wall of large radius, a rigid bottom at large depth, and by a liquid-air interface. The explosion is assumed to occur on the axis of symmetry. Calculations are carried out for the motion of an underwater explosion bubble in the presence of gravity using initial conditions supplied by H. Snay. This case corresponds to the detonation of a TNT sphere of 354 pounds at a depth of 81 feet.

II. OUTLINE OF THE MAC METHOD

1. Differential Equations

The equations solved by the present MAC code are the unsteady, incompressible, axisymmetric, inviscid flow equations with the effect of gravity included, and are given as follows. The continuity equation for conservation of mass is

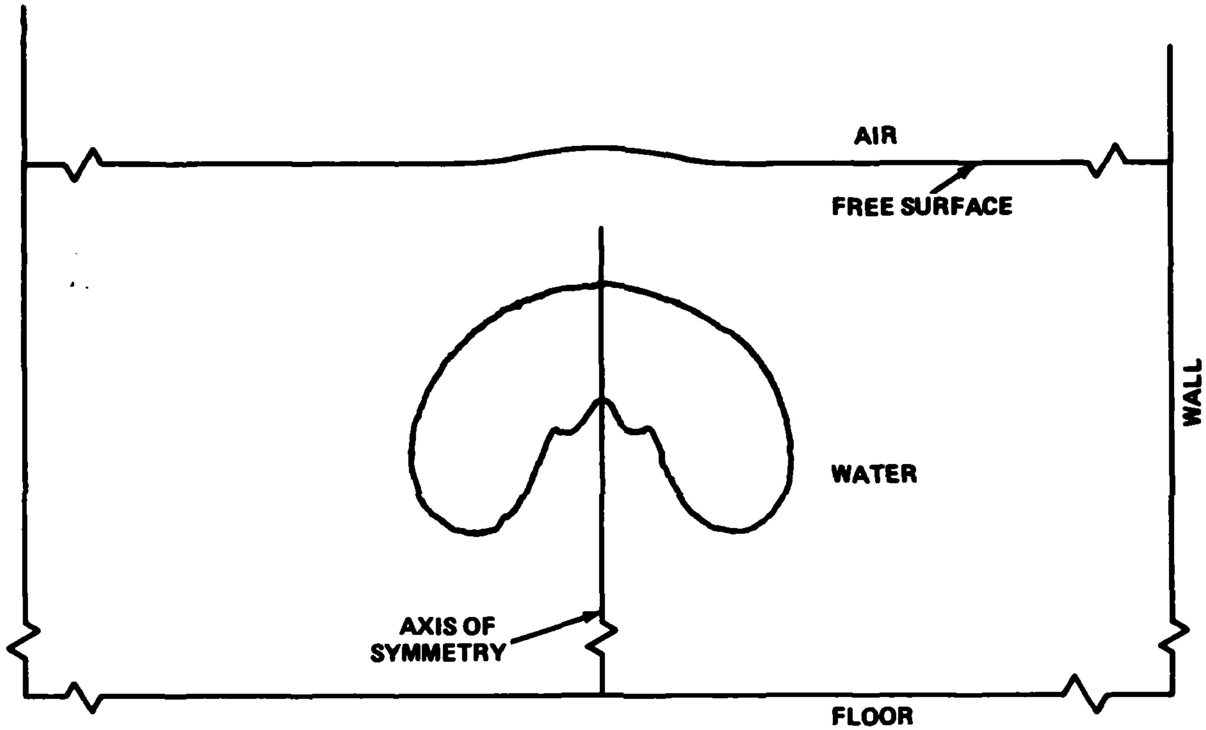

FIG. 1 SCHEMATIC OF THE UNDERWATER EXPLOSION BUBBLE PROBLEM.

(2.1) $$\frac{1}{r}\frac{\partial(ru)}{\partial r} + \frac{\partial v}{\partial z} = 0,$$

where r and z are cylindrical coordinates and u and v are the velocity components in the r- and z-directions, respectively. The radial and axial accelerations are given by the Euler equations

(2.2) $$\frac{\partial u}{\partial t} + u\frac{\partial u}{\partial r} + v\frac{\partial u}{\partial z} + \frac{\partial \phi}{\partial r} = 0$$

and

(2.3) $$\frac{\partial v}{\partial t} + u\frac{\partial v}{\partial r} + v\frac{\partial v}{\partial z} + \frac{\partial \phi}{\partial z} = g$$

respectively, with $\phi = p/\rho$, where p is the pressure, ρ is the constant density, and g is the acceleration due to gravity. Many forms of the convection terms in (2.2) and (2.3) have been used. The results presented in this paper use the form obtained by combining these terms with (2.1) to get

(2.4) $$u\frac{\partial u}{\partial r} + v\frac{\partial u}{\partial z} = \frac{1}{r}\frac{\partial (ru^2)}{\partial r} + \frac{\partial (uv)}{\partial z}$$

(2.5) $$u\frac{\partial v}{\partial r} + v\frac{\partial v}{\partial z} = \frac{1}{r}\frac{\partial (ruv)}{\partial r} + \frac{\partial (v^2)}{\partial z}.$$

For the linearized model equations, it is well known [18] that if centered differences are used to approximate the convective terms in the explicit forward time discretization of (2.2) and (2.3), then the difference scheme is unstable. However if, in addition to the usual Courant condition, a sufficiently large viscous-like damping term is added to the equation, the scheme becomes stable. Similarly Hirt [19] has shown in an heuristic stability analysis, that centered finite differences introduce error terms which are like negative viscosity terms and that for stability these negative contributions can be counterbalanced by introducing a numerical viscosity, ν, to the momentum equations. The final form of the momentum equations used by the program is then

(2.6) $$\frac{\partial u}{\partial t} = -\frac{1}{r}\frac{\partial (ru^2)}{\partial r} - \frac{\partial (uv)}{\partial z} - \frac{\partial \phi}{\partial r} + \nu\frac{\partial}{\partial z}\left(\frac{\partial u}{\partial z} - \frac{\partial v}{\partial r}\right)$$

and

(2.7) $$\frac{\partial v}{\partial t} = -\frac{1}{r}\frac{\partial (ruv)}{\partial r} - \frac{\partial v^2}{\partial z} - \frac{\partial \phi}{\partial z} - \frac{\nu}{r}\frac{\partial}{\partial r}\left[r\left(\frac{\partial u}{\partial z} - \frac{\partial v}{\partial r}\right)\right] + g$$

where for stability, using a notation described in [5], we have

$$\nu \geq 0.7\ \left[(\Delta X)^2\ \left|\frac{\partial u}{\partial X}\right|\right]_{max},\quad \Delta t \leq \frac{(\Delta X)^2_{min}}{\nu}.$$

Differentiating the continuity equation (2.1) with respect to t and substituting the momentum equations (2.6) and (2.7) in the resulting equation gives

$$(2.8)\qquad \frac{1}{r}\frac{\partial}{\partial r}\left(r\frac{\partial\phi}{\partial r}\right) + \frac{\partial^2\phi}{\partial z^2} = -Q,$$

where the viscous terms vanish and Q is just the divergence of the convection terms. We have

$$(2.9)\qquad Q = \frac{1}{r}\frac{\partial}{\partial r}\left[\frac{1}{r}\frac{\partial(ru^2)}{\partial r} + \frac{\partial(ru^2)}{\partial r} + \frac{\partial(uv)}{\partial z}\right] + \frac{\partial}{\partial z}\left[\frac{1}{r}\frac{\partial(ruv)}{\partial r} + \frac{\partial(v^2)}{\partial z}\right].$$

When u and v are known, (2.8) is a Poisson equation for ϕ.

2. Boundary Conditions

Since solid walls are impermeable and the fluid is assumed to be inviscid, the appropriate boundary condition at rigid walls is the "free-slip" condition, in which only the normal component of velocity is constrained to be zero. To obtain an additional condition at rigid walls when the numerical viscosity coefficient ν is nonzero, we require the viscous stress $\partial u/\partial x + \partial v/\partial r$ to be zero there. The velocity boundary conditions on the axis of symmetry are the same as the preceding boundary conditions at a rigid wall, since we have $u = 0$ and $\partial v/\partial r = 0$.

On free surfaces the pressure, p, is prescribed. On the air surface, in Figure 1, p is assumed to be a constant applied pressure, usually one atmosphere. On the bubble surface p is given by an equation of state such as the adiabatic gas law pV^γ = constant. The boundary condition for the pressure on a solid boundary is obtained from the momentum equations and the velocity boundary conditions. For example on a vertical wall, since $u = 0$, $\frac{\partial u}{\partial t}$, $u\frac{\partial u}{\partial r}$ and $\frac{\partial u}{\partial z}$ all vanish in (2.2), and the appropriate condition is $\partial\phi/\partial r = 0$. Similarly $\partial\phi/\partial z = g$ on horizontal walls.

In addition, the velocity near or on the free surface is constrained by the free surface pressure condition through the terms $\partial\phi/\partial r$ and $\partial\phi/\partial z$ in the momentum equations (2.2) and (2.3).

3. Development of the Computational Procedure

The development of the method is based on a procedure due to Chorin [20]. This development is equivalent to the usual one, but the difference equations for the pressure at solid boundaries are obtained more naturally.

In the present version of the MAC method a non-uniform mesh is used, as shown in Figure 2, and flow quantities are evaluated at the locations shown in Figure 3. Thus, the pressure is calculated in the interior of a cell, u is calculated on vertical edges, and v on horizontal edges.

Let D represent the discrete divergence operator used to approximate the continuity equation (2.1), and let $\overline{G}$ be the discrete gradient operator used to evaluate $\partial\phi/\partial r$ and $\partial\phi/\partial z$ in (2.6) and (2.7). Let $\overline{w} = (u, v)$. Using the notation established in Figure 3 our approximations to these operators are

$$(2.10) \qquad (D\overline{w})_{i,j} = \frac{r_{i+\frac{1}{2}}\, u_{i+\frac{1}{2},j} - r_{i-\frac{1}{2}}\, u_{i-\frac{1}{2},j}}{r_i \Delta\nu_i} + \frac{v_{i,j+\frac{1}{2}} - v_{i,j-\frac{1}{2}}}{\Delta z_j}$$

and

$$(2.11) \qquad \overline{G}\phi = (G_r\phi,\ G_z\phi),$$

where

$$(2.12) \qquad (G_r\phi)_{i+\frac{1}{2},j} = \frac{\phi_{i+1,j} - \phi_{i,j}}{\Delta r_{i+\frac{1}{2}}},$$

$$(2.13) \qquad (G_z\phi)_{i,j+\frac{1}{2}} = \frac{\phi_{i,j+1} - \phi_{i,j}}{\Delta z_{j+\frac{1}{2}}}.$$

Replacing derivatives with respect to time, t, by forward divided differences using a time increment Δt that is calculated at each time step to insure stability, we symbolically write first order approximations to (2.6) and (2.7) as

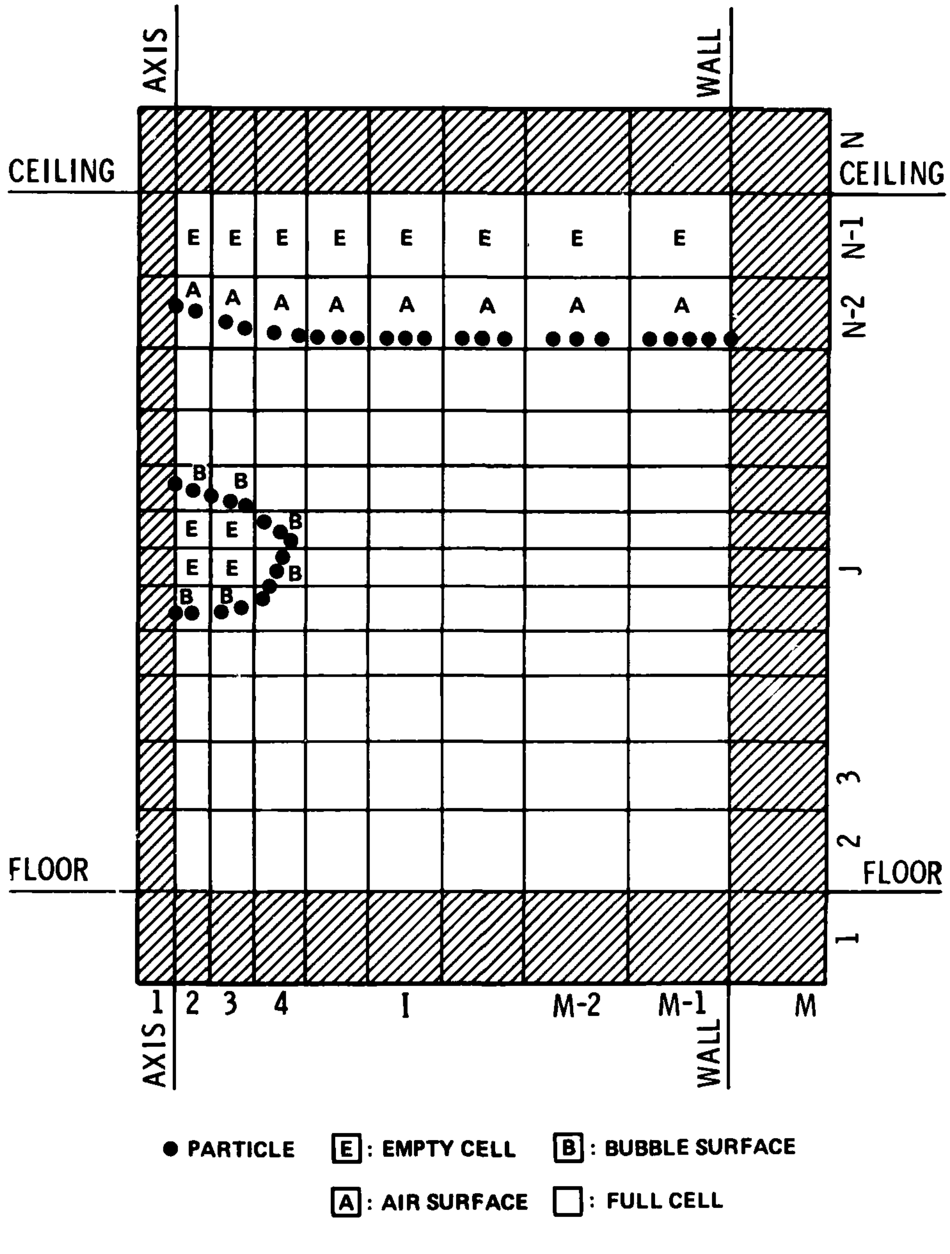

FIG. 2 THE COMPUTING MESH

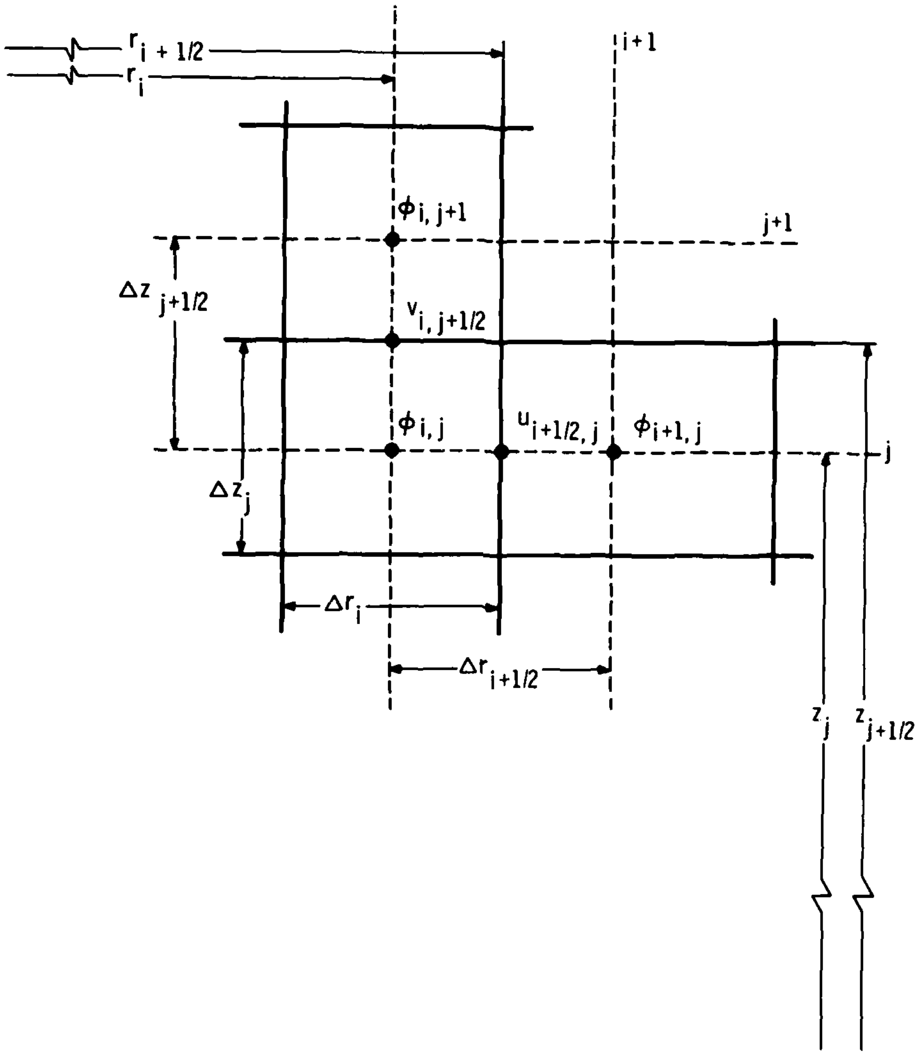

FIG. 3 CELL NOMENCLATURE.

$$(2.14) \qquad u^{n+1}_{i+\frac{1}{2},j} = u^{n}_{i+\frac{1}{2},j} - \Delta t^{n}\, [C_r + G_r\phi - \Lambda_r]^{n}_{i+\frac{1}{2},j}$$

$$(2.15) \qquad v^{n+1}_{i,j+\frac{1}{2}} = v^{n}_{i,j+\frac{1}{2}} - \Delta t^{n}\, [C_z + G_z\phi - g - \Lambda_z]^{n}_{i,j+\frac{1}{2}}$$

where the superscript n represents the nth time level, $(C_r)_{i+\frac{1}{2},j}$ and $(C_z)_{i,j+\frac{1}{2}}$ are the discretized convection terms, and $(\Lambda_r)_{i+\frac{1}{2},j}$ and $(\Lambda_z)_{i,j+\frac{1}{2}}$ are the discretized damping terms. The finite difference approximations to the convection and diffusion terms used in the present calculations are due to Pritchett [5], but the convection terms of [5] are not first order on the mesh shown in Figure 3. Hence, the present calculations cannot show the effect of the new positioning of the dependent variables. However, a calculation for a different example, comparing the approximations of [5] with a fully first order set of equations, shows little difference in bubble profiles or bubble periods.

If we write

$$(2.16) \qquad u^{aux}_{i+\frac{1}{2},j} = u^{n}_{i+\frac{1}{2},j} - \Delta t^{n}\, [C_r - \Lambda_r]^{n}_{i+\frac{1}{2},j}\ ,$$

$$(2.17) \qquad v^{aux}_{i,j+\frac{1}{2}} = v_{i,j+\frac{1}{2}} - \Delta t^{n}\, [C_z - g - \Lambda_z]^{n}_{i,j+\frac{1}{2}}\ ,$$

then

$$(2.18) \qquad u^{n+1}_{i+\frac{1}{2},j} = u^{aux}_{i+\frac{1}{2},j} - \Delta t^{n}\, (G_r\phi)^{n}_{i+\frac{1}{2},j}\ ,$$

$$(2.19) \qquad v^{n+1}_{i,j+\frac{1}{2}} = v^{aux}_{i,j+\frac{1}{2}} - \Delta t^{n}\, (G_z\phi)^{n}_{i,j+\frac{1}{2}}\ .$$

The requirement that mass be conserved, (2.1), is

$$(2.20) \qquad (D\bar{w})^{n+1}_{i,j} = 0.$$

Substituting (2.18) and (2.19) into (2.20) gives for each cell (i,j)

$$(2.21) \qquad (D\,\bar{G}\phi)^{n}_{i,j} = (D\bar{w}^{aux})_{i,j}/\Delta t^{n}.$$

If in addition we require that $\bar{\Lambda} = (\Lambda_r, \Lambda_z)$ be of a form so that $D\bar{\Lambda} = 0$ then (2.21) is the discrete analog of the Poisson equation (2.8).

Referring to the numbering system for the finite difference mesh as shown in Figures 2 and 3 we expand (2.20) for each fluid cell i,j with

$$u^{n+1}_{i+\frac{1}{2},j} = u^{aux}_{i+\frac{1}{2},j} = 0 \text{ or } v^{n+1}_{i,j+\frac{1}{2}} = v^{aux}_{i,j+\frac{1}{2}} = 0$$

as appropriate on rigid walls. We then obtain a system of linear algebraic equations in the unknown $\phi^n_{i,j}$ of the form

$$\alpha_{1,j}\,\phi^n_{i,j-1} + \beta_{1,i}\,\phi^n_{i-1,j} - (\alpha_{1,i} + \alpha_{2,j} + \beta_{1,i} + \beta_{2,i})\,\phi^n_{i,j} + \beta_{2,i}\,\phi^n_{i+1,j} + \alpha_{2,j}\,\phi^n_{i,j+1} = R_{i,j} \tag{2.22}$$

where

$$R_{i,j} = D(\overline{w}^{aux})_{i,j}/\Delta t \tag{2.23}$$

$$\alpha_{1,j} = \begin{cases} \dfrac{1}{\Delta z_j \Delta z_{j-\frac{1}{2}}}, & j = 3 \text{ to } N-1 \\ 0 & \text{otherwise} \end{cases} \tag{2.24}$$

$$\alpha_{2,j} = \begin{cases} \dfrac{1}{\Delta z_j \Delta z_{j+\frac{1}{2}}}, & j = 2 \text{ to } N-2 \\ 0 & \text{otherwise} \end{cases} \tag{2.25}$$

$$\beta_{1,i} = \begin{cases} \dfrac{r_{i-\frac{1}{2}}}{r_i \Delta r_i \Delta r_{i-\frac{1}{2}}}, & i = 3 \text{ to } M-1 \\ 0 & \text{otherwise} \end{cases} \tag{2.26}$$

$$\beta_{2,i} = \begin{cases} \dfrac{r_{i+\frac{1}{2}}}{r_i \Delta r_i \Delta r_{i+\frac{1}{2}}}, & i = 2 \text{ to } M-2 \\ 0 & \text{otherwise} \end{cases} \tag{2.27}$$

This system automatically includes the rigid wall boundary conditions for the pressure, and as shown below, is equivalent to the system generated by the more conventional derivation. Moreover the system (2.22) to (2.27) immediately gives rise to an efficient algorithm, since the boundary conditions are implemented by merely setting to zero the appropriate positions in the arrays which contain the coefficients, $\alpha_{k,j}$ and $\beta_{k,i}$.

In the usual development of the MAC method, the discrete five point Laplacian, $D\bar{G}\phi$, is made to hold for cells adjacent to solid boundaries as well as for interior cells by introducing a layer of "fictitious" cells adjacent to the boundary. The finite difference approximation to the normal derivative boundary condition is expressed in terms of the pressure in the fictitious cell and the pressure in the adjacent boundary cell. The boundary condition for the pressure is imposed by combining this equation with the discrete five point Laplacian for the interior boundary cell to give an expression for the pressure which does not involve the fictitious cell. We verify below that this is equivalent to Chorin's procedure on the boundary $z = 0$.

On the floor, $z = 0$, the substitution $v = 0$ in (2.3) gives the Neumann condition $\partial\phi/\partial z = g$. Using a fictitious row of cells below the floor as in Figure 3, we can approximate this condition by

$$\frac{\phi_{i,2} - \phi_{i,1}}{\Delta z_{3/2}} = g \tag{2.28}$$

or

$$\phi_{i,1} = \phi_{i,2} - g\Delta z_{3/2}. \tag{2.29}$$

After introduction of fictitious cells, the usual discrete Poisson equation for the pressure in the row of floor cells, $j = 2$ and $3 \leq i \leq M-2$, is the same as (2.22) with $\alpha_{1,2}$ replaced by

$$\alpha'_{1,2} = \frac{1}{\Delta z_2 \Delta z_{3/2}}, \tag{2.30}$$

and with $R_{i,2}$ replaced by

$$R'_{i,2} = (D\overline{w}^{aux})_{i,2}/\Delta t. \tag{2.31}$$

In equation (2.31), the standard interior form (2.17) for the velocity $v^{aux}_{i,3/2}$ is used in forming the expression $(D\overline{w}^{aux})_{i,2}$. Noting that $(C_z)_{i,3/2} = 0$ on the boundary, we obtain

$$v^{aux}_{i,3/2} = (g + \Lambda_z)\,\Delta t.$$

AD-A119 315 DAVID W TAYLOR NAVAL SHIP RESEARCH AND DEVELOPMENT CE--ETC F/G 20/4
FIRST INTERNATIONAL CONFERENCE ON NUMERICAL SHIP HYDRODYNAMICS --ETC(U)
1975 J W SCHOT, N SALVESEN

UNCLASSIFIED NL

3 OF 8
AD A
119315

On substituting (2.29) into this modified form of (2.22), we obtain the finite difference equation to be satisfied in floor cells,

$$(2.32)\qquad \beta_{1,i}\,\phi^n_{i-1,2} - (\alpha_{2,2} + \beta_{1,i} + \beta_{2,i})\,\phi^n_{i,2} + \beta_{2,i}\,\phi_{i+1,2} + \alpha_{2,2}\,\phi_{i,3} = R'_{i,2} + \alpha'_{i,2}\,g\Delta z_{3/2},$$

In order to show that (2.32) is identical with (2.22) for floor cells, we need to verify that

$$(2.33)\qquad R'_{i,2} + \alpha'_{i,2}\,g\Delta z_{3/2} = R_{i,2}.$$

From (2.23), we have

$$(2.34)\qquad R_{i,2} = \left\{\frac{1}{r_i\Delta r_i}\left[r_{i+\frac{1}{2}}\,(u - C_r\,\Delta t)^n_{i+\frac{1}{2},2} - r_{i-\frac{1}{2}}\,(u - C_r\,\Delta t)^n_{i-\frac{1}{2},2}\right] + \frac{1}{\Delta z_2}\,[v - \Delta t\,(C_z - g)]^n_{i,5/2}\right\}/\Delta t.$$

The requirement that $D\bar{A} = 0$ leads to

$$(2.35)\qquad R'_{i,2} = \left\{\frac{1}{r_i\Delta r_i}\left[r_{i+\frac{1}{2}}\,(u - C_r\,\Delta t)^n_{i+\frac{1}{2},2} - r_{i-\frac{1}{2}}\,(u - C_r\,\Delta t)^n_{i-\frac{1}{2},2}\right] + \frac{1}{\Delta z_2}\,[v - \Delta t\,C_z]^n_{i,3/2}\right\}.$$

Finally, (2.33) follows from (2.34), (2.35), and (2.30). A similar analysis for axis, wall, and ceiling cells shows that equations (2.22) through (2.27) are equivalent to the usual MAC procedure.

4. Order of Accuracy of the Discrete Laplacian

In the original MAC formulation, the pressure is defined at the centers of cells, and the horizontal and vertical components of velocity are defined at the centers of vertical and horizontal sides, respectively. It will be shown below that some of the terms of the difference equations are not accurate to first order for arbitrary grid spacing as the maximum grid size goes to zero. However, with the pressure and the velocity components defined at the points shown in Figure 3, these terms become

accurate to first order, and in particular, the discrete Laplacian is then first order, while remaining in the form of the divergence of a gradient, as in (2.21). For equal mesh spacing, the original and the new positions are of course the same. As in Figure 3, the points at which the pressure is defined are such that the midpoint of the line connecting two adjacent points is on a cell side, and a radial or vertical velocity component, as the case may be, is defined at this intersection point. Such a mesh is determined uniquely when the points of definition of the pressure are assigned.

To show the validity of this modification, we consider the one-dimensional operator $\partial^2\phi/\partial z^2$. Its first order Taylor series approximation is

$$\text{(2.36)} \qquad \Delta^T_{ij}\,\phi = \left[\frac{\phi_{i,j+1} - \phi_{i,j}}{\Delta z_{j+\frac{1}{2}}} - \frac{\phi_{i,j} - \phi_{i,j-1}}{\Delta z_{j-\frac{1}{2}}}\right] \Big/ \left[\frac{\Delta z_{j+\frac{1}{2}} + \Delta z_{j-\frac{1}{2}}}{2}\right]$$

To satisfy the criterion that $\frac{\partial^2\phi}{\partial z^2}$ be numerically of the form $\frac{\partial}{\partial z}\,[\frac{\partial\phi}{\partial z}]$ as in (2.21), the usual MAC approximation is

$$\text{(2.37)} \qquad \Delta^M_{i,j}\,\phi = \left[\frac{\phi_{i,j+1} - \phi_{i,j}}{\Delta z_{j+\frac{1}{2}}} - \frac{\phi_{i,j} - \phi_{i,j-1}}{\Delta z_{j-\frac{1}{2}}}\right] \Big/ \; \Delta z_j$$

Under the original formulation, where the pressure is defined at cell centers, the MAC expression (2.37) is related to the Taylor series expression (2.36) by

$$\text{(2.38)} \qquad \Delta^M_{i,j}\,\phi = \Delta^T_{i,j}\,\phi\left[\frac{1}{2} + \frac{\Delta z_{j+1} + \Delta z_{j-1}}{4\Delta z_j}\right]$$

The quantity in brackets is unity only if

$$\text{(2.39)} \qquad \Delta z_j = \Delta z_o + (\Delta z_1 - \Delta z_o)j,$$

which includes the evenly spaced mesh as a special case. By requiring instead that

$$\text{(2.40)} \qquad \Delta z_j = \frac{1}{2}\,[\Delta z_{j+\frac{1}{2}} + \Delta z_{j-\frac{1}{2}}]$$

(2.36) and (2.37) become equal. This equation together with a similar equation for r_i, defines the new positioning of the dependent variables shown in Figure 3.

We note that the expression within the square brackets in (2.38) remains close to unity when the mesh size varies gradually enough.

5. Solution of the System of Linear Algebraic Equations

The system (2.22) is solved by use of the successive overrelaxation (SOR) method. The original MACYL code used the five point form of the discrete Laplacian in (2.21) for all boundary as well as full cells. The boundary conditions were satisfied by appending the linear equations, involving the pressure in fictitious cells, consisting of (2.29) together with similar equations at vertical walls and the axis of symmetry. Weber [21] showed, and we verified numerically, that when the SOR method is used to solve this enlarged system, the solution may diverge. On the other hand, he demonstrated that the system (2.22) to (2.27), or the equivalent set exemplified by (2.32), satisfies sufficient conditions for convergence of the SOR method (such as those given in [22], for example).

In the underwater explosion bubble calculations, the solution of the Poisson equation for the pressure at a given time is carried out by using the solution at the preceding time as an initial guess. When M radial and N vertical grid points are used, we find that the number of iterations required for a root-mean-square relative error of 10^{-4} is roughly equal to max(M, N).

6. Numerical Treatment of the Boundary Conditions

a. The boundary region

The region in which the equations are solved is defined by four fixed boundaries, axis, wall, floor and ceiling, and by the free surfaces. A free surface is composed of a sequence of massless marker particles. These particles are introduced at known locations in the beginning, and are moved at each time step according to the local velocities. The velocity components at each particle location are computed by interpolation, assuming that the velocity components vary linearly between points of definition of the grid velocities.

It is necessary to distinguish between empty, surface, and full cells in the calculation, as shown schematically in Figure 1. The type of a given cell is denoted by means of a flag, which in the present program is a signed integer associated with the cell. The cells are reflagged at each time step after the particles have been moved.

In a study sponsored by the Office of Naval Research, Berger and Vander Vorst [23] solved the Poisson equation (2.8) using the finite element method with linear triangular elements constrained to lie within the finite difference mesh. For this study they developed a procedure to form a polygonal approximation to the surface from the locations of the marker particles. This polygonal surface consists of a sequence of connected straight line segments such that, as shown in Figure 4a, each surface cell contains only one such segment. The polygonal surface is utilized in the present code for the calculation of surface normals and the formation of the irregular stars which are described later in this section. In addition it is used to calculate the bubble volume for use in the equation of state. This polygonal surface is used for two reasons. First and most important, since the polygonal surface has only one segment per cell, it is computationally more efficient to describe and traverse than the marker particle surface. Second, if the arrangement of the particles becomes very irregular we can use the polygonal surface to smooth the particle surface by distributing the particles onto the polygon.

b. Velocity boundary conditions

In order to satisfy the velocity boundary conditions in the finite-difference version of the problem, we follow the usual MAC methodology and introduce fictitious cells adjacent to the rigid boundaries and the axis of symmetry. The values of the flow quantities at points of these fictitious cells are determined so that both the finite difference equations and the finite difference forms of the boundary conditions are satisfied.

For simplicity, we do not use special backward differences near surfaces to evaluate the convection and damping terms, $\overline{C}$ and $\overline{\Lambda}$, of the discrete momentum equations, (2.14) and (2.15); instead, we extend the velocity field across the computational polygonal surface by linear extrapolation from a direction normal to the surface. The original MAC [3] as well as the later SMAC [7] and MACYL [5] codes set these

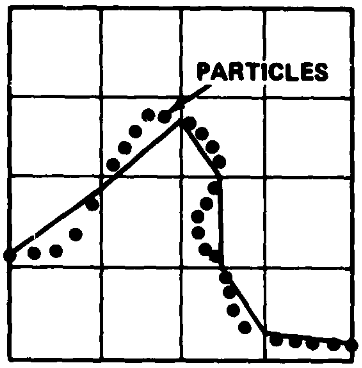

a. LINE SEGMENT BOUNDARY

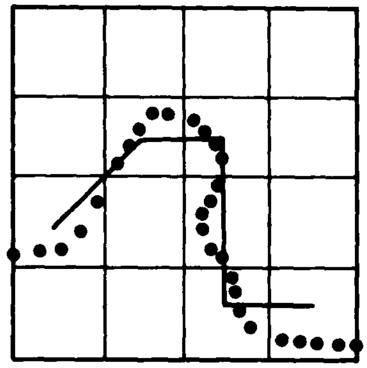

b. EFFECTIVE BOUNDARY USING REGULAR STARS

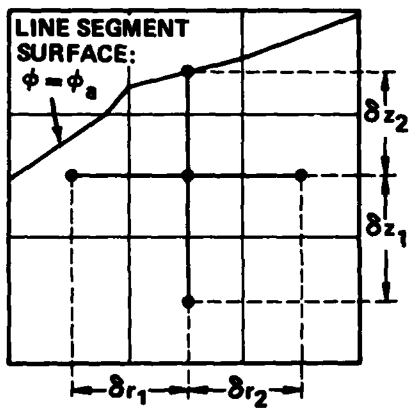

c. IRREGULAR STARS IN A FULL CELL

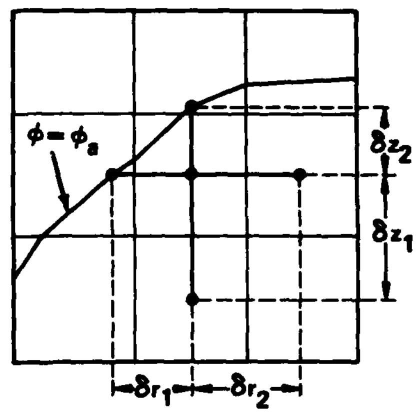

d. IRREGULAR STARS IN A SURFACE CELL

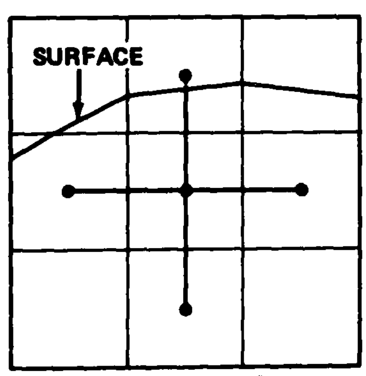

e. AMSDEN'S PRESSURE EXTRAPOLATION

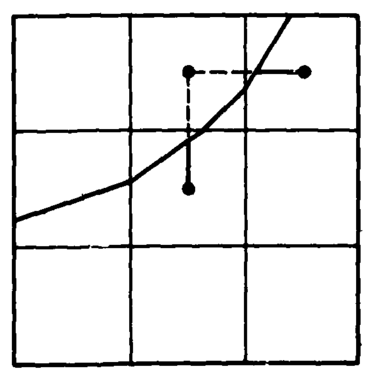

f. EXTRAPOLATION DOUBLY DEFINED

FIG. 4 FREE SURFACE BOUNDARY CONDITION.

velocities on the empty faces of a surface cell so that the discrete divergence vanishes as if the cell were entirely full. Chan and Street [10], on the other hand, introduced extrapolation along cell lines to calculate these velocities. They found that linear extrapolation gave better results for water wave problems than was obtained by setting $D\tilde{w} = 0$ in surface cells. Shere and Vander Vorst [15] reached the same conclusion by using a version of the SMAC code, which they had modified so that the velocity field is extended by extrapolation, to compute the flow produced when a large mass of water with a plane surface impacts on a vertical cylinder with large velocity. In their case, when the velocity field was extended by forcing zero divergence in surface cells, large nonphysical velocities occurred at the impact of the water mass with the cylinder, and the calculation could not be continued. However, when the velocity field was extended by linear extrapolation, the resulting flow agreed with experiment. For the underwater explosion bubble problem, we find that extrapolation in a direction normal to the surface produces slightly better results than extrapolating along cell lines in either a vertical or horizontal direction.

c. Pressure boundary conditions

As shown earlier, the Neumann boundary conditions for the pressure on the vertical and horizontal rigid boundaries are implicitly satisfied in the set of linear equations (2.22) to (2.27). However, the Dirichlet condition, ϕ = constant, on free surfaces must still be satisfied. The SMAC and MACYL codes implemented this condition by fixing $\phi_{i,j} = \phi_a$ at the center of all air-surface cells, and $\phi_{i,j} = \phi_b$ at the centers of bubble surface. The discrete Poisson equation (2.22) is then enforced only on full cells, that is, cells whose four neighbors are either surface or full. This gives an effective computational surface connecting the centers of surface cells, as shown in Figure 4b. The MACBUB code implements the free surface boundary condition by using the irregular star technique to difference (2.8) near the polygonal surface.

The "regular star" equation (2.22) applies to full cells such that the centers of all four neighbors lie in the fluid. In all other cases a surface segment cuts through the cell or a neighboring cell such that the center of one or more of the four adjacent cells is outside

the fluid. Two examples of this are shown in Figure 4. Using the nomenclature established in Figure 4 for these irregular cells, we approximate the Poisson equation (2.9) to first order as the irregular star equation

$$(2.41)\qquad \frac{1}{r_i}\left[(r_i + r_2^*)\frac{\phi_{i+1,j} - \phi_{i,j}}{\delta r_2} - (r_1^* + r_i)\frac{\phi_{i,j} - \phi_{i-1,j}}{r_1}\right]/(\delta r_1 + \delta r_2) + \left[\frac{\phi_{i,j+1} - \phi_{i,j}}{\delta z_2} - \frac{\phi_{i,j} - \phi_{i,j-1}}{\delta z_1}\right]/\left[\frac{\delta z_1 + \delta z_2}{2}\right] = R_{i,j}.$$

We have

$$\delta r_1 = \begin{cases} \Delta r_{i-\frac{1}{2}} \text{ if } (r_{i-1}, z_j) \text{ is inside the fluid} \\ = r_i - r_s \text{ otherwise,} \end{cases}$$

where r_s is the value of r on the polygonal boundary for $z = z_j$, and similarly for δr_2, δz_1, and δz_2. Any of the quantities $\phi_{i+1,j}$, $\phi_{i-1,j}$, $\phi_{i,j-1}$, and $\phi_{i,j+1}$ are equal to the surface pressure where applicable. We see that (2.41) reduces to (2.22) in the case of a regular star. In the present calculations, $R_{i,j}$ is calculated in both full cells and partially filled cells by the same procedure. This procedure is not accurate in the case of partially filled cells, and may contribute to some of the difficulties found at the bubble surface. A more accurate method for calculation of $R_{i,j}$ in partially filled cells has been developed by Vander Vorst and Rogers [24], but has not yet been used in bubble calculations.

To be consistent, the irregular star procedure also requires that the pressure gradient approximation (2.11) and (2.12) to $\frac{\partial\phi}{\partial r}$ and $\frac{\partial\phi}{\partial z}$ be rewritten for the irregular sides of the star. For example in Figure 6a

$$(2.42)\qquad \left.\frac{\partial\phi}{\partial z}\right|_{i,j+\frac{1}{2}} = \frac{\phi_a - \phi_{i,j}}{\delta z_2}.$$

Figure 5 gives a comparison of calculations with and without the use of irregular stars. Amsden [8] outlined an alternate procedure for implementing the irregular star method which is computationally more

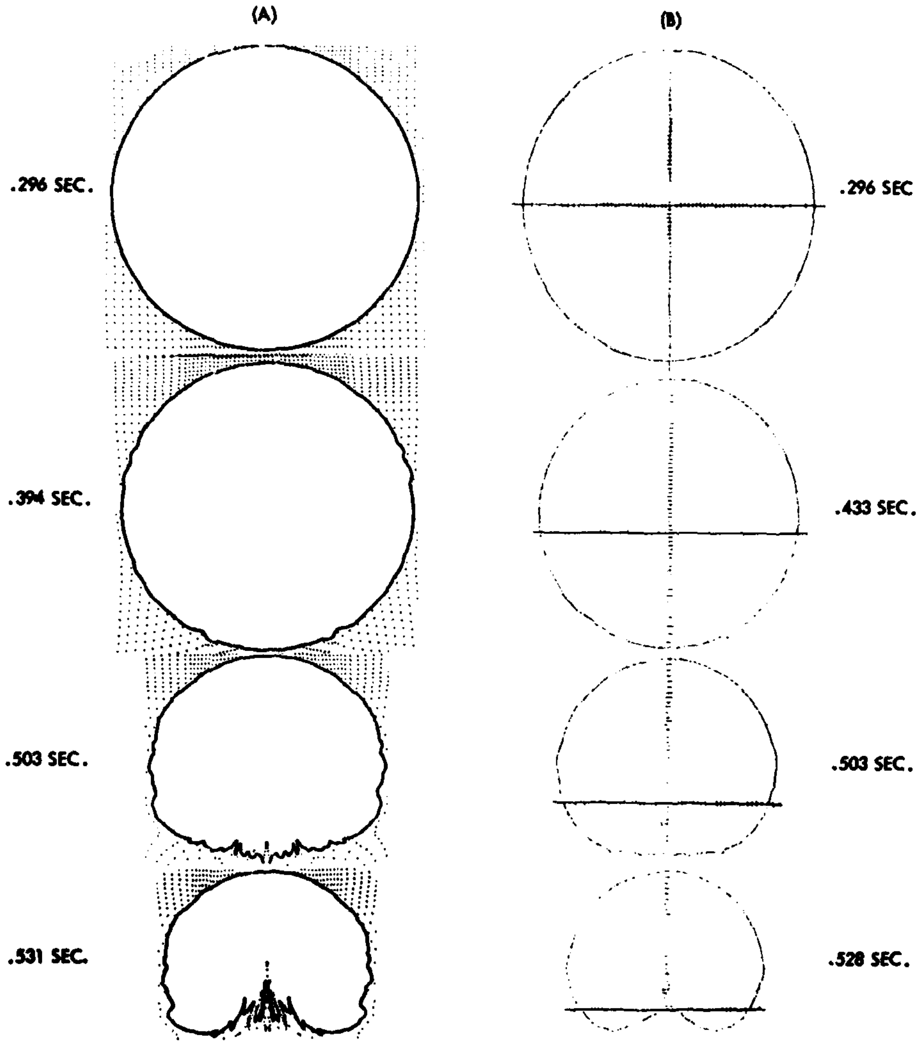

FIG. 5 BUBBLE PROFILES RESULTING FROM DETONATION OF A 354 LB. CHARGE OF TNT AT A DEPTH OF 80.8 FT. (A) PROFILES USING REGULAR STARS AND VELOCITY EXTRAPOLATION ALONG GRID LINES. (B) PROFILES USING IRREGULAR STARS AND NORMAL EXTRAPOLATION.

efficient than the procedure of Chan and Street. They use the regular star equation in all cells whose center is in the fluid; however, as illustrated in Figure 4e, at the beginning of each SOR sweep, the pressure in cells whose centers lie just outside the surface are set by a linear extrapolation in the vertical direction across the surface. These extrapolated pressures are used as the boundary values in the subsequent iteration.

Previous to this, we had independently rejected this extension procedure for two reasons. First, the more complicated surface geometry of the underwater bubble requires that the pressure extrapolation be done in either a horizontal or vertical direction. In some such cases, as shown in Figure 4f, an extrapolated pressure may be doubly defined, say from above and from the left. Secondly, an analysis similar to that of Weber [21] predicts that unless a sufficiently small over-relaxation factor is used, the SOR iteration may diverge. This can be circumvented by using a smaller over-relaxation factor for the irregular cells than for the regular cells, but this adds a degree of complexity back into the algorithm.

III. THE MACBUB COMPUTER PROGRAM

To run a problem we really need to consider four distinct computer programs: MACEDIT, MACIN, MACBUB, and MACPLT.

MACEDIT is a small program which utilizes an editor to change all of the FORTRAN dimension statements in the other three programs to correspond to the desired finite difference mesh size for a particular problem.

MACIN creates the initial data as cycle 0 on a magnetic tape. Input to this program consists of all the parameters necessary to describe the initial state of the problem, including the grid dimensions, grid cell size, bubble location, bubble radius, bubble migration rate, bubble expansion (or contraction) rate, location of free surface, and the number and locations of free surface and interior marker particles.

MACBUB is the major program; it carries out the MAC solution as outlined below in steps 0 through 12:

0. Read in running parameters: starting cycle; ending cycle; smoothing cycle/do not smooth; overrelaxation factor; maximum number of iterations; Courant number; print frequency; dump frequency; SOR accuracy parameter. Read in initial data at starting cycle from magnetic tape.

1. Increment cycle counters.
2. Find polygonal free surface from particles.
3. If this cycle is to be smoothed put particles on polygonal surface.
4. Calculate pressure coefficients (2.37) for irregular star cells and label those cells.
5. Calculate auxiliary velocities from (2.16) and (2.17).
6. Compute inhomogeneous Poisson term, R (2.23).
7. To find pressure, iterate on (2.22) and (2.37) by SOR method until solution is within desired relative accuracy or maximum number of iterations have been completed.
8. Find new velocities from auxiliary velocities using (2.18) and (2.19).
9. Extend velocities by normal extrapolation.
10. Move particles by local fluid velocity.
11. Dump onto magnetic tape, or print as demanded by counters.
12. If cycle does not equal ending cycle, go to step 1; otherwise, stop.

The program MACPLT reads the magnetic tape produced by MACBUB and produces particle, isobar, and vector plots on an electrostatic plotter.

IV. THE UNDERWATER BUBBLE CALCULATION

1. Computations

The problem of determining the fluid flow generated by an underwater detonation of an explosive charge has been addressed experimentally, analytically, and numerically in the literature. A compendium of reports selected by the Office of Naval Research [25] presents the major historical results to 1950. Snay and coworkers [26-28] have contributed much experimental as well as one-dimensional and quasi two-dimensional analysis.

For purely radial motion in incompressible flow, the radius of the bubble produced by an underwater explosion satisfies the differential equation

$$(4.1) \qquad r\ddot{r} + \frac{3}{2}\dot{r}^2 - \frac{1}{\rho}[p(r) - p_\infty] = 0$$

(Cole [29], page 273), where $r(t)$ is the radius of the bubble at time t, $p(r)$ is the pressure inside the bubble, and p_∞ is the pressure at infinity. The pressure $p(r)$ inside the bubble can be calculated when the equation of state of the explosion products is known. A commonly used isentropic form of the equation of state is $p = p_o(\rho/\rho_o)^\gamma$, where p_o and ρ_o are the pressure and density at some initial time, and γ is a constant. In this case, $p(r) = p_o(r_o/r)^{3\gamma}$, where r_o is the initial bubble radius. Given the values

of $r(0)$ and $r(0)$, the equation for r can be solved numerically [30]. Such a solution is shown in Figure 6 corresponding to the case of an explosion bubble produced by a 354 pound charge of TNT at a depth of 81 feet, where p_∞ is taken equal to the hydrostatic pressure at the charge depth. The given function $p(r)$ is taken as above, with p_o, γ, and $r(0) = r_o$ as shown under Figure 6, and with $\dot{r}(0) = 0$.

For axisymmetric flow that includes the effects of gravity and the water surface, calculations have been carried out by MACBUB for the case of an explosion bubble produced by a 354 pound charge of TNT at a depth of 81 feet, with the equation of state of the explosion products of the form $p = p_o(\rho/\rho_o)^\gamma$. The calculation was begun at the first bubble maximum, using a value of γ and initial conditions furnished by Snay [31]. The parameters used are:

$\gamma = 1.25402$
Time at first maximum = 0.296037 sec.
Bubble radius = 18.8943 ft.
Bubble pressure = 2.08412 psi.
Migration velocity = 11.8231 ft./sec.

The initial conditions were calculated by Snay by an approximate analytical method in which the bubble is assumed to remain spherical. Up to the first maximum, the bubble remains nearly spherical. As the first step in the MACBUB calculation, the velocity in the water due to the motion of a sphere of the above radius translating upward with the given migration velocity was calculated at grid points by use of well-known results from potential theory, given conveniently in [25], page 136, for example.

The pressures near the first minimum are such that the water should be considered slightly compressible. However, the present calculation was continued through the first minimum as incompressible, and energy was not subtracted at the first minimum as in [5] and [6].

Figure 7 shows a sequence of photographs of a scaled explosion of a 354 pound charge of TNT at a depth of 81 feet. Figures 8 and 9 show the bubble profiles and isobars obtained by the MACBUB calculations just described. The tic marks on the reference lines in Figures 8 and 9 represent the grid spacing. As seen in Figure 8, the bubble remains toroidal during its second expansion. The persistence of such a toroidal shape when the gravity effect is strong enough is mentioned by Pritchett

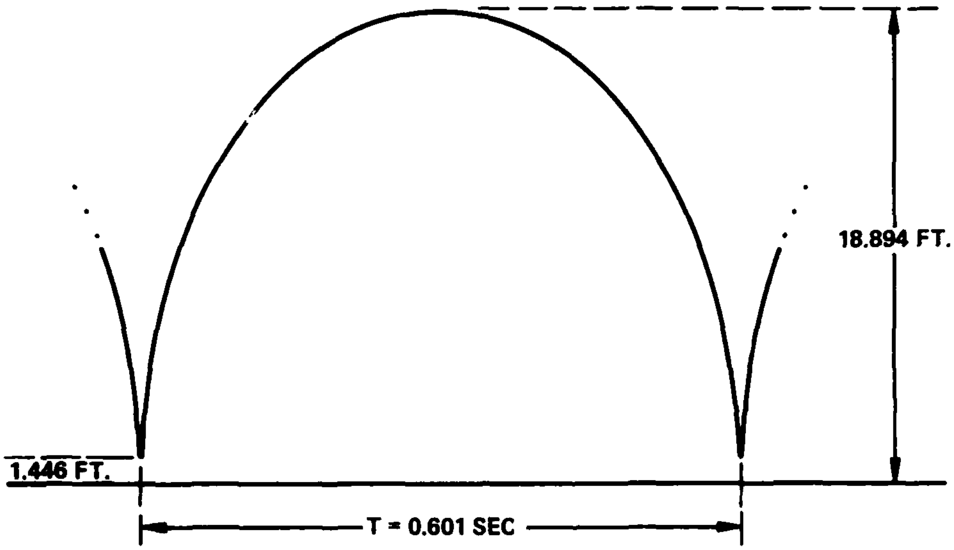

TIME VS RADIUS

EQUATION OF STATE: $PV^{\gamma} = C; \gamma = 1.254$
INITIAL RADIUS: $R_o = 18.894$ FT.
INITIAL BUBBLE PRESSURE: $P_o = 2.08412$ PSI
AMBIENT PRESSURE: 50.7 PSI

FIG. 6 PERIODIC SPHERICAL NON-MIGRATING SOLUTION FOR A 354 LB TNT CHARGE AT 81 FEET.

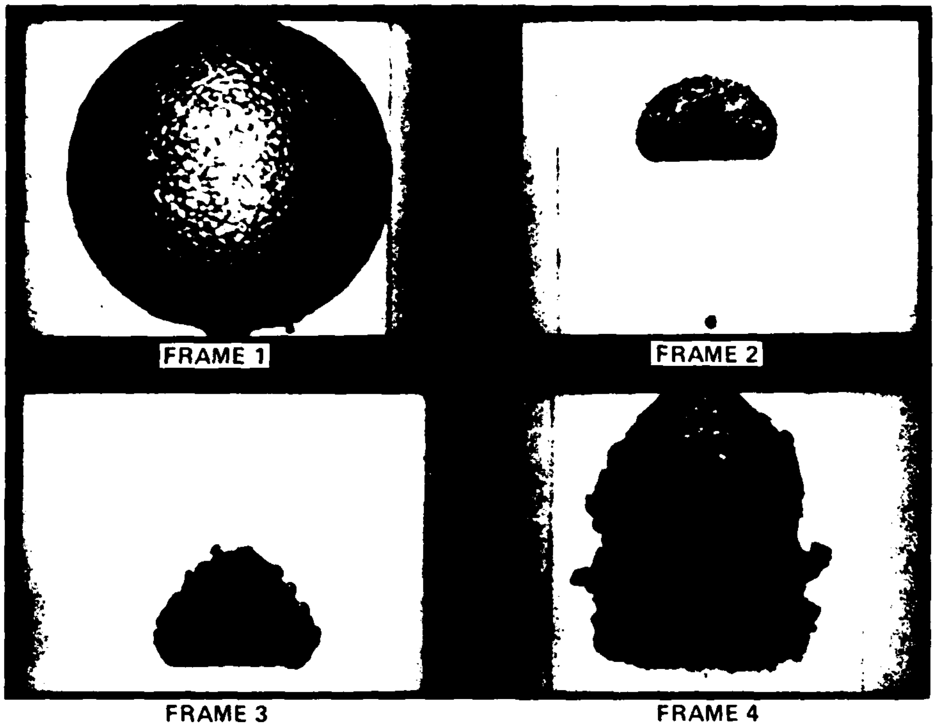

FRAME 1. BUBBLE MAXIMUM
FRAME 2. SHORTLY BEFORE MINIMUM
FRAME 3. SHORTLY AFTER MINIMUM
FRAME 4. SECOND BUBBLE MAXIMUM

FIG. 7 GAS BUBBLE FORMED BY AN UNDERWATER EXPLOSION
(SNAY, GOERTNER, and PRICE [27])

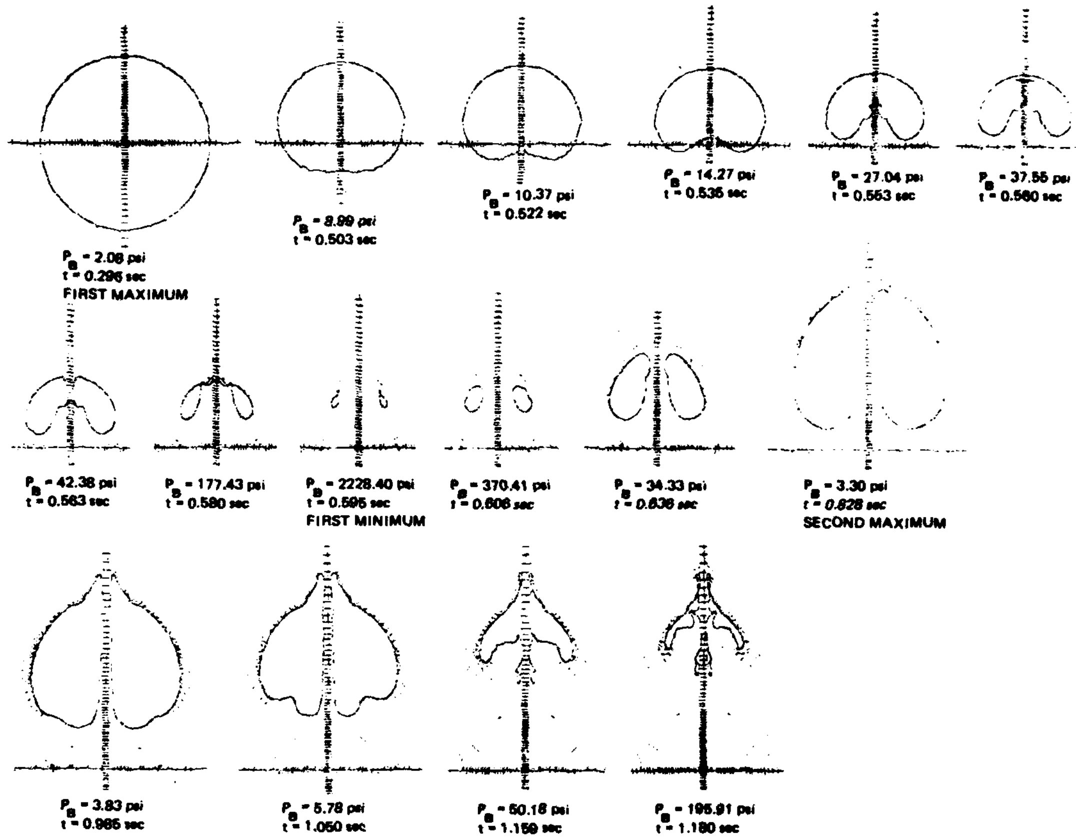

FIG. 8 EXPLOSION BUBBLE RESULTING FROM DETONATION OF A 354 LB. CHARGE OF TNT AT A DEPTH OF 81 FT.

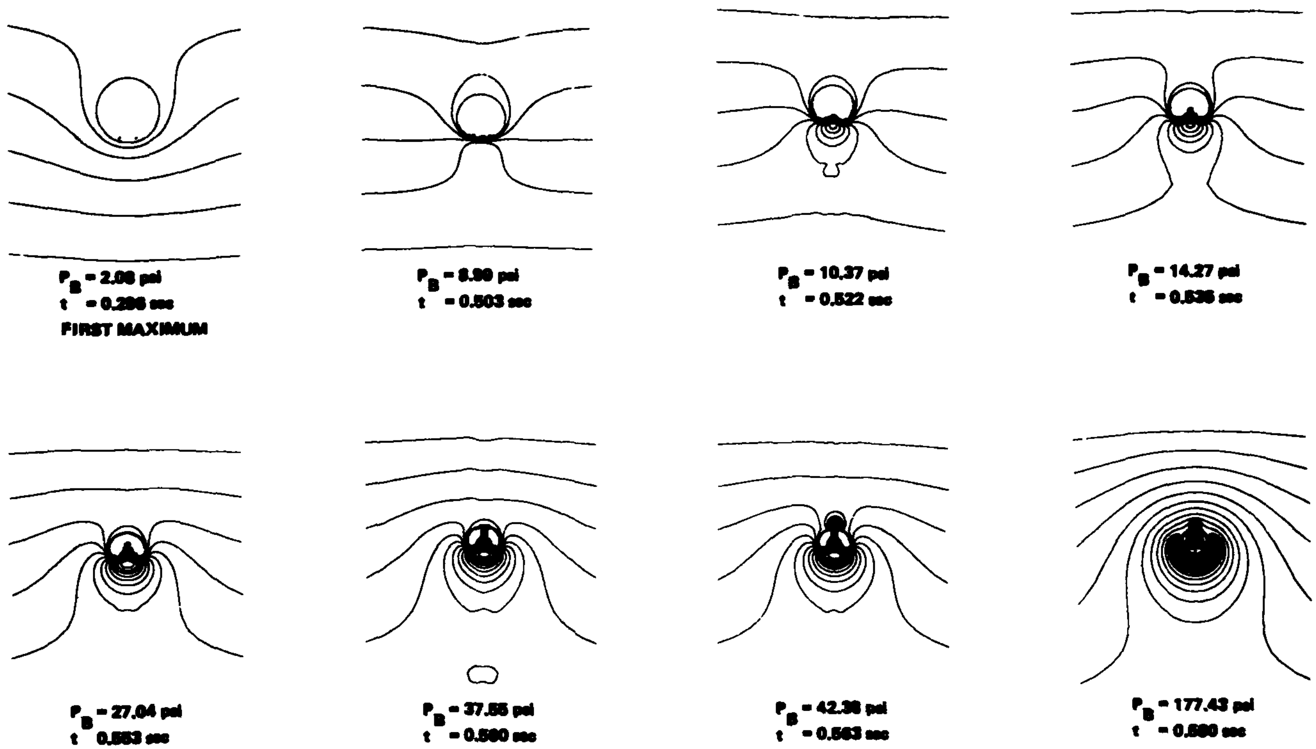

FIG. 9 ISOBARS AT 1 ATM. INTERVALS FROM DETONATION OF A 354 LB. TNT CHARGE AT A DEPTH OF 81 FT.

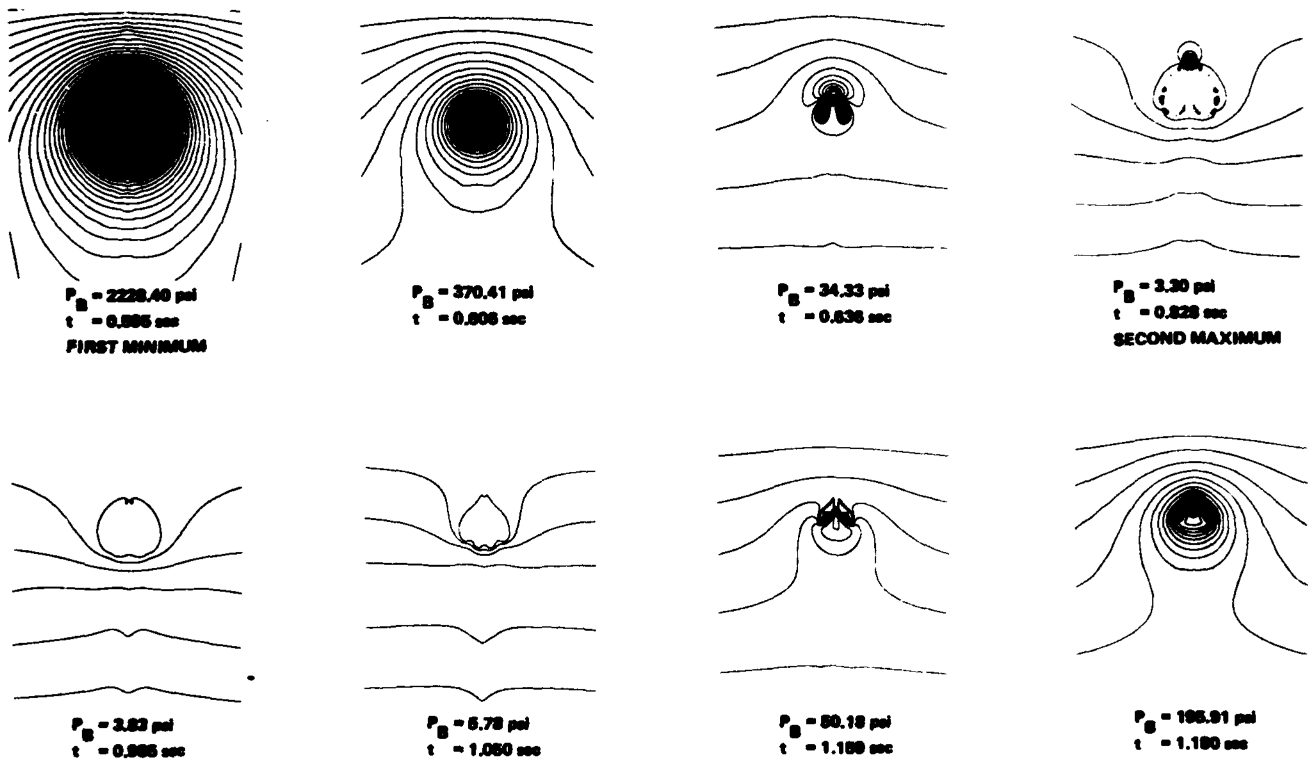

FIG. 9 (CONT'D)
ISOBARS AT 1 ATM. INTERVALS FROM DETONATION OF A 354 LB. TNT CHARGE AT A DEPTH OF 81 FT.

([32], page 423). This toroidal shape appears to be the cause of the plume of debris jetting from the top of the bubble in other photographs of this experiment in [27]. During the second contraction in Figure 8, a secondary ring-shaped jet forms on the lower side of the bubble. Before the second minimum is reached, this secondary jet folds over onto the primary jet, forming a single jet. This phenomenon would be difficult to observe experimentally, although it should be expected for the same reason that a jet is formed during the first contraction. In the present calculation, the bubble would continue to pulsate and migrate until it reaches the surface. We stopped our sample calculation near the second minimum only because the bubble had migrated into a region in which the finite difference mesh was too coarse to resolve the bubble adequately.

Comparison of computational and experimental results is difficult because of several circumstances. First, experimental pressure data for the scaled tests corresponding to our calculations were not taken due to lack of suitable instrumentation. Pressure data are available for some full-scale tests, but for these, no photographs were taken. In addition, due to explosion products and debris the bubble is opaque, and bubble profiles are therefore difficult to interpret. Finally, the experiment shown in Figure 7 was performed under scaled conditions, while the corresponding computations shown in Figures 8 and 9 are for a full-scale charge. Hence, the accuracy of the scaling laws also enters into the comparison. A comparison of the experimental profiles in Figure 7 with the computational profiles in Figure 8 shows an agreement of about 10 percent.

Perhaps a better measure of the accuracy of the calculations is the comparison between the numerical solution of equation (4.1) and the two-dimensional MACBUB solution of the same problem, in which the acceleration due to gravity is set equal to zero. Some time ago, using a less accurate version of the MACBUB code, such a calculation was carried out in the case of a one-dimensional spherical problem corresponding to the detonation of a blasting cap at a depth of 15 feet (Willis [25], page 13). The time and bubble radius at the first maximum agreed with the values obtained from the solution of equation (4.1) to within 10 percent.

2. Bubble Instability

The principal difficulty which we found when we began our calculations was an instability exhibited by the bubble during the contraction phase. This instability became evident immediately following the bubble maximum, when small ripples appeared on the bubble surface. These ripples continued to grow, and in some cases, completely dominated the solution near the bubble minimum. The instability near the maximum is not a manifestation of Taylor instability, since the bubble pressure at the maximum is smaller than the ambient pressure, and the acceleration is radially inward. Furthermore, an increase in the value of the numerical viscosity did not alter the nature of the instability or improve the computation. Birkhoff [33] showed that an instability which is not a Taylor instability also occurs during the collapse of a small vapor bubble.

By computing the flow more accurately near free surfaces, we were able to reduce these disturbances considerably in our sample problem shown in Figure 8. The most significant factor in gaining this accuracy was the addition of the irregular star technique. The introduction of an extrapolation procedure to extend the velocity field from within the fluid instead of requiring zero divergence in partially filled cells was also an important, although less significant, addition to the code.

However, in the calculation of the solution of other bubble problems, we have observed that this instability still persists to a greater extent than in the present example. Two possible areas of future investigation and experimentation in connection with this problem are the use of more accurate or more stable finite difference approximations to the momentum equations, and the use of a more accurate calculation for movement of the particles. As one of the second possibilities, for example, we can use $x_{n+1} = x_n + \frac{1}{2}(u_n + u_{n+1})\,\Delta t$ instead of $x_{n+1} = x_n + u_n\Delta t$ in the calculation of the new particle positions, and similarly for the other coordinates.

Acknowledgments

We would like to thank Ralph Ferguson and Larry Hieb for providing the contour program which was used to generate the isobar plots shown in Figure 8. This work was supported by the Naval Sea Systems Command under Task No. SEA-332-001-AA4-33/SF33-354-315.

REFERENCES

1. F. H. Harlow and J. E. Welch, "Numerical Calculation of Time-Dependent Viscous Incompressible Flow of Fluid with Free Surface," Phys. Fluids 8, 2182 (1965).
2. F. H. Harlow and J. E. Welch, "Numerical Study of Large-Amplitude Free-Surface Motions," Phys. Fluids, 9, 845 (1966).
3. J. E. Welch, F. H. Harlow, J. P. Shannon, and B. J. Daly, "The MAC Method - A Computing Technique for Solving Viscous, Incompressible, Transient Fluid-Flow Problems Involving Free Surfaces," Los Alamos Scientific Laboratory, LA-3425 (Mar. 1966).
4. C. W. Hirt and F. H. Harlow, "A General Corrective Procedure for the Numerical Solution of Initial Value Problems," J. Comp. Phys. 2, 114-119 (1967).
5. J. Pritchett, "MACYL—A Two Dimensional Cylindrical Coordinate Incompressible Hydrodynamic Code," Naval Radiological Defense Laboratory Technical Report USNRDL-TR 67-97 (20 Oct. 1967).
6. J. Pritchett and J. Pestaner, "A Numerical Calculation of the Water Flow Following the WIGWAM Underwater Explosion," Naval Radiological Defense Laboratory Technical Report USNRDL-TR 69-48 (20 May 1969).
7. A. A. Amsden and F. H. Harlow, "The SMAC Method: A Numerical Technique for Calculating Incompressible Fluid Flows," Los Alamos Scientific Laboratory LA-4370 (May 1970); A. A. Amsden and F. H. Harlow, "A Simplified MAC Technique for Incompressible Fluid Flow Calculations," J. Comp. Phys. 6, 322-325 (1970).
8. A. A. Amsden, "Numerical Calculation of Surface Waves: A Modified Zuni Code with Surface Particles and Partial Cells," Los Alamos Scientific Laboratory LA-5146 (May 1973).
9. C. W. Hirt, B. D. Nichols, and N. C. Romero, "SOLA-A Numerical Solution Algorithm for Transient Fluid Flows," Los Alamos Scientific Laboratory LA-5852 (April 1975).
10. R. K. C. Chan and R. L. Street, "A Computer Study of Finite-Amplitude Water Waves," J. Comp. Phys. 6, 68-94 (1970).
11. R. K. C. Chan and R. L. Street, "SUMMAC - A Numerical Model for Wake Wave," Stanford University, Department of Civil Engineering TR-135 (Aug. 1970).
12. C. R. Easton and J. B. Nelson, "The MDAC-WO Version of the Marker-and-Cell Program," McDonnell Douglas Astronautics Company, MDAC-62426 (1969).
13. J. Viecelli, "Test Calculations with the ABMAC Incompressible Hydrodynamic Code," Lawrence Radiation Laboratory UCID-15681 (1970).
14. J. Viecelli, "A Computing Method for Incompressible Flows Bounded by Moving Walls," J. Comp. Phys., 8, 119-143 (1971).
15. K. D. Shere and M. J. Vander Vorst, "Vertical Water Entry of Finite Cones - A Numerical Calculation," Naval Ordnance Laboratory, NOLTR 73-22 (1973).

16. H. M. Sternberg and W. A. Walker, "Calculated Flow and Energy Distribution Following Underwater Detonation of a Pentolite Sphere," Phys. Fluids, 14, 1869-1878 (1971).

17. H. G. Snay, "Underwater Explosion Phenomena: The Parameters of Migrating Bubbles," Naval Ordnance Laboratory NAVORD 4185 (1962).

18. K. W. Morton, "Stability and Convergence in Fluid Flow Problems," Proc. Roy. Soc. Lond. A. 323, 237-253 (1971).

19. C. W. Hirt, "Heuristic Stability Theory for Finite-Difference Equations," J. Comp. Phys., 2, 339-355 (1968).

20. A. J. Chorin, "Numerical Solution of the Navier-Stokes Equations," Math. Comp. 22, 745-762 (1968).

21. C. Weber, private communication, Naval Ordnance Laboratory, White Oak, Silver Spring, Maryland, October 1970.

22. R. S. Varga, Matrix Iterative Analysis, Prentice Hall Inc., 1962.

23. A. E. Berger and M. J. Vander Vorst, "Use of the Finite Element Method Within a Marker and Cell Code for the Solution of the Underwater Explosion Bubble Problem," Naval Surface Weapons Center, White Oak Laboratory NSWC/WOL/TR (to appear).

24. M. J. Vander Vorst and J. C. W. Rogers, "The Partial Cell Marker and Cell Method and the Numerical Calculation of Vertical Water Entry of Finite Cones," Naval Surface Weapons Center, White Oak Laboratory NSWC/WOL/TR 75-172 (to appear).

25. Underwater Explosions Research, A Compendium of British and American Reports, Volume II, The Gas Globe, Office of Naval Research, 1950.

26. H. G. Snay, "Hydrodynamics of Underwater Explosions," Naval Hydrodynamics, NAS-NRC Publication 515, 325-351 (1957).

27. H. G. Snay, J. F. Goertner, and R. S. Price, "Small Scale Experiment to Determine Migration of Explosion Gas Globes," Naval Ordnance Laboratory NAVORD 2280 (1952).

28. T. E. Farley and H. G. Snay, "A Simplified Analysis of the Bubble Jet Pulse," Naval Ordnance Laboratory NOLTR 68-42 (1968).

29. R. H. Cole, Underwater Explosions, Princeton University Press, 1948.

30. R. E. Ferguson and T. A. Orlow, "FNOL3, A Computer Program to Solve Ordinary Differential Equations," Naval Ordnance Laboratory NOLTR 71-2 (1971).

31. H. Snay, private communication, Naval Ordnance Laboratory, White Oak, Silver Spring, Maryland (1970).

32. J. W. Pritchett, "Incompressible Calculations of Underwater Explosion Phenomena," Proceedings of the Second International Conference on Numerical Methods in Fluid Dynamics, Springer, 1971, pp. 422-428.

33. G. Birkhoff, "Note on Taylor Instability," Quarterly of Applied Mathematics, 12, 306-309 (1954).

A LOCALIZED FINITE-ELEMENT METHOD FOR STEADY, TWO-DIMENSIONAL FREE-SURFACE FLOW PROBLEMS

Kwang June Bai*

Department of Ocean Engineering
Massachusetts Institute of Technology
Cambridge, Massachusetts 02139 U.S.A.

ABSTRACT

A numerical method is presented for solving two-dimensional uniform flow problems with a linearized free-surface boundary condition. The boundary-value problem governed by Laplace's equation is replaced by a weak formulation (also known as Galerkin's method) with certain essential boundary conditions. The infinite domain of the fluid is reduced to a finite domain by utilizing known solution spaces in certain subdomains. The bases for the trial and test functions are chosen from the same subspace of the polynomial function space in the reduced subdomain. The essential boundary conditions are properly taken into account by an unconventional choice of the basis for the trial functions, which is different from that for the test functions in other subdomains. This method is tested for the two-dimensional steady flow past a submerged circular section. The method is also applied to the problem of a surface pressure distribution and to a bump on the bottom.

1. Introduction

A uniform flow problem in an inviscid, incompressible fluid with a free surface is described by a boundary-value problem governed by Laplace's equation. In the past, problems of this type were generally solved by distributing sources (and/or dipoles) on the body boundary and using Green's theorem to obtain an integral equation for the strength of these boundary singularities or, alternatively, by using sources and higher order multipole expansions at an interior point within the body, the strength of these singularities being determined so as to satisfy the body boundary condition. In all cases, it is conventional to utilize the

*Present address is David W. Taylor Naval Ship R & D Center, Bethesda, Md. 20084

singularities which are solutions of the boundary-value problem stated above, except that the body boundary condition is invoked separately to determine the singularity distribution. For two- and three-dimensional motions with a fluid of infinite depth, or of finite but constant depth, the required singularities are well-known, although of rather complicated analytical form, so that the approach described above corresponds to solving a Fredholm integral equation over the body surface, with a rather complicated kernel function.

In this paper, a numerical method based on Galerkin's method is introduced as an alternative approach to the solution of the problem. A similar method, which employs variational functionals, has been used for time-harmonic water-wave problems by Bai (1972, 1975), Berkhoff (1972), Bai and Yeung (1974), and by Chen and Mei (1974). The fluid domain is divided into a number of finite elements, and the potential is approximated by a set of polynomial bases for both the trial and the test functions. The known analytic solutions in certain subdomains are also utilized to reduce the size of the fluid domain. We shall call this numerical method a localized finite-element method. Thus, in effect, an integral equation over the body boundary with a complicated kernel is replaced by a system of equations over a much larger fluid domain, but a much simpler kernel.

Previously the finite-element method has been applied only to time-harmonic water-waves problems which can in general be reduced to symmetric matrix equations. For time-harmonic problems, all the boundary conditions are usually taken into account in the functional form, or Galerkin form, as natural boundary conditions. This enables one to choose symmetrical (identical) bases for the trial and test functions for the approximate solution. The major difference between the uniform-flow problems and the time-harmonic problems is that in the uniform-flow case the upstream and downstream conditions are not symmetric. In this paper we will concentrate on establishing the validity of this new finite-element method by comparing results obtained by this method to known results.

Due to the limit on the length of this paper, several steps, particularly in the numerical procedures, are left out. A paper which includes more detail about the procedure and more results is in preparation.

2. Formulation of the Uniform Flow Problem

We consider here steady uniform flow past a fixed two-dimensional body submerged in a fluid or past a specified pressure distribution on a finite segment on the free surface. The coordinate system is right-handed and rectangular. The y-axis is directed oppositely to the force of gravity, and the x-axis coincides with the undisturbed free surface. We neglect surface tension and assume that the fluid is inviscid, incompressible, and that the motions are irrotational.

The steady two-dimensional flow is described by a total velocity potential

$$\Phi(x, y) = Ux + \phi(x, y) \tag{2.1}$$

where ϕ is the perturbation potential, which must satisfy

$$\nabla^2 \phi(x, y) = 0 \tag{2.2}$$

in the fluid domain D shown in Figure 1. It will be assumed that the free-surface disturbances are all small so that the linearized free-surface boundary condition

$$U^2 \phi_{xx} + g\phi_y = \begin{cases} 0 & \text{on } S_F \\ -\frac{U}{\rho} p_x & \text{on } S_p \end{cases} \tag{2.3}$$

can be applied.

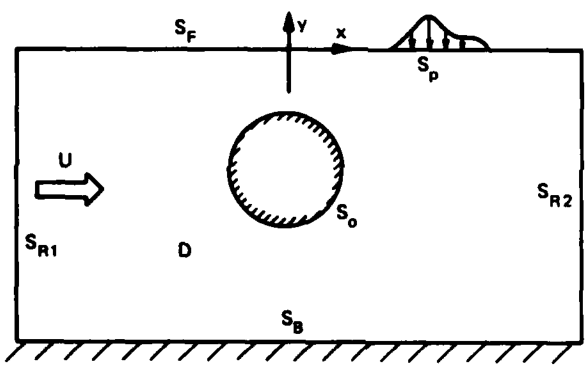

Figure 1 – Configuration of the Boundary Geometry

The body boundary condition is

$$\phi_n = V_n \tag{2.4}$$

to be satisfied on the body surface, S_o. Here the normal velocity V_n is given as

$$V_n = -Un_1 \tag{2.5}$$

where $\vec{n} = (n_1, n_2)$ is outward normal vector. The bottom condition for finite depth, H is

$$\phi_n = 0, \text{ at } y = -H. \tag{2.6}$$

As the radiation condition we require that no disturbances exist far upstream, i.e.,

$$\lim_{x \to -\infty} |\nabla \phi| = 0 \tag{2.7}$$

and that the potential ϕ is bounded far downstream

$$\lim_{x \to +\infty} \phi < \infty \tag{2.8}$$

The solution of equations (2.2) through (2.8) is unique to within an arbitrary additive constant. To eliminate the abritrary constant in the solution, we require a Dirichlet-type boundary condition at any one point in the fluid domain or on its boundary. For this purpose, we simply require, without loss of generality

$$\phi(x, y)\big|_{\substack{x=0\\y=0}} = 0. \tag{2.9}$$

Now the solution of equations (2.2) through (2.9) can be determined uniquely. It is of interest to note that in the analytical approach, the upstream condition is given as

$$\lim_{x \to -\infty} \phi = 0. \tag{2.10}$$

which replaces (2.7) and (2.9). In the present numerical scheme, these equivalent upstream conditions were tested. The results were the same in both cases except for an additive constant.

3. Localized Finite Element Method

When we reduce our problem to an operational form by introducing finite elements in the fluid domain, we obtain a set of linear algebraic equations. The size of the matrix equation is mainly dependent on the size of the fluid domain. In order to reduce the fluid domain where the finite-element method is applied, the known solution space will be used in certain subdomains, which will be defined later, and an appropriate condition will be specified along the interface between adjacent subdomains. This modification has been applied to the steady-oscillatory water-wave problem by Bai and Yeung (1974) and Chen and Mei (1974). The same procedure is applied here to the uniform flow problem.

Let us draw two imaginary lines J_1 and J_2 which separate the fluid into the three regions: D_o, D_1, and D_2, shown in Figure 2. We assume that D_o includes the submerged body or the pressure distribution on the free surface S_p. The boundaries of D_o, D_1, and D_2 are denoted respectively by

$$\begin{aligned} \partial D_o &= S_F + S_p + J_1 + J_2 + S_B + S_o \\ \partial D_i &= S_{Fi} + S_{Ri} + S_{Bi} + J_i, \; i = 1, 2. \end{aligned} \tag{3.1}$$

In Figure 2, the points $p_1(x_1, 0)$, $p_2(x_2, 0)$, $p_3(x_3, 0)$, and $p_4(x_4, 0)$ are, respectively, the intersection points of J_1, S_{R1}, J_2, and S_{R2} with the free surface.

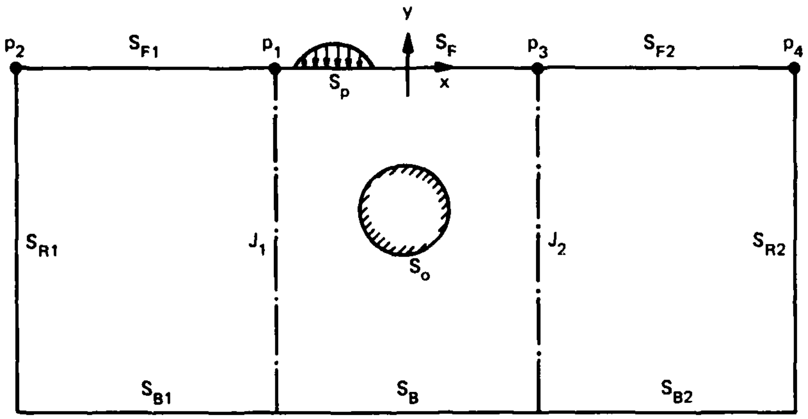

Figure 2 – Boundary Configuration of the Three Subdomains

Let ϕ_o, ϕ_1 and ϕ_2 denote the perturbation potentials defined in the subdomains D_o, D_1, and D_2 and on the boundaries, ∂D_o, ∂D_1, and ∂D_2, respectively. Then we have, from equations (2.2) through (2.9), that ϕ_o must satisfy

$$\begin{aligned}
&\nabla^2 \phi_o = 0 && \text{in } D_o \\
&\phi_{oy} = \begin{cases} -\dfrac{U^2}{g}\phi_{oxx} & \text{on } S_F \\ -\dfrac{U^2}{g}\phi_{oxx} - \dfrac{U}{\rho g}p_x, & \text{on } S_p \end{cases} \\
&\phi_{on} = 0 && \text{on } S_B \\
&\phi_{on} = -Un_1 && \text{on } S_o \\
&\phi_o(0,0) = 0
\end{aligned} \tag{3.2}$$

and that ϕ_i, i = 1, 2, must satisfy

$$\begin{aligned}
&\nabla^2 \phi_i = 0 \\
&\phi_{iy} = -\frac{U^2}{g}\phi_{ixx} && \text{on } S_{Fi} \\
&\phi_{in} = 0 && \text{on } S_{Bi}
\end{aligned} \tag{3.3}$$

with the upstream condition

$$\lim_{x \to -\infty} |\nabla \phi_1| = 0$$

and with the downstream condition

$$\lim_{x \to +\infty} \phi < \infty .$$

In addition, we have the matching conditions

$$\phi_o = \phi_i \text{ and } \phi_{on} + \phi_{in} = 0, \text{ on } J_i, \ i = 1,2 \tag{3.4}$$

where the normal vector n is taken outwards from the fluid region, i.e.,

$$\begin{aligned} \phi_{1n} &= \phi_{1x}, \quad \phi_{on} = -\phi_{ox} \quad \text{on } J_1 \\ \phi_{2n} &= -\phi_{2x}, \quad \phi_{on} = \phi_{ox} \quad \text{on } J_2 \end{aligned} \tag{3.5}$$

It is easy to show, by use of Green's theorem, that the solutions, ϕ_o, ϕ_1, and ϕ_2 of the above coupled problems (3.2) through (3.4) are identical in each corresponding subdomain to the solution ϕ of (2.2) through (2.9).

As the basis of the present numerical procedure, Galerkin's method will be used. One important step in this procedure is the introduction of the weak formulation. The three coupled functionals will be defined later. From these functional equations a set of linear algebraic equations will be obtained. More details on this procedure will appear in a future paper. We will consider (3.2) through (3.4) by using the following weak form (Strang and Fix, 1973):

$$\iint_{D_i} (\nabla^2 \phi_i)\, \psi_i \, dxdy = 0, \ (i = 0,1,2) \tag{3.6}$$

for all ψ_i in some test space. Integrating by parts, (3.6) reduces to

$$\iint_{D_o} \nabla\phi_o \, \nabla\psi_o \, dxdy - \oint_{\partial D_o} \phi_{on}\, \psi_o \, dS = 0, \text{ for all } \psi_o, \tag{3.7}$$

$$\oint_{\partial D_i} (\psi_i \phi_{in} - \psi_{in} \phi_i)\, dS = 0, \tag{3.8}$$

for all ψ_i, i = 1, 2. Here ϕ_i, ψ_i, i = 1, 2, are solutions of Laplace's equation.

Let $\overline{\phi}_o$, $\overline{\phi}_1$, and $\overline{\phi}_2$ denote the trial functions in the subspace of the solution space in the subdomains D_o, D_1, and D_2, respectively and let $\overline{\psi}_o$, $\overline{\psi}_1$ and $\overline{\psi}_2$ denote the test functions in the subspace of the test space in D_o, D_1, and D_2, respectively. We define the functionals F_o, F_1, and F_2 in D_o, D_1, and D_2, respectively, as follows

$$F_o\left\{\bar{\phi}_o, \bar{\phi}_1, \bar{\phi}_2 ; \bar{\psi}_o\right\} = \iint_{D_o} \nabla\bar{\phi}_o \nabla\bar{\psi}_o \, dxdy - \frac{U^2}{g}\int_{S_F+S_p} \bar{\phi}_{ox} \bar{\psi}_{ox} \, dS + \frac{U}{\rho g}\int_{S_p} p_x \bar{\psi}_o \, dS$$

$$+ U\int_{S_o} n_1 \bar{\psi}_o \, dS + \int_{J_1} \bar{\phi}_{1x} \bar{\psi}_o \, dS - \frac{U^2}{g}\left[\bar{\phi}_{1x} \bar{\psi}_o\right]_{P_1} \tag{3.9}$$

$$- \int_{J_2} \bar{\phi}_{2x} \bar{\psi}_o \, dS + \frac{U^2}{g}\left[\bar{\phi}_{2x} \bar{\psi}_o\right]_{P_3}$$

$$F_1\left\{\bar{\phi}_1, \bar{\phi}_o ; \bar{\psi}_1\right\} = \int_{J_1} \bar{\phi}_{1x} \bar{\psi}_1 \, dS - \frac{U^2}{g}\left[\bar{\phi}_{1x} \bar{\psi}_1\right]_{P_1} + \frac{U^2}{g}\left[\bar{\phi}_{1x} \bar{\psi}_1 - \bar{\psi}_{1x} \bar{\phi}_1\right]_{P_2}$$

$$- \int_{S_{R1}} (\bar{\phi}_{1x} \bar{\psi}_1 - \bar{\psi}_{1x} \bar{\phi}_1) \, dS + \frac{U^2}{g}\left[\bar{\phi}_o \bar{\psi}_{1x}\right]_{P_1} - \int_{J_1} \bar{\phi}_o \bar{\psi}_{1x} \, dS \tag{3.10}$$

$$F_2\left\{\bar{\phi}_2, \bar{\phi}_o ; \bar{\psi}_2\right\} = - \int_{J_2} \bar{\phi}_{2x} \bar{\psi}_2 \, dS + \frac{U^2}{g}\left[\bar{\phi}_{2x} \bar{\psi}_2\right]_{P_3} + \int_{S_{R2}} (\bar{\phi}_{2x} \bar{\psi}_2 - \bar{\psi}_{2x} \bar{\phi}_2) \, dS$$

$$- \frac{U^2}{g}\left[\bar{\phi}_{2x} \bar{\psi}_2 - \bar{\psi}_{2x} \bar{\phi}_2\right]_{P_4} - \frac{U^2}{g}\left[\bar{\phi}_o \bar{\psi}_{2x}\right]_{P_3} + \int_{J_2} \bar{\phi}_o \bar{\psi}_{2x} \, dS \tag{3.11}$$

Finally we obtain the following functional equations with certain essential boundary conditions:

$$F_o\left\{\bar{\phi}_o, \bar{\phi}_1, \bar{\phi}_2 ; \bar{\psi}_o\right\} = 0 , \quad \text{for all } \bar{\psi}_o \tag{3.12}$$

with the condition $\bar{\phi}_o(0,0) = 0$

$$F_1\left\{\bar{\phi}_1, \bar{\phi}_o ; \bar{\psi}_1\right\} = 0 , \quad \text{for all } \bar{\psi}_1 \tag{3.13}$$

with the condition $\lim_{x \to -\infty} |\nabla\bar{\phi}_1| = 0$, and

$$F_2\left\{\bar{\phi}_2, \bar{\phi}_o ; \bar{\psi}_2\right\} = 0 , \quad \text{for all } \bar{\psi}_2 \tag{3.14}$$

with the condition that $\bar{\phi}_2$ is bounded as $x \to \infty$.

In the coupled functional equations (3.12) through (3.14), all the boundary conditions are properly taken into account as natural boundary conditions except the essential conditions specified in the above functional equations. The essential conditions play the role

of an additional condition to the functional equations given in (3.12) through (3.14) and have to be properly taken into account in constructing the trial functions.

In the localized finite-element region D_o, the basis for the trial and test functions are chosen from a polynomial basis. Specifically, 8-node isoparametric quadrilateral elements were used in the present numerical procedures. We will omit the description of this procedure and of the computation of (3.9). One can find this in Bai (1972, 1975).

As mentioned earlier, the trial and test functions in D_1 and D_2 will be chosen from a subspace of the solution space which satisfies the Laplace equation with the free-surface condition and the bottom condition. The eigenfunctions or the Green functions of the above problem can represent the solution space. We will choose the eigenfunction space in this paper for its simplicity. F_1 and F_2 can be given in simple analytic forms except for the integrals along the juncture boundaries, i.e., J_1 and J_2. Therefore, the integral expressions for the functionals are involved only with subdomain D_o, which we shall call the localized-finite-element domain. If one takes the localized finite-element domain to be small, then the domain over which the integrals have to be computed will also be small. On the other hand, one has to take many terms (eigenfunctions) to represent the trial and test functions for $\overline{\phi}_1$ and $\overline{\psi}_1$ or $\overline{\phi}_2$ and $\overline{\psi}_2$ in the computation of the approximate solutions, and vice versa.

The coupled Galerkin equations (3.12) through (3.14) go into operational form in the following way. Let $q_{i1}, \cdots, q_{iM_i}$, $(i = 0, 1, 2)$ be the basis for the M_i-dimensional subspace of the solution space and let

$$\psi_{i1}, \psi_{i2}, \cdots, \psi_{iN_i}, (i = 0, 1, 2)$$

be the basis for the N_i-dimensional subspace of the test space defined in the subdomains D_i, $i = 0, 1, 2$. Then the solution is assumed to be

$$\overline{\phi}_i = \sum_{j=1}^{M_i} \varphi_{ij}\, q_{ij} \quad \text{in } D_i, \quad i = 0, 1, 2. \tag{3.15}$$

where φ_{ij} are coefficients to be determined. By substituting (3.15), the coupled functional equations, (3.12) through (3.14), finally reduce to the following sets of linear algebraic equations:

$$\begin{aligned} &\sum_{j=1}^{M_o} \varphi_{oj}\, F_o\left\{q_{oj}, 0, 0; \psi_{ok}\right\} + \sum_{j=1}^{M_1} \varphi_{1j}\, F_o\left\{0, q_{1j}, 0; \psi_{ok}\right\} \\ &+ \sum_{j=1}^{M_2} \varphi_{2j}\, F_o\left\{0, 0, q_{2j}; \psi_{ok}\right\} = 0, \; (k = 1, \cdots, N_o) \end{aligned} \tag{3.16}$$

with the condition $\bar{\phi}(0,0) = 0$.

$$\sum_{j=1}^{M_1} \varphi_{1j} F_1 \left\{q_{1j}, 0; \psi_{1k}\right\} + \sum_{j=1}^{M_o} \varphi_{oj} F_1 \left\{0, q_{oj}; \psi_{1k}\right\} = 0, \ (k = 1, \cdots, N_1) \quad (3.17)$$

with the condition $\lim_{x \to -\infty} |\nabla q_{1j}| = 0$ for all j

$$\sum_{j=1}^{M_2} \varphi_{2j} F_2 \left\{q_{2j}, 0; \psi_{2k}\right\} + \sum_{j=1}^{M_o} \varphi_{oj} F_2 \left\{0, q_{oj}; \psi_{2k}\right\} = 0, \ (k = 1, \cdots, N_2) \quad (3.18)$$

with the condition $\lim_{x \to \infty} |q_{2j}| < \infty$ for all j. It should be noted that the last two expressions in (3.16) and the second term in (3.17) and (3.18) are the coupling terms due to the matching conditions along J_1 and J_2.

The eigenfunctions which satisfy the Laplace's equation with the free-surface and bottom conditions, are given for subcritical flow as

$$\left\{x,\ 1,\ \cos m_o x \frac{\cosh m_o(y+H)}{\cosh m_o H},\ \sin m_o x \frac{\cosh m_o(y+H)}{\cosh m_o H},\ e^{\pm m_1 x} \cos m_1(y+H), \cdots\right\} \quad (3.19)$$

where

$$\frac{U^2}{g} m_o = \tanh m_o H \quad (3.20)$$

$$\frac{U^2}{g} m_i = \tan m_i H, \quad i = 1, 2, \quad (3.21)$$

From the complete set of eigenfunctions, the basis for the trial functions is chosen so that all the trial functions satisfy the essential boundary conditions. In the choice of the basis for the test functions, we eliminate the terms which result in a trivial zero row vector, a row vector linearly related to another row vector, or an unbounded integral.

The bases are chosen as

$$\left\{q_{21}, \cdots, q_{2M_2}\right\} = \left\{1,\ \cos m_o x \frac{\cosh m_o(y+H)}{\cosh m_o H},\ \sin m_o x \frac{\cosh m_o(y+H)}{\cosh m_o H},\right.$$
$$\left. e^{-m_1 x} \cos m_1(y+H), \cdots, e^{-M_L x} \cos m_L(y+H)\right\} \quad (3.22)$$

with $M_2 = L + 3$,

$$\left\{\psi_{21}, \cdots, \psi_{2N_2}\right\} = \left\{x, \sin m_o x \frac{\cosh m_o(y+H)}{\cosh m_o H}, e^{-m_1 x} \cos m_1(y+H), \right.$$
$$\left. \cdots, e^{-m_L x} \cos m_L(y+H)\right\} \tag{3.23}$$

with $N_2 = L + 2$,

$$\left\{q_{11}, \cdots, q_{1M_1}\right\} = \left\{1, e^{m_1 x} \cos m_1(y+H), \cdots, e^{m_L x} \cos m_L(y+H)\right\} \tag{3.24}$$

with $M_1 = L + 1$, and

$$\left\{\psi_{11}, \cdots, \psi_{1N_1}\right\} = \left\{x, \sin m_o x \frac{\cosh m_o(y+H)}{\cosh m_o H}, e^{m_1 x} \cos m_1(y+H), \right.$$
$$\left. \cdots, e^{m_L x} \cos m_L(y+H)\right\} \tag{3.25}$$

with $N_1 = L + 2$. Here the integer index L of m_L in (3.22) and (3.23) is not necessarily the same as that in (3.24) and (3.25). In a similar procedure the bases for the trial and test functions for supercritical flow are obtained. Once the bases for the trial and test functions are constructed, then the computations of (3.16), (3.17), and (3.18) are straightforward.

Finally, the essential condition in (3.16) is treated simply by substituting the nodal value of zero for $\bar{\phi}(0,0)$ in the solution vector, since we require the potential ϕ at (0, 0) to be zero in equation (2.9). After assembling all the equations obtained from (3.16) through (3.18), we have to solve $(M_o + M_1 + M_2)$ linear algebraic equations. Unfortunately, the final coefficient matrix is not symmetric because of the non-symmetry of the infinity conditions. However, the matrix does have the desirable property of being banded, if the nodes are properly numbered.

4. Results and Discussions

After the velocity potential has been obtained, the pressure can be computed by Bernoulli's equation

$$p = -\rho U \phi_x - \frac{1}{2}(\phi_x^2 + \phi_y^2) \tag{4.1}$$

where the static pressure has been neglected. The free-surface elevation η is given by

$$\eta(x) = -\frac{U}{g} \phi_x(x, o) \tag{4.2}$$

and the far downstream elevation is

$$\lim_{x \to \infty} \eta(x) = \eta_0 \sin(m_0 x + \theta) \tag{4.3}$$

where θ is a phase angle, m_0 is the wave number defined by (3.20) and η_0 is the asymptotic wave amplitude which can be expressed by (3.15) and (3.22) as

$$\eta_0 = \frac{Um_0}{g} (\varphi_{22}^2 + \varphi_{23}^2)^{1/2} \tag{4.4}$$

The force and moment acting on a submerged body S_0 are, respectively,

$$\vec{F} = \int_{S_0} p\vec{n}\, dS \tag{4.5}$$

$$\vec{M} = \int_{S_0} p(\vec{r} \times \vec{n})\, dS \tag{4.6}$$

$\vec{F} = (X, Y)$; $\vec{r} = (x, y)$ is the position vector; and $\vec{n} = (n_1, n_2)$ is the normal vector into the body. The resistance X can also be expressed in terms of wave amplitude η_0 as

$$X = \frac{1}{4} \rho g \eta_0^2 \left(1 - \frac{2m_0 H}{\sinh 2m_0 H}\right) \tag{4.7}$$

where m_0 is defined by (3.20).

It is of interest to note that for finite depth water the mean potentials far upstream and far downstream are different. This mean-potential jump between the two infinities defines the so-called blockage parameter which is discussed by Newman (1969) in connection with channel flow. The potential jump is defined by the difference in the two constants at both infinities

$$C = \varphi_{21} - \varphi_{11} \tag{4.8}$$

where φ_{21} and φ_{11} are defined in (3.15).

In presenting the results, we will make use of the depth Froude number defined as

$$F_H = \frac{U}{\sqrt{gH}} \tag{4.9}$$

and the submergence Froude number defined as

$$F_h = \frac{U}{\sqrt{gh}} \tag{4.10}$$

In the following three subsections, three specific types of disturbances are considered.

4.1 Submerged Body

A submerged cylinder with a circular cross section will be used to test the present numerical method since there exist several other solutions for this simple geometry. Let a circular section of radius a be submerged at a depth h below the free surface in water of finite depth H as shown in Figure 3.

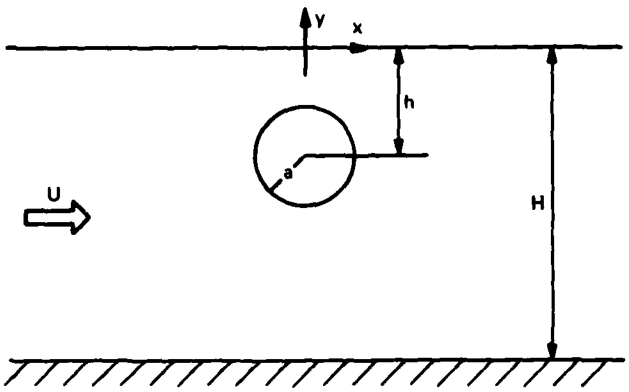

Figure 3 – A Submerged Circular Section

The wave resistance and lift force are computed for $h/a = 2$ and for a large depth, $H = 20h$ in such a range of Froude numbers that the effect of the finite depth is negligible. Havelock (1938) considered this problem for infinite depth with a linearized free surface condition and presented two sets of results: One, obtained by satisfying an approximate body boundary condition; the other, satisfying the exact body boundary condition. In Figure 4 our results are compared with those of Havelock and they agree well with his exact body-boundary-condition results.

Computations were also made for the finite-depth case of $h/a = 2$, $H/h = 5$, for both sub- and super-critical Froude numbers. The potential and the free-surface elevation are shown in Figure 5 and 6 for depth Froude numbers 0.8 and 1.2, respectively. The wave resistance and lift force are shown in Figure 7. The result of Haskind (1945) shown in Figure 7 was obtained by using a first-order approximation to the body boundary condition, while our numerical results satisfy the body boundary condition exactly. The relative wave resistance show the same general trend as the two wave resistances of Havelock shown in Figure 4. The lift force shown in Figure 7 becomes negative at around $F_H = 0.37$ and its magnitude increases monotonically as F_H increases with a discontinuity occurring at the critical Froude number of unity.

The mean potential jump is shown in Figure 8. The magnitude of the blockage parameter C increases indefinitely as the Froude number approaches unity whereas $C(1 - F_H^2)/UH$ stays nearly constant for all Froude numbers with a slight discontinuity at the critical Froude number.

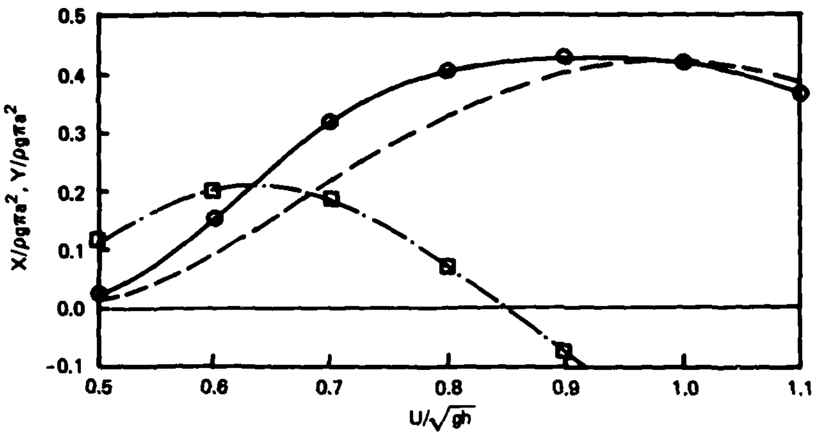

Figure 4 – Comparisons of the Wave Resistance and Lift Force with the Results of Havelock

——— resistance with exact body condition
— — — resistance with approximate body condition
—·— lift force with exact body condition, all by Havelock
O resistance □ lift force by the present method

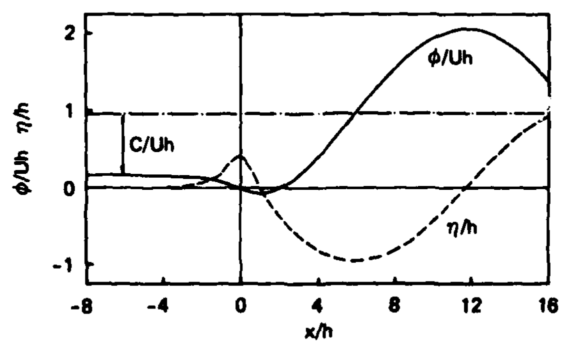

Figure 5 – Potential and Wave Elevation on the Free Surface for a Submerged Circular Section
$U/\sqrt{gH} = 0.8$, $H/h = 5$, $h/a = 2$

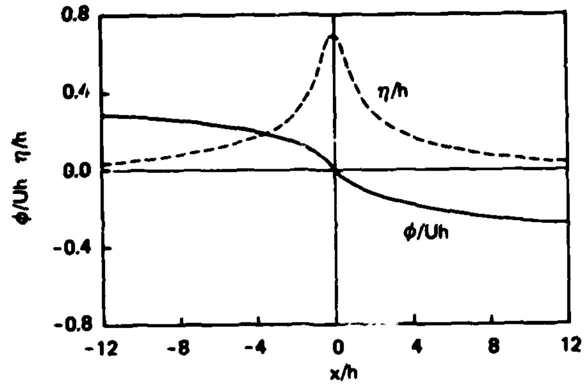

Figure 6 – Potential and Wave Elevation on the Free Surface for a Submerged Circular Section
U/gH = 1.2, H/h = 5, h/a = 2

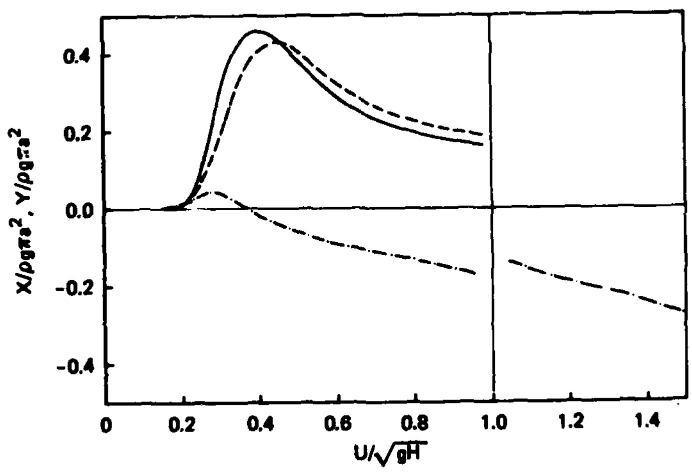

Figure 7 – Wave Resistance and Lift Force of a Circular Section in Water of Finite Depth
H/h = 5, and h/a = 2
——— present method
– – – Haskind, both are $X/\rho g \pi a^2$
—·— $Y/\rho g \pi a^2$, present method

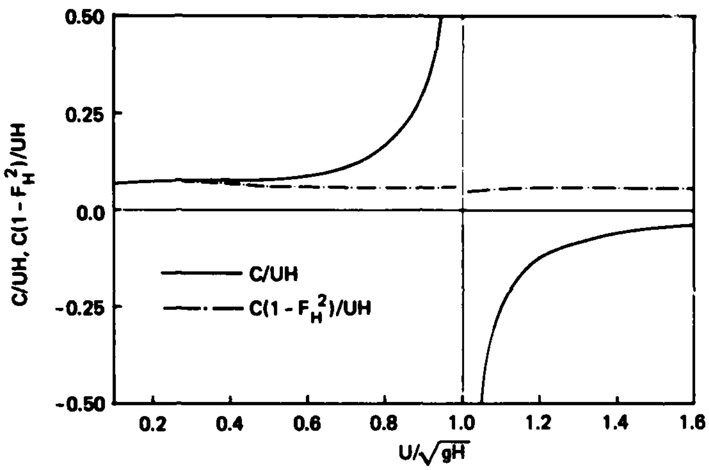

Figure 8 – Blockage Parameter of a Circular Section

4.2 Bottom Obstruction

A sinusoidal bump on the bottom as shown in Figure 9 is considered. The bottom shape is given by

$$y = \begin{cases} -H + \frac{h}{2}\left(1 + \cos\frac{\pi x}{a}\right), & \text{for } |x| \leq a \\ -H & , \text{for } |x| > a \end{cases} \tag{4.11}$$

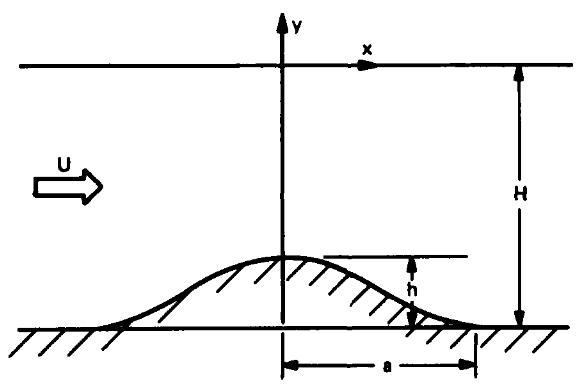

Figure 9 – Bottom Geometry

Computations were made for h/a = 0.05 and a/H = 1. The computed potential and free-surface elevation are shown in Figures 10 and 11, respectively, for F_H = 0.6 and 1.2 and the potential jumps are well illustrated in these figures.

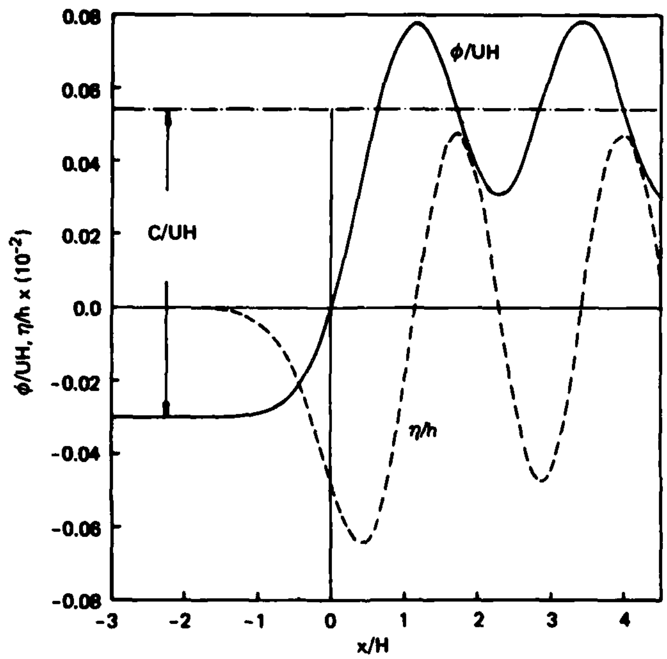

Figure 10 – Potential and Wave Profile on the Free Surface
h/a = 0.05, a/H = 1, F_H = 0.6

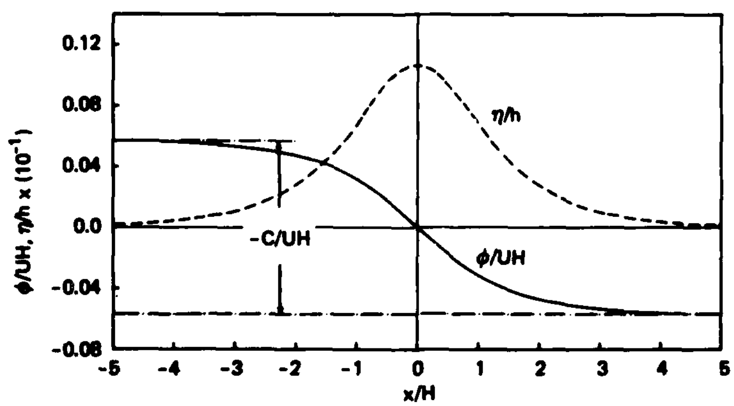

Figure 11 – Potential and Wave Profile on the Free Surface
F_H = 1.2, h/a = 0.05, a/H = 1

In order to test the present numerical method, computations were also made with a linearized body boundary condition since the analytical solution for the asymptotic wave amplitude η_0 can be obtained easily by using the far downstream wave term in the Green function given in Wehausen and Laitone (1960, p. 490). The analytical solution can be expressed as

$$\eta_0 = \frac{2\pi\nu h U^2 \sin m_0 a \cosh m_0 H}{g(\pi^2 - a^2 m_0^2)(\nu H - \cosh^2 m_0 H)} \tag{4.12}$$

where $\nu = \frac{g}{U^2}$ and m_0 is as defined earlier.

It is of interest to note that the wave amplitude becomes zero for $m_0 a = n\pi$, $n = 2, 3, \ldots$ The wave amplitude η_0 and wave resistance X obtained by the present numerical method are compared in Figure 12 with the analytical solutions. Our results agree with the analytical solution within three significant digits. It is of interest to remark that $C(1 - F_H^2)/UH = 0.05$ for all Froude numbers. This shows that $C(1 - F_H^2)/UH$ is constant for all Froude numbers when the disturbance is given only on the bottom, $y = -H$, or $y = 0$. We will show an example of the latter case in the next subsection.

4.3 Pressure Distribution on the Free Surface

In this example, the pressure on the free surface is given by

$$p(x) = \begin{cases} \frac{p_0}{2}\left(1 + \cos\frac{\pi x}{a}\right), & \text{for } |x| \leq a \\ 0, & \text{for } |x| > a \end{cases} \tag{4.13}$$

Figures 13 and 14 show the computed potential and wave elevation on the free surface, together with the potential jump, for $\frac{\pi p_0}{2\rho g a} = 1$, $\frac{a}{H} = 1$, at Froude numbers $F_H = 0.6$ and 1.2, respectively.

For this pressure problem one can readily obtain an analytical solution for the asymptotic wave amplitude by using Green's function. The analytical solution of η_0 for the pressure distribution given by (4.13) can be expressed as

$$\eta_0 = \frac{2\pi^2 \nu U^2 p_0 \sin m_0 a \cosh^2 m_0 H}{\rho g^2 (\pi^2 - a^2 m_0^2)(\nu H - \cosh^2 m_0 H)} \tag{4.14}$$

where ν and m_0 are as defined earlier. Computations were made for $a/H = 0.25$ and $\frac{\pi p_0}{2\rho g a} = 1$ and the numerical and the analytical results are compared in Figure 15. Our numerical results were identical to the analytical solution to within three significant figures.

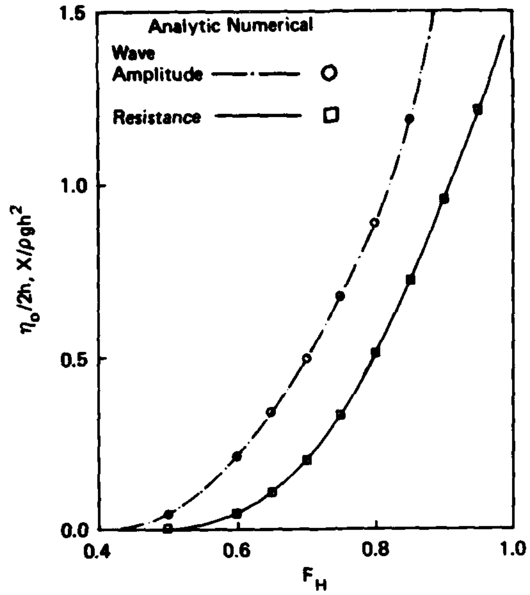

Figure 12 – Wave Amplitude and Resistance with the Linearized Body Boundary Condition
h/a = 0.05, a/H = 1

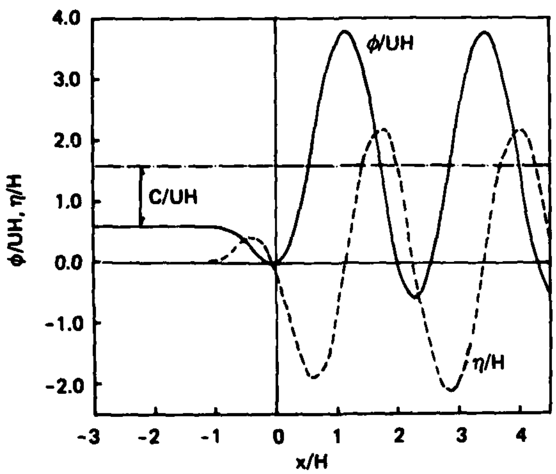

Figure 13 – Potential and Wave Profile on the Free Surface
F_H = 0.6, a/H = 1, $\pi p_o/2\rho g a$ = 1

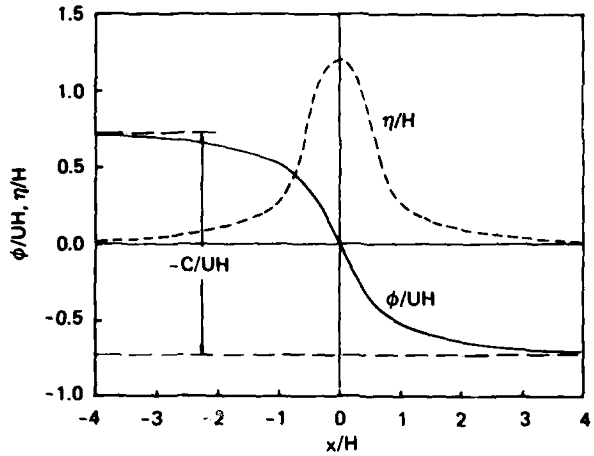

Figure 14 – Potential and Wave Profile on the Free Surface
$\pi p_o/2\rho ga = 1,\ a/H = 1,\ F_H = 1.2$

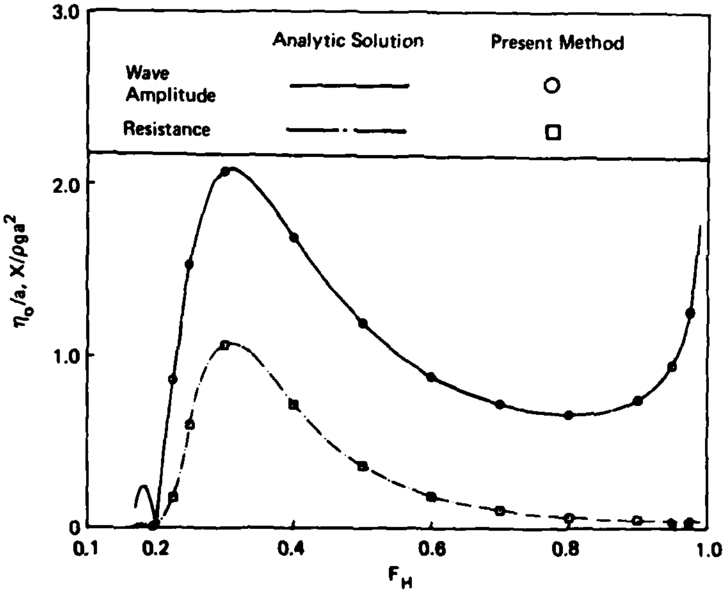

Figure 15 – Wave Amplitude and Resistance for the Pressure Distribution on the Free Surface
$\pi p_o/2\rho ga = 1$

As mentioned at the end of the previous subsection, the potential jump $C(1 - F_H^2)/UH$ was 0.039977 over the entire range of Froude numbers, for both sub- or super-critical flows. However, when a body is present, $C(1 - F_H^2)/UH$ is no longer a constant independent of Froude numbers. The value is in general a function of Froude number with a discontinuity at the critical Froude number. It is of interest to note that when the flow is supercritical the wave profiles are symmetric with respect to the y-axis for each of the three disturbances discussed.

5. Concluding Remarks

In the previous section the numerical results for several problems were shown to agree well with known analytical solutions. The main advantage of the present method is that any complex body (or bodies) geometry can be easily accommodated with a reasonable computation time. In all the problems treated here, for example, on an IBM 370 computer for each Froude number, the central processor unit time was between 0.5 and 6.0 seconds depending on the specific problem.

The present method can be extended to the wave-resistance problem for a general three-dimensional body in restricted water if it is assumed that the cross section of the canal is uniform. The complete set of eigenfunctions can then be easily obtained. This method can also be extended to solve the problem of two-dimensional uniform flow past a step (i.e., both infinities have different constant depths) and the problem of a body oscillating in a uniform stream. Finally, the method may be used to obtain non-linear effects by formulating the problem in terms of a higher-order perturbation scheme.

6. Acknowledgments

The author is grateful to Professor J.N. Newman for suggesting this topic and to Mr. Yoonho Kim for his assistance. He owes thanks to Professor C.C. Mei and Dr. H.S. Chen for useful discussions.

This research was supported by the David W. Taylor Naval Ship Research and Development Center, Contract N00014-67-A-0204-0081, by the Office of Naval Research, Contract N00014-67-A-0204-0023, NR 062-411, and by the National Science Foundation, Grant GK 43886X. This research was also supported partially by the Numerical Naval Hydrodynamics Program at the David W. Taylor Naval Ship Research and Development Center.

References

Bai, K.J., 1972, "**A Variational Method in Potential Flows with a Free Surface,**" PhD. Dissertation, Department of Naval Architecture, University of California, Berkeley.

Bai, K.J., 1975, "**Diffraction of Oblique Waves by an Infinite Cylinder,**" Journal of Fluid Mechanics, 68, 513-535.

Bai, K.J. and Yeung, R.W., 1974, "**Numerical Solutions to Free-Surface Flow Problems,**" The Tenth Symposium on Naval Hydrodynamics, Office of Naval Research, held at Massachusetts Institute of Technology.

Berkhoff, J.C.W., 1972, "**Computation of Combined Refraction-Diffraction,**" Proc. 13th Coastal Eng. Conference, 2, ASCE, 471-490.

Chen, H.S. and Mei, C.C., "**Oscillations and Wave Forces in a Man-Made Harbor in the Open Sea,**" The Tenth Symposium on Naval Hydrodynamics, Office of Naval Research, held at Massachusetts Institute of Technology.

Haskind, M.D., 1945, "**Translational Motion of Bodies under the Free Surface of a Heavy Fluid of Finite Depth,**" Translation (1952), NACA TM 1345, pp. 20.

Havelock, T.H., F.R.S., 1938, "**The Forces on a Circular Cylinder Submerged in a Uniform Stream,**" The Collected Papers of Sir Thomas Havelock on Hydrodynamics, Office of Naval Research, Department of the Navy, ONR/ACR-103.

Newman, J.N., 1969, "**Lateral Motion of Slender Body Between Two Parallel Walls,**" Journal of Fluid Mechanics, 39, pp. 97-115.

Strang, G. and Fix, G., "**An Analysis of the Finite Element Method,**" Prentice-Hall, 1973, pp. 360.

Wehausen, J.V. and Laitone, E.V., "**Surface Waves,**" Handbuch der Physik, 9, pp. 446-778, Springer-Verlag, Berlin, 1960.

A COMPARISON OF NUMERICAL METHODS FOR SOLVING WAVE EQUATIONS

Vassilios A. Dougalis and Garrett Birkhoff
Mathematics Department, Harvard University
Cambridge, Massachusetts 02138 U.S.A.

ABSTRACT

Many numerical methods have been proposed in the literature for solving linear and nonlinear wave equations. Analytical and numerical comparisons are given below of some of the most attractive methods for solving linear, constant-coefficient wave equations in one and two dimensions. Thus, comparisons are made between two-step schemes for solving second-order equations and one-step schemes for solving first-order systems, and between difference and finite element methods. Finally, a brief discussion is given of methods for solving numerically the initial value problem for "plane waves of finite amplitude."

1. Introduction

A basic problem of numerical fluid mechanics is to develop good computer programs for solving initial value problems involving the linear, constant-coefficient wave equation

$$(1.1)\quad u_{tt} = c^2\nabla^2 u, \qquad \nabla^2 u = \sum_{k=1}^{m} \partial^2 u/\partial {x_k}^2 ,$$

and its nonlinear and variable coefficient analogues. We have been trying to determine the best algorithms for solving such problems, with reference to their accuracy and economy, for the past 18 months; we present here some of our most interesting conclusions to date. Not all of these conclusions are new; however, we hope their systematic presentation will be of interest. Moreover since the cases $m = 1$ and 2 of (1.1) correspond to the usual linearization of shallow water waves, they are relevant to this Conference.

Computationally, the case $m = 1$ of the one-dimensional wave equation $u_{tt} = c^2 u_{xx}$ is of purely academic interest, because it has the exact solution

(1.2) $$u_j^{n+1} = u_{j-1}^n + u_{j+1}^n - u_j^{n-1} ,$$

on any rectangular mesh with $\Delta x = c\Delta t$. However, even in this case the conversion of the usual initial conditions

(1.2') $$u(x,0) = f(x), \qquad u_t(x,0) = g(x)$$

and general boundary conditions such as

(1.2") $$\cos \alpha \, u(a,t) + \sin \alpha \, u_x(a,t) = f(t),$$

into conditions at mesh-points is non-trivial.

The m-dimensional analogue of (1.2) is the (2m +2)-point formula

(1.3) $$u_{\underline{j}}^{n+1} = \frac{1}{m} \Diamond_h u_{\underline{j}}^n - u_{\underline{j}}^{n-1} ,$$

on a square mesh of side h in planes $t = nk$ and $\Diamond_h u_{\underline{j}}$ is the sum of the values of $\underline{u}$ at mesh-points adjacent to $\underline{j}$. This was proposed in 1928 by Courant, Friedrichs and Lewy in their celebrated 1928 paper [4, esp. pp. 62-67]; it has $O(h^2)$ accuracy for $m > 1$. It is obtained by central difference approximation from (1.1), and has the largest stable time-step $\Delta t = rh/c$ that is compatible with the standard (2m + 4)-point explicit discretization of (1.1), namely

(1.4) $$u_{\underline{j}}^{n+1} = 2u_{\underline{j}}^n - u_{\underline{j}}^{n-1} + r^2 \nabla_h{}^2 u_{\underline{j}}^n .$$

We have not yet found any other algorithm that seems preferable to (1.3), which is just the special case $r^2 = 1/m$ of (1.4).

One of our ultimate objectives is to construct portable, optimal codes for solving the two- and three-dimensional wave equations in general domains, and to find out in particular what kinds of problems can be handled with how much accuracy in different price ranges such as 50¢, \$5, \$50, and \$500. The other objective is to construct similar codes for solving the Riemann problem for plane waves of finite amplitude, with and without shocks.

There is a large literature concerning both kinds of hyperbolic differential equations. For the linear, constant-coefficient wave equation (1.1) in $m > 1$ dimensions, most of this is analytical; we do not know of any computer programs that have been extensively used on a wide variety of problems, and would be glad to test such programs. In this spirit, we have just begun to adapt to the M.I.T.-Harvard computing system a program based on [3] kindly supplied to us by Dr. Leventhal of the U.S. Naval Surface Weapons Center.

As regards the Riemann problem, we have only made preliminary tests of an extract from Professor Moretti's codes for solving more general problems; this already uses 1300 cards! We have not yet tested programs developed at the Courant Institute, based on the Lax-Wendroff formula to be described below. Neither have we consulted R.D. Richtmyer to find out what he now thinks is the best code, although we have studies carefully his discussion of the problem in [11].

2. Difference Methods: $m = 1$.

This section and the next will be concerned with difference algorithms for solving $u_{tt} = u_{xx}$. Though of no practical interest, they illustrate important ideas. Most noteworthy are the standard 5-point explicit scheme

$$\delta_t^2 u_j^n = r^2 \delta_x^2 u_j^n \quad , \qquad r = ck/h \, , \quad h = \Delta x, \qquad k = \Delta t, \tag{2.1}$$

and the more general 9-point implicit scheme of von Neumann

$$\delta_t^2 u_j^n = r^2 [\alpha \delta_x^2 u_j^{n+1} + (1 - 2\alpha)\delta_x^2 u_j^n + \alpha \delta_x^2 u_j^{n-1}] \, . \tag{2.2}$$

We recall from [11, Ch. 10] that (2.1) is only stable for $r \leq 1$, whereas (2.2) is stable for all r if $\alpha \geqq 1/4$ (for $r \leqq 1/\sqrt{1 - 4\alpha}$ if $\alpha < 1/4$). This stability is the attraction of (2.2): for $\alpha \geqq 1/4$, it permits one to take arbitrarily large time steps.

To the above two schemes, we would add the following, apparently new predictor-corrector modification of (2.2):

Predictor: $\quad \bar{u}_j^{n+1} = 2u_j^n - u_j^{n-1} + r^2\delta_x{}^2u_j^n$.

Corrector: $\quad \delta_t{}^2u_j^n = r^2[\alpha\delta_x{}^2\bar{u}_j^{n+1} + (1-2\alpha)\delta_x{}^2u_j^n + \alpha\delta_x{}^2u_j^{n-1}]$.

Like (2.1) when $r = 1$, this scheme is <u>exact</u> for $\alpha = 1/16$, $r = 2$;like both (2.1) and (2.2), it has $O(h^2 + k^2)$ accuracy in general.
Finally, if $\alpha \geq 1/16$, it is stable for all $r \leq 1/2\sqrt{\alpha}$.

<u>Semi-discretization</u>. Note that as $r \downarrow 0$, the approximation (2.1) tends to the <u>semi-discretization</u>

$$(2.3) \qquad u_j''(t) = (c^2/h^2)\delta_x{}^2u_j$$

of $u_{tt} = c^2u_{xx}$. This semi-discretization corresponds to the celebrated "beads on a string" mechanical model of a vibrating string invented by Daniel Bernoulli in 1753. Generalizations of this model were studied in depth by Cauchy, Born, and others as <u>molecular models</u> for crystals; see L. Brillouin, <u>Wave Propagation in Periodic Structures</u>, McGraw-Hill , 1946.

More relevant for us is the fact that if we rewrite (2.3) as a second-order <u>vector</u> ordinary DE of the form

$$(2.4) \qquad \underline{u}''(t) = L[\underline{u}],$$

we can recognize the difference equations (2.1) and (2.2) as straightforward extensions of well-known algorithms for solving DE's of the form (2.4) -- such as $\delta_t{}^2[\underline{u}^n] = k^2L[\underline{u}^n]$ and $\delta_t{}^2[\underline{u}^n] = k^2\{\alpha L[\underline{u}^{n+1}] + (1-2\alpha)L[\underline{u}^n] + \alpha L[\underline{u}^{n-1}]\}$.

<u>Dispersion</u>. We shall discuss here only <u>linear constant-coefficient</u> approximations to wave equations, and indeed only models in which the wave velocity approaches c as the dimensionless molecular spacing $h/\lambda \downarrow 0$. For such approximations, since the schemes are conservative (i.e., non-dissipative), the <u>dispersion</u> (i.e., variation in the wave velocity c_h with the dimensionless wave-length λ/h [15, pp. 46-52]) is a good measure of the error. This is because multivariate Fourier analysis resolves any local disturbance into simply harmonic waves of the form

$$(2.5) \qquad w_h(x,t) = \exp i(kx - \omega_h t) ,$$

and these travel without change of form with wave velocity $c_h = \omega_h/k = \omega_h\lambda/2\pi$ Hence errors are due to deviations in the wave velocities c_h of solutions (2.5) from the wave velocity of the model. Moreover, the exact wave equation (1.1) is non-dispersive: the propagation velocity is exactly c for all wave-lengths $\lambda > 2h$ and in all directions. (For wave lengths $\lambda < 2h$, see §8.)

The variation in wave velocity c_h with wave length λ in discretizations (i.e.,the dispersion [15, 46-52]) is easily computed by substituting a general complex periodic solution $w_h = \exp i(kx-\omega_h t)$ of (2.5) into the relevant formulas. The formulas for the dispersion become simplest when put into dimensionless form -- i.e., by considering $\gamma_h = c_h/c$ as a function of $\sigma = \pi h/\lambda$. For the discretizations (2.1) and (2.2), we then have the following relations:

$$\text{(2.1')} \qquad \sin(r\sigma\gamma_h) = r \sin \sigma$$

$$\text{(2.2')} \qquad \sin(r\sigma\gamma_h) = \frac{r \sin \sigma}{\sqrt{1+4\alpha r^2 \sin^2\alpha}}$$

The relation is $\sin(r\sigma\gamma_h) = r \sin \sigma \sqrt{1-4\alpha r^2\sin^2\sigma}$ for our predictor- corrector scheme. In the limiting case $r\downarrow 0$ of (2.3), $\gamma_h = (\sin\sigma)/\sigma$.

Figure 1 shows the dispersion of various discretizations and semi-discretizations of $u_{tt} = c^2 u_{xx}$ by plotting $\gamma_h \equiv c_h/c$ as a function of h/λ. Note that the finite difference approximations that we have discussed so far always give $c_h \le c$.

3. Associated first-order systems.

It is very well-known that $u_{tt} = c^2 u_{xx}$ is essentially equivalent to the first-order hyperbolic system

$$\begin{bmatrix} \frac{\partial u}{\partial u} \\ \\ \frac{\partial v}{\partial t} \end{bmatrix} = \begin{bmatrix} 0 & c \\ \\ c & 0 \end{bmatrix} \begin{bmatrix} \frac{\partial u}{\partial x} \\ \\ \frac{\partial v}{\partial x} \end{bmatrix}$$

Moreover, as is pointed out in [11, p. 262], the standard 5-point explicit

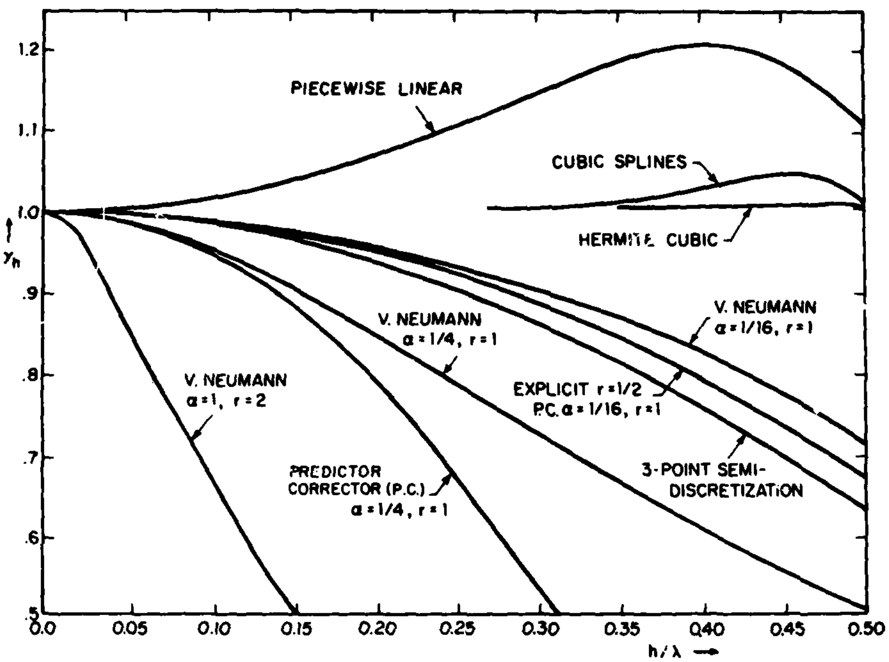

FIG. 1. VARIATION OF γ_h WITH h/λ

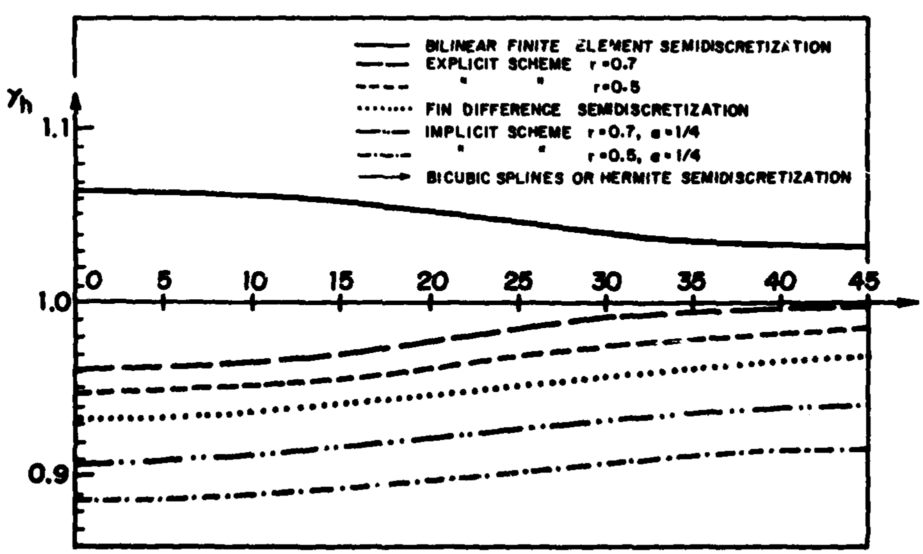

FIG. 2 VARIATION OF γ_h WITH θ FOR h/λ = 0.2

scheme (2.1) is equivalent to a very simple discretization of the system (3.1) on a staggered mesh. Namely, setting $r = c\Delta t/\Delta x$ and

$$u_j^{n-1/2} = (w_j^n - w_j^{n-1})/\Delta t \quad \text{and} \quad v_{j-1/2}^n = c(w_j^n - w_{j-1}^n)/\Delta x,$$

we obtain

$$(3.2) \quad u_j^{n+1/2} - u_j^{n-1/2} = r(v_{j+1/2}^n - v_{j-1/2}^n)$$

and

$$(3.2') \quad v_{j+1/2}^{n+1} - v_{j+1/2}^n = r(u_{j+1}^{n+1/2} - u_j^{n+1/2}) ,$$

Like (1.2), this system is stable for $r \leq 1$, exact for $r = 1$, and has second-order accuracy ("consistency") for all r.

In this section, we shall review other schemes for integrating (3.1) numerically. Indeed, many authors advocate replacing second-order DE's like $u_{tt} = c^2u_{xx}$ systematically by their first-order equivalents, partly with the aim of covering all hyperbolic problems by a unified theory. Actually, one of us has already reviewed in [1, pp. 293-4] five other schemes for integrating numerically a slight generalization of (3.1) (i.e., the first-order system equivalent to the telegraph equation). In discussing them, it is convenient to first diagonalize (3.1) by the substitution $U = u+v$, $V = u - v$, to get the equivalent system

$$(3.3) \qquad \frac{\partial}{\partial t}\begin{bmatrix} U \\ V \end{bmatrix} = \begin{bmatrix} c & 0 \\ 0 & -c \end{bmatrix} \frac{\partial}{\partial x}\begin{bmatrix} U \\ V \end{bmatrix}.$$

Only two of these five schems have second-order accuracy, and we shall confine our discussion to them.

Lax-Wendroff method. The first of these is a variant of the widely used Lax-Wendroff method (see [7] and [11, Sec. 12.7]). For the diagonalized system (3.3), this is

$$(3.4) \qquad U_j^{n+1} = \frac{1}{2}(r^2 + r)U_{j+1}^n + (1 - r^2)U_j^n + \frac{1}{2}(r^2 - r)U_{j-1}^n$$

$$(3.4') \qquad V_j^{n+1} = \frac{1}{2}(r^2 - r)V_{j+1}^n + (1 - r^2)V_j^n + \frac{1}{2}(r^2 + r)V_{j-1}^n$$

As is shown in [11, pp. 303-4], the preceding scheme is second-order accurate for all r, and stable if and only if $r \leq 1$. Moreover for $r = 1$ it reproduces exact solutions of the equation at mesh-points. But for $r < 1$ it is not only dispersive but dissipative as well.† More precisely, it is dissipative of order four in the sense of Kreiss [1, p. 53]. The dispersion (variation in $\gamma_h = c_h/c$ with $\sigma = \pi h/\lambda$) is given by

$$(3.5) \qquad \sin(2\gamma_h r\sigma) = r \sin 2\sigma/\sqrt{1-4r^2(1-r^2)\sin^4\sigma}$$

For these reasons, it seems inappropriate for our problem

Box Scheme. The second scheme having $O(h^2)$ accuracy discussed in [1,pp. 293-4] was the following implicit Box Scheme

$$(3.6) \qquad \tau U_j^{n+1} + U_{j-1}^{n+1} = U_j^{\,n} + \tau U_{j-1}^n, \qquad V_j^{n+1} + \tau V_{j-1}^{n+1} = \tau V_j^{\,n} + V_{j-1}^n$$

where $\tau = (1-r)/(1+r)$, with $r = c\Delta t/h$ as usual. This scheme was apparently first proposed by H.A. Thomas in his 1937 Ph.D. Thesis. It is also second-order accurate, neutrally stable (energy-conserving) for all $r>0$ and exact for $r = 1$. The dispersion satisfies

$$(3.7) \qquad \sin(2\gamma_h r\sigma) = \frac{r \sin 2\sigma}{\cos^2\sigma + r^2\sin^2\sigma};$$

hence there is no dispersion for $r = 1$. In series form, (3.7) gives:

$$(3.7') \qquad c_h/c = 1 + \tfrac{1}{3}(1 - r^2)\sigma^2 + O(\sigma^4)$$

4. Plane Analogs.

We next consider some plane analogs of the schemes described in §§2-3. The natural plane analog of Daniel Bernoulli's "beads on a string" model is the "beads on a square mesh" semi-discretization

$$(4.1) \qquad \underline{u}''(t) = c^2\nabla_h^{\,2}\underline{u}, \qquad \nabla_h^{\,2} = \delta_x^{\,2} + \delta_y^{\,2},$$

---

†i.e., its amplification matrix is not similar to a unitary matrix -- whereas central difference approximations to $u_{tt} = c^2 u_{xx}$ have a basis of solutions of the form $\exp[i(kx-\omega_h t)]$.

where $\underline{u}$ is the vector of nodal values $u_{j\ell} = u(jh, \ell h)$. This is a conservative (i.e. non-dissipative) Lagrangian dynamical system that approximates the continuum "vibrating membrane" model with $O(h^2)$ accuracy. Moreover central difference approximations to (4.1) are conservative, so that for them, the dispersion (usually anisotropic) is the only error).

To each scheme for integrating systems of second-order ordinary DE"s of the form $\underline{u}'' = F(\underline{u})$ or $\underline{u}'' = F(\underline{u}, t)$, there corresponds a full discretization of (4.1). For example, the second central difference approximation $\delta_t^2 u = k^2 F(\underline{u})$ gives the explicit standard 7-point difference approximation:

(4.2) $$u_{j\ell}^{n+1} = (2-4r^2)u_{j\ell}^n - u_{j\ell}^{n-1} + r^2 \Diamond u_{j\ell}^n$$

where $r = c\Delta t/\Delta x$ is the stability ratio (the Courant number) as before and $\Diamond u_{j\ell}^n = u_{j+1,\ell}^n + u_{j,\ell+1}^n + u_{j-1,\ell}^n + u_{j,\ell-1}^n$. This is obviously just the plane analog of the standard 5-point approximation (2.1) of $u_{tt} = c^2 u_{xx}$, and also has $O(h^2)$ accuracy for any fixed r. However, it is not exact for $r=1$, and is only stable for $r \le 1/\sqrt{2}$. The best choice is $r = 1/\sqrt{2}$; it gives the 6-point discretization (1.4) of [4]:

(4.2') $u_{j\ell}^{n+1} = \frac{1}{2}\Diamond u_{j\ell}^n - u_{j\ell}^{n-1}$, which we recommend most highly among $O(h^2)$ methods.

Similar considerations lead to the following 15-point plane analog of von Neumann's 5-point implicit scheme (2.2):

(4.3) $$\delta_t^2 u_{j\ell}^n = r^2 \left[\alpha \nabla_h^2 u_{j\ell}^{n+1} + (1-2\alpha)\nabla_h^2 u_{j\ell}^n + \alpha\nabla_h^2 u_{j\ell}^{n-1}\right].$$

This also has $O(h^2)$ accuracy for any fixed $r>0$. For $\alpha \ge 1/4$ it is unconditionally stable; for $\alpha < 1/4$, it is stable when $r \le 1/\sqrt{2(1-4\alpha)}$.

As in the one-dimensional case, there also exists an explicit predictor-corrector version of (4.3) having $O(h^2)$ accuracy. If $\alpha \ge 1/16$, this is stable for $r \le 1/\sqrt{8\alpha}$.

Dispersion. To find the dispersion of the semi-discrete model (4.1), simply substitute the trial function $u_{j\ell} = \exp[i(pjh + q\ell h - \omega t)]$ into (4.1) and set $p = k\cos\theta$, $q = k\sin\theta$, where $k = \sqrt{p^2 + q^2} = 2\pi/\lambda$,

λ being the wave length.

For each real (p, q), mesh-length h, and Courant number, every central difference approximation determines a real $\omega_h = \omega(p,q\ ;\ h)$ as before. Hence such models are conservative, with easily computable wave speed $c_h = \omega_h/k$. The dispersion, measured by the variation in $\gamma_h = c_h/c = \gamma_h(\sigma,\theta)$ is therefore again a good measure of the error.

For the semi-discretization (4.1), this dispersion is

$$(4.1') \qquad \gamma_h = c_h/c = \frac{1}{\sigma}\sqrt{\sin^2(\sigma\cos\theta) + \sin^2(\sigma\sin\theta)}$$

For the 7-point explicit scheme (4.2), a similar procedure gives the implicit equation

$$(4.2') \quad \sin^2(r\sigma\gamma_h) = r^2[\sin^2(\sigma\cos\theta) + \sin^2(\sigma\sin\theta)].$$

This has, for $r<1/\sqrt{2}$, the following series expansion:

$$(4.2'') \qquad \gamma_h = 1 - \sigma^2(\cos^4\theta + \sin^4\theta - r^2)/6 + O(\sigma^4).$$

The corresponding relations for the implicit 15-point approximation (4.3) are

$$(4.3') \quad \sin(r\sigma\gamma_h) = r\sqrt{A/(1+4\alpha A)}\ , \ A = \sin^2(\sigma\cos\theta) + \sin^2(\sigma\sin\theta).$$

and

$$(4.3'') \qquad \gamma_h = 1 - \sigma^2[\cos^4\theta + \sin^4\theta + r^2(12\alpha - 1)] + O(\sigma^4),$$

which evidently reduce to (4.2") when $\alpha = 0$.

Note that in the plane, the dimensionless dispersion $c_h/c = \gamma_h(\sigma,\theta)$ is a function of the direction θ as well as the dimensionless node spacing $\sigma = \pi h/\lambda$. In other words, the disturbance is anisotropic; see Figure 2.

5. First-order Schemes.

Because the general theory of first-order hyperbolic systems and their numerical solution is attractive, we tried to apply it to $u_{tt} = c^2(u_{xx} + u_{yy})$. For doing this, the best procedure seems to be to adopt the usual physical model for sound propagation [6, Art. 285], namely

$$p_t = c(u_x + v_y), \quad u_t = cp_x, \quad v_t = cp_y \tag{5.1}$$

We adopted this model, but discovered that (5.1) is not equivalent to $u_{tt} = c^2(u_{xx} + u_{yy})$. What is true is that the subspace of irrotational sound vibrations with $u_y = v_x$, or equivalently $(u,v) = \nabla\phi$ the gradient of a velocity potential ϕ, is invariant under (5.1). In this subspace, (5.1) is equivalent to $\phi_{tt} = c^2(\phi_{xx} + \phi_{yy})$.

We next semi-discretized the system (5.2), using a square mesh with mesh-length h as in §4, but staggered mesh-points:

$$u_{j',\ell}, \quad v_{j,\ell}, \quad p_{j,\ell}, \quad j' = j + \frac{1}{2}, \quad \ell' = \ell + \frac{1}{2}, \tag{5.2}$$

The discrete analog of irrotationality can then be taken as the condition

$$u_{j',\ell} + v_{j+1,\ell'} - u_{j',\ell+1} - v_{j,\ell'} = 0 \tag{5.3}$$

for all j, ℓ. The semi-discretization of (5.1) can be taken as the system

$$p'_{j,\ell}(t) = \frac{c}{h}[u_{j',\ell} - u_{j'-1,\ell} + v_{j,\ell'} - v_{j,\ell'-1}] \tag{5.4}$$

$$u'_{j,\ell}(t) = \frac{c}{h}[p_{j+1,\ell} - p_{j,\ell}], \qquad v'_{j,\ell'}(t) = \frac{c}{h}[p_{j,\ell+1} - p_{j,\ell}].$$

Observe that the discrete 'irrotationality' condition (5.3) is conserved by (5.4), since the sum of the time-derivatives is the sum of the pressure differences around a square:

$$\frac{d}{dt}(u_{j',\ell} + v_{j+1,\ell'} - u_{j',\ell+1} - v_{j,\ell'}) = 0$$

To discretize (5.4), we applied the trapezoidal method. This gives the 10-point discretization

$$(5.5)\quad p^{n+1}_{j,\ell} - \frac{r}{2}(u^{n+1}_{j',\ell} - u^{n+1}_{j'-1,\ell}) - \frac{r}{2}(v^{n+1}_{j,\ell'} - v^{n+1}_{j,\ell'-1})$$

$$= p^{n}_{j\ell} + \frac{r}{2}(u^{n}_{j',\ell} - u^{n}_{j'-1,\ell}) + \frac{r}{2}(v^{n}_{j,\ell'} - v^{n}_{j,\ell'-1})$$

$$(5.5')\quad u^{n+1}_{j',\ell} - \frac{r}{2}(p^{n+1}_{j+1,\ell} - p^{n}_{j,\ell}) = u^{n}_{j',\ell} + \frac{r}{2}(p^{n}_{j+1,\ell} - p^{n}_{j,\ell})$$

$$(5.5'')\quad v^{n+1}_{j,\ell'} - \frac{r}{2}(p^{n+1}_{j,\ell+1} - p^{n+1}_{j,\ell}) = v^{n}_{j,\ell'} + \frac{r}{2}(p^{n}_{j,\ell+1} - p^{n}_{j,\ell})$$

This scheme also conserves the discrete irrotationality condition (5.3)‡. Moreover it has $O(h^2)$ accuracy, and is conditionally stable. Its biggest drawback is that it is implicit (see § 6).

Lax-Wendroff scheme. As an alternative, we tried to apply a Lax-Wendroff scheme to (5.1). We rewrote it for this purpose in the vector form

$$(5.6)\quad Z_t = AZ_x + BZ_y$$

with

$$(5.6')\quad Z = \begin{bmatrix} p \\ u \\ v \end{bmatrix}, \quad A = c\begin{bmatrix} 0 & 1 & 0 \\ 1 & 0 & 0 \\ 0 & 0 & 0 \end{bmatrix}, \quad B = C\begin{bmatrix} 0 & 0 & 1 \\ 0 & 0 & 0 \\ 1 & 0 & 0 \end{bmatrix}.$$

We then applied to (5.6) - (5.6') the Lax-Wendroff scheme

$$Z(t+\Delta t) = [I + \frac{r}{2}(A\delta_x + B\delta_y) + \frac{r^2}{2}(A^2\delta_{xx} + \frac{1}{4}(AB + BA)\delta_x\delta_y + B^2\delta_{yy}]\, Z(t),$$

where A and B are as above, and $\delta_x u_{j\ell} = u_{j+1,\ell} - u_{j-1,\ell}$, $\delta_{xx} = u_{j+1,\ell} - 2u_{j,\ell} + u_{j-1,\ell}$, and similarly for δ_y and δ_{yy}. This scheme is stable for $r \le 1/\sqrt{8}$; but, it is dissipative and fails to preserve irrotationality. Though we are hopeful that a different staggered mesh analog (5.2) of this scheme will conserve irrotationality, we have not derived such a scheme.

Dispersion. Instead, we have computed the dispersions of the schemes (5.4) and (5.5), based on staggered mesh-points. For the semi-discretization (5.4), the dispersion is

$$(5.8)\quad \gamma_h = \sigma^{-1}\sqrt{\sin^2(\sigma\cos\theta) + \sin^2(\sigma\sin\theta)},$$

‡ This is true because if $\underline{u}_t = L[\underline{u}]$ is a linear system of ordinary differential equations, S is a linear subspace invariant under L, and $\underline{u}^{n+1} = R(L)[\underline{u}^n]$ is a discretization of the system with R a rational function, then a solution initially in S stays in S.

the same as for the "beads on a mesh" model. Likewise, those for the trapezoidal scheme (5.5) are the same as for von Neumann's implicit scheme for solving $u_{tt} = c^2(u_{xx} + u_{yy})$ with $\alpha = 1/4$. It may therefore be presumed that, for irrotational motions the pairs of schemes referred to are in some sense equivalent.

6. Fourth-order methods.

To summarize, our very thorough exploration failed to bring to light any difference method for solving $u_{tt} = c^2(u_{xx} + u_{yy})$ with second-order accuracy that was superior to the standard 7-point difference method with $r = 1/\sqrt{2}$. We shall next give a brief progress report on our search for difference methods having fourth-order accuracy, and afterwards discuss some finite element methods for solving the same equation.

Methods for solving $u_{tt} = c^2(u_{xx} + u_{yy})$ with $O(h^4)$ ("fourth-order") accuracy have been Collatz [8, pp. 52-56] and Fairweather and Mitchell [5]. The method proposed in [5] has been extended to (linear) wave equations having variable coefficients by Ciment and Leventhal [3], and programmed at the U.S. Naval Ordnance Laboratory. We have just begun testing this program, in consultation with the authors.† In this brief summary, we shall only review very briefly the ideas underlying the construction of $O(h^4)$ approximations, the formulas to which they lead, and their stability.

For the one-dimensional wave equation, one can achieve $O(h^4)$ accuracy for any $r>0$ by using the implicit formula

$$(5 + r^2)\delta_t^2 u_i^n = (1 + 5r^2)\delta_x^2 u_i^n - (1 - r^2)\,\Box u_i^n \tag{6.1}$$

where $\Box u_i^n = u_{i+1}^{n-1} + u_{i+1}^{n+1} + u_{i-1}^{n+1} + u_{i-1}^{n-1} - 4u_i^n$. This is stable if and only if $r \le \sqrt{7}/2$ (the stability limit seems to be new).

The formulas of Collatz involve a free parameter; they are all linear combinations of two special 19-point formulas that involve only five unknowns at the advanced time step (and, by symmetry, five known values from the earliest time step). The stencils involved are displayed below for the special cases of maximum stable Courant numbers $r = c\Delta t/\Delta x$ equal to $1/\sqrt{2}$ and $1/\sqrt{3}$ respectively.

† The authors have warned us that the paper by McKee cited in [3] contains many misprints.

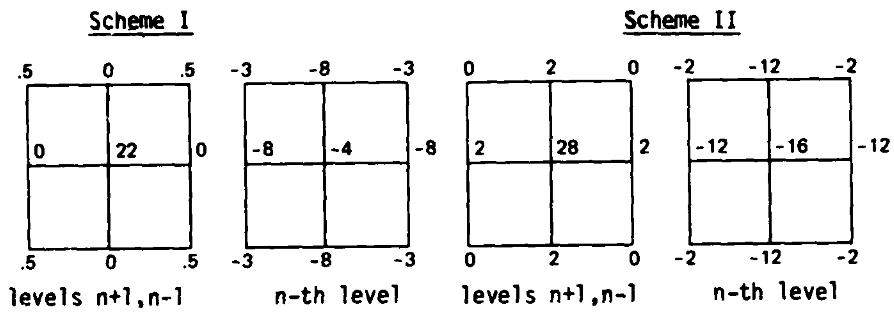

Collatz himself proposed using a Gauss-Seidel iterative method to solve the resulting implicit system

(6.1) $$C\underline{u}^{n+1} = 2E\underline{u}^{n} - C\underline{u}^{n-1}$$

for the $u^{n+1}_{j,\ell}$ as unknowns, at each time step, remarking that this should converge rapidly because C is so heavily diagonally dominant. Although we have not yet tried the method, this proposal seems very reasonable. The standard 7-point explicit method could be used as a "predictor" to find a good first approximation.

7. Finite Element Methods.

In numerical solid mechanics, new finite element methods have almost entirely replaced difference methods during the past decade. This naturally suggests the idea that the same change would be advantageous in fluid mechanics. We doubt that this is the case for the wave equation (1.1), which is of hyperbolic type, noting that the problems in solid mechanics solved so successfully by finite element methods are typically elliptic (even if they involve incremental loads). Nevertheless, we have made a careful theoretical analysis of the possibilities. The following paragraphs summarize our theoretical conclusions; we hope to test them soon by numerical experiments.

We will begin with the general observation that for small oscillations of (conservative) Lagrangian systems like those to which the wave equation (1.1), applies, finite element methods lead naturally to implicit semi-discretizations of the form

(7.1) $$B\ddot{q} = Aq ,$$

where B is an inertial and A a stiffness matrix, and the q_i are (generalized)

coordinates. Specifically, to restrict semi-discretizations to lie in a (linear) "approximating subspace" is equivalent to imposing a set of "workless constraints", replacing an infinite-dimensional model from theoretical continuum mechanics by a finite-dimensional Lagrangian system.

In particular, by constraining $u(x,t)$ to be piecewise linear for fixed t and $u(x,y,t)$ to be piecewise bilinear, we get a semi-discretization of the form (7.1) having <u>second</u>-order accuracy. By constraining them to be piecewise cubic and bicubic, respectively, with additional smoothness constraints (of being C^1 or C^2), we get Hermite and spline semi-discretizations having <u>fourth</u>-order accuracy. These approximations are discussed in Strang and Fix [14], where equations of the form (7.1) are obtained by the Galerkin method. The approach described in the preceding paragraph is closer to Rayleigh's ideas.

For simplicity we consider first the one-dimensional case. A complex normal mode is given by:

$$u = e^{i\omega_h t}\, w_h(x) \tag{7.2}$$

where w_h is a piecewise linear, cubic spline, or cubic Hermite function that <u>interpolates</u> to $w = e^{ikx}$ at the nodes $x_j = jh$. From the principle of interchange of energy between the kinetic and the potential phases of the standing wave (7.2), we have:

$$\omega_h^2/c^2 \equiv R_h(k) = \int \left|w_h'(x)\right|^2 dx \Big/ \int \left|w_h(x)\right|^2 dx. \tag{7.3}$$

Here R_h is the Rayleigh quotient of the finite element approximation. We can calculate R_h easily by self=similarity. Using (7.3), we conclude that $\gamma_h = c_h/c = \lambda\sqrt{R_h(k)}/2\pi$.

Straightforward computations give the following formulas for γh:

$$\gamma_h = (\sqrt{3}\sin\sigma)/\sigma\sqrt{1+2\cos^2\sigma} = 1 + \sigma^2/6 - \sigma^4/120 + 0(\sigma^6) \tag{7.4}$$

for piecewise linear elements, and

$$\gamma_h = 1 + \sigma^6/945 + 0(\sigma^8) \tag{7.5}$$

for piecewise <u>cubic</u> Hermite and spline elements. Note that the finite element approximations tend to <u>stiffen</u> the system (i.e., $c_h > c$), whereas finite differences tend to <u>soften it</u> ($c_h < c$); see Fig. 1. This tendency can be

rationalized as follows.

THEOREM. For any given wave-length λ, the wave velocity is increased by any workless constraint.

Proof. In (7.3), R_h is minimized by the complex wave profile $w(x) = e^{ikx}$ with respect to all waves with wave-length λ or less. Hence a constraint can only increase R_h and $\gamma_h = \lambda\sqrt{R_h(k)}/2\pi$.

Although quadratic functions might provide a desirable compromise between the linear and cubic approximations described above, we have seen no reason for preferring other finite elements. We have also tentatively decided to use spline rather than Hermite approximations in numerical experiments, because of the practical difficulty of matching closely the initial values of u_{xt}, etc.

In the plane, a basis for the finite element subspace consists of products of their one-dimensional counterparts, and:

$$R_h(p,q) = R_h(p) + R_h(q) \ . \tag{7.6}$$

The dispersion therefore satisfies

$$\gamma_h = 1 + \sigma^2(\cos^4\theta + \sin^4\theta)/6 + O(\sigma^4) \tag{7.4'}$$

for piecewise bilinear elements, and

$$\gamma_h = 1 + \sigma^6(\cos^8\sigma + \sin^8\theta)/945 + O(\sigma^8) \tag{7.5'}$$

for bicubic Hermite and spline elements.

The matrices B and A in (7.1) depend on the choice of basis in the approximating finite element subspace [14, pp. 252-4]. With "tent" functions as a basis, the q_j are just the nodal values $x_j(t)$ of the solution. Eq. (7.1) simplifies with this choice of basis to

$$\ddot{b}_{j-1} + 4\ddot{b}_j + \ddot{b}_{j+1} = 6c^2[b_{j-1} - 2b_j + b_{j+1}]/h^2 \ . \tag{7.7}$$

By noting the resemblance of (7.7) with the 3-point semidiscretization (2.2), and especially the fact that the $O(\sigma^2)$ terms in the asymptotic formula for the dispersion of (7.7) and (2.2), are equal in magnitude but opposite in sign, we average to:

$$\frac{1}{12}[\ddot{b}_{j-1} + \ddot{b}_j + \ddot{b}_{j+1}] = c^2[b_{j-1} - 2b_j + b_{j+1}]/h^2 \ , \tag{7.8}$$

whose dispersion is indeed smaller:

$$(7.8') \qquad \gamma_h = 1 - \sigma^4/30 + O(\sigma^6)$$

To obtain full discretizations in time, one can approximate second-order time derivatives by central difference quotients in (7.7), getting a 3-level tridiagonal implicit scheme that is stable for $r<1\sqrt{3}$. For (7.8), by applying the 4-th order accurate Størmer-Numerov formula in time, we recapture the 9-point $O(h^4)$ approximation (6.1). In the plane, one can use tensor products of these formulas; see (7.6).

Note that cubic and bicubic finite element semi-discretizations reproduce wave velocities with sixth-order accuracy, but wave profiles with only fourth-order accuracy. The sixth-order accuracy is achieved only at meshpoints, as is customary with superconvergence.

The greatest defect of finite element methods for solving $u_{tt} = c^2(u_{xx} + u_{yy})$ is the difficulty of integrating efficiently the implicit systems of DE's of the form (7.1) to which they lead. We have not yet decided on the best way to resolve this difficulty. Milton Lees has suggested using ADI methods (J. SIAM 10 (1962), 610-16); see also [5]. We plan to try following a standard 6-point explicit predictor by an explicit corrector based on Scheme I, possibly iterated once.

8. The Riemann Problem

We conclude with a few remards on the numerical solution of the initial value problem for "plane waves of finite amplitude," which Riemann tried to solve analytically in a famous paper written in 1860. Von Neumann tried to solve this in 1944 by a straightforward generalization of Daniel Bernoulli's "beads on a string" model. He did this by using Lagrangian coordinates in which h is a mass-increment. Setting $\xi_j = x_j/h$, where x_j is the position of the j-th particle, the simplest 3-point central difference approximation then gives a system of 3-point non-linear ordinary DE's of the form

$$(8.1) \qquad \xi_j''(t) = [F(\xi_{j+1} - \xi_j) - F(\xi_j - \xi_{j-1})]/h^2 ,$$

where F is the adiabatic pressure as a function of scaled density. These he discretized to

$$(8.2) \qquad \xi_j^{n+1} = 2\xi_j^n - \xi_j^{n-1} + r^2[F(\xi_{j+1}^n - \xi_j^n) - F(\xi_j^n - \xi_{j-1}^n)] \ .$$

Until a shock forms and destroys the entropy conservation, this seems to us as effective as any other method having only second-order accuracy.

Since 1944, many other schemes have been proposed for handling the general case in which shocks occur. Most notable among these are probably the von Neumann-Richtmyer method of 1950, and various Lax-Wendroff methods. An excellent and authoritative review of these methods is given in [11, Chap. 12]. Nevertheless, Moretti [9] could ask in 1971: "is a computer program available [for solving one-dimensional compressible flow problems, which is] easy to use, general, safe, accurate and fast?...the answer seems to be negative." One of us made a similar observation at the ONR Workshop on Numerical Hydrodynamics held in 1974‡, Prof. Moretti responded by supplying us with a deck of about 1300 cards to do the job.

We have made a few simple, quite successful experiments with this deck (following some minor modificaitons). However, we think that a good deal more work will be required to make it truly "easy to use, general, safe, accurate and fast"; see §9. We plan to do this work, testing at the same time other codes based on Lax-Wendroff methods that have been developed at the Courant Institute by S. Burstein.

Treatment of Shocks. After shocks form, one must introduce the entropy as an additional, third dependent variable. All existing codes treat the resulting model as a system of three first-order hyperbolic equations. However, where most authors use an "artificial viscosity" to smear out the shock, "capturing" it in a band a few mesh-lengths thick, Moretti adopts a "shocklocating" technique that assigns to shocks a negligible width. We plan to find out also whether, for flows containing only a few shocks, a similar "shocklocating" technique could be incorporated into the scheme (8.1) - (8.2), modifying $F(\xi_{j+1}^n - \xi_j^n)$ to allow for a change in the entropy of the j-th interval each time that a shock passes.

Gibbs phenomenon. Von Neumann's original numerical experiments, and most later ones based on "shock-capturing" techniques, tend to produce spurious oscillations or " wiggles" behind shocks. See [12, p. 161 and Sec. V - C]. However, whereas these oscillations are commonly attributed to

‡ See the Proceedings of this Workshop, published by the U.S. National Academy of Sciences, 1975, pp. 140, 158.

iterative instability, nonlinearities, or spatially varying coefficients, their presence is really just a "Gibbs phenomenon" associated with analytical treatments of jumps. Thus they arise also in the (linear) acoustic approximation to steady flow across jumps [12, p. 161], and even with interpolation through discontinuities. Specifically, if one discretizes the step-function sgn(x) through its values on a uniform mesh, and then reconstructs it by Whittaker's cardinal interpolation formula, one gets spurious oscillations near the discontinuity; see Fig. 3.

9. WAVPAK

We are glad to report that the algorithms described in §§2-4 have been incorporated, together with some others, into a versatile package of Fortran programs called WAVPAK, designed and implemented at Harvard by Surender Gulati. Using this package, one can for example trace the evolution of a wave generated at one corner of a square, on a 40 x 40 mesh, for 200 time steps, at a cost of about $3 per case plus $3 for the job run (compiling, listing, printing, etc.) This is long enough for the wave to travel from one corner along the diagonal diameter to the opposite corner, all the way back, and half-way across again.

Mr. Gulati plans to incorporate into WAVPAK the best of the other algorithms discussed in the body of this paper, as well as treating more general domains and boundary conditions. When documented, this package might serve as a pilot model for a standard package of computer programs for solving simple hyperbolic problems at modest cost.

We realize that such programs cannot compete with the far more sophisticated programs developed at Los Alamos and other major government laboratories for solving practical problems. However, such sophisticated programs are best run at the laboratories that designed them. We hope that the simplicity, economy, ease of use, and portability of WAVPAK will make it generally useful as an introduction to the subject. Mr. Gulati plans to describe its design and capabilities in another publication.

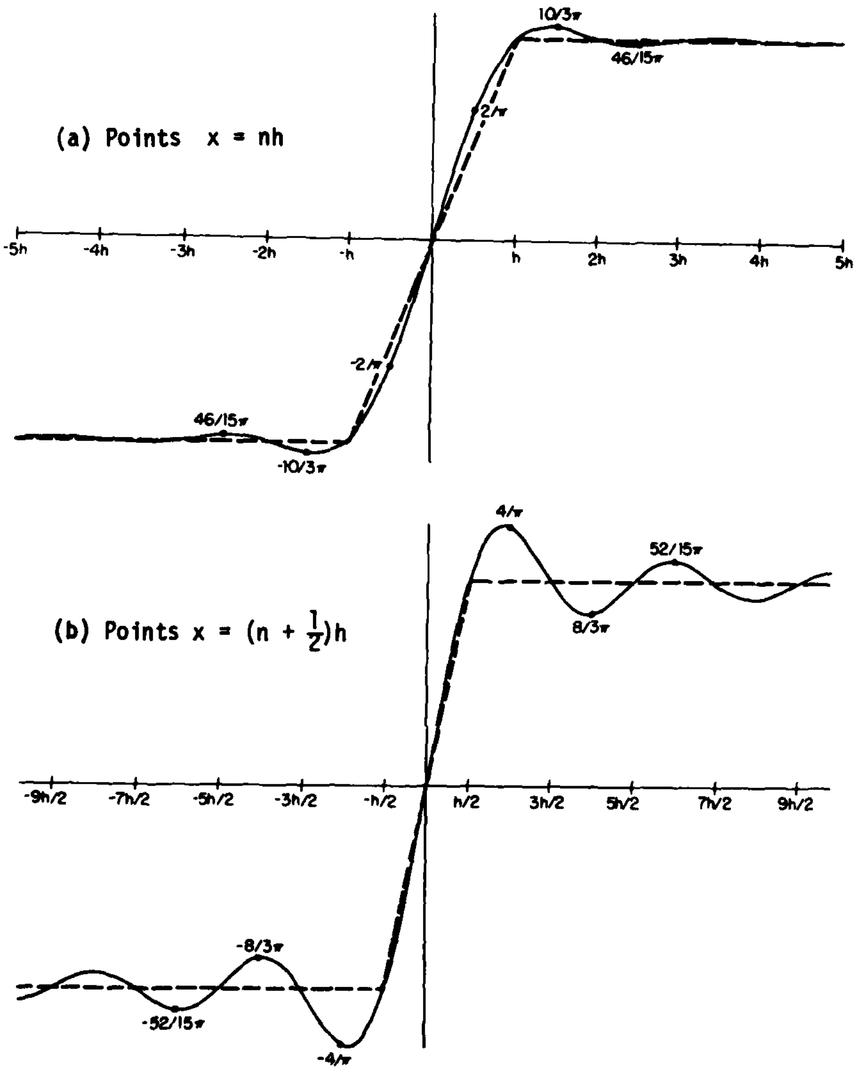

Fig. 3. Whittaker Interpolants to sgn(x)

REFERENCES

[1] J.H. Bramble (ed.), Numerical Solution of Partial Differential Equations, Academic Press, 1966.

[2] S.Z. Burstein and A.A. Mirin, "Third order difference methods for hyperbolic equations," J. Comp. Phys. 5 (1970), 547-71.

[3] M. Ciment and S.H. Leventhal, "Higher order compact implicit schemes for the wave equation", NOLTR 74-159, 1974. (To be published in Math. Comp., Oct., 1975).

[4] R. Courant, K.O. Friedrichs, and H. Lewy. "Uber die partiellen Differenzengleichungen der mathematischen Physik," Math. Annalen 100 (1928), 32-74.

[5] G. Fairweather and A.R. Mitchell, "A high accuracy alternating direction method for the wave equation", J. Inst. Maths Applics. (1965), 309-16.

[6] H. Lamb, Hydrodynamics, 6th ed., 1932.

[7] Peter D. Lax and B.S. Wendroff, "Difference schemes for hyperbolic equations with high orders of accuracy," Comm. Pure Appl. Math. 13 (1960), 217-37.

[8] J.J. Miller (ed.), Topics in Numerical Analysis, Academic Press, 1973.

[9] G. Moretti, "The Choice of a Time-Dependent Technique in Gas Dynamics" (1969), "Complicated One-Dimensional Flows" (1971), "Thoughts and Afterthoughts about Shock Computations" (1973), PIBAL Reports Polytechnic Institute of Brooklyn.

[10] G.G. O'Brien, M.A. Hyman and S. Kaplan, "A study of the numerical solution of partial differential equations", J. Math, and Physics 29 (1951), 223-51.

[11] R. D. Richtmyer and K.W. Morton, Difference Methods for Initial-Value Problems, Wiley-Interscience, 1967.

[12] Patrick J. Roache, Computational Fluid Dynamics, Hermosa Publ., Albuquerque, N.M., 1972.

[13] E.L. Rubin and S.Z. Burstein, "Difference equations for the inviscid and viscous equations of a compressible gas," J. Comp. Phys. 2 (1967), 178-96.

[14] G. Strang and George J. Fix, An Analysis of the Finite Element Method, Prentice-Hall, 1973.

[15] R. Vichnevetsky (ed.), Advances in Computer Methods for Partial Differential Equations, AICA Publ. of University of Ghent, 1975.

[16] G.B. Whitham, Linear and Nonlinear Waves, Wiley, 1974.

METHODS FOR CALCULATING MULTI-DIMENSIONAL, TRANSIENT, FREE SURFACE FLOWS PAST BODIES

B. D. Nichols and C.W. Hirt

Los Alamos Scientific Laboratory of the
University of California
Los Alamos, New Mexico 87545 U.S.A.

I. Introduction

In this paper we discuss numerical methods for calculating multi-dimensional, transient, free surface flows interacting with general curved boundaries. To effectively model a free surface, three problems must be resolved: the surface must be numerically defined, a prescription must be provided to advance it in time, and appropriate boundary conditions must be applied at the location of the surface. The schemes chosen to meet these conditions must be compatible.

Before discussing methods that model free surfaces, we first review the basic notions of Lagrangian and Eulerian finite difference representations. In each representation the fluid region is subdivided into a finite grid, or mesh, of computing cells. Associated with each cell are local values of the appropriate field variables. The Lagrangian viewpoint utilizes a mesh of grid points embedded in the fluid and moving with it. Thus, a free boundary will always be coincident with a mesh boundary, which simplifies the application of boundary conditions. The Eulerian viewpoint treats the mesh as a fixed reference frame through which the fluid moves. In this case, some additional means must be supplied to locate a free boundary within the mesh. Furthermore, since the boundary is not likely to be coincident with the mesh lines, application of boundary conditions requires some interpolative subcell resolution scheme. For low amplitude free surface configurations, various methods are available that work more or less equally well. For example, several Lagrangian techniques have been developed to calculate incompressible flows with a free surface; see Hirt, et al. (1970), Brennen and Whitney (1970), and Chan (1975). These techniques, however, are not applicable to highly contorting or shearing free surface flows in which the Lagrangian meshes would be distorted so severely as to

produce serious questions of accuracy.

Eulerian schemes are more frequently used for calculating free surface flows because they do not necessarily have the low amplitude restriction. For example, the Marker-and-Cell (MAC) method developed by Harlow and Welch (1965) is an Eulerian technique that has been extensively used to calculate multi-dimensional free surface phenomena. The basic technique has been improved by various users. In the original formulation the fluid is represented by marker particles, which are moved by the local fluid velocity. The fluid surface is defined by the location of these particles. The free surface boundary conditions are applied at the center of cells containing the interface. No attempt is made to determine the exact location of the surface within a calculational cell. This free surface treatment was improved by Chan and Street (1970). For low amplitude surface deformations, they defined the free surface by its height above the horizontal axis, which eliminated the need for marker particles. However, they also developed an alternative scheme that used marker particles only on the free surface. More importantly, in both schemes, they applied free surface boundary conditions at the actual location of the free surface. This practice eliminated small scale surface irregularities present in the original MAC formulation. Viecelli (1969) further extended the Marker-and-Cell method to include impenetrable, curved boundaries. He treats these boundaries analogous to a free surface, but applies a pressure at the boundary in such a way that the velocity of the fluid normal to the boundary vanishes. Thus, the difference between the treatment of cells containing free surfaces and those containing the impenetrable boundaries is that the cell pressures are computed from a Neumann (specified derivative) rather than a Dirichlet (specified value) condition. This technique was later extended by Viecelli (1971) to calculate flexible curved walls. Nichols and Hirt (1971) adapted and extended Chan's surface marker particle scheme to calculate highly contorted, multi-valued, free surfaces and applied better approximations for the normal and tangential stress conditions.

The assimilation of all these improvements into one general technique could result in a useful but very complicated technique. Realizing the need for these capabilities to be generally available in an easily used

form, we have developed an Eulerian code, SOLA-SURF, which is capable of handling free and curved rigid surfaces that are single valued functions of height. The original SOLA code is based on the Marker-and-Cell method, but is written in a simplified form to facilitate its use by persons with little or no experience in numerical fluid dynamics. Because of its simplicity it is easy to add special boundary conditions to calculate, for example, flow past fixed or moving prismatic structures. In the SOLA-SURF version, which has the free surface capability, these structures may be completely submerged or may penetrate the free surface. The SOLA and SOLA-SURF codes are available from the Argonne Code Center and the basic algorithm and free surface scheme are described in a report by Hirt, et al. (1975).

Numerical techniques for calculating free surface flows in three space dimensions pose the same problems as the two-dimensional techniques discussed above, except they have the added requirement of making efficient use of computer time and storage. Nichols and Hirt (1973) developed a numerical technique for three-dimensional free surface flows. The technique is based on the Chan and Street version of the Marker-and-Cell method in which the free surface is defined by its height at the center of each vertical column of cells in the mesh. Because the surface must remain single valued and because of the manner in which boundary conditions are applied, the maximum surface slope must be less than that of a diagonal on the vertical face of any cell. While this does limit the amplitude of surface distortions, flow over and around some structures is possible in this technique.

Nichols (1973) has also employed marker particles for defining three-dimensional free surfaces. In this case, logic was established that permitted surface boundary conditions to be applied with arbitrary surface deformations. Although more general, there are problems associated with the use of marker particles for surface definition. The essential difficulty is associated with the lack of a suitable scheme to add additional surface markers in regions of surface expansion, for example, near the corner of obstacles that penetrate the surface.

Because of the difficulties associated with previous schemes, two new techniques are being developed. In one, surfaces are defined by a

volume-fraction function that specifies the fractional fluid filled volume per unit volume. Surfaces are moved by fluxing the volume fraction from cell to cell. This eliminates the explicit setting and moving of a discretely defined free surface. The direction of maximum gradient of the volume-fraction function defines a surface normal direction, and this together with the volume-fraction values can be used to reconstruct an average interface location in each surface cell.

In the second alternative, a variable density fluid is assumed. The fluid has density normalized to unity, while in the void there is a very small density (for example, 10^{-6}). No special boundary conditions are used in this method. For efficiency, these latter techniques are being developed initially for only two space dimensions.

All of the free surface schemes discussed in the following sections of this paper are couched in one basic solution algorithm, which is a direct extension of the Marker-and-Cell method. This algorithm is briefly described in section II. Following this a more detailed description, including the advantages and disadvantages, is given of free surface computational schemes that make use of the surface height function (section III), surface marker particles (section V), and the volume fraction and variable density schemes (section VI).

Before making a critical comparison of these different techniques, however, we illustrate how even the simplest method can be used to compute reliable and useful results. In section IV, following a description of the surface height function scheme, a study is presented of the added mass and damping coefficients computed for rectangular cylinders undergoing forced oscillation. These results are compared with the experimental data of Vugts (1968). An interpretation is also given of some nonlinear effects.

II. The Basic Solution Algorithm

The finite difference solution of the Navier-Stokes equations is achieved by a direct extension of the Marker-and-Cell method. A stationary network of rectangular cells is used to divide the calculational region into a finite number of elements with which the fluid variables are associated. The primary field variables are the velocity components and the

pressure. Each of the velocity components is specified at the center of the cell face to which it is normal and the pressure is specified at the cell center.

In several of the free surface schemes it is expedient to flag each mesh cell to denote whether it is an empty cell containing no fluid; a surface cell, which contains fluid but is not adjacent to an empty cell; or an obstacle cell, which is impervious to fluid flow. All remaining cells are interior fluid cells. Additional flags can be used to designate the rigid boundary cells, including interior obstacles, as either free-slip, which require zero normal velocity and zero shear stress, or no-slip, which require zero normal and zero tangential velocity at the boundary. Input and continuative outflow boundaries are also possible.

The fluid motion is numerically determined by advancing the fluid configuration through a series of small time increments. During each time step the solution to the momentum equation is obtained in two phases. First, the known velocities and pressures from the previous time step are used to determine the fluid velocities in each cell, with the initial conditions used for the first time step. This explicit calculation does not necessarily ensure incompressiblity; therefore, in the second phase the tentative velocity field is adjusted through changes in the pressure field. This was accomplished in the original Marker-and-Cell method by solving a Poisson equation derived from the constraint that the velocity divergence be zero in each cell at the end of the time step. The basic idea of the present algorithm is to adjust the pressure in each mesh cell to drive the velocity divergence in that cell to zero. The pressure and velocity distributions must be obtained by iteratively adjusting these velocities in each cell in the mesh (see, for example, Hirt, et al. 1975).

III. Free Surface Definition by a Surface Height Function

The surface height function is generally more efficient and logically simpler than surface treatments involving marker particles. For this reason, this was the first method used to define the free surface in a three-dimensional technique; see Nichols and Hirt (1973).

The fluid surface is single valued and is initially defined by specifying the surface height above the bottom of the mesh at the center of each

vertical column of cells. The change in the surface elevation is determined by the local fluid velocity, that is, by the vertical component of the fluid motion plus the horizontal convection of the surface elevation from adjacent cell columns.

The free surface boundary conditions require that the normal and tangential velocities immediately outside the surface be chosen to ensure a zero transfer of momentum through the surface. Velocities normal to the surface are set to satisfy the incompressibility condition in the surface cells where the free surface is located. The tangential velocities in the cells immediately outside the fluid are set equal to the adjacent interior velocities. This is consistent with zero shear stress at the surface for an inviscid fluid. The pressure in surface cells is determined by a linear interpolation or extrapolation between the pressure in the fluid cell immediately below the surface cell and a specified pressure at the surface.

A new three-dimensional version of this free surface technique, SOLA-3D, has been developed recently by Stein and Hirt (1975). The solution technique and the capabilities of the code are similar to the one described above, except that it has a variable mesh and the code has been written in a simpler, more versatile, and efficient manner. The following examples, however, have been computed using the original three-dimensional code.

All examples have been run on a CDC-7600 computer. A fast core memory of 64,000 words is available and a large core memory makes an additional 400,000 words accessible, although the large core is not a direct access core and does slow the calculation speed somewhat. The grind time, that is, calculation time per cycle per cell, for typical calculations varies from 0.8 to 1.6 ms/cycle/cell. We have chosen two examples to illustrate the three-dimensional free surface features of this method. In Fig. 1, we show the perspective view of the free surface configuration resulting from flow over a rectangular structure. (Rigid bodies may be created in the fluid region by designating any number or configuration of cells as obstacle cells.) A 3 x 3 x 3 cell structure is located in a 15 x 15 x 7 cell mesh. The leftmost boundary is a fluid input boundary. The opposite end of the mesh is an outflow boundary. All other rigid boundaries are free-slip walls, that is, walls where the fluid is subjected to a zero normal velocity and a zero shear stress. The fluid is initially 3.5 cells deep

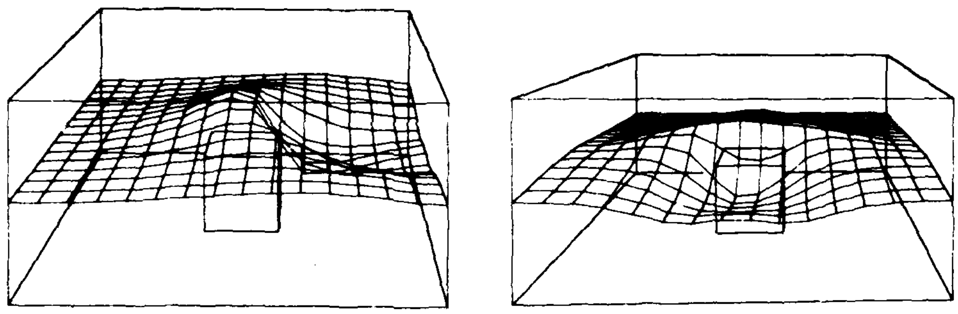

(a) (b)

Fig. 1. Perspective views of the free surface configuration re-resulting from flow over a submerged structure as seen from (a) the side, with input from the left, and (b) downstream.

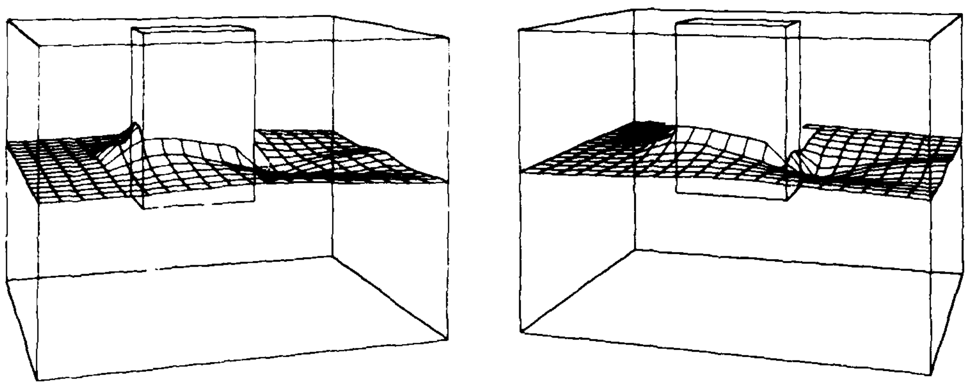

Fig. 2. Perspective views of the free surface configuration resulting from flow past a partially submerged blunt body.

and the Froude number is 2.0, based on initial depth and input velocity. The plots shown are at a nondimensional time of 2.0, after 20 calculational cycles. Perspective views from two separate viewing positions are shown. The plot on the left shows the fluid flowing through the mesh from left to right. The rightmost plot views the flow from a centered, downstream position.

Figure 2 shows two views of the free surface configuration resulting from fluid flowing from left to right past a partially submerged blunt body with a length to width ratio of 2.0, a width to draft ratio of 1.5, and a draft Froude number (based on the body draft and the input velocity) of 2.0. No frictional drag forces are assumed in the calculation. The wall boundary conditions are the same as in the previous example. At the calculation time of 3.5 (35 cycles) that is shown, the flow has reached steady state.

These examples are typical of the kinds of calculations possible using three-dimensional techniques with the free surface defined by a surface height function. The free surface is easily defined initially and the surface movement is straightforward. The free surface boundary conditions are easy to apply, even when adjacent to interior obstacles. The computer storage requirement for the free surface definition is minimal, since only two height values for each vertical column of cells are required, one old and one new time value. This free surface scheme can be used tc calculate meaningful results in a low amplitude free surface environment, as demonstrated with the two-dimensional SOLA-SURF calculations presented in the following section. The only major disadvantage of this scheme is that it is restricted to a single valued free surface and, thus, to relatively low amplitude surface distortions.

IV. Experimental Verification

To illustrate the utility of finite difference techniques we present a study performed to obtain the hydrodynamic coefficients of a rectangular cylinder. Added mass and damping coefficients are determined by computing the dynamic pressure force on the cylinder during forced heave. These calculations are compared with the experimental data of Vugts (1968).

The two-dimensional SOLA code, SOLA-SURF, which defines the free surface by a surface height function, was used for these calculations. The mesh size for the calculations varied from 100 to 250 cells in the horizontal direction, depending on the period of the forced motion, and there were 22 cells in the vertical direction. The mesh cells were of uniform size, $\delta x = 0.1$ and $\delta y = 0.2$. Five cells were used to resolve the half width of the cylinder, which was located at a plane of symmetry at the left mesh boundary. To model the harmonic motion of the cylinder, special boundary conditions were added to the SOLA code. At the rigid boundary of the cylinder bottom, the cell pressure is derived from the constraint that the normal fluid velocity be equal to that of the body. The SOLA-SURF boundary conditions restrict the surface slope to be less than that of a cell diagonal. We eliminated this restraint at the vertical side of the cylinder, however, by aligning the side with a cell boundary line and adding boundary conditions that set to zero all velocities on and normal to the side of the cylinder.

The vertical displacement of the rectangular cylinder from its mean position is given by

$$\alpha = a \sin \omega t \ .$$

The linearized equation of motion for the cylinder in forced heave is, see for example Wehausen (1971),

$$\left(m + \mu_{22}\right) \ddot{\alpha}_2 + \lambda_{22} \dot{\alpha}_2 + c_{22} \alpha_2 = Z$$

where

m = mass of the cylinder,

μ_{22} = hydrodynamic or "added" mass in heave,

λ_{22} = damping coefficient against vertical motion,

c_{22} = hydrostatic restoring coefficient against vertical displacement,

Z = external driving force,

and the raised dot notation indicates differentiation with time. The total hydrodynamic force, that is, total force minus static force, F_b, acting on the body in the vertical direction is

$$F_b(t) = - \mu_{22} \ddot{\alpha}(t) - \lambda_{22} \dot{\alpha}(t) \ .$$

Assuming this hydrodynamic force is a harmonic function in time and can be written as

$$F_b(t) = \gamma \sin(\omega t - \beta) ,$$

the hydrodynamic coefficients are obtained by equating these two expressions for F_b,

$$\mu_{22} = \frac{\gamma \cos \beta}{\omega^2 a}$$

and

$$\lambda_{22} = \frac{\gamma \sin \beta}{\omega a} .$$

The amplitude γ and phase shift β were obtained by comparing plots of the displacement and dynamic pressure force F_b acting on the cylinder as functions of time and measuring the shift in phase.

The calculated coefficients are compared with experimental data in Fig. 3. The coefficients are normalized by ρA and $\sqrt{\frac{B}{2g}}$, where ρ is the fluid density, A is the mean submerged area, B is the cylinder beam, and g is the acceleration of gravity. The calculations were for $B/T = 2.0$, where T is the cylinder draft at its mean location. The amplitude of motion normalized by B was 0.025 and 0.05. Vugts' experiments were conducted in fluid depths, normalized by B, varying from 4.50 to 5.625. The normalized depth was 4.0 for the calculated results. The calculated data generally agrees very well with the experimental data as shown in Fig. 3.

The discrepancy in the calculated damping coefficient at the normalized frequency of 1.25 is probably due to an error in determining the phase shift β, since it is very small at this beam width and frequency. To check this, another calculation was made, which is not shown in Fig. 3, for $B/T = 8$ and $\omega\sqrt{\frac{B}{2g}} = 1.25$. In this case the phase shift is much larger, and the added mass coefficient agrees closely with the experimental data. The calculated damping coefficient in this case is slightly lower than the experimental data, but is higher than the linear theory.

There is a discrepancy between the experimental data and linear theory for the added mass coefficient at normalized frequencies below 0.5.

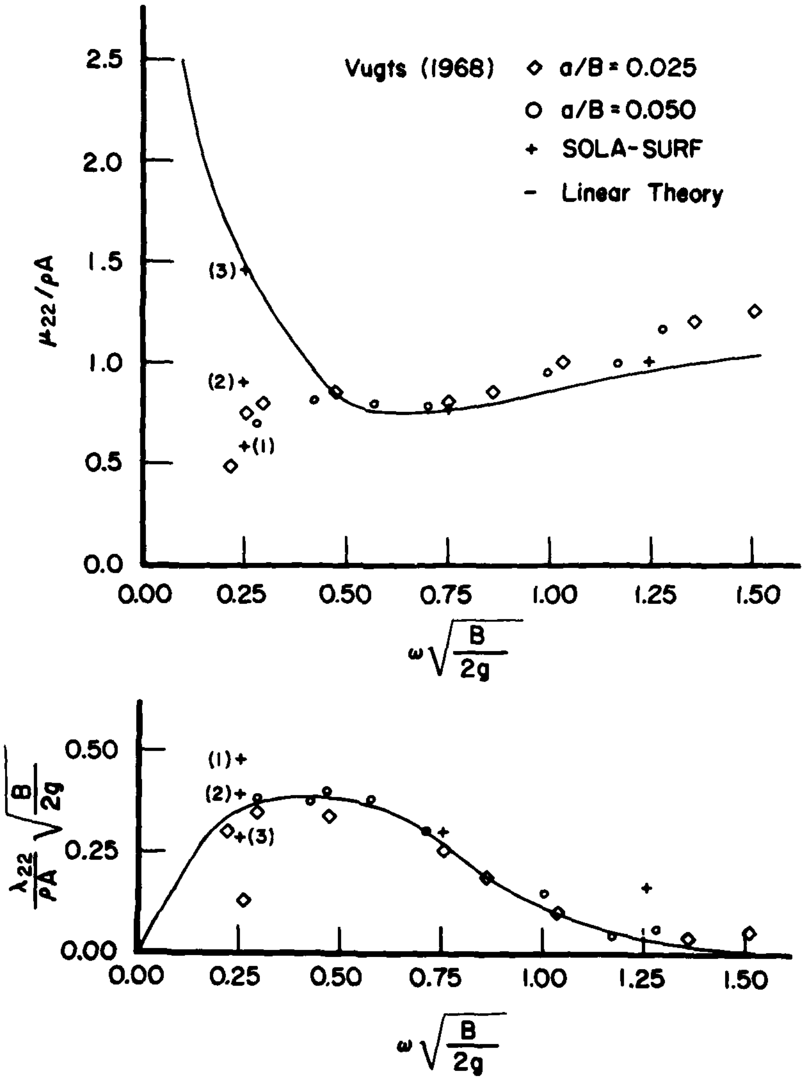

Fig. 3. A comparison of numerically calculated and experimental values of added mass (top) and damping (bottom) coefficients from a rectangular cylinder in forced heave for B/T = 2.0.

Vugts explains this as being caused by experimental inaccuracies. With a normalized fluid depth of 4.0, the calculated coefficient at a frequency of 0.25 is slightly higher than the experiments. (This is the middle point marked (2) in Fig. 3 at this frequency.) However, calculations with a fluid depth of 2.0, marked (1), and a fluid depth of 8.0, marked (3), show clearly that the finite depth is the cause of the disagreement with linear theory. The added mass coefficient for the shallower fluid depth is slightly less than the experimental data, but with the normalized depth of 8.0 the calculated coefficient agrees with the linear theory, which assumes an infinite depth.

These calculations were done using a relatively coarse convergence criterion for solving the implicit pressure equation. Calculation times required from 3 to 15 minutes of CDC-7600 time, depending on the period of oscillation. At the low frequency, that is, $\omega\sqrt{\frac{B}{2g}} = 0.25$, we observed a low amplitude, short wavelength disturbance superimposed on the hydrodynamic force. The disturbance appeared only on the positive increasing side of the force versus time curve, and can be eliminated by tightening the convergence criterion to increase the number of iterations per time cycle from 12 to approximately 60. The average magnitude and period of the force plots were not significantly changed by this, however, indicating that the coarser criterion is sufficient.

We observed some nonlinear effects in these calculations. As the rectangular cylinder is moving upward, a "wake" eddy forms near the bottom edge. On the downward motion this eddy dissipates somewhat as it is pushed from beneath the cylinder, but reforms as the cylinder velocity decreases, as seen in the velocity vector plot in Fig. 4. The development of this secondary flow is expected to increase the damping coefficient somewhat. According to Fig. 3, the calculated results are, in fact, higher than either linear theory or the experimental data. The experimental data at higher frequencies show significantly larger damping coefficients than predicted by the irrotational theory, but significantly smaller than the calculated results. We believe the calculated results are qualitatively correct, but are too large because they over-emphasize the secondary flow effects through numerical diffusion errors.

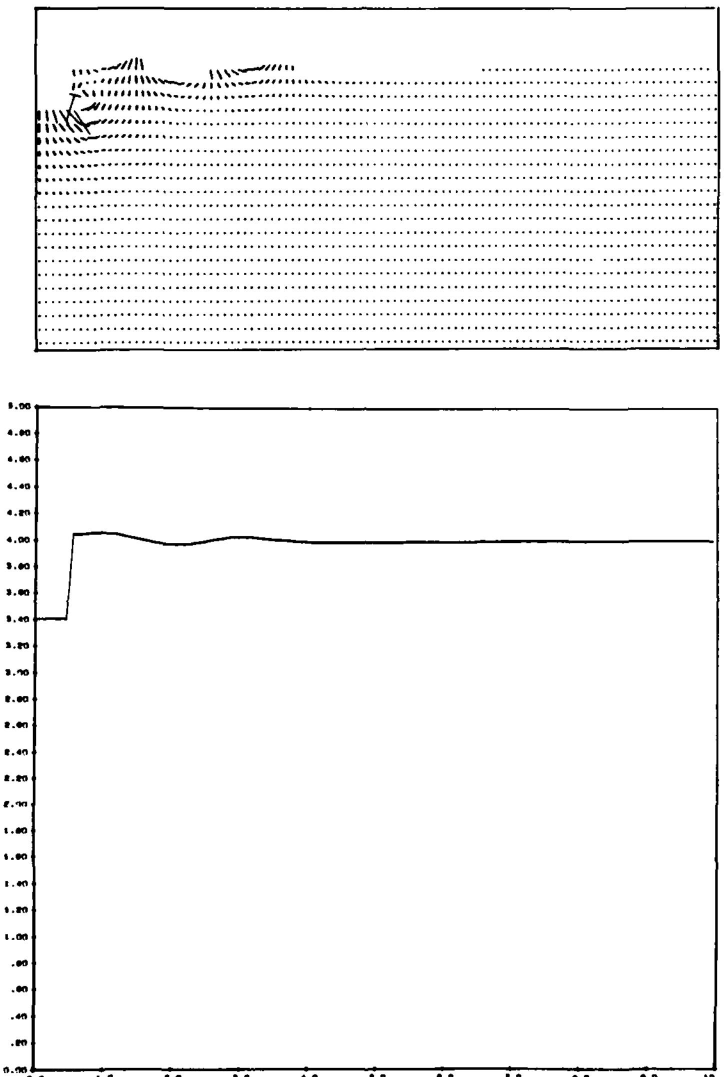

Fig. 4. Velocity vectors of the fluid (top) in which a rectangular cylinder is in forced heave at the left mesh boundary (vectors have their bases aligned on horizontal lines). This velocity field and the free surface configuration (bottom), which has a vertical magnification of 2.0, are after 2.53 periods.

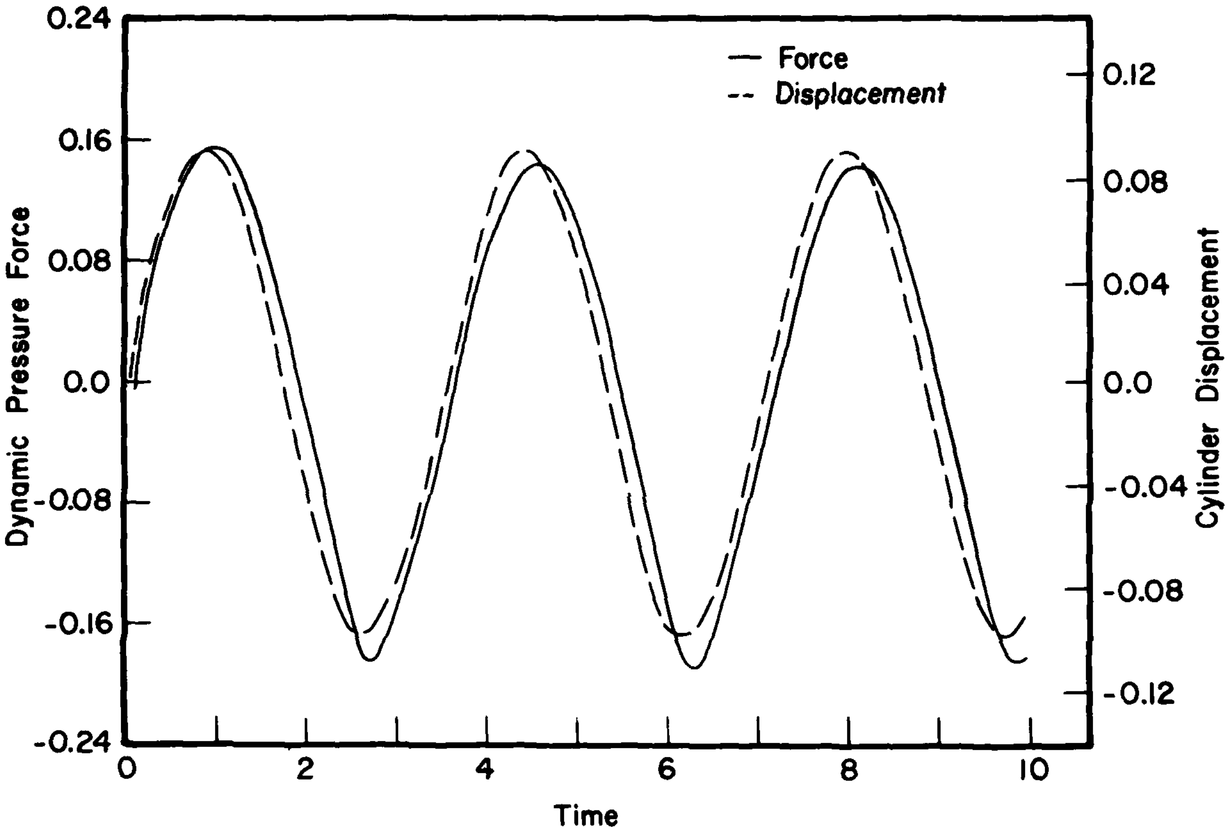

Fig. 5. Hydrodynamic force and cylinder displacement versus time for a rectangular cylinder in forced heave with $\omega\sqrt{\frac{B}{2g}} = 1.25$ and $a = 0.095$.

Another kind of nonlinear effect is responsible for asymmetries observed in the force versus time plot in Fig. 5. This calculation was at a normalized frequency of 1.25, with an amplitude of motion normalized by B of 0.095. At this larger amplitude, the damping coefficient is larger than the value calculated with an amplitude of 0.05, but the added mass coefficient is about the same. It is seen in Fig. 5 that the magnitude of the hydrodynamic force experienced by the cylinder at its maximum elevation is less than the force magnitude it experiences at its minimum elevation. Because the added mass coefficient is principally a reflection of the force amplitude, we can interpret this result as predicting a reduced added mass when the cylinder is at its crest and an enhanced added mass when at its trough. This result is reasonable as there is less fluid surrounding the body when it is raised, hence less that needs to be accelerated, and more when the body is at its low point. Linear theory does not predict this asymmetry because it applies free surface boundary conditions at the initial undisturbed boundary location.

V. Free Surface Definition by Surface Marker Particles

We now consider a scheme to remove the low amplitude restriction in surface deformations. The original Marker-and-Cell method could be directly extended into three dimensions. However, the use of marker particles throughout the fluid volume would be costly and, as already mentioned, the application of boundary conditions at surface cell centers is sufficiently crude that bothersome fluctuations are generated. With these limitations in mind, Nichols (1973) replaced the surface height function technique described in section III with a free surface defined by marker particles. That is, particles are only used on the surface and boundary conditions are applied by interpolation at the surface position. The fluid motion is governed by conservative equations numerically solved with the solution algorithm described in section II.

Marker particles defining a free surface can initially be placed in any configuration within the three-dimensional mesh and are set in a staggered pattern for better surface coverage. For calculations involving inflow and outflow boundaries, particles are input as necessary to maintain coverage of new surface area flowing into the calculational region and are

deleted as they flow from the calculational region.

A volume weighting scheme analogous to the area weighting scheme described by Welch, et al. (1966) is used to obtain interpolated cell velocities to move the surface marker particles. This is straightforward except in the vicinity of obstacles. For each of the three components of velocity, the volume weighting scheme must interpolate between eight neighboring velocities. Cells contiguous to these eight velocities are tested to determine if any are obstacle cells. If such is the case, the component of particle velocity parallel to the obstacle boundary must be determined as if the obstacle cell did not exist. If the component of particle velocity is normal to the obstacle boundary, the velocities used in the interpolation must not allow the particle to move into the obstacle cell.

In regions of large velocity gradients or expanding surface areas particles must be added to ensure uniform surface coverage. To add surface marker particles, an approximate surface plane in each surface cell is determined by first locating the approximate normal to the surface by considering the empty-full cell configuration about the surface cell. This surface plane is then projected onto the horizontal or vertical plane of the cell whose normal vector is closest in angle to the normal vector of the surface plane. This projected surface plane is then divided into 4 equal parts by the rectangular coordinate axes lying in that plane. One particle near the surface cell boundary is chosen from each of the three quadrants containing the most particles. The location of these particles is used to define the approximate plane of the free surface. Particles are added in this plane if the total number of particles in the cell becomes less than some prescribed number, such as half of the number used initially. This scheme functions very well, except in the regions downstream of obstacles and in flow around sharp corners. Without surface marker particles flowing into the cells in these areas, it is difficult to keep enough particles in the cells to accurately define the surface.

The free surface boundary conditions are imposed by setting the normal velocities to satisfy the incompressibility condition in the surface cells and the tangential velocities immediately outside the fluid to ensure zero shear stress. These are the same conditions used in the low amplitude technique described above and are appropriate for inviscid flow.

In the general case, however, there are 64 possible empty-full cell configurations about a surface cell, compared to 16 possibilities in the single valued surface case.

To prooftest this technique, we made a variety of calculations, each of which tested a feature of the method. We have chosen two of these to present here. The grind time for the calculations varied from 2 to 8 ms/cycle/cell. Adequate free surface definition required from 16 to 36 particles per cell, which is 3600 to 8100 particles for a mesh with 15 x 15 cells in a horizontal plane.

The surface configuration resulting from flow over and around a submerged obstacle is shown in Fig. 6. The calculational mesh is composed of 15 x 15 x 8 cells and the obstacle size is 3 x 3 x 3 cells with the initial fluid depth equivalent to 4 cells. A fluid input boundary is at the left and an output boundary is at the right. All other mesh boundaries are rigid and free-slip. The Froude number, based on the input velocity and initial fluid depth, is 2.0. The surface plane in each cell is initially defined by 36 marker particles. The plots are at nondimensional times of 0.0, 0.5, and 1.0, and the calculational time step is 0.1. At each of these times, two perspective-view plots are shown, which are viewed from the same horizontal eye position but different vertical positions. In the plot on the right, the surface observed below the initial height shows the underside of the surface, while the surface above the initial height is the top side of the surface. The free surface and obstacles are transparent in these plots. The deformation of the free surface is caused by the initial impulse of flow past the obstacle and is completely formed by a time of 1.0. This surface deformation agrees qualitatively with the low amplitude calculation of a similar problem shown in Fig. 1.

We calculated flow past a partially submerged blunt body to test the free surface and particle movement boundary conditions near obstacles that penetrate the free surface. The calculational mesh is composed of 16 x 10 x 12 cells and the obstacle size is 10 x 2 x 8 cells located at a plane of symmetry. The draft is initially 2 cells. The fluid input boundary is at the left; the output boundary is at the right. All other boundaries are rigid, free-slip. Free surface configurations resulting from this flow are shown in Fig. 7. The plots are at nondimensional times 0.0, 1.5, 3.0, and

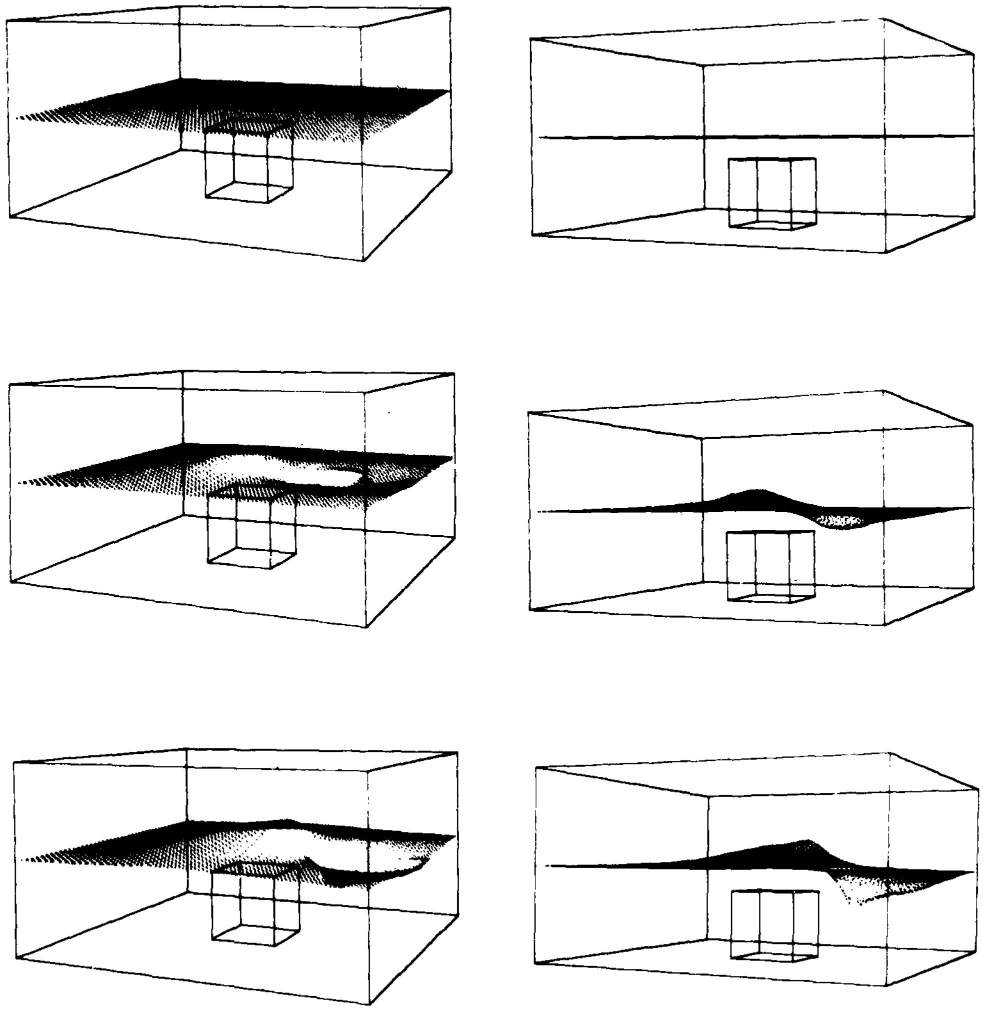

Fig. 6. Perspective views of the free surface configuration resulting from flow, input from the left, over a submerged structure. The right column of plots corresponds in time to those on the left but is viewed from a lower vertical position and shows both the top side and underside of the surface.

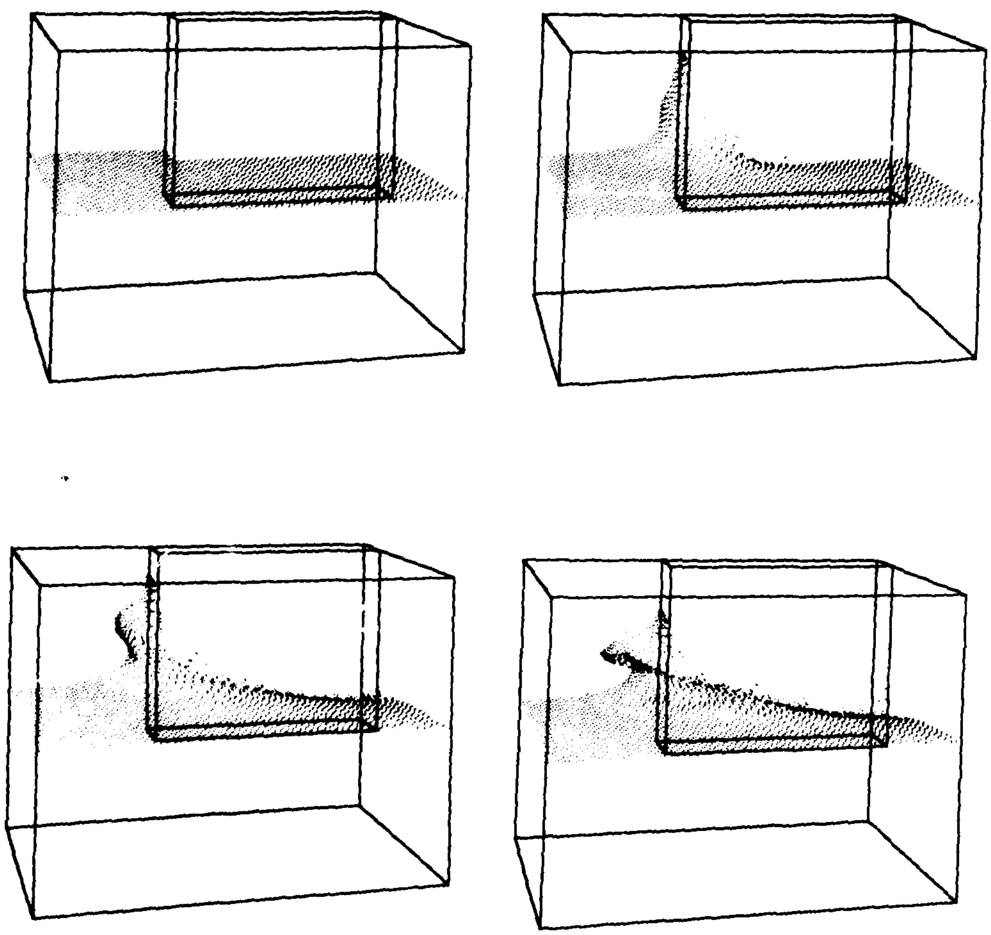

Fig. 7. Perspective views of the free surface configuration resulting from impulsively started flow past a partially submerged blunt body.

4.5, reading from left to right. The calculational time step is 0.1. The draft Froude number, based on the input velocity and obstacle draft, is 2.0. At a time of 1.5, the fluid has reached its maximum height on the obstacle front and has begun to fall back. At a time of 4.5, the fluid is beginning to fold onto the incoming fluid below.

In contrast to the surface height function, this technique is more complicated and less efficient, but does calculate multivalued free surface flows. The free surface is easily defined initially and the surface movement is straightforward, except near interior obstacles. More testing is involved in setting the free surface boundary conditions, because the free surface configuration can be more contorted than the low amplitude method. As described above, the major problem with the technique is in keeping the surface adequately defined in regions of highly contorted flow, especially on the downstream side of obstacle boundaries. This is a useful scheme for some multivalued free surface flows, but in its present form is not suitable in general.

VI. Volume-Fraction Function

Realizing the limitation of the surface height function method and finding the surface marker particle scheme not totally satisfactory, we attempted a method of defining the free surface through a volume-fraction function. This method has the simplicity needed in three-dimensional calculations and does handle highly contorted surfaces. This free surface scheme is used with the solution algorithm described in section II, except for the flagging scheme.

The cell centered volume-fraction function F is the ratio of fluid volume in each Eulerian cell to the cell volume, that is, $F = 1$ in cells full of fluid, $F = 0$ in empty cells, and F has intermediate values in surface cells. The surface is located at $F = 1/2$. The basic equation solved is the convection equation written in conservative form for two space dimensions

$$\frac{\partial F}{\partial t} + \frac{\partial Fu}{\partial x} + \frac{\partial Fv}{\partial y} = 0 .$$

The F function is fluxed out of the positive face of each cell. For example, the F function is fluxed through the positive x-coordinate face of a

cell by

$$V_x = \frac{\delta t\, u}{\delta x} ,$$

where δt is the time increment of the calculation, u is the velocity specified normal to the cell face, in the x-direction, and δx is the cell dimension along this axis. The sign of V_x defines the donor and acceptor cells (that is, the cells losing and gaining fluid volume, respectively). The amount of F fluxed out of this cell face each time step is

$$F = \text{MIN} \left\{ F_{AD} \mid V_x \mid + \text{MAX} \left[(1.0 - F_{AD}) |V_x| - (1.0 - F_D),\ 0.0 \right],\ F_D \right\} ,$$

where the subscripts A and D denote the acceptor and donor cells and AD is either A or D, depending upon the orientation of the interface, as explained below. The "MIN" feature negates fluxing more fluid than is available, while the "MAX" feature assures the fluxing of material from a partially filled cell. The amount of F fluxed is added to the acceptor cell and subtracted from the donor cell. Whether the acceptor or donor cell is used to determine the volume fluxed is dependent upon the orientation of the surface. The acceptor cell is used when the interface is convected normal to itself, and the donor cell is used when the interface is translating parallel with the interface orientation. However, if the acceptor is an empty cell, it is used to determine the flux, regardless of the orientation of the interface, thus allowing the donor cell to fill before any fluid is fluxed into this adjacent, downstream cell.

The values of the function F assigned to each cell serve as a flag, which is used in setting the free surface boundary conditions. The normal velocities are set to satisfy the incompressibility condition in surface cells. The tangential velocities immediately outside the fluid are specified to ensure zero shear stress at the surface. These are the same conditions set for the techniques described in sections III and V.

A useful calculation for testing this scheme, which was written as a two-dimensional code with plane or cylindrical coordinates and variable cell dimension capabilities, was one in which a cylindrical volume of fluid splashed into a quiescent pool. We defined the problem in cylindrical coordinates with the initial fluid volumes set by specifying values for the F function in appropriate cells. The cylindrical drop of fluid was com-

posed of 7 vertical cells with a radius equivalent to 5 cells and the pool was 10 cells deep. There were 40 x 25 cells in the calculational mesh. A grind time of 2.6 ms/cycle/cell was required for this calculation. Many aspects of the code were tested with this problem. First, the calculation demonstrated its ability to calculate a body of fluid falling through space, while maintaining integrity of the body shape. Then, the free surface boundary condition logic and the volume-fraction function flux equations were given a severe test as the bottom surface of the cylindrical drop approached and collided with the free surface of the pool. Finally, momentum from the falling cylinder of fluid was imparted to the fluid in the pool as they coalesced, causing a contorted free surface, thus testing the codes' ability to handle these conditions. Figure 8 shows a sequence of free surface configuration plots for this calculation. Data is not available for direct comparison, but this calculation is in good qualitative agreement with a previous numerical calculation of a spherical drop of equal mass splashing into a shallow pool.

Because the free surface is defined by a cell quantity, this method is inherently less accurate than the other methods discussed. For very contorted free surfaces, setting the surface boundary conditions or selecting the correct F function to convect can become complex. This scheme is much simpler, however, than the surface marker particle treatment.

Attempting to further simplify the free surface treatment, we modified the equations of motion to treat a variable density fluid. The fluid density is normalized to unity, while in the void a very small density (for example, 10^{-6}) is assumed. The donor-acceptor flux scheme is used to convect density in order to maintain sharp density interfaces. This scheme is presently being developed and does show definite promise. This scheme, if successful, will eliminate the explicit setting of the free surface boundary conditions, and will be useful for two fluid problems as well. A similar scheme has recently been developed by Spalding (1975).

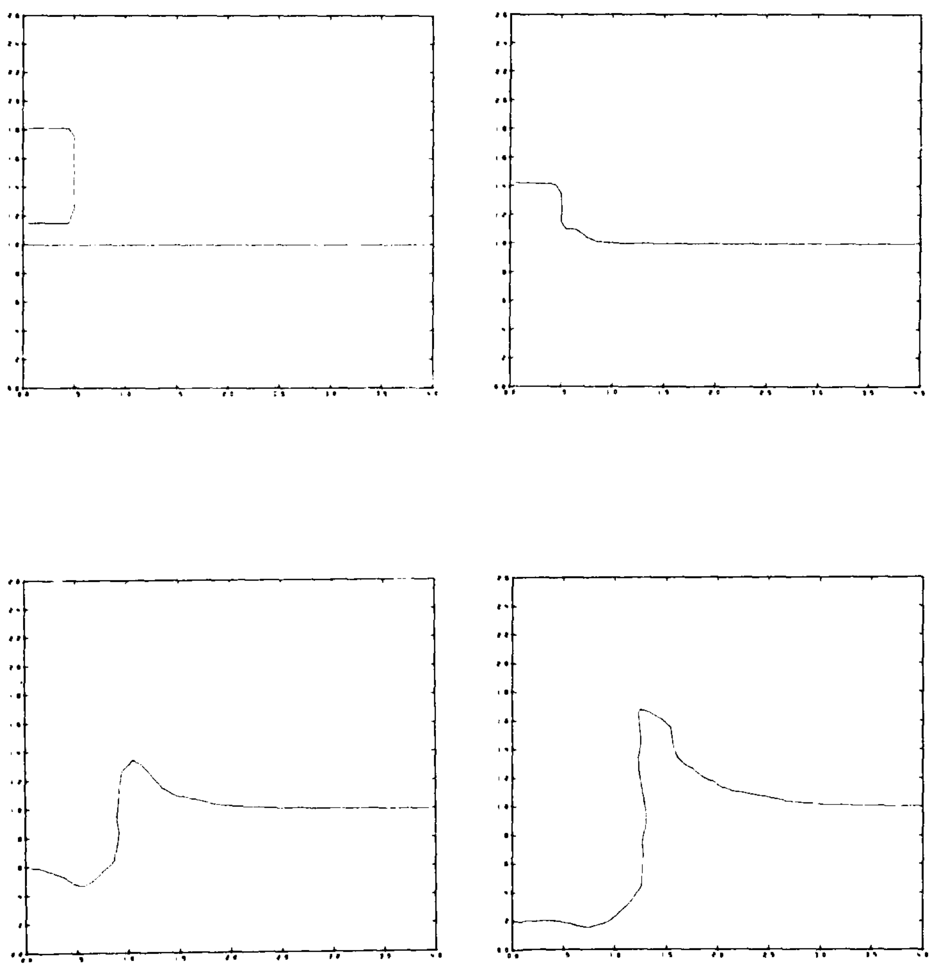

Fig. 8. Free surface configurations resulting from a cylinder of fluid splashing into a pool. Left edge of each frame is an axis of cylindrical symmetry.

Acknowledgment

The authors wish to thank R. K.-C. Chan for his interest and helpful comments on the material presented in this paper. This work was partially supported by the Office of Naval Research, ONR Task #NR 062-455 and by the United States Energy Research and Development Administration.

References

Brennen, C. B. and Whitney, A. K., "Unsteady, Free Surface Flows: Solutions Employing the Lagrangian Description of the Motion," Proceedings of the 8th Symposium on Naval Hydrodynamics, Pasadena, California, 117 (1970).

Chan, R. K.-C. and Street, R. L., "SUMMAC - A Numerical Model for Water Waves," Stanford University Technical report No. 135 (1970); "A Computer Study of Finite-Amplitude Water Waves," J. Comp. Phys., 6, 68 (1970).

Chan, R. K.-C., "A Generalized Arbitrary Lagrangian-Eulerian Method for Incompressible Flows with Sharp Interfaces," J. Comp. Phys., 17, 311 (1975).

Harlow, F. H. and Welch, J. E., "Numerical Calculation of Time-Dependent Viscous Incompressible Flow of Fluid with Free Surface," Phys. Fluids 8, 2182 (1970).

Hirt, C. W., Cook, J. L., and Butler, T. D., "A Lagrangian Method for Calculating the Dynamics of an Incompressible Fluid with Free Surface," J. Comp. Phys., 5, 103 (1970).

Hirt, C. W. and Cook, J. L., "Calculating Three-Dimensional Flows around Structures and over Rough Terrain," J. Comp. Phys., 10, 324 (1972).

Hirt, C. W., Nichols, B. D., and Romero, N. C., "SOLA - A Numerical Solution Algorithm for Transient Fluid Flows," Los Alamos Scientific Laboratory report LA-5852 (1975).

Nichols, B. D. and Hirt, C. W., "Improved Free Surface Boundary Conditions for Numerical Incompressible-Flow Calculations," J. Comp. Phys., 8, 434 (1971).

Nichols, B. D. and Hirt, C. W., "Calculating Three-Dimensional Free Surface Flows in the Vicinity of Submerged and Exposed Structures," J. Comp. Phys., 12, 234 (1973).

Nichols, B. D., unpublished work performed for the Office of Naval Research under contract No. NA-onr-2-73, (1973).

Spalding, D. B., personal communication (1975).

Stein, L. R. and Hirt, C. W., "SOLA-3D: A Solution Algorithm for Transient, Three-Dimensional Fluid Flows," Los Alamos Scientific Laboratory report in preparation (1975).

Viecelli, J. A., "A Method for Including Arbitrary External Boundaries in the MAC Incompressible Fluid Computing Technique," J. Comp. Phys., 4, 543 (1969).

Viecelli, J. A., "A Computing Method for Incompressible Flows Bounded by Moving Walls," J. Comp. Phys., 8, 119 (1971).

Wehausen, J. V., "The Motion of Floating Bodies," Annual Review of Fluid Mechanics, 3, 237 (1971).

Welch, J. E., Harlow, F. H., Shannon, J. P., and Daly, B. J., "The MAC Method, A Computing Technique for Solving Viscous, Incompressible, Transient Fluid-Flow Problems Involving Free Surfaces," Los Alamos Scientific Laboratory report LA-3425 (1966).

Vugts, J. H., "The Hydrodynamic Coefficients for Swaying, Heaving, and Rolling Cylinders in a Free Surface," International Shipbuilding Progress, 15, 251 (1968).

NUMERICAL SOLUTIONS OF TWO-DIMENSIONAL NONLINEAR BODY-WAVE PROBLEMS

N. Salvesen and C.H. von Kerczek

David W. Taylor Naval Ship Research and Development Center
Bethesda, Maryland 20084 U.S.A.

ABSTRACT

Numerical solutions of the nonlinear problem of steady potential flow past a submerged two-dimensional body are obtained by an iterative numerical procedure. The Laplace equation is solved by finite differences in a field bounded by an assumed free-surface shape which is systematically corrected until it satisfies the nonlinear free-surface boundary conditions. Free-surface profiles and wave resistances computed by the numerical method are compared with experimental results. Fairly good agreement is found, but some discrepancies exist which may be related to the Kutta condition.

1. Introduction

In this paper a direct numerical method for solving two-dimensional nonlinear water-wave problems is used to solve the problem of the flow past a submerged foil and comparison of these solutions is made with experimental results. This numerical method which models the exact nonlinear problem of the irrotational flow past a disturbance was first used by von Kerczek and Salvesen[1] to solve the problems of the flow past a submerged vortex and past a free-surface pressure distribution. For the cases solved in [1], the steepness of the waves is so small that the nonlinear effects are of little significance. In fact, the wave steepnesses are all less than one third the steepness shown in the experiments by Salvesen[2] to be on the verge of breaking.

In a continuation of their work, Salvesen and von Kerczek[3] were able to obtain solutions for cases with very steep waves. They obtained results where the maximum $H/\lambda = 0.12$ which is about 15 percent less than the theoretical upper limit and very close to the maximum experimental value for non-breaking waves. For free waves, the maximum theoretical H/λ in potential flow has been computed by various authors to be between 0.141 and 0.145[3] and in Salvesen's experiments[2], the steepest non-breaking waves have $H/\lambda \leqslant 0.11$.

Figure 1 shows the steepest wave obtained in [3], by the numerical method, for uniform flow past a vortex, at submergence depth b, and with positive circulation strength, τ (counter-clockwise circulation). Free-surface elevations predicted by first-, second-, and third-order theories are also given in Figure 1. It is seen that fairly food agreement is obtained between third-order theory and the numerical results even for these very steep waves; there is considerable discrepancy between the numerical results and the results given by both first- and second-order theory.

Figure 2, which is also taken from reference [3] shows the wave resistance as a function of both positive and negative circulation for fixed values of uniform stream velocity, stream depth, and submergence depth of a vortex. It is seen in Figure 2 that the nonlinear effects are much larger than had generally been recognized previously, particularly for the case of negative circulation (clockwise circulation or downward lift force).

For the positive circulation cases, good agreement exists between the numerical and the third-order results in the entire range, whereas the first-order and second-order theories predict wave resistances which are, respectively, up to 30 percent smaller and up to 50 percent larger than those given by the numerical method. For the negative circulation cases shown in Figure 2, good agreement is obtained between the numerical and perturbation predictions of resistance only for very weak vortices. For the stronger negative circulation vortices, large discrepancies exist between the numerical and the third-order as well as the

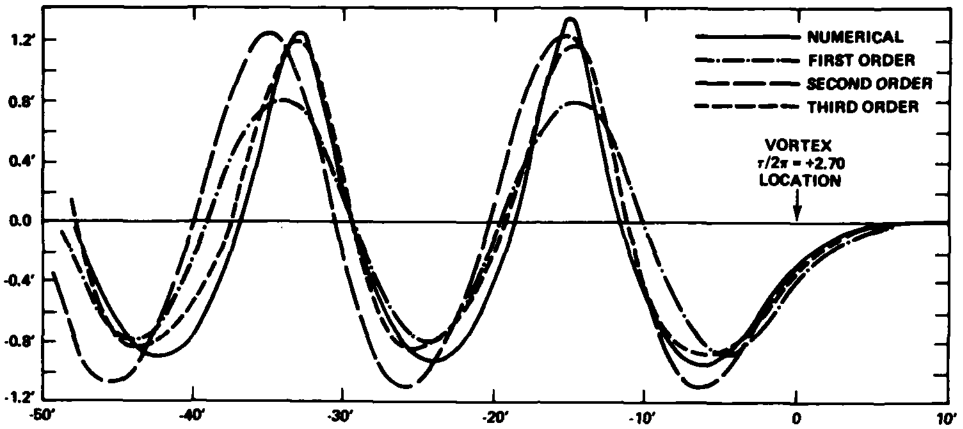

Figure 1 – Wave Elevations Generated by Submerged Vortex (b = 4.5 ft) in Uniform Stream (U = 10 ft/sec)
(Depth is 9.5 ft for numerical results and infinite for analytical results.)

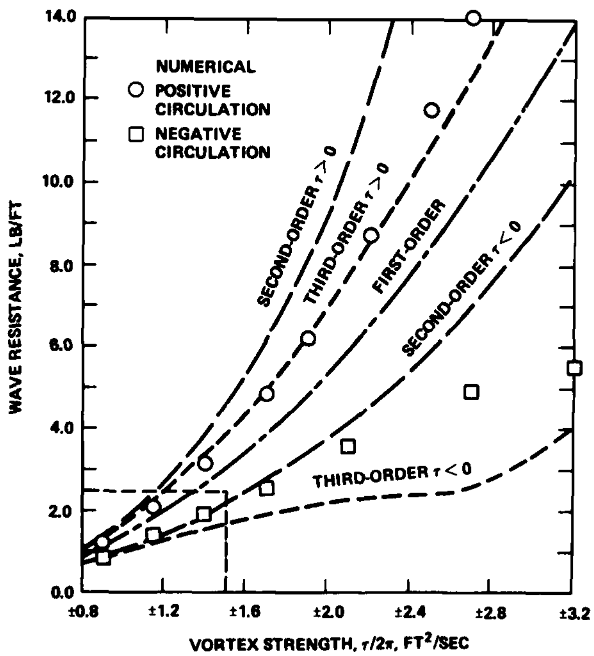

Figure 2 – Wave Resistance as a Function of Vortex Strength
(Uniform stream velocity is 10 ft/sec, vortex submergence is 4.5 ft and depth is 9.5 ft for numerical and infinite for analytical results.)

first- and second-order results. If it is assumed that the numerical predictions are correct, these results seem to indicate that the perturbation method may not converge at all for a vortex with large negative circulation.

From these results, the following overall conclusions are drawn in reference [3]: "The adequacy of perturbation theory for flow past an obstruction depends not only on its strength and the resulting height of the waves left behind, but also on the type of obstruction. The quality of the third-order perturbation theory for the submerged vortex is very different for positive and negative circulation. Most practical applications involving obstructions in a steady-stream would probably behave at least in the far downstream effects like a vortex with positive circulation and hence we might expect that third-order perturbation theory is an adequate approximation for such problems."

In this paper, the application of the numerical method to the flow past a submerged foil is discussed. It is shown that the computed results agree fairly well with experimental results, but there are some discrepancies which may be due to the Kutta condition as used in the potential flow.

2. Mathematical Formulation

An infinitely long cylinder is moving at constant velocity U in a direction perpendicular to its axis in water with uniform depth D and at a fixed distance b below the undisturbed free surface. The problem is to determine the surface waves and the wave resistance, as well as to obtain a description of the complete flow field.

The flow is treated as steady in a coordinate system moving with the body. A two-dimensional coordinate system with the y-axis pointing upward and the x-axis located in the undisturbed free surface with x positive in the direction of motion of the cylinder is shown in Figure 3. It is assumed that the fluid is inviscid, incompressible and without surface tension, and that the flow is irrotational.

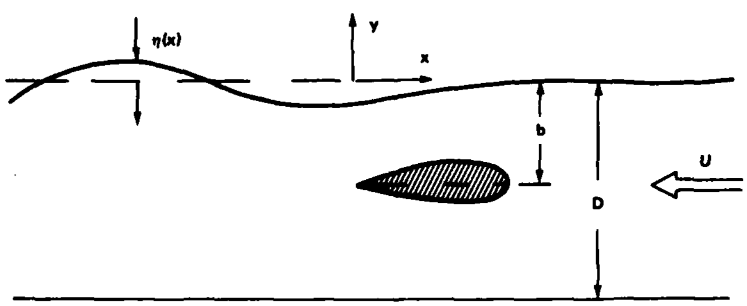

Figure 3 – Coordinate System and Body Orientation

This two-dimensional steady-state potential-flow problem is formulated in terms of a stream function $\psi(x,y)$ which satisfies the Laplace equation

$$\nabla^2\psi = \psi_{xx} + \psi_{yy} = 0 \tag{2.1}$$

everywhere in the fluid domain. The stream function must also satisfy the following boundary conditions: On the unknown free surface, $y = \eta(x)$, the kinematic condition is

$$\psi = 0 \tag{2.2}$$

and the dynamic condition is

$$\frac{1}{2}\left|\nabla\psi\right|^2 + gy = \frac{1}{2}U^2 \tag{2.3}$$

where g is the acceleration of gravity. On the cylinder surface, the condition is

$$\psi = \text{constant} \tag{2.4}$$

where the constant must be chosen so that the Kutta condition is satisfied at the trailing edge of the cylinder. The Kutta condition specifies that the trailing edge is a stagnation point.

Far upstream the flow is assumed to be uniform with no waves so that

$$\lim_{x\to\infty} \vec{k} \times \nabla\psi = -U\vec{i} \tag{2.5}$$

where $\vec{i}$ is the unit vector in the positive x-direction $\vec{k} = \vec{i} \times \vec{j}$ and $\vec{j}$ is the unit vector in the positive y-direction. Far downstream it is assumed that there is a train of periodic waves with as yet unknown wave length λ; hence,

$$\psi(x,y) = \psi(x+\lambda, y) \text{ as } x\to-\infty \tag{2.6}$$

The bottom condition for finite uniform depth D is

$$\psi = -UD \tag{2.7}$$

3. Numerical Method

The problem for ψ as stated in Section 2 is approximated by a finite difference problem obtained for a rectangular grid system overlaying the fluid domain as shown in Figure 4. In the outer region, the grid spacing is approximately one-twentieth of the wave length while a finer grid system with half the spacing is used in the region close to the body. Laplace's equation is approximated by a five-point finite difference equation obtained by approximating the second derivatives by second-order central difference formulae. The flow-field grid is not uniform in the vicinity of both the free surface, and the cylinder surface. The kinematic free-surface condition (2.2), the body condition (2.4), and the bottom condition (2.7) are

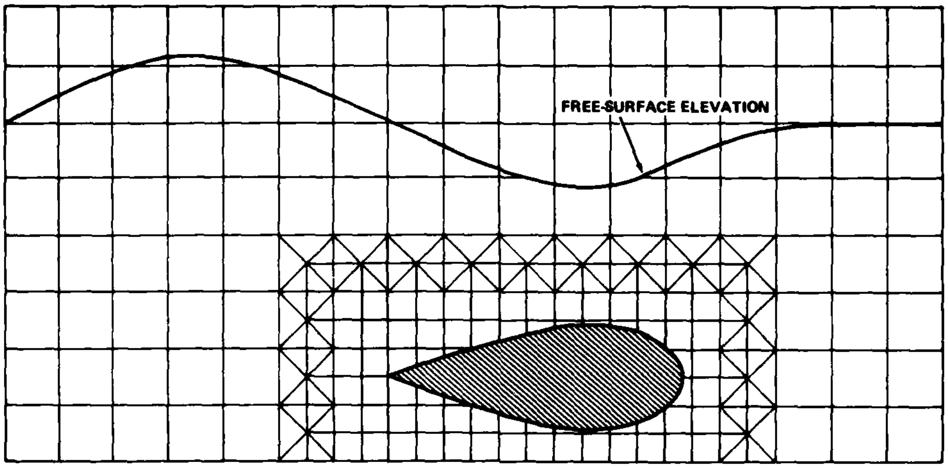

Figure 4 – Finite Difference Grid System

incorporated into the difference method at the points where the grid intersects the boundary.

It is an easy matter to satisfy the body boundary condition (2.4) if the value of the constant required to satisfy the Kutta condition is known. Since it is not known, it is found iteratively as follows. The finite difference field equations are solved iteratively by successive overrelaxation. In the initial relaxation pass through the finite difference field, the value of the stream function ψ at the body grid points, ψ_B, marked B in Figure 5, is given an arbitrary constant value. At the completion of the relaxation pass, the value of the stream function ψ at point K, ψ_K is evaluated using the finite difference form of Laplace's equation and the values of ψ at neighboring points. Then ψ_B is set equal to ψ_K and the next relaxation pass is begun. Upon convergence, the body streamline leaves the body tangent to the trailing edge (thin plate in Figure 5) and thus satisfies the Kutta condition.

The upstream infinity condition (2.5) is applied at a distance of about one wave length ($\lambda_1 = 2\pi U^2/g$)* in front of the body by requiring that the flow be uniform with velocity $-U\vec{i}$ and have a horizontal free surface there. The downstream closure condition is somewhat more difficult since λ is unknown and hence the periodicity condition (2.6) cannot be applied directly. Because the problem is steady and because the upstream boundary condition does not admit waves propagating upstream, it would appear that all that is necessary is that the downstream boundary condition assures the proper mass flux out of the region.

*Note that the actual wave length is unknown so that the wave length used here is the wave length given by first-order theory for infinite depth.

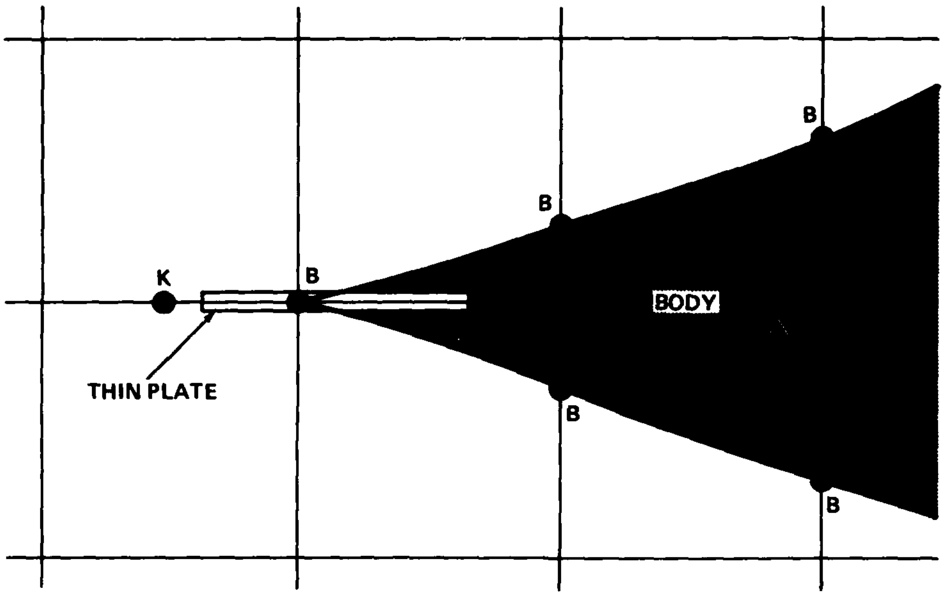

Figure 5 – The Grid System at the Trailing Edge

It has been assumed, therefore, that the field can be truncated at a finite distance downstream of the disturbance and that closure of the finite difference equations can be achieved by setting the value of the stream function ψ, on the last column of grid points, equal to extrapolated values of ψ using grid points immediately upstream. A three-point Lagrange extrapolation formula is used. This downstream closure condition seems to work well and it has been found to affect the accuracy of the computations up to a distance of less than half a wave length in front of the section where it is applied. Computations have shown that the downstream condition can be applied as close as only one and one-half wave lengths behind the body with no discernable effect on the computed forces.

Starting with an assumed free-surface elevation, the field equations are solved by sucessive overrelaxation with an overrelaxation factor of 4/3 on the uniform part of the finite difference grid. After the field equations have been solved, selected test points on the assumed free surface are checked to see if the dynamic free-surface condition (2.3) is satisfied there. In (2.3), the gradient $\nabla\psi$ is approximated by approximating $\partial\psi/\partial y$ with a five-point forward difference formula and the slope of the free-surface by a five-point central difference formula. The assumed free-surface elevation is systematically changed by an iteration scheme until condition (2.3) is satisfied at all of the free-surface grid points.

The problem is then essentially completed. For a detailed description of this procedure, the reader is referred to references [1] and [3].

The final step in the numerical procedure is the determination of the wave resistance of the body. This can be obtained in a variety of ways. The two most convenient ways, which also serve as a consistency check if they agree, are use of the downstream stream function to compute the change of momentum of the fluid as it passes the body and the use of Blasius' theorem integrating along any path enclosing the body.

4. Model Experiments

For the purpose of evaluating the present numerical method, we first considered using the results from the experiments conducted by Salvesen[2] at The University of Michigan. An 11-foot-span asymmetric foil with cross-sectional dimensions twice those given in Figure 6 was used in those experiments. The foil was equipped with endplates which were attached to a carriage, and the tank was 20 feet wide. The ends of the foil and the endplates introduced disturbances so that the waves were two-dimensional for only a relatively short distance behind the body. Furthermore, the foil tested at The University of Michigan had a finite-angle wedge-shaped trailing edge. It was felt that the Kutta condition used in potential theory and discussed in the previous section could be more precisely modeled in a real fluid if the model were equipped with a plate at the trailing edge (see Figure 5) to better simulate potential flow about the trailing edge. Because no precise record of the measured wave elevation from the Michigan experiments was preserved, it was decided to conduct a new set of experiments at the David W. Taylor Naval Ship Research and Development Center (DTNSRDC) using a two-foot strut with cross-sectional dimensions as shown in Figure 6. The major purpose of this new set of experiments was to make a detailed investigation of wave breaking

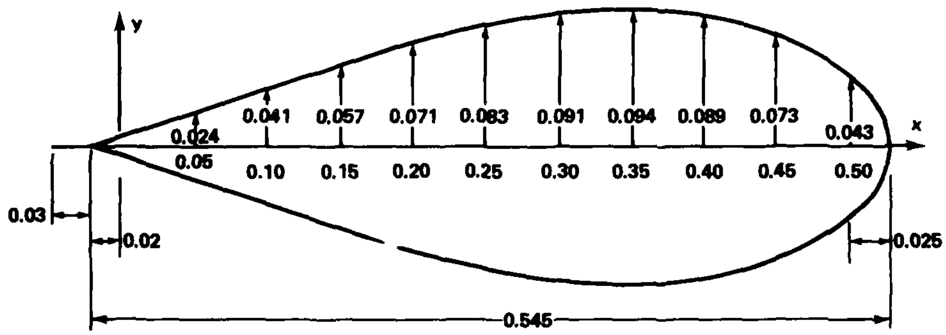

Figure 6 – Cross-Section of Body (dimensions in feet)

in deep water and of nonlinear effects in shallow water; however, these aspects of the experiments will not be discussed here.

The DTNSRDC experiments were conducted in a 40-foot tank with a two-by-two foot cross-section. The foil span is 1'-11 7/8" leaving only a 1/16-inch clearance between the tank side walls and end of the foils. The foil is supported on each side by steel beams which are welded to the sides of the tank at a distance of 1.20 feet above the bottom. In order to minimize the free-surface disturbances generated by the towing system, the foil was towed by a submerged wire running the entire length of the tank. It was found that this configuration generates waves which are fairly uniform across the width of the tank as shown in Figure 7.

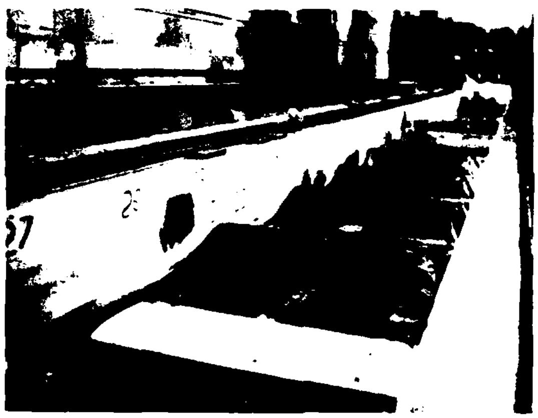

Figure 7 – Actual Test Case with U = 3.38 Ft/Sec and h = 5.50 Inches

The free-surface elevations were measured by both a sonic transducer and a resistance wire probe. Unfortunately, the sonic transducer failed to measure waves steeper than about 12 deg and hence, most of the data used in this report were measured only by the resistance probe. However, the sonic transducer was extremely useful in calibrating and checking the accuracy of the resistance probe. In these experiments, the wave resistance and the lift force were not measured. A more detailed description of these experiments and the results will appear in a forthcoming report.

5. Comparison of Numerical and Experimental Results

Comparisons of numerical and experimental results are presented here for two foil speeds, $U = 3.18$ ft/sec and 3.85 ft/sec. In both cases, the foil submergence $h = 7.50$ inches, and the water depth, $D = 1.825$ feet, were the same. The first-order infinite-depth wave

AD-A119 315 DAVID W TAYLOR NAVAL SHIP RESEARCH AND DEVELOPMENT CE--ETC F/G 20/4
FIRST INTERNATIONAL CONFERENCE ON NUMERICAL SHIP HYDRODYNAMICS --ETC(U)
1975 J W SCHOT, N SALVESEN

UNCLASSIFIED NL

4 OF 8
AD A
119315

length, λ, for the case with U = 3.18 ft/sec is 1.97 feet and for U = 3.85 ft/sec is 2.89 feet, which gives a depth-wave-length ratio, D/λ, of 0.93 and 0.64, respectively. These are sufficiently deep so that they may be considered comparable to infinite depth.

Wave elevation curves obtained by the present numerical method and as measured in the DTNSRDC experiments are shown in Figure 8 for the case of U = 3.18 ft/sec. Results obtained by linear theory following reference [4] are also shown. It is seen that the agreement between the numerical and the experimental results is good with only a small discrepancy in free-surface elevation at the first small hump above the body. We have no explanation for this particular discrepancy. Further downstream it is seen that the agreement is very good. Although not reported here, both the computed and the measured far downstream wave elevations are extremely close to the results shown for the last wave length in Figure 8.

	FIRST CREST	DOWNSTREAM		
	η	η_{max}	η_{min}	λ
LINEAR THEORY	0.079	0.073	0.073	1.97
NON-LINEAR NUMERICAL	0.090	0.089	0.075	1.90
EXPERIMENTAL	0.096	0.088	0.074	1.88
THIRD-ORDER THEORY				1.87

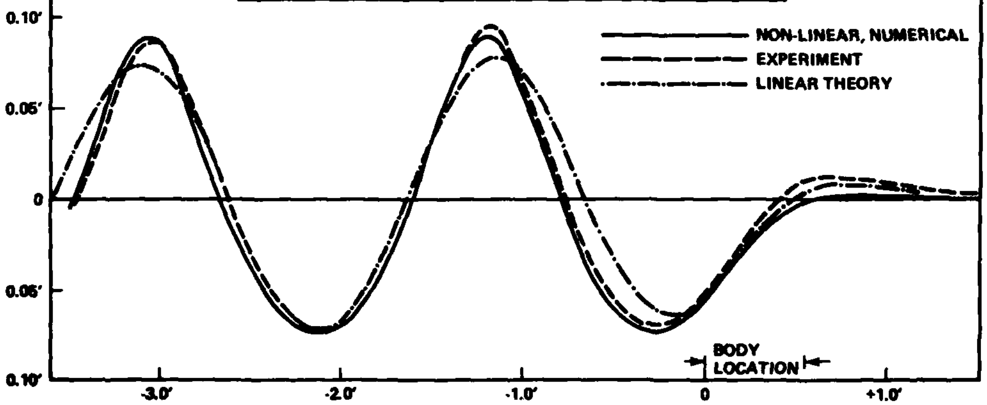

Figure 8 – Wave-Elevation Curves for U = 3.18 Ft/Sec and b = 7.50 Inches

Comparing the wave lengths tabulated in Figure 8, it is seen that the lengths obtained by the numerical method and the experiment agree well and that they are somewhat shorter than given by the linear theory. The third-order theory for Stokes waves predicts the wave length

$$\lambda_3 = \lambda_1 (1 - \nu^2 a^2) \qquad (5.1)$$

where $\lambda_1 = 2U^2/g$ is the first order wave length and a is the first-order wave amplitude. Applying (5.1) to the case presented in Figure 8, we have that λ_3 = 1.87 feet which can be seen from the tabulated values in Figure 8 to be in good agreement with both the numerical and experimental wave lengths.

Table 1 gives the far downstream wave heights obtained by the present numerical method, the DTNSRDC experiments, the University of Michigan experiments, and second-order theory for both foil speeds, U = 3.18 ft/sec and U = 3.85 ft/sec. It is seen that there is only an 0.5 percent difference in wave height between the numerical and the DTNSRDC experiment for the case of U = 3.18 ft/sec, while the difference is about 5 percent for the higher speed case, U = 3.85 ft/sec. This large difference in the discrepancy for these two speeds is surprising. One possible explanation may be that according to reference [4], there is very little lift and cross flow at the lower speed, while there is considerably more lift and cross flow at the higher speed. The Kutta condition as used in the potential flow model requires that the stagnation streamline leaves the body tangent to the trailing edge. Available data shows that because of viscous effects, the lift computed by imposing this Kutta condition can be in error by as much as 20 percent at large (unstalled) angles of attack. Thus, when a free surface is present, one can expect some error in the prediction of wave drag when applying the Kutta condition in potential flow. This may not be the only reason for the larger discrepancy between the numerical and experimental results at the higher speed, U = 3.85 ft/sec; however we believe it is probably the main reason for this difference.

It is interesting to note that there is very good agreement (less than 2 percent difference) between the experimental wave heights measured at DTNSRDC and at The University of Michigan. This close agreement was unexpected, since the foil at DTNSRDC was equipped

TABLE 1
Computed and Experimental Far Downstream Wave Heights for 7.50-Inch Submergence

	Wave Heights			
	Nonlinear Numerical	Experiments DTNSRDC	Experiments U of M[2]	Second-Order Theory[4]
U = 3.18 ft/sec	0.164	0.163	0.160	0.152
U = 3.85 ft/sec	0.180	0.171	0.172	0.152

with a thin plate at the trailing edge as shown in Figure 5, while the foil used at The University of Michigan had an included angle of about 40 deg at the trailing edge. This might mean that there is some separation near the trailing edge and that the plate is merely immersed in the separated region and thus ineffective. These explanations are speculative at the present time, but indicate some of the difficulties involved in comparing potential flow results with experimental results.

Far-downstream wave heights computed by second-order theory[4] are also given in Table 1. It is seen that for the lower speed case, the second-order theory underpredicts the measured wave height by about 7 percent and at the higher speed, the difference is about 11 percent.

The forces on the body are usually of more concern to the designer than the wave profile. While direct force measurements were not made, application of higher-order wave theory and the momentum theorem at any vertical plane far behind the disturbance where the measured waves can be assumed to have the shape of third-order Stokes waves, results in an experimentally-based third-order wave resistance formula;

$$R_3 = \frac{1}{4}\rho g\left(\frac{H}{2}\right)^2\left\{1 - 2\nu^2\left(\frac{H}{2}\right)^2\right\} + O(\epsilon^5) \tag{5.2}$$

where H is trough-to-crest wave height.[3] Similarly, we have the second-order and linear wave resistance formulae

$$R_2 = \frac{1}{4}\rho g\left(\frac{H}{2}\right)^2 + O(\epsilon^4) \tag{5.3}$$

$$R_1 = \frac{1}{4}\rho g\, a^2 + O(\epsilon^3) \tag{5.4}$$

where a is the first-order wave amplitude.

Applying (5.2) and (5.3) to the experimentally measured far-downstream wave heights, H, the wave resistance curves shown in Figure 9 are obtained. (We note that wave-resistance according to the linear theory (5.4) cannot be obtained from experiment.) Figure 9 shows that there is a considerable difference between the wave-resistance curves obtained using second- and third-order formulas (5.3) and (5.2), respectively.

The wave resistance computed by the numerical method using Blasius' theorem is shown as points 1 in Figure 9. The wave resistance obtained by the third-order formula (5.2) using the numerically computed far-downstream wave height, H, is shown as points 2.

The difference between these two methods of computing the wave resistance is about 4 percent at the lower speed and 2.5 at the higher speed. This difference can be due to several sources of error. Bottom effects may introduce a discrepancy because (5.2) is valid only for infinite depth. We expect bottom effects to introduce differences of about 1 percent (see [3]). Third-order theory, rather than exact, can account for an additional part of the discrepancy. However, the most likely cause of the major part of the discrepancy between the two methods of computing wave resistance is that application of Blasius' theorem on a contour close to the body may not be as accurate as obtaining wave resistance from a momentum balance far downstream. This is because the Blasius theorem requires calculation

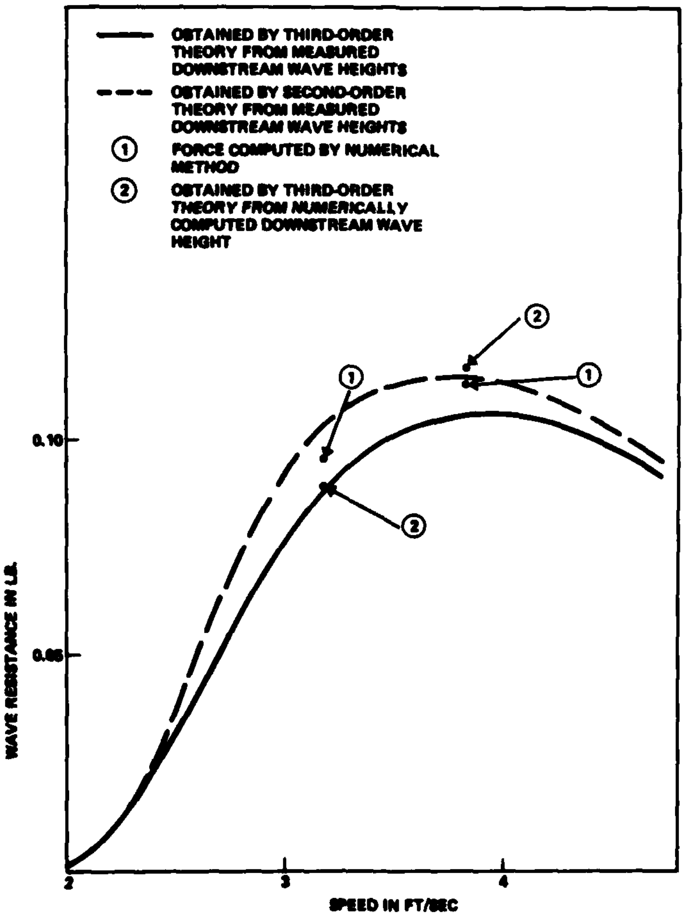

Figure 9 – Wave Resistance as Function of Speed for b = 7.50 Inches

of velocities and hence gradients of ψ very close to the body where this numerical calculation can be inaccurate.

In summary, then, the difference between the wave resistance obtained from the numerical solution of the exact potential problem and that determined from (5.2) using experimental values of H is essentially due to the difference in computed and measured wave heights. We attribute this discrepancy primarily to the difference in the flow around a submerged foil in an inviscid and a viscous fluid. Satisfaction of the Kutta condition in a potential flow simulates only approximately the lifting effect of a foil in a viscous flow.

6. Concluding Remarks

The work described in this paper brings to a conclusion an effort that had two main objectives.

The first objective was to thoroughly test and verify the numerical method[1] for computing steady two-dimensional flow past submerged obstacles by extensive comparison with analytical and experimental results. In [1] we described this method in detail and made some preliminary comparisons with perturbation theory to show that the method did indeed seem to solve nonlinear body-wave problems. The subsequent study reported in [3] explored the numerical method further for problems in which the wave height to length ratios approached, within 15 percent, the theoretical maximum where nonlinear effects are prominent. Consistency of our numerical results with other numerical solutions of irrotational free waves gives us confidence that the numerical method yields accurate results, within 2 or 3 percent, for the nonlinear potential problems considered.

As a result of the confidence established in the numerical method, our second objective was to use the method to test the adequacy of perturbation theory. It has been found in [3] that even third-order perturbation theory can be inaccurate in some cases. This depends more on the type of disturbance than its severity (by severity we mean the height of the waves left behind). The present paper continues the evaluation of certain aspects of perturbation theory and evaluates exact potential theory as a model for real viscous flow around a foil. We find that the exact potential flow model gives good approximations except for some small discrepancies in the forces on the foil which may be due to viscous effects.

This discrepancy is mainly associated with the lift produced by the foil and hence emphasizes the approximate nature of the potential flow circulation model for lifting effects in a viscous fluid.

Acknowledgment

The authors wish to express their appreciation to Ms Nancy C. Groves for assisting us with the computer work, to Dr. Thomas Langan for helping us with the experiment and to Mr. John Hess of Douglas Aircraft Co. for an enlightening discussion concerning the Kutta condition. This work has been supported by the Numerical Naval Hydrodynamics Program at the David W. Taylor Naval Ship Research and Development Center. This program is jointly sponsored by the Office of Naval Research, the Naval Sea Systems Commands, and DTNSRDC.

REFERENCES

[1] von Kerczek, C.H. and N. Salvesen, "**Numerical Solutions of Two-Dimensional Nonlinear Wave Problems,**" ONR 10th Naval Hydrodynamics Symposium, Cambridge, Mass. (1974)

[2] Salvesen, N., "**Second-Order Wave Theory for Submerged Two-Dimensional Bodies,**" ONR 6th Naval Hydrodynamics Symposium, Wash., D.C., pp. 595-636 (1966)

[3] Salvesen, N. and C.H. von Kerczek, "**Comparison of Numerical and Perturbation Solutions of Two-Dimensional Nonlinear Water-Wave Problems,**" to appear in Journal of Ship Research (1976).

[4] Salvesen, N., "**On Higher-Order Wave Theory for Submerged Two-Dimensional Bodies,**" Journal of Fluid Mechanics, Vol. 38, Part 2, pp. 415-423 (1969)

FINITE-DIFFERENCE METHODS FOR TRANSIENT POTENTIAL FLOWS WITH FREE SURFACES

H.J. Haussling and R.T. VanEseltine

David W. Taylor Naval Ship Research and Development Center
Bethesda, Maryland 20084 U.S.A.

ABSTRACT

Finite-difference methods have been developed for the treatment of transient potential flow problems associated with water waves. The marching scheme couples a solution of the Laplace equation with numerical approximations to the time-dependent free-surface boundary conditions. Two methods have been studied for treating the Laplace equation, a series expansion technique and a finite-difference scheme.

1. Introduction

In recent years there has been considerable interest in the numerical solution of free-surface flow problems. One popular technique is the marker-and-cell (MAC) method[1] in which finite differences are employed to find approximate solutions to the Navier-Stokes or Euler equations for viscous or inviscid flows. In an alternative approach for inviscid flows numerical schemes are used to solve potential-flow problems.

Easton and Catton[2] surveyed a series of papers reporting results for transient nonlinear free-surface potential flows in containers. These results were obtained with a combination of spectral and finite-difference methods. Multer[3] used a similar scheme for transient nonlinear potential flows in a wave generator. Bai[4] has obtained periodic two-dimensional linear solutions for a variety of potential-flow problems using a finite-element method. Von Kerczek and Salvesen[5] used finite differences to solve steady-state nonlinear wave problems. Chan and Hirt[6] reported on transient potential-flow solutions for the motion of floating bodies. They investigated nonlinear effects through the use of Taylor series expansions about the mean level of the free surface.

In a previous paper[7] the present authors reported on a combined spectral finite-difference method for two-dimensional, transient, linear and nonlinear free-surface potential flows of both contained and uncontained fluids. The method involved extensions and modifications of the method discussed by Easton and Catton.[2] Recently a pure finite-difference scheme has been considered and applied to two- and three-dimensional linear and nonlinear problems.

In this paper the basic features of both the spectral and finite-difference methods are outlined and results presented. Indications are that these two methods yield accurate solutions to the problems considered. The finite-difference scheme seems the more desirable for general use chiefly because of its flexibility. Higher-order finite-difference schemes and expanding grid systems are easily employed.

2. Mathematical Formulation

The problem on which the schemes are tested concerns the flow generated by a pressure disturbance moving across the free surface. A right-handed (x,y,z)-coordinate system is chosen with the origin in the undisturbed free surface. The y-axis points upward and the x-axis points in the direction opposite to the movement of the pressure disturbance. The coordinate system moves with the disturbance. The region of non-constant surface pressure is of length L in the x-direction and has a width-to-length ratio of b. In this study the values of b considered are $b=1$ and $b=\infty$. Initially the disturbance is at rest over a motionless fluid and is then accelerated impulsively to a constant speed U. The formulation presented here applies to this particular problem but can easily be extended to more general cases.

It is assumed that the flow is irrotational and that the fluid is incompressible and lacks surface tension. The flow takes place in a region bounded by $x = \pm\infty$, $z = \pm\infty$, a solid boundary at $y = -d$ where d may be infinite, and a free surface. It is assumed that the surface elevation can be described at any time t by specifying y as a single-valued function of x and z: $y = \eta(x,z,t)$.

The variables are nondimensionalized according to the scheme

$$(x', y', z') = L(x,y,z) \qquad t' = \frac{L}{U}t$$
$$\phi' = LU\phi \qquad p' = Pp \qquad \eta' = L\eta \tag{1}$$

where the primes denote dimensional variables, $\phi(x,y,z,t)$ is the velocity potential relative to a non-moving reference frame, p is pressure, and P is the maximum pressure in the surface distribution.

The initial/boundary-value problem in the moving reference frame is written in the form

$$\phi_{xx} + \phi_{yy} + \phi_{zz} = 0 \qquad -\infty<x<\infty,\ -d<y<\eta,\ -\infty<z<\infty \tag{2}$$

$$\eta_t = -U\,\eta_x - \phi_x\eta_x - \phi_z\eta_z + \phi_y \qquad \text{at } y = \eta \tag{3}$$

$$\phi_t = -U\,\phi_x - \frac{1}{Fr^2}\eta - \frac{1}{2}(\phi_x^2+\phi_y^2+\phi_z^2) - \frac{\delta}{Fr^2}p \quad \text{at } y = \eta \tag{4}$$

$$\phi_x = 0 \qquad \text{at } x = \pm\infty \tag{5}$$

$$\phi_z = 0 \qquad \text{at } z = \pm\infty \tag{6}$$

$$\phi_y = 0 \qquad \text{at } y = -d \tag{7}$$

$$\phi = 0,\ \eta = -\delta p \qquad \text{at } t = 0 \tag{8}$$

where subscripts x, y, z, and t denote differentiation. The dimensionless parameters are $Fr = U/\sqrt{gL}$, the Froude number based on L, and $\delta = P/\rho gL$. The gravitational acceleration is denoted by g and ρ is the constant density. The second parameter δ can be regarded as the ratio of two length scales. The length $P/\rho g$ is the hydrostatic surface displacement caused by the surface pressure P. The initial surface elevation in Equation (8) is the hydrostatic displacement due to the pressure disturbance.

The disturbance is assigned one of two forms:

$$p(x,y{=}\eta,z) = \begin{cases} \sin^2(\pi(x-x_0)) & x_0\le x\le x_0+1,\ -\infty<z<\infty \\ 0 & \text{otherwise} \end{cases} \tag{9}$$

or

$$p(x,y{=}\eta,z) = \begin{cases} \sin^2(\pi(x-x_0))\sin^2(\pi(z-\frac{1}{2})) & x_0\le x\le x_0+1,\ -\frac{1}{2}\le z\le\frac{1}{2} \\ 0 & \text{otherwise} \end{cases} \tag{10}$$

where x_0 defines the location of the disturbance relative to the origin of the coordinate system. The distribution of Equation (9) generates a two-dimensional flow.

Energy conservation serves as a useful check on the validity of numerical solutions. The kinetic and potential energies (per unit length in the 2-D case) are nondimensionalized with respect to $\rho L^3U^2(\rho L^2U^2)$ and the wave resistance is normalized with respect to $\rho L^2U^2(\rho LU^2)$. Formulas for the kinetic and potential energies of the fluid, the rate of work performed by the pressure on the fluid, and the resistance experienced by the pressure to its movement across the fluid are

$$KE = \frac{1}{2}\int\int \{\phi(\phi_y - \phi_x\eta_x - \phi_z\eta_z)\}_{y=\eta}\, dxdz \tag{11}$$

$$PE = \frac{1}{2Fr^2}\int\int \eta^2\, dxdz \tag{12}$$

$$W = -\frac{\delta}{Fr^2}\int\int \{p(\phi_y - \phi_x\eta_x - \phi_z\eta_z)\}_{y=\eta}\, dxdz \tag{13}$$

and

$$R = -\frac{\delta}{Fr^2}\int\int p(y=\eta)\eta_x\, dxdz \tag{14}$$

respectively. The total energy is then expressed by $E \equiv KE+PE$. Energy conservation is represented by

$$W = \frac{dE}{dt} \tag{15}$$

When wave slopes are small, the linearized surface boundary conditions

$$\left.\begin{aligned} \eta_t &= -U\,\eta_x + \phi_y \\ \phi_t &= -U\,\phi_x - \frac{1}{Fr^2}\eta - \frac{\delta}{Fr^2}p \end{aligned}\right\} \text{ at } y = 0 \tag{16}$$

often provide sufficient accuracy.

3. Numerical Schemes

The Nonlinear Numerical Methods

As the first approximation for the numerical schemes, the boundary conditions of Equations (5) and (6) are replaced by

$$\begin{aligned} \phi_x &= 0 \quad \text{at} \quad x = \pm L_1/2 \\ \phi_z &= 0 \quad \text{at} \quad z = \pm L_2/2 \end{aligned} \tag{17}$$

The error introduced by replacing the boundary conditions at infinity with those of Equation (17) is small if L_1 and L_2 are large. In the two-dimensional case $L_2 = \infty$.

The nonlinear methods have been applied to two-dimensional examples. For simplicity, the formulation is presented for two dimensions. The extension to three dimensions is straightforward.

The computational region is displayed in Figure 1. The complexity and time dependence of the upper boundary are the cause of much of the difficulty connected with the solution of the nonlinear problems.

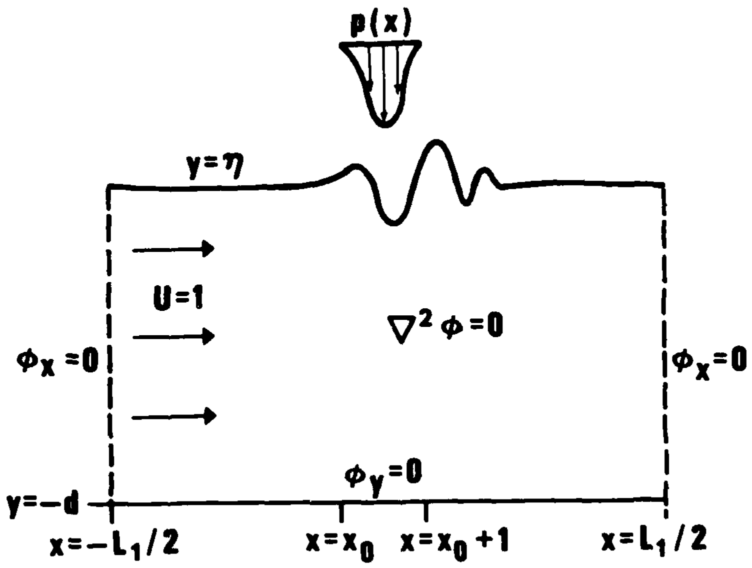

Figure 1. The Two-Dimensional Computational Region in a Reference Frame Moving with the Pressure Distribution.

The procedure for advancing the solution in time consists of two basic parts. The first concerns the solution of the Laplace equation (2) given η and subject to the boundary conditions of Equations (7), (17) and

$$\phi(y=\eta) = \phi_s \tag{18}$$

where ϕ_s represents the values of ϕ on the free surface which are considered to be known at this step. Two methods are considered for solving this Laplace problem: a spectral method and a finite-difference approach.

The spectral approach was previously described by Haussling and VanEseltine.[7] Briefly, a series expansion which satisfies Equations (2), (7), and (17) is assumed for the potential

$$\phi(x,y,t) = \sum_{n=0}^{\infty} C_n(t)\cosh\frac{n\pi(y+d)}{L_1}\cos\frac{n\pi(x+L_1/2)}{L_1} \tag{19}$$

The C_n's are then chosen such that the free-surface conditions of Equations (3) and (4) and the initial conditions of Equation (8) are satisfied. The free surface is represented by a series of grid points located at $x = -L_1/2 + (i-1)\Delta x$ with $i=1,\dots,M_x$. The series of Equation (19) is truncated and evaluated at the surface such that

$$\phi_s \simeq \sum_{n=0}^{N} C_n(t)\cosh\frac{n\pi(\eta+d)}{L_1}\cos\frac{n\pi(x+L_1/2)}{L_1} \tag{20}$$

The C_n's are then chosen to minimize the mean square error of the approximation (20) over the M_x grid points. This leads to the problem of solving an NxN positive definite system of linear algebraic equations for the N C_n's.

In the finite-difference method the following transformation is applied

$$\xi = y+d/(\eta(x,t) + d) \tag{21}$$

This maps the original computational region into a time-invariant region in the (x,ξ)-plane as shown in Figure 2. In the (x,ξ)-coordinate system

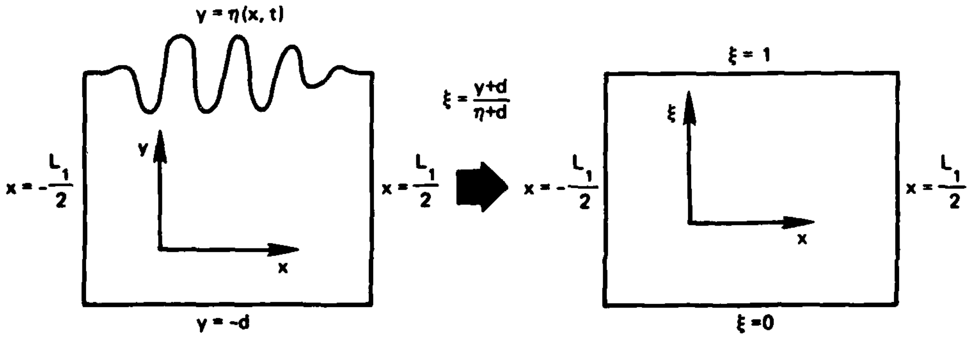

Figure 2. Transformation from (x,y)-space to (x,ξ)-space.

the two-dimensional counterparts of Equations (2)-(7) take the form

$$\phi_{xx} + (1+\xi^2\eta_x^2)\phi_{\xi\xi}/(\eta+d)^2 + \xi(2\eta_x^2/(\eta+d)-\eta_{xx})\phi_\xi/(\eta+d) - 2\xi\eta_x\,\phi_{x\xi}/(\eta+d) = 0 \tag{22}$$

$$\eta_t = (-U + \phi_x - \eta_x\phi_\xi/(\eta+d))\eta_x + \phi_\xi/(\eta+d) \qquad \text{at } \xi = 1 \tag{23}$$

$$\phi_t = -U(\phi_x - \eta_x\phi_\xi/(\eta+d)) - \eta/Fr^2 - (\phi_x-\eta_x\phi_\xi/(\eta+d))^2/2 - \phi_\xi^2/(\eta+d)^2 - \delta p/Fr^2 + \eta_t\phi_\xi/(\eta+d) \quad \text{at } \xi = 1 \tag{24}$$

$$\phi_x - \xi\,\eta_x\,\phi_\xi/(\eta+d) = 0 \qquad \text{at} \quad x = -L_1/2 \tag{25}$$

$$\phi_x - \xi\,\eta_x\,\phi_\xi/(\eta+d) = 0 \qquad \text{at} \quad x = L_1/2 \tag{26}$$

$$\phi_\xi = 0 \qquad \text{at} \quad \xi = 0 \tag{27}$$

In experiments with the spectral approach an instability arising at the upstream boundary was encountered. This instability was removed through the application of a weak pressure at the intersection of the surface with this boundary. It was found that the effects of this instability are absent if the upstream boundary is sufficiently far from the region of interest. With the finite-difference method an additional transformation of coordinates can be carried out so that the upstream boundary is removed from the region of interest through use of an expanding grid system. The transformation

$$x = \ell - e^{-\zeta} + 1 \qquad \zeta \le 0 \tag{28}$$

is applied for $-L_1/2 \le x < \ell$ and in this region Equations (24)-(27) are written in terms of ζ and ξ before being replaced by finite-difference approximations. The domain of integration is replaced by a uniformly spaced $M_x \times M_y$ grid system in the (x,ξ) and (ζ,ξ) planes. Equation (22) and its counterpart within the expanding grid are replaced by difference equations involving variables at the grid points. Standard second-order central difference schemes are employed. One-sided second-order difference

schemes are used to simulate the boundary conditions of Equations (25)-(27). At the surface

$$\phi_{i,j=1} = \phi_{s,i} \tag{29}$$

where i refers to the x (or ζ)-location of the grid point and j refers to the ξ-location with j=1 corresponding to the free surface ξ=1. For convenience Gauss-Seidel successive overrelaxation is used to solve the resulting system of equations.

The second basic part of the over-all marching scheme deals with the advancement of η and ϕ_s in time according to the 2-d forms of Equations (3) and (4) under the spectral approach or to Equations (23) and (24) when the finite-difference scheme is used for the interior of the fluid. Euler's modified method is used to replace these differential equations by difference equations of the form

$$\left.\begin{aligned} \eta_i^{m+1} &= \eta_i^m + \frac{\Delta t}{2}\left(F_i^{m+1} + F_i^m\right) && (30) \\ \text{and} \qquad & \\ \phi_{s,i}^{m+1} &= \phi_{s,i}^m + \frac{\Delta t}{2}\left(G_i^{m+1} + G_i^m\right) && (31) \end{aligned}\right\} 1<i<M_x$$

where the superscripts refer to time levels, Δt is the time increment, and F_i and G_i are approximations to the right-hand sides of the free-surface boundary conditions. When the spectral method is employed, the quantities ϕ_x and ϕ_y which appear in Equations (3) and (4) are found by differentiating the series of Equation (20). Otherwise derivatives are approximated with difference schemes. Second-order central spatial differencing was used initially for approximating ϕ_x and η_x. However, it was found that use of third-order upstream differencing, namely

$$\eta_{x_i} = (2\eta_{i+1} + 3\eta_i - 6\eta_{i-1} + \eta_{i-2})/6\Delta x \tag{32}$$

and

$$(\phi_x)_{s,i} = (2\phi_{s,i+1}+3\phi_{s,i}-6\phi_{s,i-1}+\phi_{s,i-2})/6\Delta x \tag{33}$$

at time level m+1 combined with downstream differencing

$$\eta_{x_i} = (-2\eta_{i-1} - 3\eta_i + 6\eta_{i+1} - \eta_{i+2})/6\Delta x \tag{34}$$

and

$$(\phi_x)_{s,i} = (-2\phi_{s,i-1} - 3\phi_{s,i} + 6\phi_{s,i+1} - \phi_{s,i+2})/6\Delta x \tag{35}$$

at level m is effective in increasing the stability of the over-all scheme and thus allowing longer time integrations.

Equations (30) and (31) are solved iteratively. The iterative solution of these equations is combined with the solution of the Laplace equation. An updating of η and ϕ_s according to Equations (30) and (31) is followed by an updating of ϕ below the surface, either by computing new C_n's, if the series expansion is employed, or by carrying out one sweep of the mesh in the finite-difference approach. Latest values are used as soon as they are available. Before the iteration procedure is started initial estimates of η_i^{m+1} and $\phi_{i,j}^{m+1}$ are obtained by extrapolating from previous time levels. The iteration process is halted after the k^{th} iteration when

$$|\eta_i^{k+1} - \eta_i^k| < \varepsilon_1 \, |\eta_i^{k+1}| \tag{36}$$

for all i where $|\eta_i^{k+1}| > \varepsilon_2$. The numbers ε_1 and ε_2 can be chosen such that the desired accuracy is achieved.

The procedure for advancing the quantities in time is carried out repeatedly to simulate the flow development with the initial conditions of Equation (8) serving as the starting point. The kinetic energy, potential energy, rate of work, and resistance are computed from Equations (11)-(14) by numerical integration. The rate of change of energy is computed according to the scheme

$$\frac{dE^m}{dt} = (3E^m - 4E^{m-1} + E^{m-2})/2\Delta t \tag{37}$$

and is compared with the rate of work as a check on the energy conservation property of Equation (15).

Linear Numerical Methods

Although the particular problems being considered can be solved exactly by analytic methods in the linearized case,[8] it is useful to investigate the properties of the numerical methods when they are applied to the linear equations. Many of the hurdles to be overcome in the nonlinear

case occur in the linear case as well and can be dealt with more easily in the absence of nonlinear complications. Also, a numerical method which works well for the linear problems considered here may be useful on other linear problems where exact solutions do not exist or are difficult to evaluate.

The fact that the linear boundary conditions of Equation (16) are applied at $y=0$ rather than at $y=\eta$ greatly simplifies the computations. In the spectral approach the C_n's become Fourier coefficients and the N x N system of equations is replaced by the direct computation of N of these coefficients. In the finite-difference approach the transformation of Equation (19) is no longer necessary and the standard Laplace equation is solved in a region bounded by plane surfaces. Both second-order and fourth-order finite-difference schemes have been applied to the two-dimensional linear problem. The fourth-order method employs the well-known nine-point scheme for the Laplace equation

$$\begin{aligned}\phi_{i,j} = &(\phi_{i+1,j+1} + \phi_{i-1,j+1} + \phi_{i+1,j-1} + \phi_{i-1,j-1})/20 \\ &+(\phi_{i+1,j} + \phi_{i-1,j} + \phi_{i,j+1} + \phi_{i,j-1})/5\end{aligned} \tag{38}$$

which requires equal mesh spacing in the x- and y-directions.

The use of the pressure distribution of Equation (10) necessitates the approximate solution of the full three-dimensional initial/boundary-value problem. The methods discussed above can be extended directly to the 3-d case. The chief difficulty is in obtaining an accurate scheme which can be applied to 3-d problems without excessive use of computer time. To achieve such a scheme for the 3-d linear problem a direct fourth-order Laplace solver developed by Ohring[9] is combined with fourth-order approximations to the spatial derivatives at the free surface. The Euler modified iterative method is retained for the time advancement. The symmetry about $z=0$ allows the restriction of the computation to $0 \le z \le L_2/2$.

4. Results

Two-Dimensional Motion

The linear and nonlinear schemes were tested on the two-dimensional

flows generated by the pressure distribution of Equation (9). Two Froude numbers were considered, Fr = $(4\pi)^{-1/2}$ and Fr = $(2\pi)^{-1/2}$. Time histories of the surface elevations are displayed in Figures 3 and 4 for the linear problems with δ = 0.01 and d = 100 as computed with the spectral method. It

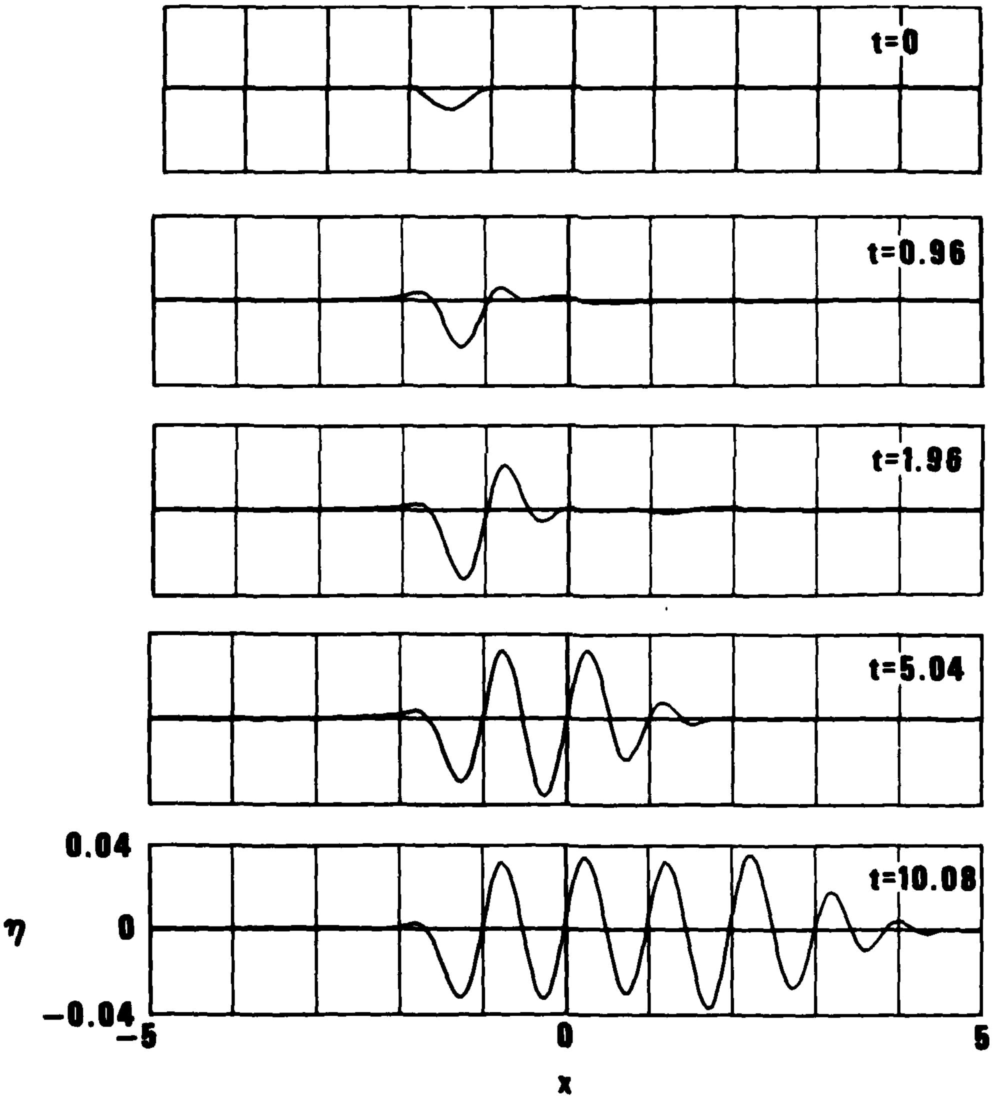

Figure 3. Sequence of Surface Elevations for Fr = $(2\pi)^{-1/2}$, δ = 0.01 as Computed with the Linear Spectral Method.

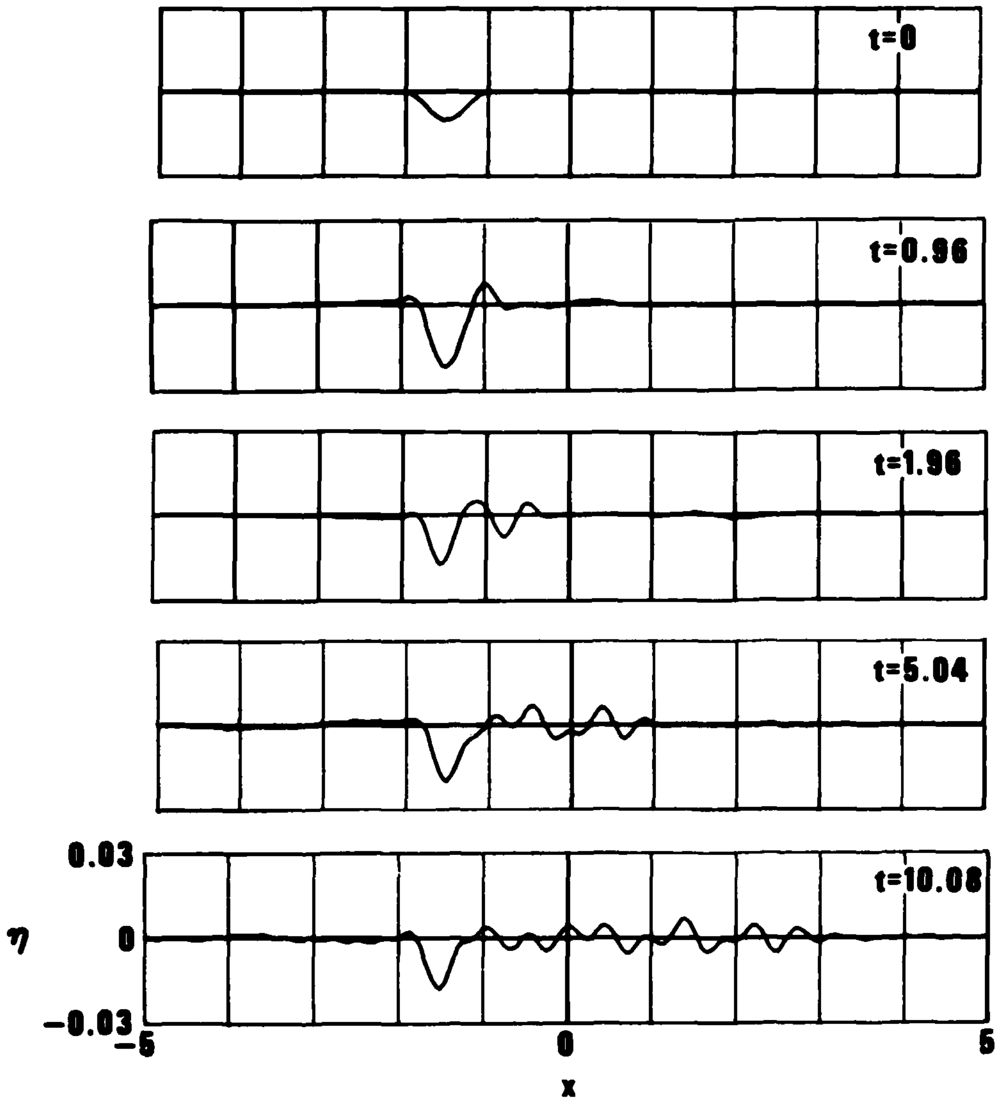

Figure 4. Sequence of Surface Elevations for $Fr = (4\pi)^{-1/2}$, $\delta = 0.01$ as Computed with the Linear Spectral Method.

was shown by Haussling and VanEseltine[7] that the numerical results generated by the linear and nonlinear spectral methods appear qualitatively correct and show good quantitative agreement with exact linear solutions and perturbation results. The surface elevations of Figure 3 approach uniform downstream waves with increasing time while those of Figure 4 approach the condition of no downstream

waves which is the exact linear solution at $Fr = (2\pi)^{-1/2}$.

The linear problem with $Fr = (4\pi)^{-1/2}$ and $\delta = 0.01$ was considered using the second-order finite-difference approach with three different grid spacings as a test of the convergence properties of the schemes (Figure 5).

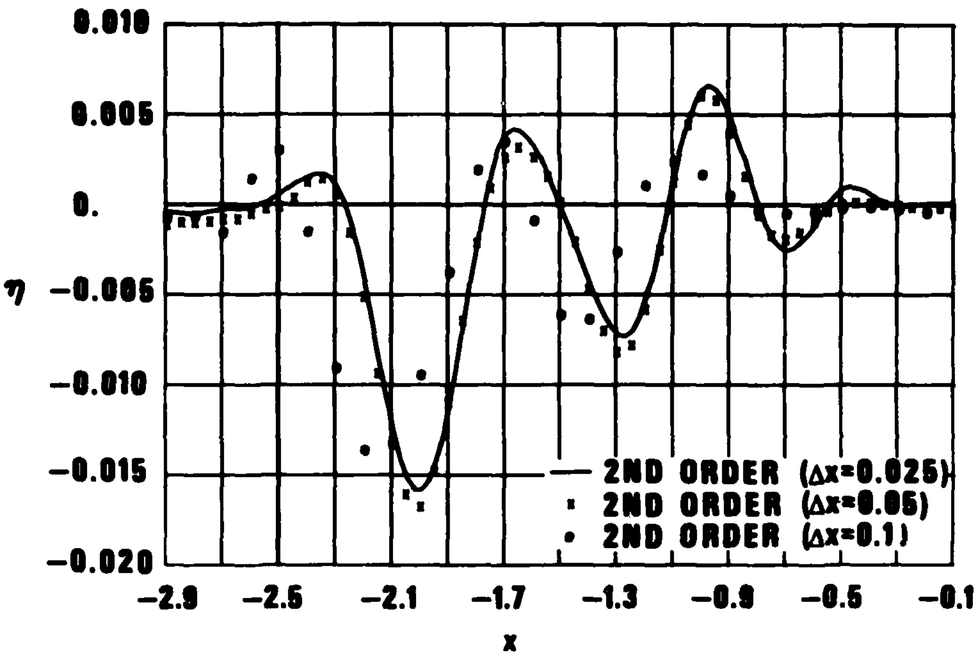

Figure 5. Surface Elevations at $t = 2.16$ for $Fr = (4\pi)^{-1/2}$, $\delta = 0.01$ as Computed with the Linear Finite-Difference Method using Three Different Grid Spacings.

The spacings used are $\Delta x = 0.1$, 0.05, and 0.025 (i.e., 10, 20, and 40 grid points in the x-direction over the region of nonzero pressure). In all cases the depth d is unity and $\Delta y = \Delta x$. The grid spacing in the region of the expanding grid was chosen so as to achieve a smooth transition from the uniform to the expanding grid. The time increment Δt is limited by accuracy and was decreased as Δx was reduced. The results indicate that the numerical solutions converge to a solution which is close to that generated by the spectral method. The results for $\Delta x = 0.025$ were obtained using a region of length $L_1 = 10$. The leading edge of the pressure distribution was at $x_0 = -2.5$. The grid extended upstream from the pressure distribution a

distance of 2.5 units, 2 units of which were covered by the expanding grid. The mesh extended downstream from the disturbance a distance of 6.5 units. A grid system of 361 x 41 points was used. With $\epsilon_1 = 0.001$, $\epsilon_2 = 0.0005$, and $\Delta t = 0.0075$ the number of combined iterations on η and ϕ varied between 4 and 10 per time step. About 500 seconds of CDC 6600 computer time were used to simulate the time development from t=0 to t=2.16. The results for $\Delta x = 0.05$ were generated with about 100 seconds of computer time. Corresponding results were generated with the spectral method using $\Delta x = 0.05$ and about 150 seconds of computer time.

The results generated with the fourth-order finite-difference scheme apparently converge to the same solution as the second-order results when the grid spacings and time increment approach zero (Figure 6). The fourth-order solution for $Fr = (4\pi)^{-1/2}$, $\delta = 0.01$ at $t = 2.16$ with $\Delta x = 0.05$ is

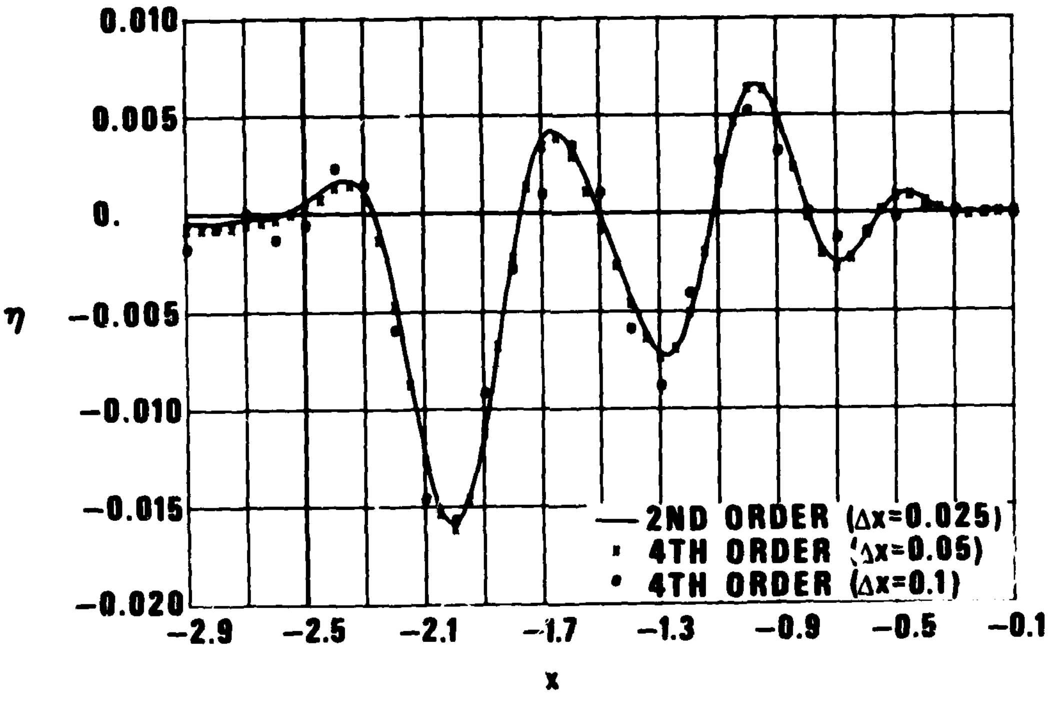

Figure 6. Surface Elevations at $t = 2.16$ for $Fr = (4\pi)^{-1/2}$, $\delta = 0.01$ as Computed with the Linear Finite-Difference Method.

very close to the second-order solution generated with $\Delta x = 0.025$ but the computation of the fourth-order solution used only about 100 seconds of computer time, a saving of 80%. Thus it appears that use of the fourth-order difference scheme is advisable when high accuracy is necessary for these problems.

A comparison of surface elevations for the linear and nonlinear, spectral and finite-difference methods is presented in Figure 7. These results indicate that the errors introduced by the numerical approximations are smaller, for the grid sizes considered, than the differences between the linear and nonlinear solutions.

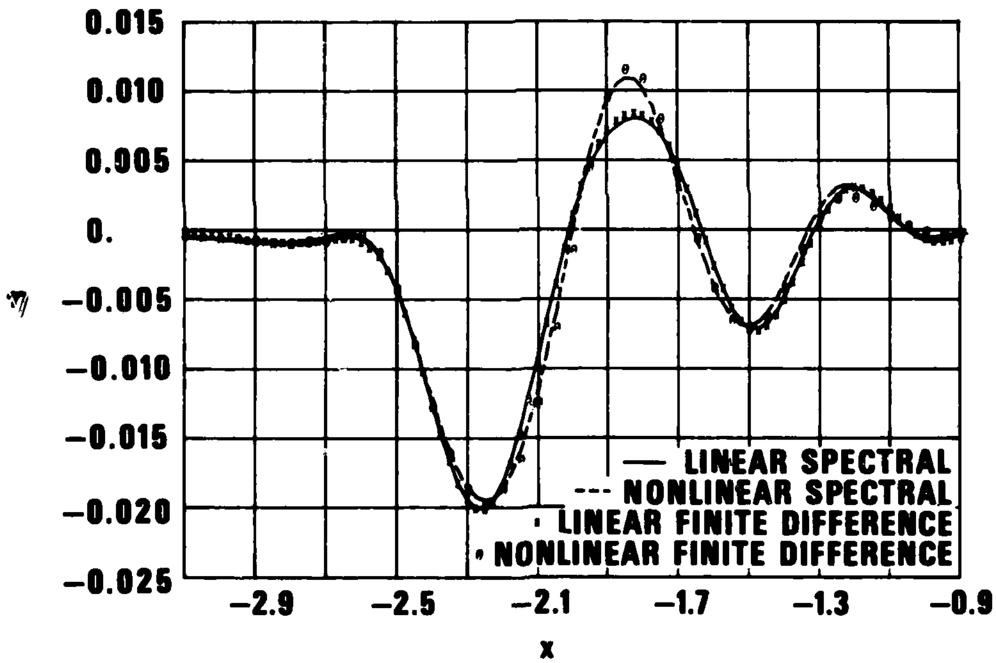

Figure 7. Surface Elevations at $t = 1.68$ for $Fr = (4\pi)^{-1/2}$, $\delta = 0.01$ as Computed with the Linear and Nonlinear Spectral and Finite-Difference Methods.

The finite-difference scheme seems to have a computer-time advantage over the spectral method for nonlinear problems. The nonlinear results in Figure 7 were generated in about 220 seconds of CDC 6600 time using the

finite-difference method.

Both nonlinear methods exhibit instability during long time integrations when steep waves occur. The immediate lack of energy conservation reported by Easton and Catton[2] with a scheme employing a series expansion is not present. Instead, energy conservation is maintained quite well for a certain time interval but is then lost rapidly as the instability becomes apparent. The instability is independent of Δt. Various modifications of the nonlinear numerical schemes were attempted to stabilize the computations. Use of Euler backward time differencing as suggested by Easton and Catton was unsuccessful. Upstream differencing, which has been used widely to stabilize other numerical schemes, stabilizes these schemes but is acceptable only if high accuracy is not needed since the waves are drastically damped with the amplitude diminishing rapidly in the downstream direction. As mentioned in the previous section the use of third-order upstream differencing at time level m+1 and third-order downstream differencing at level m in place of central differencing for η_x and ϕ_x has a stabilizing influence and allows longer time integrations with a closer approach to an accurate steady state near the pressure disturbance.

Three-Dimensional Motion

The fourth-order three-dimensional scheme was tested using the pressure distribution of Equation (10). The depth was $d = 1.6$ and $\Delta x = \Delta y = \Delta z = 0.1$. Seventeen levels resolved the region from $y=0$ to $y=-d$. Each level consisted of a 65 x 65 mesh. Thus 65 x 65 x 17 = 71,825 grid points were used. Figure 8 displays surface elevations at $t = 2.16$ after the abrupt start. The results at this early time already give a qualitative picture of the steady-state situation in the neighborhood of the disturbance. With $\epsilon_1 = .01$, $\epsilon_2 = .001$, and $\Delta t = .03$ two iterations on the free-surface conditions are carried out per time step. The development from $t = 0$ to $t = 2.16$ consumed about 110 seconds of CDC 6600 time. The results compare favorably with numerical evaluations of an analytic solution constructed by Haussling and VanEseltine[8] (Table 1).

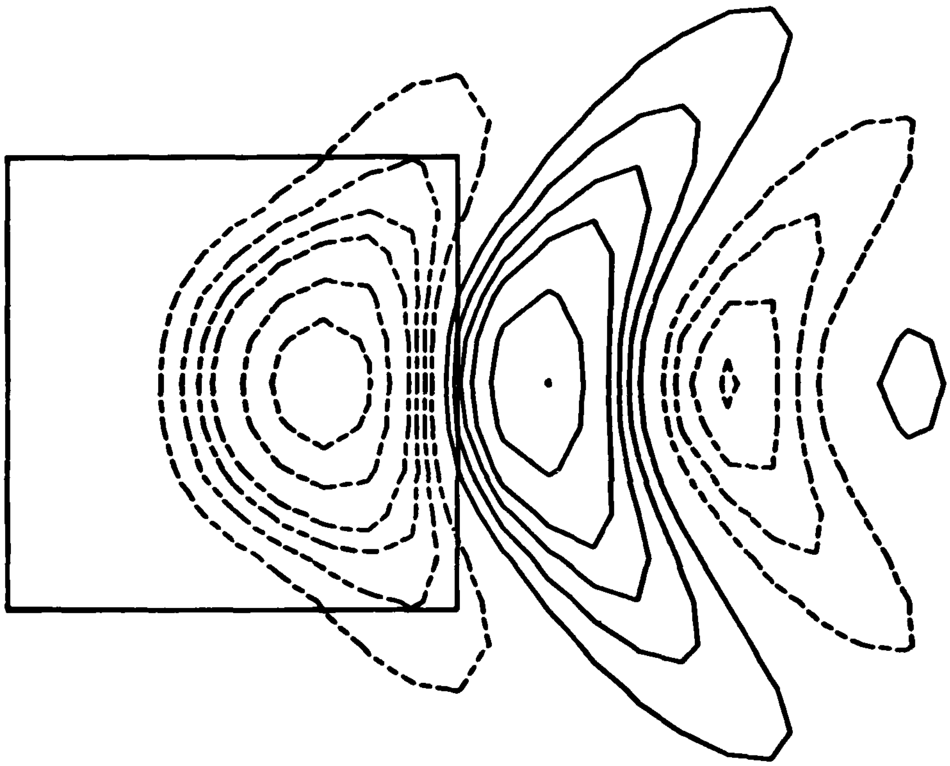

Figure 8. Surface Elevations at $t = 2.16$, for $Fr = (2\pi)^{-1/2}$, $\delta = 0.01$, $b = 1$ as Computed with the 3-D Linear Finite-Difference Method. The contours plotted are $\eta = \pm 0.02, \pm 0.015, \pm 0.01, \pm 0.0075, \pm 0.005, \pm 0.0025$ with negative values represented by broken lines.

t	R x 10^3		W x 10^3	
	ANALYTIC	NUMERICAL	ANALYTIC	NUMERICAL
0.12	0.0122	0.0119	0.1324	0.1304
0.24	0.0669	0.0649	0.1914	0.1908
0.36	0.1306	0.1290	0.2014	0.2011
0.48	0.1669	0.1663	0.2119	0.2109
0.60	0.1856	0.1847	0.2280	0.2280
0.72	0.2019	0.2011	0.2402	0.2410

Table 1. Comparison of 3-D Linear Finite-Difference Results with Values Computed from an Exact Linear Solution for $Fr = (2\pi)^{-1/2}$, $\delta = 0.01$, $b = 1$.

5. Conclusions

Results indicate that, except for the instability which appears in long time integrations for steep nonlinear waves, these numerical schemes for simulating transient free-surface potential flows are convergent. Also, reasonable accuracy is attainable for the two-dimensional linear and nonlinear as well as the three-dimensional linear problems on which the methods have been tested. The solution of three-dimensional nonlinear problems seems possible but would be very time consuming.

The finite-difference method for solving the Laplace equation seems to be superior for general use to the spectral method because of its flexibility. Higher-order finite-difference schemes and expanding grid systems are effective in improving accuracy and/or reducing computer time.

Since the methods discussed in this paper have yet to be proven best for these problems, other alternatives such as finite-element techniques, for example, should be considered.

The use of energy absorbing boundary conditions or matching to far-field solutions in place of conditions such as those of Equation (17) should allow the use of much smaller computational regions and less computer time in numerical calculations.

Acknowledgment

This work has been supported by the Numerical Naval Hydrodynamics Program at the David W. Taylor Naval Ship Research and Development Center. This program is jointly sponsored by the Office of Naval Research, the Naval Sea Systems Command , and DTNSRDC.

References

1. Nichols, B.D. and C.W. Hirt, "Calculating Three-Dimensional Free Surface Flows in the Vicinity of Submerged and Exposed Structures," J. Computational Physics, Vol. 12, p. 234 (1973).
2. Easton, C.R. and I. Catton, "Initial Value Techniques in Free-Surface Hydrodynamics," J. Computational Physics, Vol. 9, p. 424 (1972).
3. Multer, R.H., "Exact Nonlinear Model of Wave Generator," J. Hydraulics Div. ASCE, Vol. 99, p. 31 (1973).
4. Bai, K.J., "A Variational Method in Potential Flows with a Free Surface," College of Engineering Report No. NA 72-2, Univ. of Calif., Berkeley (1972).
5. von Kerczek, C.H. and N. Salvesen, "Numerical Solutions of Two-dimensional Nonlinear Wave Problems," Proceedings of the Tenth Symposium on Naval Hydrodynamics, MIT (June 1974).
6. Chan, R.K.-C. and C.W. Hirt, "Two-dimensional Calculations of the Motion of Floating Bodies," Proceedings of the Tenth Symposium on Naval Hydrodynamics, MIT (June 1974).
7. Haussling, H.J. and R.T. VanEseltine, "A Combined Spectral Finite-Difference Method for Linear and Nonlinear Water Wave Problems," Naval Ship Research and Development Center Report No. 4580 (1974).
8. Haussling, H.J. and R.T. VanEseltine, "Unsteady Air-Cushion Vehicle Hydrodynamics Using Fourier Series," (to appear in Journ. of Ship Research).
9. Ohring, S., "A Fast Fourth Order Laplace Solver for Application to Numerical 3-d Water Wave Problems," Proceedings of the First International Conference on Numerical Ship Hydrodynamics, Naval Ship Research and Development Center (October 1975).

TWO-DIMENSIONAL TIME-DEPENDENT CALCULATIONS OF LARGE-AMPLITUDE SURFACE GRAVITY WAVES DUE TO A SURFACE DISTURBANCE

R. K.-C. Chan

JAYCOR
1401 Camino Del Mar
Del Mar, California 92014 U.S.A.

ABSTRACT

The Generalized Arbitrary Lagrangian-Eulerian (GALE) computing technique has been employed to study the nonlinear, large-amplitude gravity waves generated by a moving surface disturbance, which, for the purpose of comparison with other works, is represented by a pressure distribution. To allow computations in a domain of finite size without serious interferences by waves reflected from the boundaries, an artifice is used which depletes the energy of the outgoing waves. It has been found that, although the GALE method is capable of producing quite accurate simulations, the treatment of wave reflection is essential to its practical application. Discussed in this paper are the results of a series of numerical experiments to study the properties of a wave-damping device.

1. Introduction

A number of direct numerical techniques for obtaining solutions to large-amplitude, nonlinear, surface gravity wave problems have become available due to the effort of many investigators in the last decade or so. In the present discussion, we consider only those formulations in which the prescribed free-surface pressure condition is applied at the instantaneous location of the free surface and that either the Euler's equation of motion or the potential flow is simulated. Thus, we exclude those techniques that attempt to solve equations that

contain further approximations or simplifications, e.g. the shallow-water equations, Korteweg-deVries equation, etc. Consequently, the problems we are concerned with are necessarily two-dimensional or three-dimensional in nature.

A brief citation of the contributions to finite difference techniques for solving the nonlinear gravity waves as defined above may be of interest. Techniques for calculating a steady-state wave system have been proposed by von Kerczek and Salvesen[(1)] for a two-dimensional potential flow past a disturbance, and by Chan[(2)] for a large-amplitude solitary wave. For two-dimensional, time-dependent calculations, the technique for potential flows by Fangmeier[(3)], the SUMMAC method by Chan and Street[(4)], the Lagrangian technique by Brennen and Whitney[(5)], the ALE method of Hirt, Amsden, and Cook[(6)], and the GALE technique by Chan[(7)] are some examples. Spectral methods or combined spectral-finite-difference methods have also been proposed by various investigators and these have been summarized by Haussling and van Eseltine[(8)].

One serious difficulty encountered in the study of infinite wave trains is the prescription of the upstream and downstream boundary conditions. Consider the wave train produced by an obstacle held stationary in a steady stream. Depending on the nature of the blockage, the stationary waves produced by the disturbance may extend to infinity both upstream and downstream of the obstacle. Cost and computer storage, however, dictate the use of a relatively small computational region which contains only a small number of the dominant waves. In a steady-state formulation, one simply does not know what to specify at the upstream and downstream boundaries, while in an initial-value formulation the usual use of rigid walls leads to wave reflections which soon contaminate the region of interest, rendering the solution useless. Nonreflecting boundary conditions for simulations in which the linear, time-dependent wave equation with constant coefficients is used,

i. e. for nondispersive waves, have been proposed and used successfully by several authors (see (9) and the reference given therein). However, for the problem considered here, the waves are in general nonlinear, dispersive and governed by equations that are more complicated than the wave equation. Thus, no simple "radiation boundary conditions" seem to be available. To reduce wave reflection for a wider class of time-dependent problems, one would naturally think of a damping region near the upstream and downstream boundaries of the computational domain to absorb waves incident upon it. Thus, the outgoing waves would be removed by dissipation rather than by being transmitted out of the domain. The efficiency of this artifice obviously depends on how the damping term is added to the governing equations, on the magnitude and spatial variation of the viscosity in the damping zone, and on the length of the damping zone relative to the wavelength of the various components in the wave system.

The objective of the present research, which is not yet completed, is to study the nonlinear, large-amplitude waves generated by a moving disturbance at the free surface by applying the Generalized Arbitrary Lagrangian-Eulerian (GALE) computing technique. The surface disturbance is represented by the same localized pressure distribution used by von Kerczek and Salvesen[(1)] in their steady-state formulation of the problem. In the present study, the pressure disturbance is at rest at t=0 and is located at some distance from the left wall of the two-dimensional wave tank. Then the disturbance starts moving at a constant speed toward the right wall. Given sufficient length for the tank, a train of nearly periodic waves is expected to follow the disturbance, which is steady relative to the disturbance. From previous experience[(7)] there is no doubt that the GALE method can produce very accurate solutions. After a few test calculations in the present study, however, it became apparent that one can not

meaningfully compare the results with the steady-state solutions, analytic or numerical, without first treating adequately those aspects that contaminate the physical processes of interest. At present, two interfering elements are recognized: wave reflection, as has already been described, and the starting process, i.e. how the pressure disturbance accelerates to the constant cruising speed. A violent starting process tends to impart excessive energy to the waves during their early development, thus requiring much longer computation to reach a practically steady state.

In this paper detailed discussion on the use of artificial damping to absorb incident waves is given. The form of the damping term, to be derived in the following section, is quite general and can be used in conjunction with many types of governing equations and the corresponding finite-difference models, e.g. SUMMAC, GALE, wave equation. In the case of the wave equation, of course, one could use radiation boundary conditions[9]. Once the interfering elements are understood and removed, the original task of studying the nonlinearity using the GALE method and comparing the results with steady-state solutions by other methods can be completed. This, however, shall be the subject of a future report.

2. Wave Absorption by Damping

To derive a form for the artificial damping which is easy to implement in a wide variety of schemes, we add linear damping terms to the momentum equations to obtain

$$\frac{\partial u}{\partial t} + \frac{\partial (u^2)}{\partial x} + \frac{\partial (uv)}{\partial y} = - \frac{\partial (p/\rho)}{\partial x} - \nu u \qquad (1)$$

$$\frac{\partial v}{\partial t} + \frac{\partial (uv)}{\partial x} + \frac{\partial (v^2)}{\partial y} = - \frac{\partial (p/\rho)}{\partial y} - g - \nu v \qquad (2)$$

where u and v are the velocity components in the x- and y-directions, respectively, p is the fluid pressure, ρ

is the density and ν is the artificial viscosity which is generally a function of x and y. The two-dimensional flow is assumed to occur on the x-y plane with gravity pointing to the negative y-axis. If Eqs. (1) and (2) are to be written in finite difference form, as in MAC[10], u and v in the damping terms must be treated implicitly, i.e. evaluated at the advanced time level, to avoid numerical instability when the viscosity ν exceeds a certain limit. Implicit treatment of the damping terms would require major modification of many finite-difference schemes; thus it is desirable to find an alternative form for the damping terms which could be evaluated explicitly, i.e. at the old time level.

Consider the simple equation

$$\frac{du}{dt} = - \nu u \tag{3}$$

for which the solution is $u = e^{-\nu t}$. The value of u at the time level $t+\delta t$, where δt is the time step, is

$$u^{n+1} = e^{-\nu(t+\delta t)} = u^n e^{-\nu\delta t} \tag{4}$$

The superscript n refers to the time level. Equation (4) can be manipulated into

$$\frac{u^{n+1}-u^n}{\delta t} = u^n \left(\frac{e^{-\nu\delta t}-1}{\delta t}\right) \tag{5}$$

By considering the left side of Eq. (5) as an approximation for $\frac{du}{dt}$ and comparing Eqs. (3) and (5), the term $u^n\left(e^{-\nu\delta t}-1\right)/\delta t$ is equivalent to the damping term $-\nu u$. Thus, Eqs. (1) and (2) may be replaced by

$$\frac{\partial u}{\partial t} + \frac{\partial (u^2)}{\partial x} + \frac{\partial (uv)}{\partial y} = - \frac{\partial (p/\rho)}{\partial x} + u^n\left(\frac{e^{-\nu\delta t}-1}{\delta t}\right) \tag{6}$$

$$\frac{\partial v}{\partial t} + \frac{\partial (uv)}{\partial x} + \frac{\partial (v^2)}{\partial y} = - \frac{\partial (p/\rho)}{\partial y} - g + v^n\left(\frac{e^{-\nu\delta t}-1}{\delta t}\right) \tag{7}$$

Equations (6) and (7) are identical with Eqs. (1) and (2) only in the limit of vanishing $\nu\delta t$. However, we are only concerned with dissipating the waves and any simple artifice that serves the purpose is useful. Note also that even as $\nu\partial t$ becomes infinitely large, the damping terms in Eqs. (6) and (7) do not lead to numerical instability when they are evaluated explicitly.

To explore the properties of the wave damper just derived, we add the damping term to the linearized one-dimensional shallow-water equations for a constant depth

$$\frac{\partial u}{\partial t} + g\,\frac{\partial \eta}{\partial x} = u\left(\frac{e^{-\nu\delta t}-1}{\delta t}\right) \tag{8}$$

$$\frac{\partial \eta}{\partial t} + h\,\frac{\partial u}{\partial x} = 0 \tag{9}$$

where h is the water depth and η the surface elevation. The time-centered finite-difference representations of Eqs. (8) and (9) are

$$\frac{u_i^{n+1}-u_i^n}{\delta t} = -\,g\left(\frac{\eta_i^n-\eta_{i-1}^n+\eta_i^{n+1}-\eta_{i-1}^{n+1}}{2\delta x}\right) + u_i^n\left(e^{-\nu_i\delta t}-1\right)/\delta t \tag{10}$$

$$\frac{\eta_i^{n+1}-\eta_i^n}{\delta t} = -\,h\left(\frac{u_{i+1}^n-u_i^n+u_{i+1}^{n+1}-u_i^{n+1}}{2\delta x}\right) \tag{11}$$

where δx is the constant spacing of mesh points in this one-dimensional wave problem. The variables u_i and η_i are defined at staggered mesh points, i.e. η_i is located half way between u_i and u_{i+1}.

As shown in Fig. 1, in the numerical experiment a train of sinusoidel waves are generated at the left edge (x=0) of the one-dimensional domain by specifying

$$\eta = \sin \omega t$$

$$\frac{\partial u}{\partial x} = - \frac{1}{h} \frac{\partial \eta}{\partial t} = - \frac{\omega}{h} \cos \omega t \qquad (12)$$

at x=0. The artificial viscosity ν is set to zero everywhere except in the damping zone where $x \geq x_o$. In the present investigation the length of the damping zone has been chosen to be 2λ, λ being the wavelength of the sinusoidal waves. Both uniform and linear distribution of viscosity in the damping zone have been examined. For linear distribution the following formula is used

$$\nu_i = \nu_{max} (x_i - x_o)/(2\lambda). \qquad (13)$$

The time history of η at station A (Fig. 1) is to be used to monitor wave reflection. In Fig. 2, the wave amplitude at station A is plotted against $\tau = t\omega/2\pi$, which is the time normalized by the period of the incident waves, for the case of no damping (ν=0). The front of the initial right-going wave train reaches station A at $\tau \sim 3.0$, and the wave amplitude there remains at the exact value of 1.0 until $\tau \sim 11.0$. At this time the waves reflected from the right-hand wall amplifies the amplitude to the expected value of 2.0. In Fig. 3 a similar plot is shown for the case in which the viscosity is distributed as in Eq. (13), with ν_{max}=0.5. It can be seen that

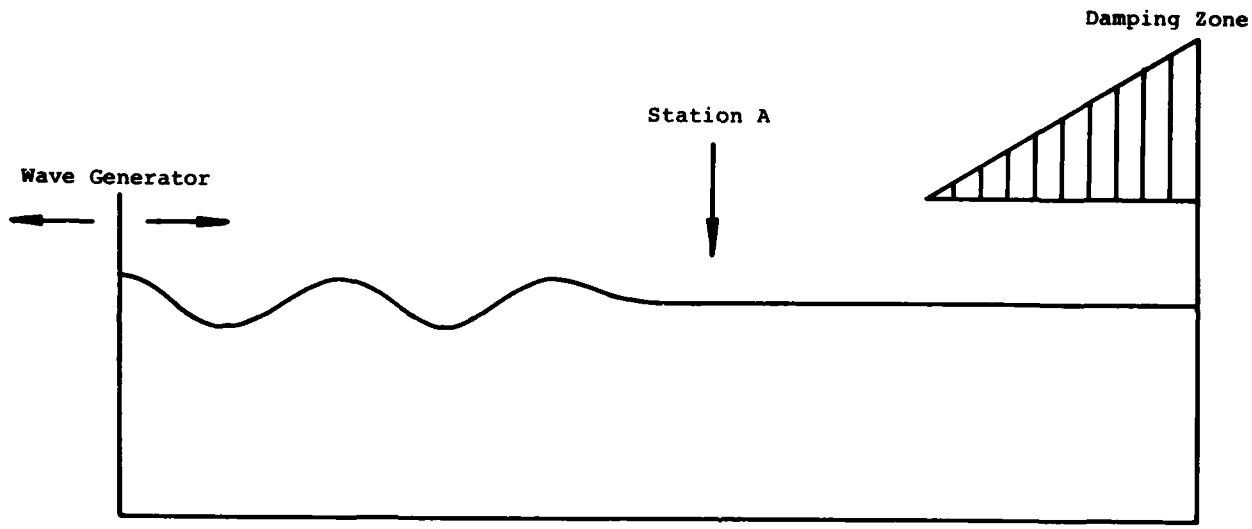

Figure 1. Schematic of the problem for testing the properties of the Wave Damping Device.

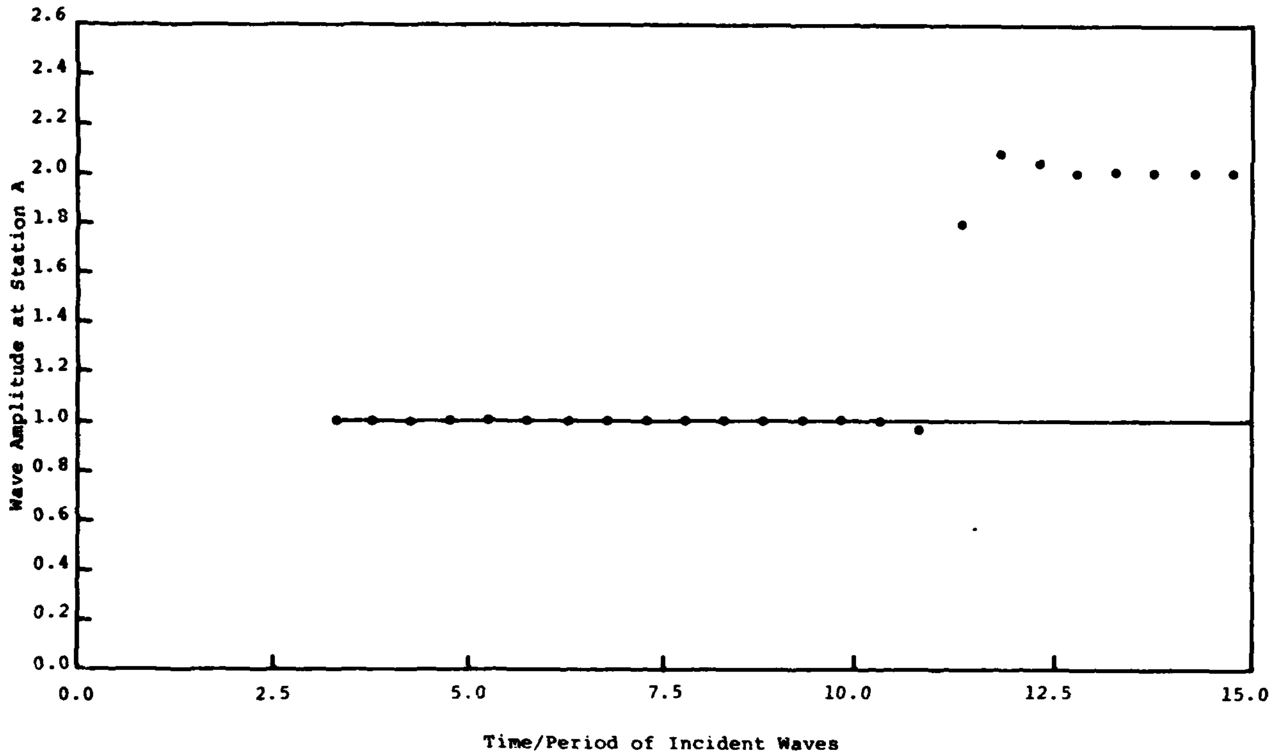

Figure 2. Time History of Wave Amplitudes at Station A (No Damping)

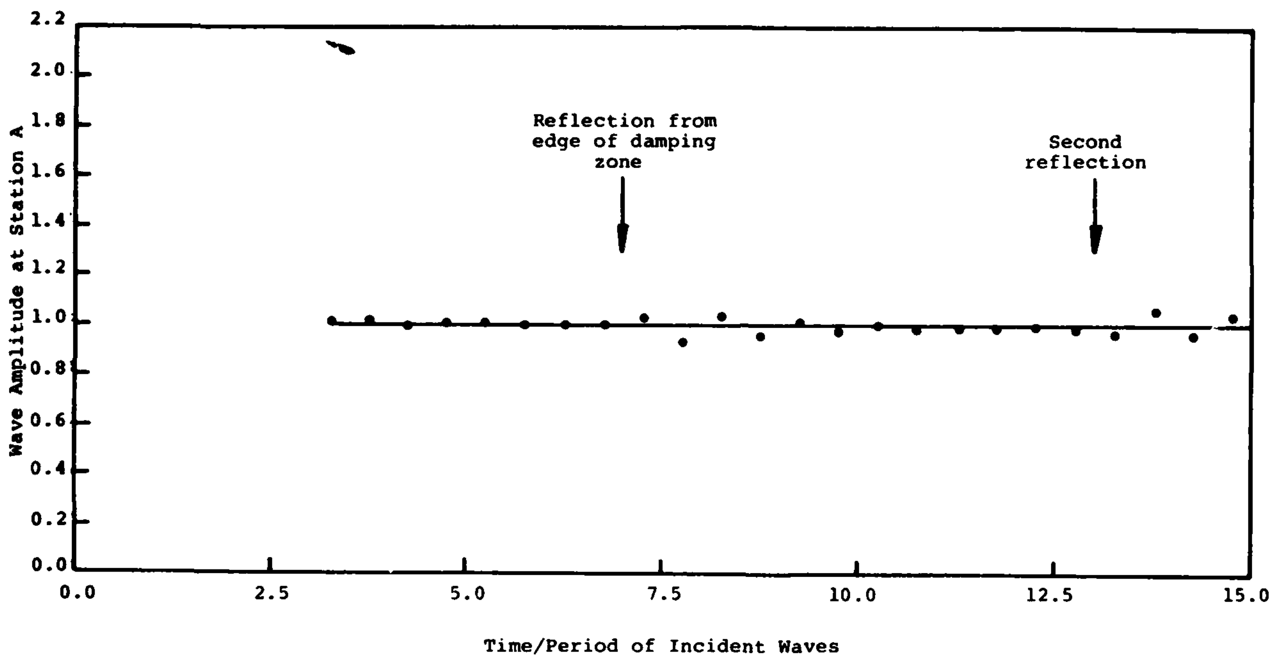

Figure 3. Time History of Wave Amplitudes at Station A. (Linear Variation of Viscosity, $\nu_{max} = 0.5$)

reflections have been drastically reduced. At $\tau \sim 7.0$ some reflection from the edge of the damping zone distorts the amplitudes slightly. This reflected wave travels to the left, hits the left boundary and again travels to the right. When this second reflection occurs (at $\tau \sim 13.0$) the wave amplitude at station A is again distorted slightly. If, on the other hand, a uniform viscosity $\nu \equiv 0.5$ is applied in the damping zone, the discontinuity in viscosity at the edge of the damping zone leads to significant amount of reflection (Fig. 4).

A series of numerical experiments, using the system represented by Eqs. (10), (11), (12) and (13), have been conducted to study the effect of various types of damping zones. Figure 5 summarizes the present effort, with two primary findings. The first finding is that sharp discontinuity in viscosity, e.g. ν = constant in the damping zone and $\nu=0$ elsewhere, is very inefficient in the reduction of wave reflections. A smooth variation in ν works out much better. The second finding is that for the parameters chosen in the present study, i.e. the length of damping zone = 2λ and ν is specified by Eq. (13), there exists an optimum value for ν_{max}, at which the damping is most efficient. As shown in Fig. 5, the use of $\nu_{max} \sim 0.5$ in Eq. (13) has resulted in only about 1.3% reflection.

Obviously, further work should be performed to explore other aspects of the damping device, such as alternative distribution for ν and the effect of varying the length of the damping zone. These topics will be considered in the future. Application of the present damping device to other types of equations and their corresponding finite-difference schemes is quite simple. For example, Eqs. (6) and (7) can be directly used in the SUMMAC method, while for application to the GALE technique one only has to replace Eq. (7) in Reference 7 with

$$\xi = \rho u_{i,j}^{n}\left(e^{-\nu_i \delta t}-1\right)/\delta t$$

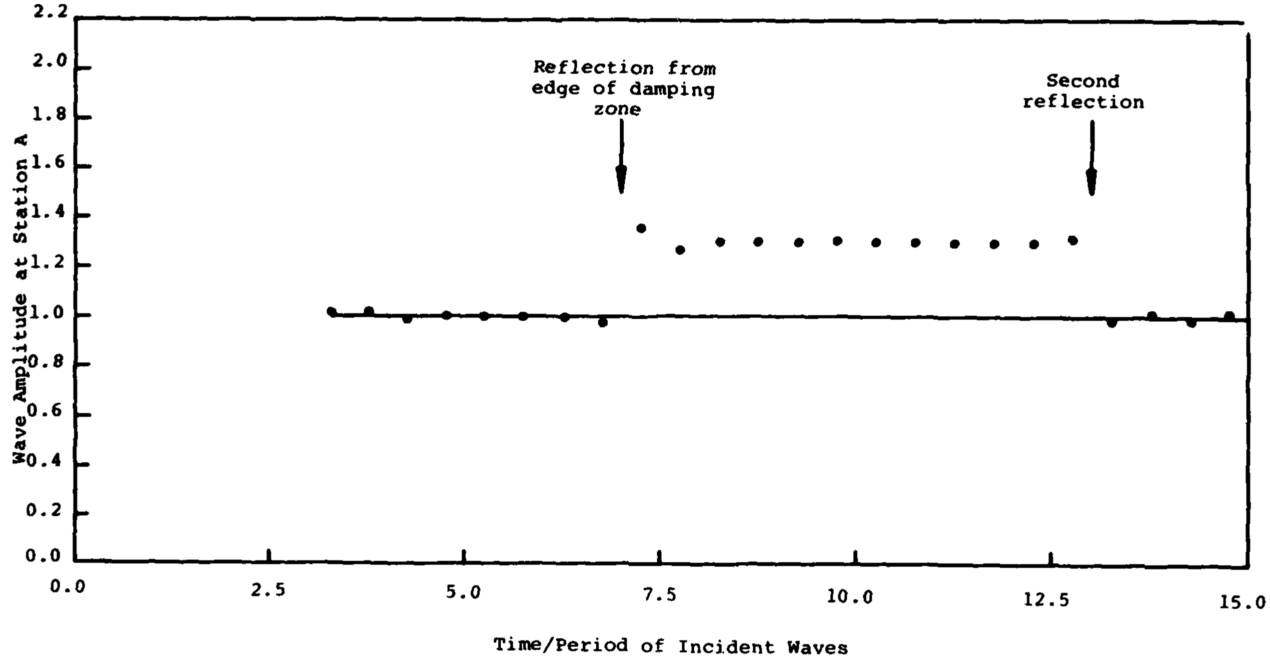

Figure 4. Time History of Wave Amplitudes at Station A. (Uniform viscosity in the damping zone, $\nu = 0.5$)

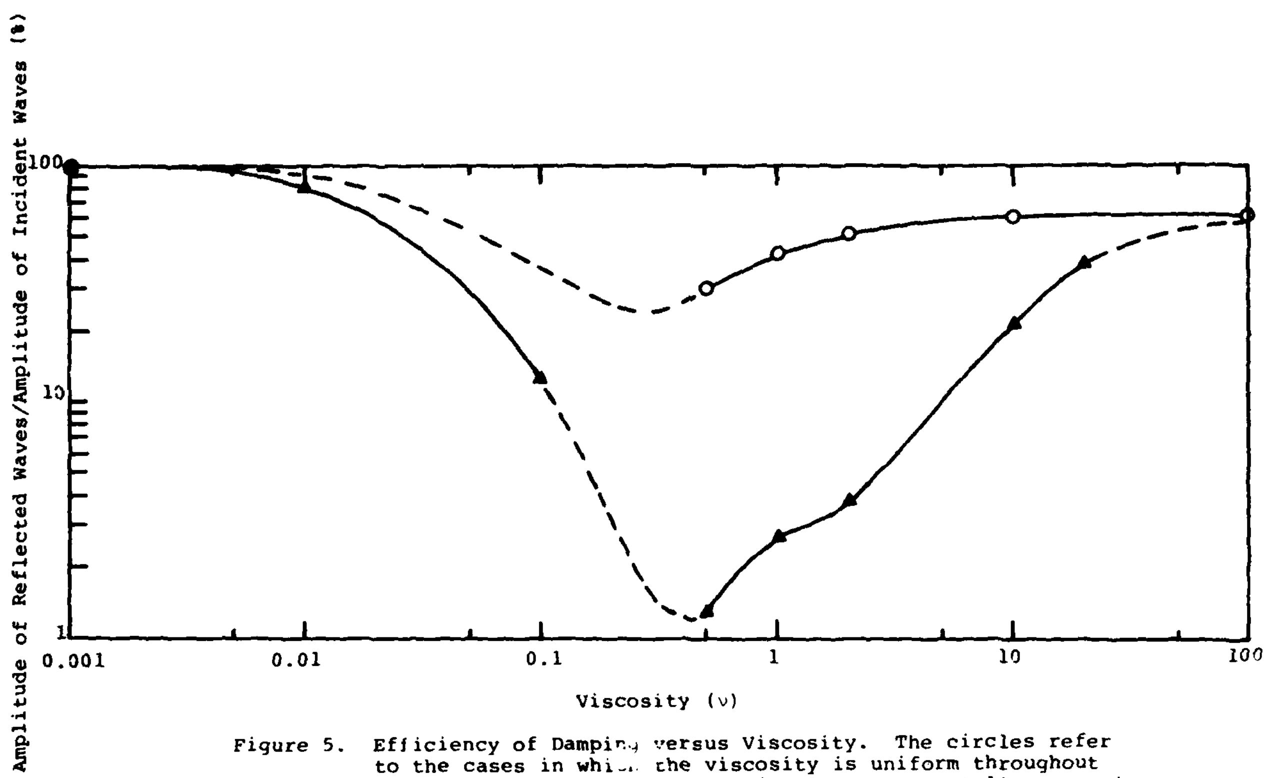

Figure 5. Efficiency of Damping versus Viscosity. The circles refer to the cases in which the viscosity is uniform throughout the damping zone, while the triangles represent linear variation of viscosity in the damping zone. The dashed portion of the curves is merely an estimate.

$$\eta = \rho v_{i,j}^{n}\left(e^{-\nu_i \delta t}-1\right)/\delta t$$

where ξ, η, and ρ are defined in the cited reference.

3. Preliminary Calculation of Large-Amplitude Waves Generated by a Moving Surface Disturbance

The Lagrangian part of the GALE method has been chosen in the present research to study the nonlinear effects in waves generated by a moving surface disturbance. The reason for employing a Lagrangian description is the ease of representing the free surface without the need of interpolation, as is the case in SUMMAC. Detailed description of GALE can be found in Reference 7.

A two-dimensional wave tank, 200 ft. long and 9.5 ft. deep, is considered. At t=0 the water in the tank is at rest and a pressure distribution

$$p = \begin{cases} 8.6\ \cos^2\left[\dfrac{2\pi(x-x_1)}{20}\right]\ \text{lb/ft}^2, & \text{for } |x-x_1| \leq 5 \\ 0 & \text{, elsewhere} \end{cases}$$

is applied at the free surface. Subsequently, the pressure distribution moves to the right at the constant speed of 10 ft/sec, that is

$$x_1(t) = 20 + 10t$$

The region $0<x<26.0$ is prescribed as the damping zone, with $\nu_{max} = 10.0$. The calculation shown in Fig. 6 had been made before the series of numerical experiments on the properties of artificial damping was conducted. Thus a serious mistake was inadvertently made by assigning too large a value for ν_{max}, which resulted in significant reflections. The waves reflected from the edge of the damping zone immediately follow the moving pressure, thus contaminating the wave field behind the pressure disturbance. At this point one could only

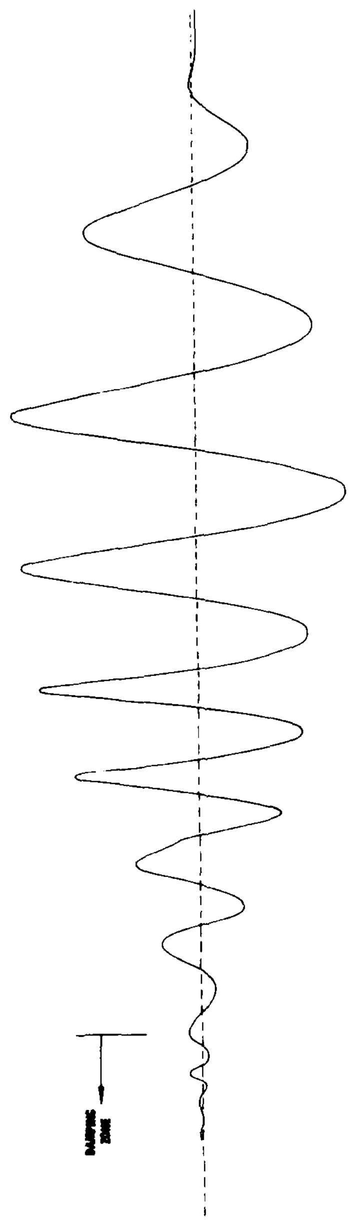

Figure 6

say that the calculation has been stable, requiring an average of ten iterations per time step to solve the velocity field, and that characteristics of nonlinear waves, i.e. sharpened crests and broadened troughs, have been produced. A definitive study of the nonlinearity and comparisons with results of other investigations must await future calculations in which reflections are properly handled in the light of the discussions in Section 2.

REFERENCES

1. von Kerczek, C. H. and Salvesen, N., "Numerical Solutions of Two-Dimensional Nonlinear Wave Problems," Proceedings of the Tenth Naval Hydrodynamics Symposium, Boston, Massachusetts, June 1974.

2. Chan, R. K.-C., "A Discretized Solution for the Solitary Wave," Journal of Computational Physics, Vol. 16, No. 1, September 1974.

3. Fangmeier, D. D., Dissertation submitted to University of California (Davis) in partial satisfaction of Ph.D. requirements, 1967.

4. Chan, R. K.-C. and Street, R. L., "A Computer Study of Finite-Amplitude Water Waves," Journal of Computational Physics, Vol. 6, No. 1, August 1970.

5. Brennen, C. B. and Whitney, A. K., "Unsteady, Free Surface Flows; Solutions Employing the Lagrangian Description of the Motion," Proceedings of the Eighth Naval Hydrodynamics Symposium, Pasadena, California, 1970.

6. Hirt, C. W., Amsden, A. A. and Cook, J. L., Journal of Computational Physics, Vol. 14, 1974.

7. Chan, R. K.-C., "A Generalized Arbitrary Lagrangian-Eulerian Method for Incompressible Flows with Sharp Interfaces," Journal of Computational Physics, Vol. 17, No. 3, 1975.

8. Haussling, H. J. and van Eseltine, R. T., "A Combined Spectral Finite-Difference Method for Linear and Nonlinear Water Wave Problems," Naval Ship Research and Development Center Report 4580, Bethesda, Maryland, November 1974.

9. Lindman, E. L., "Free-Space Boundary Condition for the Time Dependent Wave Equation," Journal of Computational Physics, Vol. 18, No. 1, May 1975.

10. Harlow, F. H. and Welch, J. E., "Numerical Calculation of Time Dependent Viscous Incompressible Flow," Physics of Fluids, Vol. 8, p.2182, 1965.

NUMERICAL SOLUTION FOR HYDRODYNAMIC FORCES ON A SURFACE-PIERCING PLATE OSCILLATING IN YAW AND SWAY

R.B. Chapman

David W. Taylor Naval Ship Research and Development Center
Bethesda, Maryland 20084 U.S.A.

ABSTRACT

The numerical solution for a surface-piercing flat plate at a steady angle of attack is extended, by superposition, to a plate oscillating in yaw and sway. Force and moment coefficients are computed as functions of nondimensional length and frequency and are compared with experimental values. The relationship of this formulation to classical strip theory is discussed, and it is established that the two theories are equivalent in the zero Froude number limit.

1. Introduction

A typical monohull may be modeled as a slender body translating on a free-surface. A catamaran may be regarded as a pair of slender bodies. The hydrodynamic forces acting on a slender body due to lateral motion (yaw and sway) are fundamental to the maneuvering and seakeeping properties of the craft represented by the body. Calculation of these forces is greatly simplified by the slender-body approximation that the flow field varies an order of magnitude more rapidly in the transverse plane than it does in the longitudinal direction. This approximation changes the character of the longitudinal variable in the free-surface problem from spatial to time-like. A steady problem in three dimensions reduces to a form equivalent to unsteady two-dimensional flow in the transverse plane with initial conditions at the leading edge and the advancement of time equivalent to translation of the solution plane aft. In this way, a steady three-dimensional problem may be solved by numerical methods suitable for unsteady two-dimensional free-surface flows.

This approach has been applied by the author[1] to the case of a flat plate piercing the free surface at a constant angle of attack. In [1] finite-difference methods produced solutions with linear and nonlinear boundary conditions. Side force and yawing moment coefficients

were compared with experimental results of Van den Brug, Beukelman, and Prins[2]. The nonlinear boundary conditions had only a small effect on these coefficients.

This paper examines the extension of the linear solution obtained in reference [1] to oscillatory sway and yaw. Force and moment coefficients are developed and compared with strip theory and with experimental values. It is necessary to formulate the linearized equations governing unsteady yaw and sway of a slender body.

2. Linearized Formulation

A left-handed Cartesian coordinate system (x, y, z) is fixed in space and another system (x′, y′, z′) is fixed on the body such that the two systems coincide in the absence of yaw and sway. The x-coordinate is aligned in the direction of the free-stream velocity U, that is x is positive aft. The z-coordinate is positive upward and y is positive to port. When the two systems coincide, the common origin is on the longitudinal center-plane of the body at the intersection of the leading edge and the undisturbed free surface. Yawing moment is measured about an axis A′ parallel to the z axis at the mid-body point ($x' = \ell/2$, $y' = 0$) where ℓ is the body length. Rotation about this axis is positive in the right-hand sense; that is the leading edge moves to port. This geometry is illustrated in Figure 1.

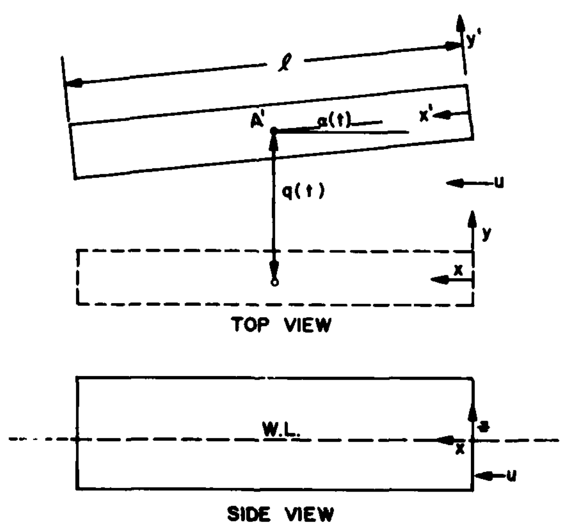

Figure 1 – Coordinate Geometry

If the body is translated a small distance q(t) on the y axis and is rotated by a small angle $\alpha(t)$ about axis A′ fixed in the body, then in the linearized limit, the body and space coordinates are related by

$$
\begin{aligned}
x' &= x - y\alpha(t) \\
y' &= y - q(t) - \alpha(t)\left(\frac{1}{2}\boldsymbol{\ell} - x\right) \\
z' &= z\,,
\end{aligned}
\tag{1}
$$

and the velocity components in the two systems are related by

$$
\begin{aligned}
\dot{x}' &= \dot{x} - y\dot{\alpha}(t) - \dot{y}\alpha(t) \\
\dot{y}' &= \dot{y} - \dot{q}(t) - \dot{\alpha}(t)\left(\frac{1}{2}\boldsymbol{\ell} - x\right) + \alpha(t)\dot{x} \\
\dot{z}' &= \dot{z}
\end{aligned}
\tag{2}
$$

It is assumed that the flow is irrotational and may be described by a velocity potential. Since the problem is linearized, this potential may be written as

$$\Phi = Ux + \varphi_A(x,y,z) + \varphi(x,y,t) \tag{3}$$

where $Ux + \varphi_A(x,y,z)$ represents the potential in the absence of lateral motion and $\varphi(x,y,z,t)$ is the perturbation potential caused by yaw and sway. It is assumed that the velocity perturbations due to $\varphi_A(x,y,z)$ and $\varphi(x,y,z,t)$ are both an order of magnitude smaller than U. Let the body be represented by

$$F(x',y',z') = 0 \tag{4}$$

with F positive on the exterior and negative on the interior of the body. Then the Neumann boundary condition on the body is

$$\dot{x}'\frac{\partial F}{\partial x'} + \dot{y}'\frac{\partial F}{\partial y'} + \dot{z}'\frac{\partial F}{\partial z'} = 0 \quad \text{on } F(x',y',z') = 0 \tag{5}$$

By substitution of equation (2), the body boundary condition may be written as

$$
\begin{aligned}
&\left(\frac{\partial \Phi}{\partial x} - y\dot{\alpha}(t) - \frac{\partial \Phi}{\partial y}\alpha(t)\right)\frac{\partial F}{\partial x'} + \\
&\left(\frac{\partial \Phi}{\partial y} - \dot{q}(t) - \dot{\alpha}(t)\left(\frac{1}{2}\boldsymbol{\ell} - x\right) + \alpha(t)\frac{\partial \Phi}{\partial x}\right)\frac{\partial F}{\partial y'} + \frac{\partial \Phi}{\partial z}\frac{\partial F}{\partial z'} = 0
\end{aligned}
\tag{6}
$$

In the linearized limit, the body boundary condition is satisfied on the boundary of the static body, i.e. on $F(x,y,z) = 0$. After the body-boundary condition for the static part of the potential $(Ux + \varphi_A(x,y,z))$ is subtracted from equation (5) and terms involving products

of $\dot{\alpha}(t)$ and the perturbation velocities are neglected, equation (6) reduces to the form,

$$\left(\frac{\partial\varphi}{\partial x} - y\dot{\alpha}(t)\right)\frac{\partial F}{\partial x} + \left(\frac{\partial\varphi}{\partial y} - V_B(x,t)\right)\frac{\partial F}{\partial y} + \frac{\partial\varphi}{\partial z}\frac{\partial F}{\partial z} = 0 \tag{7}$$

where $V_B(x, t)$ is a function of the sway velocity $V_o(t)$ and the yaw velocity $\dot{\alpha}(t)$,

$$\begin{aligned} V_B(x,t) &= V_o(t) + \left(\frac{1}{2}\ell - x\right)\dot{\alpha}(t) \\ V_o(t) &= \dot{q}(t) - U\alpha(t) \end{aligned} \tag{8}$$

The potential must satisfy Laplace's equation throughout the flow,

$$\frac{\partial^2\varphi}{\partial x^2} + \frac{\partial^2\varphi}{\partial y^2} + \frac{\partial^2\varphi}{\partial z^2} = 0 \quad z<0,\ F(x,y,z)>0. \tag{9}$$

Also, the potential must satisfy the linearized free-surface condition on $z = 0$,

$$\left(\frac{\partial}{\partial t} + U\frac{\partial}{\partial x}\right)^2 \varphi = -g\frac{\partial\varphi}{\partial z}. \tag{10}$$

Finally, $\varphi(x, y, z\ t)$ must satisfy some initial condition *throughout the lower half plane at* some initial time t_o. For the oscillatory problem, this transforms to a radiation condition.

3. Slender Body Approximation

The slender-body approximation may be implemented by assigning orders of magnitude to the spatial differential operators,

$$\frac{\partial}{\partial x} = O(\ell^{-1}),\ \frac{\partial}{\partial y} = O(a^{-1}),\ \frac{\partial}{\partial z} = O(a^{-1}) \tag{11}$$

where a is a characteristic dimension of the body cross-section and ℓ is the body length. The ratio $\epsilon = a/\ell$ is assumed to be small. If the terms of order ϵ^2 are neglected, Laplace's equation immediately reduces to two dimensions,

$$\frac{\partial^2\varphi}{\partial y^2} + \frac{\partial^2\varphi}{\partial z^2} = 0. \tag{12}$$

On the body $y = O(a)$ so from equation (8)

$$(y\dot{\alpha}(t)\ V_B^{-1}(x,t)) = O(y/\ell) = O(\epsilon) \tag{13}$$

and the body boundary condition (7) reduces to the two-dimensional form,

$$\left(\frac{\partial\varphi}{\partial y} - V_B(x,t)\right)\frac{\partial F}{\partial y} + \frac{\partial\varphi}{\partial z}\frac{\partial F}{\partial z} \approx 0 \quad \text{on } F(x,y,z) = 0 \tag{14}$$

Since the order of magnitudes of the temporal differential operator and of the acceleration of gravity are left unspecified, the free-surface condition (10) is unchanged.

The slender-body approximation eliminates the x variable from the field equation. In the body boundary condition, x remains only as a parameter. The governing equations (10), (12), and (14) have characteristic lines in the x-t plane defined by

$$t - xU^{-1} = \text{constant} \tag{15}$$

The position of a point on a characteristic line is specified by

$$s = \frac{1}{2}(t + xU^{-1}). \tag{16}$$

This variable transforms the free-surface condition into

$$\frac{\partial^2\varphi}{\partial s^2} = -g\frac{\partial\varphi}{\partial z} \quad \text{on } z = 0,\ t - xU^{-1} = \text{constant}. \tag{17}$$

If initial conditions are specified over the entire space at $t = t_o$, then the solution is determined for all $t \geq t_o$.

Several points are worth noting. First, since the solution on any characteristic line is independent of conditions on any other characteristic, the flow in the plane $x = x_1$ at time $t = t_1$ is independent of the flow in plane $x = x_2$ at time $t = t_2$ unless

$$t_2 - t_1 = (x_2 - x_1)U^{-1} \tag{18}$$

Second, when the solution is constructed for an initial-value problem, the solution at any point $s = s_1$ on a characteristic line depends only on conditions for $s < s_1$. Thus, the solution at $x = x_1$ and $t = t_1$ is independent of conditions downstream $(x_2 > x_1)$ or at a later time in the sense that it is not influenced by the body boundary condition. Finally, it is obvious that an initial condition of identically zero perturbation potential requires the solution to remain zero ahead of the leading edge for all time. These considerations remain applicable to the oscillatory problem and may be regarded as consequences of a radiation condition.

4. Oscillating Cylinder

For the special case of an harmonically oscillating truncated cylinder, the body surface is defined by

$$F(y,z) = 0,\ O < x < \ell. \tag{19}$$

and the function $V_B(x,t)$ defined in equation (8) has the form

$$V_B(x,t) = b(x)\, e^{i\omega t} \quad \text{on } F(y,z) = 0,\ O < x < \ell. \tag{20}$$

For rigid body motion such as yaw and sway, b(x) is a linear function. A more general form would be suitable for hydroelastic problems. For the present analysis b(x) may be assumed to be a differentiable function of x. It is convenient to express the equation in terms of a nondimensional set of independent variables,

$$
\begin{aligned}
\bar{x} &= x(g/a)^{1/2}\, U^{-1} \\
\bar{y} &= ya^{-1} \\
\bar{z} &= za^{-1} \\
\bar{t} &= t(g/a)^{1/2}
\end{aligned}
\tag{21}
$$

and to define a nondimensional frequency and body length,

$$\bar{\omega} = \omega\,(a/g)^{1/2} \text{ and } \bar{\mathcal{L}} = \mathcal{L}\ (g/a)^{1/2}\ U^{-1} \tag{22}$$

The free-surface and body boundary conditions are then

$$\left(\frac{\partial}{\partial \bar{t}} + \frac{\partial}{\partial \bar{x}}\right)^2 \varphi = -\frac{\partial \varphi}{\partial \bar{z}} \quad \text{on } \bar{z} = 0 \tag{23}$$

and

$$\frac{\partial \varphi}{\partial \bar{y}}\frac{\partial \bar{F}}{\partial \bar{y}} + \frac{\partial \varphi}{\partial \bar{z}}\frac{\partial \bar{F}}{\partial \bar{z}} = ab(\bar{x})\, e^{i\bar{\omega}\bar{t}}\, H(\bar{x})\frac{\partial \bar{F}}{\partial \bar{y}} \quad \text{on } F(\bar{y},\bar{z}) = 0 \tag{24}$$

where $\bar{F}(\bar{y},\bar{z}) = F(y,z)$ and $H(\bar{x})$ is the step function, which arises from the condition of zero disturbance ahead of the leading edge ($\bar{x} = 0$).

A special case of this problem is steady flow ($\bar{\omega} = 0$) with $b(\bar{x}) = a^{-1}$ corresponding to a constant angle of attack. Let the potential for this problem be defined as $f(\bar{x},\bar{y},\bar{z})$. In addition to the two-dimensional Laplace's equation, $f(\bar{x},\bar{y},\bar{z})$ satisfies a free-surface condition,

$$\frac{\partial f^2}{\partial \bar{x}^2} = -\frac{\partial f}{\partial \bar{z}} \quad \text{on } \bar{z} = 0 \tag{25}$$

the body boundary condition,

$$\frac{\partial f}{\partial \bar{y}}\frac{\partial \bar{F}}{\partial \bar{y}} + \frac{\partial f}{\partial \bar{z}}\frac{\partial \bar{F}}{\partial \bar{z}} = H(\bar{x})\frac{\partial \bar{F}}{\partial \bar{y}} \quad \text{on } \bar{F}(\bar{y},\bar{z}) = 0 \tag{26}$$

and a radiation condition,

$$\bar{f}(\bar{x},\bar{y},\bar{z}) = 0,\ \bar{x} < 0.$$

Reference [1] demonstrates that this function may be determined by an unsteady two-dimensional calculation.

The general solution satisfying equations (23) and (24) may be expressed by linear superposition of the special solution $f(\bar{x},\bar{y},\bar{z})$. Let the variables $\bar{s}$ and $\bar{q}$ be defined by the linear transformation

$$\bar{s} = \frac{1}{2}(\bar{t} + \bar{x})$$
$$\bar{q} = \frac{1}{2}(\bar{t} - \bar{x}) \tag{27}$$

with the inverse

$$\bar{t} = \bar{s} + \bar{q}$$
$$\bar{x} = \bar{s} - \bar{q}\,. \tag{28}$$

The free-surface condition becomes

$$\frac{\partial^2\varphi}{\partial\bar{s}^2} = -\frac{\partial\varphi}{\partial z} \quad \text{on } \bar{z} = 0 \tag{29}$$

and the body boundary condition is

$$\frac{\partial\varphi}{\partial\bar{y}}\frac{\partial\bar{F}}{\partial\bar{y}} + \frac{\partial\varphi}{\partial\bar{z}}\frac{\partial\bar{F}}{\partial\bar{z}} = a\,e^{2i\bar{\omega}\bar{q}}\;b(\bar{s}-\bar{q})\,H(\bar{s}-\bar{q})\,e^{i\bar{\omega}(\bar{s}-\bar{q})}\,\frac{\partial\bar{F}}{\partial\bar{y}} \tag{30}$$

By the principle of linear superposition, any solution of the form

$$\begin{aligned}\varphi(\bar{s},\bar{q},\bar{y},\bar{z}) &= Af(\bar{s}-\bar{q},\bar{y},\bar{z}) + \int_0^\infty d\sigma\,B(\sigma)\,f(\bar{s}-\bar{q}-\sigma,\bar{y},\bar{z})\\ &= Af(\bar{s}-\bar{q},\bar{y},\bar{z}) + \int_0^{\bar{s}-\bar{q}} d\sigma\,B(\sigma)\,f(\bar{s}-\bar{q}-\sigma,\bar{y},\bar{z})\end{aligned} \tag{31}$$

satisfies the two-dimensional Laplace's equation and the free-surface condition (29) for arbitrary A and $B(\sigma)$. It may be shown from equation (26), using integration by parts, that

$$\varphi(\bar{s},\bar{q},\bar{y},\bar{z}) = a\,e^{2i\bar{\omega}\bar{q}}\left[f(\bar{s}-\bar{q},\bar{y},\bar{z}) + \int_0^{\bar{s}-\bar{q}} d\sigma\,f(\bar{s}-\bar{q}-\sigma,\bar{y},\bar{z})\,\frac{d}{d\sigma}\left(b(\sigma)\,e^{i\bar{\omega}\sigma}\right)\right] \tag{32}$$

satisfies the body-boundary condition (30) as well. In terms of $(\bar{x},\bar{y},\bar{z},\bar{t})$ the general solution is

$$\begin{aligned}\varphi(\bar{x},\bar{y},\bar{z},\bar{t}) = a\,e^{i\bar{\omega}\bar{t}}\Big[&f(\bar{x},\bar{y},\bar{z})\,b(o)\,e^{i\bar{\omega}\bar{x}} +\\ &\int_0^{\bar{x}} d\bar{q}\,f(\bar{q},\bar{y},\bar{z})(i\bar{\omega}\,b(\bar{x}-\bar{q})) + b'(\bar{x}-\bar{q})\Big]\end{aligned} \tag{33}$$

where $b'(\bar{x})$ is the derivative of $b(\bar{x})$. Uniqueness is assured by the radiation condition.

5. Side Force and Yawing Moment

The linearized dynamic pressure on the body is

$$p(x,y,z,t) = -\rho U \frac{\partial\varphi}{\partial x} - \rho \frac{\partial\varphi}{\partial t} = -\rho\left(U\frac{\partial}{\partial x} + i\omega\right)\varphi(x,\,y,z,t) \qquad (34)$$

Let Y(x, t) be the side force acting on the portion of the body forward of point x. Then

$$Y(x,t) = -\int_0^x dq \int_{ABC} dz\; p(q,y,z,t) \qquad (35)$$

where ABC is the body contour, F(y, z) = 0 in the lower half-plane as shown in Figure 2.

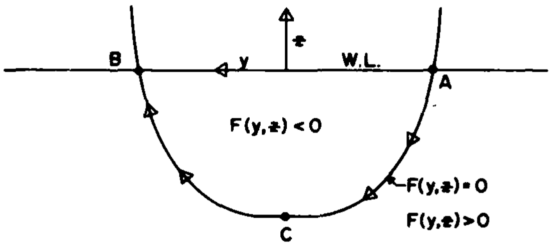

Figure 2 – Section Contour, Aft View

Expressions (34) and (35) combine to produce

$$Y(x,t) = \rho U \int_{ABC} dz\; \varphi(x,y,z,t) + \rho i\omega \int_0^x dq \int_{ABC} dz\; \varphi(q,y,z,t) \qquad (36)$$

In terms of nondimensional variables, the side force is

$$Y(\bar{x},t) = \rho U a\,[1 + i\bar{\omega} I] \int_{ABC} d\bar{z}\; \varphi(\bar{x},\bar{y},\bar{z},\bar{t}) \qquad (37)$$

where I is an operator defined by

$$I \cdot h(\bar{x},\bar{y},\bar{z},\bar{t}) = \int_0^{\bar{x}} d\bar{q}\; h(\bar{q},\bar{y},\bar{z},\bar{t}) \qquad (38)$$

Let the function $g(\bar{x})$ be defined by

$$g(\bar{x}) = -\frac{1}{2}\int_{ABC} d\bar{z}\; f(\bar{x},\bar{y},\bar{z}) \qquad (39)$$

Then substitution of (33) and (34) into (37) yields

$$Y(\bar{x},\bar{t}) = -\rho U a^2 e^{i\bar{\omega}\bar{t}}\, 2(1 + i\bar{\omega}l)[g(\bar{x})\, b(o)\, \bar{e}^{i\bar{\omega}\bar{x}} + i\bar{\omega}\int_o^{\bar{x}} d\bar{q}\; g(\bar{q})\, \bar{e}^{i\bar{\omega}\bar{q}}\, b(\bar{x}-\bar{q}) + \int_o^{\bar{x}} d\bar{q}\; g(\bar{q})\, \bar{e}^{i\bar{\omega}\bar{q}}\, b'(\bar{x}-\bar{q})] \tag{40}$$

with yawing moment about $\bar{x} = \bar{\boldsymbol{\ell}}/2$,

$$N(\bar{\boldsymbol{\ell}},\bar{t}) = \int_o^{\bar{\boldsymbol{\ell}}} \left(\frac{1}{2} - x\right) \frac{\partial Y(\bar{x},\bar{t})}{\partial \bar{x}}\, dx \tag{41}$$

6. **Sway and Yaw Modes**

Equation (40) may be evaluated for specified modes of motion. For the sway mode of harmonic oscillation defined by

$$V_B(x,t) = i\omega y_o\, e^{i\omega t} \tag{42}$$

the function $b(x)$ is a constant,

$$b(x) = i\omega y_o \tag{43}$$

The complex force coefficient defined as

$$Y^*(\bar{x},\bar{\omega}) = Y(\bar{x},\bar{t}) \cdot \left(\frac{1}{2}\rho a^2 U y_o\, e^{i\omega t}\omega\right)^{-1} \tag{44}$$

may be written as

$$Y^*(\bar{x},\bar{\omega}) = -4i\,[1 + i\bar{\omega}l] \left(g(\bar{x})\, \bar{e}^{i\bar{\omega}\bar{x}} + i\bar{\omega}\int_o^{x} g(\bar{q})\, \bar{e}^{i\bar{\omega}\bar{q}}\, d\bar{q}\right) \tag{45}$$

which reduces to

$$Y^*(\bar{x},\bar{\omega}) = -4i\, g(\bar{x})\, \bar{e}^{i\bar{\omega}\bar{x}} + q\bar{\omega}\int_o^{\bar{x}} g(\bar{q})\, \bar{e}^{i\bar{\omega}\bar{q}}\, d\bar{q} + 4i\bar{\omega}^2\int_o^{\bar{x}} (\bar{x}-\bar{q})\, g(\bar{q})\, \bar{e}^{i\bar{\omega}\bar{q}}\, d\bar{q} \tag{46}$$

Once $Y^*(\bar{x},\bar{\omega})$ is computed from (46), the yawing moment coefficient defined by

$$N^*(\bar{\boldsymbol{\ell}},\bar{\omega}) = N(\bar{\boldsymbol{\ell}},\bar{t}) \cdot \left(\frac{1}{2}\rho a^2 U y_o\, \omega\, e^{i\omega t}\boldsymbol{\ell}\right)^{-1} \tag{47}$$

may also be established.

The yawing mode of oscillation has two possible definitions. One definition, used in reference [2], requires that $V_o(t)$ in equation (8) remain zero. The second definition, used in reference [3], requires that $\dot{q}(t)$ in equation (8) remain zero. Both definitions have

certain minor advantages. Coefficients produced by the first definition are independent of the orientation of the space-fixed system; while the second definition leads to simpler inertial terms in the equations of motion. The first definition will be used in the present analysis. The function b(x) for the yawing mode is then

$$b(x) = i\omega\left(\frac{1}{2}\ell - x\right)a_o \tag{48}$$

and the complex force coefficient defined as

$$Y^*(\bar{\ell},\bar{\omega}) = Y(\bar{\ell},\bar{t})\cdot\left(\frac{1}{2}\rho a^2 U\omega\ell a_o e^{i\omega t}\right)^{-1} \tag{49}$$

may be written as

$$Y^*(\bar{\ell},\bar{\omega}) = \frac{1}{2}Y^*(\bar{\ell},\bar{\omega}) + 4i[1+i\bar{\omega}I]\int_0^{\bar{\ell}} g(\bar{q})\,\bar{e}^{i\bar{\omega}\bar{q}}\,(1+i\bar{\omega}(\bar{\ell}-\bar{q}))\,d\bar{q} \tag{50}$$

$$= \frac{1}{2}Y^*(\bar{\ell},\bar{\omega}) + 4i\int_0^{\bar{\ell}} d\bar{q}\,g(\bar{q})\,\bar{e}^{i\bar{\omega}\bar{q}}\left(1+2i\bar{\omega}(\bar{\ell}-\bar{q}) - \frac{\bar{\omega}^2}{2}(\bar{\ell}-\bar{q})^2\right) \tag{51}$$

The corresponding yaw moment coefficient is

$$N^*(\bar{\ell},\bar{\omega}) = N(\bar{\ell},\bar{t})\cdot\left(\frac{1}{2}\rho U a^2\omega\ell^2 a_o e^{i\omega t}\right)^{-1} \tag{52}$$

7. Strip Theory

The above slender-body theory may be compared with classical strip theory. In strip theory, the flow is assumed to be entirely two-dimensional in the transverse plane so that the solution is not only independent of downstream conditions, as is the case with slender-body theory, but is independent of upstream conditions as well. Under the assumption that the longitudinal perturbation velocity is zero, the potential may be written as

$$\varphi(\bar{x},\bar{y},\bar{z},\bar{t}) = H(\bar{x})\,b(\bar{x})\,\hat{\varphi}(\bar{x},\bar{y},\bar{z},\bar{t}) \tag{53}$$

where $\hat{\varphi}$ is the two-dimensional solution in the y-z plane for the section at x oscillating along the y axis with velocity $V_B(t) = \exp(i\omega t)$. The potential $\hat{\varphi}$ depends on $\bar{x}$ only as a parameter specifying the cross-section. The added mass and damping, $m(x,\omega)$ and $d(x,\omega)$ of the cross-section at x are defined by

$$m(\bar{x},\bar{\omega}) + d(\bar{x},\bar{\omega})(i\omega)^{-1} = a\rho\,\bar{e}^{i\omega t}\int_{ABC} d\bar{z}\,\varphi(\bar{x},\bar{y},\bar{z},\bar{t}) \tag{54}$$

Then from equation (37), the force forward of $\bar{x}$ is

$$Y(\bar{x},\bar{t}) = -U[1+i\bar{\omega}I]\,b(\bar{x})(m(\bar{x},\bar{\omega}) + d(\bar{x},\bar{\omega})(i\omega)^{-1})\,e^{i\omega t} \tag{55}$$

After equation (55) is reduced to coefficient form and notation is suitably altered, it may be seen that (55) is equivalent to the lateral-motion coefficients in reference [3]. For the case of a cylinder in sway, the complex force and moment coefficients are

$$Y^*(\bar{x}, \bar{\omega}) = (\bar{\omega}\bar{x} - i)(\bar{m}(\bar{\omega}) + \bar{d}(\bar{\omega})(i\bar{\omega})^{-1}) \tag{56}$$

and

$$N^*(\bar{x}, \bar{\omega}) = -\frac{1}{2}\, i\, (\bar{m}(\bar{\omega}) + \bar{d}(\bar{\omega})(i\bar{\omega})^{-1}) \tag{57}$$

where

$$\bar{m}(\bar{\omega}) \equiv m(\bar{\omega}) \cdot \left(\frac{1}{2}\,\rho\, a^2\right)^{-1} \tag{58}$$

and

$$\bar{d}(\bar{\omega}) \equiv \bar{\omega}\, d(\bar{x}, \bar{\omega}) \cdot \left(\frac{1}{2}\,\rho\, a^2\, \omega\right)^{-1} \tag{59}$$

with similar expressions for the yawing mode.

Strip theory can be related to slender-body theory by considering an infinite cylinder in sway. At large values of $\bar{x}$, the effects of the leading edge diminish and the solution should approach the stationary solution with the step function in equation (24) replaced by unity. In this limiting case of infinite $\bar{x}$, the slender-body solution is identical to the strip-theory solution. It may also be seen that the sectional added mass and damping may be determined from

$$\lim_{\bar{x} \to \infty} \left[\left(\frac{\partial Y^*(\bar{x}, \bar{\omega})}{\partial x}\right)_{\text{strip}} - \left(\frac{\partial Y^*(\bar{x}, \bar{\omega})}{\partial x}\right)_{\substack{\text{slender} \\ \text{body}}} \right] = 0 \tag{60}$$

or

$$\bar{m}(\bar{\omega}) - i\bar{d}(\bar{\omega})\bar{\omega}^{-1} = \lim_{\bar{x} \to \infty} 4 \left[g(o) + \int_0^{\bar{x}} g'(\bar{q})\, \bar{e}^{i\bar{\omega}\bar{q}}\, d\bar{q} - ig'(\bar{x})\, \bar{e}^{i\bar{\omega}\bar{x}} \right] \tag{61}$$

where $g(\bar{x})$ is the function defined in equation (39) and $g'(\bar{x})$ is its derivative. These equations indicate that the present slender-body formulation reduces to strip theory as $\bar{x}$ defined in equation (21) becomes infinite. Thus, the two formulations are identical in the zero-speed limit; and the slender-body formulation may be considered as a generalization of strip theory.

8. Flat Plate

The function $g(\bar{x})$ defined in equation (39) represents the force coefficient for a body of nondimensional length $\bar{x}$ at a steady angle of attack. Figure 3 shows this function as calculated for a flat plate of depth a in reference [1]. Note that $g(\bar{x})$ approaches its theoretical limit of $\pi/4$ for large values of $\bar{x}$. The derivative of this function may be interpreted as proportional to the incremental force along the length of the plate.

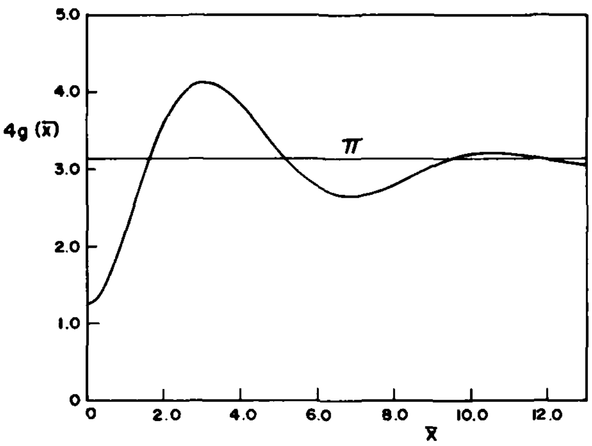

Figure 3 – Finite Difference Solution for Force Coefficient of Flat Plate

The numerical solution was a marching method with standard overrelaxation solution of the finite-difference representation of Laplace's equation.

One check on the numerical solution for $g(\bar{x})$ is to compare theoretical values from strip theory for added-mass and damping coefficients with real and imaginary parts of the expressions on the right-hand side of equation (61) evaluated at a large value of $\bar{x}$. Added-mass and damping coefficients calculated from equation (61) using the finite-difference solution for $g(\bar{x})$ over $0 \leq x \leq 13.0$ are compared in Figure (4) with coefficients for infinite $\bar{x}$ calculated from Ursell's[4] analysis of a flat plate oscillating in two dimensions. Leading edge effects are evidently small at $\bar{x} = 13.0$.

The slender-body formulation described in this paper is best illustrated by comparing theoretical and experimental hydrodynamic coefficients. Force coefficients reported in reference [2] for the sway mode are defined by

$$(-\bar{\omega}\bar{x}\, Y_{\dot{v}}'(\bar{x},\bar{\omega}) + i\, Y_v'(\bar{x},\bar{\omega})) = \epsilon\, Y^*(\bar{x},\bar{\omega})$$

and (62)

$$(-\bar{\omega}\bar{x}\, N_{\dot{v}}'(\bar{x},\bar{\omega}) + i\, N_v'(\bar{x},\bar{\omega})) = \epsilon\, N^*(\bar{x},\bar{\omega})$$

where $Y^*(\bar{x},\bar{\omega})$ and $N^*(\bar{x},\bar{\omega})$ are the functions defined in equations (44) and (47). Coefficients in the yawing mode are similarly defined by

$$(-\bar{\omega}\bar{x}\, Y_{\dot{r}}'(\bar{x},\bar{\omega}) + i\, Y_r'(\bar{x},\bar{\omega})) = \epsilon\, Y^*(\bar{x},\bar{\omega})$$

and (63)

$$(-\bar{\omega}\bar{x}\, N_{\dot{r}}'(\bar{x},\bar{\omega}) + i\, N_r'(\bar{x},\bar{\omega})) = \epsilon\, N^*(\bar{x},\bar{\omega})$$

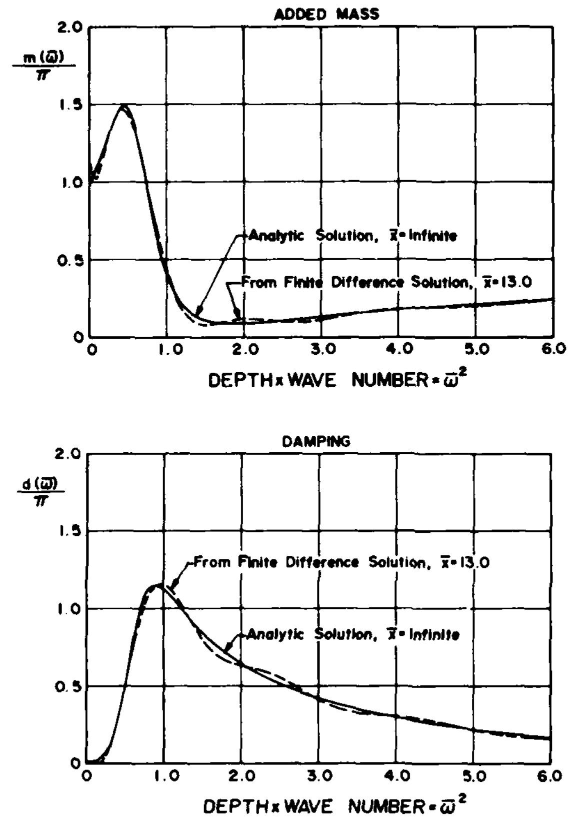

Figure 4 – Damping and Added Mass

These coefficients are presented in Figures 5 through 12 as functions of a nondimensional frequency,

$$\omega' = \bar{\omega}(\ell/a)^{1/2} \tag{64}$$

and Froude number

$$F_n = \bar{x}(\ell/a)^{1/2} \tag{65}$$

Experimental coefficients for sway and yaw modes of a plate with a one-meter chord and $(a/\ell) = 0.20$ are reproduced from [2] in Figures 5 through 12 with corresponding coefficients from slender-body theory and from strip theory. Certain coefficients in strip theory are independent of Froude number and may be represented by a single line. In other cases, where Froude number dependence is small, strip theory is plotted only for the highest and lowest experimental Froude numbers.

Slender-body theory gives generally satisfactory agreement with the experimental coefficients throughout the range of Froude numbers and frequencies. Strip theory fails at all but the lowest Froude number ($F_n = 0.16$, $\bar{x} = 14.0$) where it approximates experimental sway and added mass adequately, but still fails in the coupling coefficients for the sway mode and in all coefficients for the yaw mode. Perhaps this is because the error in strip theory due to forward speed is greater near the leading edge, where $\bar{x}$ is small, and the sway added-mass and damping coefficients are least affected by an error near the leading edge. It should be pointed out, however, that for many problems with smaller aspect ratios or Froude numbers, $\bar{x}$ is much greater than considered here so that the effect of forward speed is small and strip theory should be adequate. In other cases, it may be possible to obtain good results with slender-body theory over a forward portion of the body and strip theory further aft.

9. Conclusions

This example of a flat plate illustrates the potential utility of numerical solutions based on a slender-body formulation of a type first proposed by Ogilvie[5]. Comparisons with experimental results indicate that, for problems with significant forward speed effects, this slender-body approach produces far more satisfactory results than does strip theory for the hydrodynamic coefficients associated with sway and yaw.

References

[1] Chapman, R.B., "**Free-Surface Effects for Yawed Surface-Piercing Plates,**" submitted to Journal of Ship Research.

[2] Van Den Brug, J.B., Beukelman, W. and Prins, G.J., "**Hydrodynamic Forces on a Surface-Piercing Flat Plate,**" Report NR 325, Shipbuilding Laboratory, Delft University (1971).

[3] Salvesen, N., Tuck, E.O. and Faltinsen, O., "**Ship Motions and Sea Loads,**" Trans. Society of Naval Architects and Marine Engineers, Vol. 78 (1970).

[4] Ursell, F., "**On the Waves Due to the Rolling of a Ship,**" Quarterly Journal of Mechanics and Applied Mathematics, Vol. 1 (1948).

[5] Ogilvie, T.F., "**Nonlinear High-Froude Number Free-Surface Problems,**" Journal of Engineering Mathematics, Vol. 1 (July 1966).

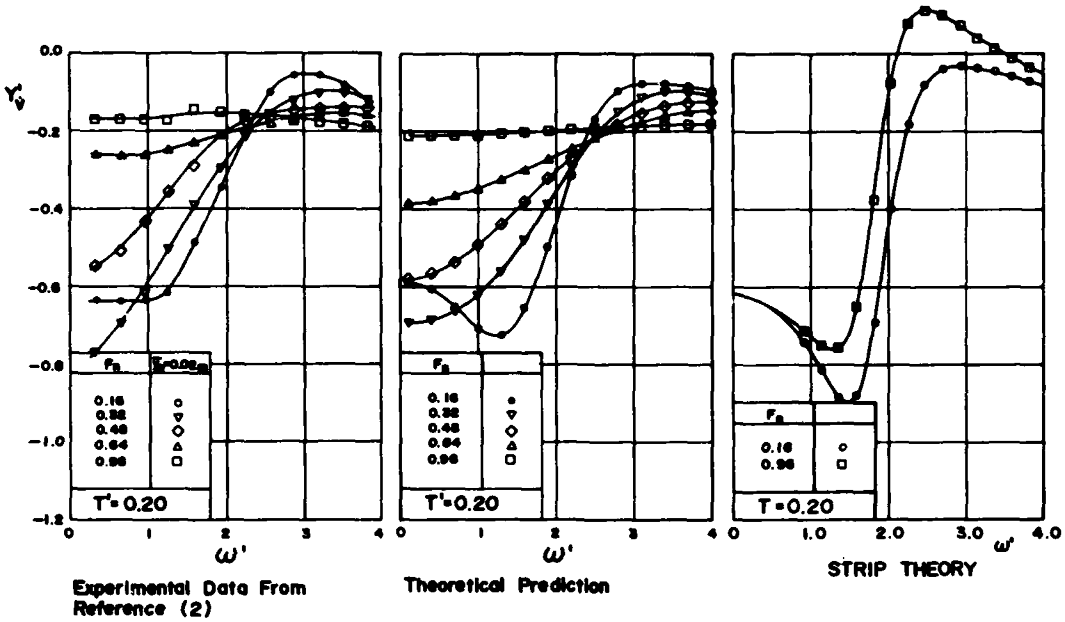

Figure 5 – Flat Plate Sway Added Mass

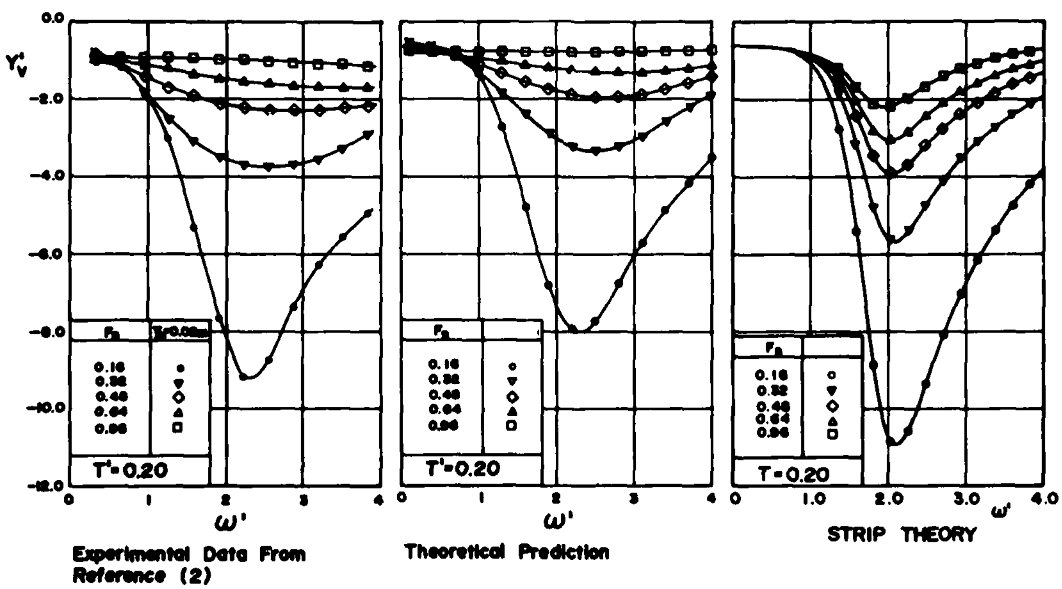

Figure 6 – Flat Plate Sway Damping

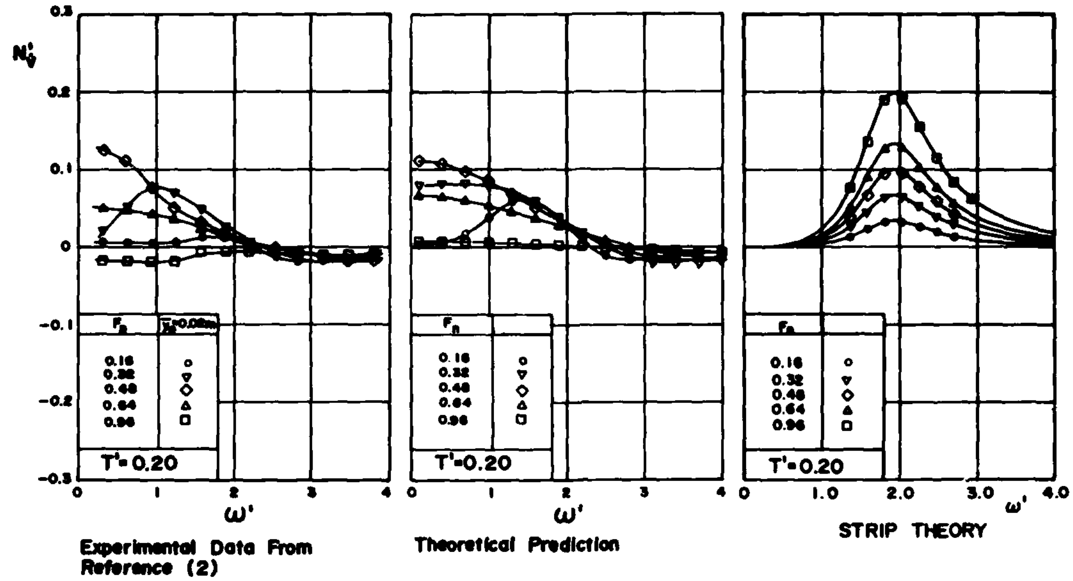

Figure 7 – Flat Plate Coupling of Sway into Yaw

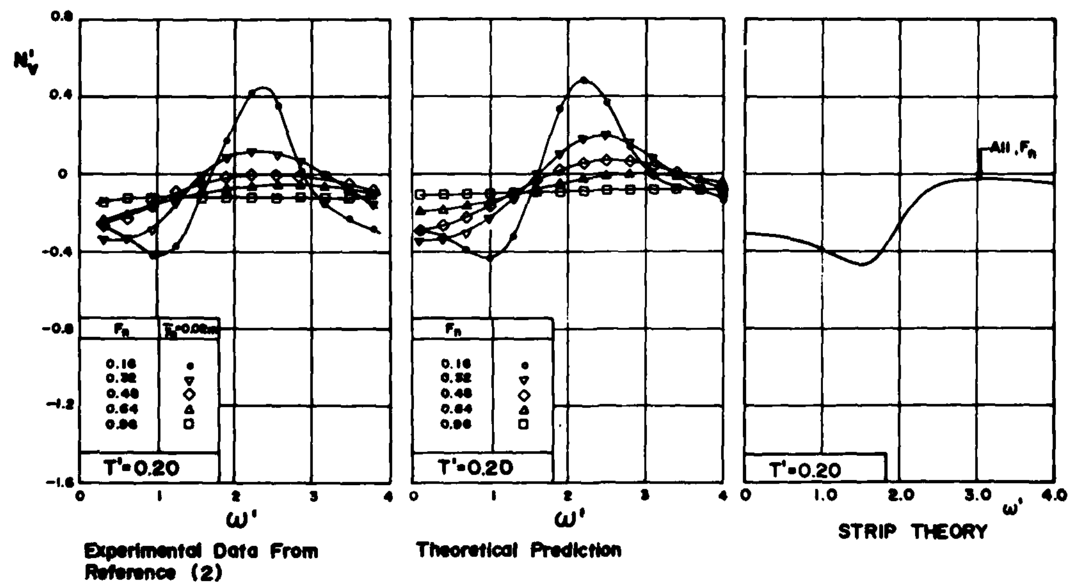

Figure 8 – Flat Plate Coupling of Sway into Yaw

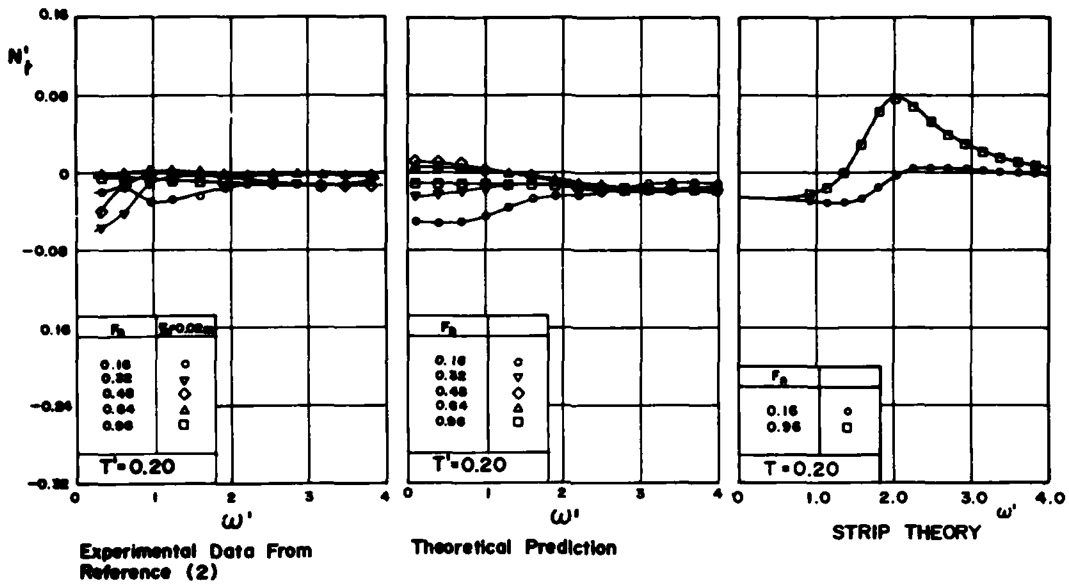

Figure 9 – Flat Plate Yaw Added Mass

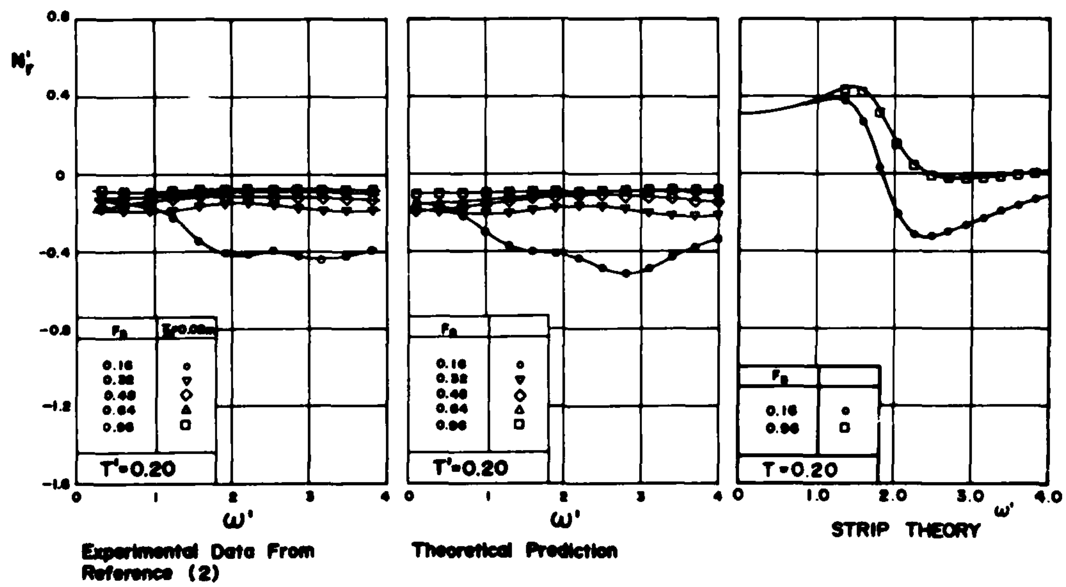

Figure 10 – Flat Plate Yaw Damping

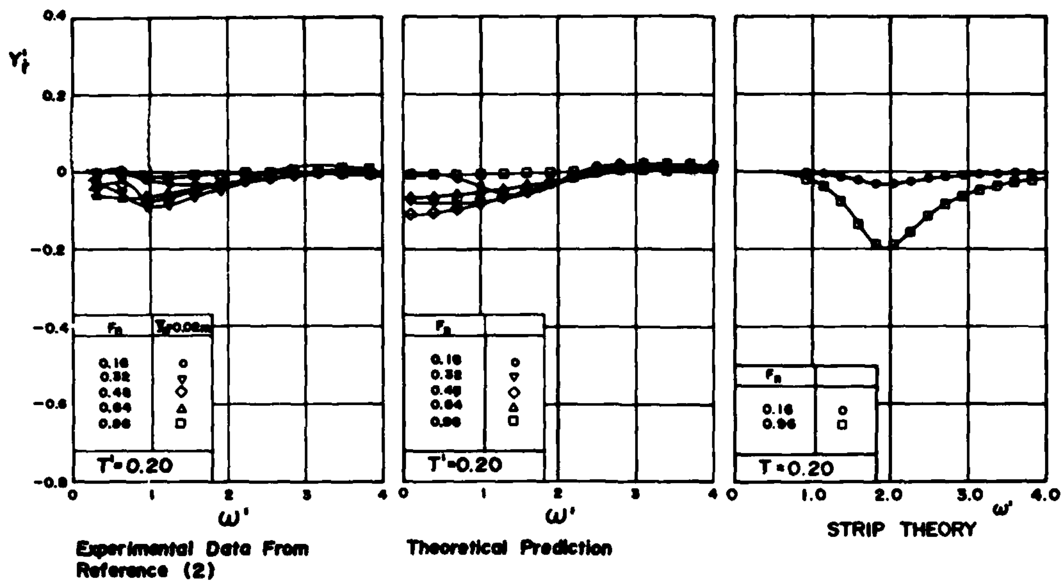

Figure 11 – Flat Plate Coupling of Yaw into Sway

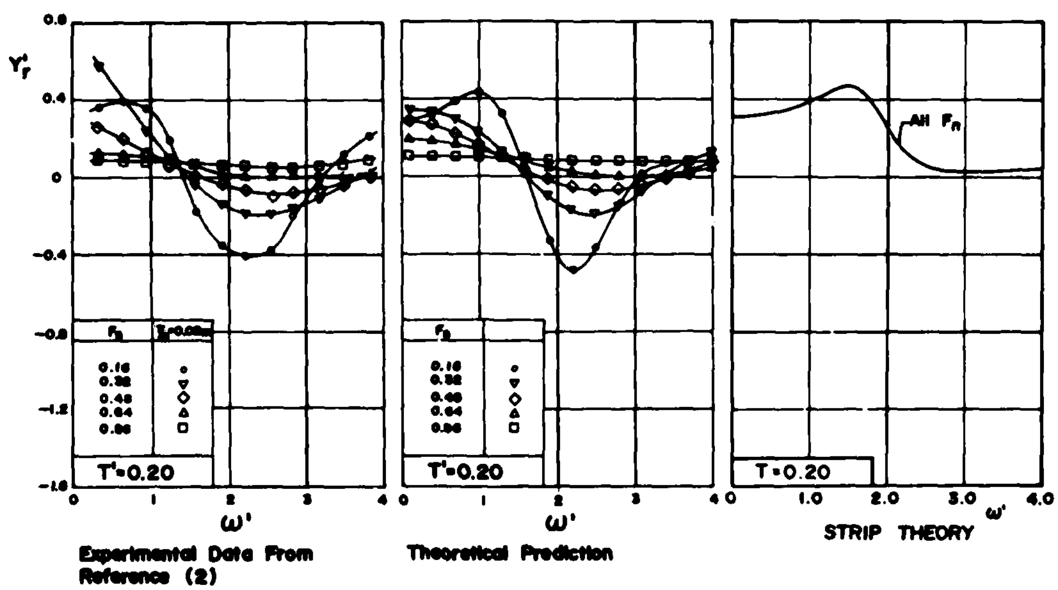

Figure 12 – Flat Plate Coupling of Yaw into Sway

NUMERICAL SOLUTION OF THE INCOMPRESSIBLE NAVIER STOKES EQUATIONS FOR TWO DIMENSIONAL FLOWS AT HIGH REYNOLDS NUMBER*

R.T. Davis

Department of Aerospace Engineering
University of Cincinnati
Cincinnati, Ohio 45221 U.S.A.

ABSTRACT

Over the past several years the author and co-workers have developed a numerical technique for solving the Navier Stokes equations for steady plane incompressible laminar flows. The method can be described as a boundary-layer like technique since it uses boundary-layer type coordinates and similarity variables and solves the full equations using an *alternating direction* implicit technique with the boundary-layer terms totally contained in one sweep. The second sweep in the ADI technique then corrects for the additional terms in the equations.

The technique was therefore developed specifically for solving high Reynolds number laminar steady flow problems and it has been found to converge very rapidly for cases where the flow is unseparated. More recently the method has been applied to separated flows, and while the convergence rate is slower, it still appears to be faster than many other methods.

The initial calculations were done using the finite difference technique in the entire flowfield. However, more recently the outer inviscid portion of the flowfield has been removed from the finite difference calculation and replaced by an integral formulation. This refinement improves the accuracy of the method. In addition, the same integral technique has been used to do interacting boundary-layer calculations.

*This research was supported by the Office of Naval Research under contract N00014-76-C-0364.

Results are presented for high Reynolds number flow past some two dimensional semi-infinite bodies. The bodies considered are ones for which under certain conditions the flow separates but reattaches before reaching downstream infinity. Improvements in the method such as the use of optimal coordinates are also discussed.

1. Introduction

The purpose of this paper is to discuss some of the difficulties the author and his co-workers have encountered in attempting to find accurate numerical solutions for high Reynolds number separated flows. It is the author's belief that in order to efficiently find accurate numerical solutions for flows under high Reynolds number conditions, more than an understanding of numerical analysis is needed. We have repeatedly found that a combined analytical-numerical approach is necessary. In the discussion which follows, we will consider only steady plane incompressible laminar flows. Accurate numerical solutions are scarce for even this case at high Reynolds number.

Until the present we have considered, with one exception, plane flows with very simple geometries. Initially the problems considered were unseparated flows past bodies like parabolas (Davis (1972)), paraboloids (Davis and Werle (1972)) and wedges (Davis, U. Ghia and K.N. Ghia (1974a,b)). All of these bodies are semi-infinite and are of such a shape that the outer inviscid flow is known at infinite Reynolds number. In addition, in every case, the downstream boundary conditions are known and are members of the Falkner Skan family of similarity solutions. Choosing simple flows of this type and thereby removing as much uncertainty from the problems as possible, we were able to focus attention on such questions as which coordinate system to use, what dependent variables to use, how to remove singularities (such as occur at the sharp tip of the wedge) and finally which numerical technique to use

to most efficiently handle a particular problem with high accuracy. The author believes that all of these items are interconnected.

With this approach, we were led into studying the ideas of Kaplun (1954) on optimal coordinates and were led to believe that a boundary-layer like ADI scheme, in similarity type variables, would be one of the most efficient and accurate methods for solving the Navier Stokes equations at high Reynolds number. Our numerical results on these problems tended to support this approach. In every case where we were able to compare with analytical or other numerical results, we were able to show excellent accuracy with generally higher convergence rates than found in other numerical methods. This exercise also pointed out to us, that in spite of the enormous amount of numerical fluid mechanics work being done on the Navier Stokes equations, there is very little in the way of highly documented simple flow solutions. It is interesting to note, for example, that the Navier Stokes solutions for flow past a semi-infinite flat plate were not done correctly until around 1970-72 by Dennis and Walsh (1971), Botta, Dijkstra and Veldman (1972), van de Vooren and Dijkstra (1970), Yoshizawa (1970) and Davis (1972). There is still a definite need to provide more of these types of highly accurate simple solutions to be used as check cases before we proceed on to the solution of complicated separated flow problems.

Our next step was to proceed slightly away from the unseparated plane case to consider steady plane flows with small separated bubbles. A typical flow of this type is shown in figure 1. The figure shows calculated streamlines for a flow coming from the left past a blunted flat plate of finite thickness. The Reynolds number for the case shown is about 250 based on the plate thickness. More detailed results are presented in U. Ghia and Davis (1974). The important features are that the body shape is generated from the conformal coordinate lines obtained from mapping the flow past a flat

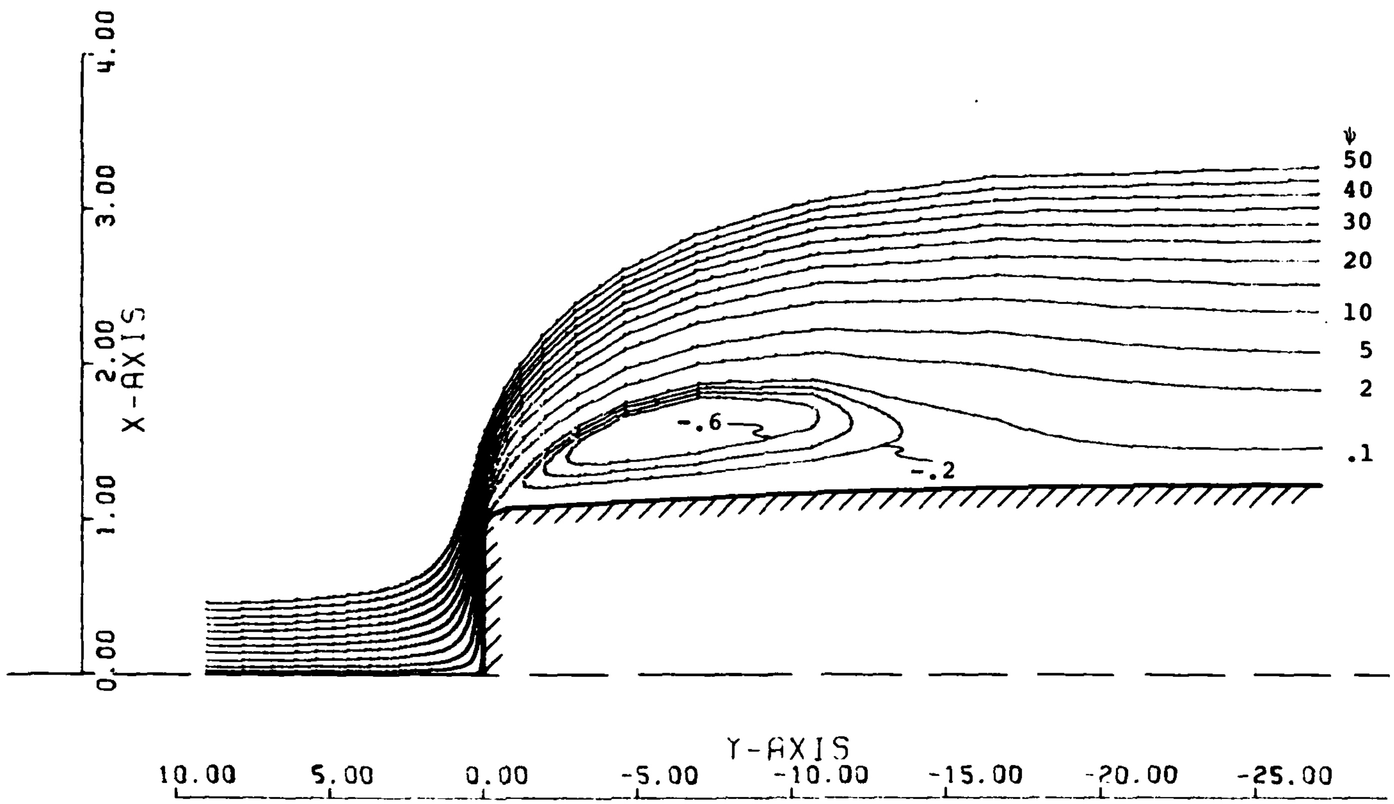

Figure 1. Streamlines for flow past a blunted plate at a Reynolds number of approximately 250 based on plate thickness.

plate of finite thickness to a stagnation point flow. The numerical calculations are thus carried out in the conformal plane. It can easily be shown that far downstream on the plate the flow approaches the Blasius flat plate flow providing the downstream boundary condition. The outer inviscid flow at high Reynolds number is found to be nearly the solution for inviscid flow past the body shape, except for interaction effects which arise near the corner due to the separated bubble and corner expansion.

The separation problem mentioned above represents separation from an exterior corner. At the same time Napolitano and Werle (1975) are studying separation ahead of an interior corner using the model problem of symmetric flow past a wedge with a flat plate attached to the leading edge. Again, this flow approaches a similarity solution far downstream.

In examining separated flow problems we have encountered several difficulties which we had not experienced in the fully attached cases. While we have been able to obtain accurate solutions for separated flows at low Reynolds number, the high Reynolds number cases have presented resolution problems. The recent asymptotic analysis of Sychev (1972) and Messiter and Enlow (1973), see figure 2, provides some explanation. We have been using scaling normal to the body surface proportional to $Re^{-1/2}$. This scaling is correct for unseparated flows, but as figure 2 indicates, as the separation point is approached, one will experience resolution problems unless scaling of the order $Re^{-5/8}$ in the tangential direction and of the order $Re^{-3/8}$ in the normal direction is used in the region near the wall. The alternative to this is to use an extremely fine grid system in the whole flowfield at high Reynolds numbers, which will cause extreme computing times and require large storage. Downstream of separation, additional scaling problems occur. However, figure 2 does demonstrate the first obstacle which must be overcome if accurate solutions are to

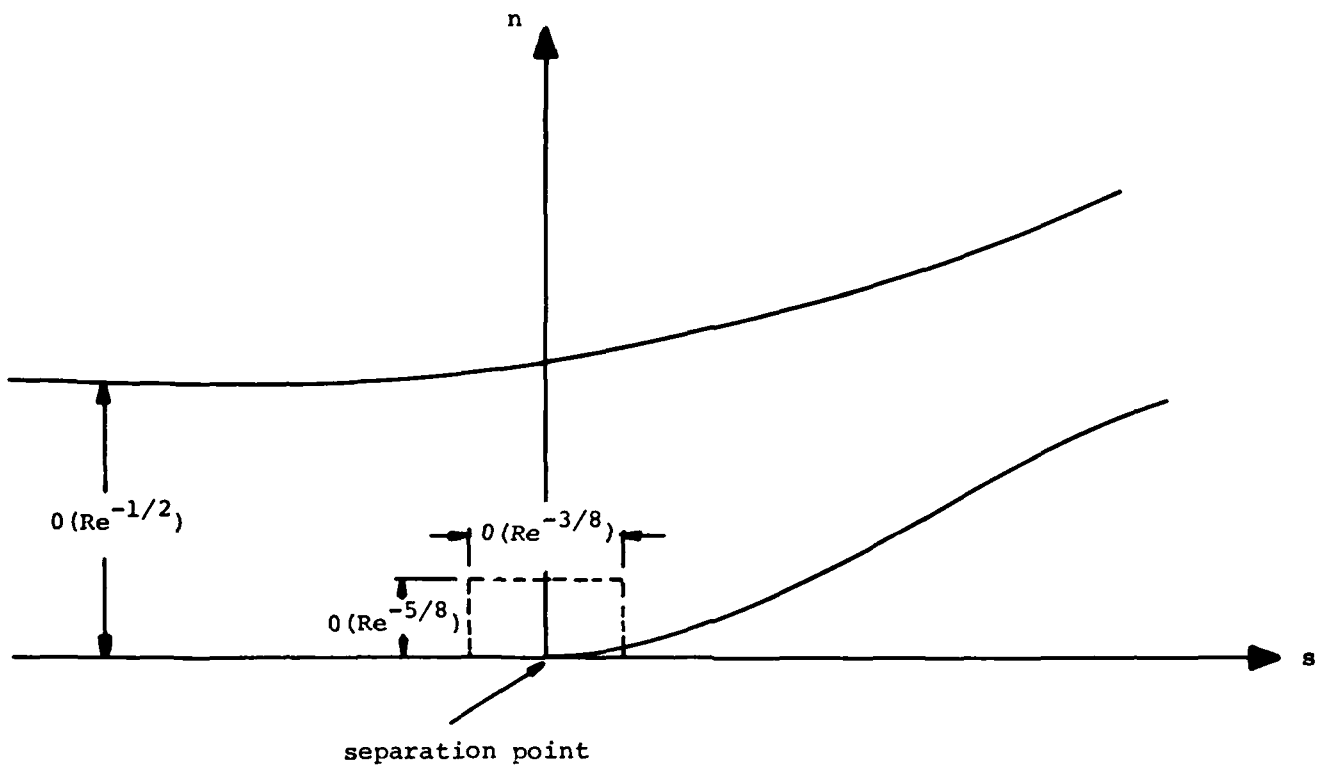

Figure 2. Scaling near incompressible laminar separation at high Reynolds number, after Sychev (1972) and Messiter and Enlow (1973).

be obtained at high Reynolds number. Jenson, Burggraf, and Rizzetta (1974) have provided the order of magnitude and asymptotic analysis for supersonic flow past the ramp shown in figure 3. The pioneering work of Stewartson and Williams (1969, 1973) and Stewartson (1974) has made such a "triple deck" analysis possible. Burggraf, Werle, Rizzetta and Vatsa (1975) have shown that the numerical results for interacting boundary-layer flow past such a ramp clearly indicate that the scaling is correct and that accurate numerical solutions are efficiently obtained if the scaling is honored in the numerical scheme.

It thus seems important that we understand and incorporate the results of high Reynolds number asymptotic analysis into our numerical schemes if we are to accurately and efficiently compute high Reynolds number separated flows.

In order to more fully understand our Navier Stokes calculations, we have also been doing interacting boundary-layer calculations. For many flows involving limited separations, there appears to be no doubt that interacting boundary-layer theory is adequate. In the cases of separated flow where direct comparisons have been made, the interacting boundary-layer calculations have shown excellent agreement with Navier Stokes calculations, even at fairly low Reynolds number, see Carter and Wornom (1975) and Briley and McDonald (1975) for example. It is the author's belief that a boundary-layer like theory with interaction is capable of predicting many separated flows of practical interest, making solution of the full Navier Stokes equations unnecessary in those cases. One purpose of our research has been to make comparisons of Navier Stokes and interacting boundary-layer calculations under identical conditions in order to determine the practical limitations of boundary-layer theory.

In summary, the important points in developing an accurate and efficient numerical scheme for solving the Navier Stokes equations at high Reynolds number are: 1. determination of an

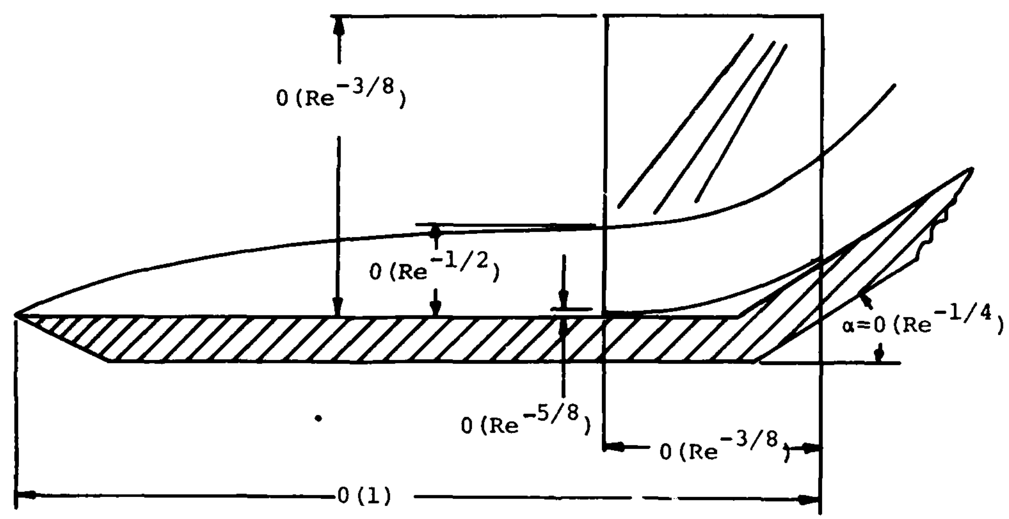

Figure 3. Triple Deck Structure, after Jenson, Burggraf, and Rizzetta (1974).

appropriate coordinate system with proper scaling of the independent variables, 2. determination of appropriate dependent variables which reflect similarity and remove singularities as much as possible, 3. determination of outer and downstream boundary conditions and 4. development of numerical techniques which best incorporate the above.

This paper will briefly discuss the pertinent work done on the above items.

2. Coordinate Systems (Optimal Coordinates)

One is always faced with the question of what is the best coordinate system to use in order to find an analytical solution to a given problem. There is no doubt that the same is true in finding numerical solutions. Choice of a correct coordinate system is important in finding separable solutions. In solving the boundary-layer equations, for example, it is important from a numerical standpoint that similarity type independent variables be used so that the equations can be reduced to ordinary differential equations when similarity conditions are satisfied. It is then easier to produce accurate numerical solutions to the resulting ordinary differential equations than the original partial differential equations. Even when similarity does not exist in all parts of the flowfield, similarity type variables tend to minimize variations in one coordinate direction allowing one to take larger step sizes in that direction in a finite difference method.

In studying coordinate systems in boundary-layer theory Kaplun (1954) discovered that solutions to the first-order boundary-layer equations depend upon the coordinate system. Wall quantities such as shear, heat transfer, etc. turn out to be independent of coordinate systems, whereas asymptotic quantities outside of the boundary layer are not. This dependence of asymptotic quantities on coordinate systems allows one to find coordinate systems such that the boundary-layer solution contains not only the outer inviscid flow, but also the flow

due to displacement thickness. These coordinates are called optimal coordinates by Kaplun. Legner (1971) extended this idea to arbitrary order and Davis (1974) generalized Legner's results.

The determination of coordinate systems for solving the Navier Stokes equations has been considered by several authors. For example Thompson, Thames and Mastin (1974) have developed a numerical procedure for generating coordinate systems. In order to generate a coordinate system in their manner, criteria must be stated which the coordinate system must satisfy. If one uses the criteria for optimal coordinates, optimal coordinates may be generated numerically in a manner similar to that used by Thompson et. al. Davis (1974) has shown how this can be done.

Why does one want to consider optimal coordinates as candidates for best coordinate systems for solving the Navier Stokes equations? First, by their fundamental nature, they confine the viscous part of the solution to boundary-layer like equations and the inviscid part of the solution to coordinate equations which account for displacement effects. Therefore, they partially take care of the scaling problems which occur between viscid and inviscid regions at high Reynolds number, since different scales can be used in the two separate, but coupled (through boundary conditions) sets of viscid and inviscid equations. Second, the determination of optimal coordinates is not unique and therefore, enough arbitrariness is left to satisfy similarity conditions and possibly remove singularities at leading edges and corners. Third, once an optimal coordinate system is determined which satisfies similarity conditions and removes as many singularities as possible, the predominate terms in the Navier Stokes equations should be the boundary-layer like terms and therefore one can develop a numerical method which takes advantage of this. One such method is the ADI scheme developed by Davis (1972).

Davis (1974) has shown that, for plane symmetric flows,

if one uses Legner's (1971) conditions for optimal coordinates and assumes the coordinates are orthogonal, the coordinates must be conformal coordinates. Thus, for example, the only orthogonal coordinates for symmetric flow past the semi-infinite flat plate which can be optimal according to Legner's results are parabolic coordinates. These coordinates were therefore used in Davis' (1972) numerical scheme for viscous flow over a parabola, which becomes a flat plate as the nose radius of curvature approaches zero. While these coordinates are not completely optimal, they can be shown to be optimal to third order in terms of boundary-layer theory. They also have the proper form for removing the singularity at the leading edge of the plate. Unfortunately, the conformal coordinate system for symmetric flow past a wedge, while also optimal to third order, does not remove the singularity at the leading edge except when the wedge half angle is 0° (flat plate) or 90° (vertical wall), see Davis, U. Ghia, and K.N. Ghia (1974a,b). The consideration of more general optimal coordinates should allow the arbitrariness needed to remove this singularity.

In the numerical work done to the present, there appears to be an advantage in using coordinates which are at least partially optimal. It is felt that properly chosen completely optimal coordinates will be even more advantageous.

In the remainder of this paper conformal coordinates will be used, since in the spirit of optimal coordinates, they are the best orthogonal coordinates.

3. Navier Stokes Equations for Plane Flow

The Navier Stokes equations for plane flow in terms of stream function ψ and vorticity ω are written as follows in dimensionless form:

$$\frac{D\omega}{Dt} = \nabla^2\omega \qquad (3.1a)$$

and

$$\nabla^2\psi = -\omega \quad , \tag{3.1b}$$

where lengths are nondimensionalized by ν/U, t is nondimensionalized by ν/U^2, and ψ and ω are nondimensionalized by ν and U^2/ν respectively. The quantity ν is the kinematic viscosity and U is the freestream speed. Equations (3.1) are therefore expressed in Oseen variables.

In view of the discussion of section 2 on optimal coordinates, the governing equations (3.1) are next transformed to conformal coordinates. Let $z = x+iy$ be the physical plane and $\zeta = \xi+i\eta$ be the conformal plane, see figure 4. The conformal transformation is given by $z = f(\zeta)$ and the resulting Navier Stokes equations are

$$\psi_{\eta\eta} + \psi_{\xi\xi} = -\frac{1}{H}\,\omega \tag{3.2a}$$

and

$$\omega_{\eta\eta} + \omega_{\xi\xi} + \psi_{\xi}\,\omega_{\eta} - \psi_{\eta}\,\omega_{\xi} = \frac{1}{H}\,\omega_t \tag{3.2b}$$

where

$$z = x+iy = f(\zeta) \quad , \tag{3.3a}$$

$$\zeta = \xi+i\eta \quad , \tag{3.3b}$$

$$h = |f'(\zeta)| \quad , \tag{3.3c}$$

and

$$H = \frac{1}{h^2} \quad . \tag{3.3d}$$

Figure 4 shows the physical and transformed planes for a particular body shape, in this case the flat plate of finite thickness considered by U. Ghia and Davis (1974). Notice that the flow past the body is transformed to a stagnation point type flow. All flows past bodies in our investigations are handled in a stagnation point plane, since in this plane the Navier Stokes equations reduce to the Falkner Skan equations at downstream infinity and therefore directly produce the downstream boundary conditions as solutions of ordinary

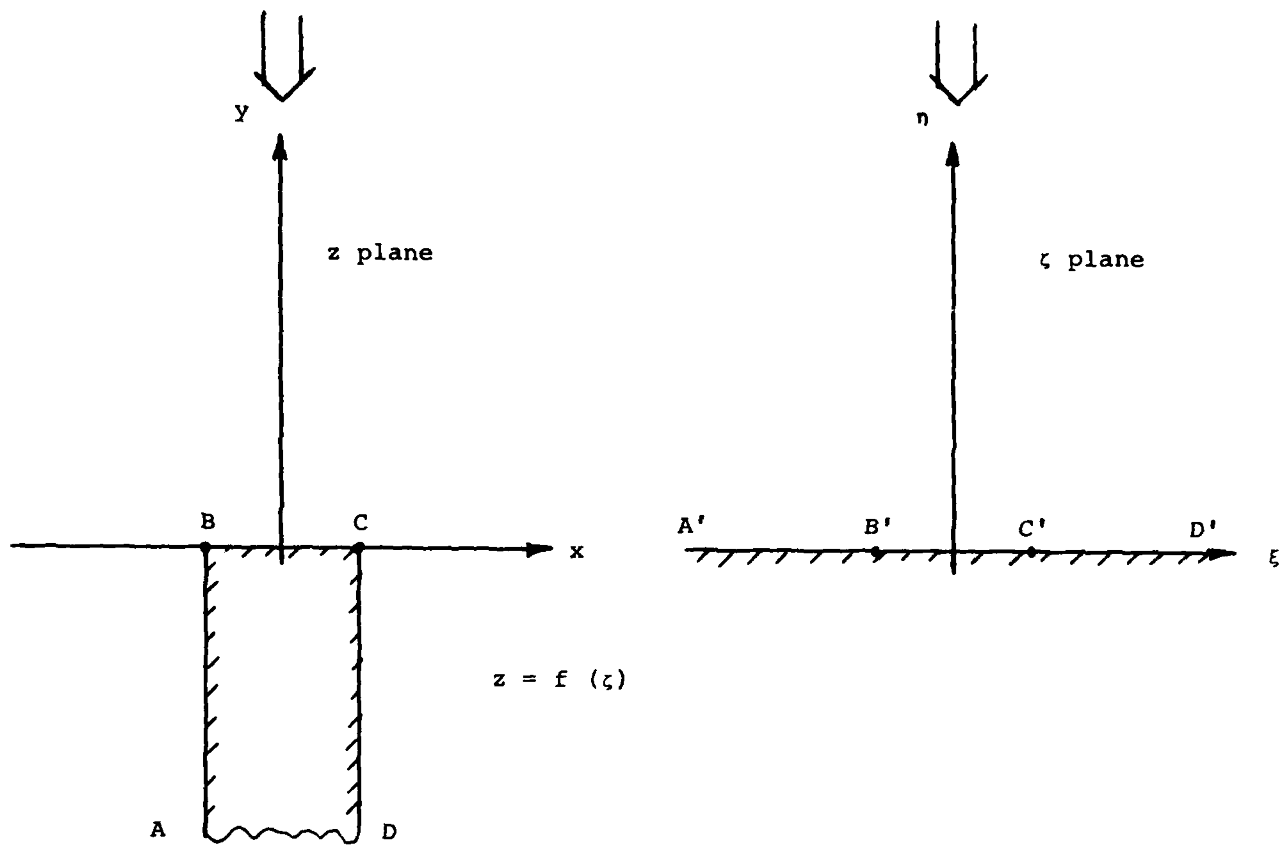

Figure 4. Transformation from physical to conformal plane, see U. Ghia and Davis (1974).

differential equations.

In view of the fact that the streamfunction is an odd function of ξ about the stagnation point, and that the form of the outer potential flow is $\psi = \xi\eta$, a transformed streamfunction is introduced as

$$\psi = \xi f(\xi,\eta) \quad . \tag{3.4a}$$

Substituting (3.4a) into the transformed streamfunction equation (3.2a) it is easily shown that the most proper form for the vorticity transformation is

$$\omega = - \xi H g(\xi,\eta) \quad . \tag{3.4b}$$

In these variables the transformed streamfunction equation (3.2a) becomes

$$f_{\eta\eta} + f_{\xi\xi} + \frac{2}{\xi} f_{\xi} = g + \frac{\partial f}{\partial v} \tag{3.5a}$$

where a fictitious time derivative $\partial f/\partial v$ has been added, which we will discuss later.

The transformed vorticity equation becomes from equation (3.2b)

$$\begin{aligned} g_{\eta\eta} &+ [2 \frac{H_\eta}{H} + f + \xi f_\xi] g_\eta + [\frac{2}{\xi} \frac{H_\xi}{H} + \frac{H_\eta^2 + H_\xi^2}{H^2} + \frac{H_\eta}{H} (f + \xi f_\xi) \\ &- f_\eta (1 + \xi \frac{H_\xi}{H})] g + [2 \frac{H_\xi}{H} - \xi f_\eta] g_\xi + g_{\xi\xi} + \frac{2}{\xi} g_\xi \\ &= \frac{1}{H} \frac{\partial g}{\partial t} \quad . \end{aligned} \tag{3.5b}$$

Some lengthy algebra is required in reducing terms involving the scale factor H to the form shown in the coefficient of the g term.

An important feature of equations (3.5) is that they reduce to the Falkner Skan equations at downstream infinity, see U. Ghia and Davis (1974). This gives additional support to the choice of the streamfunction and vorticity transformations given by equations (3.4).

Another important feature to notice is that the boundary conditions are free of any ξ dependence. They can be written as follows (see figure 4):

$$f_\xi(0,\eta) = 0 \quad , \tag{3.6a}$$

$$f(\xi,0) = 0 \quad , \tag{3.6b}$$

$$f_\eta(\xi,0) = 0 \quad , \tag{3.6c}$$

$$f_\eta(\xi,\infty) = 1 \quad , \tag{3.6d}$$

$$g(\xi,\infty) = 0 \quad , \tag{3.6e}$$

$$f(\infty,\eta) = \text{Falkner Skan solution} \tag{3.6f}$$

and

$$g(\infty,\eta) = \text{Falkner Skan solution.} \tag{3.6g}$$

We see that f and g are therefore similarity-type variables for the Navier Stokes equations.

4. Integral Equation Formulation and Solution for the Outer Inviscid Flow

Equations (3.5) have been solved with finite difference methods which will be discussed later. However, rather than integrate to $\eta = \infty$ with a finite difference method, one can solve the external inviscid flow problem by means of an integral equation method. Botta and Dijkstra (1970) have discussed one such method using a Green's function approach.

Inside the region near the body surface the vorticity function g is nonzero. However, away from the body surface the vorticity g dies out exponentially and the streamfunction variable f approaches an inviscid potential flow. In this potential flow region the flow can be represented by any one of several integral equations. In the conformal (ξ,η) plane these integral equations become particularly simple.

If we let $f = \eta + h$ to remove the first order inviscid part of the flow and consider h to be the perturbation on the outer flow due to viscous effects we can write the following integral

equation for h for a source distribution on $\eta = N$ (see figure 5)

$$\xi h_{\eta} + \frac{1}{\pi} \int_{-\infty}^{\infty} \frac{\xi - x}{r^2} \frac{d}{dx} (xh) \, dx = 0 \quad . \tag{4.1}$$

The integral equation for a vortex distribution on $\eta = N$ is

$$(\xi h)_{\xi} - \frac{1}{\pi} \int_{-\infty}^{\infty} \frac{\xi - x}{r^2} \, x h_{\eta} \, dx = 0 \quad . \tag{4.2}$$

The results for a Green's function approach can be found in Botta and Dijkstra (1970).

Hess and co-workers have extensive experience in solving integral equations of the type (4.1) or (4.2), see Hess (1975) for example. Following their procedure, the source distribution, $\frac{d}{dx}$ (xh), or the vortex distribution, xh_{η}, on $\eta = N$ is assumed to be a constant over an element as a first approximation, or to vary linearly over an element as a second approximation. The integration is then performed analytically for a single element with the assumed source or vortex distribution and the integrals in (4.1) and (4.2) are replaced with summations over all of the elements. When the resulting expressions are evaluated at $\eta = N$ a set of simultaneous algebraic equations result. These equations can then be used to replace the outer boundary condition (3.6d).

The advantage in using this formulation is that greater accuracy can be achieved in the solution of the outer flowfield since one does not need to address the question of how to place grid points near infinity in a finite difference method to properly handle the asymptotic approach of the inviscid flow to the conditions at infinity. In addition, this approach should require less computer time since many mesh points can be eliminated from the finite difference computation. We have used this method in a limited number of cases and found that it should be pursued further. We do not yet have enough experience in using the method to make it as efficient as we feel it

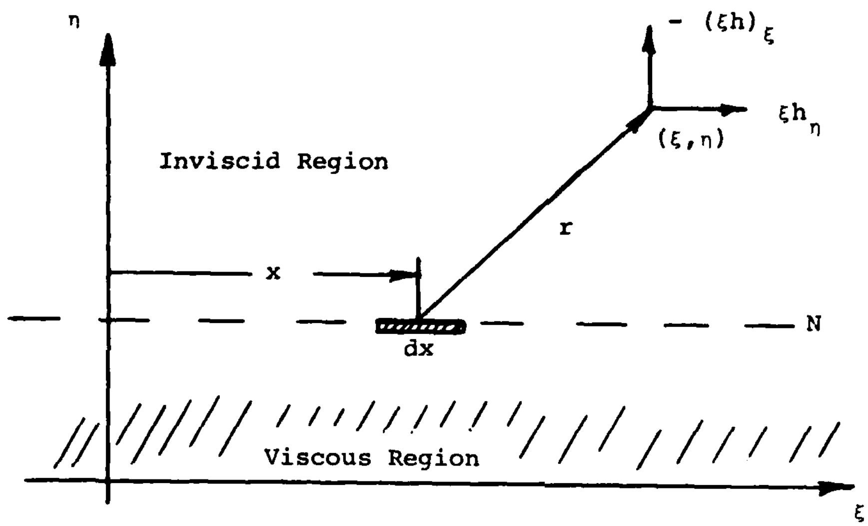

Figure 5. Schematic for formulation of the integral equations.

should be.

Wu and Thompson (1973) have developed a method which solves the vorticity equation coupled to an integral equation relating vorticity to the velocity components. This integral equation replaces the streamfunction equation in the entire flowfield. The method thus removes the inviscid portion of the flowfield from the computation. If one counts the number of steps required to solve this integral equation, it becomes clear that even though the method is attractive from a theoretical viewpoint, it is inefficient for numerical calculations unless a much faster method than presently exists is developed for solving the integral equation. Our limited experience with the method has led us to abandon it at present for this reason. We have some ideas on how the integral equation may be solved more efficiently, but have not yet explored them.

5. Interacting Boundary-Layer Theory

There is growing evidence that the boundary-layer equations, including interaction with the external inviscid flow, are sufficient for handling many separated flow problems. Werle and Vatsa (1974) have developed an efficient method for handling some types of supersonic separated flows. Carter (1974), Carter and Wornom (1975), Klineberg and Steger (1974) and Briley and McDonald (1975) have presented methods for handling the incompressible separated flow problem. However, all of these methods have problems which indicate that improvements are needed. For example, all of the methods developed for incompressible flows show very slow convergence.

We can easily develop interacting boundary-layer type equations in conformal coordinates from the full Navier Stokes equations (3.5). Expressing the equations in boundary-layer variables we find that the $g_{\xi\xi} + \frac{2}{\xi} g_{\xi}$ terms in equation (3.5b) are of third order importance in terms of boundary-layer theory. These are the terms which make the vorticity equation elliptic in the spacial variables. Therefore, neglecting them

results in a vorticity equation which is parabolic in space and at the same time is valid to second order. We have called this equation a parabolized vorticity equation, see U. Ghia and Davis (1974). Therefore, one type of interacting boundary-layer theory has been explored by solving the parabolized vorticity equation along with the full streamfunction equation (3.5a). This set of equations is valid in the entire flow-field. Excellent agreement has been found between solutions to this set of equations and the full Navier Stokes equations for separated and unseparated flows, even at fairly low Reynolds numbers. From a numerical viewpoint there is no advantage to go further with the vorticity equation and reduce it to the first-order boundary-layer equation since the parabolized vorticity equation is already of parabolic type. However, Werle and Bernstein (1975) have explored further simplifications in the vorticity equation and compared the results to solutions of the full Navier Stokes equations. They find excellent agreement at moderate to high Reynolds numbers.

The numerical advantage in the use of a parabolized vorticity equation with the full streamfunction equation is that it reduces computer time by about 25% when compared to the solution of the full Navier Stokes equations. However, of more importance from a theoretical viewpoint, is the excellent agreement found between the exact and parabolized vorticity models. These calculations show that a boundary-layer like vorticity equation is entirely adequate for calculating separated flows of the type we have considered. The coordinate system in which the parabolic approximation is made is undoubtedly important. Even in flows with large separations, the parabolic approximation may be adequate if the correct coordinate system is used. It can be shown that a coordinate system based on the inviscid streamlines, including displacement effects, is always optimal. Such a coordinate system could be the best one for making the parabolic approximation.

We can proceed on and develop a true interacting boundary-

layer theory. The streamfunction equation (3.5a) is simplified by neglecting all terms of higher order than second in boundary-layer theory. This involves neglecting the $f_{\xi\xi} + \frac{2}{\xi} f_\xi$ terms in equations (3.5a). At the same time the $\partial f/\partial v$ term is deleted since it serves no purpose except in the numerical solution of the full equations. The resulting set of equations are no longer valid in the entire flowfield, i.e. they are now only valid in the boundary-layer region near the body surface. Higher order boundary-layer theory shows that the external inviscid flow is disturbed by the effect of the boundary-layer displacement thickness. This flow due to displacement thickness can be calculated by one of the integral methods discussed in section 4. It can be shown that to second order in terms of boundary-layer theory (see Van Dyke (1962)) the correct equations are

$$g_{\eta\eta} + [2 \frac{H_\eta}{H} + f + \xi f_\xi] g_\eta + \{\frac{2}{\xi} \frac{H_\xi}{H} + \frac{H_\eta^2 + H_\xi^2}{H^2} + \frac{H_\eta}{H} (f + \xi f_\xi)$$

$$- f_\eta \ (1 + \xi \frac{H_\xi}{H})\} g + [2 \frac{H_\xi}{H} - \xi f_\eta] \ g_\xi = \frac{1}{H} \frac{\partial g}{\partial t} \qquad (5.1a)$$

and

$$f_{\eta\eta} = g \quad . \qquad (5.1b)$$

The appropriate boundary and matching conditions are

$$f(\xi,0) = 0 \quad , \qquad (5.2a)$$

$$f_\eta(\xi,0) = 0 \quad , \qquad (5.2b)$$

$$g(\xi,\eta) \sim 0 \text{ as } \eta \to \infty \quad , \qquad (5.2c)$$

and

$$\text{prescribe } f_\eta,\ f,\ \eta f_\eta - f, \text{ or ? as } \eta \to \infty \quad . \qquad (5.2d)$$

The outer edge matching condition (5.2d) can be handled in several ways. For example, if we let $f = \eta + h$ to remove the first order inviscid flow we can show from asymptotic matching that

$$\left.\begin{aligned} \eta h_\eta - h &= D(\xi) = \int_0^\infty \eta g d\eta, \qquad &(5.3a)\\ h_\eta &= h_{i\eta}(\xi,0) \quad , \qquad &(5.3b)\end{aligned}\right\} \text{as } \eta \to \infty$$

and

$$h_i(\xi,0) = - D(\xi) \tag{5.3c}$$

where

$$D(\xi) = [1+h_{i\eta}(\xi,0)]\bar{\delta}(\xi) \quad . \tag{5.3d}$$

The quantities $h_{i\eta}(\xi,0)$ and $h_i(\xi,0)$ are the inviscid values evaluated on the body surface.

Thus, if we use a surface source distribution, we solve the integral equation (4.1) evaluated on $\eta = 0$,

$$\xi h_{i\eta}(\xi,0) = \frac{1}{\pi} \int_{-\infty}^{\infty} \frac{\xi-x}{r^2} \frac{d}{dx} (xD(x))\, dx \quad , \tag{5.4a}$$

to produce an edge condition for h of the form

$$h = \eta h_{i\eta}(\xi,0) - D(\xi) \quad \text{as} \quad \eta \to \infty \quad . \tag{5.4b}$$

The quantity $D(\xi)$, which is related to displacement thickness, is determined from the boundary-layer equations through equation (5.3a).

If we use a surface vortex distribution, we solve the integral equation (4.2) evaluated on $\eta = 0$,

$$[\xi D(\xi)]_\xi = - \frac{1}{\pi} \int_{-\infty}^{\infty} \frac{\xi-x}{r^2}\, x\, h_{i\eta}(x,0)\, dx \quad , \tag{5.5a}$$

to produce an edge condition for $\eta h_\eta - h$ of the form

$$\eta h_\eta - h = D(\xi) \quad \text{as} \quad \eta \to \infty \quad . \tag{5.5b}$$

The equations (5.1) with boundary and matching conditions (5.2) and (5.4a,b) or (5.5a,b) form a closed set. Messiter's (1975) equations for separated boundary layers contain no

additional terms and therefore these equations are appropriate for calculating separated flows. The coupling between the equations is complicated and for this reason, numerical solution of the equations is difficult and until the present time unsatisfactory from a rate of convergence viewpoint. Even though equations (5.1) are parabolic in space, the total set of equations is effectively elliptic through the edge conditions (5.4a,b) or (5.5a,b). Information also propagates upstream through the coefficients in (5.1a) in a manner which is still not completely understood. Werle and Vatsa (1974) have found that even in the supersonic case, the interacting boundary-layer equations are boundary value in nature due to upstream propagation of information through the coefficients of the momentum equation. The very slow convergence of Carter's (1974) method for the incompressible case is perhaps due to a somewhat less than optimal handling of some terms in forming his difference equations. All incompressible interacting boundary-layer methods developed to date seem to possess slow convergence.

We will not go into the details of how we are handling the interacting boundary-layer equations here. We will present some results in section 7 for comparison with Navier Stokes solutions. Details of the numerical scheme will be presented in a paper which will appear shortly.

It is important to study interacting boundary-layer theory for two reasons. First, better numerical schemes for handling interacting boundary-layer theory should result in better schemes for solving the Navier Stokes equations. Second, it is important to determine under what conditions interacting boundary-layer theory is adequate so that one can bypass the computationally time consuming Navier Stokes solutions whenever possible.

6. Numerical Method for Solution of the Navier Stokes Equations

The present numerical method being used to solve the Navier Stokes equations is essentially the same as that described in Davis (1972) or U. Ghia and Davis (1974). Some minor modifications have been made in the method to incorporate the integral conditions described in section 4. In addition, a version exists for solving the equations in the completely optimal coordinates described in Davis (1974). Slow convergence of the method for high Reynolds number separated flows has led us to spend more time on interacting boundary-layer theory to try to determine the reason for slow convergence. At the conclusion of this study of interacting boundary-layer theory, it is anticipated that some fairly major modifications will be made to the Navier Stokes solution method, at least for high Reynolds number separated flow cases.

Basically the present method consists of the following. Equations (3.5a) and (3.5b) have been developed so that they contain the similarity type boundary-layer terms. Therefore, one would expect that the major contribution to the solution of the equations comes from those terms. An ADI scheme is therefore most appropriate in solving the equations since the boundary-layer like terms can be gathered in one sweep and corrections made to them in a second sweep. The fictitious $\partial f/\partial v$ term was therefore added to equation (3.5a) in order to fully employ an ADI method. This term disappears when the solution approaches the steady state. With this modification the application of the ADI scheme is straightforward and the first sweep consists of a boundary-layer like calculation performed in space variables in a manner similar to the method developed by Blottner and Flügge-Lotz (1963) for solving the boundary-layer equations. The second sweep consists of gathering the remaining terms and performing what may be viewed as a correction to boundary-layer theory.

As would be expected, the method converges rapidly at all

Reynolds numbers for unseparated problems which are boundary-layer like. The method converges at a slower rate for separated flows. It is expected that the reason for slower convergence of the Navier Stokes solution method for separated flows is the same as the reason for slow convergence of interacting boundary layer methods. This is likely since the Navier Stokes method relies heavily on a boundary-layer like solution method in the first sweep. We anticipate that any modifications which improve convergence in the interacting boundary-layer calculations will result in the same for the Navier Stokes solutions. Thus far, we have found this to be the case.

We still must face the scaling problems which arise in high Reynolds number separated flows as has been indicated by Messiter (1975) for example. At present we are using a finer mesh near the separation point, but in the future we need to more fully explore transformations to stretch the regions of difficulty. This will ultimately be necessary in order to efficiently and accurately calculate high Reynolds number separated flows.

7. Results and Conclusions

The accuracy and efficiency of the ADI numerical scheme developed and used by the author and his co-workers has been well documented for some simple unseparated flows. For example, Davis (1972) has shown three place agreement with several other authors for skin friction distributions on parabolas and a semi-infinite flat plate. At the same time the numerical procedure converged faster than others. Davis and Werle (1972) have found the same type of convergence and accuracy for flow past a paraboloid. They also present results which indicate how convergence rate depends upon time steps.

U. Ghia and Davis (1974) have presented results for low Reynolds number separated and unseparated flows past a blunted flat plate. Some additional calculations have been performed in order to examine solutions for separated flows past these

bodies at high Reynolds number. While it appears that we have accurate solutions for the separated flows at low Reynolds number, step size studies indicate that the high Reynolds number separated flow solutions tend to be inaccurate and tend to converge slowly. We feel that the accuracy problem is due to poor resolution due to the scaling problems associated with high Reynolds number separation.

In order to demonstrate some of the points made in this paper, we will consider some solutions for flow past the blunted flat plate used by U. Ghia and Davis (1974). Figure 6 shows the geometry of the bodies. The flow at infinity approaches from the left along the y axis. The quantity α is a parameter which determines the body shape. Three cases are shown in the figure. If $\alpha = 0$, the body is a flat plate of finite thickness and some results for this case are presented in U. Ghia and Davis (1974). The body shapes represented by $\alpha = 0.2$ and $\alpha = 0.1$ are chosen for this study since the flows over them will not separate ($\alpha = 0.2$) and nearly separate or separate ($\alpha = 0.1$).

In applying our numerical procedures, the infinite region extending from $\xi = 0$ to $\xi = \infty$ in the conformal plane (see figure 4) is transformed to a finite region extending from $s = 0$ to $s = 1$, see U. Ghia and Davis (1974). The locations of several values of s are shown in figure 6 for reference. The η coordinate is also transformed to a N coordinate, see U. Ghia and Davis (1974), but we do not need to discuss that since results will only be presented for skin friction on the body surface.

The Navier Stokes equations (3.5a,b) and the interacting boundary-layer equations (5.1a,b) and (5.4a,b) have been integrated numerically under identical conditions. The same transformations, variables, and step sizes have been used.

Figure 7 presents results for the surface skin friction function g_w for the case of $\alpha = 0.2$ with 40 steps in the s direction and 100 steps in the N (transformed η) direction.

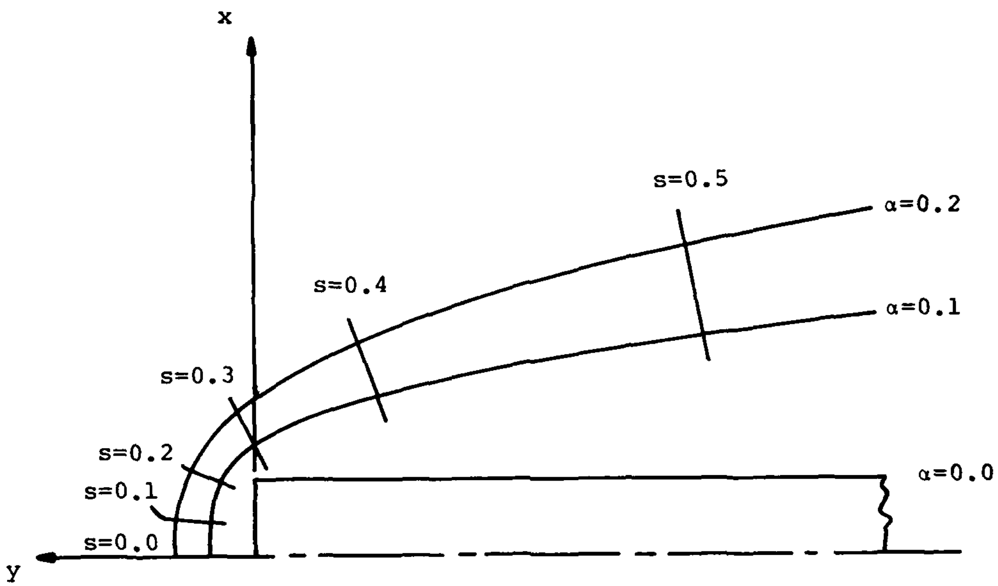

Figure 6. Body geometries.

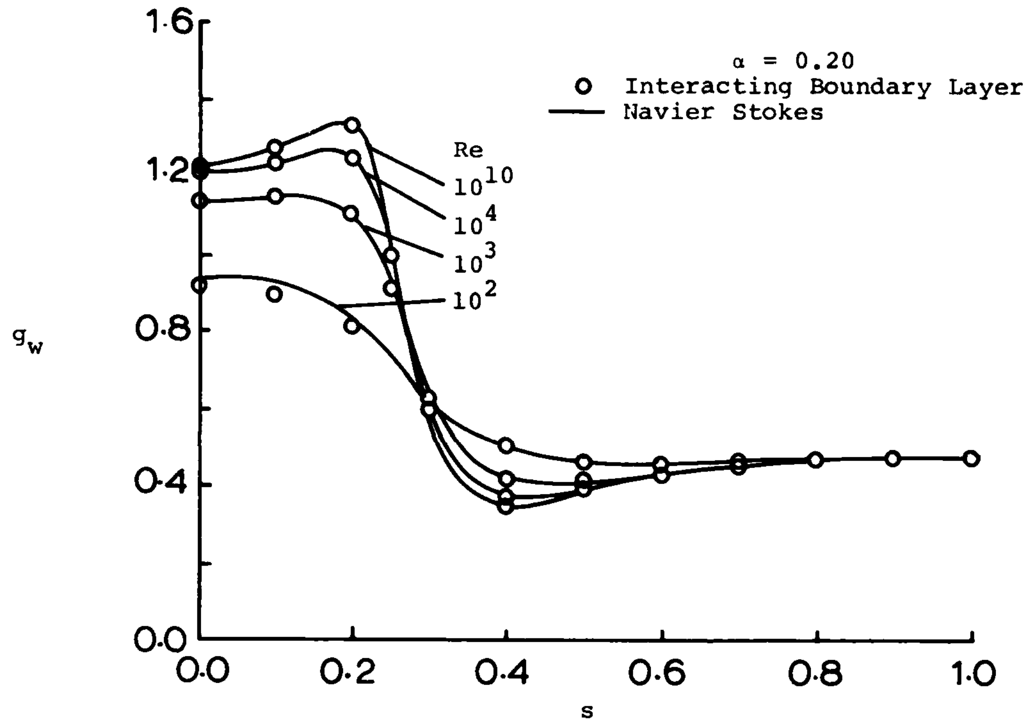

Figure 7. Comparison of interacting boundary layer with Navier Stokes solutions.

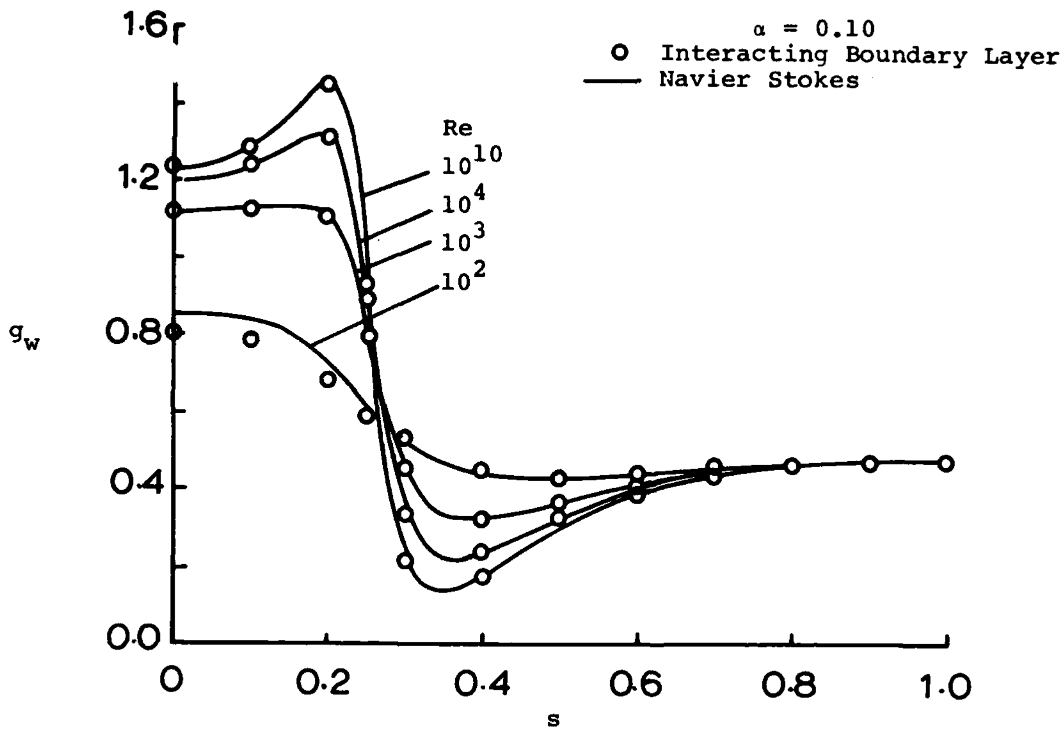

Figure 8. Comparison of interacting boundary layer with Navier Stokes solutions.

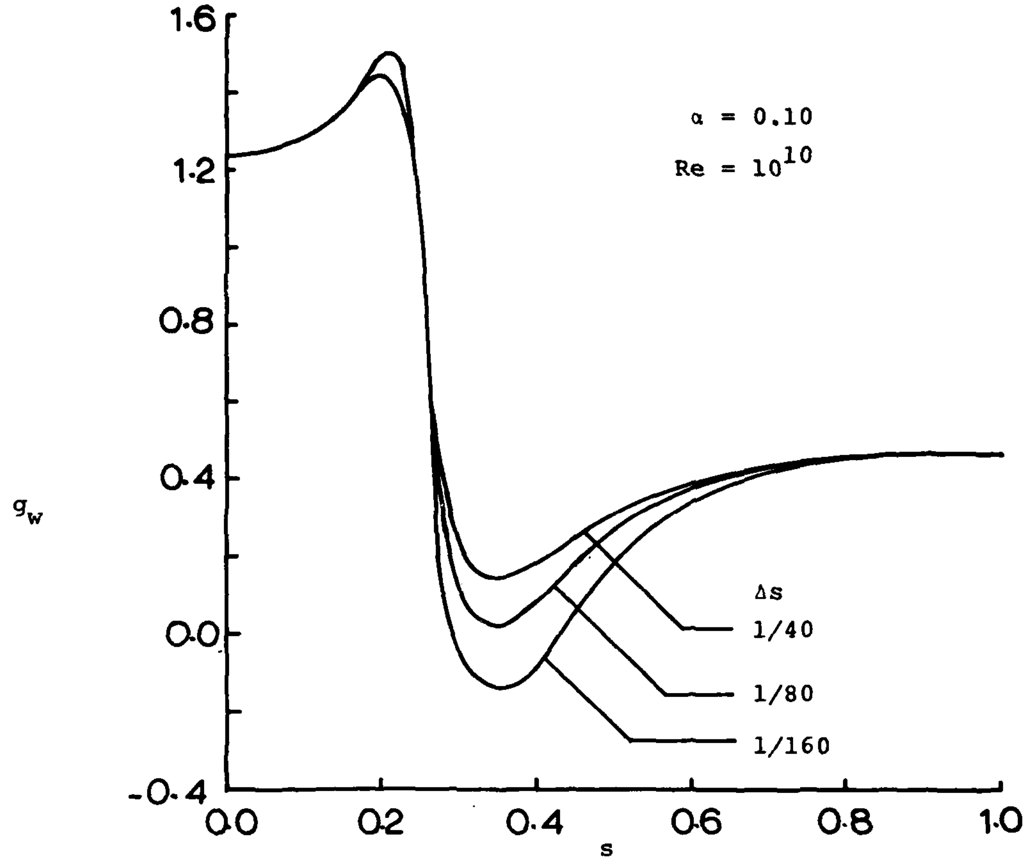

Figure 9. Step size study for an interacting boundary layer calculation.

The Reynolds number, Re, is based on the body nose radius of curvature. The interacting boundary-layer calculations are in excellent agreement with the Navier Stokes calculations for high Reynolds numbers. At a Reynolds number of 100 one notices a departure between the two results, which is to be expected.

In figure 8 one notices a similar trend for $\alpha = 0.1$. However, this case indicates that at high Reynolds number the flow is nearly separated at around $s = 0.35$. Figure 9 indicates that on closer examination with more grid points, the flow is in fact separated around $s = 0.35$ at $Re = 10^{10}$ and that many more grid points are needed to properly resolve the separated flow region.

This last calculation, shown in figure 9, demonstrates one of the main problems associated with high Reynolds number separated flows. The problem of resolution in a separation region for low Reynolds number flows will not demonstrate nearly as severe a problem. We hope to be able to demonstrate that the inaccuracy at high Reynolds number is associated with the severe scaling problems indicated by Messiter (1975) and Sychev's (1972) theory.

References

Blottner, F.G. and Flügge-Lotz, I. (1963), "Finite-Difference Computation of the Boundary-Layer with Displacement Thickness Interaction," Journal de Mecanique, Vol. II, No. 4, 1963, pp. 397-423.

Botta, E.F.F. and Dijkstra, D. (1970), "An Improved Numerical Solution of the Navier-Stokes Equations for Laminar Flow Past a Semi-Infinite Flat Plate," Mathematisch Instituut Rijksuniversiteit Groningen, Report TW-80, July 1970.

Botta, E.F.F., Dijkstra, D. and Veldman, A.E.P. (1972), "The Numerical Solution of the Navier-Stokes Equations for Laminar, Incompressible Flow Past a Parabolic Cylinder," J. Eng. Math, 6, 1972, pp. 63-81.

Briley, W.R. and McDonald, H. (1975), "Numerical Prediction of Incompressible Separation Bubbles," J. Fluid Mech., Vol. 69, part 4, 1975, pp. 631-656.

Burggraf, O.R., Werle, M.J., Rizzetta, D., and Vatsa, V.N. (1975), "Effect of Reynolds Number on Laminar Separation of a Supersonic Stream," paper in preparation.

Carter, J.E. (1974), "Solutions for Laminar Boundary Layers with Separation and Reattachment," AIAA Paper No. 74-583, presented at the AIAA 7th Fluid and Plasma Dynamics Conference, Palo Alto, California, June 1974.

Carter, J.E. and Wornom, S.F. (1975), "Solutions for Incompressible Separated Boundary Layers Including Viscous-Inviscid Interaction," NASA SP-347, pp. 125-150.

Davis, R.T. (1972), "Numerical Solution of the Navier Stokes Equations for Symmetric Laminar Incompressible Flow Past a Parabola," Journal of Fluid Mechanics, Vol. 51, Part 3, pp. 417-433, 1972.

Davis, R.T. and Werle, M.J. (1972), "Numerical Solutions for Laminar Incompressible Flow Past a Paraboloid of Revolution," AIAA Journal, Vol. 10, No. 9, September 1972.

Davis, R.T., Ghia, U. and Ghia, K.N. (1974a), "Laminar Incompressible Flow Past Blunted Wedges Using the Navier Stokes Equations," Aerospace Engineering Report No. AFL 73-7-2, University of Cincinnati, also, International Journal of Computers and Fluids, Vol. 2, pp. 211-223, 1974.

Davis, R.T., Ghia, U. and Ghia, K.N. (1974b), "Laminar Incompressible Flow Past Sharp Wedges," Aerospace Engineering Report No. AFL 73-7-3, University of Cincinnati, also, presented at the Symposium on Application of Computers to Fluid Dynamic Analysis and Desgin, January 1973, Polytechnic Institue of Brooklyn, International Journal of Computers and Fluids, Vol. 2, pp. 225-235, 1974.

Davis, R.T. (1974), "A Study of the Use of Optimal Coordinates in the Solution of the Navier-Stokes Equations," Department of Aerospace Engineering, University of Cincinnati, Report No. AFL 74-12-14, December, 1974.

Dennis, S.C.R. and Walsh, J.D. (1971), "Numerical Solutions for Steady Symmetric Viscous Flow Past a Parabolic Cylinder in a Uniform Stream," J. Fluid Mech., 50, pp. 801-814.

Ghia, U. and Davis, R.T. (1974), "Solution of Navier Stokes Equations for Flow Past a Class of Two Dimensional Semi-Infinite Bodies," preliminary version published as AIAA Paper No. 74-12, also, final version in AIAA Journal, Vol. 12, No. 12, December 1974.

Hess, J.L. (1975), "Review of Integral-Equation Techniques for Solving Potential-Flow Problems with Emphasis on the Surface-Source Method," Computer Methods in Applied Mechanics and Engineering, Vol. 5, 1975, pp. 145-196.

Jenson, R., Burggraf, O., and Rizzetta, D. (1974), "Asymptotic Solution for Supersonic Viscous Flow Past a Compression Corner," presented at the 4th International Conference on Numerical Methods in Fluid Dynamics, Boulder, Colorado, June 1974.

Kaplun, S. (1954), "The Role of Coordinate Systems in Boundary-Layer Theory," ZAMP, Vol. 5, pp. 111-135.

Klineberg, J.M. and Steger, J.L. (1974), "On Laminar Boundary-Layer Separation," AIAA Paper, No. 74-94.

Legner, H.H. (1971), "On Optimal Coordinates and Boundary-Layer Theory," Ph.D. dissertation, Department of Aeronautics and Astronautics, Stanford University, July 1971.

Messiter, A.F. and Enlow, R.L. (1973), "A Model for Laminar Boundary-Layer Flow Near a Separation Point," SIAM J. Appl. Math, Vol. 25, No. 4, Dec. 1973, pp. 655-670.

Messiter, A.F. (1975), "Laminar Separation - A Local Asymptotic Flow Description for Constant Pressure Downstream," in AGARD Conference Pre-Print No. 168 on Flow Separation, May 1975.

Napolitano, M. and Werle, M.J. (1975), "Numerical Solution of Navier-Stokes Equations for Flow Past a Compression Corner - Including Separation," M.S. Thesis, Department of Aerospace Engineering, University of Cincinnati, 1975, to appear in report form.

Stewartson, K. and Williams, P.G. (1969), "Self-Induced Separation," Proc. Roy. Soc. London, A 312, pp. 181-206.

Stewartson, K. and Williams, P.G. (1973), "Self-Induced Separation II," Mathematika, 20, pp. 98-108.

Stewartson, K. (1974), "Multistructured Boundary Layers on Flat Plates and Related Bodies," from Advances in Applied Mechanics, Vol. 14, pp. 145-239, Academic Press, Inc.

Sychev, V.V. (1972), "On Laminar Separation," Mekhanika Zhidkosti i Gaza, No. 3, 1972, pp. 47-59.

Thompson, F.C., Thames, F.C., and Mastin, C.W. (1974)," Automatic Numerical Generation of Body-Fitted Curvilinear Coordinate System for Field Containing Any Number of Arbitrary Two-Dimensional Bodies," Journal of Computational Physics, Vol. 15.

van de Vooren, A.I. and D. stra, D. (1970), "The Navier-Stokes Solution for Laminar Flow Past a Semi-Infinite Flat Plate," Journal of Engineering Mathematics, Vol. 4, 1970, pp. 9-27.

Van Dyke, M.D. (1962), "Higher Approximations in Boundary Layer Theory. Part I: General Analysis," Journal of Fluid Mechanics, Vol. 14, pp. 161-177.

Werle, M.J. and Bernstein, J.M. (1975), "A Comparative Numerical Study of Models of the Navier Stokes Equations for Incompressible Separated Flows," Paper No. 75-8, presented at the AIAA 13th Aerospace Sciences Meeting, Pasadena, California, January 1975.

Werle, M.J. and Vatsa, V.N. (1974), A New Method for Supersonic Boundary Layer Separations," AIAA Journal, pp. 1491-1497, November 1974.

Wu, J.C. and Thompson, J.F. (1973), "Numerical Solutions of Time - Dependent Incompressible Navier-Stokes Equations Using an Integro-Differential Formulation," Computers and Fluids, Vol. 1, pp. 197-217, 1973.

Yoshizawa, A. (1970), "Laminar Viscous Flow Past a Semi-Infinite Flat Plate," J. Phys. Soc. Japan, 28, 1970, pp. 776-779.

A CALCULATION METHOD FOR THREE-DIMENSIONAL TURBULENT BOUNDARY LAYERS ON SHIPLIKE BODIES

L. Larsson

Swedish State Shipbuilding Experimental Tank
Box 24001, S-400 22 Gothenburg, Sweden

ABSTRACT

Since the boundary layer equations for the present case must be written in curvilinear coordinates, a procedure for calculation of metrics and curvatures for two coordinate axes must be available. This paper gives a brief description of such a procedure, which also includes streamline tracing, based on the Hess & Smith method for potential flow.

The boundary layer equations are solved in their integral form, using empirical relations due to Michel et al. Crosswise derivatives are taken into account in an iterative way, so the solution is not restricted to small cross-flows. The boundary layer on a ship model is used as a test case and comparisons are given with previous measurements by the author.

1. Introduction

The interest in calculations of the flow around ship hulls has grown rapidly during the last few years. One reason may be that the present day lack of knowledge of the fundamental nature of the flow has made it very difficult to make resistance predictions for modern ships which are not within the limits of previous experience. Wake prediction in connection with propeller construction is another field where increased knowledge of the governing flow laws would be very welcome. This holds also for the design of other appendages such as rudders, bilge keels, scoops, etc.

The boundary layer is characterized as the flow region where viscous forces play a part. To first approximation, this region is thin compared to any relevant dimension of the body and has therefore by assumption no influence on the outer potential flow which must be calculated to obtain the pressure distribution. A survey of methods for the computation of three-dimensional turbulent boundary layers has been written by the author /1/.

Some attempts have been made to calculate the boundary layer on ships and ship models /2/. In what appears to be the first approach, Uberoi in 1968 developed a method which was purely two-dimensional. This method is unsatisfactory, since strong three-dimensional effects occur in ship boundary layers. Later Gadd, Webster & Huang and von Kerczek developed procedures which take the main three-dimensional effects into account, although in an approximate manner. (They use the small cross-flow approximation explained below.) The most ambitious calculation method reported up to now is the one of Himeno & Tanaka. While the other procedures are based on methods previously developed, Himeno & Tanaka employed an equation (the moment of momentum equation) which has not previously been used in three-dimensional calculations. Furthermore, their method is fully three-dimensional. In all calculation methods the integrated forms of the governing equations have been employed, see Chapter 2.

2. Governing equations

The coordinate system to be used is shown in Figure 1. It is an orthogonal curvilinear system based on the streamlines and equipotential lines of the potential flow. Since the boundary layer is assumed to be thin, these lines, calculated at the surface, are assumed to coincide with the projection of their counterparts just outside the boundary layer in the real case. Another implication of the boundary layer approximation is that the bending of the z-axis (normal to the surface) within the

layer is negligible. The system is thus curved only in x and y.

Due to the bending of the axes the corresponding coordinates are stretched (cf Figure 1) in a non-uniform manner. The stretching is taken into account by the metrics h_1 and h_2, which are functions of x and y. An element of length, dl, in this coordinate system may thus be written

$$dl^2 = h_1{}^2 dx^2 + h_2{}^2 dy^2 + dz^2 \tag{1}$$

The geodesic curvatures K_{12} of the x-axis and K_{21} of the y-axis are connected to the metrics via the relations

$$K_{12} = \frac{1}{h_1 h_2} \frac{\partial h_1}{\partial y} \qquad K_{21} = \frac{1}{h_1 h_2} \frac{\partial h_2}{\partial x} \tag{2}$$

In the present calculation method an integrated form of the governing equation is used. The integration has been carried out in the z-direction and the following variables appear

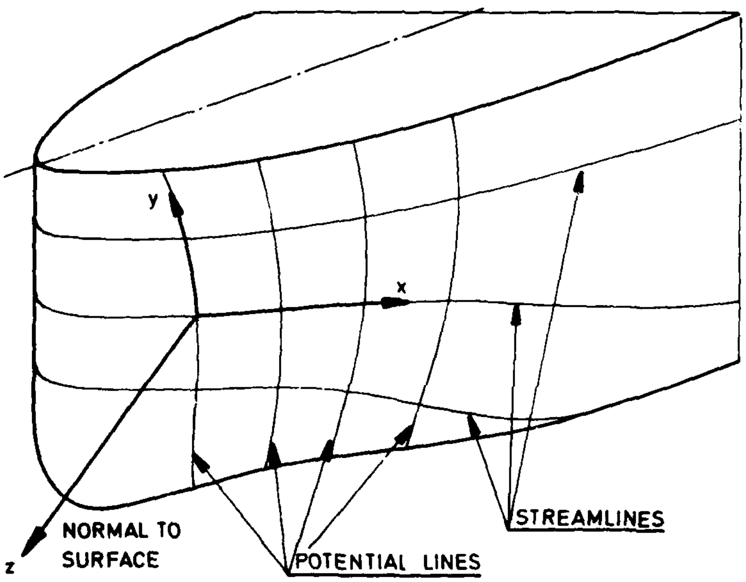

Fig 1. Surface coordinate system

AD-A119 315 DAVID W TAYLOR NAVAL SHIP RESEARCH AND DEVELOPMENT CE--ETC F/G 20/4
FIRST INTERNATIONAL CONFERENCE ON NUMERICAL SHIP HYDRODYNAMICS --ETC(U)
1975 J W SCHOT, N.SALVESEN

UNCLASSIFIED NL

AD A
119315

$$\delta_1 = \int_0^\infty (1 - \frac{u}{u_e}) dz \qquad \delta_2^* = - \int_0^\infty \frac{v}{u_e} dz$$

$$\theta_{11} = \int_0^\infty (1 - \frac{u}{u_e}) \frac{u}{u_e} dz \qquad \theta_{12} = \int_0^\infty (1 - \frac{u}{u_e}) \frac{v}{u_e} dz$$

$$\theta_{21} = - \int_0^\infty \frac{uv}{u_e^2} dz \qquad \theta_{22} = - \int_0^\infty \frac{v^2}{u_e^2} dz \qquad (3)$$

where $\mathbf{v} = (u, v, w)$ is the mean velocity vector, whose magnitude is equal to u_e at the boundary layer edge.

The governing equations become in terms of these quantities

$$\frac{1}{h_1} \frac{\partial \theta_{11}}{\partial x} + \frac{1}{h_2} \frac{\partial \theta_{12}}{\partial y} + \frac{1}{h_1 u_e} \frac{\partial u_e}{\partial x} (2\theta_{11} + \delta_1) + K_{12}(\theta_{12} + \theta_{21}) +$$

$$+ K_{21}(\theta_{11} - \theta_{22}) + \frac{1}{h_2 u_e} \frac{\partial u_e}{\partial y} (\theta_{12} + \theta_{21}) = \frac{\tau_{wx}}{\rho u_e^2} \qquad (4a)$$

$$\frac{1}{h_1} \frac{\partial \theta_{21}}{\partial x} + \frac{1}{h_2} \frac{\partial \theta_{22}}{\partial y} + \frac{2}{h_1 u_e} \frac{\partial u_e}{\partial x} \theta_{21} + \frac{2}{h_2 u_e} \frac{\partial u_e}{\partial y} \theta_{22} -$$

$$- K_{12}(\theta_{11} + \delta_1 - \theta_{22}) + 2K_{21}\theta_{21} = \frac{\tau_{wy}}{\rho u_e^2} \qquad (4b)$$

$\boldsymbol{\tau}_w = (\tau_{wx}, \tau_{wy}, 0)$ is the wall shear stress vector defined by

$$\tau_{wx} = \rho(\nu \frac{\partial u}{\partial z} - \overline{u'w'})_{z=0}, \qquad \tau_{wy} = \rho(\nu \frac{\partial \bar{v}}{\partial z} - \overline{v'w'})_{z=0}$$

The primed quantities u', v', w' are the fluctuating parts of the components of the velocity vector.

Calculation methods of this type - integral methods - are mathematically simpler than the so called finite difference methods. The latter are based on the equations from which (4a, b) have been obtained by integration in the z-direction. On the other hand more empirical input is needed to connect the integral quantities to each other in the first case. In Chapter 4 the relations used in the present method are given. First, however, an account will be given of the method for calculation of metrics and curvatures.

3. Calculation of geometrical properties

A non-trivial part of a calculation procedure of this kind is the construction of the coordinate system and the calculation of the metrics h_1 and h_2 and the curvatures K_{12} and K_{21}. There are two principal approaches which have been in use for such a calculation. Either the shape of the surface may be transformed by conformal mapping to a simpler one and the geometrical properties calculated analytically, or the surface may be approximated by spline functions, in which case h_1, h_2 etc are obtained entirely by numerical methods. The latter method is employed here.

3.1 Streamline tracing (GEOM 1)

The coordinate system, x, y, z, for the boundary layer equations is based on the streamlines and equipotential lines on the surface of the hull. These lines are obtained from a potential flow solution using the Hess & Smith (Douglas) method /3/. Since this method produces "correct" results only at a limited number of points, null points, on the surface, an interpolation procedure has to be adopted.

To facilitate this interpolation (and also the tracing), the projection of the hull surface in the X, Z' plane is considered, according to Figure 3. X, Y, Z are Cartesian coordinates defined in Figure 2. Transformation of the coordinates and direction cosines (α, β, γ) from this system to the primed one is trivial.

Given the starting point for each streamline the tracing is carried out by numerically integrating the relation

$$\frac{dZ'}{dX} = k \tag{5}$$

where $k = \gamma'/\alpha$ is known at each projected null point. To interpolate between the known k's the method shown in Figure 4 has been adopted. By matching a spline function through the values of k obtained along each row of null points its value at, say, $X = X_0$ may be obtained at a number of Z' coordinates. Then

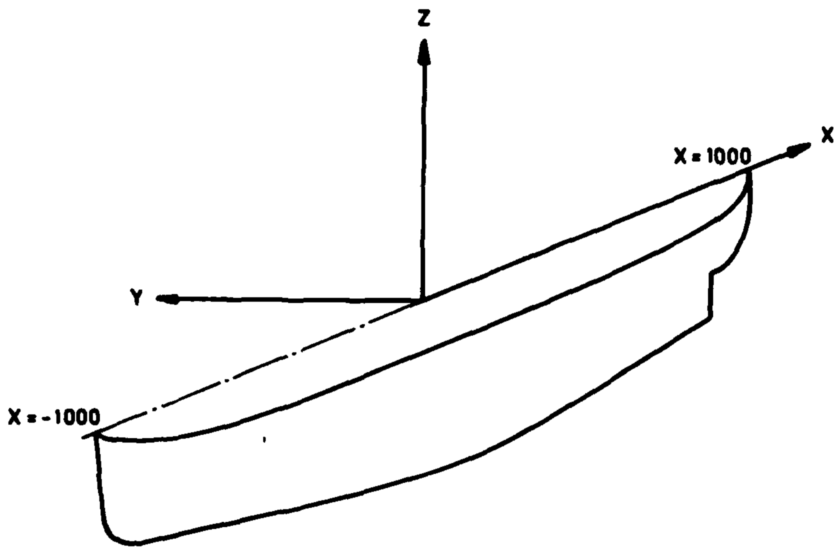

Fig 2. Space coordinate system

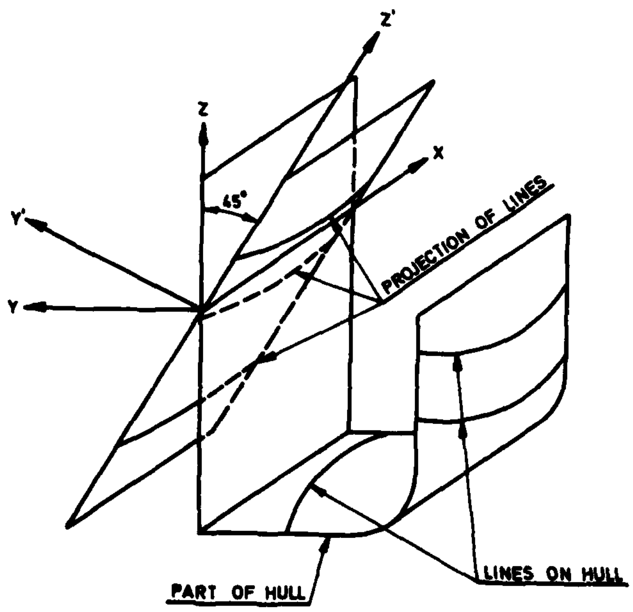

Fig 3. Definition of the X, Z' plane

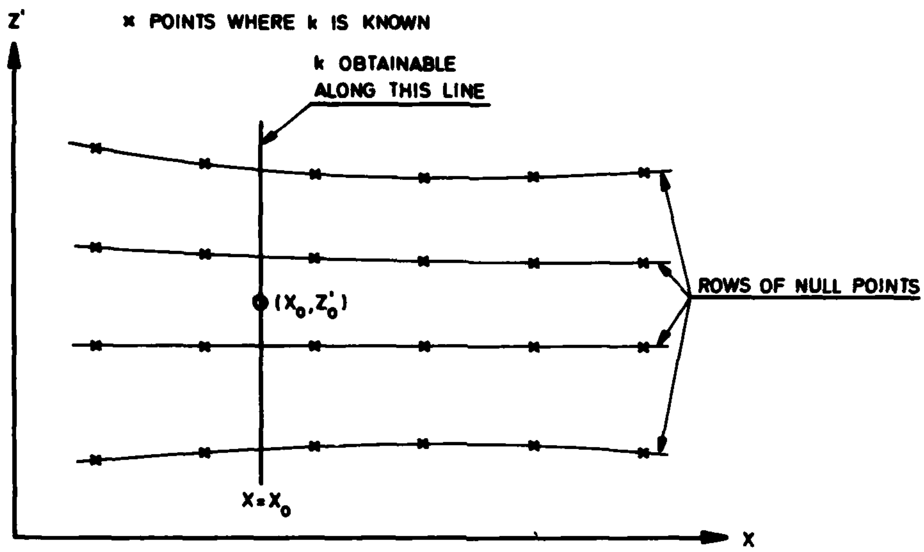

Fig 4. Interpolation in the X, Z' plane

applying the function to these calculated values, k may be obtained at an arbitrary coordinate $Z' = Z'_0$. It is required that the projection of the null points in the X, Z' plane lie on smooth lines. This is easily obtained, however, by defining the surface in a regular manner in the input to the Douglas program.

The integration of equation (5) is carried out using the Runge-Kutta method. All streamlines are traced simultaneously with the same step size, which reduces the storage requirements. Only two cross-wise (along X = const) splines are then needed for all lines when marching forward one step.

3.2 Calculation of pressure derivatives, metrics and curvatures (GEOM 2)

The main task for this program is to calculate the curvatures K_{12} and K_{21} defined by equations (2). Thus, the metrics and their derivatives must be obtained first. Since all calcu-

lations are carried out in the X, Z' plane a transformation of derivatives to the hull surface must be carried out. The slope of the hull function Y' = Y'(X, Z') is then needed. Since the longitudinal pressure derivative must also be known to solve the governing equations, it appears that there are four dependent variables in this program. They are: the metrics h_1 and h_2, the hull function Y' and the pressure coefficient C_p.

Three sets of independent variables are used. x and y are already defined, s and n are the corresponding arc lengths and s' and n' are the lengths along the projected lines. It should be mentioned that s, n and s', n' do not form coordinate systems which implies that partial derivatives with respect to these variables strictly speaking have no meaning. However, for the ordinary derivative along a streamline, a symbol s is used as shorthand and along its projection the index s'; n and n' are used correspondingly.

The first metric h_1 is easily calculated from the formula $h_1 = 1/u_e$, which is obtained by putting $dx = d\phi$, where ϕ is the velocity potential. The relation is obvious for a coordinate system based on the potential flow, since by definition

$$u_e = \left(\frac{d\phi}{ds}\right)_s \quad \text{and} \quad ds = h_1 dx \quad \text{(along a streamline)}$$

The calculation of h_2 is considerably more complicated. In Reference /5/ a derivation is given of the following expression

$$h_2 = \frac{1}{\frac{\partial y}{\partial Z'}} \left| \frac{\left(\frac{dX}{dZ'}\right)^2_{n'} + 1 + \left\{\frac{\partial Y'}{\partial X}\left(\frac{dX}{dZ'}\right)_{n'} + \frac{\partial Y'}{\partial Z'}\right\}^2}{\left(1 - \left(\frac{dZ'}{dX}\right)_{s'}\left(\frac{dX}{dZ'}\right)_{n'}\right)^2} \right|^{1/2} \qquad (6)$$

Thus h_2 is inversely proportional to $\partial y/\partial z'$, which is a measure of the closeness of the projected streamlines (y = const) in the X, Z' plane. The expression within brackets appears because the hull surface is not parallel to the plane and the projected lines are not parallel to the Z' axis.

There are two types of derivatives within the brackets. $(dZ'/dX)_{s'}$ and $(dX/DZ')_{n'}$ are the slopes of the streamlines and equipotential lines respectively (the inverse, in the

latter case) in the X, Z' plane. The first one is already known as k from the streamline tracing, while the second one must be calculated according to a formula derived in /5/, namely,

$$\left(\frac{dX}{dZ'}\right)_{n'} = - \frac{\frac{\partial Y'}{\partial Z'}\left(\frac{dY'}{dX}\right)_{s'} + \left(\frac{dZ'}{dX}\right)_{s'}}{\frac{\partial Y'}{\partial X}\left(\frac{dY'}{dX}\right)_{s'} + 1} \tag{7}$$

The other types of derivatives, appearing in (6) as well as in (7) are connected with the hull function $Y' = Y'(X, Z')$. They are in fact the partial derivatives with respect to X and Z'.

The hull function is defined by the points used as input in the Douglas program. In order to obtain its value at points along the projected streamlines the interpolation procedure described above for k has been used. Thus the derivative in the Z' direction is obtained directly from the "cross-wise" spline connecting values at $X = X_0$, Figure 4. The derivative along s' is easily obtained by applying the spline to the values calculated along each streamline. If X is taken as the independent variable, $(\partial Y'/\partial X)_{s'}$ is obtained. Using these two derivatives of Y', the partial derivative in the X direction may easily be calculated,

$$\frac{\partial Y'}{\partial X} = \left(\frac{dY'}{dX}\right)_{s'} - \frac{\partial Y'}{\partial Z'}\left(\frac{dZ'}{dX}\right)_{s'} \tag{8}$$

Thus all derivatives necessary to compute h_2 have been obtained. However, some further comments will be given.

It will be seen that h_2 appears in the final equations only in the expression for K_{21}. Since the h_2 derivative there is divided by h_2 itself, only the relative change along x is important. Its absolute value as well as its derivative in the y direction at the starting point of each streamline may thus be chosen arbitrarily. In this method the value of y (cf equation (6)) for each streamline (y = const) has been chosen as the Z' coordinate for its starting point, i e $\partial y/\partial Z'$ is unity at this point.

It now remains to calculate the derivatives with respect to y for h_1 and with respect to x for h_2. According to defini-

tions of h_1 and h_2 an element of length along the hull may be written

$$dl^2 = h_1{}^2 dx^2 + h_2{}^2 dy^2 \tag{9}$$

Along a potential line dx = 0, which implies

$$h_2 = \frac{dn}{dy} \quad \text{and} \quad \left(\frac{d}{dn}\right)_n = \frac{\partial}{\partial y}\frac{dy}{dn}\text{ , i e } \left(\frac{d}{dn}\right)_n = \frac{1}{h_2}\frac{\partial}{\partial y} \tag{10}$$

K_{12} may thus be calculated using the formula

$$K_{12} = \frac{1}{h_1}\left(\frac{dh_1}{dn}\right)_n \tag{11}$$

Now the derivative along n may be obtained from the derivative along n',

$$\left(\frac{dh_1}{dn}\right)_n = \left(\frac{dh_1}{dn'}\right)_{n'}\frac{dn'}{dn} \quad \text{where} \quad \frac{dn'}{dn} = \left\{1 + \left(\frac{dY'}{dn'}\right)_{n'}\right\}^{-1/2} \tag{12}$$

In /5/ there is a derivation of an expression for (d/dn'), given the derivatives $(d/ds')_{s'}$ and $\partial/\partial Z'$

$$\left(\frac{dh_1}{dn'}\right)_{n'} = \left\{\frac{\partial n_1}{\partial Z'}\left[1 - \left(\frac{dZ'}{dX}\right)_{s'}\left(\frac{dX}{dZ'}\right)_{n'}\right] + \right.$$

$$\left. + \left(\frac{dh_1}{ds'}\right)_{s'}\left(\frac{dX}{dZ'}\right)_{n'}\left[1 + \left(\frac{dZ'}{dX}\right)_{s'}\right]^{1/2}\right\}\left\{1 + \left(\frac{dX}{dZ'}\right)_{n'}\right\}^{-1/2} \tag{13}$$

The derivatives of h_1 appearing in this expression are easily obtained by putting splines through the values of h_1 along s' and Z'. Other derivatives have been given previously.

The curvature, K_{21}, can be calculated from the formula

$$K_{21} = \frac{1}{h_2}\left(\frac{dh_2}{ds}\right)_s \tag{14}$$

By using formulae analogous to (12) this curvature may also be evaluated.

The final point to be mentioned in this section is the calculation of the longitudinal pressure derivative. No complication occurs using the relevant parts of the above analysis, i.e. interpolations are carried out in the same way as for k and derivatives along s are then obtained as for h_2.

3.3 Tests

GEOM 1 and GEOM 2 were tested on an ellipsoid 2.0:1.5:1.0, parallel to the flow. Three runs were made: one using analytical input to the GEOM programs, another using results from the Douglas program and a third using the same results smoothed in a separate procedure.

The error in the streamline tracing was found to be extremely small. Thus, when tracing a line from a point close to the nose up to the middle of the body, in no case was the deviation from the analytical streamline greater than 0.01% of the minor axis. Forty steps were used in the calculations.

In Figure 5 the calculated K_{12} and K_{21} are shown. Comparing them with the analytical value it is seen that the errors are of the order of a few per cent if input from the Douglas program is used. However, using exact input to GEOM 1 and GEOM 2, the errors are virtually zero. It may be remarked that smoothing was applied to the output from the Douglas pro-

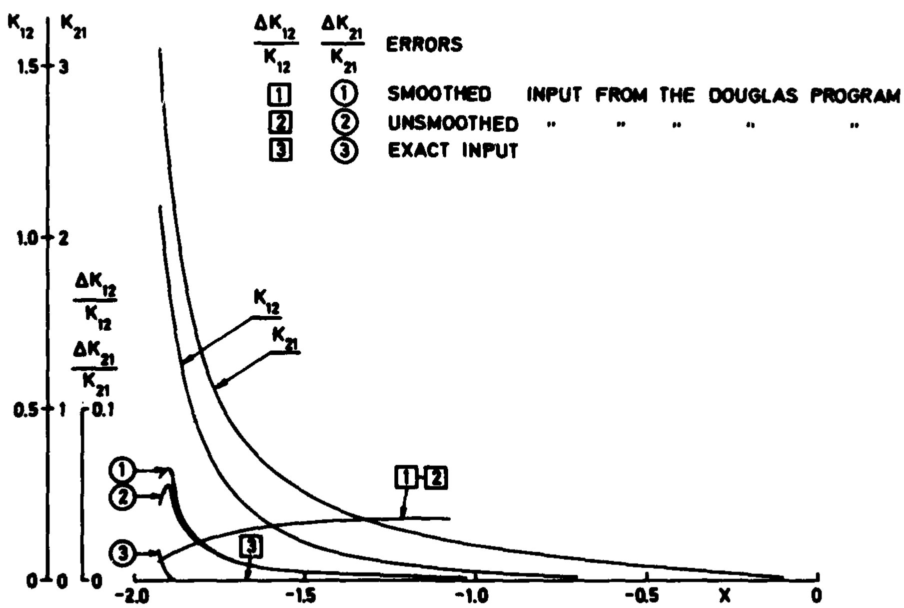

Fig 5. Curvatures on an ellipsoid

gram only to test the smoothing procedure. In cases where these calculations are based on input obtained from a working drawing, smoothing is essential.

4. Calculations of the boundary layer

As mentioned in Chapter 2 the present method is of the integral type, based on the equations (4). It is seen that these relations contain seven unknowns: five integral properties according to (3) and two shear stresses. Since there are only two equations five further relations must be found. The ones used here may be classified as

1. An auxiliary equation
2. A skin friction relation
3. A velocity profile family

The first two are necessary also in two-dimensional calculations, while the third point is specified for three-dimensional cases. A profile family represents the three-dimensional velocity profile, Figure 6, thus providing relations between the integral properties according to (3).

In earlier work the author /4/ tested a large number of assumptions under points 2 and 3. Comparing quantities measured in the boundary layer on a ship model with the results of the assumptions, it was found that most skin friction laws produced very good results, while the velocity profiles were rather poorly predicted in the cross-wise direction. Longitudinal velocity profiles were, however, quite well represented. As a result of this work the skin friction and profile relations of Michel et al were adopted. The entrainment equation, due to Head, was taken as the auxiliary equation, as in practically all other three-dimensional integral methods.

4.1 Boundary layer equations

In equations (4) the following relations are introduced

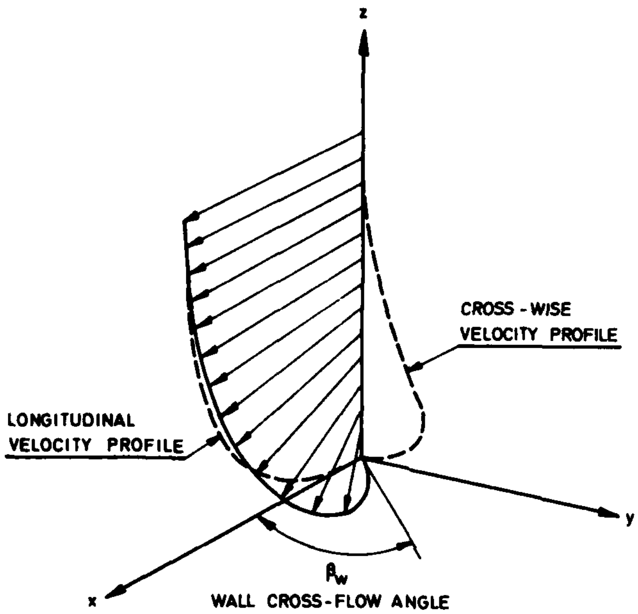

Fig 6. A three-dimensional velocity profile

$$H_{12} = \frac{\delta_1}{\theta_{11}} \qquad \beta_w = \arctan \frac{\tau_{wy}}{\tau_{wx}} \tag{15}$$

$$C_1 = \frac{1}{h_2} \frac{\partial \theta_{12}}{\partial y} \qquad C_2 = \frac{1}{h_2} \frac{\partial \theta_{22}}{\partial y} \tag{16}$$

$$\frac{\tau_{wx}}{\rho u_e^2} = \frac{c_{fx}}{2} \qquad \frac{\tau_{wy}}{\rho u_e^2} = \frac{c_{fx}}{2} \tan \beta_w \tag{17}$$

C_1 and C_2 are cross-wise derivatives, which are calculated after taking one step along each streamline. When taking this step they are thus considered as constants. The differential equations then become ordinary ones and may be solved along each streamline separately. Replacing $1/h_1 \cdot \partial/\partial x$ by d/ds (cf equation (10)), (4) may be written

$$\frac{d\theta_{11}}{ds} = \frac{c_{fx}}{2} - \frac{\theta_{11}}{u_e} \frac{du_e}{ds}(2 + H_{12}) - K_{21}(\theta_{11} - \theta_{22}) - C_1 \tag{18a}$$

$$\frac{d\theta_{21}}{ds} = \frac{c_{fx}}{2} \tan \beta_w - 2\theta_{21}\left(\frac{1}{u_e}\frac{du_e}{ds} + K_{21}\right) +$$

$$+ K_{12}\theta_{11}(1 + H_{12}) + K_{12}\theta_{22} - C_2 \tag{18b}$$

The entrainment equation reads, according to Michel et al

$$\frac{d(\delta - \delta_1)}{ds} = P\gamma - (\delta - \delta_1)\left(\frac{1}{u_e}\frac{du_e}{ds} + K_{21}\right) + C_3 \tag{19}$$

where

$$P = 0.074\ G - \frac{1.0957}{G} \qquad \gamma = \sqrt{\frac{c_{fx}}{2}} \qquad G = \frac{H_{12} - 1}{\gamma H_{12}}$$

$$C_3 = \frac{1}{h_2}\frac{\partial \delta_2}{\partial y}, \text{ another cross-wise derivative} \tag{20}$$

and δ is the boundary layer thickness.

The skin friction c_{fx} is calculated from the relation

$$\frac{1}{\gamma} = \sqrt{\frac{2}{c_{fx}}} = \frac{1}{\kappa} \ln \frac{u_e \delta_1}{\nu} + D^*(G) \tag{21}$$

where

$$D^*(G) = 2\,G - 4.25\,G^{1/2} + 2.12 \qquad (G < 300)$$

Michel's cross-flow relations are very lengthy and will not be written out here. They may be found in /5/. In principle an equation for δ_2 as a function of θ_{21} is solved first, and the parameters β_w, θ_{12} and θ_{22} are obtained thereafter by putting δ_2 in analytical formulae. The quantities to be obtained by the relations (18a, b), (19) and (21) are thus: θ_{11}, θ_{21}, H_{12} and c_{fx}.

4.2 Solution procedure

In most calculation methods the derivatives C_1-C_3 are put equal to zero. The so called "small cross-flow approximation" is then obtained. As a measure of the applicability of this approximation the wall cross-flow angle β_w is usually used. It is obvious, however, that it is not the magnitude of β_w, but

its derivative in the cross-wise direction which is important. Previous measurements by the author /4/ have shown that this derivative is not small at the afterbody of a ship.

Therefore, an attempt has been made here to extend the method to take cross-wise derivatives into account in an iterative way. As explained above, C_1-C_3 are considered as constants when taking one step along each streamline. After taking the step the derivatives are calculated by matching spline functions through the values obtained for all streamlines at this X position. The cross-wise derivative (along x = const) is then obtained by a special routine, NODER, which makes use of the derivatives for constant X and the derivative along the streamline, several properties calculated in GEOM 2 then being used.

The updated values of C_1-C_3 are put in and the step is repeated until the value of C_1 changes less than one per cent between two iterations. For the ship model described below this usually occurs after 5-6 iterations over the main part of the hull. At the afterbody, however, more iterations are needed. The initial guess for one step is taken as the converged solution from the previous step. Integration is carried out using the Runge-Kutta method.

4.3 Tests

Cumpsty & Head's /6/ infinite swept wing has been used as a test case for the boundary layer program. This is an analytically specified case in which the chordwise velocity falls linearly across the wing. Since no derivatives occur spanwise, a relation between stream- and cross-wise derivatives may be deduced

$$\frac{1}{h_2}\frac{\partial}{\partial y} = -\frac{u_\eta}{u_\xi}\frac{1}{h_1}\frac{\partial}{\partial x} \qquad (22)$$

where u_ξ and u_η are the external velocities along and normal to streamlines respectively.

In Figure 7 two fully three-dimensional calculations using the present method are compared with the calculations of Cumpsty

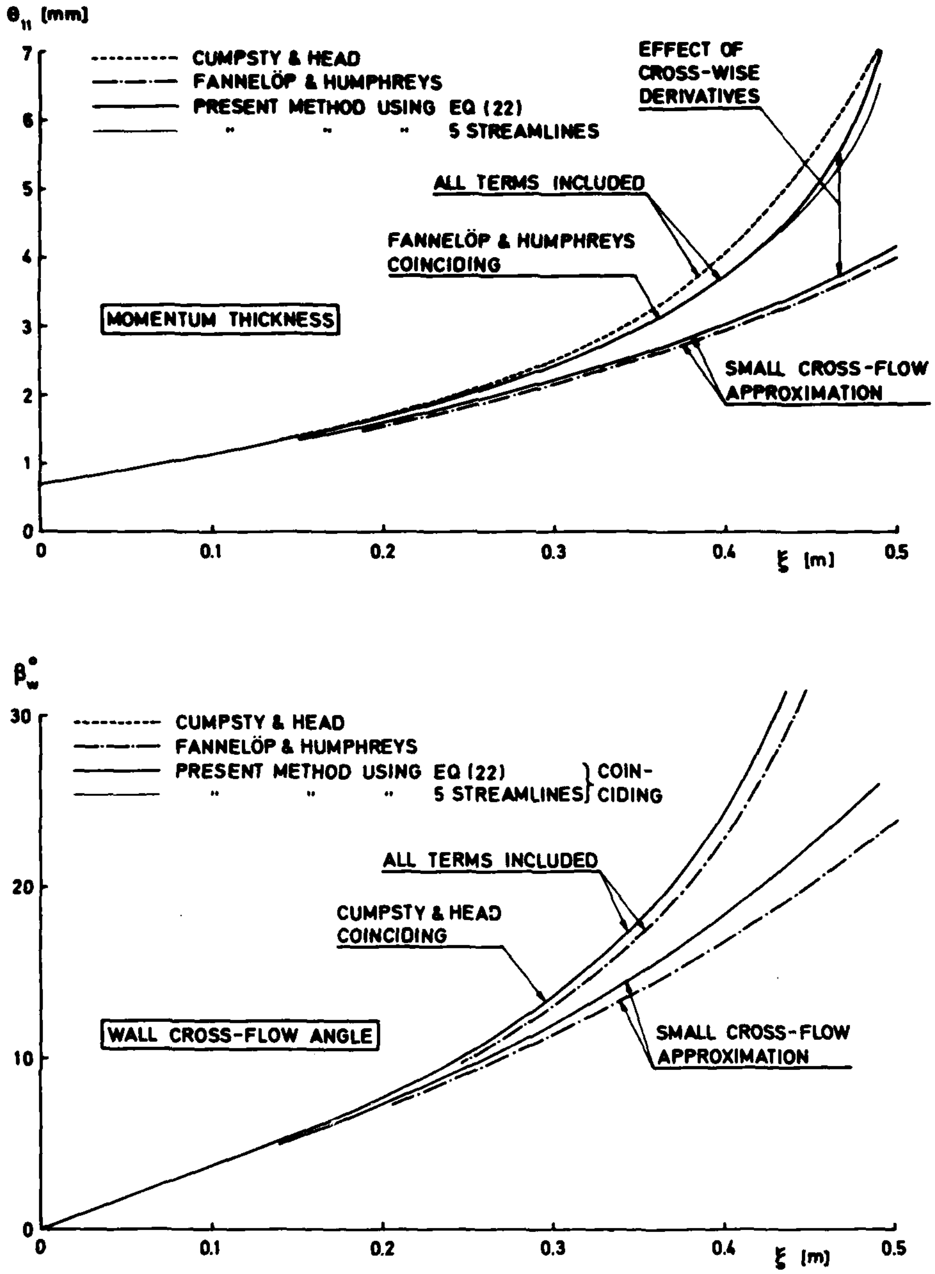

Fig 7. Results for the swept wing ($\alpha_0 = 35^{\circ}$, $k = 0.82$ m)

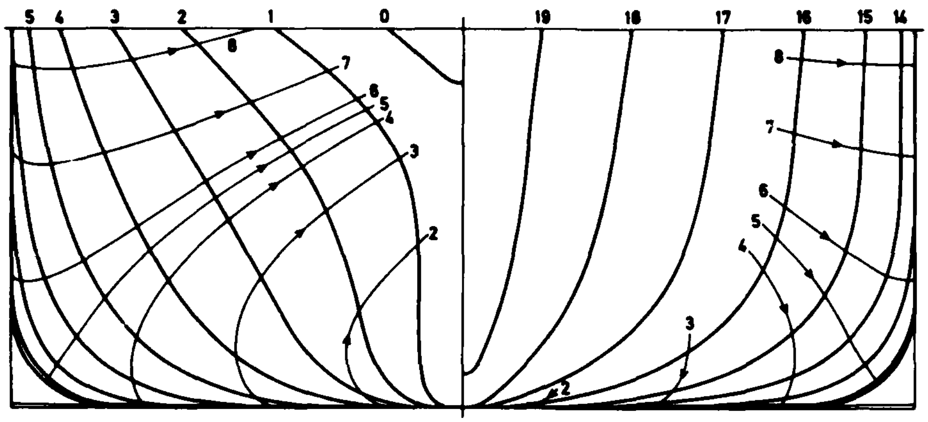

Fig 8. Model 720 SSPA. Calculated streamlines

& Head and Fannelöp & Humphreys /7/. In one of the present runs equation (22) was used, as in the other two methods. The most interesting curve is, however, the one representing the fully three-dimensional calculation, using five adjacent streamlines and the above theory. Obviously three-dimensional effects are well predicted in this case.

5. Calculations for a ship model

In Reference /4/ an experimental investigation of the boundary layer on a ship model is described. Three-dimensional velocity profiles have been measured at a number of stations along eight streamlines, see Figure 8.

Results from a calculation using the present method are compared with measurements in Figure 9a, b, c. Curves are shown for Streamlines Nos 2 and 5, both of which are in important characteristic regions of the flow. Streamline No 2 passes through a region of the afterbody where the boundary layer is fairly thin, i. e. where the boundary layer approximation should be applicable. On the other hand, this streamline bends more sharply than the others, which means that large three-dimensional effects must occur.

Streamline No 5 passes the bilge and goes into a region of

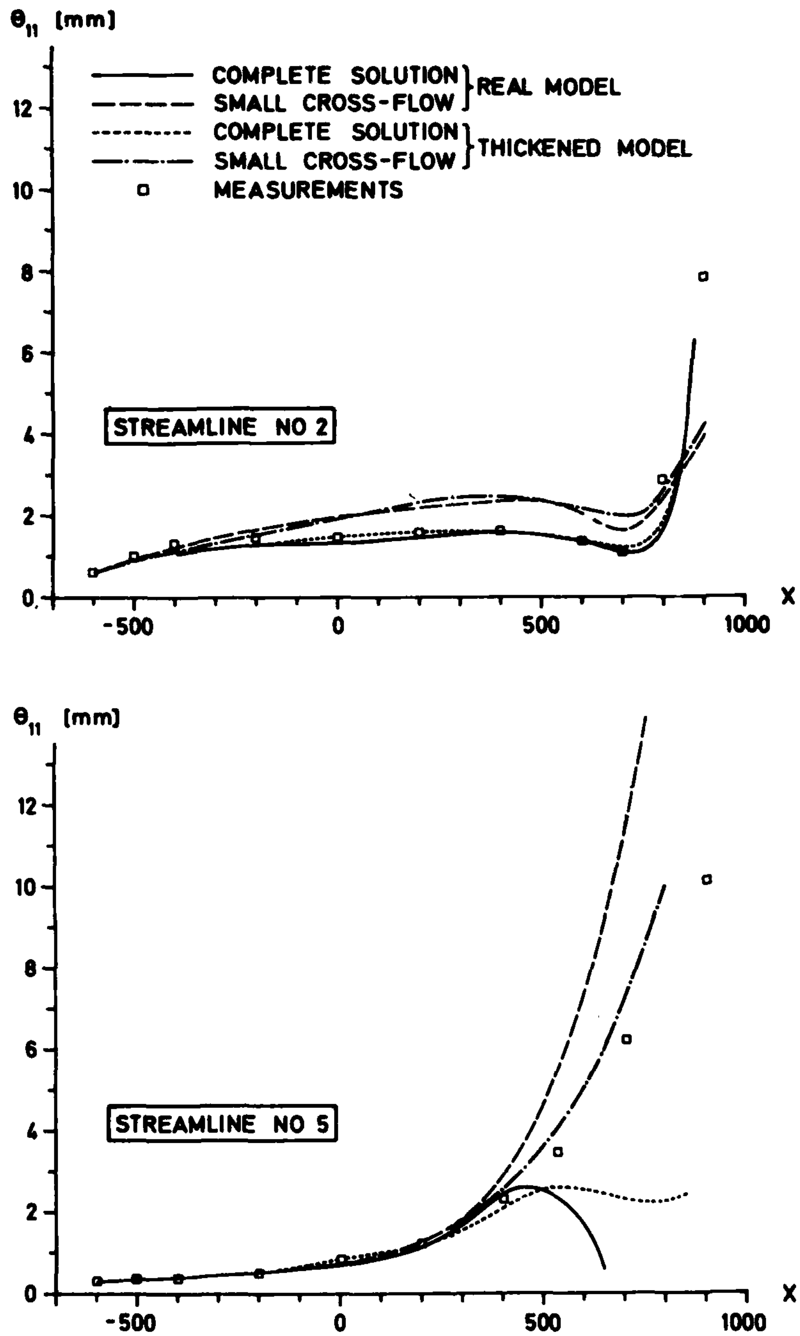

Fig 9a. Momentum thickness. Model 720

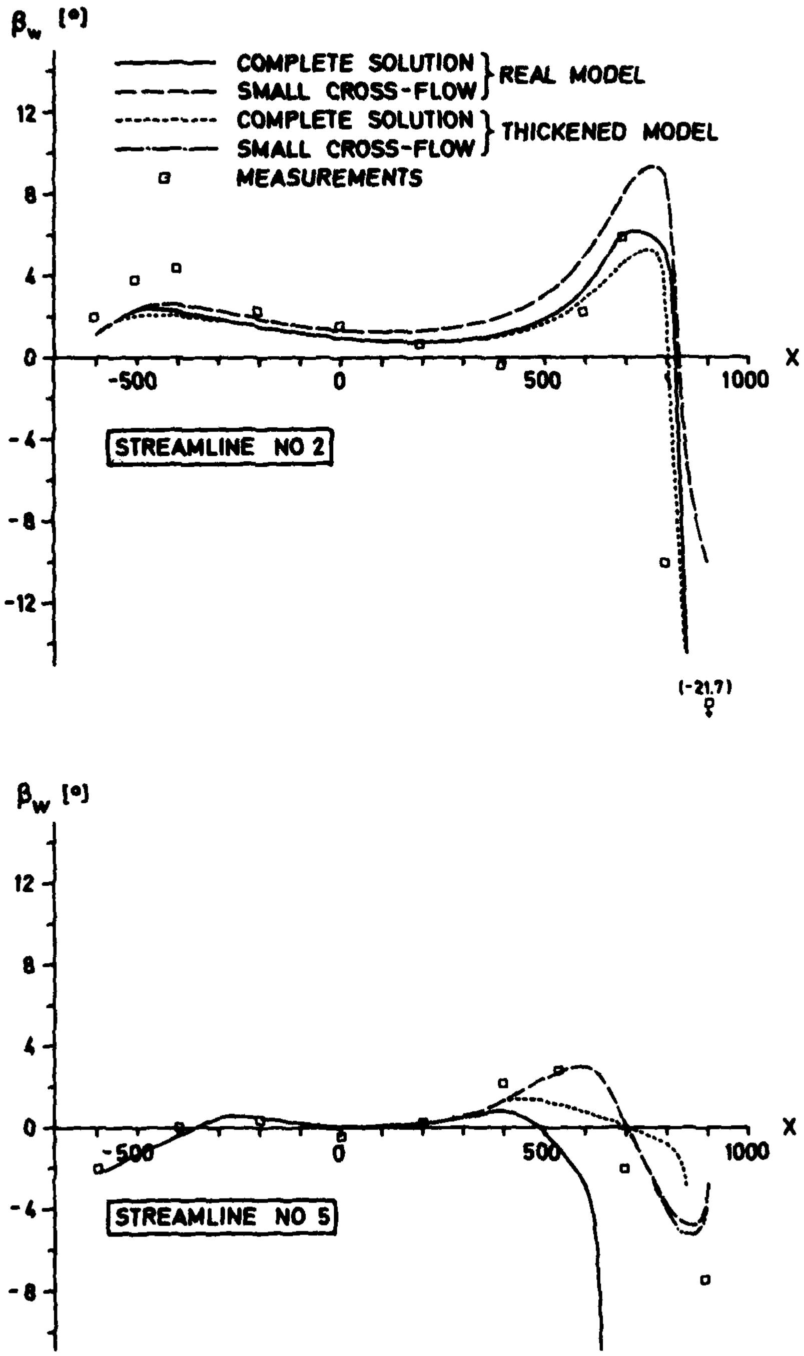

Fig 9b. Wall cross-flow angle. Model 720

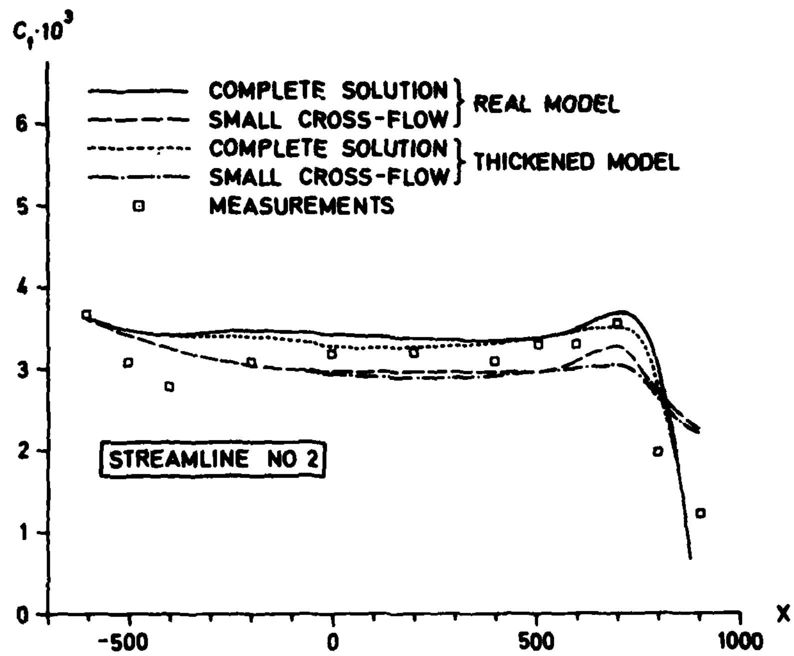

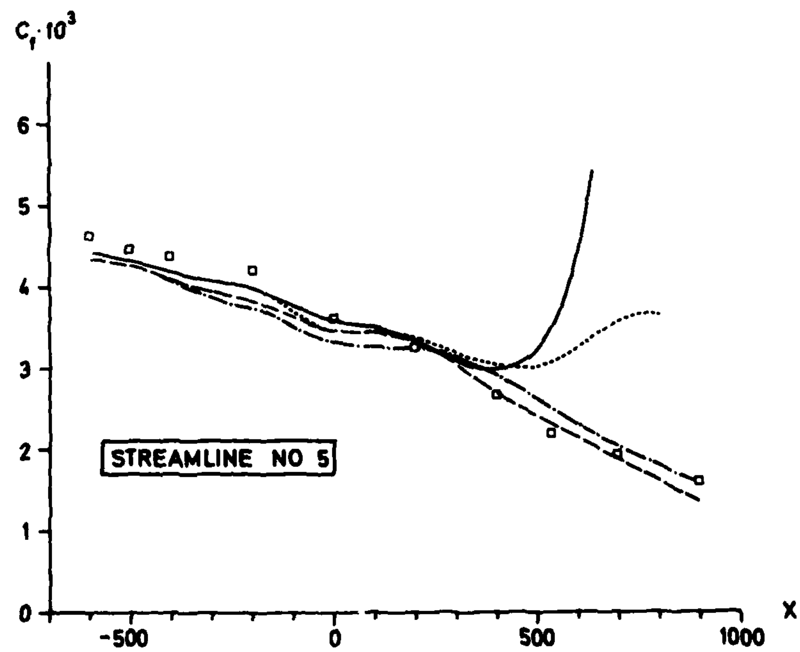

Fig 9c. Skin friction. Model 720

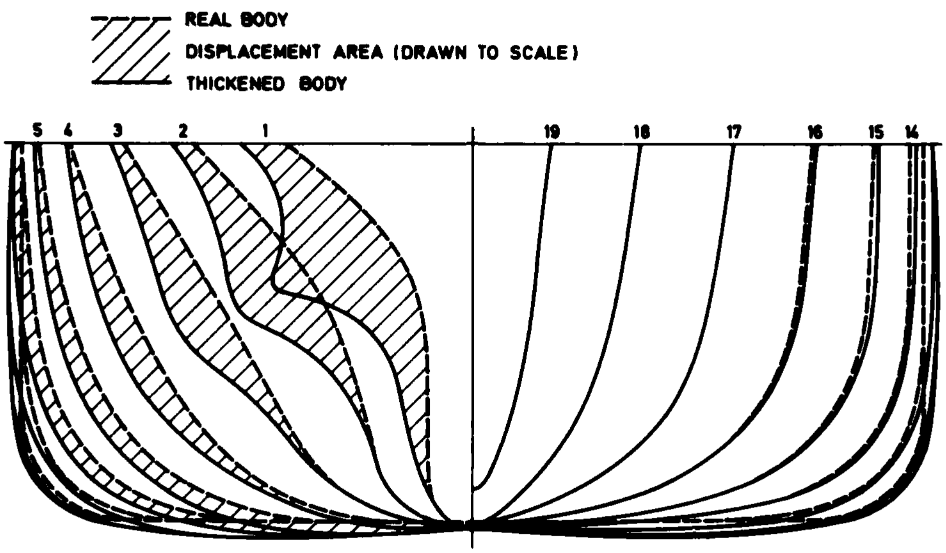

Fig 10. Model 720 thickened by the displacement thickness

very convergent streamlines at the afterbody. Thus the boundary layer thickness increases very rapidly and it may be suspected that the governing equations do not hold. It should be remarked that although the line is fairly straight, large cross-flow derivatives occur, since the surrounding lines are bent in different directions.

Four calculations are shown in Figure 9a, b, c. Complete solutions as well as small cross-flow solutions have been obtained for two pressure distributions. Thus the potential flow has been calculated not only for the real model, but also for a model thickened by the measured displacement thickness, Figure 10.

It appears from Figure 9a that both small cross-flow solutions yield too large momentum thicknesses for Streamline No 2, while the solutions using the complete equations are very good. The difference between the two potential flows is small here and the corresponding solutions are very similar. For Streamline No 5, however, the calculation for the thickened model is better than the one for the real model using the small cross-flow ap-

proximation, while both fully three-dimensional calculations produce very poor results at X > 500, due to excessively large cross-wise derivatives.

The sharp bends in the cross-flow angle distributions, Figure 9b, along Streamline No 2 are quite well reproduced, indicating that three-dimensional effects are well accounted for as long as the boundary layer is thin. Unfortunately this is not the case over the main part of the afterbody. The solution is poor not only on Streamline No 5, but also on Nos 4 and 6, which are not shown. For Nos 7 and 8 the wrong sign of β_w is predicted at the aftermost stations.

Like the momentum thickness the skin friction in Figure 9c exhibits a peculiar development along Streamline No 2. The c_f rises in the region X = 500-700, thereafter dropping rapidly. The predictions are, however, quite good.

In the complete calculations presented the cross-wise derivatives have been obtained by using five adjacent streamlines (more closely spaced than in Figure 8) and the solution procedure according to 4.2. Initial values for each streamline have been taken from measurements at X = - 600. By using this procedure solutions in regions where the boundary layer is thin may be obtained up to X = 900, while in other regions the solutions break down much earlier.

Of course erroneous boundary conditions are used in a method of this kind, so a check was carried out of the errors introduced in this way. This was done by calculating a solution for 23 streamlines between the LWL and the ℄. Outside these lines, which lie in planes of symmetry, calculations were made simultaneously for three extra streamlines. The boundary conditions at the planes of symmetry were thus quite well satisfied. Fortunately the solution deviated very slightly from the results presented here up to X = 650, where the calculations broke down at Streamline No 5.

In all calculations described 75 steps were used between X = - 600 and X = 900. However, to investigate the influence of the longitudinal step size a separate run was made using all

streamlines and the step size reduced to 1/5 for $X > 400$. The solution was nearly identical to the one mentioned above, so it may be concluded that 75 steps is enough.

Calculations of this flow have also been carried out by Cebeci et al /8/. They used a finite difference method and only small cross-flow solutions were obtained. In /8/ the results along Streamlines Nos 3 and 5 are given. To the accuracy of the diagrams they coincide with the corresponding solution using the present method (potential flow for the real body). Although both calculations are based on geometrical properties from GEOM, it is surprising that the two boundary layer calculation methods, being of very different types, can produce nearly identical results.

6. Conclusions

A method for the calculation of three-dimensional turbulent boundary layers around shiplike bodies has been presented. In the first part geometrical properties related to the coordinate system are calculated. This procedure has produced very accurate results when applied to an analytical case.

In the second part the boundary layer equations are solved in integral form. Cross-wise derivatives are taken into account by iteration. When applied to a well known test case this part of the method produced results very similar to those obtained by two other methods.

Calculations for a ship model showed good agreement with measurements over the main part of the hull. However, at the afterbody reliable solutions could be obtained only in a small region. Elsewhere the boundary layer equations are thought not to be valid, due to the thick boundary layer. Nearly identical results have been obtained by the present method and a finite difference method due to Cebeci et al.

7. Acknowledgement

This project was supported by the Swedish Board for Techni-

cal Development under the Contracts No 734125U and No 74-4033. It was carried out as a cooperative effort between the Department of Applied Thermo and Fluid Dynamics at Chalmers University of Technology and the Swedish State Shipbuilding Experimental Tank.

8. References

/1/ Larsson, L: Boundary Layers of Ships. Part I: A Literature Survey on Investigations of Three-Dimensional Turbulent Boundary Layers. Swedish State Shipbuilding Experimental Tank (SSPA) Allmän Rapport nr 44, 1974

/2/ Larsson, L: Boundary Layers of Ships. Part II: A Literature Survey on Investigations of Ship and Model Boundary Layers. SSPA Allmän Rapport nr 45, 1974

/3/ Hess, J L and Smith, A M O: Calculations of Potential Flow about Three Dimensional Bodies. Douglas Aircraft Company Report No E.S. 40622, 1962

/4/ Larsson, L: Boundary Layers of Ships. Part III: An Experimental Investigation of the Turbulent Boundary Layer on a Ship Model. SSPA Allmän Rapport nr 46, 1974

/5/ Larsson, L: Boundary Layers of Ships. Part IV: Calculations of the Turbulent Boundary Layer on a Ship Model. SSPA Allmän Rapport nr 47, 1974

/6/ Cumpsty, N A and Head, M R: The Calculation of Three-Dimensional Turbulent Boundary Layers. Part I: Flow over the Rear of an Infinite Swept Wing. Aeronautical Quarterly, Vol XVIII, 1967

/7/ Fannelöp, T and Humphreys, D A: A Simple Finite Difference Method for Solving the Three-Dimensional Turbulent Boundary Layer Equations. American Institute of Aeronautics and Astronautics, 12th Aerospace Sciences Meeting, Washington D C, January 1974

/8/ Cebeci, T et al: A General Method for Calculating Three-Dimensional Incompressible Laminar and Turbulent Boundary Layers III. Three-Dimensional Flows in Curvilinear Orthogonal Coordinates. Douglas Aircraft Company Report MDC J6867, 1975

Note: The References /1/, /2/, /4/ and /5/ by the author are also available from the Department of Applied Thermo and Fluid Dynamics, Chalmers University of Technology, as Publications 74/2, 74/3, 74/7 and 74/8 respectively.

CALCULATION OF THREE-DIMENSIONAL BOUNDARY LAYERS ON SHIP HULLS

Tuncer Cebeci, Kalle Kaups and Judy Ramsey

Douglas Aircraft Company
Long Beach, California 90846 U.S.A.

ABSTRACT

This paper describes a general method for calculating three-dimensional laminar and turbulent boundary layers. The method, developed under a three-year NSRDC Contract, uses the eddy-viscosity concept to model the Reynolds shear-stress terms. The governing equations are solved by a very efficient two-point finite-difference method used earlier by Keller and Cebeci for two-dimensional flows and later by Cebeci for three-dimensional flows.

During the three-year period this method has been used to compute laminar and turbulent flows past infinite swept cylinders, flows restricted to small cross-flow, and fully three-dimensional flows in general curvilinear orthogonal coordinates. The accuracy of the method was thoroughly studied with the available experimental data and with the results obtained by Bradshaw's method. Based on these studies we find the method to be quite accurate and efficient. A typical computation time for a laminar or turbulent flow consisting of thirty streamwise stations, fifteen crosswise stations with thirty points across the boundary layer is approximately 30 seconds of CPU-time on an IBM 370/165 computer.

Principal Notation

A	Van Driest damping parameter, see (3.4b)
c_{f_s}	local skin friction coefficient in streamwise direction
f	transformed vector potential for ψ
g	transformed vector potential for ϕ
h_1, h_2	metric coefficients

h_j net spacing in η-direction
H boundary-layer shape factor, see (6.4)
k_n net spacing in x-direction
K_1, K_2 geodesic curvatures, see (2.4b)
L modified mixing length, see (3.4a)
p static pressure
$\vec{q}$ velocity vector parallel to surface
q magnitude of velocity vector
q_e magnitude of velocity vector at the boundary-layer edge
R_s Reynolds number, $u_e s_1/\nu$
s arc length along coordinate line
$\vec{S}$ shear vector $\partial\vec{q}/\partial y$
u, v, w velocity components in the x, y, z directions
x curvilinear surface coordinate
y distance normal to the body surface
z curvilinear surface coordinate orthogonal to the x-coordinate
β cross-flow angle relative to inviscid flow direction
δ boundary-layer thickness
ε eddy viscosity
ε^+ dimensionless eddy viscosity, ε/ν
η similarity variable for y, see (4.1)
μ dynamic viscosity
ν kinematic viscosity
ρ density
τ shear stress
ϕ, ψ two-component vector potential, see (4.3)

Subscripts

e boundary-layer edge
s streamwise direction
w wall

Primes denote differentiation with respect to η

1. Introduction

The capability to calculate boundary layers on ship hulls is not only desirable from the standpoint of determining the frictional resistances

accurately but also from the standpoint of predicting boundary-layer separation and accounting for the displacement effect. Because of the complexity of flow around ship hulls, one can expect the boundary layer to be always three-dimensional, in the most general way. Progress in developing methods for calculating such flows is quite difficult and must proceed step-by-step from the simplest to more complicated flows. This paper is a summary of work done under a three-year NSRDC contract, No. N00014-72-C-0111, to develop a general method for calculating three-dimensional laminar and turbulent boundary layers on ship hulls. Details of the results are given in three separate reports, [1], [2], [3]. The first report deals with the calculation of restricted three-dimensional turbulent boundary layers over yawed infinite cylinders and under small cross-flow assumption. As can be seen from the results presented in this paper, calculations with small cross-flow assumption can give reasonable answers with the economy of two-dimensional calculations. The second report covers the calculation of three-dimensional turbulent boundary layers in Cartesian coordinates with emphasis on flow approaching separation. The third report contains the formulation of the problem as well as development of calculation methods in curvilinear orthogonal coordinate systems.

The following sections describe the general three-dimensional boundary-layer equations, the transformations used to bring them into more tractable form, and the eddy-viscosity formulation for three-dimensional flows. The numerical method employed is demonstrated with an illustrative example, and finally, four calculated sample cases and comparisons with experimental data are presented.

2. The Boundary-Layer Equations

The governing boundary-layer equations for three-dimensional incompressible flows in a curvilinear orthogonal coordinate system are given by the following equations:

Continuity

$$\frac{\partial}{\partial x}(h_2 u) + \frac{\partial}{\partial z}(h_1 w) + \frac{\partial}{\partial y}(h_1 h_2 v) = 0 \tag{2.1}$$

x-Momentum

$$\frac{u}{h_1}\frac{\partial u}{\partial x} + \frac{w}{h_2}\frac{\partial u}{\partial z} + v\frac{\partial u}{\partial y} - uwK_1 + w^2K_2 = -\frac{1}{\rho h_1}\frac{\partial p}{\partial x} + \frac{\partial}{\partial y}\left(\nu\frac{\partial u}{\partial y} - \overline{u'v'}\right) \quad (2.2)$$

z-Momentum

$$\frac{u}{h_1}\frac{\partial w}{\partial x} + \frac{w}{h_2}\frac{\partial w}{\partial z} + v\frac{\partial w}{\partial y} - uwK_2 + u^2K_1 = -\frac{1}{\rho h_2}\frac{\partial p}{\partial z} + \frac{\partial}{\partial y}\left(\nu\frac{\partial w}{\partial y} - \overline{w'v'}\right) \quad (2.3)$$

where h_1 and h_2 are metric coefficients, and they are functions of x and z, that is,

$$h_1 = h_1(x,z) \qquad , \qquad h_2 = h_2(x,z) \quad (2.4a)$$

The parameters K_1 and K_2 are known as the geodesic curvatures of the curves z = const. and x = const., respectively. They are given by

$$K_1 = -\frac{1}{h_1h_2}\frac{\partial h_1}{\partial z} \quad , \qquad K_2 = -\frac{1}{h_1h_2}\frac{\partial h_2}{\partial x} \quad (2.4b)$$

At the edge of the boundary layer, (2.2) and (2.3) reduce to

$$\frac{u_e}{h_1}\frac{\partial u_e}{\partial x} + \frac{w_e}{h_2}\frac{\partial u_e}{\partial z} - u_ew_eK_1 + w_e{}^2K_2 = -\frac{1}{\rho h_1}\frac{\partial p}{\partial x} \quad (2.5a)$$

$$\frac{u_e}{h_1}\frac{\partial w_e}{\partial x} + \frac{w_e}{h_2}\frac{\partial w_e}{\partial z} - u_ew_eK_2 + u_e{}^2K_1 = -\frac{1}{\rho h_2}\frac{\partial p}{\partial z} \quad (2.5b)$$

The boundary conditions for (2.1) to (2.3) for zero mass transfer are:

$$y = 0 \qquad u,w = 0 \qquad v = 0 \quad (2.6a)$$

$$y \to \infty \qquad u \to u_e(x,z) \qquad w \to w_e(x,z) \quad (2.6b)$$

3. Closure Assumptions for the Reynolds Shear Stresses

The solution of the system given by (2.1) to (2.6) requires closure assumptions for the Reynolds shear stresses, $-\rho\overline{u'v'}$, $-\rho\overline{w'v'}$. As in our previous studies we use the eddy-viscosity concept and define

$$-\overline{u'v'} = \varepsilon_1\frac{\partial u}{\partial y} \quad , \qquad -\overline{w'v'} = \varepsilon_2\frac{\partial w}{\partial y} \quad (3.1)$$

As in [2], we assume that $\varepsilon_1 = \varepsilon_2 = \varepsilon$ and define ε by two separate formulas. With the definition of the velocity vector parallel to the wall, $\vec{q} = (u,w)$ and the shear or strain vector $\vec{S} = \partial\vec{q}/\partial y = (\partial u/\partial y, \partial w/\partial y)$, the eddy-viscosity formulas for the inner and outer regions are

$$\varepsilon = \begin{cases} \varepsilon_i = L^2 \,|\, \vec{S}(y) \,| & \varepsilon_i \leq \varepsilon_o \qquad (3.2) \\[2ex] \varepsilon_o = 0.0168 \displaystyle\int_0^\infty \left(|\vec{q}_e| - |\vec{q}(y)|\right) dy & \varepsilon_i \geq \varepsilon_o \qquad (3.3) \end{cases}$$

Here

$$L = 0.4\, y\, [1 - \exp(-y/A)] \tag{3.4a}$$

$$A = 26\, (\nu/|\vec{S}_w|)^{\frac{1}{2}} \tag{3.4b}$$

4. Transformation of the Governing Equations

The boundary-layer equations (2.1) to (2.3) can be solved when they are expressed either in physical coordinates or in transformed coordinates. Each coordinate system has its own advantages. In problems where the computer storage becomes important, the choice of using transformed coordinates becomes necessary, as well as convenient, since the transformed coordinates allow large steps to be taken in the x and z directions. The reason for this is that the profiles expressed in the transformed coordinates do not change as rapidly as they do when they are expressed in physical coordinates. The use of transformed coordinates stretches the coordinate normal to the wall and takes out much of the variation in boundary-layer thickness for laminar flows.

We first define the transformed coordinates by

$$x = x\,, \qquad z = z\,, \qquad \eta = \left(\frac{u_e}{\nu s_1}\right)^{\frac{1}{2}} y \tag{4.1}$$

and introduce a two-component vector potential such that

$$h_2 u = \frac{\partial\psi}{\partial y}\,, \qquad h_1 w = \frac{\partial\phi}{\partial y}\,, \qquad h_1 h_2 v = -\left(\frac{\partial\psi}{\partial x} + \frac{\partial\phi}{\partial z}\right) \tag{4.2}$$

In addition we define dimensionless variables f and g related to variables ψ and ϕ by

$$\psi = (u_e \nu s_1)^{\frac{1}{2}} h_2 \, f(x,z,\eta) \tag{4.3a}$$

$$\phi = (u_e \nu s_1)^{\frac{1}{2}} h_1 \frac{w_e}{u_e} g(x,z,\eta) \tag{4.3b}$$

Here s_1, which denotes the arc length along the x-coordinate, is defined by

$$s_1 = \int_0^x h_1 \, dx + s_1(0) \tag{4.4}$$

Introducing the expressions (4.1) to (4.3) into (2.2) and (2.3), we get, after considerable algebra,

x-momentum equation

$$(bf'')' + P_1 ff'' + P_2[1 - (f')^2] + P_5[1 - f'g'] + P_6 f''g + P_8[1 - (g')^2]$$
$$= xP_{10}\left[f' \frac{\partial f'}{\partial x} - f'' \frac{\partial f}{\partial x} + P_7\left(g' \frac{\partial f'}{\partial z} - f'' \frac{\partial g}{\partial z}\right)\right] \tag{4.5}$$

z-momentum equation

$$(bg'')' + P_1 fg'' + P_4(P_{11} - f'g') + P_3[1 - (g')^2] + P_6 gg'' + P_9[1 - (f')^2]$$
$$= xP_{10}\left[f' \frac{\partial g'}{\partial x} - g'' \frac{\partial f}{\partial x} + P_7\left(g' \frac{\partial g'}{\partial z} - g'' \frac{\partial g}{\partial z}\right)\right] \tag{4.6}$$

Here the primes denote differentiation with respect to η and

$$P_1 = \frac{1}{2}(1 + P_2) - s_1 K_2, \qquad P_2 = \frac{s_1}{u_e h_1} \frac{\partial u_e}{\partial x}, \qquad P_3 = P_2 \tag{4.7a}$$

$$P_4 = \frac{s_1}{w_e h_1} \frac{\partial w_e}{\partial x} - s_1 K_2, \qquad P_5 = \frac{s_1}{u_e h_2} \frac{w_e}{u_e} \frac{\partial u_e}{\partial z} - s_1 K_1 \left(\frac{w_e}{u_e}\right) \tag{4.7b}$$

$$P_6 = P_2 + \frac{w_e}{2u_e}\left(\frac{1}{h_1}\frac{\partial s_1}{\partial z} - \frac{s_1}{u_e h_2}\frac{\partial u_e}{\partial z}\right) - s_1 K_1\left(\frac{w_e}{u_e}\right), \quad P_7 = \frac{h_1}{h_2}\frac{w_e}{u_e}$$

$$P_8 = s_1 K_2\left(\frac{w_e}{u_e}\right)^2, \quad P_9 = s_1 K_1\left(\frac{w_e}{u_e}\right), \quad P_{10} = \frac{s_1}{h_1 x}, \quad P_{11} = 1.0 \qquad (4.7b)$$

The boundary conditions (2.6) become

$$\eta = 0 \qquad f = g = f' = g' = 0 \qquad (4.8a)$$

$$\eta = \eta_\infty \qquad f' = g' = 1 \qquad (4.8b)$$

Introducing the transformation (4.1) to (4.3) into the eddy-viscosity formulas (3.2) to (3.4), we get

$$\varepsilon_i^+ = [0.4\ \eta\ (1 - \exp(-y/A))]^2 \left\{R_s\left[f''^2 + \left(\frac{w_e}{u_e} g''\right)^2\right]\right\}^{1/2} \qquad (4.9a)$$

$$\varepsilon_0^+ = 0.0168\ R_s^{1/2} \left\{\frac{q_e}{u_e}\eta_e - \int_0^{\eta_e}\left[f'^2 + \left(\frac{w_e}{u_e} g'\right)^2\right]^{1/2} d\eta\right\} \qquad (4.9b)$$

Here

$$R_s = \frac{u_e s_1}{\nu} \qquad (4.10a)$$

$$y/A = (\eta/26)\left\{R_s\left[f_w''^2 + \left(\frac{w_e}{u_e} g_w''\right)^2\right]\right\}^{1/4} \qquad (4.10b)$$

$$q_e/u_e = (1 + (w_e/u_e)^2)^{1/2} \qquad (4.10c)$$

5. Numerical Method

We use the Box method to solve the system of equations described in section 4. This method was developed by H. B. Keller [4] and has successfully been applied to the two-dimensional boundary-layer equations by Keller and Cebeci [5], [6] and to the three-dimensional laminar and turbulent

boundary layers by Cebeci and his associates [1], [2], [3]. A detailed description of the method for two-dimensional flows is presented in [6] and [7], and for three-dimensional flows in [2]. For completeness, a brief description of it will be repeated here for three-dimensional flows.

According to the Box method we first reduce the system (4.5), (4.6), (4.8) to a system of six first-order equations by introducing new dependent variables $u(x,z,\eta)$, $v(x,z,\eta)$, $w(x,z,\eta)$ and $t(x,z,\eta)$ and write (4.5), (4.6), (4.8) as

$$f' = u \tag{5.1a}$$

$$u' = v \tag{5.1b}$$

$$g' = w \tag{5.1c}$$

$$w' = t \tag{5.1d}$$

$$(bv)' + P_1fv + P_2(1-u^2) + P_5(1-uw) + P_6vg + P_8(1-w^2) = xP_{10}\left[u\frac{\partial u}{\partial x} - v\frac{\partial f}{\partial x} + P_7\left(w\frac{\partial u}{\partial z} - v\frac{\partial g}{\partial z}\right)\right] \tag{5.1e}$$

$$(bt)' + P_1ft + P_4(P_{11}-uw) + P_3(1-w^2) + P_6gt + P_9(1-u^2) = xP_{10}\left[u\frac{\partial w}{\partial x} - t\frac{\partial f}{\partial x} + P_7\left(w\frac{\partial w}{\partial z} - t\frac{\partial g}{\partial z}\right)\right] \tag{5.1f}$$

$$\eta = 0 \qquad f = g = u = w = 0 \tag{5.2a}$$

$$\eta = \eta_\infty \qquad u = w = 1 \tag{5.2b}$$

We next consider the net cube shown in figure 1 and introduce the net points by

$$\begin{array}{llll} x_0 = 0, & x_n = x_{n-1} + k_n & n = 1, 2, \ldots, N & \\ z_0 = 0, & z_i = z_{i-1} + r_i & i = 1, 2, \ldots, I & \\ \eta_0 = 0, & \eta_j = \eta_{j-1} + h_j & j = 1, 2, \ldots, J & \eta_J = \eta_\infty \end{array} \tag{5.3}$$

The net spacings, k_n, r_i and h_j are arbitrary and indeed may have large variations in practical calculations. This is especially important in turbulent boundary-layer calculations which are characterized by large boundary

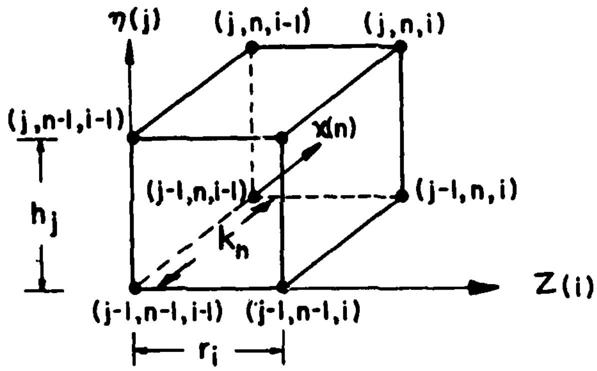

Figure 1. Net cube for the difference equations for three-dimensional flows.

layer thicknesses. To get accuracy near the wall, small net spacing is required while large spacing can be used away from the wall.

We approximate the quantities (f, u, v, g, w, t) at points (x_n, z_i, η_j) of the net by net functions denoted by $(f_j^{n,i}, u_j^{n,i}, v_j^{n,i}, g_j^{n,i}, w_j^{n,i}, t_j^{n,i})$. The equations (5.1a,d) are approximated using centered difference quotients and averaged about the midpoint $(x_n, x_i, \eta_{j-1/2})$, that is:

$$\frac{f_j^{n,i} - f_{j-1}^{n,i}}{h_j} = u_{j-1/2}^{n,i} \tag{5.4a}$$

$$\frac{u_j^{n,i} - u_{j-1}^{n,i}}{h_j} = v_{j-1/2}^{n,i} \tag{5.4b}$$

$$\frac{g_j^{n,i} - g_{j-1}^{n,i}}{h_j} = w_{j-1/2}^{n,i} \tag{5.4c}$$

$$\frac{w_j^{n,i} - w_{j-1}^{n,i}}{h_j} = t_{j-1/2}^{n,i} \tag{5.4d}$$

where, for example,

$$u_{j-1/2}^{n,i} = \frac{1}{2}(u_j^{n,i} + u_{j-1}^{n,i})$$

The difference equations which are to approximate (5.1e,f) are rather lengthy. To illustrate the difference equations, we consider the following model equation

$$v' + P_1 fv = x\left(u\frac{\partial u}{\partial x} + P_7 w\frac{\partial u}{\partial z}\right) \tag{5.5}$$

The difference equations for this equation are

$$\frac{\bar{v}_j - \bar{v}_{j-1}}{h_j} + (P_1)^{n-1/2}_{i-1/2}\,(\overline{fv})_{j-1/2} = x^{n-1/2}\Bigg[\bar{u}_{j-1/2}\left(\frac{\bar{u}_n - \bar{u}_{n-1}}{k_n}\right)$$

$$+ (P_7)^{n-1/2}_{i-1/2}\,\bar{w}_{j-1/2}\left(\frac{\bar{u}_i - \bar{u}_{i-1}}{r_i}\right)\Bigg] \tag{5.6}$$

where, for example,

$$\bar{v}_j = \frac{1}{4}\left(v_j^{n,i} + v_j^{n,i-1} + v_j^{n-1,i-1} + v_j^{n-1,i}\right)$$

$$\bar{u}_n = \frac{1}{4}\left(u_j^{n,i} + u_j^{n,i-1} + u_{j-1}^{n,i} + u_{j-1}^{n,i-1}\right)$$

$$\bar{u}_i = \frac{1}{4}\left(u_j^{n,i} + u_j^{n-1,i} + u_{j-1}^{n,i} + u_{j-1}^{n-1,i}\right)$$

$$(P_1)^{n-1/2}_{i-1/2} = \frac{1}{4}\left(P_i^n + P_{i-1}^n + P_i^{n-1} + P_{i-1}^{n-1}\right)$$

The boundary conditions (5.2) yield at $x = x_n$, and $z = z_i$:

$$f_0^{n,i} = 0, \quad g_0^{n,i} = 0, \quad u_0^{n,i} = 0, \quad w_0^{n,i} = 0, \quad u_J^{n,i} = 1, \quad w_J^{n,i} = 1 \tag{5.7}$$

The equations (5.4) and the difference equations for (5.1e,f) are imposed for $j = 1, 2, \ldots, J$. If we assume $(f_j^{n-1,i-1}, u_j^{n-1,i-1}, v_j^{n-1,i-1}, g_j^{n-1,i-1}, w_j^{n-1,i-1}, t_j^{n-1,i-1})$, $(f_j^{n,i-1}, u_j^{n,i-1}, v_j^{n,i-1}, g_j^{n,i-1}, w_j^{n,i-1}, t_j^{n,i-1})$, and $(f_j^{n-1,i}, v_j^{n-1,i}, g_j^{n-1,i}, t_j^{n-1,i})$ to be known for $0 \le j \le J$, the differenced equations (5.4) and the difference equations for (5.1e,f) for $1 \le j \le J$ and the boundary conditions (5.7) yield an implicit nonlinear algebraic system of $6J + 6$ equations in as many unknowns $(f_j^{n,i}, u_j^{n,i}, v_j^{n,i}, g_j^{n,i}, w_j^{n,i}, t_j^{n,i})$. We first use Newton's method to linearize the

system and then use the block elimination method discussed by Isaacson and Keller [8] to solve the resulting linear system.

6. Results

The method discussed in the previous sections is applicable to both laminar and turbulent boundary layers. For laminar layers, the accuracy of the method depends on the accuracy of the numerical method. According to the study conducted in [2], the accuracy of the method is quite good for laminar flows. Highly accurate solutions can be obtained by taking 25 to 30 points across the boundary layer. Although a higher degree of accuracy can be obtained with less points by using Richardson extrapolation, the accuracy obtained with 25 to 30 points is sufficient for most laminar layers.

For turbulent flows, the accuracy of the method depends also on the accuracy of the turbulence model for the Reynolds stresses. While the experimental data for full three-dimensional turbulent boundary layers are limited, there are a number of experimental data for restricted quasi-three-dimensional flows, such as flows over infinite swept wings and small cross flows. For this reason, we at first studied the accuracy of our method for those quasi-three-dimensional turbulent flows before applying it to full three-dimensional flows.

6.1 Infinite Swept-Wing Calculations

Equations (4.5) and (4.6) are applicable to the general three-dimensional flows in orthogonal curvilinear coordinates. For flows with yawed infinite cylinder or swept-wing approximations in Cartesian coordinates, where the spanwise flow is independent of the z-coordinate, these equations simplify considerably. The metric coefficients h_1, h_2 become unity and the geodesic curvature parameters K_1, K_2 become zero. In addition, the coefficients P_i $(i = 3 \text{ to } 9)$ become zero and

$$P_1 = \frac{1 + P_2}{2}, \qquad P_2 = \frac{x}{u_e}\frac{du_e}{dx}, \qquad P_{10} = x$$

In [1], a number of flows that fall in this class were considered. Here we present the results for the 45° infinite swept-wing data of Bradshaw and

Terrell [9]. This experiment was set up especially to test the outer-layer assumptions made in extending the boundary-layer calculation method of Bradshaw et al [10] from two dimensions to three. Measurements were made only on the flat rear of the wing in a region of nominally zero pressure gradient and decaying cross flow. See the sketch in figure 2a. Spanwise and chordwise components of mean velocity and shear stress, and all three components of turbulence intensity, were measured at a number of distances $x' = 0, 4, 10, 16$ and 20 inches from the start of the flat portion of the wing (see figure 2). The surface shear stress, measured with a Preston tube, was constant along a generator at the start of the flat part of the wing, except for a few inches at each end and except for small undulations of small spanwise wave length caused by residual nonuniformities in the tunnel flow.

Figure 2 shows the results calculated by the yawed infinite cylinder approximation compared with experimental results and those obtained by Bradshaw's method [11]. Our calculations were started at $x' = 0$ by using the procedure described in [1]. The initial values for c_{f_s} and $R_{\delta_1^*}$

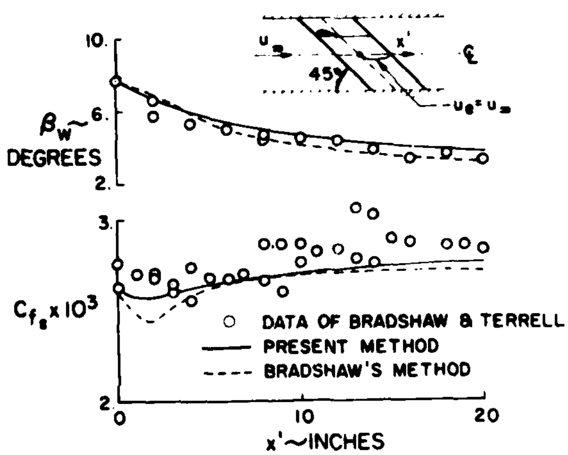

Figure 2. Results for the relaxing flow of Bradshaw and Terrell. (a) Wall cross-flow angle and local skin friction.

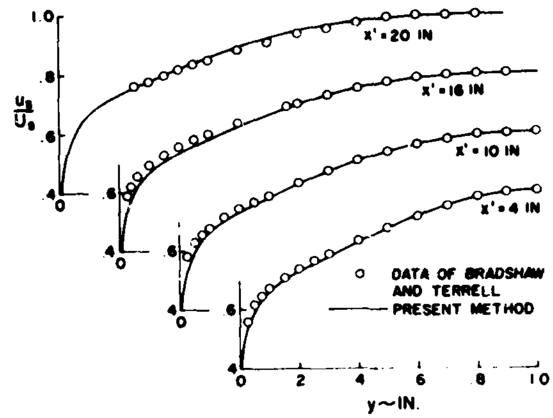

Figure 2. Continued. (b) Velocity profiles.

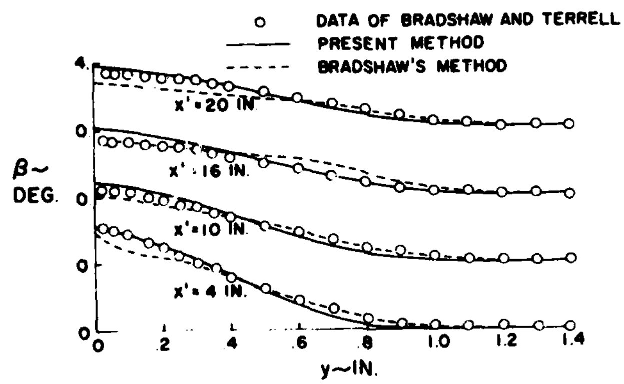

Figure 2. Continued. (c) Cross-flow angle distributions.

were taken as 2.62×10^{-3} and 1.13×10^{4}, respectively. Also, the cross-flow angle distribution, given by experiment, was used in the initial velocity profile.

6.2 Small Cross-Flow Calculations

When the variations in cross-flow direction are so small that they can be neglected, the general governing equations in streamline coordinates simplify considerably by setting $\partial u/\partial z = \partial w/\partial z = \partial/\partial z\ (h_1 w) = 0$ in (2.1) and (2.3). The transformed equations applicable to the small cross flow cannot be derived directly from (4.5) and (4.6) because $w_e = 0$ in streamline coordinates. However, if we define a new dimensionless variable $g' = w/u_s$ and introduce the following stream function and transformations

$$
\begin{aligned}
h_2 u &= \frac{\partial \psi}{\partial y} & h_2 v &= -\frac{1}{h_1}\frac{\partial \psi}{\partial x} \\
ds &= h_1 dx & \eta &= \left(\frac{u_s}{\nu s}\right)^{1/2} y \\
\psi &= (\nu u_s s)^{1/2} h_2 f(s_1 \eta)
\end{aligned}
\tag{6.1}
$$

then we can bring equations (2.1) to (2.3) into the form of (4.5) and (4.6). Note that u_s is the inviscid velocity at the edge of the boundary layer, and s is the distance along a given streamline. The outer boundary conditions in (4.8b) now become:

$$
\eta = \eta_\infty \qquad f' = 1 \qquad g' = 0
$$

and the coefficients in (4.5) and (4.6) become

$$
\begin{aligned}
&P_1 = \frac{1}{2}(1 + P_2) - sK_2, \quad P_2 = \frac{s_1}{u_e}, \quad P_3 = 0, \quad P_4 = P_2 - sK_2 \\
&P_5 = P_5 = P_6 = P_7 = P_8 = 0, \quad P_9 = sK_1, \quad P_{10} = \frac{s}{h_1 x}, \quad P_{11} = 0
\end{aligned}
\tag{6.2}
$$

Here K_2 is the geodesic curvature of the orthogonal trajectory to the streamline; the geodesic curvature of the streamline, K_1, is related to the cross-flow pressure gradient by

$$
K_1 = \frac{1}{\rho u_s^2 h_2}\frac{\partial P}{\partial z} \tag{6.3}
$$

To check the accuracy of our method for flows with small cross-flow approximation, we have considered the experimental data of Larsson [12] taken on the model of a cargo ship. The model of 2.0m length was tested in the low-speed wind tunnel at Chalmers University of Technology in Sweden at a free-stream velocity of 40m/sec corresponding to a unit Reynolds number of approximately 2.68×10^6/m (0.816×10^6/ft). The water surface was approximated by a plane at the load waterline as shown in figure 3, and in this way the effects of waves were ignored, i.e., the Froude number was zero. This plane was obtained in the wind tunnel as plane of symmetry by joining two models of the submerged part of the hull. At station 18 the boundary layer was tripped by cylindrical turbulence studs of 3 mm diameter and 0.8m height, spaced by 9 mm.

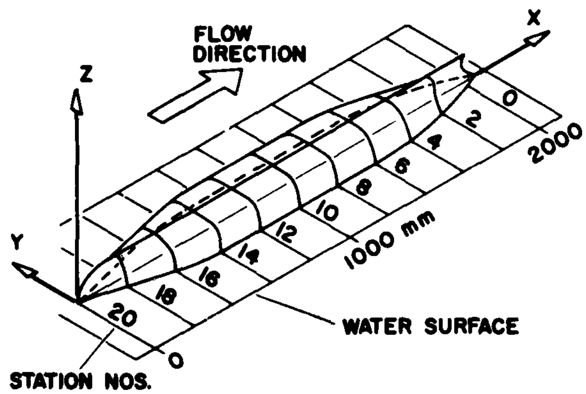

Figure 3. Hull model of cargo liner, SSPA model 720, tested by Larsson [12]. Actual model consists of two shapes, as shown, to produce plane of symmetry at load waterline.

Static pressures were measured by orifices on the model surface. The boundary layer was traversed with a hot-wire probe with a single wire parallel to the local surface-tangent plane. Magnitude and direction of the mean flow velocity were obtained by taking two readings at each traversing location, with the probe rotated 45 degrees left and right of an estimated edge streamline direction about an axis normal to the surface. The velocity

vector was determined from the two signals by using calibration curves (the surface-normal component was assumed zero).

The locations of boundary-layer traverses were selected on inviscid surface-streamlines to facilitate comparison with boundary-layer calculations that proceed along such streamlines. The streamlines had to be known beforehand and they were integrated from the output of the Douglas Neumann three-dimensional potential flow program [13]. Two such streamlines are shown in figure 4. Nine to twelve profiles were measured on each of seven streamlines between stations 16 and 1. Unfortunately some of the edge streamline directions, as measured by the hot-wire probe, disagreed with the calculated inviscid flow directions by as much as two degrees in the forward half of the model and seven degrees in the aft half.

A comparison of calculated and experimental results for the streamlines, Nos. 3 and 5, are shown in figures 5 and 6. The calculations were started at the first measured station, No. 16, located at $x = 0.4m$ from the bow, i.e., at 20 percent of the total model length. The initial velocity profile on each streamline was generated by using the procedure described in [1]. The boundary-layer parameters R_θ, H are calculated from

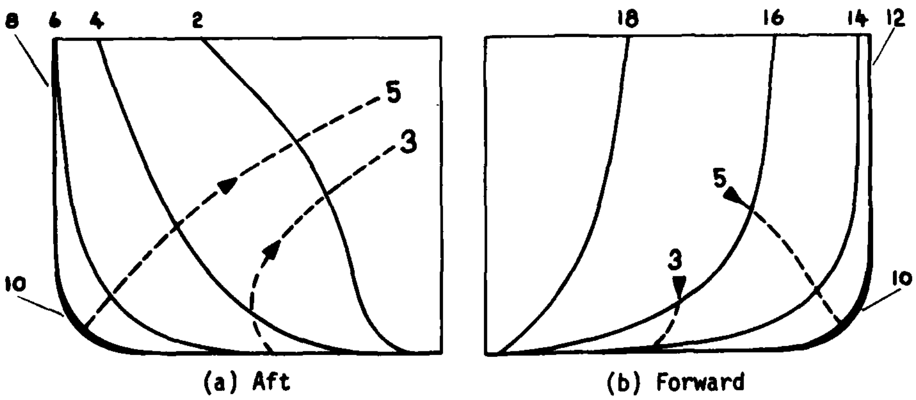

Figure 4. Sections through ship body normal to x-axis (station nos. same as in figure 3). Streamlines Nos. 3 and 5 are indicated by dashed curves. (a) Aft. (b) Forward.

$$R_\theta = \frac{\theta_{11} u_s}{\nu} \quad , \quad H = \frac{\delta_1^*}{\theta_{11}} \tag{6.4}$$

Here u_s is the local streamwise edge velocity and

$$\theta_{11} = \int_0^\infty \frac{u}{u_s}\left(1 - \frac{u}{u_s}\right) dy \tag{6.5}$$

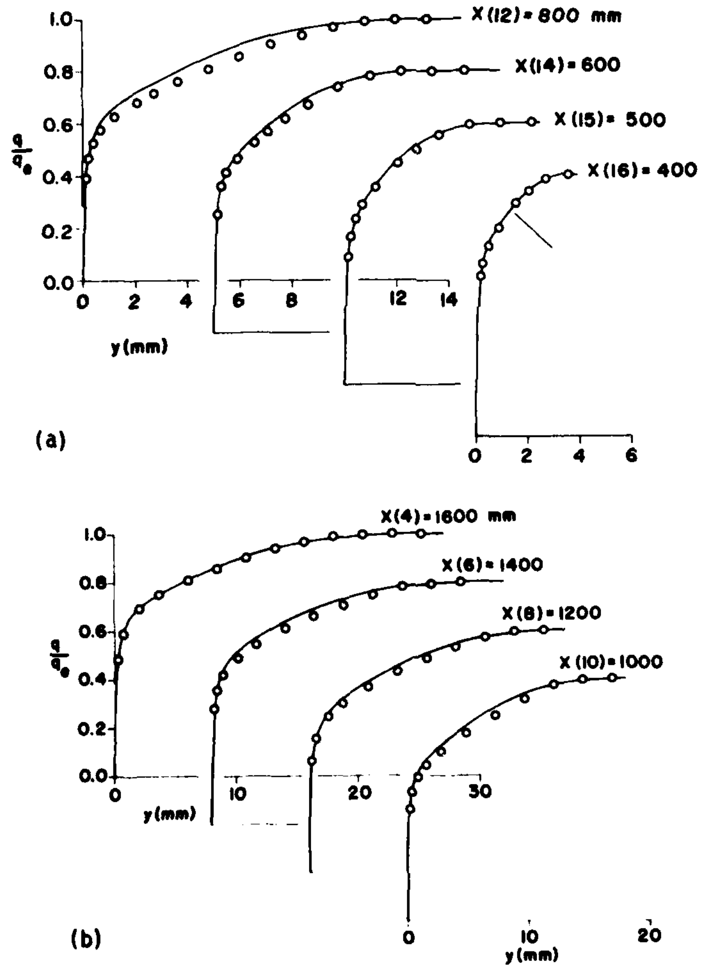

Figure 5. Comparison of calculated and experimental velocity profiles for the data of Larrson. (a) For streamline No. 3. (b) For streamline No. 3.

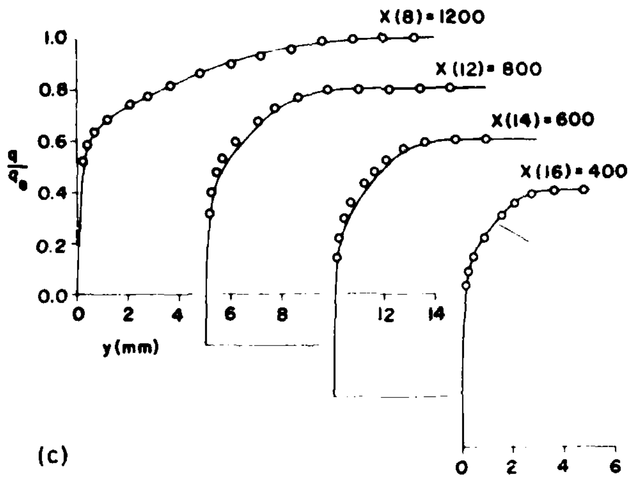

(c)

Figure 5. Continued. (c) For streamline No. 5.

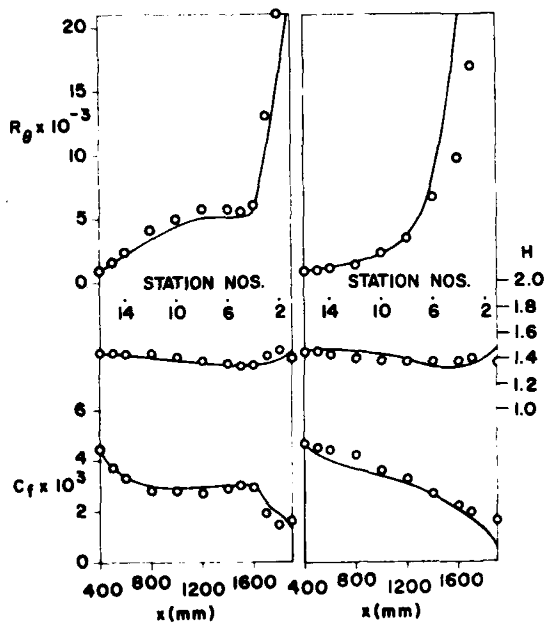

(a) (b)

Figure 6. Comparison of calculated and experimental results for the data of Larrson. (a) Streamline No. 3. (b) Streamline No. 5.

$$\delta_1^* = \int_0^\infty \left(1 - \frac{u}{u_s}\right) dy \tag{6.6}$$

6.3 Three-Dimensional Flows in Cartesian Coordinates

To check the accuracy of our method for fully three-dimensional turbulent boundary layers, we have considered two sets of experimental data: they are due to Johnston [14] and East and Hoxey [15].

Data of Johnston:

Johnston's experimental apparatus consisted of a rectangular inlet duct from which an issuing jet impinged on an end wall 48 inches from the outlet of the channel. The jet was confined on the top and bottom by flat surfaces, and the boundary layer which developed on the floor of the test section was probed. Figure 7 shows the schematic drawing of Johnston's test geometry and figure 8 shows the locations where the measurements were conducted.

In our method, the solution begins on the attachment line at $x = 0$, $z = 0$, and proceeds downstream. At station $x = 0$, $z = 0$, the flow is laminar, and it becomes turbulent at any specified station where $x > 0$, $z > 0$. The calculations can be started at any x-location by inputting the initial velocity profiles. Reference 5 describes such a procedure. For the data of Johnston, we have started the calculations at $x = 0$, $z = 0$, and matched the initial experimental velocity profile as closely as possible.

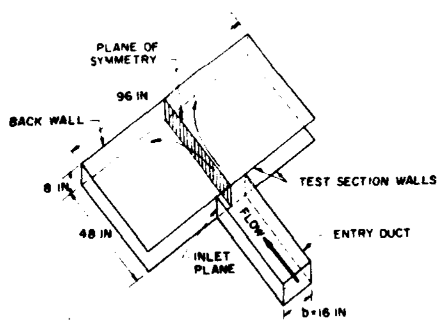

Figure 7. Schematic drawing of Johnston's test geometry.

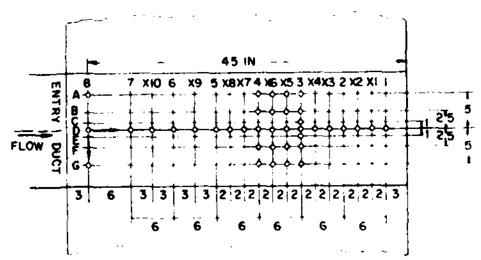

Figure 8. Sketch showing the measured stations.

Figure 9 shows the results for the attachment-line flow. These calculations and others described for this flow were made by using the inviscid external velocity distribution described in [2] and starting the calculations at $x = 0$, $z = 0$. The flow was laminar and was made turbulent at $x = 0.1$ by activating the eddy-viscosity formulas. With this procedure, we matched the first experimental velocity profile, D-8 at $x = 6$, by using a total of four x-stations although we used 26 x-stations to do the calculations up to D-3.

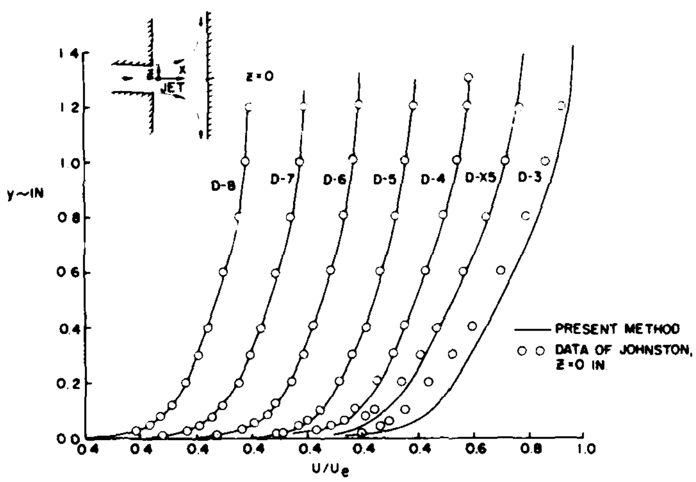

Figure 9. Results for the attachment-line flow.

Figure 10 shows the velocity profiles off the line of symmetry. The calculations were made by taking $z = 2.5$ and 5 inches. As in the attachment-line flow, the agreement with experiment is good.

Data of East and Hoxey:

The data of East and Hoxey [15] was obtained from a flow formed by placing an obstruction in an initially planar boundary layer. The strong adverse pressure gradients imposed by the obstruction, see figure 11, caused the boundary layer to become three-dimensional, and eventually to

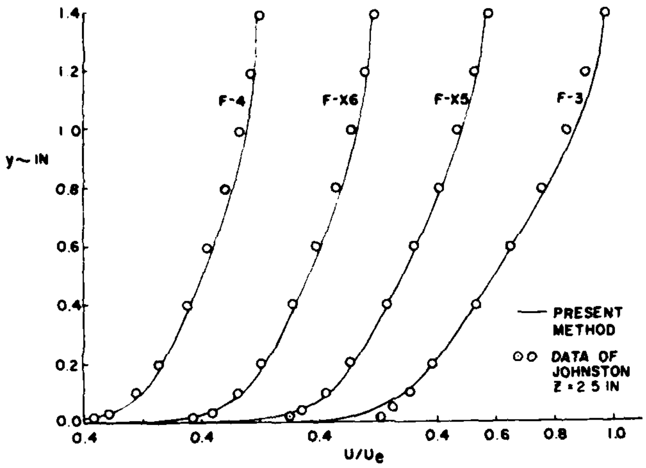

(a)

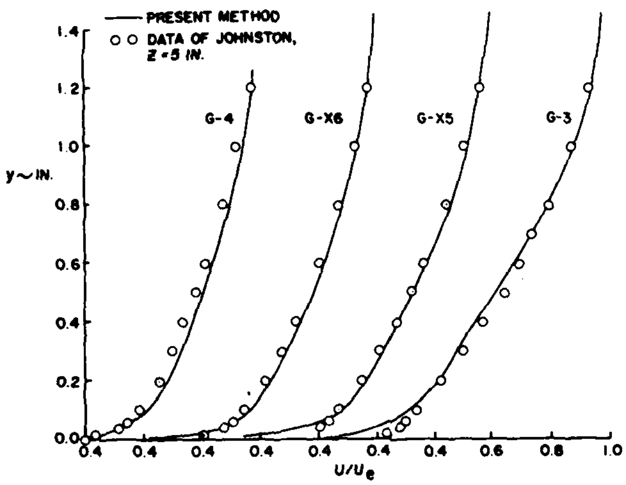

(b)

Figure 10. Results for the flow off the line of symmetry. (a) z = 2.5. (b) z = 5.0.

separate. The measurements were made in the three-dimensional boundary layer upstream of and including the separated region. Calculations are with fully three-dimensional flow model in Cartesian coordinates. Figure 12 shows the calculated velocity profiles for the plane of symmetry flow directly upstream of the obstacle. These calculations were made by inputting the initial velocity profile at station x = 30 in.

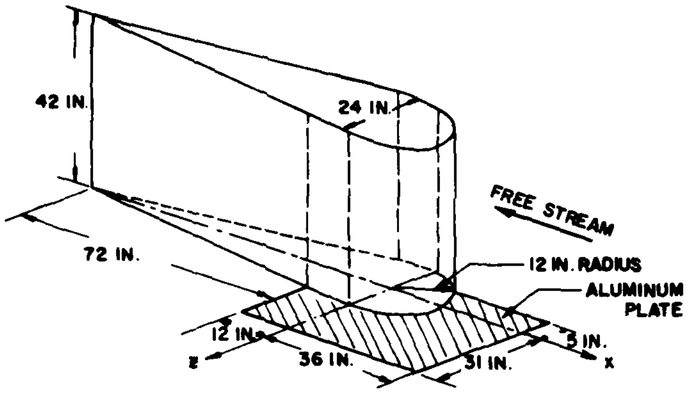

Figure 11. Schematic drawing of East and Hoxey's test setup.

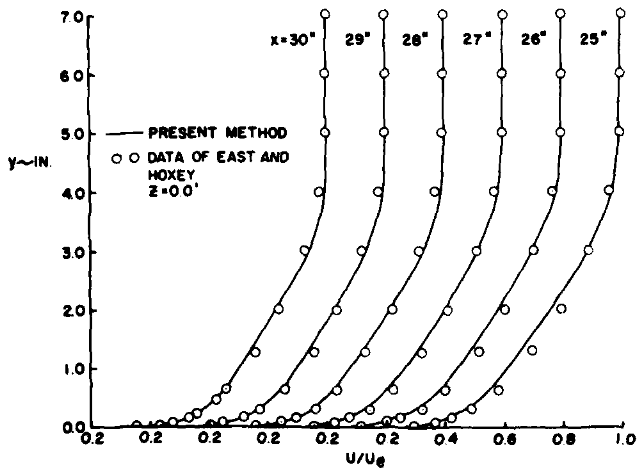

Figure 12. Results for attachment-line flow.

Figure 13 shows the velocity profiles off the line of symmetry. Again, experimental data were used as initial conditions to start the calculations.

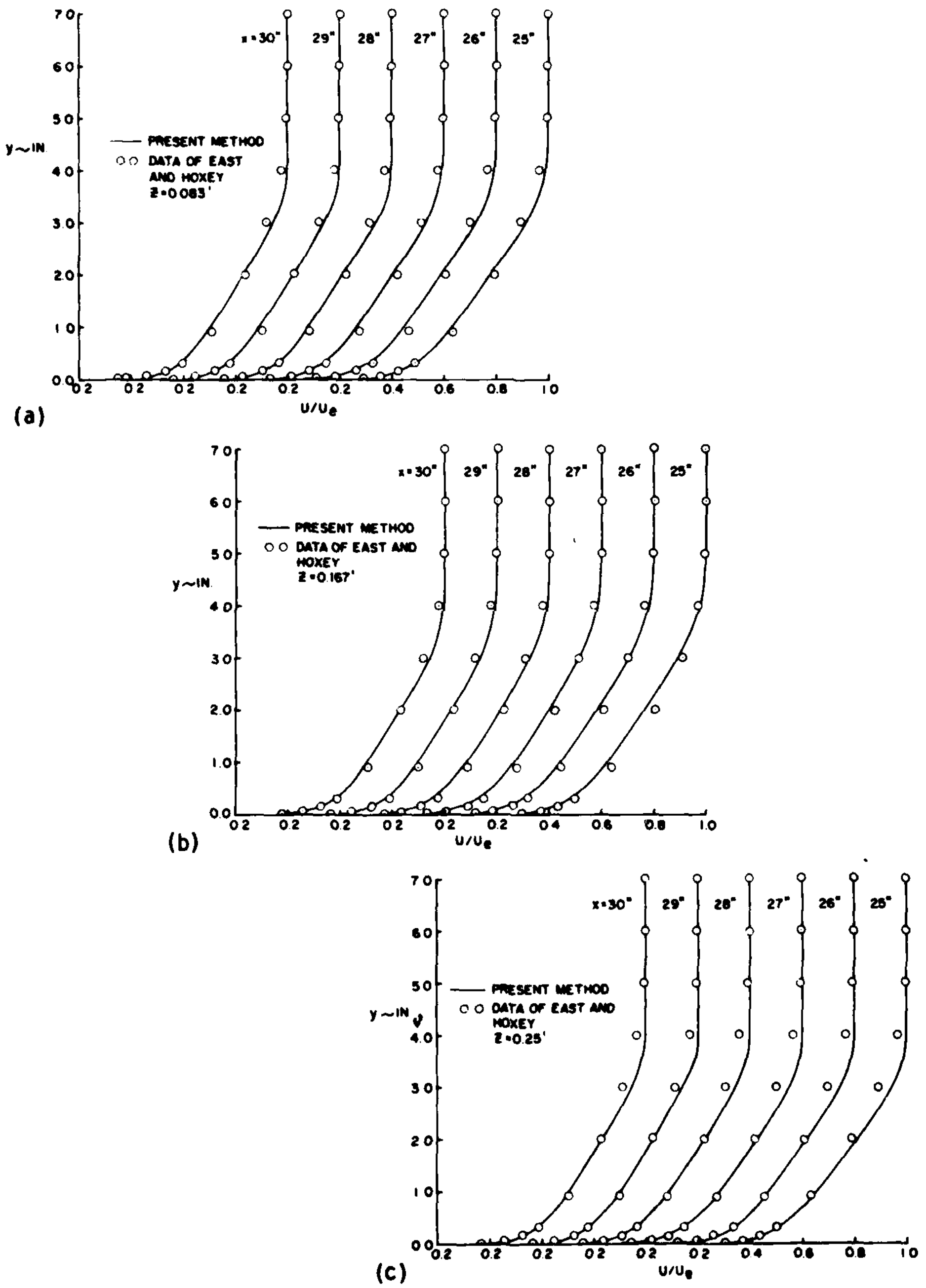

Figure 13. Results for the flow off the line of symmetry. (a) z = 0.083 feet. (b) z = 0.167 feet. (c) z = 0.25 feet.

References

1. Cebeci, T., Mosinskis, G.J., and Kaups, K.: Calculation of Three-Dimensional Boundary Layers. I. Swept Infinite Cylinders and Small Cross-Flow. Douglas Aircraft Co. Rept. MDC J5694, November 1972, Also in AIAA J., Vol. 12, No. 6, June 1974, pp. 779-786.

2. Cebeci, T.: Calculation of Three-Dimensional Boundary Layers. II. Three-Dimensional Flows in Cartesian Coordinates. Douglas Aircraft Co. Rept. MDC J6517, March 1974. Also to appear in AIAA J., 1975.

3. Cebeci, T., Kaups, K., and Moser, A.: A General Method for Calculating Three-Dimensional Incompressible Laminar and Turbulent Boundary Layers. III. Three-Dimensional Flows in Curvilinear Orthogonal Coordinates. Douglas Aircraft Co. Rept. MDC J6867, April 1975.

4. Keller, H.B.: A New Difference Scheme for Parabolic Problems. Numerical Solutions of Partial Differential Equations, II, J. Bramble (ed.) Academic Press, New York, 1970.

5. Keller, H.B. and Cebeci, T.: Accurate Numerical Methods for Boundary Layers. I. Two-Dimensional Laminar Flows. Proceedings of the Second International Conference on Numerical Methods in Fluid Dynamics. Lecture Notes in Physics, Vol. 8, Springer-Verlag, New York, 1971.

6. Keller, H.B. and Cebeci, T.: Accurate Numerical Methods for Boundary Layers. II. Two-Dimensional Turbulent Flows. AIAA J., Vol. 10, No. 9, p. 1197-1200, Sept. 1972.

7. Cebeci, T. and Smith, A.M.O.: Analysis of Turbulent Boundary Layers. Academic Press, Nov. 1974.

8. Isaacson, E. and Keller, H.B.: Analysis of Numerical Methods. Wiley, New York, p. 58, 1966.

9. Bradshaw, P. and Terrell, M.G.: The Response of a Turbulent Boundary Layer on an Infinite Swept Wing to the Sudden Removal of Pressure Gradient. Nat. Phys. Lab. Aero Rept. No. 1305, 1969.

10. Bradshaw, P., Ferriss, D.H. and Atwell, N.P.: Calculation of Boundary Layer Development Using the Turbulent Energy Equation. J. of Fluid Mech., Vol. 28, Pt. 3, pp. 593-616, 1967.

11. Bradshaw, P.: Calculation of Three-Dimensional Turbulent Boundary Layers. J. of Fluid Mech., Vol. 22, Pt. 3, pp. 217-445, 1971.

12. Larsson, L.: Boundary Layers of Ships. III. An Experimental Investigation of the Turbulent Boundary Layer on a Ship Model. The Swedish State Shipbuilding Experimental Tank, Report No. 46, Sept. 1974.

13. Hess, J.L. and Smith, A.M.O.: Calculation of Nonlifting Potential Flow about Arbitrary Three-Dimensional Bodies. Douglas Aircraft Co. Rept. E.S. 40622, Mar. 1962.

14. Johnston, J. P.: Three-Dimensional Turbulent Boundary Layer. M.I.T. Gas Turbine Laboratory Rept. No. 39, 1957.

15. East, L.D. and Hoxey, R.P.: Low-Speed Three-Dimensional Turbulent Boundary-Layer Data. Royal Aircraft Establishment, Farnborough, England Rept. TR 69041, Pt. I, March 1969.

FLUID FLOW AROUND A SHIP'S HULL

Bruce H. Adee

Department of Mechanical Engineering
University of Washington
Seattle, Washington 98195 U.S.A.

ABSTRACT

One of the primary goals of ship hydrodynamics is a theoretical prediction of the resistance of a ship as it moves through the water. Present theoretical treatments aimed at determining the fluid flow around a ship hull, and the resistance, require a separation of the calculation into an inviscid and a viscous-fluid-flow portion. Under the assumption of an inviscid fluid, a linearized boundary-value problem may be formulated for the velocity potential. When the velocity potential is determined, the streamlines over the hull surface may be computed. These streamlines then serve as input for the calculation of the development of the three-dimensional turbulent boundary layer. Streamlines determined in this manner are shown for several Froude numbers and compared to those obtained using a double-model approximation and those found using a zero-Froude-number approach. The free-surface elevation along the hull is also shown and compared with experimental measurements.

INTRODUCTION

Hull-surface streamlines play an important role in examining the fluid flow around a ship's hull. By themselves they indicate the general flow pattern over the hull. They are also critical in calculating the development of the three-dimensional turbulent boundary layer.

The procedure for determining the hull-surface streamlines presented in this paper requires the following steps:

a. Determination of the velocity potential and fluid velocities at "control points" on the hull.

b. Formulation and numerical integration of the "streamline equations" in the appropriate coordinate system.

The boundary-layer development may then be computed by formulating

the boundary-layer equations in the curvilinear coordinate system based on the hull-surface streamlines.

Several other methods have been proposed for finding hull-surface streamlines. These include the zero-Froude-number approximation of Tuck and von Kerczek (1968), and the double-model approximation employed by Uberoi (1969).

THE VELOCITY POTENTIAL

The determination of the inviscid-fluid flow around a ship's hull requires the formulation and solution of a boundary-value problem for the velocity potential. At present, a solution for the velocity potential assuming only an inviscid fluid is impossible because the free-surface boundary condition is nonlinear. By expanding the velocity potential in a power series, "linearization" of the free-surface boundary condition is possible and an approximate solution for the velocity potential may be obtained.

The technique employed in the present work to determine the velocity potential extends the pioneering efforts of Hess and Smith (1964, 1967) to fluid flow with a free surface present. A detailed description of the method used in solving for the velocity potential is given by Adee (1973).

In this approach, the actual hull surface is approximated using flat-plate elements. A "control point" is selected on each plate element at the position where the hull-surface boundary condition is satisfied. Singularities of unit strength (sometimes referred to as "Kelvin sources") are then distributed over the hull surface at the control points. These singularities satisfy the Laplace equation and all the boundary conditions except the hull-surface boundary condition. The strengths of the individual sources are then calculated to insure satisfaction of the hull-surface boundary condition.

HULL-SURFACE STREAMLINES

The potential-flow calculation provides the fluid velocities at the control points on the hull. These are transformed into streamlines on the hull surface and velocities at discrete points along these streamlines. In addition to their use in the boundary-layer calculations, the hull-surface streamlines provide an excellent means of displaying the inviscid-

fluid flow around the hull.

The procedure developed to calculate streamlines requires two steps. First, the streamline at the free surface is determined. When this calculation is completed, streamlines below the free surface may be computed using the fluid velocities at the control points and along the free-surface streamline as input data.

Free-Surface Streamline

The elevation of the free surface is calculated in the rectangular coordinate system illustrated in Figure 1 by applying the linearized-free-surface boundary condition

$$\gamma(x,z) = \frac{V}{g}\,\phi_x(x,0,z) \tag{1}$$

at the stations along the hull where the control points are defined.

In computing the velocity potential for the case of 100 control points on each side of the Series 60, block coefficient 0.60 hull, the control points nearest the free surface are located four feet below the undisturbed waterplane. Rather than using $\phi_x(x,0,z)$ in the linearized free-surface boundary condition, $\phi_x(x,-4,z)$ was used since it was readily available. The results were checked by actually computing the velocity induced at $y = 0$ by the 100 sources distributed at the control points. No major differences were found between the calculated free-surface elevations at Froude numbers equal to 0.259 or 0.345. Consequently, only the results obtained using $\phi_x(x,-4,z)$ are illustrated here.

Application of the linearized-free-surface boundary condition in the present case yields the free-surface elevation at twenty points along the hull. After computing the position and fluid velocity at points along the free-surface streamline these are added to the matrix of control points used in determining all other hull-surface streamlines.

The offset, or z coordinate, at any point along the free-surface streamline is found by interpolating within the hull offset table. An equation of the form

$$z = f(x,y) = A_1x^2 + A_2x + A_3xy + A_4y^2 + A_5y + A_6 \tag{2}$$

is used to represent the local hull surface. The nine points nearest a

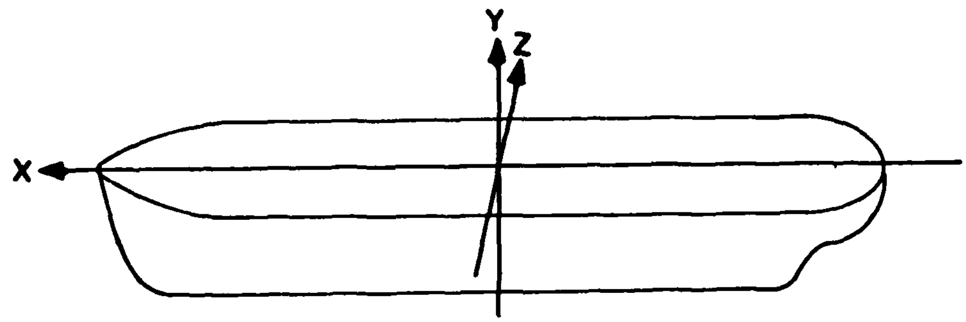

Figure 1. Rectangular coordinate system

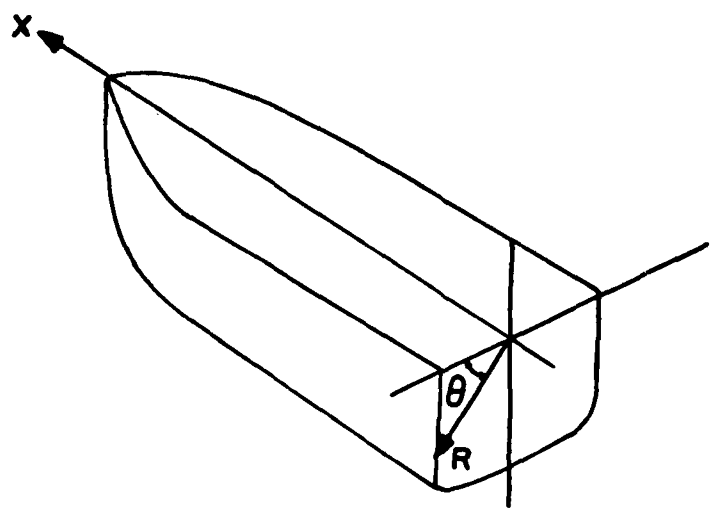

Figure 2. Cylindrical coordinate system

free-surface point are used in performing a least-squares fit to determine the coefficients A_i for $i = 1$ to 6. A Gaussian reduction method is employed to solve the six simultaneous equations for the coefficients.

The position of the free-surface streamline is now determined at several points. If more points are required, then the y and z coordinates are found by using the equations:

$$y = A_1x^2 + B_1x + C_1 , \tag{3}$$

and

$$z = A_2x^2 + B_2x + C_2 . \tag{4}$$

At any desired x location the coefficients in equations (3) and (4) are determined using the three nearest free-surface points.

To complete the calculation of the free-surface streamline, the fluid velocity must be found at the points defining its position. This information is required in the subsequent calculation of the other hull-surface streamlines and for use in the boundary-layer calculations. The procedure developed for calculating fluid velocity is based on three equations. The first is a form of Bernoulli's equation

$$v_x{}^2 + v_y{}^2 + v_z{}^2 + 2g\gamma = V^2 . \tag{5}$$

The second expresses the requirement that the velocity vector is tangent to the streamline

$$\vec{v} = \text{constant} \cdot [\vec{i} + \frac{\partial y}{\partial x}\vec{j} + \frac{\partial z}{\partial x}\vec{k}] , \tag{6}$$

while the third is the vector representation of velocity

$$\vec{v} = v_x\vec{i} + v_y\vec{j} + v_z\vec{k} . \tag{7}$$

With the constant in equation (6) equal to v_x, equations (6) and (7) yield:

$$v_x = v_x ,$$
$$v_y = v_x \frac{\partial y}{\partial x} , \tag{8}$$

and

$$v_z = v_x \frac{\partial z}{\partial x} .$$

Combining these with equation (5) yields the x component of velocity

$$v_x^{\,2} = \frac{v^2 - 2g\gamma}{[1 + (\frac{\partial y}{\partial x})^2 + (\frac{\partial z}{\partial x})^2]} . \tag{9}$$

The problem in using this technique is to accurately determine the partial derivatives $\frac{\partial y}{\partial x}$ and $\frac{\partial z}{\partial x}$. Here, the parametric representation previously discussed was employed. As long as the magnitude of v_x remains approximately an order of magnitude larger than v_y and v_z the derivatives obtained in this manner are satisfactory.

In order to check the procedure for calculating fluid velocity along the free-surface streamline the hull-surface boundary condition may be used. The equation

$$Vn_x = \vec{v} \cdot \vec{n} = v_x n_x + v_y n_y + v_z n_z \tag{10}$$

expresses this boundary condition. Using equation (2) to perform a least-squares surface fit the components of the hull-surface normal may be calculated. These are

$$n_x = \frac{1}{k} \frac{\partial z}{\partial x} ,$$

$$n_y = \frac{1}{k} \frac{\partial z}{\partial y} \tag{11}$$

and

$$n_z = \frac{1}{k} .$$

Here,

$$k = \sqrt{1 + (\frac{\partial z}{\partial x})^2 + (\frac{\partial z}{\partial y})^2} .$$

Using equation (10) the velocity of the hull surface and the fluid velocity at the hull surface may be compared. Differences have typically ranged between .01 and .5 per cent of the ship speed.

Free-surface streamlines calculated for a Series 60, block coefficient 0.60 ship are illustrated in Figures 3 through 6. In each case a wave profile experimentally measured on a twenty foot model by Huang and von Kerczek (1972) is included. The four computed wave profiles are also plotted together in Figure 7.

Comparison of the theoretically predicted and experimentally measured wave profiles shows reasonable agreement (note that Froude number matching is not exact). The phase of the predicted and measured wave patterns is in general agreement with the theoretical profiles shifted slightly aft of the experimental profiles. In each case, the amplitude of the bow wave is underestimated while the stern wave, except at the Froude number 0.345, is overestimated.

As the Froude number increases the prediction of the profile weakens, particularly in the stern region. At a Froude number of 0.302 the final trough is out of phase by over one station and the steepness of the stern wave is overpredicted. At the Froude number of 0.345 there is considerable difference aft of station 9.

There are two potential sources of explanation for the discrepancies between wave profiles in the stern region. The hull-surface geometry in this region is quite complex with large changes in curvature. As a result there may be some inaccuracy in solving for the velocity potential because the hull was not divided into a sufficient number of flat-plate elements to accurately model the surface geometry. The second possible source of error is the effect of fluid viscosity and boundary-layer growth on the calculations. This effect is likely to increase from bow to stern and is not accounted for in the present analysis.

The general trend followed by the wave profile as forward speed increases may be seen in Figure 8 where the wave profiles calculated at various Froude numbers are superimposed. The height of the bow wave increases and the crest shifts aft as speed increases. A similar trend is observed in the experimental data. Aft of the initial crest at the bow, the remaining portion of the wave profile including a crest in the midship area and near the stern also tend to shift aft as speed increases. Between Fr = 0.302 and Fr = 0.345 the very large stern wave predicted at lower Froude numbers disappears giving the wave profile at FR = 0.345 a

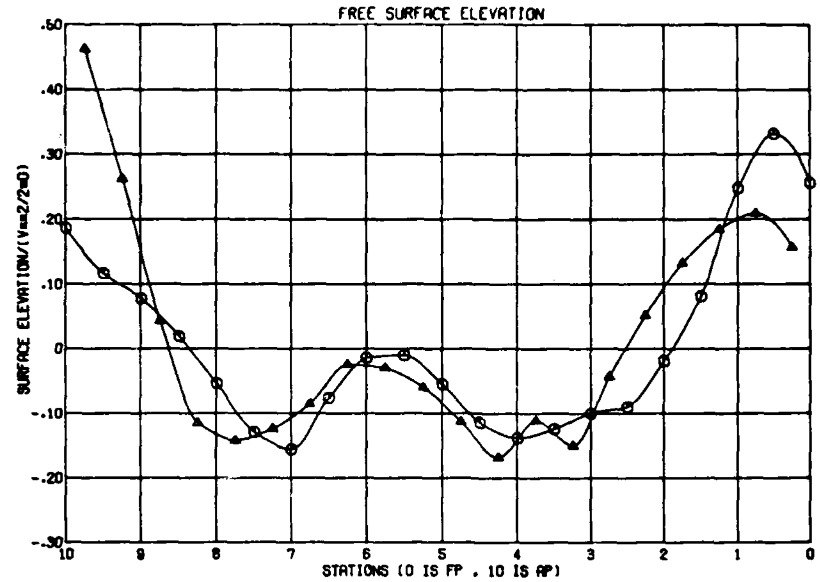

▲ NONDIMENSIONAL FREE SURFACE ELEVATION FROM SURFACE-SOURCE DISTRIBUTION, FR = .259
○ NONDIMENSIONAL FREE SURFACE (HUANG AND VON KERCZEK - 1972), FR = .250

Figure 3. Nondimensional free-surface elevation Series 60, C_B = 0.60

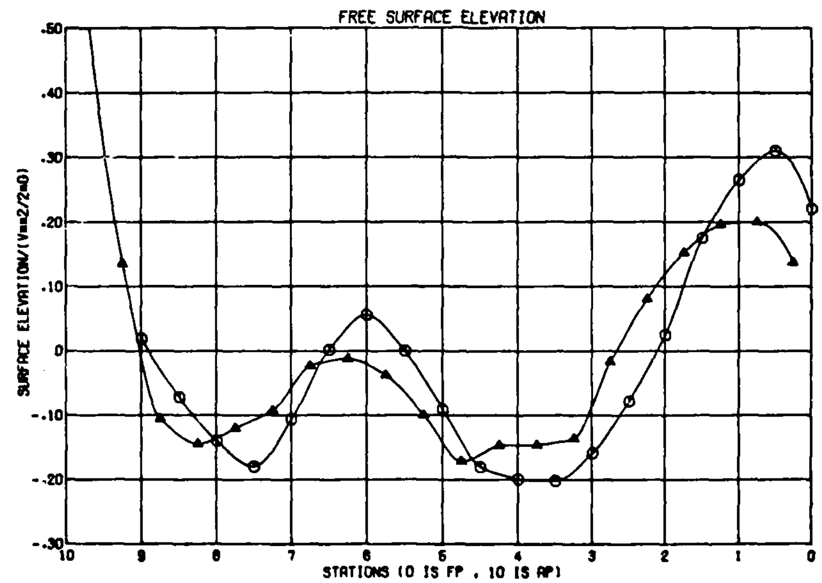

▲ NONDIMENSIONAL FREE SURFACE ELEVATION FROM SURFACE-SOURCE DISTRIBUTION, FR = .281
○ NONDIMENSIONAL FREE SURFACE (HUANG AND VON KERCZEK - 1972), FR = .280

Figure 4. Nondimensional free-surface elevation Series 60, C_B = 0.60

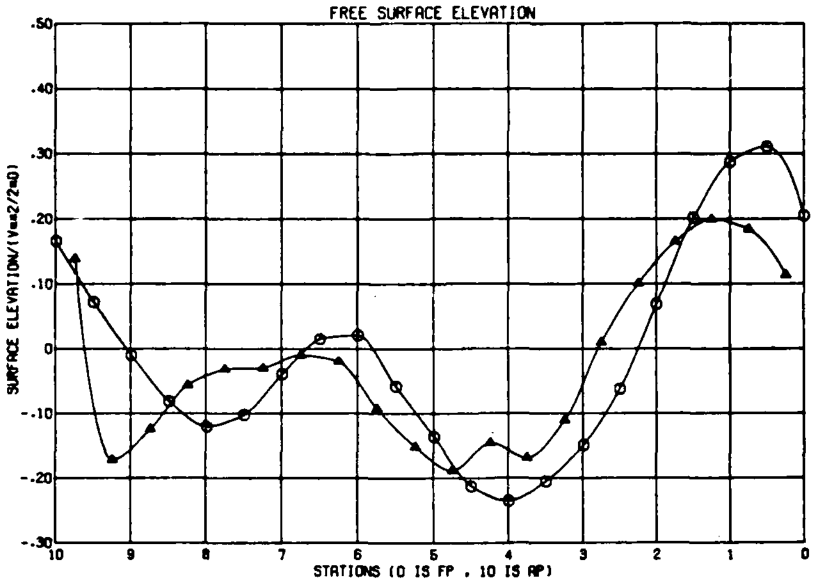

▲ NONDIMENSIONAL FREE SURFACE ELEVATION FROM SURFACE-SOURCE DISTRIBUTION, FR = .302

○ NONDIMENSIONAL FREE SURFACE (HUANG AND VON KERCZEK - 1972), FR = .300

Figure 5. Nondimensional free-surface elevation Series 60, C_B = 0.60

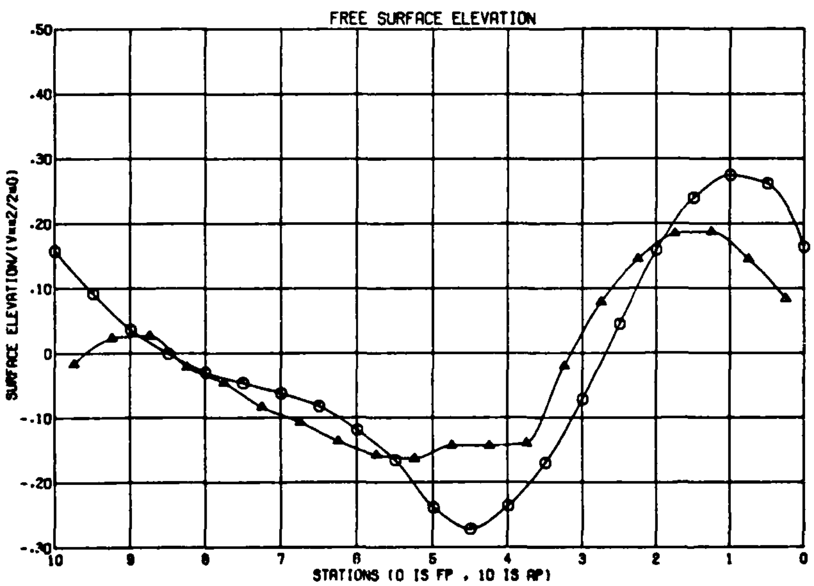

▲ NONDIMENSIONAL FREE SURFACE ELEVATION FROM SURFACE-SOURCE DISTRIBUTION, FR = .345

○ NONDIMENSIONAL FREE SURFACE (HUANG AND VON KERCZEK - 1972), FR = .360

Figure 6. Nondimensional free-surface elevation Series 60, C_B = 0.60

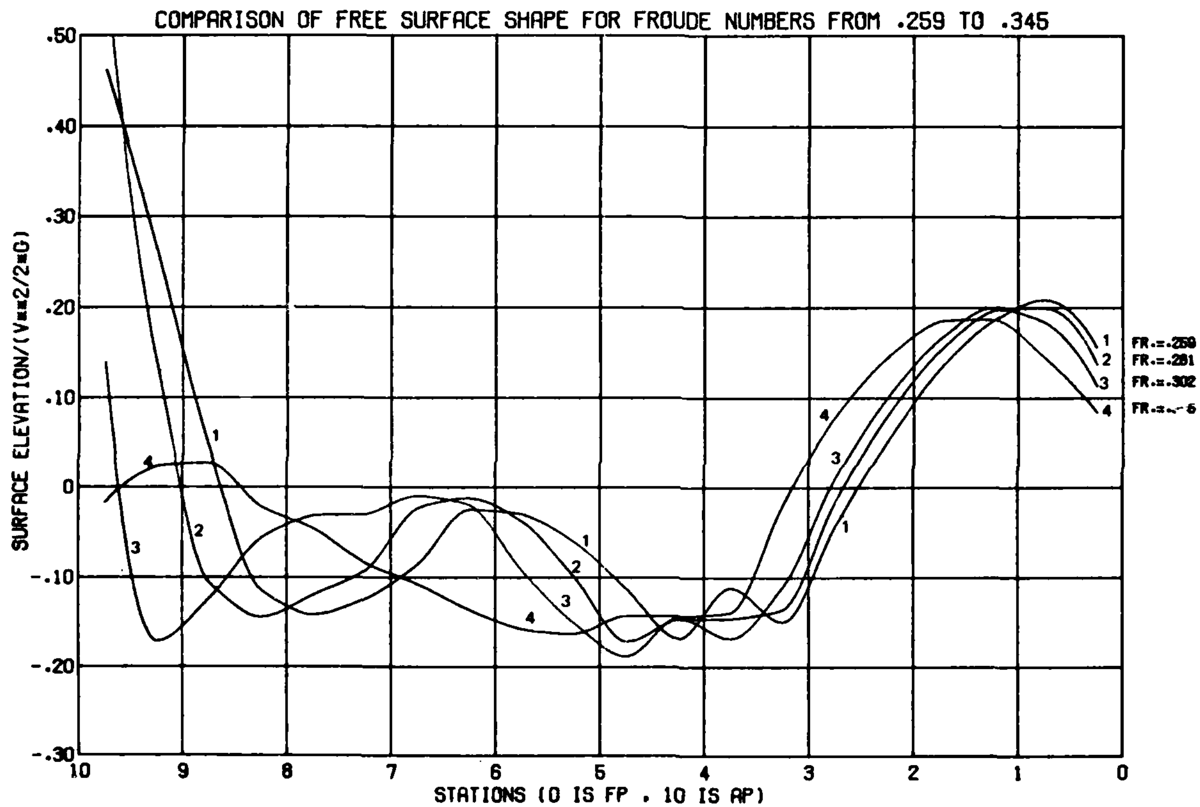

Figure 7. Series 60, block coefficient 0.60

considerably different appearance.

Other Hull-Surface Streamlines

Using the free-surface streamline and the fluid velocities at the control points, the calculation of the other hull-surface streamlines can proceed. The method developed for finding these streamlines is an improvement on the technique described by Adee (1973). The new procedure appears to produce better quality streamlines with a more straightforward computer program.

The original technique for determining the hull-surface streamlines used a rectangular coordinate system with x and y as independent variables when the streamline was on the side of the hull and x and z when the streamline turned under the bilge and proceeded along the bottom. This technique was first modified so that the cylindrical coordinate system shown in Figure 2* was used exclusively. The change simplified the computer program but produced streamlines which were not smooth in the bow and stern regions where the radial dimension of the hull is small. Finally, a third system was tried where calculations in the bow and stern regions were performed in a rectangular coordinate system while in the midbody region a cylindrical system was used. Several combinations of lengths for each coordinate system were tried with the best streamlines resulting from a 10-75-15 system. Over the first 10 per cent of the length of the hull a rectangular system was used followed by 75 per cent of the length using a cylindrical system and returning to a rectangular system over the final 15 per cent of the length.

Streamlines are calculated by solving two simultaneous differential equations. These are of the form

$$\frac{dx}{dt} = v_x(v,y,f(x,y)) \ ,$$
$$\frac{dy}{dt} = v_y(x,y,f(x,y)) \qquad (12)$$

in rectangular coordinates, and

$$\frac{dx}{dt} = v_x(x,\theta,F(x,\theta)) \ ,$$

*See page 438

$$\frac{d\theta}{dt} = v_\theta(x,\theta,F(x,\theta)) \tag{13}$$

in cylindrical coordinates.

In computing streamlines a starting point near the bow and a time step Δt are selected. The calculation proceeds aft from the starting point in a step-by-step manner. The time increment between points calculated along the streamline is a function of several variables. For instance, when 60 points are desired along a streamline for a ship of 600 feet traveling at 36 feet per second, the time increment should be

$$\Delta t \approx \frac{L}{nV} = .28 \text{ seconds.} \tag{14}$$

To integrate the differential equations, values of the components of velocity at any point on the hull are found by interpolating among the known velocities at the control points and along the free-surface streamline. The technique for calculating velocities on the hull surface is similar to the method of interpolation used with the offset table. Nine control points nearest to the streamline-point are used to perform a least-squares fit using the equations

$$\begin{aligned} v_x &= A_1x^2 + A_2x + A_3xy + A_4y^2 + A_5y + A_6 , \\ v_y &= B_1x^2 + B_2x + B_3xy + B_4y^2 + B_5y + B_6 \end{aligned} \tag{15}$$

for rectangular coordinates, and

$$\begin{aligned} v_x &= D_1x^2 + D_2x + D_3x\theta + D_4\theta^2 + D_5\theta + D_6 \\ v_\theta &= E_1x^2 + E_2x + E_3x\theta + E_4\theta^2 + E_5\theta + E_6 \end{aligned} \tag{16}$$

in the cylindrical coordinates. Using the interpolation formulas (15) and (16), the change in position of a fluid particle traveling along the streamline during the time step Δt may be calculated. In this manner a step-by-step procedure may be developed for finding each hull-surface streamline. The results are the positions of points along each streamline and the fluid velocity at each of these points. For convenience, all results are expressed in the rectangular coordinate system.

Hull-surface streamlines were obtained for Froude numbers 0.259, 0.281, 0.302 and 0.345 on the Series 60, block coefficient 0.60 hull. These are illustrated in Figures 8 through 11.

Since there is very little experimentally obtained streamline data available, it is difficult to predict the accuracy of these streamlines. In general, they follow the expected trend of turning sharply around the bilge forward, flowing aft along the bottom and emerging from the bottom to rise rapidly in the stern region. As previously discussed, the free-surface streamline shows reasonable comparison with wave profiles measured on a model.

Streamline data which is available for comparison is the result of assuming a double model in an infinite fluid (see Uberoi, 1969) or the zero-Froude-number approximation of Tuck and von Kerczek (1967). To provide some comparison with these streamlines, calculations were performed assuming a double model in an infinite fluid.

Comparisons between the double-model streamlines calculated here and the zero-Froude-number streamlines of Tuck and von Kerczek (1968) appear in Figures 12 and 13. In Figure 12, for a Froude number of 0.036, the streamlines are all very close. This is true at lower Froude numbers as well. As the Froude number increases to 0.259 (see Figure 13), there is a consistent difference in the midship area with the double-model streamlines tending to be deeper than the zero-Froude-number streamlines. Comparisons at the other Froude numbers higher than 0.259 are very similar to the case of 0.259 and have not been included.

Figure 14 shows a comparison of streamlines computed using a linearized-free-surface boundary condition (Kelvin source streamlines) and the zero-Froude-number approximation. There are considerable differences between the two sets of streamlines over the length of the hull. These differences are greatest in the region near the free surface and diminish with increasing depth.

Comparisons between streamlines resulting from the double-model approximation and those including the linearized-free-surface boundary condition are contained in Figures 15 and 16 for Froude numbers of 0.259 and 0.302, respectively. Again the effect of the presence of the free surface is evident in the streamlines near the free surface. Deeper

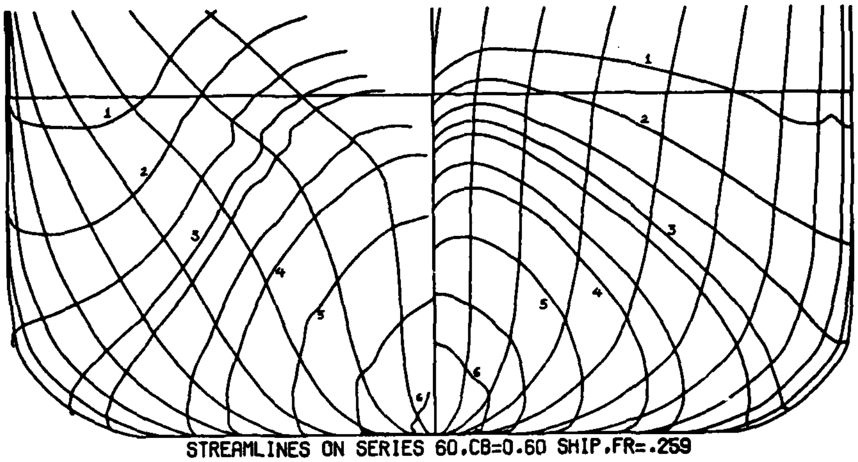

Figure 8. Streamlines including free surface

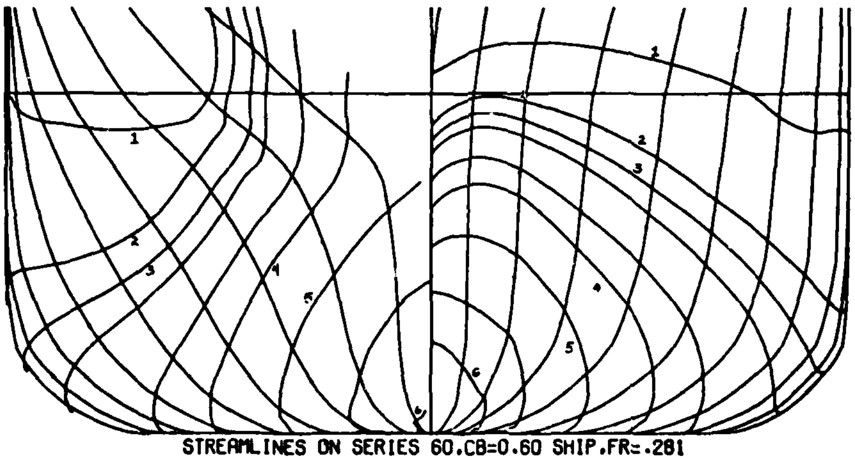

Figure 9. Streamlines including free surface

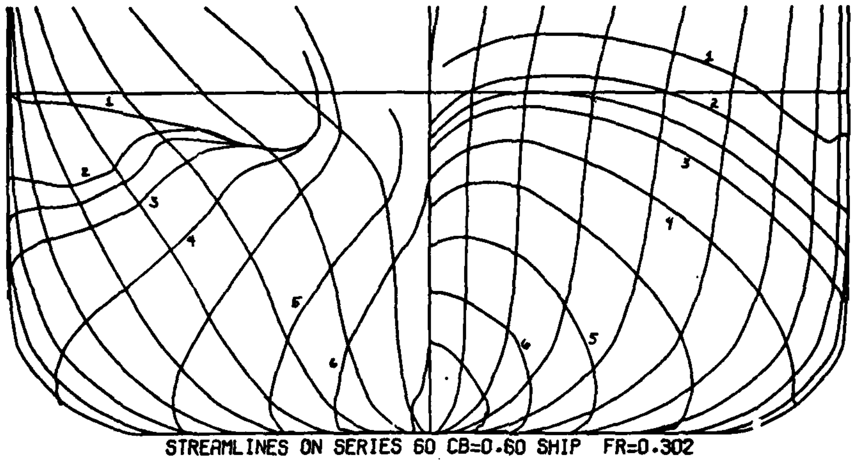

Figure 10. Streamlines including free surface

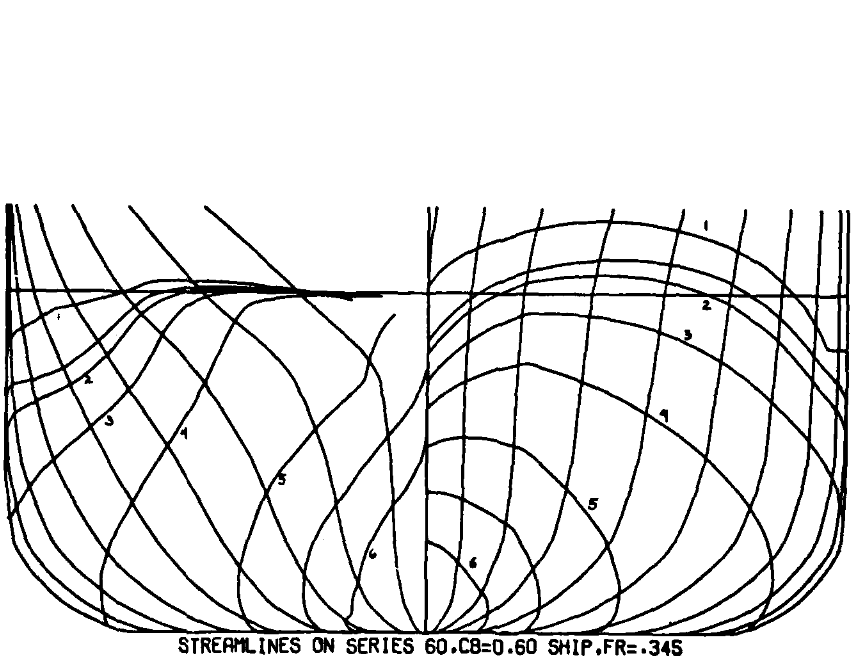

Figure 11. Streamlines including free surface

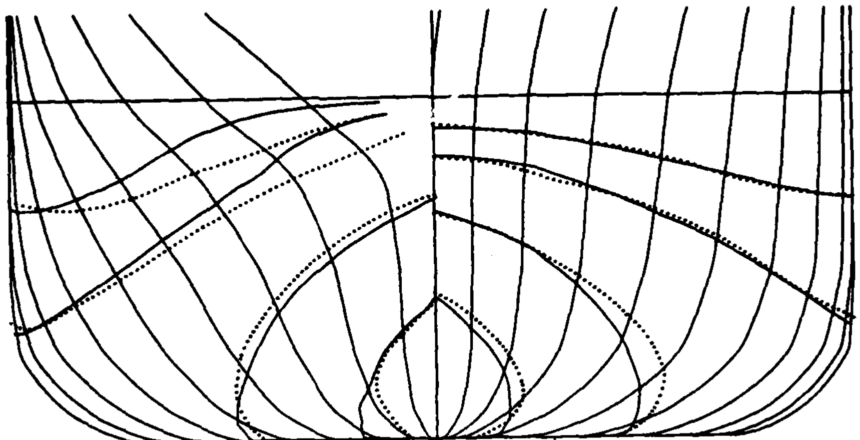

STREAMLINES ON SERIES 60.CB=0.60 SHIP.FR=.036

—— DOUBLE - MODEL STREAMLINES - PRESENT WORK - 100 SOURCES

—— ZERO FROUDE NUMBER STREAMLINES-HUANG AND VON KERCZEK (1972)

Figure 12

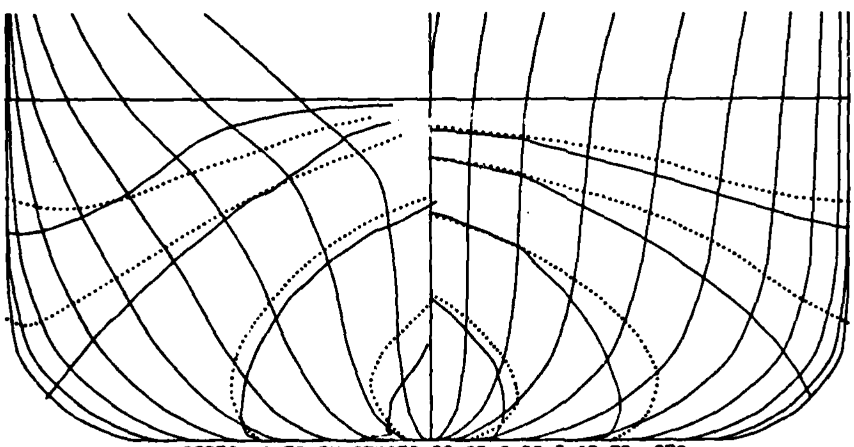

STREAMLINES ON SERIES 60.CB=0.60 SHIP.FR=.259

—— DOUBLE - MODEL STREAMLINES - PRESENT WORK - 100 SOURCES

- - - - ZERO FROUDE NUMBER STREAMLINES-HUANG AND VON KERCZEK (1972)

Figure 13

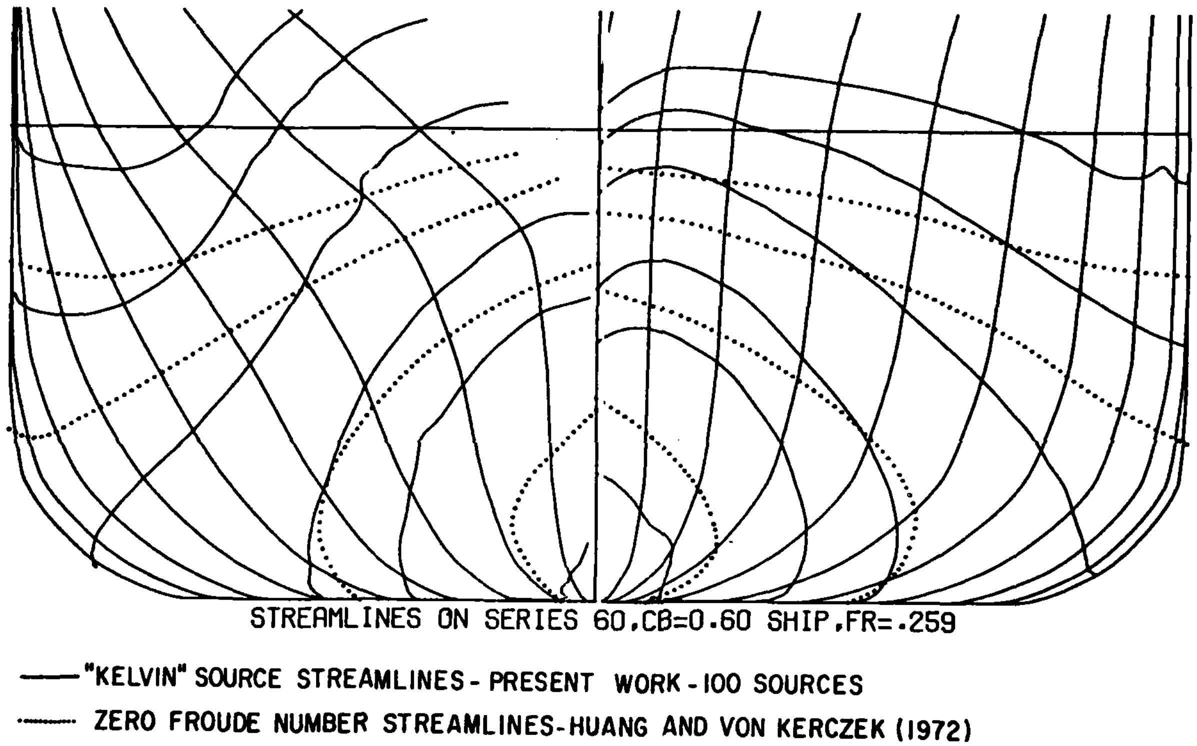
STREAMLINES ON SERIES 60,CB=0.60 SHIP,FR=.259
"KELVIN" SOURCE STREAMLINES - PRESENT WORK - 100 SOURCES
ZERO FROUDE NUMBER STREAMLINES-HUANG AND VON KERCZEK (1972)

Figure 14.

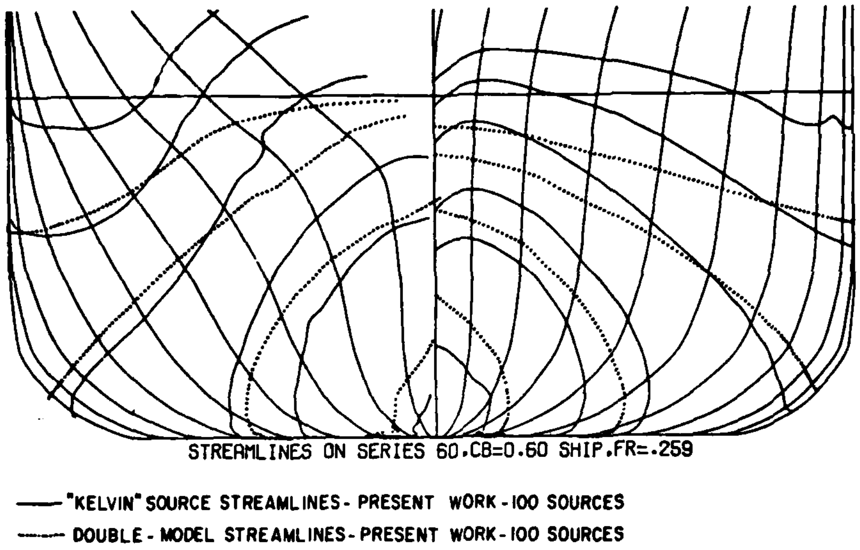

Figure 15

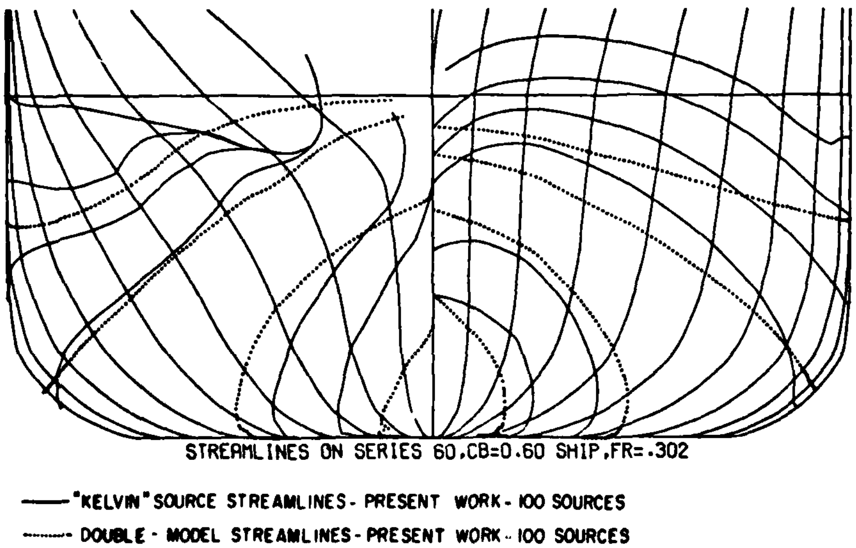

Figure 16.

streamlines are quite similar using either method of calculating the velocity potential.

CONCLUSION

At the present time computational techniques have been developed to obtain hull-surface streamlines for ships of arbitrary hull shape. The effect of the free surface is included by using a linearized-free-surface boundary condition when determining the velocity potential.

The streamline calculations illustrated here indicate significant differences among the three approaches considered. The zero-Froude-number and double-model streamlines are close for very low Froude numbers. However, there is a difference between these results as speed increases. Including the linearized-free-surface boundary condition yields results which are different than the other two calculations. These differences decrease with increasing depth.

Comparisons of the computed and measured wave profile along the hull are good in the forward portion of the hull but the correlation decreases in the stern region.

The major impediment to the widespread application of these calculations is the large amount of computer time required to obtain the velocity potential. With 100 control points on each side of the hull it takes about 3.5 hours on a CDC 6400 to compute a set of streamlines. However, there is a very good chance of reducing the computer time requirements as the numerical techniques employed in the computer program are refined.

ACKNOWLEDGEMENT

The support of the Fluid Mechanics Program, Division of Engineering, National Science Foundation is gratefully acknowledged. The contribution of Philip J. Harvey who served as a research assistant under this grant was invaluable in completing this research effort.

NOMENCLATURE

$f(x,y)$	Distance from centerplane to hull surface in rectangular coordinates
$F(x,\theta)$	Radial distance to hull surface in cylindrical coordinates

g	Acceleration of gravity
L	Ship length
$\vec{n}$	Exterior unit normal of the hull surface
n_x, n_y, n_z	Components of $\vec{n}$ in a rectangular system
v_x, v_y, v_z	Fluid velocities in the x,y,z directions, respectively
x, y, z	Rectangular coordinates
x, θ, r	Cylindrical coordinates
γ	Free-surface elevation
ϕ	Velocity potential

REFERENCES

Adee, B., "Calculation of the Streamlines About a Ship Assuming a Linearized Free-Surface Boundary Condition," Journal of Ship Research, Vol. 17, No. 3, Sept. 1973, pp. 140-146.

Hess, J.L., Smith, A.M.O., "Calculation of Nonlifting Potential Flow About Arbitrary Three-Dimensional Bodies," Journal of Ship Research, Vol. 8, No. 2, Sept. 1964, pp. 22-44.

Hess, J.L., Smith, A.M.O., "Calculation of Potential Flow About Arbitrary Bodies," Progress in Aeronautical Sciences, Pergamon Press, New York, 1967, pp. 1-138.

Huang, T.T., von Kerczek, C., "Shear Stress and Pressure Distribution on a Surface Ship Model: Theory and Experiment," Ninth Symposium of Naval Hydrodynamics, Paris, France, August, 1972.

Tuck, E.O., von Kerczek, C., "Streamlines and Pressure Distribution on Arbitrary Ship Hulls at Zero Froude Number," Journal of Ship Research, Vol. 12, No. 3, Sept. 1968, pp. 231-236.

Uberoi, S.B.S., "Viscous Resistance of Ships and Ship Models," Hydro- and Aerodynamics Laboratory, Report No. Hy-18, Lyngby, Denmark, Sept. 1969.

ON THE CALCULATION OF STATIONARY SHIP FLOW COMPONENTS

K.W.H. Eggers and H.S. Choi

Institut für Schiffbau, Hamburg University
2 Hamburg 60, Lämmersieth 90

ABSTRACT

A procedure is described for evaluating flow components, pressure and first-order wave resistance for polynomial ship forms. Second-order corrections are determined, and the resistance components are estimated by use of a reverse flow principle. The subdivision for quadrature of second-order Lagally force is controlled through checking an identity *between first-order* Lagally force and resistance from far-field waves. The resistance obtained from pressure integration over the submerged hull should deviate therefrom by a line integral over square of wave height along the free-surface intersection, provided there is no flow through the hull. This correlation is studied numerically. It is confirmed that line integrals within the second-order potential can be eliminated; however, the potential differs from that for a submerged thin body by a certain line integral. For integration over polygon-shaped surfaces, two procedures are described; one for flow components due to a polynomial source distribution, leading through recursion to four elementary expressions to be evaluated at corner points (in generalisation of the result of Hess and Smith). The other is for integration of exponential functions with argument linear in space coordinates, resulting in a sum of exponentials from the corner points times geometric characteristics. The program was extended to calculate the derivatives of the "displacement potential" in the sense of Noblesse's analysis.

Introduction

In the early sixties, there was a world-wide interest in determining wave resistance from *wave pattern geometry.* At that time, the first author initiated a computer program for

calculating wave fields due to a linear source distribution on a vertical rectangular plane in order to examine wave analysis methods numerically.

The program was gradually extended in various directions owing to different trends in wave resistance research. One of them was to produce all three flow components in the entire fluid domain, and another was to include more general source distributions to cover a broader class of ship forms such as ships with parallel middle body. In particular, the program was revised for evaluating second-order resistance contributions, as described in an ONR Symposium lecture (Eggers 1966) and a subsequent modification (Eggers 1970). It was eventually recognised, however, that the regular second-order perturbation approach could not provide significant improvement to the classical Michell thin-ship theory for actual ship forms.

The program is nevertheless still a useful device of generating theorectical flow fields for numerical experiments. For example, through numerical integration of the flow, the velocity potential could be obtained; thereby different types of "line integral contributions" to the flow and to the wave resistance could be evaluated, thus equivalence relations between different expressions for wave resistance were investigated numerically.

At this conference, the concept underlying the program shall be discussed together with some miscellaneous topics which are frequently encountered in the *numerical solution of the* ship-wave problem.

1 First-Order Flow Components

1.1 Notation

We restrict our analysis to ship forms with fore and aft symmetry and which can be described through a product of polynomials as

$$y = \pm \epsilon f(x) h(z) \tag{1}$$

with $f(x) = 1$ for $|x| \leq p < 1$,

$f(x) = 1 - \Sigma a_i \, ((|x| - p)/(1 - p))^i$ for $p \leq |x| \leq 1$,

and $h(z) = 1 - (z/D)^m$ for $-D \leq z \leq 0$.

Here ϵ is the half beam, p is half the length of the parallel middle body, and D is the draft. The problem has been normalized by setting half the length of the ship equal to unity (See Figure 1). Due to the symmetry assumed, all a_i with i odd vanish, and we have $\Sigma a_i = 1$. For rectangular frames we may formally set $m = \infty$. The ship is advancing with uniform speed V in + x direction, and z = o is the undisturbed free surface.

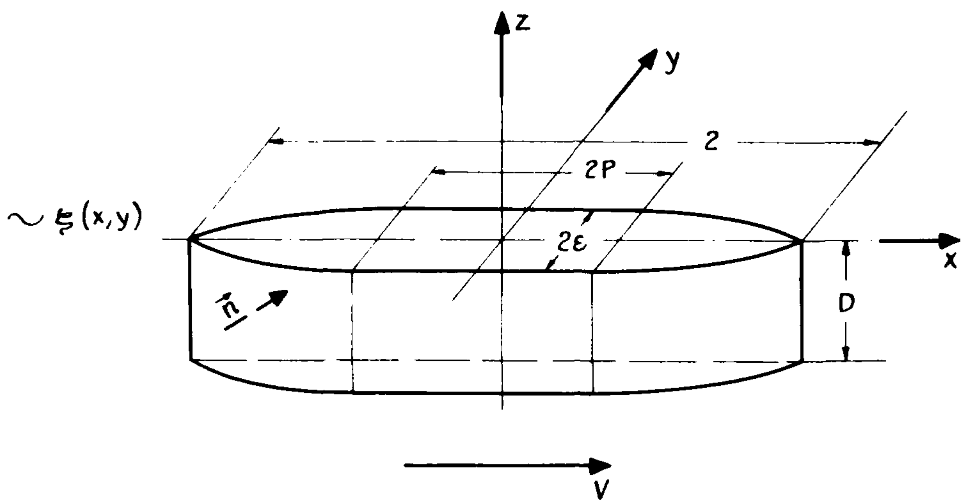

Figure 1 – Coordinate System

Following first-order thin-ship theory, we let $\sigma(x,z) = -2\epsilon V f_x(x) h(z)$ be the "source distribution" over the longitudinal centerplane $-1 \leq x \leq 1$, $-D \leq z \leq 0$ and it generates a velocity potential φ which can be expressed in terms of the "Havelock source potential" G as

$$* \qquad \varphi = -1/4\pi \int_{-D}^{0} \int_{-1}^{1} \sigma(x',z')\, G(x-x', y, z-z', z+z')\, dx'\, dz' \tag{2}$$

G may be conveniently decomposed into three parts:

$$G = G^{basic} + G^{local} + G^{free},$$

where
$$G^{basic} = (r_1 - r)/r r_1$$

with
$$r = \sqrt{(x-x')^2 + y^2 + (z-z')^2}, \quad r_1 = \sqrt{(x-x')^2 + y^2 + (z+z')^2}$$

G^{local} and G^{free} depend only on three variables, i.e. $x-x'$, y and $z+z'$:

$$G^{local} = +2k_o/\pi \, \mathrm{Re}\left\{ \int_{-\infty}^{\infty} e^{ik_o uy} du \int_{|u|}^{\infty} \frac{\exp(-k_o w\,|x-x'| + ik_o v(z+z'))}{v - iw^2}\, dw \right\}, \tag{3}$$

with
$$v = \sqrt{w^2 - u^2},$$

$$G^{free} = -k_o \frac{(1-\mathrm{sign}(x-x'))}{2} \mathrm{Im}\left\{ \int_{-\infty}^{\infty} \frac{\exp(ik_o uy + ik_o s(x-x') + s^2 k_o(z+z'))4s}{\sqrt{1+4u^2}}\, du \right\} \tag{4}$$

*In this and in succeeding equations read $-1/4\pi$ as $(-1/4\pi)$.

with $$s = s(u) = \sqrt{(1+\sqrt{1+4u^2})/2}.$$

Here $k_o = g/V^2$ stands for the principal wave number (g is the acceleration due to gravity). For calculating vertical flow components (i.e. z-derivatives) it is appropriate to use another decomposition:

$$G = G_o^{basic} + G_o^{local} + G^{free}$$

with $$G_o^{basic} = +(r+r_1)/rr_1 \text{ and } G_o^{local} = G^{local} - 2/r_1$$

This ensures that there will be no contribution from G^{basic} to φ_x and φ_y, and no contribution from G_o^{basic} to φ_z at the undisturbed free surface $z = 0$. It can be shown (Eggers 1970) that for any pair z, z' with $z+z'<0$, we have $G_{oz}^{local} = -1/k_o\, G_{xx}^{local}$. Accordingly it is not necessary to calculate G_o^{local}. All local flow components may be expressed through G_x^{local}, G_y^{local} and G_{xx}^{local}. It is convenient to define a "reverse-flow source potential" $\widetilde{G}$ related to G by

$$\widetilde{G}(x-x', y, z-z', z+z') = G(x'-x, -y, z-z', z+z')$$
$$= G - G^{free}(x-x', y, z+z') + G^{free}(x'-x, -y, z+z') \qquad (5)$$

(note that G^{basic} and G^{local} are even functions of $x-x'$ and y). Thus $\widetilde{G}$ is the source potential under a reversed radiation condition, i.e. with waves not behind, but ahead of the ship.

The first-order flow components φ_y and φ_z derived from (2) may now be decomposed as

$$\begin{aligned}\varphi_y = &-\epsilon Vy/2\pi \int_{-D}^{0}\int_{-1}^{1} f_x(x')h(z')(1/r^3 - 1/r_1^3)\,dx'\,dz' \\ &-\epsilon V k_o^2/\pi^2\, \mathrm{Im}\left\{\int_{-\infty}^{\infty} u e^{ik_o uy}\,du \int_{|u|}^{\infty} \frac{F^{\ell}(w)\,H^{\ell}(v)\,e^{ik_o vz}}{v-iw^2}\,dw\right\} \\ &+2\epsilon V k_o^2/\pi\, \mathrm{Re}\left\{\int_{-\infty}^{\infty} u\cdot s\, e^{ik_o uy}\,\frac{F^f(s)\,H^f(s)\,e^{k_o s^2 z}}{\sqrt{1+4u^2}}\,du\right\}\end{aligned} \qquad (6)$$

$$\begin{aligned}\varphi_z = &-\epsilon V/2\pi \int_{-D}^{0}\int_{-1}^{1} f_x(x')h(z')((z-z')/r^3 + (z+z')/r_1^3)\,dx'\,dz' \\ &-\epsilon V k_o^2/\pi^2\, \mathrm{Re}\left\{\int_{-\infty}^{\infty} e^{ik_o uy}\,du \int_{|u|}^{\infty} \frac{w^2 F^{\ell}(w)\,H^{\ell}(v)\,e^{ik_o vz}}{v-iw^2}\,dw\right\} \\ &-2\epsilon V k_o^2/\pi\, \mathrm{Im}\left\{\int_{-\infty}^{\infty} e^{ik_o uy}\,\frac{s^3 F^f(s)\,H^f(s)\,e^{k_o s^2 z}}{\sqrt{1+4u^2}}\,du\right\}\end{aligned} \qquad (7)$$

with $$F^{\ell}(w) = \int_{-1}^{1} f_x(x') e^{-k_o w |x-x'|} dx', \quad H^{\ell}(v) = \int_{-D}^{0} e^{ik_o v z'} h(z')\, dz'$$

$$F^f(s) = \int_{-1}^{1} \left\{ \frac{1-\mathrm{sign}(x-x')}{2} \right\} f_x(x') e^{ik_o s(x-x')} dx'$$

$$H^f(s) = \int_{-D}^{0} h(z')\, e^{k_o s^2 z'} dz'.$$

The expression for φ_x is only slightly different. The wave elevation $\zeta(x,y)$ is given as $\zeta = V/g\, \varphi_x(x,y,0)$ within the first-order theory. Far enough behind the ship, only the free waves persist, and we have

$$\zeta(x,y) \sim +2\epsilon k_o/\pi \;\mathrm{Re}\left\{ \int_{-\infty}^{\infty} \frac{e^{ik_o uy}\, s^2 F^f(s) H^f(s)}{\sqrt{1+4u^2}} du \right\} \tag{8}$$

For $x < -1$, $F^f(s)$ simplifies to $e^{ik_o sx}\, F^f_o(s)$,

with $$F^f_o = \int_{-1}^{1} f_x(x')\, e^{-ik_o sx'} dx',$$

which is no longer dependent on x. The first-order wave resistance $R^{(1)}$ associated with the far-field wave pattern (8) is

$$R^{(1)} = 2\rho g k_o \epsilon^2/\pi \int_{-\infty}^{\infty} \frac{|F^f_o(s)\, H^f(s)|^2 s^2}{\sqrt{1+4u^2}} du \tag{9}$$

where ρ stands for the fluid density.

1.2 Numerical procedures for first-order flow components.

By use of a binomial expansion, all basic flow components can be reduced to elementary indefinite integrals

$$E^{i,k}(X,Y,Z) = \int^{X}\!\!\int^{Z} x^i z^k/R^3\, dx\, dz \tag{10}$$

with $R = \sqrt{x^2+Y^2+z^2}$, $i = 0,1,2,\ldots$, $k = 0,1,2,\ldots$.

By a recursion formula derived in Appendix A we can express all $E^{i,k}$ in terms of a linear combination of four elementary integrals

$$E^{0,0} = \frac{1}{Y}\arctan(XZ/RY),\; E^{0,1} = -\ln(X+R),\; E^{1,0} = -\ln(Z+R),\; E^{1,1} = -R \tag{11}$$

with rational coefficients.

For the purpose of performing the w-integration of the local flow components, we first express $F^{\ell}(w)$ and $H^{\ell}(v)$ in closed form by use of multiple partial integration. This leads to terms of type $e^{-Aw - iBv}$ within the integrands of (6) and (7). For not too small positive A, we may use a Laguerre-Gauss quadrature formula

$$\int_C^{\infty} e^{-wA}\, f(w)\, dw \sim e^{-CA}/A \sum_i f(w_i/A + C)\, g_i$$

with weights g_i and abscissae w_i. If B is not too small, one may as well integrate with regard to v by use of dw = v dv/w. The oscillatory factor e^{-iBv} may be replaced by a factor with exponential decay through complex contour integration (Yeung 1972). If both A and B vanish, the interval may be reduced to finite length by use of a rational transformation and then Simpson's rule may be applied. But the above procedures can not be applied to the entire range of w-integration: Near $w = |u|$ there is a virtual infinity of the integrand due to $v = 0$ in the denominator. The numerator has to be expanded in a Taylor series to introduce a multiple zero which keeps the integrand finite. But this holds only for the total numerator, not for each separate component obtained from the partial integrations. Thus for a certain finite initial range, the combined integrand must undergo quadrature.

The u-integration, both for local and for free flows, may be performed by truncating for $|u|$ sufficiently large. If the trapezoidal rule is used for the finite interval thus obtained, the step width Δu is related to the effect of finite tank width b through $\Delta u = 2\pi/k_0 b$ (Eggers 1966).

2 Wave Resistance

2.1 Additional expressions for first-order resistance, used for control of numerical accuracy.

For numerical evaluation of the second-order correction to wave resistance $R^{(2)}$, it becomes necessary to calculate first-order flow even close to the ship and to integrate over the longitudinal centerplane. Considering the oscillations of the flow over the hull, the subdivision which is necessary for numerical quadrature will depend on the Froude number. We control it by calculating first-order resistance in the same way. Applying Lagally's law to the first-order source distribution σ, we obtain a resistance expression

$$R^{(1)}_{\sigma Lag} = \rho \int_{-D}^{0} \int_{-1}^{1} \sigma(x,z)\, \varphi_x(x,0,z)\, dx\, dz \tag{12}$$

(observing that resistance is minus the x-component of the force acting on the distribution).

But it is known that $R^{(1)}$ and $R^{(1)}_{\sigma\,\mathrm{Lag}}$ must be the same and we have tested this fact under different subdivisions and Froude numbers, approximating

$$R^{(1)}_{\sigma\,\mathrm{Lag}} \sim 2\rho D/(NX \cdot NZ) \sum_{k=1}^{NZ} \sum_{i=1}^{NX} \sigma(x_i, z_k)\, \varphi_x(x_i, 0, z_k),$$

$$x_i = (2i-1)/NX - 1,\; z_k = -(2k-1)/2NZ.$$

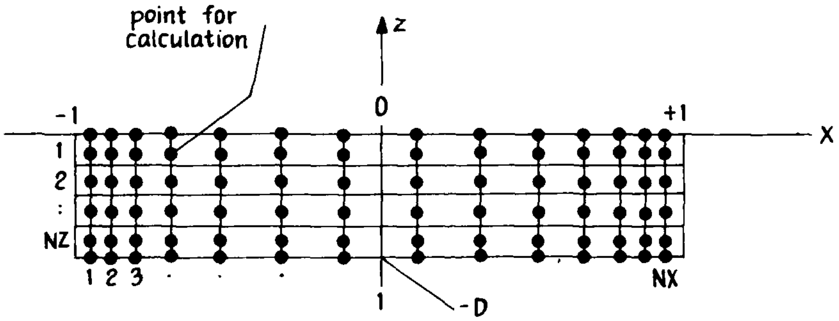

Figure 2 – Subdivision of the Longitudinal Centerplane

The second-order correction to σ is

$$\sigma^{(2)} = 2\epsilon \left\{ h(z)(f(x)\varphi_x)_x + f(x)(h(z)\varphi_z)_z \right\}. \tag{13}$$

The Lagally force due to this correction, may be expressed as

$$R^{(2)}_{\sigma\,\mathrm{Lag}} = \rho \int_{-D}^{0} \int_{-1}^{1} \sigma^{(2)}(x,z)\, \varphi_x(x,0,z)dxdz + \rho \int_{-D}^{0} \int_{-1}^{1} \sigma(x,z)\, \varphi_x^{(2)}(x,0,z)dxdz \tag{14}$$

The second term represents the force acting on the first-order distribution σ due to the flow from the potential $\varphi^{(2)}$, which is generated through $\sigma^{(2)}$ in analogy to (2). It may be evaluated without calculation of $\varphi^{(2)}$ in terms of the first-order reversed flow potential $\widetilde{\varphi}$ given as

$$\widetilde{\varphi}(x,y,z) = -1/4\pi \int_{-D}^{0} \int_{-1}^{1} \sigma(x',z')\widetilde{G}(x-x', y, z-z', z+z')dx'\,dz' \tag{15}$$

It is easily seen that

$$\int_{-D}^{0}\int_{-1}^{1}\sigma\varphi_x^{(2)}\,dxdz = -1/4\pi\int_{-D}^{0}\int_{-1}^{1}\sigma(x,z)\int_{-D}^{0}\int_{-1}^{1}G_x(x-x',y,z-z',z+z')\,\sigma^{(2)}\,dx'dz'\,dxdz$$

$$= \int_{-D}^{0}\int_{-1}^{1}\sigma^{(2)}\tilde{\varphi}_x\,dx\,dz \tag{16}$$

For a symmetric ship, we have $\tilde{\varphi}(x,y,z) = \varphi(-x,y,z)$ and we may substitute

$$\int_{-D}^{0}\int_{-1}^{1}\sigma\,\varphi_x^{(2)}\,dx\,dz = -\int_{-D}^{0}\int_{-1}^{1}\sigma^{(2)}\varphi_x(-x)dxdz$$

i.e. neither $\varphi_x^{(2)}$ nor $\tilde{\varphi}_x$ needs to be calculated explicitely.

Within a consistent approach, another second-order correction has to be applied according to the free-surface boundary condition. We have to add a potential $\varphi_\delta^{(2)}$ due to a source distribution $\delta(x,y)$ over the plane $z = 0$,

$$\varphi_\delta^{(2)}(x,y,z) = -\,1/4\pi k_o\int_{-\infty}^{\infty}\int_{-\infty}^{\infty}\delta(x',y')G(x-x',y-y',z-0,z+0)dx'\,dy'$$

with $$V\delta(x,y) = (\varphi_x^2+\varphi_y^2+\varphi_z^2)_x - 1/k_o\varphi_x(\varphi_{xx}+k_o\varphi_z)_z \tag{17}$$

The second-order Lagally force due to this flow acting on the first-order distribution $\sigma(x,z)$ may be expressed as

$$R_{\delta\,Lag}^{(2)} = \rho\iint\sigma\varphi_{\delta\,x}^{(2)}\,dxdz = -\,\rho/k_o\int_{-\infty}^{\infty}\int_{-\infty}^{\infty}\delta(x,y)\,\varphi_x(-x,-y,0)\,dx\,dy \tag{18}$$

by using the reversed flow principle. For the classical experiment of Weinblum, Kendrick and Todd (1952) the second-order corrections $R_{\sigma\,Lag}^{(2)}$ and $R_{\delta\,Lag}^{(2)}$ have been evaluated, and their contribution to covering the gap between experiment and theory is shown in Figure 3.

2.2 Relation to pressure resistance

There is another analytical relation which we may use for testing the first-order flow approximation and for checking our calculations. The condition of no flow through the ship's hull surface may be expressed as

$$\delta_s \equiv \epsilon h f_x(\varphi_x - V) - \varphi_y + \epsilon f h_z \varphi_z = 0 \text{ for } y = \epsilon f(x)h(z). \tag{19}$$

Now it can be shown that (Eggers 1975)

$$R^{(1)} = R_p^{hull} - R_p^{prof} + \Delta R \tag{20}$$

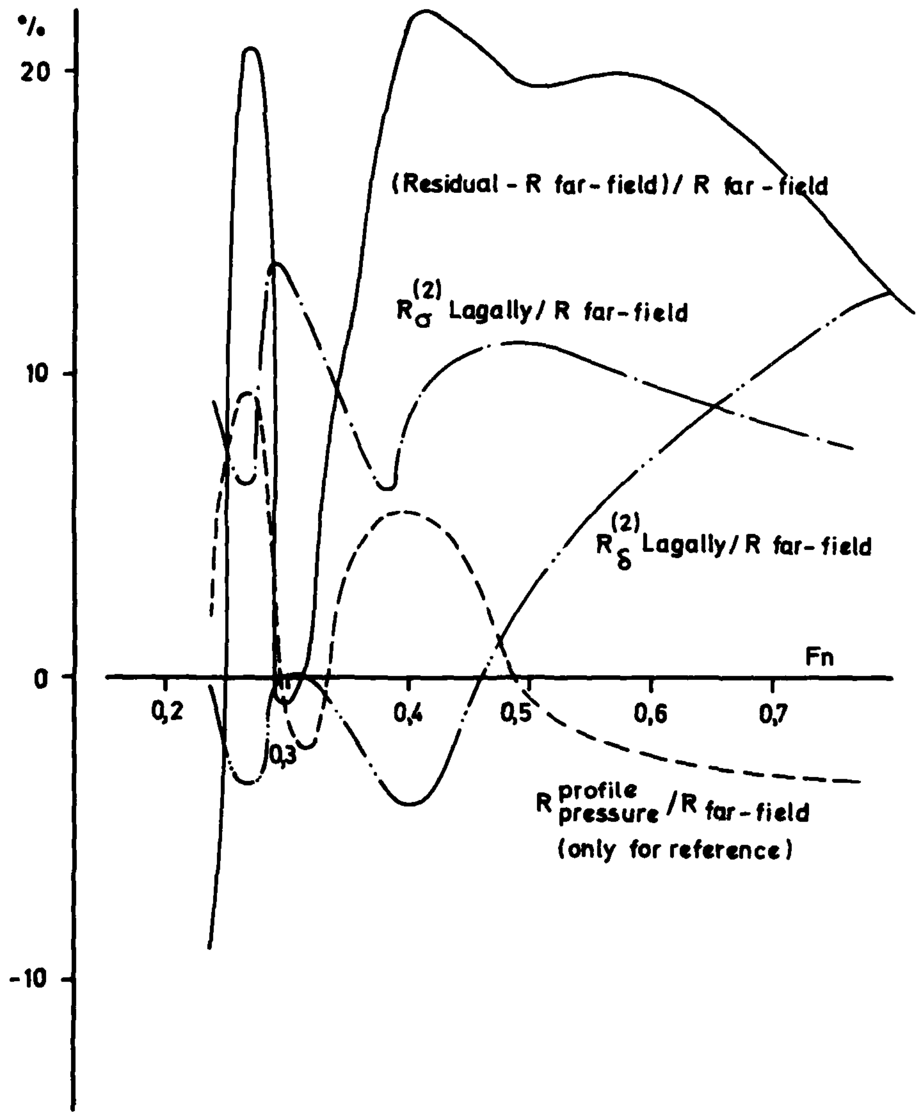

Figure 3 – Second-Order Corrections to Linear Wave Resistance for Weinblum-Kendrick-Todd Plank

with $$R_p^{hull} = 2\rho\epsilon \int_{-D}^{0}\int_{-1}^{1} ((\varphi_x^2 + \varphi_y^2 + \varphi_z^2)/2 - V\varphi_x)\, f_x(x)h(z)dxdz,$$

where φ_x, φ_y and φ_z should be evaluated for $y = \epsilon f(x)h(z)$,

$$R_p^{prof} = -\rho\epsilon/k_o \int_{-1}^{1} \varphi_x^2(x, \epsilon f(x)h(0),0)\, f_x(x)\, dx \text{ and}$$

$$\Delta R = -2\rho\epsilon \int_{-D}^{0}\int_{-1}^{1} \delta_s \varphi_x(x, \epsilon f(x)h(z), z)\, dx\, dz.$$

Thus ΔR is a measure of the invalidity of the body boundary condition, and ΔR should tend to zero even if divided by $R^{(1)}$. Our calculations, both for the Weinblum-Kendrick-Todd plank with $B/L = 0.027$ and for a thin model investigated by Sharma (1968) make evident that only for F_n exceeding 0.4, do we find ΔR smaller than 10 percent of $R^{(1)}$. Thus we may conclude that the models are still not thin enough for thin-ship theory. Numerical values are given in Table 1.

2.3 Gadd's paradox

It should be noted that from naive pressure integration over the hull, observing the change in wetted area due to the first-order wave elevation, we would arrive at

$$R_p = R_p^{hull} + R_p^{prof}, \tag{21}$$

as observed by Gadd (1971). The discrepancy in sign of R_p^{prof} in (20) and in (21) corresponds to flow of x-momentum through the wave profile area. We have also calculated $R_p/R^{(1)}$ in addition. It should be noted that $R_p^{hull} - R_p^{prof}$ is essentially a part of the consistent second-order approximation $R \sim R^{(1)} + R^{(2)}_{\sigma\, Lag} + R^{(2)}_{\delta\, Lag}$. The first term in (14) may be transformed by partial integration; noting that $\varphi_z = -\varphi_{xx}/k_o$ for $z = 0$.

$$\begin{aligned}\rho\iint \sigma^{(2)}\varphi_x\, dxdz &= 2\rho\epsilon \iint ((f\varphi_x)_x h + (h\varphi_z)_z f)\,\varphi_x\, dxdz \\ &= -2\rho\epsilon \iint (hf\varphi_x\varphi_{xx} + fh\varphi_z\varphi_{xz})\, dxdz + 2\rho\epsilon \int f\varphi_z\varphi_x\, dx \\ &= 2\rho\epsilon \iint hf_x(\varphi_x^2 + \varphi_z^2)/2\, dx\, dz + \rho\epsilon/k_o \int \varphi_x^2 f_x\, dx,\end{aligned} \tag{22}$$

TABLE 1

Weinblum-Kendrick-Todd Plank, B/L = 0,027

Fn	0,24	0,27	0,29	0,32	0,38	0,50	0,71
NX	38	30	28	22	20	20	20
①	0,96	0,95	0,98	0,98	0,96	0,98	0,97
②	0,94	0,85	0,99	1,01	0,88	1,00	1,01
③	0,98	1,01	1,01	0,97	0,98	0,98	0,95
④	0,91	1,21	0,99	1,01	1,18	1,20	1,17

NZ = 4

① $R_{\text{Lagally}} / R_{\text{far-field}}$

② $\left(R^{\text{hull}}_{\text{press.}} - R^{\text{profile}}_{\text{press.}}\right) / R_{\text{far-field}}$

③ $\left(R^{\text{hull}}_{\text{press.}} + R^{\text{profile}}_{\text{press.}}\right) / R_{\text{far-field}}$

④ $R_{\text{residual}} / R_{\text{far-field}}$

Sharma's Thin Model, B/L = 0,05

Fn	0,24	0,26	0,32	0,37	0,45	0,50	0,71
NX	32	24	18	18	16	16	16
①	0,97	0,95	0,96	0,98	0,99	0,99	0,98
②	0,79	0,55	0,78	0,77	0,99	1,02	1,02
③	0,95	0,96	0,93	1,01	0,97	0,94	0,92
④	0,96	1,90	1,18	1,07	0,91	0,95	0,92

3 Extension to Related Problems

3.1 Calculation of displacement field in the sense of the analysis of Noblesse.

As an improvement to the classical thin-ship theory, Noblesse (1974) expanded coordinates as well as flow components in terms of the beam/length ratio ϵ, determining a "real hull" associated with the "linearised hull" from which we may start. The coordinate stretching thus achieved is already inherent in Wehausen's approach (1969) using Lagrangian coordinates, but Noblesse made evident that the shift may be represented as a gradient of a "displacement potential" $\psi(x, y, z)$ rather than as a time integral along streamlines. On the plane $z = 0$, *the first-order vertical displacement is defined as the first-order wave elevation, i.e.*

$$V/g\, \varphi_x(x, y, 0) = \psi_z(x, y, 0) \tag{23}$$

for all x and y. It is possible to calculate the total displacement field ψ_x, ψ_y, ψ_z through our program for φ_x, φ_y, φ_z replacing $\delta(x, z)$ in eq. (2) by an x-integrated source distribution

$$\sigma^*(x, z) = \int \sigma(x', z)\, dx'.$$

The identity (23) was used as a numerical check, and a numerical example for distortion of the wave profile was performed for a mathematical ship model of form $y = \pm\epsilon(1 - x^2)(1 - (z/D)^2)$ with $\epsilon = 0.1$, $D = 0.125$ and with $F_n = 0.25$ as shown in Figure 4.

3.2 Wave resistance of a submerged sphere.

We have calculated wave resistance of a submerged sphere in steady horizontal motion through the Hess and Smith (1964) method, modified for wave effects under the linearised free surface condition. The sphere was approximated by 108 polygon plane elements for the case of submergence depth $h = 2a$, where a is the radius of the sphere. The source distribution was determined through iteration up to error less than one percent at "null" points of elements, determined from unbounded flow. For exponential functions from wave effects, surface integrals on the polygons were evaluated by summing contributions from corner points of each element (Appendix A2). The final numerical results are shown in Figure 5 where results by Bessho (1954) and Kim (1968) are also shown.

Acknowledgement

This work has been supported by the Deutsche Forschungsgemeinschaft (lately within the framework of SFB 98) and through a grant from the Office of Naval Research (ONR263-65).

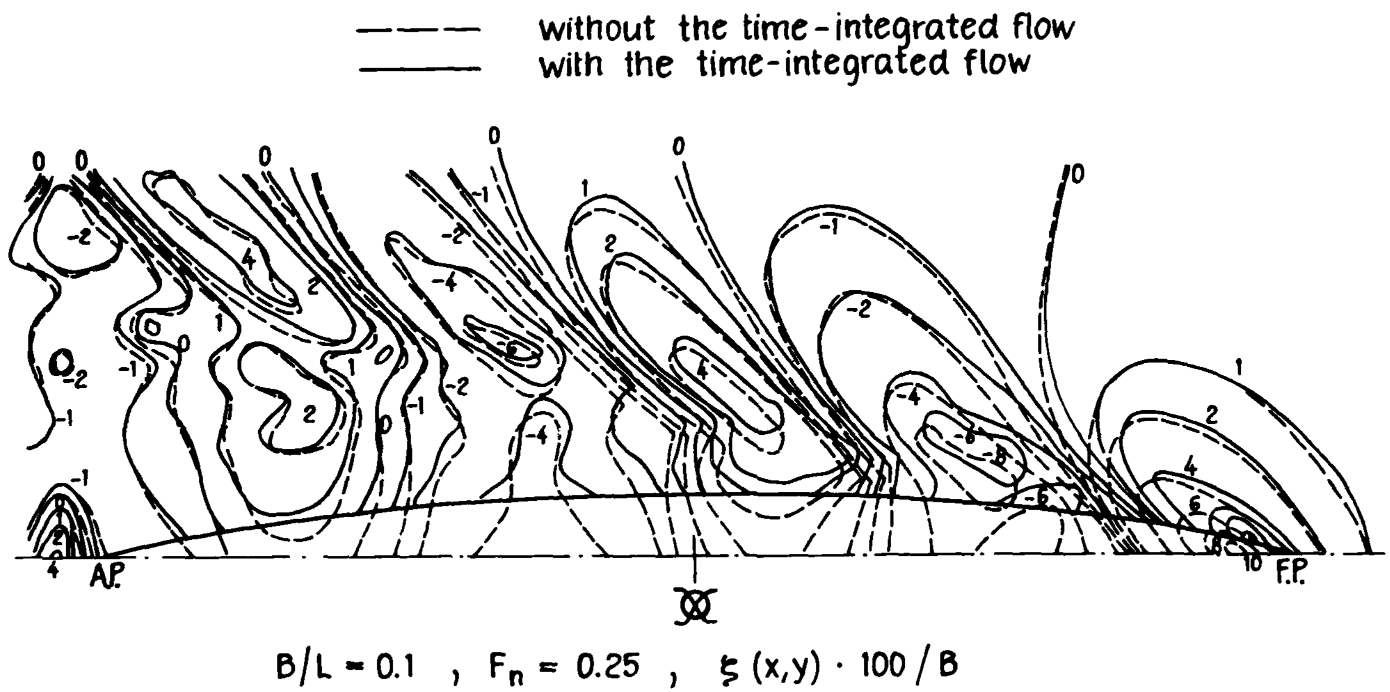

Figure 4 – Distortion of Wave Pattern for a Mathematical Model Due to the Time-Integrated Flow

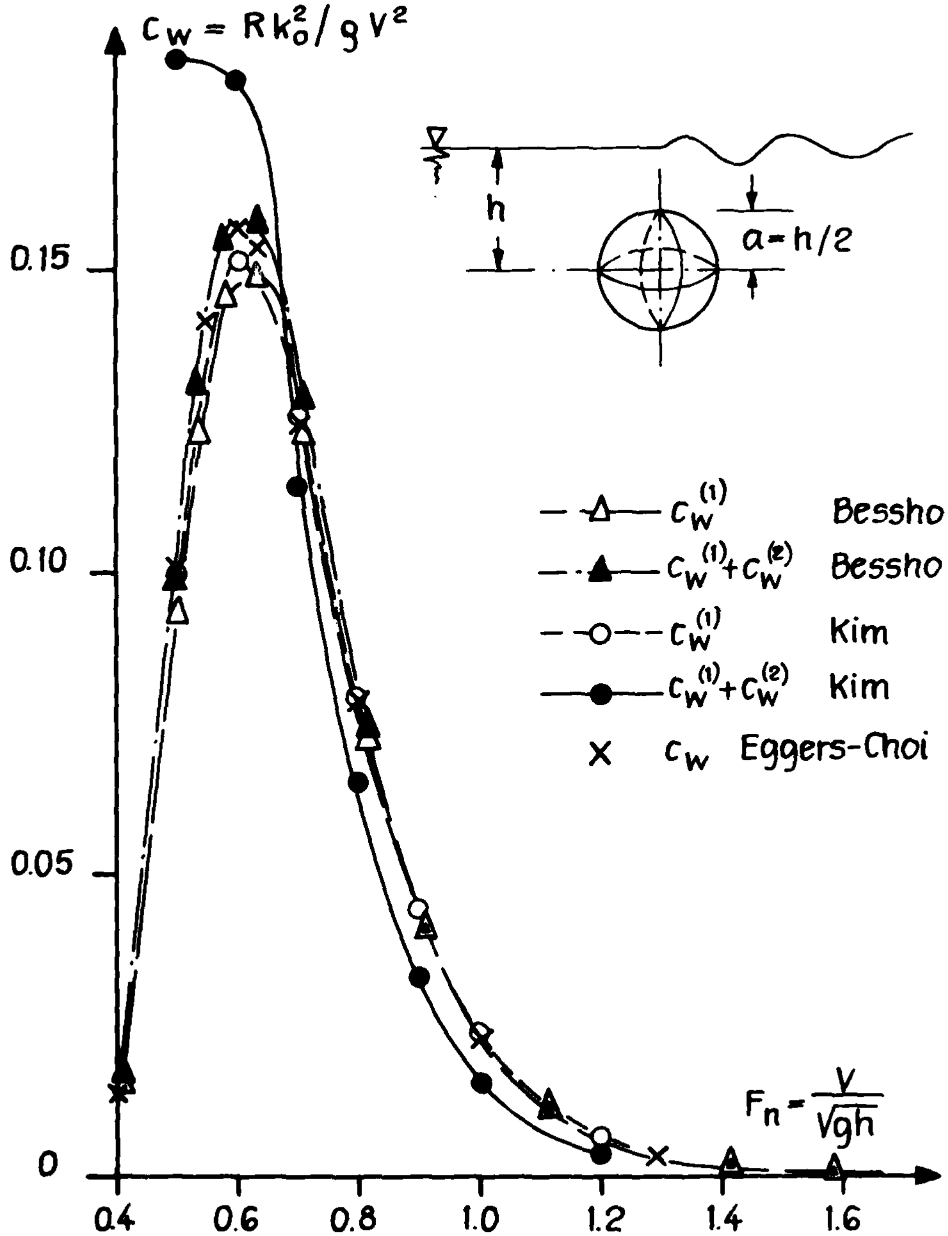

Figure 5 – Wave Resistance for a Submerged Sphere

References

Bessho, M. **Wave resistance of a sphere.** Journ. Soc. Naval Arch. Japan, Vol. 94 (1954) pp 35-41.

Eggers, K.W.H. **On second order contributions to ship waves and wave resistance.** Sixth symposium on Naval Hydrodynamics, Washington, D.C., Sept.-Oct. (1966) 26 pages.

Eggers, K.W.H. **An evaluation of the wave flow around ship forms, with application to second-order wave resistance calculations.** Stevens Inst. Tech., Davidson Lab. Rep. SIT-DL-70-1423 (1970) 32 pages.

Eggers, K.W.H. **On the role of line integral terms for the improvement of wave resistance calculations.** Contribution to the Report of the Resistance Committee, 14th ITTC Ottawa (1975) 11 pages.

Gadd, G.E. **Calculated and measured pressures on practical ship hulls.** Ship Report 156, National Physical Lab., Oct. (1971) 12 pages.

Hess, J.L. and Smith, A.M.O. **Calculation of nonlifting potential flow about arbitrary three-dimensional bodies.** Journ. Ship Res., Vol. 8, No. 2, pp 22-44. (1964)

Kim, W.D. **Non-linear free surface effects on a submerged sphere.** Stevens Inst. Tech., Davidson Lab. Rep. No. 1271 (1968) 51 pages.

Landweber, L. **Contributions on some current problems of ship resistance.** Intern. Jubilee Meeting, NSMB Wageningen (1972) pp 32-45.

Noblesse, F. **A perturbation analysis of the wavemaking of a ship with an interpretation of Guilloton's method.** Inst. Hydraulic Res., Univ. Iowa, Iowa City (1974) 37 pages.

Sharma, S.D. **Some results concerning the wavemaking of a thin ship.** Journ. Ship Res., Vol. 13 (1969) pp 72-81.

Yeung, R.W. **Sinkage and trim in first-order thin-ship theory.** Journ. Ship Res., Vol. 16 (1972) pp 47-59.

Wehausen, J.V. **An approach to thin ship theory.** Intern. Sem. Theoret. Wave Resistance, Ann Arbor (1963) pp 819-852 (disc. pp 853-855).

Wehausen, J.V. **Use of Lagrangian coordinates for ship wave resistance (first and second-order thin-ship theory).** Journ. Ship Res., Vol. 13 (1969) pp 12-22.

Weinblum, G.P., Kendrick, J.J., and Todd, M.A. **Investigation of wave effects produced by a thin body-TMB Model 4125.** DTMB Rep. 840 (1952) 14 pages.

Appendix A: Evaluation of integrals over polygon areas

A1: Recursive determination of $\varepsilon^{i,k} = \iint x^i z^k / (x^2+y^2+z^2)^{3/2}\, dx\,dz$

Let $R=\sqrt{x^2+y^2+z^2}$, and let us first consider the case where all polygon sides are parallel to the x-z coordinate axes. Let $E^{i,k}$ be a function such that $E^{i,k}_{xz} = x^i z^k / R^3$, then $\varepsilon^{i,k}$ is the sum of $E^{i,k}$ evaluated at the corner points with proper sign. For both i and k smaller than two, such set of functions is

$$E^{0,0} = \frac{1}{y} \arctan \frac{xz}{Ry} \qquad E^{1,0} = -\log(x+R)$$
$$E^{0,1} = -\log(z+R) \qquad E^{1,1} = -R \tag{A1}$$

An extension to arbitrary i and k can be recursively found in three steps:

1) For $k=1$ we define $E^{i,1} = -1/i\cdot\left(x^{i-1}R + (i-1)(z^2+y^2)E^{i-2,1}\right)$

2) For $k=0$ we define $E^{i,0} = -zE^{i-2,1} - y^2 E^{i-2,0}$

3) For i fixed, we define

$$E^{i,k} = \frac{1}{i+k-1}\left[iz^{k-1}E^{i,1} - (k-1)x^{i+1}E^{1,k-2} - (k-1)y^2E^{i,k-2}\right] \tag{A2}$$

That we really have $\partial^2 E^{i,k}/\partial x \partial z = x^i z^k / R^3$ can be verified for the right hand sides, as recursively in i and k we find that $E^{i,1}_x = -x^i/R$, $E^{1,k}_z = -z^k/R$. Note that (A2) implies a representation

$$E^{i,k} = P^{i,k}_{00}E^{0,0} + P^{i,k}_{01}E^{0,1} + P^{i,k}_{10}E^{1,0} + P^{i,k}_{11}E^{1,1} \tag{A3}$$

where the $P^{i,k}_{mn}$ are homogeneous polynominals of degree $i+k+1$; for both i and k odd, only $P^{i,k}_{11}$ is non-zero, and only $P^{i,k}_{00}$ is non-zero for both i and k even.

For arbitrary polygons, we can derive a similar result by application of Gauss' integral formula (a degenerated form of Stokes' theorem):

$$\iint F(x,z)\,dx\,dz = \oint G\big(x(z),z\big)\,dz \text{ if } G_x = F, \text{ or } -\oint H\big(x,z(x)\big)\,dx \text{ if } H_z = F \;,$$

where the line integrals along the border have to be evaluated in counterclockwise direction. For a polygon with N cornerpoints $P_j = \{x_j, z_j\}$, $j = 1,2 \ldots N$, the line integrals are composed of N integrals from P_{j-1} to P_j. (For convenience we define $P_0 = P_N$ and $P_{N+1} = P_1$).

Observing that $\int x/R^3\,dx = -1/R$, we obtain through x-partial integration

$$\iint \frac{x^i z^k}{R^3}\,dx\,dz = -\oint \frac{x^{i-1} z^k}{R}\,dz + (i-1)\iint \frac{x^{i-2} z^k}{R}\,dx\,dz \qquad \text{hence}$$

$$(i-2)\,\varepsilon^{i,k} = \sum^{N} {}^{j}I^{i-1,k} - (i-1)\,y^2\,\varepsilon^{i-2,k} - (i-1)\,\varepsilon^{i-2,k+2} \qquad \text{(A4)}$$

with ${}^{j}I^{i-1,k} = \int_{z_{j-1}}^{z_j} x^{i-1} z^k / R\,dz$; in order to eliminate $\varepsilon^{i-2,k+2}$ we can obtain an analogous relation changing the roles of x and z :

$$k\,\varepsilon^{i-2,k+2} = -\sum^{N} {}^{j}J^{i-2,k+1} - (k+1)\,y^2\,\varepsilon^{i-2,k} - (k+1)\,\varepsilon^{i,k} \qquad \text{(A5)}$$

with

$${}^{j}J^{i+2,k+1} = -\int_{x_{j-1}}^{x_j} x^{i-2}\, z^{k+1} \big/ R \;\; dx$$

and thus

$$(i+k-1)\,\varepsilon^{i,k} = -k\sum^{N} {}^{j}I^{i-1,k} - (i-1)\sum^{N} {}^{j}J^{i-2,k+2} - (i-1)\,y^2\varepsilon^{i-2,k} \qquad \text{(A6)}$$

and

$$(i+k-1)\,\varepsilon^{i,k} = i\sum^{N} {}^{j}J^{i,k-1} + (k-1)\sum^{N} {}^{j}I^{i+1,k-2} - (k-1)\,y^2\,\varepsilon^{i,k-2} \qquad \text{(A7)}$$

in particular $\quad \varepsilon^{1,k} = -\sum^{N} {}^{j}I^{0,k} \;, \quad \varepsilon^{0,k} = \sum^{N} {}^{j}I^{1,k-2} - y^2\varepsilon^{0,k-2}$

An evaluation of $\varepsilon^{0,0}$ is given by Hess and Smith (1964), thus we only have to consider expressions of type $I^{\nu,\mu}$ and $J^{\nu,\mu}$. But these integrals depend essentially only on one

integer parameter $\lambda = \nu + \mu$! Let us introduce new variables s and t through

$$s = x\cos\alpha_j + z\sin\alpha_j \quad , \qquad t = -x\sin\alpha_j + z\cos\alpha_j$$

where α_j is the angle of the line through P_{j-1} and P_j , t is constant there, $t = t_j$ (= length of perpendicular from origin). Inversely we have

$$x = s\cos\alpha_j - t_j\sin\alpha_j \qquad z = s\sin\alpha_j + t_j\cos\alpha_j$$

$$dx = ds\cos\alpha_j \qquad dz = ds\sin\alpha_j$$

$$x^2 + z^2 = s^2 + t_j^2 \text{, hence} \qquad R = \sqrt{s^2 + y^2 + t_j^2} \; .$$

But the integrals ${}^jL^\lambda = \int_{s_{j-1}}^{s_j} s^\lambda / R \, ds$ can be reduced to the cases $\lambda = 1$ and $\lambda = 0$ as

$$ {}^jL^\lambda = 1/\lambda \; \Big| sR \Big|_{s_{j-1}}^{s_j} - (\lambda-1)/\lambda \; {}^{j}L^{\lambda-2}$$

$$ {}^jL^0 = \log\Big((s_j + R_j)\Big/(s_{j-1} + R_{j-1})\Big) = \log\Big((s_{j-1} - R_{j-1})\Big/(s_j - R_j)\Big)$$

and $$ {}^jL^1 = R_j - R_{j-1} \; .$$

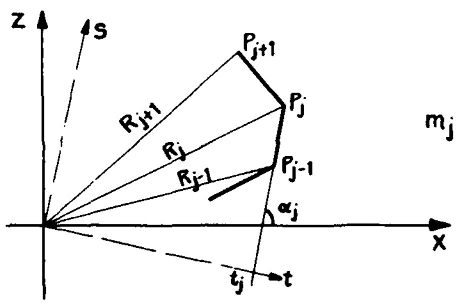

$m_j = \mathrm{ctg}\,\alpha_i$

A2: Evaluation of integrals $\iint e^{ax+bz}\,dxdz$ over polygons.

Using Gauss' integral formula mentioned above we find

$$J(a,b) = \iint \exp(ax+bz)\,dxdz = \frac{1}{a}\oint \exp(ax(z)+bz)\,dz = \frac{1}{a}\sum_{j=1}^{N}\int_{z_{j-1}}^{z_j} \exp(ax(z)+bz)\,dz$$

Along $\overline{P_{j-1}\,P_j}$ we have $x = x_{j-1} + m_j\,(z-z_{j-1})$, $m_j = \mathrm{ctg}\,\alpha_j = \Delta^- x_j \big/ \Delta^- z_j$

$$\Delta^- x_j = x_j - x_{j-1} \quad , \quad \Delta^- z_j = z_j - z_{j-1} \qquad \text{thus}$$

$$J(a,b) = \sum_{j=1}^{N} \Big(\exp(ax_j + bz_j) - \exp(ax_{j-1} + bz_{j-1})\Big) \Big/ a\,(am_j + b) \tag{A8}$$

Grouping this sum regarding common exponential factors,we obtain

$$J(a,b) = \sum_{j=1}^{N} \exp(ax_j + bz_j)\ \delta_j \Big/ \Big(\big(a\,\Delta^+ x_j + b\Delta^+ z_j\big)\big(a\Delta^- x_j + b\Delta^- z_j\big)\Big) \tag{A9}$$

with

$$\Delta^+ x_j = \Delta^- x_{j+1} \quad , \quad \Delta^+ z_j = \Delta^- z_{j+1} \quad , \quad \delta_j = \Delta^+ x_j\,\Delta^- z_j - \Delta^- x_j\,\Delta^+ z_j \ .$$

δ_j is the absolute value of the cross product of vectors $\overrightarrow{P_{j-1}\,P_j}$ and $\overrightarrow{P_j\,P_{j+1}}$ i.e. the product of their lengths and sine of the angle by which the direction of the boundary changes at P_j .

Appendix B: Line integral terms within the second-order potential.

B1: Contributions from the free surface to φ through Green's formula.

In Wehausen's approach (1963), the velocity potential is expressed in terms of boundary values over a closed surface. Due to asymptotic properties of the influence function (Havelock source potential, singular like 1/r) only contributions from the free surface S_f and from the wetted hull have to be considered. For reason of generality, we shall in the following take S_w as any control surface enclosing the wetted hull (but not the flow point) and intersecting S_f vertically along a closed line $\tilde{C}$ encircling the ship. Let C be the projection of $\tilde{C}$ on $z=0$. We thus do not impose any boundary consition on S_w, nor any assumption about smallness of its lateral extent. Let us divide S_w into S_c, the contribution from the wave profile, and S_0, the part extending up to $z=0$. Let us define corresponding components of φ such that

$$4\pi\varphi = I_f + I_c + I_0 \qquad \text{(B1)}$$

Then, following Wehausen (page 828) I_f may be expressed as

$$I_f = \iint_{S_{fp}} \Big\{ -\zeta_x(x,y)\,\varphi_x(x,y,\zeta)\,G(x,y,\zeta) - \zeta_y\varphi_y G + \varphi_z G + \zeta_x G_x \varphi + \zeta_y G_y \varphi - G_z \varphi \Big\}\, dx\,dy \qquad \text{(B2)}$$

where $\zeta(x,y)$ is the wave elevation, S_{fp} is the projection of S_f on $z=0$. (The dependence of G on flow point coordinates is suppressed in our notation.) With in our aim of determining φ up to terms of order ϵ^3 only, where ϵ is some smallness parameter ultimately related to the hull geometry, it is pertinent to substitute for ζ its linear approximation $V/g\;\varphi_x(x,y,0)$ and, after performing a Taylor

expansion of all members of the r.h.s., to delete all triple products of φ and its derivatives. If we further observe for $z=0$ that $\varphi_{xx}+\varphi_{yy}+\varphi_{zz}=O(\epsilon^2)$, $G_{xx}+k_0 G_z=0$, $G_{xx}+G_{yy}+G_{zz}=0$, with $\delta_f(x,y)\equiv\varphi_{xx}(x,y,0)+k_0\varphi_z(x,y,0)$, we finally obtain (with all integrands evaluated for $z=0$).

$$g/V\cdot I_f = \iint_{S_{fp}} \Big\{-\varphi_{xx}\varphi_x G - \varphi_{xy}\varphi_y G + \frac{g}{V}\varphi_z G - \varphi_x\varphi_{xx} G - \varphi_x\varphi_{yy} G + \varphi_{xx}\varphi G_x + \varphi_{xy}\varphi G_y - \frac{g}{V}\varphi G_z + \varphi_x\varphi G_{xx} + \varphi_x\varphi G_{yy}\Big\}\,dx\,dy + O(\epsilon^3) \tag{B3}$$

Adding - and subtracting again - $\varphi_x^2 G_x + \varphi_x\varphi_y G_y$, this may be written as

$$\begin{aligned} g/V\cdot I_f &= \iint_{S_{fp}} \Big\{\delta_f V G + V(\varphi G_x - \varphi_x G)_x - (\varphi_x^2 G)_x - (\varphi_x\varphi_y G)_y + (\varphi\varphi_x G_x)_x + (\varphi\varphi_x G_y)_y\Big\}\,dx\,dy \\ &= \iint_{S_{fp}} \delta_f V G\,dx\,dy - V\oint_C (\varphi G_x - \varphi_x G)\,dy - \oint_C \varphi\varphi_x (G_x dy - G_y dx) + \oint_C \varphi_x G(\varphi_x dy - \varphi_y dx) \end{aligned} \tag{B4}$$

save terms of order $O(\epsilon^3)$. <u>If</u> C is the load waterline, we may insert

$$\varphi_x dy - \varphi_y dx = V dy.$$

Consider now I_C , the contribution from the wave profile part of the wetted hull. Let s be some measure of arc length along C so that C may be given as $x=x(s)$, $y=y(s)$. Then

$$I_C = \oint_C \int_0^{\zeta} \Big\{\varphi_n\big(x(s),y(s),z\big)\, G\big(x(s),y(s),z\big) - \varphi G_n\Big\}\,dz\,ds \tag{B5}$$

where the index n stands for outward normal derivative. Inserting $\zeta = V/g\,\varphi_x\big(x(s),y(s),0\big)$, expanding in Taylor series and deleting triple products of flow components, we obtain

$I_C = V/g \oint \varphi_x(\varphi_n G - \varphi G_n)\,ds + O(\epsilon^3)$ with integrands evaluated for $z=0$.

With $\varphi_n ds = -\varphi_x dy + \varphi_y dx$, $G_n ds = -G_x dy + G_y dx$ for counterclockwise evaluation of the integral along C , we have

$$I_C = -V/g \oint \left\{ \varphi_x G \left(\varphi_x dy - \varphi_y dx \right) - \varphi \varphi_x \left(G_x dy - G_y dx \right) \right\} + O(\epsilon^3)$$

$$I_C + I_f = I_B + 1/k_0 \iint_{S_{fp}} \delta_f \, G \, dx \, dy + O(\epsilon^3) \tag{B6}$$

where we have defined $I_B = -1/k_0 \oint (\varphi G_x - \varphi_x G) \, dy$. This contribution to φ could alternatively have been obtained from a Green's theorem approach for the domain outside the hull bounded by the plane $z = 0$ (Eggers 1966).

B2: Reduction of the couple of line integrals I_B to integrals over surfaces plus a line integral of higher order.

Let us consider an integral expression J , symmetric regarding the functions G and φ , defined as

$$J = -\iint_{S_{op}} h(x,z) \, \overline{\left(\varphi_x G_x + \varphi_z G_z \right)} \, dx dz \tag{B7}$$

where overlining should mean the sum of contributions from $y = +h(x,z)$ and $y = -h(x,z)$, and the integration is over the vertical plane $y = 0$ which is cut out through the surface S_0 , i.e. the projection S_{op} of S_0 .

Through partial integration, regarding x for the first, regarding z for the second summand, we may either obtain

$$J = \iint_{S_{op}} \overline{\left((h\varphi_x)_x + (h\varphi_z)_z \right)} G \, dx dz - \int_{C_p} h \overline{\varphi_z G} \, dx + \iint_{S_{op}} h \underline{\left(\varphi (G_{xy} h_x + G_{zy} h_z) - \varphi_y (G_x h_x + G_z h_z) \right)} dx dz \tag{B8}$$

where C_p is the projection of C on the x-axis, and underlining stands for taking the difference of the case y positive

and y negative, or

$$\mathrm{J} = \iint_{S_{op}} \overline{\left((h\sigma_x)_x + (h\sigma_z)_z\right)\varphi}\, dxdz - \int_{C_p} \overline{h\sigma_z\varphi}\, dx + \iint_{S_{op}} h\Big(\underline{\left(\varphi_{xy}h_x + \varphi_{zy}h_z\right)\sigma} - \underline{\left(\varphi_x h_x + \varphi_z h_z\right)\sigma_y}\Big)\, dxdz \tag{B9}$$

Subtracting (B9) from (B8) we find thus that

$$\begin{aligned} I_d &= \int_{C_p} h(x,0)\, \overline{(\varphi\sigma_z - \varphi_z\sigma)}\, dx \\ &= \iint_{S_o} (\varphi\sigma_n - \varphi_n\sigma)\, dS_o - \iint_{S_{op}} \Big(h\, \overline{(\varphi\sigma_{yy} - \varphi_{yy}\sigma)} - \underline{(\varphi\sigma_y - \varphi_y\sigma)}\Big)\, dS_{op} \\ &\quad - \iint_{S_{op}} h\left(h_x\, \underline{(\varphi\sigma_y - \varphi_y\sigma)_x} + h_z\, \underline{(\varphi\sigma_y - \varphi_y\sigma)_z}\right) dS_{op} \end{aligned} \tag{B10}$$

observing that the normal vector $\vec{n}$ has the components

$$\left\{ h_x \frac{dS}{dS_{op}},\ \mp \frac{dS}{dS_{op}},\ h_z \frac{dS}{dS_{op}} \right\} \qquad \text{with} \quad dS_{op} = dxdz\,.$$

But the line integral I_c may be transformed through x-partial integration; observing that $\sigma_{xx} + k_o\sigma_z = 0,\ \varphi_{xx} + k_o\varphi_z = \delta_f(x,y)$ for $z = 0$, we find

$$\begin{aligned} k_o I_d &= \int_{C_p} h\, \overline{(-\varphi\sigma_{xx} + \varphi_{xx}\sigma - \sigma\delta_f)}\, dx \\ &= \int_{C_p} h_x\, \overline{(\varphi\sigma_x - \varphi_x\sigma)}\, dx + \int_{C_p} h h_x\, \underline{(\varphi\sigma_x - \varphi_x\sigma)_y}\, dx - \int_{C_p} h\, \overline{\delta_f\sigma}\, dx \end{aligned} \tag{B11}$$

and the first term on the r.h.s. is just k_o times I_B. Thus we can express I_B as

$$\begin{aligned} I_B &= -I_o + \iint_{S_{op}} \left\{ \underline{(\varphi\sigma_y - \varphi_y\sigma)} - h\, \overline{(\varphi\sigma_y - \varphi_y\sigma)_y} \right\} dxdz + \frac{1}{k_o}\int_{C_p} h\, \overline{\delta_f\sigma}\, dx \\ &\quad - \iint_{S_{op}} h\left(h_x\, \underline{(\varphi\sigma_y - \varphi_y\sigma)_x} + h_z\, \underline{(\varphi\sigma_y - \varphi_y\sigma)_z}\right) dxdz - \frac{1}{k_o}\int_{C_p} h h_x\, \underline{(\varphi\sigma_x - \varphi_x\sigma)_y}\, dx \end{aligned} \tag{B12}$$

where $I_o = \iint_{S_o} (\varphi_n\sigma - \varphi\sigma_n)\, dS_o$ is the third component of $4\pi\varphi$ as

defined earlier. The first line of the r.h.s. is a representation of I_B through sources, normal dipoles, y-dipoles and y-y quadrupoles on S_0 plus sources on S_{fp} if δ_f is nonzero. The terms in the second line, which are small of higher order with regard to the lateral extent of S_0 , contain x-y, and z-y quadrupoles on S_0 in addition, and x-dipoles on C . We may recall that Landweber (1972), invoking Stokes' theorem, even found a representation of I_B in terms of sources, dipoles and quadrupoles on S_0 <u>without</u> any residual line integral (assuming $\delta_f = 0$), namely

$$I_B = \frac{1}{k_0} \iint \left(\vec{n} \operatorname{curl} \left\{ (\varphi G_x - \varphi_x G) \vec{e}_2 \right\} \right) dS_0$$

where $\vec{e}_2$ is the unit vector in y-direction. But, as mentioned, the last line of (B 12) is small of order $O(\epsilon^3)$ if $h = O(\epsilon)$ as from now on we shall assume.

B3: The singularity system representing φ up to $O(\epsilon^3)$ if h is $O(\epsilon)$.

From (B1), (B6) and (B12) we obtain

$$4\pi\varphi = 1/k_0 \iint_{S_{fp}} \delta_f G \, dx dy \; - \; 1/k_0 \oint_C y \, \delta_f G \, dx$$
$$+ \iint_{S_{op}} \left((\varphi G_y - \varphi_y G) - h(\varphi G_y - \varphi_y G)_y \right) dx\,dz \; + \; O(\epsilon^3) \qquad \text{(B13)}$$

With $\delta_f = O(\epsilon^2)$, save an error $O(\epsilon^3)$ we may replace the first two terms through $1/k_0 \iint \delta_f G \, dxdy$ integrating over the entire plane $z = 0$.

Taking now S_0 as the hull surface, we may insert the body boundary condition

$$\pm \varphi_y = h_x \varphi_x + h_z \varphi_z - h_x V \quad \text{for} \quad y = \pm\, h(x,z) \qquad \text{(B14)}$$

Expanding φ and G in Taylor series with regard to y, we may easily simplify (B13) to

$$4\pi\varphi = 2V\iint_{S_{op}} h_x G\,dxdz - 2\iint_{S_{op}}\left(h_x\varphi_x + h_z\varphi_z - h\varphi_{yy}\right)dxdz + \frac{1}{K_0}\iint \delta_f G\,dxdy + O(\epsilon^3) \qquad (B15)$$

or alternatively, using the Laplace equation prior to Taylor expansion,

$$4\pi\varphi = 2V\iint_{S_{op}} h_x G\,dxdz - 2\iint_{S_{op}}\left((h\varphi_x)_x + (h\varphi_z)_z\right)G\,dxdz + \ldots \qquad (B16)$$

This expression obviously does not show line integral terms. But through partial integration we may change to a dipole representation

$$4\pi\varphi = -2V\iint_{S_{op}} h G_x\,dxdz + 2\iint_{S_{op}}\left(h\varphi_x G_x + h\varphi_z G_z\right)dxdz + I_E + \cdots \qquad (B17)$$

with

$$I_E = -2\int_{C_p} h\varphi_z G\,dx = -\frac{2}{K_0}\int_{C_p} h\varphi_x G_x dx - \frac{2}{K_0}\int_{C_p} h_x\varphi_x G\,dx - \frac{2}{K_0}\int_{C_p} h\delta_f G\,dx \qquad (B18)$$

I_E is the difference of the second-order potential for a surface piercing ship from that from the limit of a submerged thin body (which may be flat topped) approaching the free surface. For the latter case the total source output is zero, i.e. any non-zero total source output results from the second term of the r.h.s. of (B18) if δ_f is not considered. The first term of I_E - corresponding to the first term of I_σ is related to a potential due to the wave elevation pressure field within the waterplane area, the second is the degenerated version of the second term from I_B. The resistance component due to I_E in the sense of Lagally's law for a symmetric ship is a degenerated form of <u>minus</u> R_p^{prof} as could have been expected from (22). The first term alone of (B18) however would induce a resistance component $-\frac{1}{K_0}\int_{C_p}\varphi_x^2 h_x\,dx$ corresponding to plus R_p^{prof}

THE NEAR-FIELD DISTURBANCE IN THE CENTERPLANE HAVELOCK SOURCE POTENTIAL

F. Noblesse

Department of Aeronautics and Astronautics
Stanford University, Stanford, California 94305 U.S.A.

ABSTRACT

By "centerplane Havelock source potential" is meant the linearized velocity potential of the steady, inviscid, free-surface gravity flow past a unit source in an oncoming uniform stream, observed at points in the vertical plane of symmetry parallel to the oncoming stream and passing through the source. This source potential is written as the sum of three terms: (1) the potential of the source in the infinite domain, (2) the "near-field disturbance potential" which is nonoscillatory and symmetric upstream and downstream from the source, and (3) the "wave-potential" of the oscillatory wave-like disturbance trailing downstream from the source. The paper is concerned with the numerical and analytical investigation of the near-field disturbance potential.

1. Introduction

The success enjoyed by Gadd [1] in predicting the "residuary resistance" of a number of ship hulls by the method of Guilloton [2], as well as studies of Wehausen [3], Dagan [4] and Noblesse [5] rationalizing Guilloton's method and suggesting possible modifications, have called for the development of a numerical procedure for evaluating the flow around a ship hull by a Guilloton-type method. The motivation for developing such a numerical procedure has recently been strengthened by further theoretical developments of Noblesse and Dagan [6] pointing to the possibility of improving upon the method of Guilloton.

From the computational point of view, the essential feature of Guilloton's and related methods is that they involve source distributions on the ship centerplane alone, and furthermore that most quantities of practical interest, e.g., wave resistance, hydrodynamic lift and moment, sinkage and trim, velocity distribution

on the hull and free-surface profile along the hull, can be obtained from flow variables evaluated at the centerplane. This means that the computational problem in these methods of evaluating the (eminently three-dimensional) flow around a ship hull is two dimensional in nature, in that functions of two variables only need be evaluated.

The basic computational problem consists in evaluating the linearized velocity potential, say $\phi(x, y, o)$, on the ship centerplane $z = 0$, associated with a given source distribution, say of strength $\tau(x, y)$, on the centerplane, i. e.,

$$\phi(x, y, o) = \frac{1}{2\pi} \iint_{\sigma} G(x, y, o; \mu, \nu, o)\tau(\mu, \nu) d\mu d\nu \tag{1. 1}$$

where $G(x, y, o; \mu, \nu, o)$ denotes the "centerplane" Havelock source potential and σ is a given area in the lower half plane $\nu \leq o$ where the density $\tau(\mu, \nu)$ of the source distribution is defined.

The author has been engaged in the development of a numerical procedure for evaluating the centerplane potential $\phi(x, y, o)$ defined by eq. (1. 1) above. This work is not yet completed however a report on its current state of development may be found in [7]. The scope of the present paper is thus restricted to the investigation, by both analytical and numerical means, of the behavior of the centerplane Havelock source potential $G(x, y, o; \mu, \nu, o)$, a detailed knowledge of which is useful for developing a sound numerical procedure for evaluating the centerplane potential $\phi(x, y, o)$.

2. The Centerplane Havelock Source Potential

Let us consider the steady free-surface gravity flow of a uniform stream of velocity U past a unit source located at a point S below the free surface, see Fig. 1 below. The vertical plane passing through the source S and parallel to the oncoming stream U is a plane of symmetry for the flow. This plane is taken as the plane $Z = 0$ and, in reference to the thin-ship theory, will be referred to as the "centerplane". The horizontal undisturbed free surface is taken as the plane $Y = 0$ with the Y axis directed upwards. The X axis is taken parallel to the

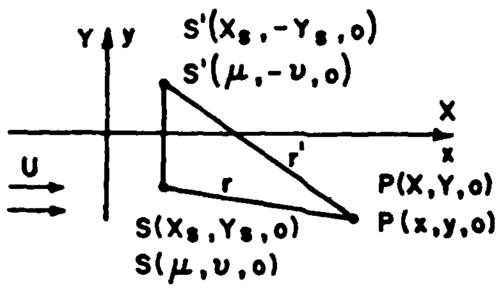

Fig. 1. Definition sketch for the centerplane Havelock source potential.

oncoming uniform stream U and pointing downstream. The (dimensional) coordinates of the source S are denoted by $\{X_S, Y_S \leq 0, 0\}$ and the field point P where the flow is observed has coordinates $\{X, Y \leq 0, 0\}$. The coordinates of the image S' of the source S with respect to the free surface are then $\{X_S, -Y_S, 0\}$.

Variables are made dimensionless with respect to the acceleration of gravity g and the velocity U taken as reference quantities. Thus, dimensionless coordinates x, y, μ, ν are defined as

$$\{x, y, \mu, \nu\} = (g/U^2)\{X, Y, X_S, Y_S\} \tag{2.1}$$

The linearized velocity potential, on the centerplane $z = 0$, for the flow described above is given by the "centerplane" Havelock source potential $G(x, y, o; \mu, \nu, 0)$, which is simply denoted by $G(x, y; \mu, \nu)$ and is written in dimensionless form as

$$G(x, y; \mu, \nu) = -[(x-\mu)^2 + (y-\nu)^2]^{-1/2} + R(x-\mu, y+\nu) \tag{2.2}$$

where $R(x-\mu, y+\nu)$ is a function of the two variables $x-\mu$ and $y+\nu$ defined — and regular — in the lower half space $y+\nu < 0$. We have

$$R(x-\mu, y+\nu) = [(x-\mu)^2 + (y+\nu)^2]^{-1/2} + \frac{4}{\pi}\int_0^{\pi/2}\int_0^{\infty} \frac{e^{k[(y+\nu)+i(x-\mu)\cos\theta]}}{k\cos^2\theta - 1}\, dk d\theta$$

$$+ 4i\int_0^{\pi/2} e^{[(y+\nu)+i(x-\mu)\cos\theta]\sec^2\theta}\sec^2\theta d\theta \tag{2.3}$$

where the convention is made that only the real part of the right-hand side is to be taken. Equation (2.3) can easily be derived from eq. (13.36), p. 485 in Wehausen [8]. It must be remembered that the equation given by Wehausen holds for the case of a uniform stream flowing past a sink in the negative x direction.

Let us introduce the complex number ζ *defined by*

$$\zeta = (y+\nu)\sec^2\theta + i(x-\mu)\sec\theta \tag{2.4}$$

Equation (2.3) can then be written as

$$R(x-\mu, y+\nu) = [(x-\mu)^2+(y+\nu)^2]^{-1/2} + \frac{4}{\pi}\int_0^{\pi/2} I(\zeta)\sec^2\theta d\theta + 4i\int_0^{\pi/2} e^{\zeta}\sec^2\theta d\theta \tag{2.5}$$

where the change of variable $k = \gamma \sec^2\theta$ was performed in the double integral, with $I(\zeta)$ defined as

$$I(\zeta) = \int_0^{\infty} \frac{e^{\gamma\zeta}}{\gamma-1} d\gamma \tag{2.6}$$

The Cauchy-principal-value integral $I(\zeta)$ can be written in terms of the complex exponential integral $E_1(\zeta)$, see Appendix 1. It yields

$$I(\zeta) = e^{\zeta}E_1(\zeta) + i\pi \operatorname{sgn}(x-\mu)e^{\zeta} \tag{2.7}$$

where $\operatorname{sgn}(x-\mu)=(x-\mu)/|x-\mu|$ and

$$E_1(\zeta) = \int_{\zeta}^{\infty} \frac{e^{-t}}{t} dt \qquad (|\arg\zeta| < \pi) \tag{2.8}$$

as defined in eq. (5.1.1) p. 228 in Abramowitz and Stegun [9].

By using eq. (2.7), eq. (2.5) can be written as

$$R(x-\mu, y+\nu) = N(x-\mu, y+\nu) + W(x-\mu, y+\nu) \tag{2.9}$$

where $N(x-\mu, y+\nu)$ and $W(x-\mu, y+\nu)$ are defined as

$$N(x-\mu, y+\nu) = [(x-\mu)^2 + (y+\nu)^2]^{-1/2} + \frac{4}{\pi}\int_0^{\pi/2} e^{\zeta}E_1(\zeta)\sec^2\theta d\theta \tag{2.10}$$

$$W(x-\mu, y+\nu) = 8iH(x-\mu)\int_0^{\pi/2} e^{\zeta}\sec^2\theta d\theta \tag{2.11}$$

In eq. (2.11), $H(x-\mu)$ is the Heaviside step function defined as $H(x-\mu) = 0$ for $x < \mu$ and $H(x-\mu) = 1$ for $x > \mu$. Only the real parts of the right-hand sides of eqs. (2.10) and (2.11) are to be taken, in accordance with the convention adopted in eq. (2.3). We have $e^{\bar{\zeta}}E_1(\bar{\zeta}) = \overline{e^{\zeta}E_1(\zeta)}$, see [9] eq. (5.1.13) p. 229, and eq. (2.10) then readily shows that $N(\mu-x, y+\nu) = N(x-\mu, y+\nu)$. This term, therefore, represents a disturbance symmetric upstream and downstream from the source. Furthermore, $N(x-\mu, y+\nu)$ represents a nonoscillatory "near-field-like disturbance", as will be seen in the following sections. The term $W(x-\mu, y+\nu)$, on the other hand, is zero upstream from the source and represents an oscillatory "wave-like disturbance". In particular, far downstream from the source, the behavior of $W(x-\mu, y+\nu)$ is given by

$$W(x-\mu, y+\nu) \sim -8(\pi/2)^{1/2} e^{y+\nu}(x-\mu)^{-1/2}\sin(x-\mu+\pi/4); \quad (x-\mu \gg 1)$$

as can readily be obtained by the method of stationary phase. It can also be easily verified that $W(x-\mu=0, y+\nu<0) = 0$, while $W(x-\mu>0, y+\nu=0) = 4\pi Y_1(x-\mu)$ where Y_1, as usual, denotes the Bessel function of the second kind (see [9], eqs. (9.1.23) and (9.1.28), pp. 360, 361).

In summary, eqs. (2.2) and (2.9) yield for the centerplane Havelock source potential

$$G(x, y;\mu, \nu) = -1/r + N(x-\mu, y+\nu) + W(x-\mu, y+\nu) \tag{2.12}$$

where $r \equiv [(x-\mu)^2 + (y-\nu)^2]^{1/2}$ denotes the distance between the field point $P(x, y)$ and the source $S(\mu, \nu)$. Thus, the linearized velocity potential of a submerged source in an oncoming uniform stream is written as the sum of three terms: (1) the potential $-1/r$ of the source in the infinite domain, (2) the symmetric, nonoscillatory "near-field disturbance potential" $N(x-\mu, y+\nu)$, and (3) the "wave potential" $W(x-\mu, y+\nu)$ of the wave-like disturbance trailing downstream from the source. It is perhaps worth emphasizing that the near-field and wave potentials N and W are universal functions which depend only upon the dimensionless (in

AD-A119 315   DAVID W TAYLOR NAVAL SHIP RESEARCH AND DEVELOPMENT CE--ETC F/G 20/4
FIRST INTERNATIONAL CONFERENCE ON NUMERICAL SHIP HYDRODYNAMICS --ETC(U)
1975   J W SCHOT, N SALVESEN

UNCLASSIFIED   NL

6 OF 8

AD A
93 5

terms of the acceleration of gravity and the velocity at infinity upstream) position vector $\overline{S'P}(x-\mu, y+\nu)$ of the field point $P(x, y)$ with respect to the mirror image $S'(\mu, -\nu)$ of the source $S(\mu, \nu)$ in the undisturbed free surface.

The idea of expressing the disturbance created by a source submerged below the free surface of an oncoming uniform stream as the sum of an oscillatory wave-like disturbance and a nonoscillatory, symmetric, near-field disturbance, is by no means new; see, in particular, Yeung [10] and Shen and Farell [11], which have been followed rather closely here. The near-field disturbance potential is kept in the form of a double integral in [10], whereas it is expressed as a simple integral in terms of the complex exponential integral in [11], a device used by others as well, e.g., Hess and Smith [12], and adopted here. The advantage of expressing the near-field disturbance potential in terms of the exponential integral results from the fact that we have an asymptotic expansion, see [9] eq. (5.1.51) p. 231, and — thanks to Hershey [13] — a rational approximation, to our disposal for evaluating the complex exponential integral.

The behavior of the wave potential $W(x-\mu, y+\nu)$ is readily understood, and its contribution to the centerplane potential $\phi(x, y, o)$ defined in eq. (1.1) may be easily evaluated, in the manner of Yeung [10], (see [7]). In the following sections, we will then exclusively be concerned with the near-field disturbance potential $N(x-\mu, y+\nu)$, which does not appear to have been thoroughly investigated in the literature.

3. Asymptotic Expansion of the Near-Field Disturbance Potential

In this section, an asymptotic expansion for the near-field disturbance potential $N(x-\mu, y+\nu)$, when $r' = [(x-\mu)^2 + (y+\nu)^2]^{1/2} \gg 1$, is derived analytically by using the asymptotic expansion for the complex exponential integral.

For simplicity, the notations $x' \equiv x-\mu$ and $y' \equiv y+\nu$ are used. It is recalled that $y' \leq 0$, while by symmetry we may assume $x' \geq 0$. The near-field disturbance potential $N(x', y')$ is given by eqs. (2.10) and (2.4) in the form

$$N(x', y') = 1/r' + \frac{4}{\pi} \int_0^{\pi/2} \mathrm{Re}\{e^{\zeta} E_1(\zeta)\} \sec^2\theta d\theta; \quad \zeta = y' \sec^2\theta + ix' \sec\theta \tag{3.1}$$

where Re{ } means "real part of". The change of variable $t = \tan\theta$ yields the alternative expression

$$N(x',y') = 1/r' + \frac{4}{\pi}\int_0^\infty \mathrm{Re}\{e^{\zeta}E_1(\zeta)\}dt; \quad \zeta = y'(t^2+1) + ix'(t^2+1)^{1/2} \tag{3.2}$$

For $|\zeta| \gg 1$, the asymptotic expansion (see [9], eq. (5.1.51) p. 231)

$$e^{\zeta}E_1(\zeta) \sim 1/\zeta + \sum_{n\geq 1}(-1)^n n!/\zeta^{n+1}; \quad (|\arg\zeta| < 3\pi/2) \tag{3.3}$$

is available. Substituting the asymptotic expansion (3.3) into eq. (3.2) yields

$$N(x',y') \sim 1/r' + \frac{4}{\pi}\int_0^\infty \mathrm{Re}\{\frac{1}{\zeta}\}dt + \sum_{n\geq 1}(-1)^n n!\,\frac{4}{\pi}\int_0^\infty \mathrm{Re}\{\frac{1}{\zeta^{n+1}}\}dt \tag{3.4}$$

It is easily verified that $R\{1/\zeta\} = y'/(y'^2t^2 + r'^2)$ and that the first integral in eq. (3.4) equals $-2/r'$. We thus obtain

$$N(x',y') \sim -1/r' + \sum_{n\geq 1}(-1)^n n!\,\frac{4}{\pi}\int_0^\infty \mathrm{Re}\{\frac{1}{\zeta^{n+1}}\}dt \tag{3.5}$$

It is convenient to introduce the notations

$$\sigma = -x'/y', \quad a = -r'/y'; \quad (\sigma^2 + 1 = a^2) \tag{3.6}$$

and to develop the analysis formally, ignoring the fact that y' may be zero. It will be seen later from the final expression of the asymptotic expansion (3.5) that no particular difficulties occur in the limit case $y' = 0$. Using the notations (3.6) and the expression (3.2) for ζ readily yields

$$\frac{1}{\zeta} = \frac{(t^2+1)^{1/2} + i\sigma}{y'(t^2+1)^{1/2}(t^2+a^2)}$$

By expanding the numerator by the binomial formula and taking the real part, we obtain

$$\operatorname{Re}\left\{\frac{1}{\zeta^{n+1}}\right\} = \frac{1}{(y')^{n+1}} \sum_{k=0}^{m} \binom{n+1}{2k} \frac{(-\sigma^2)^k}{(t^2+1)^k (t^2+a^2)^{n+1}} \;; \quad m = \begin{cases} n/2, & n \text{ even} \\ (n+1)/2, & n \text{ odd} \end{cases}$$

Substituting into eq. (3.5) then yields

$$N(x',y') \sim -1/r' - \sum_{n\geq 1} \frac{n!}{(-y')^{n+1}} \sum_{k=0}^{m} \binom{n+1}{2k} (-\sigma^2)^k \frac{4}{\pi} \int_0^\infty \frac{dt}{(t^2+1)^k (t^2+a^2)^{n+1}} \tag{3.7}$$

By using the expressions (A2.2) and (A2.4) given in Appendix 2 for the definite integrals appearing in eq. (3.7), we get

$$N(x',y') \sim -1/r' - \sum_{n\geq 1} \frac{2\, n!}{(-y'\sigma^2)^{n+1}} \left\{ c_{n+1} \frac{(\sigma^2)^{n+1}}{a^{2n+1}} + \right.$$

$$\left. + \sum_{k=1}^{m} \binom{n+1}{2k} \left[\sum_{i=1}^{k} \binom{n+k-i}{n} c_i (-\sigma^2)^i + \sum_{i=1}^{n+1} \binom{n+k-i}{k-1} c_i \frac{(\sigma^2)^i}{a^{2i-1}} \right] \right\} \tag{3.8}$$

where the coefficients c_i are defined as in eq. (A2.3) in Appendix 2. Grouping the first and last (corresponding to $i = n+1$) terms in the curly brackets in eq. (3.8), using the identity

$$1 + \sum_{k=1}^{m} \binom{n+1}{2k} = 2^n$$

(see for instance Spiegel [14], eq. (3.10) p. 4), and exchanging the order of summation on the indices k and i, we obtain

$$N(x',y') \sim -1/r' - \sum_{n\geq 1} \frac{2\, n!}{(-y'\sigma^2)^{n+1}} \left\{ 2^n c_{n+1} \frac{(\sigma^2)^{n+1}}{a^{2n+1}} + \right.$$

$$\left. + \sum_{i=1}^{m} \left[\sum_{k=i}^{m} \binom{n+1}{2k} \binom{n-i+k}{n} \right] c_i (-\sigma^2)^i + \sum_{i=1}^{n} \left[\sum_{k=1}^{m} \binom{n+1}{2k} \binom{n-i+k}{n+1-i} \right] c_i \frac{(\sigma^2)^i}{a^{2i-1}} \right\} \tag{3.9}$$

Let us introduce the notation $\alpha = -y'/r'$. Equations (3.6) then show that $a = 1/\alpha$, $\sigma^2 = (1-\alpha^2)/\alpha^2$ and $-y'\sigma^2 = r'(1-\alpha^2)/\alpha$. By substituting into eq. (3.9), and after some rearrangements, we finally obtain

$$N(r', \alpha) \sim -1/r' - \sum_{n\geq 1} 2[1.3.5 \ldots (2n-1)]\gamma_n(\alpha)/r'^{n+1} \tag{3.10}$$

where the functions $\gamma_n(\alpha)$ are defined as

$$\gamma_n(\alpha) = \alpha^n + \delta_n(\alpha)/(1+\alpha)^n \,; \qquad (0 \leq \alpha = -y'/r' \leq 1) \tag{3.11}$$

with the functions $\delta_n(\alpha)$ defined by means of

$$(1-\alpha)^n \delta_n(\alpha) = \sum_{i=1}^{m} (-1)^i a_i^n c_i^n \alpha^{n+1-2i}(1-\alpha^2)^{i-1} + \sum_{i=1}^{n} b_i^n c_i^n \alpha^n (1-\alpha^2)^{i-1} \tag{3.12}$$

and the coefficients a_i^n, b_i^n and c_i^n defined as

$$a_i^n = \sum_{k=1}^{m} \binom{n+1}{2k}\binom{n-i+k}{n} ; \quad (1 \leq i \leq m)$$

$$b_i^n = \sum_{k=1}^{m} \binom{n+1}{2k}\binom{n-i+k}{n+1-i} ; \quad (1 \leq i \leq n)$$

$$c_i^n = \frac{c_i}{2^n c_{n+1}} = \frac{1}{2^{i-1}} \frac{i(i+1)(i+2)\ldots(n-1)n}{(2i-1)(2i+1)(2i+3)\ldots(2n-1)} ; \quad (1 \leq i \leq n)$$

The functions $\delta_n(\alpha)$, $1 \leq n \leq 8$, have been determined and are given below

$$\delta_1 = -1$$

$$\delta_2 = -\alpha(2+\alpha)$$

$$\delta_3 = \frac{1}{5}(1+3\alpha-15\alpha^2-18\alpha^3-6\alpha^4)$$

$$\delta_4 = \frac{\alpha}{7}(4+16\alpha-20\alpha^2-55\alpha^3-40\alpha^4-10\alpha^5)$$

$$\delta_5 = \frac{-1}{21}(1+5\alpha-15\alpha^2-115\alpha^3-15\alpha^4+250\alpha^5+330\alpha^6+175\alpha^7+35\alpha^8)$$

$$\delta_6 = \frac{-\alpha}{11}(2+12\alpha+6\alpha^2-104\alpha^3-118\alpha^4+111\alpha^5+336\alpha^6+301\alpha^7+126\alpha^8+21\alpha^9)$$

$$\delta_7 = \frac{1}{429}(5+35\alpha-91\alpha^2-1197\alpha^3-2331\alpha^4+4515\alpha^5+12229\alpha^6+3430\alpha^7$$
$$-17654\alpha^8-27342\alpha^9-18690\alpha^{10}-6468\alpha^{11}-924\alpha^{12})$$

$$\delta_8 = \frac{\alpha}{715}(40+320\alpha+440\alpha^2-3200\alpha^3-11768\alpha^4-64\alpha^5+34200\alpha^6+38709\alpha^7$$
$$-16752\alpha^8-78324\alpha^9-83952\alpha^{10}-46530\alpha^{11}-13728\alpha^{12}-1716\alpha^{13})$$

A check of the manipulations involved in deriving the above functions $\delta_n(\alpha)$ was provided by the fact that $\alpha = 1$ had to be obtained as a root of order n of the polynomial on the right-hand side of eq. (3.12). A further check follows from the observation that the above expressions of $\delta_n(\alpha)$ can be verified to yield $\delta_n(1) = -2^n+1$, which by eq. (3.11) gives $\gamma_n(1) = 1/2^n$ in agreement with the asymptotic expansion (A3.4) obtained in Appendix 3. It may also be noted that eq. (3.12) readily yields $\delta_n(0) = 0$ when n is even and $\delta_n(0) = (-1)^m c_m^n$, with $m = (n+1)/2$, when n is odd. Finally, the integral in eq. (3.1) has been evaluated numerically, and the resulting values of $N(r', \alpha)$ compared with the values given by the above asymptotic expansion.

However, the usefulness of the asymptotic expansion (3.10) may be investigated directly, i.e., without resorting to a comparison with numerical results. Indeed, by evaluating and depicting the functions $\gamma_n(\alpha)$, $1 \le n \le 8$, for $0 \le \alpha \le 1$, it is seen that $\gamma_{2n+1}(\alpha)$, $0 \le n \le 3$, and $\gamma_{2n}(\alpha)$, $1 \le n \le 4$, have $n+1$ zeros in $0 \le \alpha \le 1$, and the behavior of these functions indicates that the accuracy of the asymptotic expansion (3.10) is fairly uniform with respect to α. Furthermore, it may be seen that the largest deviation of $\gamma_n(\alpha)$ from zero is roughly given by $\gamma_n(1) = 1/2^n$. A fair indication of the usefulness of the asymptotic expansion (3.10) may thus be obtained by simply considering the particular case $\alpha = 1$. The first neglected term in the asymptotic expansion is then given by $1.3.5 \ldots 17/2^8 r'^{10}$, see eq. (A3.4). This term will be less than ϵ if r' is greater than about $3.258/\epsilon^{1/10}$. This indicates that the nine term asymptotic expansion (3.10) should yield the value of the near-field disturbance

potential $N(r', \alpha)$ with an error not greater than 10^{-8}, 10^{-6} and 5×10^{-5} for r' greater than roughly 20, 13 and 9, respectively. Naturally, for value of r' less than about 9, fewer terms than the 9 given above need be used to obtain the best possible accuracy from the asymptotic expansion (3.10). For instance, using 7, 5 and 3 terms yield values accurate to approximately 5×10^{-4}, 5×10^{-3} and 5×10^{-2} for $r' = 7$, 5 and 3, respectively. In summary, the nine term asymptotic expansion given above may be used advantageously to evaluate the near-field disturbance potential $N(r', \alpha)$ for r' larger than, say, 15 or 20. For smaller values of r', one must resort to the numerical evaluation of the integral in eq. (3.1) for acceptable accuracy.

4. Behavior of the Near-Field Disturbance Potential in the Neighborhood of the Source

In the neighborhood of the source, i.e., for r' small, the integral in eq. (3.1) defining the near-field disturbance potential has been evaluated numerically. This integral is denoted by $N_o(x', y')$, which is thus defined as

$$N_o(x', y') = \frac{4}{\pi}\int_0^{\pi/2} \mathrm{Re}\{e^{\zeta}E_1(\zeta)\}\sec^2\theta d\theta; \ \zeta = y'\sec^2\theta + ix'\sec\theta \tag{4.1}$$

where the notations $x' = x-\mu$, $y' = y+\nu$ were used again for simplicity. The near-field disturbance potential $N(x', y')$ is then given by

$$N(x', y') = 1/r' + N_o(x', y') \tag{4.2}$$

The numerical evaluation of the integral (4.1) is discussed in Appendix 4. The results are shown in Fig. 2 where the function N_o is represented in terms of the polar-like coordinates $r' = (x'^2 + y'^2)^{1/2}$ and $\alpha' = (1 + y'/r')^{1/2} = (1-\alpha)^{1/2}$. The particular value $N(r' = 0, \alpha' = 0)$ is equal to -4, as may be verified from the series (A3.3) in Appendix 3. This series was used to check the numerical calculations for r' small and $\alpha' = 0$ (i.e., $x' = 0$). As mentioned in Section 2, the (simple) integral $N_o(x', y')$ is related to Yeung's [10] double integral $I(a, b)$; in fact, we have $N_o(x', y') = (4/\pi)I(y', x')$. The function $I(y', x')$ is represented

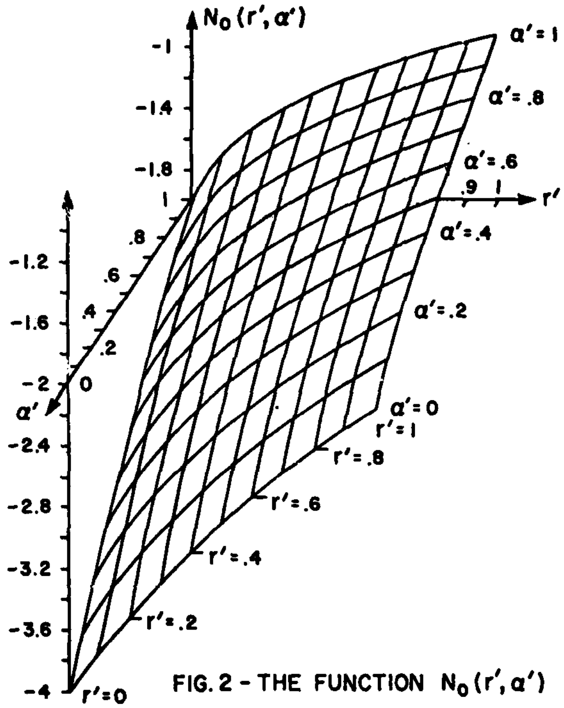

FIG. 2 - THE FUNCTION $N_0(r',\alpha')$

in [10], Fig. 19, in terms of the Cartesian coordinates x' and y'.

The behavior of the near-field disturbance potential N is depicted in Figs. 3a, b and c. In Fig. 3a, the curves $N_0(r';\alpha')$, for $\alpha' = 0$, 1/2 and 1, are represented together with the curve $-2/r'$. In agreement with the asymptotic expansion (3.10), the curves $N_0(r';\alpha')$ are seen to asymptotically approach the curve $-2/r'$ as r' increases. The asymptotic behavior of the near-field disturbance potential N appears also in Fig. 3b, where the curves $N(r';\alpha')$, for $\alpha' = 0$, 1/2 and 1, are depicted together with the curve $-1/r'$. Thus, it is seen that the near-field disturbance potential N is rightly expressed in the form (4.2) for small value of r', say for r' less than 1 or 2. For values of r'

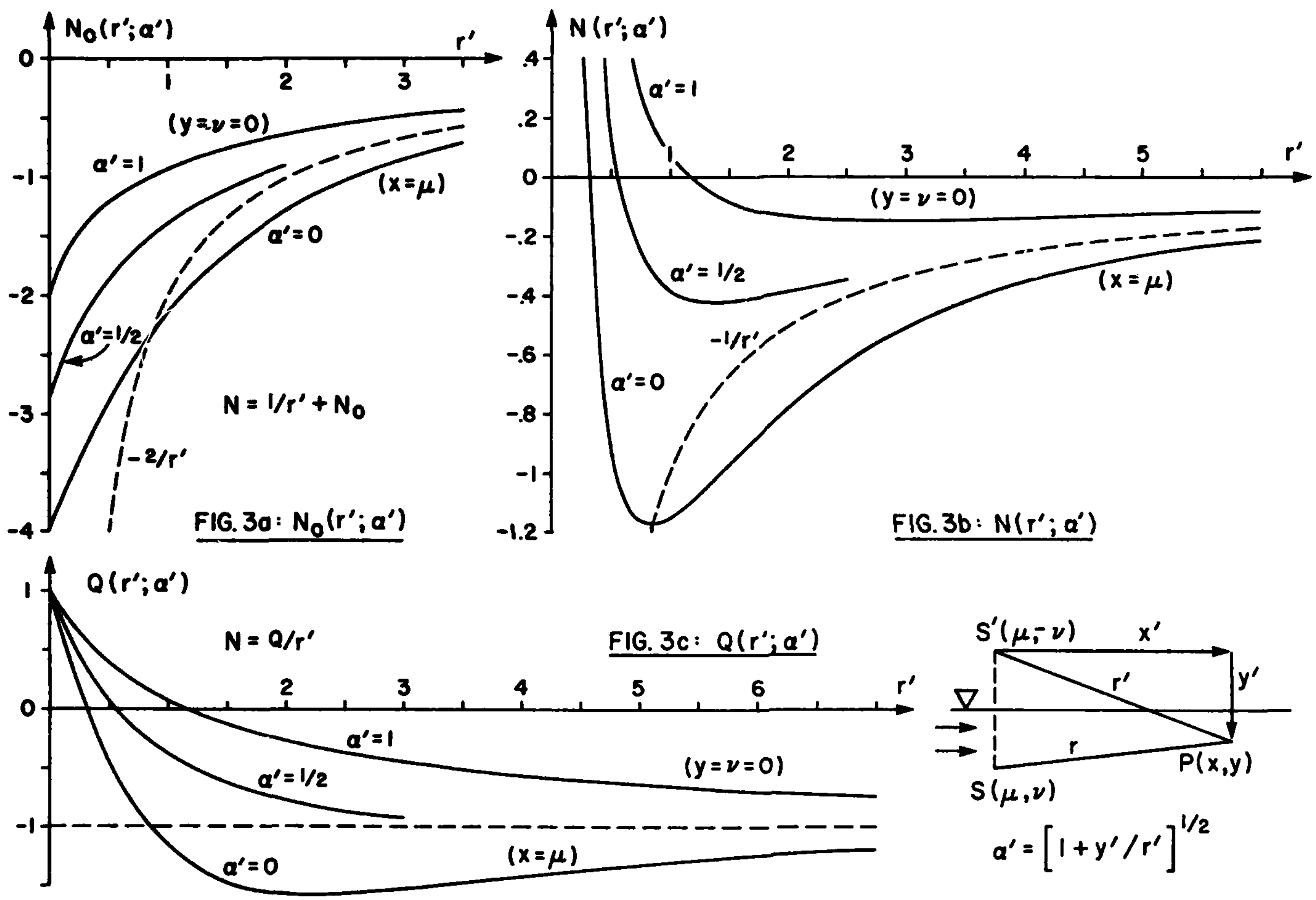

Figs. 3. Behavior of the Near-Field Disturbance Potential

greater than, say 2 or 3, it is more appropriate to write N in the form

$$N(x', y') = -1/r' + N_{\infty}(x', y') \tag{4.3}$$

where the function N_{∞} is related to N_o by $N_{\infty} = 2/r' + N_o$.

A convenient overall picture of N is obtained by expressing it in the form

$$N(x', y') = Q(x', y')/r' \tag{4.4}$$

The function $Q(x', y')$ is depicted in Fig. 3c where the curves $Q(r'; \alpha')$, for $\alpha' = 0$, 1/2 and 1, are represented; and it is seen that $Q \to 1$ as $r' \to 0$, while $Q \to -1$ as $r' \to \infty$. Equation (4.4) yields a rather simple interpretation of the near-field disturbance potential N, namely, N may be interpreted as the potential of an image sink, of strength $Q(x', y')$, in the infinite domain. Thus, the velocity potential of a submerged source in an oncoming uniform stream may be written as the sum of three terms: (1) the potential $-1/r$ of the source in the infinite domain, (2) the potential Q/r' of an image sink of strength Q in the infinite domain, and (3) the wave potential W of the wave-like disturbance trailing downstream from the source. The function $Q(x', y')$ may be interpreted as the "strength of the image singularity," and it is seen that the "image singularity" of a unit source approaches a unit source as $r' \to \infty$ (field point far from the source) or a unit sink as $r' \to o$ (field point and source near the free surface and close to each other). The function $Q(x', y')$ is represented in Fig. 4 in terms of the Cartesian coordinates x' and y'.

In concluding the above study of the behavior of the near-field disturbance potential, it may be useful to emphasize again that the results are presented in dimensionless form, with the acceleration of gravity g and the velocity at infinity upstream U used as reference quantities. In particular, the maximum value of r' for which it is required to evaluate the near-field disturbance potential N in any given ship flow problem is approximately given by $gL/U^2 = 1/F^2$, where L denotes the length of the ship and F the Froude number based on the ship length. For large values of the Froude number F, r' is seen

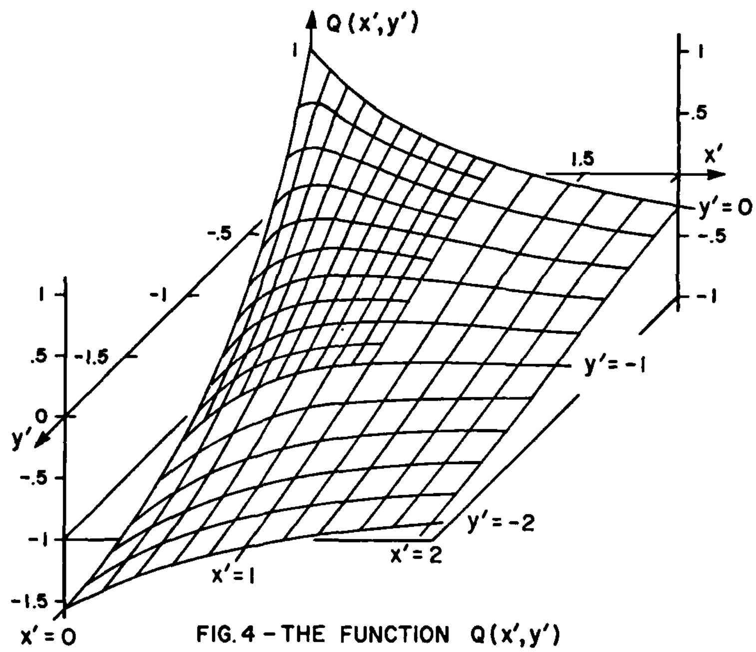

FIG. 4 - THE FUNCTION Q(x',y')

to be everywhere (i. e., for all couples of points S, P inside the ship) small, and $N = 1/r'$ thus appears to be a uniformly valid high-Froude number approximation to the near-field disturbance potential N. On the other hand, it should be realized that $N = -1/r'$ is not a uniformly valid low-Froude number approximation to N.

ACKNOWLEDGEMENTS

The present paper is based upon work started at the University of Iowa with the support of a grant from the National Science Foundation (Grant No. ENG75-03974), and continued at Stanford University with the support of the Office of Naval Research

REFERENCES

1. Gadd, G. E., 1973, "Wave resistance calculations by Guilloton's method", Trans. Royal Inst. Naval Arch., Vol. 115, pp. 377-384.

2. Guilloton, R., 1964, "L'étude théorique du bateau en fluide parfait", Bull. Assoc. Tech. Mar. Aeronautics, Vol. 64, pp. 537-561.

3. Wehausen, J. V., 1969, "Use of Lagrangian coordinates for ship wave resistance (first- and second-order thin-ship theory)," J. Ship Res., Vol. 13, pp. 12-22.

4. Dagan, G., 1975, "A method of computing nonlinear wave resistance of thin ships by coordinate straining", J. Ship Res., Vol. 19, pp. 149-154.

5. Noblesse, F., 1975, "A perturbation analysis of the wavemaking of a ship, with an interpretation of Guilloton's method", J. Ship Res., Vol. 19, pp. 140-148.

6. Noblesse, F. and Dagan, G., "Nonlinear ship waves theories by continuous mapping", submitted for publication.

7. Noblesse, F., 1975, "Numerical evaluation of the centerplane potential of a centerplane source distribution", Iowa Institute of Hydraulic Research Report No. 179.

8. Wehausen, J. V. and Laitone, E. V., 1960, "Surface waves," Handbuch der Physik, Springer-Verlag, Berlin.

9. Abramowitz, M. and Stegun, I. A., 1964, "Handbook of mathematical functions", Dover, New York.

10. Yeung, R. W., 1972, "Sinkage and trim in first-order thin-ship theory", J. Ship Res., Vol. 16, pp. 47-59.

11. Shen, H. T. and Farell, C., 1975, "Numerical calculation of the wave integrals in the linearized theory of water waves", Iowa Institute of Hydraulic Research Report No. 166.

12. Hess, J. S. and Smith, A. M. O., 1967, "Calculation of potential flow about arbitrary bodies", Progress in Aeronautical Sciences, Vol. 8, Pergamon Press, New York.

13. Hershey, A. V., 1959, "Computing programs for the complex exponential integral", NPG Report No. 1646, U. S. Naval Proving Ground, Dahlgren, VA.

14. Spiegel, M. R., 1968, "Mathematical handbook of formulas and tables", Schaum's outline series, McGraw-Hill.

Appendix 1. Expression of the Near-Field Disturbance Potential in Terms of the Complex Exponential Integral

Let the complex number ζ, defined in eq. (2.4), be written in the polar form $\zeta = ae^{i\alpha}$, where $a \geq 0$ and $\pi/2 \leq \alpha \leq 3\pi/2$ since $y+\nu \leq 0$ and $x-\mu \gtrless 0$. Following Hess and Smith [12] and others, see Yeung [10] and Shen and Farell [11], the Cauchy principal value integral $I(\zeta)$, defined in eq. (2.6), can be expressed as the sum of an oscillatory term and a nonoscillatory term by means of an appropriate contour integration in the complex γ plane. Let the complex variable γ be written in the polar form $\gamma = \rho e^{i\psi}$. We then have $\gamma\zeta = a\rho e^{i(\alpha+\psi)}$. The exponential term $e^{\gamma\zeta}$ in the integral (2.6) can be rendered monotonic decreasing by choosing $\psi = \pi-\alpha$, which yields $\gamma\zeta = -a\rho$. Performing the contour integrations shown in Fig. 5 below then yields

$$⨍_0^{\infty} \frac{e^{\gamma\zeta}}{\gamma-1}\, d\gamma \pm i\pi e^{\zeta} + \int_{\infty}^{0} \frac{e^{-a\rho}}{\rho e^{i(\pi-\alpha)}-1}\, e^{i(\pi-\alpha)} d\rho = 0$$

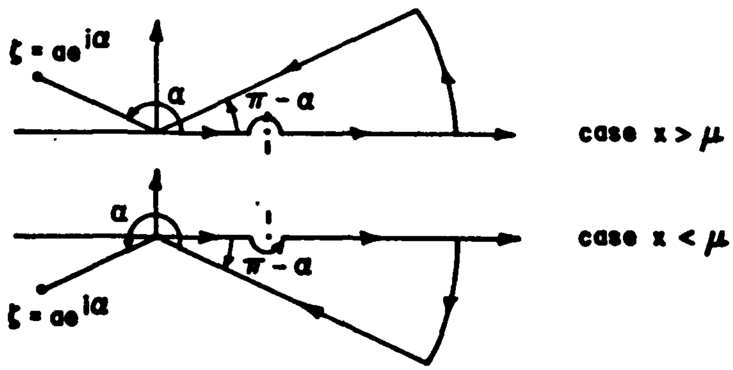

Fig. 5. Integration contours.

where the $-$ and $+$ signs correspond to the upper and lower contours (case $x-\mu>0$ and $x-\mu<0$), respectively. This readily gives

$$I(\zeta) = \pm i\pi e^{\zeta} + \int_0^{\infty} \frac{e^{-a\rho}}{\rho+e^{i\alpha}}\, d\rho$$

Equation (2. 7) is finally obtained by successively performing the change of variables $\lambda = a\rho$ and $t = \lambda+\zeta$ in the above integral.

Appendix 2. The Definite Integral $\int_0^{\infty} (t^2+a^2)^{-m}(t^2+b^2)^{-n}dt$; $(m, n \geq 1; a \neq b)$

The expression of the above definite integral, which is required for the asymptotic expansion of the near-field disturbance potential in section 3, could not be found in any table of integrals, and thus was derived.

After fairly lengthy manipulations, which are not given here, the following partial fraction decomposition can be established

$$\frac{(a^2-b^2)^m (b^2-a^2)^n}{(t^2+a^2)^m (t^2+b^2)^n} = \sum_{i=1}^{m} \binom{m+n-1-i}{n-1} \frac{(a^2-b^2)^i}{(t^2+a^2)^i}$$

$$+ \sum_{i=1}^{n} \binom{m+n-1-i}{m-1} \frac{(b^2-a^2)^i}{(t^2+b^2)^i}; \quad (m, n \geq 1; a \neq b) \qquad \text{(A2. 1)}$$

where m and n are any two integers greater than or equal to one, a and b any two different real numbers, and $\binom{p}{q}$ denotes the binomial coefficient $p!/q!(p-q)!$ as usual.

The definite integral $\int_0^{\infty} (t^2+a^2)^{-i}dt$; $(i \geq 1)$ may be obtained from tables of integrals. Indeed we have (see for instance Spiegel [14] eq. (15. 30) p. 96)

$$\frac{2}{\pi}\int_0^{\infty} \frac{dt}{(t^2+a^2)^i} = \frac{2/\pi}{a^{2i-1}} \int_0^{\pi/2} \cos^{2(i-1)}\theta d\theta = \frac{c_i}{a^{2i-1}}; \quad (i \geq 1) \qquad \text{(A2. 2)}$$

where the change of variable $t = a \tan \theta$ was performed, and the constant c_i is defined as

$$c_1 = 1; \; c_i = \frac{1.3.5\ldots(2i-3)}{2.4.6\ldots(2i-2)}; \; (i \geq 2) \quad \text{or} \quad c_i = \frac{(2i-2)!}{[2^{i-1}(i-1)!]^2}; \; (i \geq 1) \tag{A2.3}$$

Using eqs. (A2.1) and (A2.2), we readily obtain

$$\frac{2}{\pi}\int_0^\infty \frac{(a^2-b^2)^m(b^2-a^2)^n}{(t^2+a^2)^m(t^2+b^2)^n}\,dt = \sum_{i=1}^{m}\binom{m+n-1-i}{n-1}c_i\frac{(a^2-b^2)^i}{a^{2i-1}}$$

$$+\sum_{i=1}^{n}\binom{m+n-1-i}{m-1}c_i\frac{(b^2-a^2)^i}{b^{2i-1}};$$

$$(m, n \geq 1; \; a \neq b) \tag{A2.4}$$

Appendix 3. The Havelock Source Potential Along the Vertical Line Passing Through the Source

In this appendix, the Havelock source potential is examined in the particular case when the field point P is on the vertical line passing through the source S, see Fig. 1. Equations (2.4), (2.11), (2.9) and (2.2) then show that the Havelock source potential $G(y, \nu) \equiv G(0, y, 0; 0, \nu, 0)$ is given by

$$G(y;\nu) = -1/|y-\nu| + N(y+\nu) \tag{A3.1}$$

where by eq. (2.3) we have

$$N(y+\nu) = \frac{-1}{y+\nu} + \frac{4}{\pi}\int_0^{\pi/2} d\theta \int_0^\infty dk \; \frac{e^{(y+\nu)k}}{k\cos^2\theta - 1}$$

By performing the change of variable $t = \tan\theta$ and interchanging the order of integration in the above double integral, we obtain

$$N(y+\nu) = \frac{-1}{y+\nu} - \frac{4}{\pi}\int_0^\infty dk \; e^{(y+\nu)k}\int_0^\infty \frac{dt}{t^2+(1-k)}$$

The Cauchy principal value inner integral may easily be seen to yield zero when $k > 1$, while for $k < 1$ it is given by $\pi/2(1-k)^{1/2}$. We thus obtain

$$N(y+\nu) = -1/(y+\nu)-2\int_0^1 e^{(y+\nu)k}(1-k)^{-1/2}dk \qquad \text{(A3.2)}$$

By expanding $e^{(y+\nu)k}$ in Taylor series about $k = 0$, the following ascending series is obtained for $N(y+\nu)$

$$N(y+\nu) = \frac{-1}{y+\nu} - 4 - \sum_{n=1}^{\infty} \frac{2^{n+2}(y+\nu)^n}{1.3.5\ldots(2n+1)} \qquad \text{(A3.3)}$$

An asymptotic expansion for $N(y+\nu)$ may similarly be obtained by expanding $(1-k)^{-1/2}$ in Taylor series about $k = 0$. It yields

$$N(y+\nu) \sim \frac{+1}{y+\nu} - \sum_{n\geq 1} \frac{1.3.5\ldots(2n-1)}{2^{n-1}(-y-\nu)^{n+1}} \qquad \text{(A3.4)}$$

Appendix 4. Numerical Evaluation of the Near-Field Disturbance Potential

Performing the change of variable $t = c\tan\theta$, where c is an arbitrary positive constant, in the integral (4.1) yields

$$N_o(x',y') = \frac{4}{\pi}\frac{1}{c}\int_0^{\infty} \mathrm{Re}\{e^{\zeta}E_1(\zeta)\}dt \; ; \; \zeta = \frac{y'}{c^2}(t^2+c^2)+i\frac{x'}{c}(t^2+c^2)^{1/2} \qquad \text{(A4.1)}$$

The efficiency of the numerical evaluation of the above integral may be greatly improved by taking advantage of the asymptotic expansion (3.3) for $e^{\zeta}E_1(\zeta)$. The first three terms in this asymptotic expansion were retained, and eq. (A4.1) was written as

$$N_o(x',y') \simeq \frac{4}{\pi}\frac{1}{c}\int_0^{t_\infty} \mathrm{Re}\{e^{\zeta}E_1(\zeta)\}dt + \frac{4}{\pi}\frac{1}{c}\int_{t_\infty}^{\infty} \mathrm{Re}\{\frac{1}{\zeta} - \frac{1}{\zeta^2} + \frac{2}{\zeta^3}\}dt \qquad \text{(A4.2)}$$

A closed-form analytical expression has been derived for the last integral in eq. (A4.2) (setting $t_\infty = 0$ in this expression yields the first three terms of the asymptotic expansion (3.10)). The value of t_∞ can be automatically selected so as to yield the value of N_o to the specified accuracy.

The first integral in eq. (A4.2) was evaluated numerically. Simpson's integration rule was used, and the rational approximation for the complex exponential integral $E_1(\zeta)$ developed by Hershey [13] to supplement the asymptotic expansion (3.3) was used to evaluate the integrand.

The constant c in eq. (A4.2) is arbitrary, and the efficiency of the numerical evaluation of N_o does not appear to depend upon the particular value selected for c. However, as $r' \to o$, the rate $d\zeta/dt$ at which the point $\zeta = \zeta_r + i\zeta_i = (y'/c^2)(t^2+c^2)+i(x'/c)(t^2+c^2)^{1/2}$ moves along the parabola $\zeta_r = (y'/x'^2)\zeta_i^2$ tends to zero unless the constant c is properly selected. A convenient choice for this purpose is $c = (x'^2-y')^{1/2}$, which yields $\zeta = -a(t^2+c^2)+ib(t^2+c^2)^{1/2}$ where $a = \sigma/(1+\sigma)$, $b = (1+\sigma)^{-1/2}$ with $\sigma = -y'/x'^2$ (we have $0 \leq \sigma < \infty$, which gives $0 \leq a < 1$, $0 < b \leq 1$ with $a+b^2 = 1$). In addition, the logarithmic behavior of the exponential integral $E_1(\zeta)$ near the origin $\zeta = 0$ causes the computing time to increase significantly as $r' = 0$ is approached. This may be remedied by writing the integrand $\mathrm{Re}\{e^{\zeta}E_1(\zeta)\}$ as $\mathrm{Re}\{e^{\zeta}E_1(\zeta)+\ln\zeta\}-\ln|\zeta|$ for $0 \leq t \leq t_o$. The integral $\int_0^{t_o} \ln|\zeta|dt$ may readily be evaluated analytically. This device, however, has not been implemented in the computer program, and the smallest value of r' for which the function $N_o(r', \alpha')$ has been evaluated is $r' = 10^{-3}$.

COMPUTATION SYSTEM FOR SURFACE WAVE TRAINS

Allen V. Hershey

Naval Surface Weapons Center
Dahlgren, Virginia 22448 U.S.A.

ABSTRACT

A computation system has been developed for the determination of the velocity in the wave trains of ships and submarines. The first order linear approximation is used for the free boundary, while full accuracy is used for the body boundary. The body shape is expressed geometrically by orthonormal polynomials of surface coordinates, and is simulated hydrodynamically by continuous distributions of source density. The components of velocity in the wave train of a source distribution are computed by integration over the source distribution with the aid of a Fourier analysis of the components of velocity in the wave train of a point source. The system is being used to determine the flux of momentum in the wave train of a Series 60, Block 0.60 ship model. Results so far have been limited to a computation of pressure distribution and wave drag on the model at a Froude number of one third.

INTRODUCTION

For a number of years a computation system has been under development at the Dahlgren Laboratory of the Naval Surface Weapons Center. The function of the system is the computation of wave trains behind ships and submarines. Work on the system has led to a general library of subroutines which are useful for many applications. Included in the library are subroutines for exponential integrals, Fresnel integrals, Bessel functions, polynomial approximation, and matrix arithmetic.

The method of computation consists of three stages. In the first stage the surface of the ship is expressed mathematically. Surface coordinates and surface components are computed at grid points on the surface. In the second stage the velocity at each grid point is computed for a unit point source at each other grid point. The velocity is derived from the Havelock integral for a linearized free−boundary condition. In the third stage the surface of the ship is represented by a continuous distribution of source density over the surface. The velocity at each point is derived from the source densities at other points through the application of integration multipliers.

The second stage is by far the most expensive. A major objective of the development has been the design of accurate algorithms which reduce the cost of the second stage through the use of the coarsest possible grid.

Lagrange polynomials are used in the present investigation for the approximation of a function in terms of its argument. They are especially useful because they express

the coefficients of powers of the argument directly in terms of discrete values of the function. Experience with rounding errors shows that the polynomials must be derived by orthonormal expansion for arguments with Chebyshev spacing. Other polynomial expansions are less effective from the standpoint of accuracy or stability. An accuracy of six digits can be achieved with polynomials with 21 coefficients.

CARTESIAN COORDINATES AND SURFACE COMPONENTS

The preparation of fair water lines and section lines has been the goal of naval architects for many years. The truly fair line is expressed mathematically by power polynomials or by elementary functions which can be differentiated indefinitely. In the present investigation the water lines and the section lines are expressed by power polynomials of such high degree as to include such elementary functions as trigonometric functions or elliptic integrals.

In the first stage the surface of the ship is divided into quadrilaterals with curved edges. Each quadrilateral is mapped onto a square or rectangle in a plane. Isometric coordinates on the curved surface of a quadrilateral are proportional to Cartesian coordinates in the map. The Cartesian coordinates of points on the quadrilateral are expressed by power polynomials in terms of the coordinates in the map.

Inasmuch as the Series 60, Block 0.60 ship model has been the subject of experimental wake and profile surveys, it is the natural selection as a benchmark for further analysis. Data on the hull configuration have been derived from a table of offsets in NSRDC Report No. 1712[1]. The hull has flat sides and a flat bottom which are joined by a curved surface. The flat bottom intersects the curved surface along a line which is tabulated in the table of offsets. The models in the experimental investigations had various stern configurations with propellers and rudders. Only the simplest configurations at the stem and at the stern are within the scope of the present report.

The actual models which were used in the experimental work had a length of 20 ft from fore perpendicular to aft perpendicular. The mathematical models which have been adopted for the present analysis have been scaled to have the same dimensions.

The tabular data in the NSRDC report are too sparse to define the configuration mathematically. An attempt to force the section lines to be tangent to the flat bottom caused irreducible wiggles in a few of the section lines. It was necessary to assume that each section line intersects the bottom at a finite angle. The table of offsets was augmented with additional section lines and additional water lines near the edges of the sides of the model. The discrete data were compared with curved lines in large plots which could be prepared on a CalComp plotter.

Each side of the hull was simulated by a single quadrilateral which extends from the fore perpendicular to the aft perpendicular. A basic table of offsets with 27×36 entries was reduced by least squares to orthonormal polynomials with 21×17 coefficients. The arguments of polynomial approximations were proportional to the longitudinal distance to a cross section, and to the lateral distance along the section line. The table of offsets was adjusted by trial until the water lines and section lines were fair. Interpolation with the orthonormal polynomials gave the Cartesian coordinates and the surface components for Chebyshev spacing in the longitudinal distance and the distance along the section line. The results of computation are three matrices of Cartesian coordinates and three matrices of surface components for a grid of 21×7 points on the surface of each quadrilateral.

The bottom of the hull was simulated by a quadrilateral which extends from the fore perpendicular to the aft perpendicular. The arguments of polynomial approximations were proportional to the longitudinal distance and the lateral distance over the bottom. The results of computation are three matrices of Cartesian coordinates and three matrices of surface components for a grid of 21×3 points on the bottom.

The orthonormal polynomial representation of the ship model is compared with the original data in Figure 1. The computed curves agree with the tabular offsets to within the accuracy of the tabular offsets except near the stern where the models had a number of different configurations and there is no single unique configuration.

POINT SOURCE

Let x, y, z be the Cartesian coordinates of a point in the fluid, and let the origin of coordinates be at the free surface of the undisturbed fluid. The x-coordinate is the distance forward, the y-coordinate is the distance to the right, and the z-coordinate is the distance downward.

In accordance with the usual assumption of incompressible, irrotational flow, the velocity in the fluid is the negative gradient of a velocity potential which satisfies Laplace's equation. Under steady state conditions the potential in the moving reference frame is given by the expression

$$Ux + \varphi(x, y, z) \tag{1}$$

where Ux is the potential for uniform flow in a direction opposite to the motion of the source, which moves forward through still fluid with the speed U, and $\varphi(x, y, z)$ is the potential for the disturbance by the source. The Cartesian components u, v, w of velocity in the disturbance are given by the equations

$$u = -\frac{\partial\varphi}{\partial x} \qquad v = -\frac{\partial\varphi}{\partial y} \qquad w = -\frac{\partial\varphi}{\partial z} \tag{2}$$

Let the configuration of the free surface be expressed by the equation

$$z + \zeta(x, y) = 0 \tag{3}$$

For steady state conditions the velocity at the free surface is tangent to the surface and the potential obeys the boundary equation

$$\left(U + \frac{\partial\varphi}{\partial x}\right)\frac{\partial\zeta}{\partial x} + \frac{\partial\varphi}{\partial y}\frac{\partial\zeta}{\partial y} + \frac{\partial\varphi}{\partial z} = 0 \tag{4}$$

Neglect of terms of second order leads to the boundary equation

$$U\frac{\partial\zeta}{\partial x} + \frac{\partial\varphi}{\partial z} = 0 \tag{5}$$

The motion of the fluid is determined by the Bernoulli equation

$$\frac{1}{2}\left\{\left(U + \frac{\partial\varphi}{\partial x}\right)^2 + \left(\frac{\partial\varphi}{\partial y}\right)^2 + \left(\frac{\partial\varphi}{\partial z}\right)^2\right\} + \frac{p}{\rho} - gz = \tfrac{1}{2}U^2 \tag{6}$$

where ρ is the density, p is the pressure, and g is the acceleration of gravity. At the

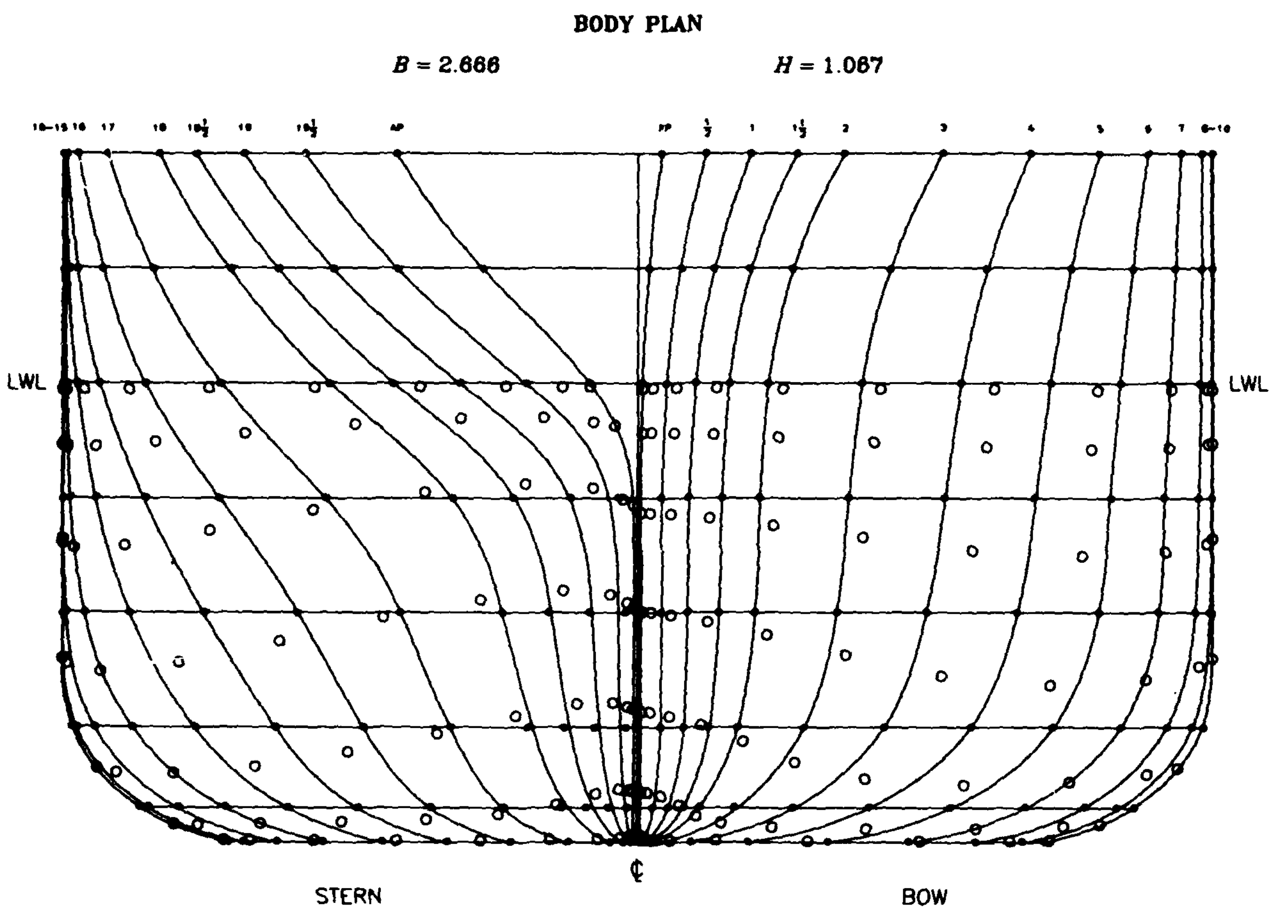

Figure 1. Section Lines of Series 60, Block 0.60 Ship Model. •, Tabular Offsets *from* NSRDC Report No. 1712; –, Orthonormal Polynomial Representation; o, Coordinates for Chebyshev Spacing along Section Line and along Longitudinal Axis.

free surface the pressure is constant. Neglect of terms of second order leads to the boundary equation

$$U\frac{\partial\varphi}{\partial x} + g\zeta = 0 \tag{7}$$

The free surface is eliminated from the equations by differentiation to give the equation

$$\frac{\partial^2\varphi}{\partial x^2} - \kappa_0\frac{\partial\varphi}{\partial z} = 0 \tag{8}$$

where κ_0 is a critical wave number and is defined by the equation

$$\kappa_0 = \frac{g}{U^2} \tag{9}$$

Along the centerline behind the source the wave length λ of the transverse waves is given by the equation

$$\lambda = \frac{2\pi}{\kappa_0} \tag{10}$$

Let the point source be at a depth h below the undisturbed free surface. Let x, y, z be the Cartesian coordinates of a point in the fluid. Let the origin of coordinates be at the undisturbed free surface above the source.

Analysis shows that the potential φ of the point source may be expressed as the sum of three potentials in accordance with the equation

$$\varphi(x, y, z) = \varphi_1(x, y, z) + \varphi_2(x, y, z) + \varphi_3(x, y, z) \tag{11}$$

where φ_1 is the potential of the source in an unbounded fluid, φ_2 is the potential of an image source over the free surface, and φ_3 is the potential of the surface wave.

The potential φ_1 is given by the equation

$$\varphi_1 = \frac{1}{\{x^2 + y^2 + (z-h)^2\}^{\frac{1}{2}}} \tag{12}$$

Its derivatives are given by the equations

$$-\frac{\partial\varphi_1}{\partial x} = \frac{x}{\{x^2 + y^2 + (z-h)^2\}^{\frac{3}{2}}} \tag{13}$$

$$-\frac{\partial\varphi_1}{\partial y} = \frac{y}{\{x^2 + y^2 + (z-h)^2\}^{\frac{3}{2}}} \tag{14}$$

$$-\frac{\partial\varphi_1}{\partial z} = \frac{z-h}{\{x^2 + y^2 + (z-h)^2\}^{\frac{3}{2}}} \tag{15}$$

which are required for the computation of flow from the point source.

The potential φ_2 is given by the equation

$$\varphi_2 = -\frac{1}{\{x^2 + y^2 + (z+h)^2\}^{\frac{1}{2}}} \tag{16}$$

Its derivatives are given by the equations

$$-\frac{\partial \varphi_2}{\partial x} = -\frac{x}{\{x^2 + y^2 + (z+h)^2\}^{\frac{3}{2}}} \tag{17}$$

$$-\frac{\partial \varphi_2}{\partial y} = -\frac{y}{\{x^2 + y^2 + (z+h)^2\}^{\frac{3}{2}}} \tag{18}$$

$$-\frac{\partial \varphi_2}{\partial z} = -\frac{z+h}{\{x^2 + y^2 + (z+h)^2\}^{\frac{3}{2}}} \tag{19}$$

which are required for the computation of flow from the image source.

The potential φ_3 is expressed as a Fourier integral. The boundary conditions at the free surface are met by the sum of the potentials if φ_3 is given by the equation

$$\varphi_3(x, y, z) = \frac{\kappa_0}{\pi} \int_{-\pi}^{+\pi} \int_0^{\infty} \frac{e^{-\kappa(z+h)+i\kappa(x\cos\theta + y\sin\theta)}}{\kappa_0 - \kappa\cos^2\theta} \, d\kappa \, d\theta \tag{20}$$

The integration can be simplified through the substitutions

$$\delta = \frac{\kappa_0}{\cos^2\theta}\left\{(z+h) - i(x\cos\theta + y\sin\theta)\right\} \tag{21}$$

and

$$\kappa = \frac{\kappa_0}{\cos^2\theta} - \frac{u}{(z+h) - i(x\cos\theta + y\sin\theta)} \tag{22}$$

where u is a new variable of integration. The function $e^{-\delta}$ satisfies both Laplace's equation and the boundary equation for the free surface. It is added in just the right amount to make the wave train trail behind the source if the path of integration with respect to u proceeds along a straight line in the complex plane from $u = -\infty$ toward the origin, bypasses the origin on a half circle of small radius at the origin, and continues on a straight line to $u = \delta$. The integrand is analytic and the path of integration may be deformed in accordance with the Cauchy theorem on analytic functions.

The potential of the surface wave is given by the equation

$$\varphi_3(x, y, z) = \frac{\kappa_0}{\pi} \int_{-\pi}^{+\pi} \frac{e^{-\delta}}{\cos^2\theta} \int_{-\infty}^{\delta} \frac{e^u}{u}\, du\, d\theta \tag{23}$$

Its derivatives are given by the equations

$$-\frac{\partial \varphi_3}{\partial x} = -i \frac{\kappa_0^2}{\pi} \int_{-\pi}^{+\pi} \frac{e^{-\delta}}{\cos^4\theta} \int_{-\infty}^{\delta} \frac{e^u}{u^2}\, du \cos\theta\, d\theta \tag{24}$$

$$-\frac{\partial \varphi_3}{\partial y} = -i \frac{\kappa_0^2}{\pi} \int_{-\pi}^{+\pi} \frac{e^{-\delta}}{\cos^4\theta} \int_{-\infty}^{\delta} \frac{e^u}{u^2}\, du \sin\theta\, d\theta \tag{25}$$

$$-\frac{\partial \varphi_3}{\partial z} = + \frac{\kappa_0^2}{\pi} \int_{-\pi}^{+\pi} \frac{e^{-\delta}}{\cos^4\theta} \int_{-\infty}^{\delta} \frac{e^u}{u^2}\, du\, d\theta \tag{26}$$

which are the foundation for one method for the computation of motion in the surface wave. Inasmuch as the variable of integration is cyclical, the high accuracy rule of integration is the trapezoidal rule. However, the integrand is oscillatory, and a large number of intervals of integration are required when the point source is close to the free surface.

A breakthrough in computation has been achieved by an integration by parts through many cycles of oscillation in each interval of the integration. It is convenient to introduce a new parameter t which is defined by the equation

$$t = \tan\theta \tag{27}$$

whence the derivatives of φ_3 are given by the equations

$$-\frac{\partial \varphi_3}{\partial x} = -i \frac{2\kappa_0^2}{\pi} \int_{-\infty}^{+\infty} \sqrt{1+t^2}\; e^{-\delta} \int_{-\infty}^{\delta} \frac{e^u}{u^2}\, du\, dt \tag{28}$$

$$-\frac{\partial \varphi_3}{\partial y} = -i \frac{2\kappa_0^2}{\pi} \int_{-\infty}^{+\infty} t\sqrt{1+t^2}\; e^{-\delta} \int_{-\infty}^{\delta} \frac{e^u}{u^2}\, du\, dt \tag{29}$$

$$-\frac{\partial \varphi_3}{\partial z} = + \frac{2\kappa_0^2}{\pi} \int_{-\infty}^{+\infty} (1+t^2)\; e^{-\delta} \int_{-\infty}^{\delta} \frac{e^u}{u^2}\, du\, dt \tag{30}$$

and the parameter δ is given by the equation

$$\delta = +\kappa_0(z+h)(1+t^2) - i\kappa_0(x+yt)\sqrt{1+t^2} \tag{31}$$

The integrands of the integrals are the products of monotonic functions of t and an oscillatory function of δ. The factors are expressed in terms of a common parameter u such that the monotonic factors are power series in u but δ is a polynomial of low degree in u. The complex phase δ is stationary at two complex points t_1 and t_2 where $d\delta/dt$ is zero.

In the convergent approximation the parameter δ is expressed as a linear function of u, and the monotonic factors are expanded as power series in u by Lagrange interpolation. Integration is completed with the aid of recurrence equations. The natural path of integration is the real axis in the t-plane, but this path passes between two singularities where $d\delta/dt = 0$. Many intervals of integration would be required in the vicinity of the singularities. These can be reduced to a single interval near the first singularity, and they can be reduced to fewer intervals near the second singularity,

if the path of integration is displaced to pass right through the first singularity. The expansions and integrations are performed in a sequence of intervals of limited range. The range of expansion of Lagrange interpolation is subject to limitations which are similar to the limitations on the range of expansion of Taylor series. In both cases the range of expansion is limited to a fraction of the radius of that circle which is centered at the center of expansion and passes through the nearest singularity.

The exponential integral is given by an asymptotic approximation when its argument is large. The asymptotic approximation is the sum of a descending series and a term $2\pi i e^{-\delta}$ when the path of integration encircles the origin. When $|x| >> \sqrt{8}|y|$ the points of stationary phase are far apart. The phase δ is expressed as a quadratic polynomial which is centered at either point t_1 or t_2. Then the integration is completed with the aid of differentiations of the error function. When $|x| \sim \sqrt{8}|y|$ the points of stationary phase are close together. The phase δ is expressed as a cubic polynomial in u such that $d\delta/du = 0$ at the same values of u that $d\delta/dt = 0$. Then the integration is completed with the aid of recurrence equations for the derivatives of the Airy function.

The analysis and the computation of the wave train of the point source have been described in more detail in a previous report[2].

SOURCE DENSITY

The boundary condition at the surface of the ship is the absence of flux through the surface. The flux from free-stream flow is cancelled by flux from source density at the surface. The flux per unit area through the surface is that component of velocity which is normal to the surface.

The velocity at one grid point on the surface of the ship is the integral over all other grid points of the product of source density, surface area, and the velocity in the wave train of a point source. The velocity in the vicinity of a point source is the sum of three terms. The first term is flow from the point source, the second term is flow from its image source, and the third term is motion in the surface wave.

Source density and surface area are approximated by power polynomials in position over the length of the ship. The wave motion is approximated by power polynomials in position over a wave length. The velocity for source flow and image flow is the quotient of a power polynomial and the cube of a radical. At a field point close to the surface of a quadrilateral the radical is small. The radical can be expanded as an ascending Taylor series only inside a zone under the field point. The radical must be expanded as a descending Taylor series outside the zone. At a distance of a half ship length from the surface of the ship the radical can be approximated by a power polynomial over the length of the ship, but at a closer distance the expansion converges rapidly only in a zone with a size equal to the distance from the surface. A grid for numerical integration must be subdivided in the vicinity of the field point, but even then convergence of the numerical integration to an accurate limit is slow. The presence of the radical can be overcome if the integration is performed analytically in the rectangular map which represents the quadrilateral. The field point near the quadrilateral is mapped into a field point over the rectangular map. The position of the field point with respect to the map is the same as the position of the field point with respect to that plane which is tangent to the quadrilateral under the field point. Thus the radical in the map deviates from the radical in the quadrilateral only at a distance from the field point.

A table of integrals can be constructed for which the integrands are the ratio between the powers of map coordinates and the cube of the distance from the point of integration to a field point. The m, n th integral in the table is given by the equation

$$\varphi_{mn} = \int_{-b}^{+b} \int_{-a}^{+a} \frac{u^m v^n}{\{(u-x)^2 + (v-y)^2 + z^2\}^{\frac{3}{2}}} \, du \, dv \tag{32}$$

where a is the half length and b is the half width of the rectangle, u, v are the Cartesian coordinates of the element of integration on the rectangle, and x, y, z are the Cartesian coordinates of a field point. The integrals of lowest order can be derived by elementary calculus. The integrals of higher order can be derived with the aid of three-term recurrence equations. A mixture of analytic manipulation with numerical evaluation provides accurate values of the integrals even when the field point is in contact with the map. The table of integrals of ratios between powers of map coordinates and the cube of the radical is multiplied by matrices of coefficients for Lagrange polynomials in order to convert it into a table which gives the integrals of the ratios of Lagrange polynomials and the cube of the radical.

The details of the algorithms for the integration over the rectangle will be documented in forthcoming reports.

From the table of integrals is derived a set of integration multipliers which are applied directly to source density in order to integrate the product of source density, surface area, and source flow. General integration multipliers for Chebyshev spacing are used for the integration of the product of source density, surface area, and wave motion.

Values of source density at each grid point are the unknowns in a set of equations which express the boundary condition at each grid point. The matrix of the equations is derived from the integration multipliers. The matrix is partitioned with one row and one column for each quadrilateral. Inversion is by the Gauss–Jordan method with pivot selection. The matrix has been found to be well conditioned.

That the rounding error in the source density is in the seventh digit of its maximum value was determined by a comparison between computations with truncated arithmetic and computations with rounded arithmetic.

The distribution of source density defines a wave motion below a reference plane on which the linearized free–boundary conditions are met. An extension of the wave motion into the space above the reference plane is obtained by a reflection of the wave motion through the reference plane. The only requirement is that the wave motion above the reference plane shall have the same velocity at $z = 0$, and shall satisfy Laplace's equation. The actual free surface is elevated with respect to the reference plane. The free surface is the envelope of streamlines which originate upstream on the reference plane. The streamlines can be constructed by trajectory integration in the complete flow field.

PROGRAMMING

The computation system consists of subroutines and programs which can be concatenated to solve various problems in connection with the global flow of fluid past a floating ship. Brief statements of the functions of the subroutines and programs are listed in Tables I and II.

TABLE I

PRINCIPAL SUBROUTINES

SUBROUTINE CHVMLT
Prepares arguments and multipliers for integration at Chebyshev spacing.

SUBROUTINE ORTHOS
Prepares a matrix of the values of orthonormal polynomials at discrete values of the argument.

SUBROUTINE ORTHOV
Computes values and derivatives of orthonormal polynomials at a given value of the argument.

SUBROUTINE ORTHOX
Prepares a matrix of the coefficients of powers of the argument in the orthonormal polynomials.

SUBROUTINE MPLNMV
Computes values and derivatives of a function which is expressed as an array of coefficients for a power polynomial.

SUBROUTINE CNTCRV
Plots contours of equal value for any continuous function of Cartesian coordinates in a rectangle.

SUBROUTINE MTRX
Performs matrix arithmetic on entire matrices which are stored in core memory.

SUBROUTINE PMTX
Performs matrix arithmetic on partitioned matrices which are stored in disk memory.

SUBROUTINE RPLTM
Prepares a matrix of integrals of the quotient of powers of surface coordinates on a rectangle and the cube of the distance to a field point.

SUBROUTINE PSWTVF
Computes the velocity components at a field point in the wave train of a point source.

TABLE II

PRINCIPAL PROGRAMS

PROGRAM LINES
Prepares plots of water lines from a table of offsets by orthonormal polynomial approximation.

PROGRAM BODY
Prepares plots of section lines from a table of offsets by orthonormal polynomial approximation.

PROGRAM SHAPE
Reduces table of offsets by orthonormal polynomial approximation to matrices of Cartesian coordinates at Chebyshev spacing along the longitudinal axis and along each section line.

PROGRAM IMLTV
Derives matrices of integration multipliers for surface integration at Chebyshev spacing along the longitudinal axis and along each section line.

PROGRAM SHSFWV
Prepares a file of velocities in the wave train at each field point for a source at each other point on the surface of the ship.

PROGRAM SHSFSD
Computes the source density at the surface of a ship from integration multipliers and velocities in the wave trains of point sources.

PROGRAM SHSFVF
Computes the velocity at the surface of a ship from source density, integration multipliers, and velocities in the wave trains of point sources.

PROGRAM SHSFPF
Computes the pressure at the surface of a ship from coordinates, velocities, and integration multipliers.

Not included in the tables are the subroutines for complex exponential integral, complex Fresnel integral, or complex Bessel functions.

WAVE RESISTANCE

The computation system has been applied so far only to a model at a Froude number of one third. Inspection of the listing of output from the system shows some surprising results. The integrated source density below the reference plane is a sink, although this sink is balanced by an image source above the reference plane. In an

open ship the sources and sinks are actually outside the fluid, and there is no requirement that their sum shall be zero below the reference plane. The source density approaches zero toward the reference plane near the bow, but approaches a finite value toward the reference plane near the stern. There is a discontinuity in source density at the reference plane near the stern, and the velocity approaches infinity toward the discontinuity.

The pressure on the hull is the sum of a hydrostatic pressure and a Bernoulli pressure. The hydrostatic pressure contributes nothing to an integral of pressure downward from the reference plane except a buoyancy force. The Bernoulli pressure is low just below the reference plane near the stern, but this region is above the wave profile, where the surface of the model would not be in contact with fluid. Along the wave profile the sum of hydrostatic pressure and Bernoulli pressure is zero. Integration of pressure downward from the reference plane includes the region of low pressure near the stern.

The present system integrates the pressure downward from the reference plane where $z = 0$. The computed value of the coefficient of wave resistance for the linearized free-boundary condition is given in Table III.

TABLE III

DIMENSIONS AND RESISTANCE
(Computed)
Series 60, Block 0.60 Model

Length	20.0	(ft)
Beam	2.666	(ft)
Draft	1.067	(ft)
Area	69.17	$(ft)^2$
Volume	34.00	$(ft)^3$
Speed	8.4556	(ft)/(sec)
Froude Number	0.3333	
Wave Resistance Coefficient	0.0049	

The Froude number is defined by the equation

$$Fn = \frac{U}{\sqrt{gL}} \tag{33}$$

where U is the speed of the model, g is the acceleration of gravity, and L is the length of the model. The coefficient of wave resistance is defined by the equation

$$Cw = \frac{R}{\frac{1}{2}\rho S U^2} \tag{34}$$

where R is the wave resistance, ρ is the density of the fluid, and S is the submerged surface area.

A smaller estimate of the wave resistance coefficient would be obtained if the system were modified so that the pressure is integrated downward from the free surface. Smaller values have been obtained in the integrations of pressure by Gadd[3] and by Adee[4]. The computed value of 0.0049 for the wave resistance coefficient is less than the experimental value of 0.0058 for the total resistance coefficient as reported by Moreno, Perez-Rojas, and Landweber[5] for a smooth model.

When vorticity is included in the flow field, the computed wave resistance will be reduced still more. The boundary conditions at the body boundary will be met partially by the vortex flow, and partially by a diminished source density.

CONCLUSION

The integrated source density is a net sink below and an image source above the reference plane where the linearized free-boundary conditions are met. The computation system must be modified so as to integrate the pressure distribution downward from the free surface.

BIBLIOGRAPHY

1. *Methodical Experiments with Models of Single-Screw Merchant Ships.*
   F. H. Todd, Naval Ship Research and Development Center Report No. 1712 (July 1963)

2. *FORTRAN Programming for Surface Wave Trains.*
   A. V. Hershey, Naval Surface Weapons Center Report TR-2714 (September 1972)

3. *A Method for Calculating the Flow over Ship Hulls.*
   G. E. Gadd, Transactions of the Royal Institution of Naval Architects, 112, 335 (1970)

4. *An Analysis of Ship Resistance.*
   B. H. Adee, and P. J. Harvey, University of Washington Report UWME-BHA-75-01 (March 1975)

5. *Effect of Wake on Wave Resistance of a Ship Model.*
   M. Moreno, L. Perez-Rojas, and L. Landweber, Iowa Institute of Hydraulic Research Report No. 180 (August 1975)

REPRESENTATION OF THREE-DIMENSIONAL PLANING SURFACES BY FINITE ELEMENTS

L.J. Doctors

School of Mechanical and Industrial Engineering
The University of New South Wales
Kensington, N.S.W. 2033, Australia

ABSTRACT

This paper presents a numerical solution for the planing of a boat over the surface of deep water. The method applies to the case of a finite Froude number and an arbitrary beam, so that the restrictions of previous theories are avoided.

Inviscid linearized potential flow is used. Thus the presence of the boat is modelled by the equivalent pressure distribution. The pressure itself is represented by a twodimensional array of elements. The pressure is allowed to vary linearly with respect to position within each element so that the overall distribution is continuous. The wave pattern produced by one such element constitutes the first part of the solution.

The second part of the solution is the assembly of these elements. A kinematic condition is required at the centre of each element. Furthermore, the Kutta condition is satisfied at a discrete number of points along the trailing edge, and the boat must be in equilibrium. These extra conditions determine the rise and trim of the boat, as well as the extent of the wetted surface.

With a very small number of elements in the longitudinal and transverse directions, the theory predicts the amount of wetted area of flat plates and prismatic hulls to within a few percent of that derived from experimental data. The proportion of the boat that rises out of the water is also computed to a similar accuracy. The lift coefficient tends to be about 30% low for a beam Froude number of two, but it is in better agreement at lower speeds.

1. Introduction

1.1 Previous Work

One of the first to study the hydrodynamics of twodimensional planing surfaces was Sretenskii [1, 2]. He applied the usual linearized potential flow theory to a flat plate. His technique represented the pressure distribution by an infinite series, the first term of which reveals a square-root singularity at the leading edge - well known in airfoil theory. Sedov [3] and Maruo [4 to 7] also treated this problem. Experimental pressure distributions of Maruo [7] tended to verify the theory - particularly at small pitch angles and away from the singularity at the leading edge.

The problem of satisfying the Kutta condition at the trailing edge, and the fact that the wetted length of the boat, and the height of its trailing edge, should be treated as unknowns (and are therefore part of the solution) were dealt with in depth by Squire [8]. Cumberbatch [9] used a high Froude number approximation. He showed that a suitably shaped parabolic plate would eliminate the leading-edge singularity (corresponding to the splash jet thrown ahead of the craft), and hence dramatically reduce the drag compared to that of a flat plate. Wehausen and Laitone [10] reviewed much of the above work.

Nonlinear aspects of twodimensional planing have also been studied - but with various restrictions. Thus Green [11 to 13] solved the case of a flat plate gliding on a stream of both finite and infinite depth using the method of conformal mapping. Wu [14] developed a singular perturbation scheme suitable for high speeds. Later Wu and Whitney [15] derived optimum shapes to generate, for example, maximum lift subject to certain restraints, such as infinite Froude number and fixed chord length, or fixed arc-length of the plate. Doctors [16] made use of finite elements to solve the linearized case at finite speed. In this way, the method of solution was greatly simplified, and the shape of the plate could be arbitrary. Certain types of optimum forms of plate were also derived - and these corresponded closely with those of Cumberbatch.

Threedimensional planing has received less attention due, primarily, to the fact that the extent of the wetted area is unknown. This difficulty is skirted in the twodimensional case, in an inverse manner, by fixing the length, and finding (for example) the weight supported by it. The

problem can be somewhat alleviated by considering either a low aspect-ratio plate, a high aspect-ratio one, or a case of high Froude number.

Thus Wagner [17] and Tulin [18] tackled the first case. Maruo [19] examined both low and high aspect-ratio plates. Shen [20] and Shen and Ogilvie [21] assumed a high aspect ratio. In the latter paper the speed was assumed to be infinite but nonlinearity was included. Wang and Rispin [22] solved the problem of a finite beam-to-length ratio plate at a high Froude number. Tuck [23] and Oertel [24] discussed the aspect of the unknown wetted area and its relation to the Kutta condition in some detail. In the latter paper, various wetted areas were assumed (at infinite Froude number) and the error in *not satisfying* the Kutta condition was computed.

A number of papers presenting experimental results have also appeared. These include work by Clement and Blount [25], Hadler [26] and Savitsky [27 to 29]. Other aspects of planing surfaces, including porpoising instability, are referred to by Du Cane [30], Parkinson [31], Angeli [32], Payne [33] and Latorre [34].

1.2 Present Work

The purpose of this paper is to extend the author's work from two dimensions to three. In particular, the method will be applied to both flat plates and prismatic hulls, shown in Fig. 1. The input parameters are: the length of the craft at rest (L_0), the amount of deadrise at the beam (d), and the speed coefficient, or beam Froude number (F_B). All horizontal distances in the results are nondimensionalized against the craft beam (B), and all quantities with a vertical sense, such as pressure (p), depth of the trailing edge below the undisturbed free surface (h) and trim angle (α) will be made nondimensional using the depth of the center of the trailing edge when at rest (h_0).

Rectangular pyramidal pressure elements of length 4a and width 4b will be used. These overlap in such a manner that the resulting pressure distribution is continuous in both the longitudinal and transverse directions, as shown in Fig. 2.

It will therefore be possible to do away with the abovementioned restrictions on the Froude number and the craft beam.

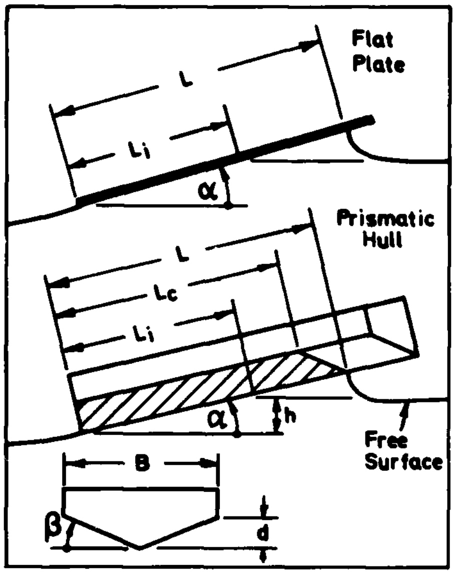

Fig. 1 Definition Sketch

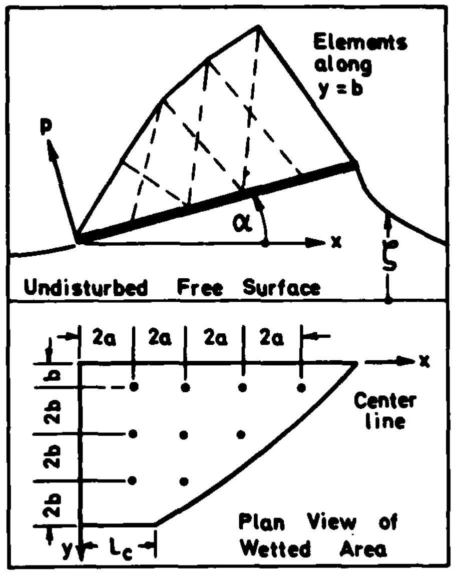

Fig. 2 Use of Finite Elements

2. Wave Pattern due to a Pressure Pyramid

2.1 Theoretical Derivation

Making the usual assumptions of inviscid linearized flow, then the potential must satisfy the Laplace equation:

$$\phi_{xx} + \phi_{yy} + \phi_{zz} = 0 \quad , \tag{1}$$

where x is measured forward and z vertically upward. The problem is made steady by imposing a uniform velocity of c (the craft speed) to the left, so that ϕ is the perturbation potential. One must also satisfy the free-surface kinematic condition:

$$\Big[\phi_z\Big]_{z=0} + c\,\zeta_x = 0 \quad , \tag{2}$$

where ζ is the free-surface elevation. The dynamic free-surface condition, obtained from the Bernoulli equation is

$$p + \rho g \zeta - \rho c \Big[\phi_x\Big]_{z=0} = 0 \quad , \tag{3}$$

where ρ is the water density, g is the acceleration of gravity and p is the pressure acting on the surface. In deep water we must also apply the condition

$$\Big[\phi_z\Big]_{z=-\infty} = 0 \quad . \tag{4}$$

The combined free-surface condition is obtained by eliminating ζ from Eqs (2) and (3):

$$\Big[\phi_{xx} + k_0 \phi_z\Big]_{z=0} = \frac{1}{\rho c} p_x \quad , \tag{5}$$

where
$$k_0 = g/c^2 \tag{6}$$
is the fundamental wave number.

The solution to Eqs (1), (4) and (5), subject to the requirement that waves should exist downstream of the pressure (the radiation condition), may be obtained by a double Fourier transform in the xy domain, and is well known (for example, see Wehausen and Laitone [10], p. 598). It is

$$\phi(x,y,z) = \frac{1}{2\pi^2 \rho c} \int_{-\pi/2}^{\pi/2} \sec\theta \, d\theta \int_0^\infty \frac{k\, e^{kz}}{k - k_1} \Big[\sin(wx + uy)\, P - \cos(wx + uy)\, Q\Big] dk \, - $$
$$- \frac{1}{2\pi \rho c} \int_{-\pi/2}^{\pi/2} \sec\theta \, k_1 \, e^{k_1 z} \Big[\cos(w_1 x + u_1 y)\, P_1 + \sin(w_1 x + u_1 y)\, Q_1\Big] d\theta \, , \tag{7}$$

where
$$P + i\,Q = \iint p(x,y) \exp[i(wx + uy)]\, dx\, dy \quad , \tag{8}$$

and
$$w + i\,u = k \exp(i\theta) \quad , \tag{9}$$

and the subscript 1 means an evaluation at the pole given by

$$k_1 = k_0 \sec^2\theta \quad . \tag{10}$$

The wave elevation may be found by substituting Eq. (7) into Eq. (3). Also, for a pressure which is symmetrical about the longitudinal axis, the range of the θ integration may be halved, and $Q = 0$. Thus

$$\zeta(x,y) = \zeta_0 + \frac{1}{\pi^2\rho g}\int_0^{\pi/2} d\theta \int_0^{\infty} \frac{k^2\cos(wx)\ \cos(uy)\ P(w,u)}{k - k_1}\, dk\ +$$

$$+\ \frac{1}{\pi\rho g}\int_0^{\pi/2} k_1{}^2\sin(w_1x)\ \cos(u_1y)\ P(w_1,u_1)\ d\theta \quad . \qquad (11)$$

where ζ_0 is the hydrostatic wave elevation (equal to $-p/\rho g$).

It is found easier to derive the wave disturbance of the pyramid, by first considering that due to a *rectangular* distribution - one in which p is constant at, say, p_0 within an area defined by $|x| < a'$ and $|y| < b'$, and is zero outside. Then

$$P = 4\,p_0 \frac{\sin(wa')}{w}\,\frac{\sin(ub')}{u} \quad . \qquad (12)$$

We substitute this result in Eq. (11). One can then combine the trigonometric functions to produce integrals involving the first of the following two auxiliary functions for the sine- and cosine-integrals:

$$g(\lambda) = \int_0^{\infty} \frac{\cos t}{\lambda + t}\, dt \quad \text{and} \quad f(\lambda) = \int_0^{\infty} \frac{\sin t}{\lambda + t}\, dt \quad , \qquad (13)$$

which are given in Abramowitz and Stegun [35], p. 232. The final result is

$$\hat{\zeta} = \frac{\rho g \zeta}{p_0}$$

$$= \hat{\zeta}_0 + \frac{1}{2\pi^2}\int_0^{\pi/2} \sec\theta\ \mathrm{cosec}\,\theta \sum\sum\sum_{i,j,m=\pm 1} m\,[-\,g|\lambda| + \pi\sin|\lambda| - i\pi\ \sin(\lambda)]\ d\theta \ , \qquad (14)$$

where $$\lambda = [(a' + ix)\cos\theta\ + m(b' + jy)\sin\theta]\, k_1 \quad . \qquad (15)$$

The wave disturbance for the pyramid may be obtained by integrating this result between the limits $0 < a' < 2a$ and $0 < b' < 2b$. Using

$$\int g|\lambda|\ d\lambda = \mathrm{sgn}(\lambda)\ [\tfrac{\pi}{2} - f|\lambda|\ ] \quad \text{and} \quad \int \mathrm{sgn}(\lambda)\ f|\lambda|\ d\lambda = g|\lambda| + \ln|\lambda| \ , \qquad (16)$$

one finally obtains

$$\hat{\zeta} = \hat{\zeta}_0 + \frac{1}{8\pi^2 abk_0^2} \int_0^{\pi/2} \cot^2\theta \sum_{i,j,k,\ell,m=\pm 1}\sum\sum\sum\sum k\ell\,[G|\lambda| + i\pi \sin(\lambda)]\, d\theta \quad , \tag{17}$$

with $$G|\lambda| = g|\lambda| + \ln|\lambda| + \frac{\pi}{2}|\lambda| - \pi \sin|\lambda| \quad , \tag{18}$$

and $$\lambda = [(a + ix + ka)\cos\theta + m(b + jy + \ell b)\sin\theta]\, k_1 \quad . \tag{19}$$

2.2 The Corner Wave Function

Examination of Eq. (17) reveals that apart from the summation with respect to m , the remaining fourfold summation reduces from 16 terms to only 9 different ones, and these can be considered to be contributions from the four corners of the pyramid, the midpoints of the four sides and the vertex.

Thus, to obtain the disturbance at various distances x and y from a pyramid of various sizes a and b , one need only compute a *twodimensional* array of values of the corner function - and not a fourdimensional one.

However, each summand in Eq. (17) is separately divergent, so that the following even and odd wave functions were defined instead:

$$F_e(X,Y) = \frac{1}{8\pi^2} \int_0^{\pi/2} \cot^2\theta \sum_{m=\pm 1} [G|\lambda| - G|\lambda_0|]\, d\theta \quad ,$$

and $$F_o(X,Y) = \frac{1}{8\pi} \int_0^{\pi/2} \cot^2\theta \sum_{m=\pm 1} [\sin(\lambda) - \sin(\lambda_0)]\, d\theta \quad , \tag{20}$$

where $$X = x\,k_0 \quad \text{and} \quad Y = y\,k_0$$

and $$\lambda_0 = \Big[\lambda\Big]_{\theta=0} \quad . \tag{21}$$

Eq. (17) may then be written as

$$\hat{\zeta} = \hat{\zeta}_0 + \frac{1}{AB}[\,T(X-2A,Y-2B) - 2\,T(X-2A,Y) + T(X-2A,Y+2B) -$$
$$-\,T(X, \quad Y-2B) + 4\,T(X, \quad Y) + 2\,T(X, \quad Y+2B) + \qquad \text{(cont.)}$$

$$+ T(X+2A,Y-2B) - 2\,T(X+2A,Y) + T(X+2A,Y+2B)] \quad , \tag{22}$$

where $$A = a\,k_0 \quad \text{and} \quad B = b\,k_0 \quad ,$$

and the total disturbance from a "corner" is

$$T(X,Y) = F_e(X,Y) + F_o(X,Y) \quad . \tag{23}$$

2.3 Numerical Evaluation

Various numerical techniques for computing the corner wave functions, Eq. (20), were tested. These took into account the oscillating behavior of the integrand in Eq. (20b). For example, as θ approaches $\pi/2$, the oscillations become so cramped that a change of variable of the form

$$\theta' = \sin\theta/\cos^2\theta$$

is suggested. Eq. (20a) contains a similar badly behaved sinusoidal term. A further point of interest is that when $x = 0$ the integrand of Eq. (20a) has a logarithmic singularity at $\theta = 0$, so that the first step in the numerical θ integration was then performed separately.

However, one must consider that it is the summation in Eq. (22) that is required accurately, and to this end, it was found that the simple trapezoidal rule was the most efficient. The integration was carried right through to $\theta = \pi/2$ (but with the last term equivalent to zero) since the integrands die out quite slowly with respect to θ. It was found that a minimum of around 512 points in the θ integral (n_θ) was required for either the even or odd term. With $n_\theta = 1024$, the maximum error in the trapezoidal rule was found to be 8×10^{-6} for $|X|$ and $|Y| < 1$. (Only positive values of X and Y need to be computed.)

2.4 Results

The corner wave function is shown in Figs 3a and b. The curves show very little curvature for the range of argument values computed and this has accuracy implications when considering the summation in Eq. (22). The curves in Fig. 3a are even with respect to X and therefore have a dis-

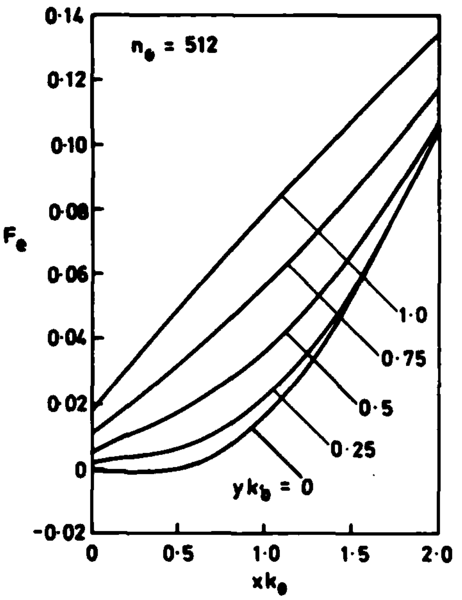

Fig. 3 Corner Wave Function
(a) Even Component

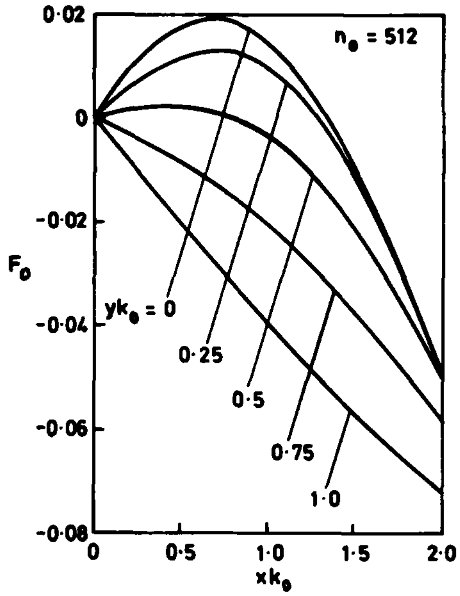

Fig. 3 Cont. (b) Odd Component

continuity in gradient at $X = 0$. Those in Fig. 3b are odd with respect to X . Both sets of curves are even with respect to Y .

The wave field itself, for a square-based pyramid ($a = b$) travelling at two different speeds is shown in Figs 4a and b. The maximum error in Fig. 4a was found to be about 0.005 - although the usual deterioration in accuracy, due to what is essentially a fourfold differentiation in Eq. (22), might suggest a still worse absolute error. The accuracy in Fig. 4b is somewhat better due to the wider spacing of the field points in the sum. (A measure of the error is also provided by the degree of smoothness in the way the wave dies away ahead of the pyramid.)

A further test of accuracy is displayed in Figs 5a and b. Here, a comparison is made with the twodimensional limit of the wave disturbance for an infinitely wide element ($b = \infty$) given by Doctors [16], and that obtained by summing up a series of threedimensional elements placed side-by-side and overlapping by the required $2b$. Any difference between the two would be attributed to the number of elements summed - as well as any error in the numerical integrations.

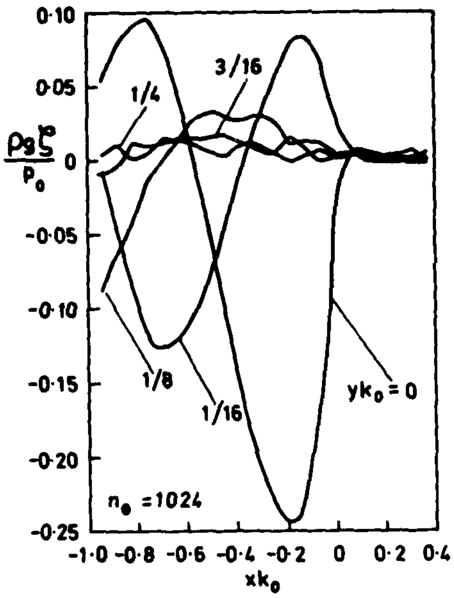

Fig. 4 Wave Field Produced by *Pressure Pyramid* (a) $ak_0 = bk_0 = 1/32$

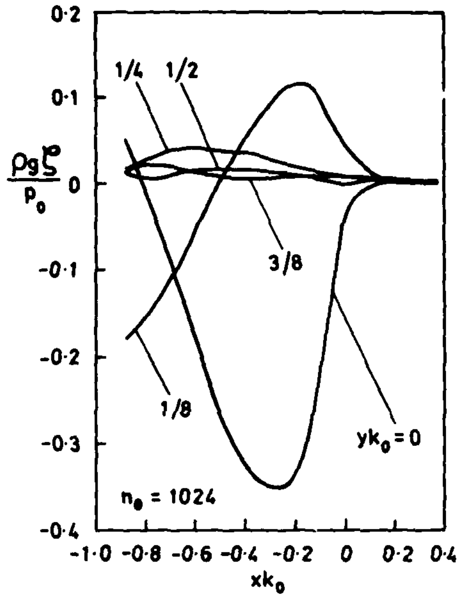

Fig. 4 Cont. (b) $ak_0 = bk_0 = 1/16$

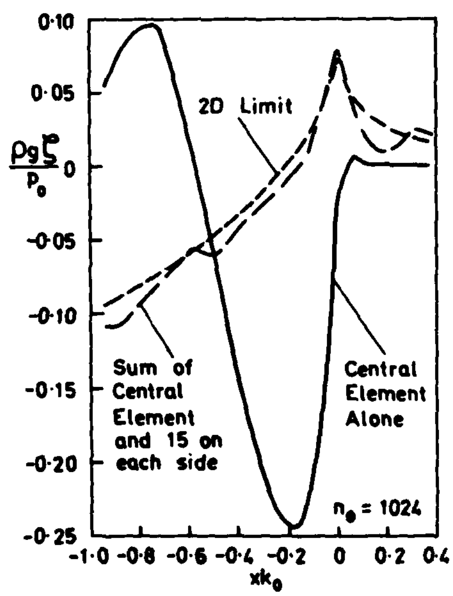

Fig 5 Twodimensional Limit of Wave Field (a) $ak_0 = bk_0 = 1/32$

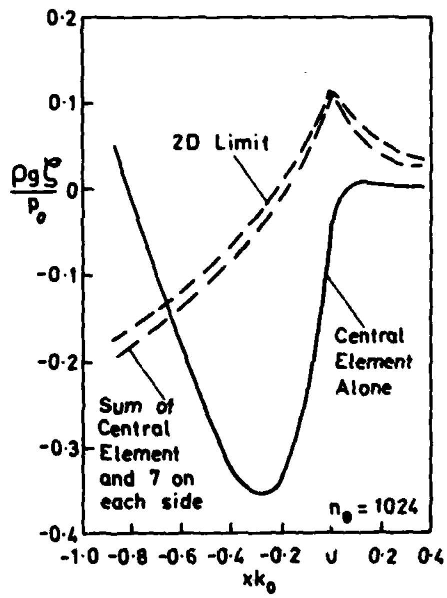

Fig 5 Cont. (b) $ak_0 = bk_0 = 1/16$

3. Combining the Elements

3.1 Use of Identical Elements

It had been planned to use elements with an arbitrary length $4a$ which would depend on the transverse position of its centroid. Thus the length of the wetted surface, which varies between L_c and L, could be composed of an integral number of elements. Unfortunately, the previously mentioned accuracy of the corner wave functions did not permit interpolation between computed points. Thus the pyramid base dimensions had to be a whole multiple of the spacing of points used in computing Fig. 3.

The array of elements shown in Fig. 2 is symmetrical about the longitudinal axis of the boat. Taking into account the image element, one obtains the wave elevation at a field point i (x_i, y_i) due to a source element j (x_j, y_j) of unit pressure as

$$\rho g K_{ij} = \hat{\zeta}(x_i-x_j, y_i-y_j) + \hat{\zeta}(x_i-x_j, y_i+y_j) \quad . \tag{24}$$

The kinematic condition on the hull requires that the sum of all such influences at each field point must equal the height of the hull there. Thus

$$\sum_{j=1}^{n_p} K_{ij}\, p_j = -h + \alpha x_i + \frac{2 d y_i}{B} \quad \text{for} \quad 1 \le i \le n_p \quad . \tag{25}$$

In this equation the unknown depth of the center of the trailing edge, the trim angle and the deadrise have been taken into account. Note that B, which has two meanings, is the craft beam here. Eq. (25) produces n_p equations (the number of field points), but there are $n_p + 2$ unknowns - the additional two being h and α.

An extra pair of equations is obtained by considering equilibrium of the boat with respect to weight and center of gravity:

$$\frac{1}{2}W = S \sum_{j=1}^{n_p} p_j \quad ,$$

and

$$\frac{1}{2}W\bar{x} = S \sum_{j=1}^{n_p} p_j\, x_j \quad , \tag{26}$$

where W is the weight of the boat and $\tilde{x}$ is the longitudinal position of its center of gravity. The nominal area of each element is given by

$$S = 4ab \quad . \tag{27}$$

3.2 Kutta Condition

Assuming an initial estimate of the wetted area shape, one can obtain the best number of elements along each buttock line and solve the $n_p + 2$ equations given by Eqs (25) and (26).

One must also satisfy the Kutta condition at the trailing edge. From a *physical* point of view this seems to be sufficient. It also gives an extra equation for each buttock - required to solve the wetted length at each such line. Oertel, in fact, gave a mathematical argument supporting this. Incidentally, in the nonlinear viscous situation with surface tension, there is effectively *a Kutta condition to be applied along the entire* perimeter of the craft.

From the estimated wetted area and the resulting pressure distribution, the error in not satisfying this condition is

$$e_i = \sum_{j=1}^{n_p} K_{ij}\, p_j + h - \frac{2\,d\,y_i}{B} \quad \text{for} \quad 1 \le i \le n_y \quad , \tag{28}$$

where n_y is the number of buttocks used and now $x_i = 0$ in Eq. (24).

A correction to each wetted length can be made by using an n_y-dimensional Newton-Raphson technique (see Carnahan, Luther and Wilkes [36], p. 319). By incrementing each buttock line by one element in turn, the various gradients can be obtained from the changes in the error given by Eq. (28). Hence

$$\frac{\partial e_i}{\partial L_j} = \Delta e_i / 2a \quad \text{(for the change in the j'th buttock)} \quad , \tag{29}$$

and the required alterations to the lengths are given by

$$\sum_{j=1}^{n_y} \frac{\partial e_i}{\partial L_j} \cdot \Delta L_j = e_i \quad \text{for} \quad 1 \le i \le n_y \quad . \tag{30}$$

This set of equations can be solved by inversion in the usual way.

The iteration can proceed until the predicted changes in length, ΔL_i , are less than the nominal element length, $2a$.

4. Results

4.1 Presentation of Data

From the dimensions of the boat in the hydrostatic condition (i.e., at rest), one can derive its weight and center of gravity:

$$W^* = \frac{W}{\rho g B^2 h_0} = \frac{1}{6} L_0^*(3 - 3\,d^* + d^{*2})$$

and

$$\bar{x}^*\, W^* = \frac{\bar{x}\, W}{\rho g B^3 h_0} = \frac{1}{24} L_0^{*2}(4 - 6\,d^* + 4\,d^{*2} - d^{*3}) \quad , \tag{31}$$

for use in Eq. (26). (Variables indicated by an asterisk have been nondimensionalized as described in the Introduction.)

An initial estimate of the wetted length was obtained from the following formula for the location of the center of pressure, taken from Savitsky [27]:

$$\bar{x}^* = \bar{L}^*\{0.75 - 1/[2.39 + 5.21(F_B/\bar{L}^*)^2]\} \quad , \tag{32}$$

where $\bar{L}$ is the average wetted length. This empirical formula indicates that there is no effect of deadrise on the center of pressure (for any *moving* wetted length).

Savitsky also gave an experimental formula for the lift coefficient for a flat plate:

$$C_L = \frac{W}{\frac{1}{2}\rho V^2 B^2} = \alpha^{1.1}\,(0.0120\,\bar{L}^{*1/2} + 0.0055\,\bar{L}^{*5/2}/F_B^{\,2}) \quad ,$$

valid for $2^\circ < \alpha < 15^\circ$. However, to make a comparison with our linear case, we let $\alpha \to 0$ and express the angle in radians to obtain

$$C_L/\alpha = 57.29\,(0.0120\,\bar{L}^{*1/2} + 0.0055\,\bar{L}^{*5/2}/F_B^{\,2}) \quad . \tag{33}$$

For a prismatic surface with a deadrise angle of β , the following empiri-

cal formula was given:

$$C_L = \Big[C_L\Big]_{\beta=0} - 0.0065\,\beta\left\{\Big[C_L\Big]_{\beta=0}\right\}^{0.60} .$$

Thus, in the limit, for small angles

$$C_L = \Big[C_L\Big]_{\beta=0} , \tag{34}$$

indicating no effect of deadrise (in the linear sense) for any particular average wetted length. The lift coefficient may also be deduced from the results of the theory as

$$C_L/\alpha = 2\,W^*/\alpha^*\,F_B{}^2 . \tag{35}$$

For a *flat* plate, Savitsky gave the following pair of formulas for the length immersed below the undisturbed free surface, L_i , as a function of the average overall wetted length:

$$L^* = L_i{}^* + 0.30 \qquad \text{for} \quad 1 \le L_i{}^* \le 4$$

and $$L^* = 1.60\,L_i{}^* - 0.30\,L_i{}^{*2} \qquad \text{for} \quad 0 \le L_i{}^* \le 1 . \tag{36}$$

On the other hand, the immersed length can be obtained from the theory using

$$L_i{}^* = h^*/\alpha^* . \tag{37}$$

4.2 Results for a Flat Plate

Figs 6a, b and c present results for the planing of a flat plate at four different beam Froude numbers, and make comparisons with Savitsky's experimental curves. Following his method, the abscissa used is the average wetted length. Examining firstly the variation of hydrostatic length with wetted length, in Fig. 6a, the theory is seen to be close to the experiment, and underpredicts by only about 4%. The weak trend of decreasing hydrostatic length with decreasing Froude number is also verified.

Excellent agreement for the immersed length is also displayed in

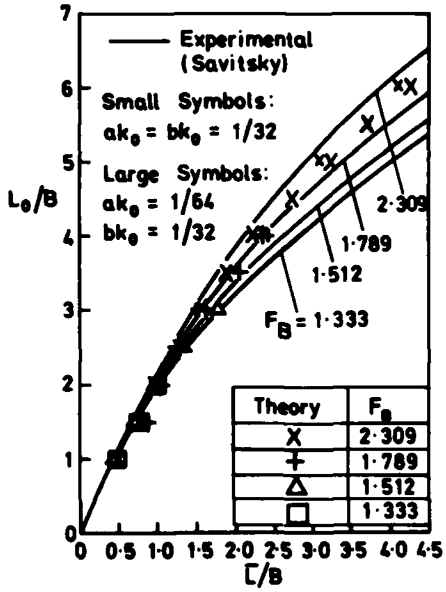

Fig 6 Results for Flat Plate
(a) Hydrostatic Length

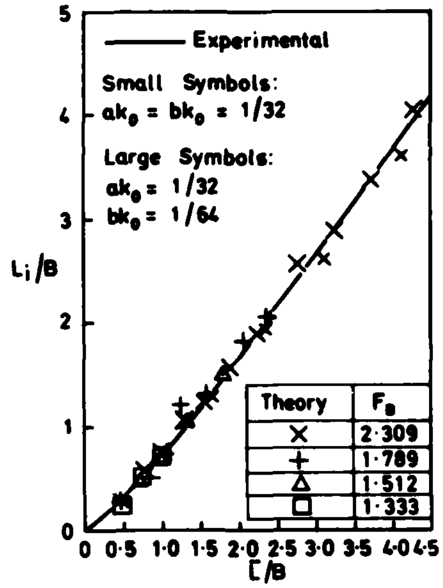

Fig 6 Cont.
(b) Wetted Area below Free Surface

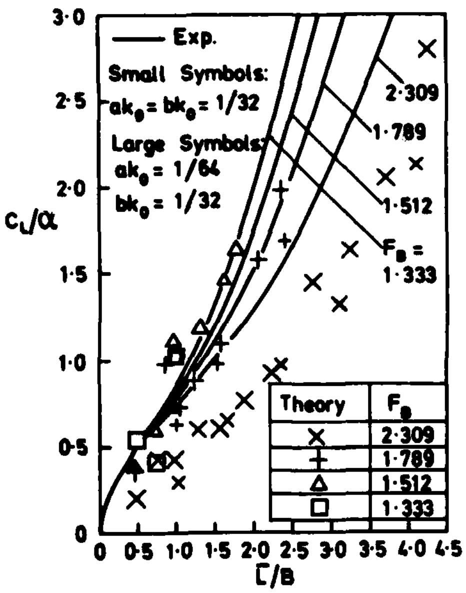

Fig 6 Cont. (c) Lift Coefficient

Fig. 6b. An interesting feature of flat-plate planing - that Froude number has no effect on the curve when plotted this way - is also verified.

Finally, the lift coefficient is shown in Fig. 6c. For length-to-beam ratios greater than about 1.0, the theory predicts a lift which is around 30% too low for a high beam Froude number. The error is, however, reduced at the lower Froude numbers. Of the two element sizes used, the smaller ones produce better results. It should be pointed out, that one should not expect too good an agreement for length-to-beam ratios less than 1.0 since only a

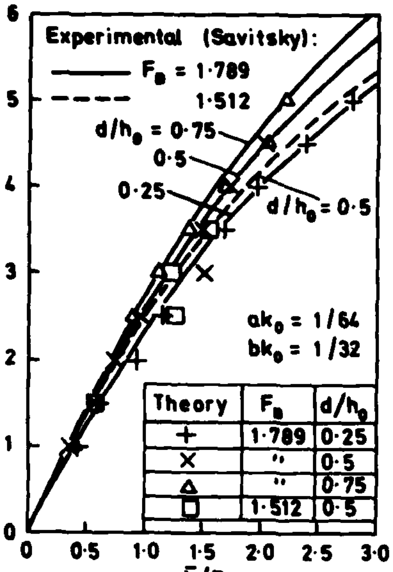

Fig 7 Results for Prismatic Hull
(a) Hydrostatic Length

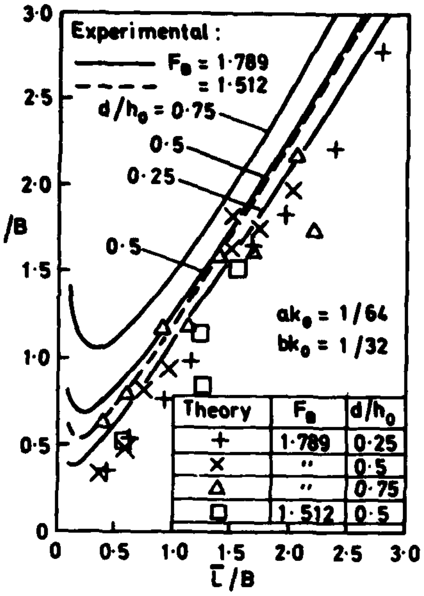

Fig. 7 Cont.
(b) Wetted Area below Free Surface

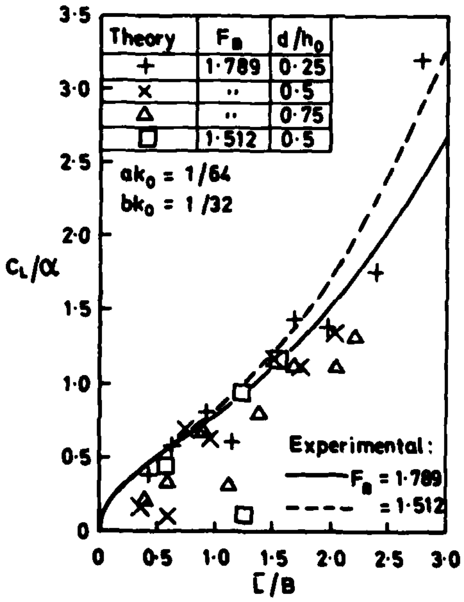

Fig. 7 Cont. (c) Lift Coefficient

small number of elements in the longitudinal direction were used then (about 4). One then needs to use somewhat shorter (longitudinally) elements.

4.3 Results for a Prismatic Hull

Figs 7a, b and c show a similar set of results for a planing surface with deadrise. Two beam Froude numbers and three amounts of deadrise are considered. Fig. 7a displays very good agreement between the theory and experiment for the hydrostatic length. In particular, the small increase in hydrostatic

length due to increasing deadrise is confirmed closely.

The wetted area below the undisturbed free surface, in Fig. 7b, is not predicted as well as for the case of the flat plate (Fig. 6b). However, the correct trend due to variations in deadrise *is* verified. It was found that the *overall* length of the boat, L , was in better agreement with these empirical curves. (Savitsky noted that, in practice, there is no build-up of water ahead of the keel of a prismatic hull at small angles of trim: that is $L = L_i$. However, the theory indicated that $L > L_i$ by perhaps 5% and this is undoubtedly partly due to the small number of elements used.)

Finally, the lift coefficient is shown in Fig. 7c. For length-to-beam ratios less than 1.5, the agreement is poor, rather similar to the case of the flat plate in Fig. 6c. The fact that the empirical formula, Eq. (34), indicates no effect of deadrise on lift coefficient at small angles of trim seems to be corroborated. One needs more computed points to confirm this.

4.4 Pressure Distributions

The last set of results displays sample longitudinal pressure distributions. An example where only one buttock line of elements is used on each side of the centerline ($n_y = 1$), for a flat plate, is shown in Fig. 8a. Various length-to-beam ratios are considered. The general form of the distribution is as one would expect: a peak near the leading edge - representing the singularity produced by the linear theory is evident. However, oscillations in the curves also occur, and a region of negative pressure near the stern is seen in two cases.

These are probably due to two causes: the imprecision of the values of K_{ij} in Eq. (25), referred to previously, and the fact that in general a whole number of elements will not fit into the length of the plate (leaving a discrepancy in a critical region).

The quality of the pressure-distribution curves deteriorates when we pass onto the cases of two and three buttock lines ($n_y = 2$ and 3) in Figs 8b and c, respectively. Unrealistic oscillations are predicted. However, the mean curves tend to be rather better. It would appear that the reason the very encouraging data points presented in Figs 6 and 7 do

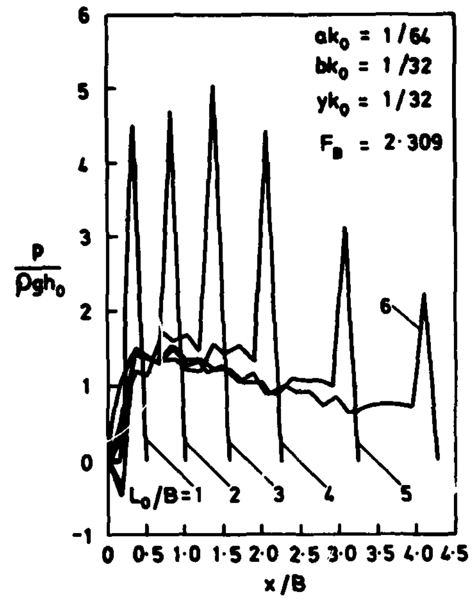

Fig. 8 Pressure Distributions
(a) Flat Plate ($n_y = 1$)

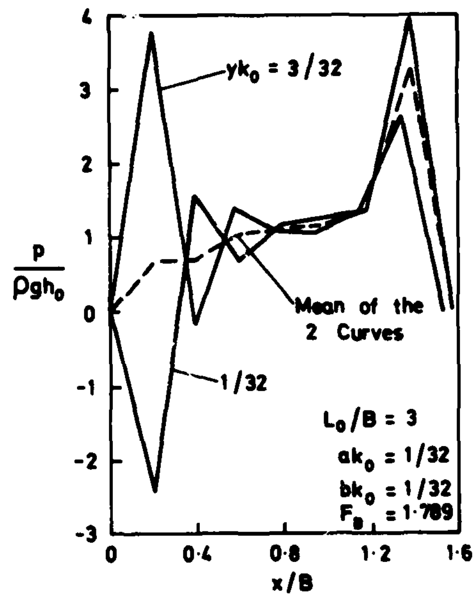

Fig. 8 Cont. (b) Flat Plate ($n_y = 2$)

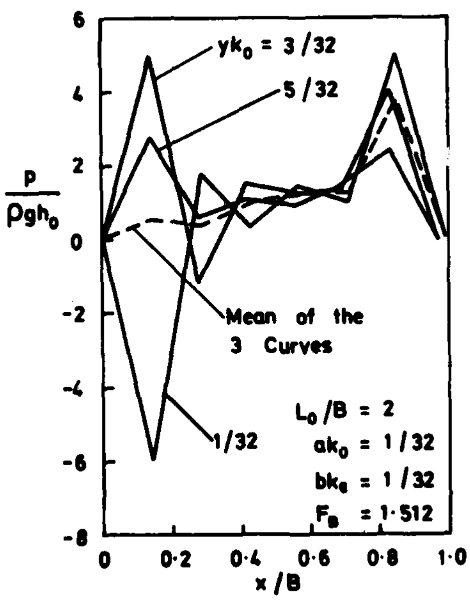

Fig. 8 Cont. (c) Flat Plate ($n_y = 3$)

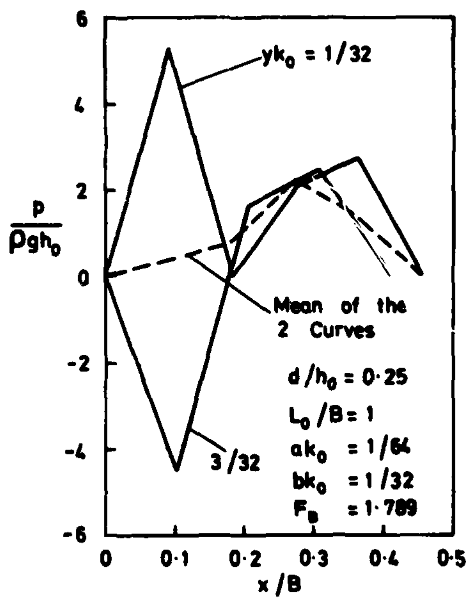

Fig. 8 Cont. (d) Prismatic Hull ($n_y = 2$)

not display this feature is that they represent an integrated effect of the pressure distibution.

An example of the distribution of pressure for a prismatic surface with $d/h_0 = 0.25$ is shown in Fig. 8d. A similar oscillatory behavior is observed.

5. Concluding Remarks

5.1 Present Work

The theoretical results presented in Figs 6 and 7 indicate that the basis of the method given here is sound. This is certainly so, when one considers that part of the error, when making comparisons with experiments, must be due to nonlinear effects, and viscosity, which are of course strictly ignored. Furthermore, the empirical results themselves represent fitted curves.

One difficulty associated with the Newton-Raphson iteration given in Eqs (29) and (30) was that the predicted wetted-length changes tended to be overestimated by around 100 - 150%. This was presumably due to the finite-difference method of computing the gradients. (It might also be related to the singularity line at the leading edge.) As a result, the iteration frequently did not converge when used in the form shown - but instead, the lengths oscillated about the correct values.

This problem was overcome by introducing a multiplicative damping factor to the right-hand side of Eq. (30). A value of 0.5 cured the oscillations and consequently convergence was usually achieved in 2 or 3 iterations.

5.2 Future Work

The first stage of refinement to the procedure should be to improve the accuracy of the results for the disturbance due to a pressure pyramid. It is felt that a simple brute-force approach - increasing the number of points in the θ integrals in Eq. (20) will not suffice. This is due to the argument of the various functions, namely λ, rapidly approaching infinity at the upper limit of the integration. Instead, it might be possible to recast the integrals in a different form.

A procedure more likely to succeed is to derive asymptotic expressions for the corner functions, F_e and F_o, valid for small values of X and Y (the high-speed limit). This would allow a completely arbitrary pyramid base size to be used, and thus permit the elements to be precisely fitted into the wetted lengths.

With such analytic expressions, the numerical differentiation, utilized in Eq. (29), could be avoided. This would eliminate the abovementioned problem of divergence in the iteration.

6. Bibliography

1. Sretenskii, L.N.: "On the Motion of a Glider on Deep Water", *Izv. Akad. Nauk SSSR., Otdel. Mat. Estest. Nauk, 1933*, pp 817-835 (in English) (1933)
2. Sretenskii, L.N.: "On the Theory of the Glider", *Izv. Akad. Nauk SSSR., Otdel. Tekhn. Nauk, 1940*, 7, pp 3-26 (in Russian) (1940)
3. Sedov, L.I.: "The Plane Problem of Gliding on the Surface of a Heavy Fluid", *Trudy Konferentsii po Teorii Volnovogo Soprotivleniya*, Moscow, pp 7-30 (in Russian) (1936). Also: *Tsentral. Aero-Gidrodinam. Inst. Moscow* (1937)
4. Maruo, H.: "Twodimensional Theory of the Hydroplane", *Proc. First Japan Nat. Cong. Appl. Mech.*, Science Council of Japan, Tokyo, pp 409-415 (1952)
5. Maruo, H.: "Hydrodynamic Researches of the Hydroplane, Part 1", *J. Zôsen Kiôkai (J. Soc. Nav. Arch. Japan), 91*, pp 9-16 (in Japanese) (1956)
6. Maruo, H.: Ibid, Part 2, *92*, pp 57-63 (1957)
7. Maruo, H.: Ibid, Part 3, *105*, pp 23-26 (1959)
8. Squire, H.B.: "The Motion of a Simple Wedge along the Water Surface", *Proc. Roy. Soc. London, Series A, 243*, pp 48-64 (1957)
9. Cumberbatch, E.: "Two-dimensional Planing at High Froude Number", *J. Fluid Mechanics, 4*, Part 5, pp 466-478 (1958)
10. Wehausen, J.V. and Laitone, E.V.: "Surface Waves", *Encyclopedia of Physics, 9,* Fluid Dynamics 3, ed. by S. Flügge, Springer-Verlag, Berlin, pp 446-815 (1960)
11. Green, A.E.: "The Gliding of a Plate on a Stream of Finite Depth, Part 1", *Proc. Cambridge Phil. Soc., 31,* pp 589-603 (1935)
12. Green, A.E.: Ibid, Part 2, *32*, pp 67-85 (1936)
13. Green, A.E.: "Note on the Gliding of a Plate on the Surface of a Stream", *Proc. Cambridge Phil. Soc., 32,* pp 248-252 (1936)
14. Wu, T.Y.: "A Singular Perturbation Theory for Nonlinear Free-Surface Flow Problems", *Int. Shipbuilding Progress, 14,* 151, pp 88-97 (1967)
15. Wu, T.Y. and Whitney, A.K.: "Theory of Optimum Shapes in Free-Surface Flows, Part 1, Optimum Profile of Sprayless Planing Surface", *J. Fluid Mechanics, 55,* Part 3, pp 439-455 (1972)
16. Doctors, L.J.: "Representation of Planing Surface by Finite Pressure Elements", *Proc. Fifth Australasian Conference on Hydraulics and Fluid Mechanics, 2,* pp 480-488 (1974)

17. Wagner, H.: "Über Stoss- und Gleitvorgänge an der Oberflächen von Flüssigkeiten", *Zeitschrift für Angewandte Mathematik und Mechanik, 12,* Heft 4, pp 193-215 (1932)

18. Tulin, M.P.: "The Theory of Slender Surfaces Planing at High Speeds", *Schiffstechnik, 4,* Heft 21, pp 125-133 (in English) (1957)

19. Maruo, H.: "High- and Low-Aspect Ratio Approximations of Planing Surfaces", *Schiffstechnik, 14,* Heft 72, pp 57-64 (in English) (1967)

20. Shen, Y.T.: "Theory of High-Aspect Ratio Planing Surfaces", Dept. Nav. Arch. and Marine Eng., Univ. Michigan, Ann Arbor, Michigan, Rep. 102, 123+vii pp (1970)

21. Shen, Y.T. and Ogilvie, T.F.: "Nonlinear Hydrodynamic Theory for Finite-Span Planing Surfaces", *J. Ship Research, 16,* 1, pp 3-20 (1972)

22. Wang, D.P. and Rispin, P.: "Three-dimensional Planing at High Froude Number", *J. Ship Research, 15,* 3, pp 221-230 (1971)

23. Tuck, E.O.: "Low-Aspect-Ratio Flat-Ship Theory", *J. Hydronautics, 9,* 1, pp 3-12 (1975)

24. Oertel, R.P.: "The Steady Motion of a Flat Ship Including an Investigation of Local Flow near the Bow", Ph. D. thesis, Dept. Applied Mathematics, Univ. Adelaide, Adelaide, Australia, 113+vii pp (1975)

25. Clement, E.P. and Blount, D.L.: "Resistance Tests of a Systematic Series of Planing Hull Forms", *Trans. Soc. Naval Architects and Marine Engineers, 71,* pp 491-579 (1963)

26. Hadler, J.: "The Prediction of Power Performance on Planing Craft", *Trans. Soc. Naval Architects and Marine Engineers, 74,* pp 563-610 (1966)

27. Savitsky, D.: "Hydrodynamic Design of Planing Hulls", *Marine Technology, 1,* 1, pp 71-95 (1964)

28. Savitsky, D.: "Planing Craft", Panel Discussion, *Proc. Seventh Symposium on Naval Hydrodynamics*, Office of Naval Research, August 25-30, Rome, pp 1163-1168 (1968)

29. Savitsky, D.: "Hydrodynamic Development of a High Speed Planing Hull for Rough Water", *Proc. Ninth Symposium on Naval Hydrodynamics*, Office of Naval Research, August 20-25, Paris, pp 419-461 (1972)

30. Du Cane, P.: *High Speed Small Craft*, Temple Press, London, 278+ ix pp (1951)

31. Parkinson, J.B.: "Hydrodynamics of High-Speed Water-Based Aircraft", *Proc. First Symposium on Naval Hydrodynamics*, Office of Naval Research, September 24-28, Washington, pp 181-213 (1956)

32. Angeli, J.C.: "Evaluation of the Trim of a Planing Boat at Inception of Porpoising", *Proc. Spring Meeting, Soc. Naval Architects and Marine Engineers*, April 2-4, Lake Buena Vista, Florida, 6 pp (1973)

33. Payne, P.R.: "Coupled Pitch and Heave Porpoising Instability in Hydrodynamic Planing", *J. Hydronautics, 8,* 2, pp 58-71 (1974)

34. Latorre, R. and Tamiya, S.: "An Experimental Technique for Studying the Planing Boat Spray and Deriving the Pressure Resistance Component", *Proc. Fourteenth International Towing Tank Conference*, Ottawa, Canada, September 2-12, 10 pp (1975)

35. Abramowitz, M. and Stegun, I.A.: *Handbook of Mathematical Functions*, Applied Mathematics Series - 55, Nat. Bureau of Standards, U.S. Govt. Printing Office, Washington, 1046+xiv pp (1965)

36. Carnahan, B., Luther, H.A. and Wilkes, J.O.: *Applied Numerical Methods*, John Wiley and Sons, Inc., New York, 604+xvii pp (1969)

HYDRODYNAMIC FORCES ON A BODY MOVING BENEATH A FREE SURFACE

M.S. Chang and P.C. Pien

David W. Taylor Naval Ship Research and Development Center
Bethesda, Maryland 20084 U.S.A.

ABSTRACT

The pressure distribution on a body moving near a free surface is calculated by numerically differentiating the velocity potential on the body's surface. This potential is obtained from a given potential inside the body surface through a singularity kernel for a doublet. The resulting wave resistance and lift for two- and three-dimensional bodies are compared with available data. The advantage of this approach in comparison to the usual source distribution method is discussed. An extension of the approach to the problem of a body moving in the free surface is also presented.

1. Introduction

There are two methods commonly used in computing hydrodynamic forces and moments acting on a body moving in or beneath a free surface; namely, the singularity method and the method of direct solution of the field equations using finite difference or finite element numerical techniques. There are certain advantages as well as disadvantages associated with each method. In a singularity method, the Laplace equation and the far-field boundary conditions are automatically satisfied by choosing a proper kernel function. However, it is quite tedious to compute the pressure distribution on the body surface from the singularity distribution. On the other hand, in a direct solution method, the velocity potential on the body surface is computed first, so that the body pressure distribution can be readily obtained. However, to satisfy the Laplace equation and far-field conditions, a finite difference or finite element method requires a large number of meshes and thus a large amount of computation. It is the intent of the present paper to describe an inner-potential doublet-distribution method which takes advantage of the two currently-used methods.

The motion of a body in an irrotational and incompressible fluid generates a potential

field in a fluid which in turn generates a dynamic pressure distribution on the body surface. This pressure distribution can be expressed in terms of the velocity potential on the body surface. Thus, the forces and moments on a moving body can be evaluated once the potential on the body surface is known. A body moving in an infinite fluid may be represented by either a sink-source distribution or a doublet distribution on the surface of the body. However, as shown in Lamb[1], if the body is represented by a doublet distribution, the potential on the body surface simply becomes the sum of the doublet strength and the velocity potential **inside** of the body surface. There is no such one-to-one correspondence if the body is represented by a source-sink distribution. Brard[2] showed that the above conclusion also applies to a body moving under a linearized free surface. For a body moving on the free surface, Brard showed that an additional line distribution of sources and doublets on the contour, C, of the intersection of the body surface and the undisturbed free surface, is required when the Kelvin singularity is used as the kernel function. However, the correspondence between the velocity potential and the doublet strength is unaltered; the correspondence is the same as that for the submerged case.

Theoretically, one may choose any type of singularities in representing a moving body. A source-sink distribution is customarily used.[3,4] For numerical computations, it was suggested by Pien and Chang[5] that the use of a doublet distribution on the body surface will have an advantage over the source-sink distribution because of the above mentioned correspondence between the velocity potential on the body surface and the strength of the doublet. Pien[6] has calculated the velocity potential for infinite-fluid body-motion problems using the method proposed by Pien and Chang[5]. He showed that, for the same accuracy of computed pressure coefficients, the use of a doublet distribution requires fewer control panels than needed when using a sink-source distribution. It has to be emphasized that in the approach of Pien and Chang, the doublet distribution is determined from the known velocity potential inside the body surface and the velocities are calculated by a finite difference scheme from the doublet strength obtained. It is thus a combined singularity and finite difference method which is different from the customarily used doublet-distribution method.[7] In the traditional method the doublet distribution is determined from the normal velocities on the body surface and the velocities on the surface are calculated from the doublets through integration. The reason the relationship between doublet strength and velocity potential has not been used in calculating velocities is that the inner potential was never considered in the previous doublet methods.

The present paper applies the approach of Pien and Chang[5] to both linearized free surface problems and unsteady infinite flow problems. In the next section a brief summary of the

approach will be given. In the following section, applications to four particular problems will be described: (1) infinite fluid unsteady flow problem; (2) free-surface problem for submerged axisymmetric body; (3) free-surface problem for submerged two-dimensional lifting body; and (4) free-surface problem for surface-piercing body.

2. Formulation of Inner-Potential Doublet Distribution Approach

2.1 Determination of Velocity Potential on Body Surface

In order to distinguish the doublet-distribution approach proposed by Pien and Chang[5] from the previous doublet-distribution methods, we will call the method of Pien and Chang the inner-potential doublet-distribution approach. The details of this approach are described in Reference 5. Only a brief summary of the basic method will be presented here.

A. Submerged Body

Let S_B be a closed surface which represents the surface of a body submerged in a fluid region R_o; let S_o be the outer boundaries of the region R_o, and R_i be the space occupied by the body. Then, from Greens theorem, the velocity potentials ϕ_o and ϕ_i, in R_o and R_i can be expressed as

$$\begin{aligned} \phi_o(P) &= -\frac{1}{4\pi}\iint_{S_B+S_o}\left[G(P,Q)\frac{\partial\phi_o(Q)}{\partial n} - \phi_o(Q)\frac{\partial G(P,Q)}{\partial n}\right]dS \quad P\epsilon R_o \\ \phi_i(P) &= -\frac{1}{4\pi}\iint_{S_B}\left[G(P,Q)\frac{\partial\phi_i(Q)}{\partial n'} - \phi_i(Q)\frac{\partial G(P,Q)}{\partial n'}\right]dS \quad P\epsilon R_i \end{aligned} \tag{1}$$

and

$$\begin{aligned} 0 &= -\frac{1}{4\pi}\iint_{S_B+S_o}\left[G(P,Q)\frac{\partial\phi_o(Q)}{\partial n} - \phi_o(Q)\frac{\partial G(P,Q)}{\partial n}\right]dS \quad P\epsilon R_i \\ 0 &= -\frac{1}{4\pi}\iint_{S_B}\left[G(P,Q)\frac{\partial\phi_i(Q)}{\partial n'} - \phi_i(Q)\frac{\partial G(P,Q)}{\partial n'}\right]dS \quad P\epsilon R_o \end{aligned} \tag{2}$$

Here, G is a Green Function with a $1/r$ singularity at P, Q is a field point and n and n′ denote the unit vector normal to the surface, directed interior to the regions R_o and R_i, respectively. If the normal velocities $\partial\phi_o/\partial n$ and $\partial\phi_i/\partial n'$ are continuous through the body surface, S_B, addition of Equations (1) and (2), shows that

$$\frac{1}{4\pi}\iint_{S_B}[\phi_o(Q)-\phi_i(Q)]\,\frac{\partial G(P,Q)}{\partial n}\,dS - \iint_{S_o}\left[G(P,Q)\frac{\partial\phi_o(Q)}{\partial n} - \phi_o(Q)\frac{\partial G(P,Q)}{\partial n}\right]dS = \begin{cases}\phi_o(P) & P\epsilon R_o \\ \phi_i(P) & P\epsilon R_i\end{cases} \tag{3}$$

This expression gives the velocity potentials ϕ_o and ϕ_i in terms of the difference between ϕ_o and ϕ_i on the surface S_B and the difference between ϕ_o and $\partial\phi_o/\partial n$ on the external boundary, S_o. If, furthermore, there exists a G such that

$$\iint_{S_o} \left(\phi_o \frac{\partial G}{\partial n} - G \frac{\partial \phi_o}{\partial n}\right) dS = 0 \text{ in } R_o \text{ and } R_i \tag{4}$$

then, with respect to this specific G, Equation (3) simply becomes,

$$\frac{1}{4\pi} \iint_{S_B} (\phi_o - \phi_i) \frac{\partial G}{\partial n} dS = \begin{cases} \phi_o(P) & P \epsilon R_o & (5) \\ \phi_i(P) & P \epsilon R_i & (6) \end{cases}$$

One can now conclude from Equation (6) that with a given ϕ_i, whose normal derivative is equal to that of ϕ_o on the surface S_B, and a given G which satisfies (4), the velocity potential on the body surface can be expressed as the sum of a doublet distribution D, and the known velocity potential ϕ_i on the inside surface of the body, where D satisfies

$$\frac{1}{4\pi} \iint_{S_B} D \frac{\partial G}{\partial n} dS = \phi_i(P) \quad P \epsilon R_i \tag{7}$$

Symbolically, one writes

$$\phi_o(P) = D(P) + \phi_i(P) \quad P \text{ on } S_B \tag{8}$$

and

$$\phi_o(P) = \frac{1}{4\pi} \iint_{S_B} D(P) \frac{\partial G(P,Q)}{\partial n_Q} dS \quad P \epsilon R_o \tag{9}$$

with D determined from Equation (7).

To obtain the velocity potential on the body surface is simple if the two assumptions which lead to Equations (8) and (9) can be easily fulfilled. Unfortunately, this is not so for an arbitrary fluid region R_o because, for an arbitrary boundary S_o, one may face difficulties in formulating a G satisfying condition (4). Yet, many problems in naval hydrodynamics do have a simple boundary S_o and the required G can be found easily. For example, G is $1/r$ for an infinite fluid, $(1/r)-(1/r^*)$ for a semi-infinite fluid with a rigid wall, and G is a Kelvin singularity for linearized free-surface problems;[2] in these cases r and r* are the distances between a field point and the source point and the image source point, respectively. To generate a velocity potential ϕ_i, which satisfies the requirement that $\partial\phi_o/\partial n = \partial\phi_i/\partial n$ is not difficult. It is[1]

$$\phi_i = -ux - vy - wz + \epsilon\chi_1 + q\chi_2 + S\chi_3 \tag{10}$$

where u, v and w are the velocity components of the moving body in the directions of the x-, y- and z-axes, respectively; and χ_1, χ_2, χ_3 are the velocity potentials generated by a unit rotation of the body surface S_B with respect to the x-, y-, z-axes, respectively. For a body undergoing only translation motion ϕ_i becomes -ux-vy-wz. It is independent of the shape of the body and the fluid boundary S_0. In this paper only velocity potentials generated by translation motions will be discussed. Without loss of generality, the body will be considered as moving only along the x-axis.

B. Bodies in Free Surface

The linearized free-surface problem for a surface piercing body differs from that of a submerged body in two respects. First, the contour C, which is the intersection of the undisturbed free surface and the ship hull is a boundary of the free surface. Second, the ship hull, S_B is not a closed surface as it is for a submerged body. Because of the contour C, the condition (4) is no longer satisfied in R_0 when a Kelvin singularity is used as G. Because the surface S_B is not closed, one does not have a closed fluid region R_i *unless some imaginary* surface, such as the undisturbed free surface enclosed in the body surface, is also considered as a part of the body surface. With the above two modifications Brard[2] showed that the velocity potentials ϕ_0 and ϕ_i are given by

$$\frac{1}{4\pi}\left[\iint_{S_B}(\phi_0 - \phi_i)\frac{\partial G}{\partial n}\,dS - \frac{1}{K_0}\int_C\left[\frac{\partial(\phi_0 - \phi_i)}{\partial x}G - (\phi_0 - \phi_i)\frac{\partial G}{\partial x}\right]dy = \begin{cases}\phi_0(P) & P\epsilon R_0 \quad (11)\\ \phi_i(P) & P\epsilon R_i \quad (12)\end{cases}\right.$$

respectively, where $K_0 = U^2/g$ is the wave number and g is the acceleration of gravity. In comparison with Equations (5) and (6) for a submerged body, an additional integral around the contour C is required for a surface piercing body. It is interesting to note from Equations (11) and (12) that, as is the case of a submerged body, the body surface is again represented by a doublet distribution alone and the strength of the doublet is again the difference of velocity potentials on the inside and the outside of the body surface.

In summary, for a body moving along the x-axis, the velocity potential on the body surface is

$$\phi_0(P) = D(P) + \phi_i(P) \text{ and } \frac{\partial\phi_0(P)}{\partial n} = -U\frac{\partial x}{\partial n} \qquad P \text{ on } S_B \tag{13}$$

providing that the singularity function, G, is chosen properly. The doublet distribution D for the surface-piercing body is obtained from

$$\phi_i(P) = \frac{1}{4\pi}\left\{\iint_{S_B} D\,\frac{\partial G}{\partial n}\,dS - \int_C \frac{1}{K_o}\left[\frac{\partial(\phi_o - \phi_i)}{\partial x}\,G - (\phi_o - \phi_i)\,\frac{\partial G}{\partial x}\right]dy\right\} \tag{14}$$

Numercially, Equation (14) is n' ' convenient to work with. A later section discusses some modifications whi. will be made when we apply the inner potential doublet distribution method to surface piercing bodies.

2.2 Evaluation of Pressure Distribution

In an irrotational flow, the pressure, p, on a body surface can be expressed in terms of the velocity potential, ϕ_o, through Bernoulli's equation[8]

$$P = \rho\left\{\frac{\partial\phi_o}{\partial t} - \frac{1}{2}\,|\,\nabla(\phi_o - Ux)\,|^2 + \frac{1}{2}\,U^2\right\} + c(t) \tag{15}$$

where ρ is the density of the fluid, ∇ is the gradient operator and c is the Bernoulli constant. Since $\nabla(\phi_o + Ux)$ can be decomposed into $\nabla_n(\phi_o + Ux)$ and $\nabla_s(\phi_o + Ux)$, where ∇_n and ∇_s denote the gradient components in directions normal and tangent to the body surface, respectively; $\nabla_n(\phi_o + Ux)$ is identically zero on the body surface. Thus, in a numerical evaluation of the body pressure only a knowledge of the velocity potential on the body surface is needed. Note that the Bernoulli constant, c, is only a function of time t for an irrotational flow and does not result in net forces and moments on the body. In the inner-potential doublet-distribution method, ϕ_o is obtained directly from (13) after the doublet distribution is determined from (14). A finite difference (or a finite element) scheme can be developed to calculate $\nabla_s(\phi_o + Ux)$ and then the body forces and moments associated with the surface gradient can be calculated. In the numerical examples given later the relative tangential velocities $\nabla_s(\phi_o + Ux)$ are calculated by a first-order finite difference scheme for three-dimensional bodies and by a second-order finite difference scheme for two-dimensional bodies. For details of the scheme one is referred to Pien[6].

The term $\partial\phi/\partial t$ and its associated forces and moments are also evaluated from the doublet distribution D. Following Lamb[1], we write $\partial\phi_o/\partial t = \partial(U\phi_1)/\partial t$ where ϕ_1 is the solution of

$$-x = \frac{1}{4\pi}\iint_{S_B}(\phi_1 + x)\,\frac{\partial G}{\partial n}\,dS$$

and we define the so-called added mass by

$$A = \rho\iint_{S_B}\phi_1\,\frac{\partial x}{\partial n}\,dS$$

By comparing the above definition of ϕ_1 with expression (7) for the doublet distribution D, it is easily seen that $\phi_1 = -\chi + D/U$. Thus, once the doublet distribution is known one can obtain the forces and moments associated with $\partial\phi_o/\partial t$ through simple integrations.

If G is time independent, by the definitions above, both D/U and the added mass, A, are also time independent and the force associated with $\partial\phi_o/\partial t$ is proportional to the acceleration:

$$\iint_{S_B} \frac{\partial\phi_o}{\partial t}\,\frac{\partial x}{\partial n}\,dS = \frac{\partial}{\partial t}\left[U\iint_{S_B}\left(\frac{D}{U} - x\right)\frac{\partial x}{\partial n}\,dS\right] = \frac{\partial(UA)}{\partial t} = A\,\frac{\partial U}{\partial t} \qquad (16)$$

To conclude this section, we state that the inner-potential doublet-distribution method is indeed a combination of the singularity and finite difference methods (or finite elements method) since it determine the velocity potential ϕ_o fron a given singularity function G and evaluates the velocities from D through a finite difference scheme.

3. Unsteady Flow Without a Free Surface

The method outlined in the previous section was used by Pien[6] to calculate the velocity field about an arbitrary body moving in an infinite fluid. In this section, some calculations of added mass and force which are proportioned to U^2 will be presented for both infinite and semi-infinite fluids.

3.1 Infinite Fluid

The added mass, A, of a body moving in an infinite fluid is calculated from Equation (16). In determining D, G has been chosen as $1/r$ and ϕ_i as $-Ux$. Table 1 presents computed added mass for some Series 58 bodies of revolution. Included in Table 1 are the added masses calculated independently by Landweber[9]. The two computations agree well. Landweber's results were obtained from a traditional doublet distribution method.[10] However, as was stated by Landweber[9], the calculation by the traditional method was quite cumbersome and he formulated another approximation which was very good for the cases he investigated.

3.2 Semi-infinite Fluid

In an infinite fluid, the added mass, A, is constant if the body is rigid. However, when a body is moving uniformly in a semi-infinite fluid near a flat wall, the added mass may no longer be time independent even though the body is rigid; it will be a function of the relative body position with respect to the rigid wall.[1] The added mass for a sphere moving away from a wall is given by Lamb[1] as $A = (2/3)\rho\pi a^3(1 + 3a^3/8y^3 + \cdots)$, where a is the radius of the sphere and y is the distance of its center from the wall. The present method has been

applied to calculation of the added mass of a sphere with varying y. Figure 1 presents the resulting added mass, in terms of a/y. In comparison with the theoretical result of Lamb (solid line), the present results seem to be accurate.

TABLE 1
Table of Added Mass Coefficients of Series 58 Models

Model No.	Present Results	Landweber's Results
4154	0.0865	0.0866
4155	0.0628	0.0629
4156	0.0480	0.0480
4158	0.0312	0.0310
4159	0.0221	0.0219
4160	0.0381	0.0385
4161	0.0378	0.0378
4162	0.0376	0.0375
4163	0.0374	0.0374
4164	0.0405	0.0404
4165	0.0383	0.0382

Due to the presence of the wall, the pressure force contributed to the y-force from the perturbation velocity term of Equation (15) is not zero, but is given by $\rho U^2(3\pi a^2/8)(a^4/y^4 + \cdots)$. Figure 2 shows the present numerical values as well as the theoretical values for the y-force. It is seen that the numerical values are almost identical with the theoretical values when $a/y < 0.5$. The deviation of the numerical calculation from the theoretical approximation for large values of a/y is due to the large variation of the velocity when the sphere is close to the wall. In this case more panels are necessary for better accuracy.

4. Force on a Body Beneath a Free Surface

With the Kelvin singularity distribution for three-dimensional flow given by,

$$G = \frac{1}{r} + \frac{1}{r^*} - \frac{K_o}{\pi}\int_{-\pi}^{\pi} d\theta \int_0^{\infty} \lim_{\mu \to o}\left(\frac{\sec^2\theta\, e^{-k\{(2f-z-z_o)+i\bar{\omega}\}}}{k - K_o\sec^2\theta + i\mu\sec\theta}\right)dk \tag{17}$$

the system of Equations (7), (8) and (9) represent the flow induced by a body moving under a linearized free surface, where $\bar{\omega} = (x - x_o)\cos\theta + (y + y_o)\sin\theta$, f is the position of the undisturbed free surface, $r^* = \sqrt{(x-x_o)^2 + (y-y_o)^2 + (z+z_o-2f)^2}$, and (x_o, y_o, z_o) is the position of the singularity. Numerical evaluation of G presents no difficulties with respect to

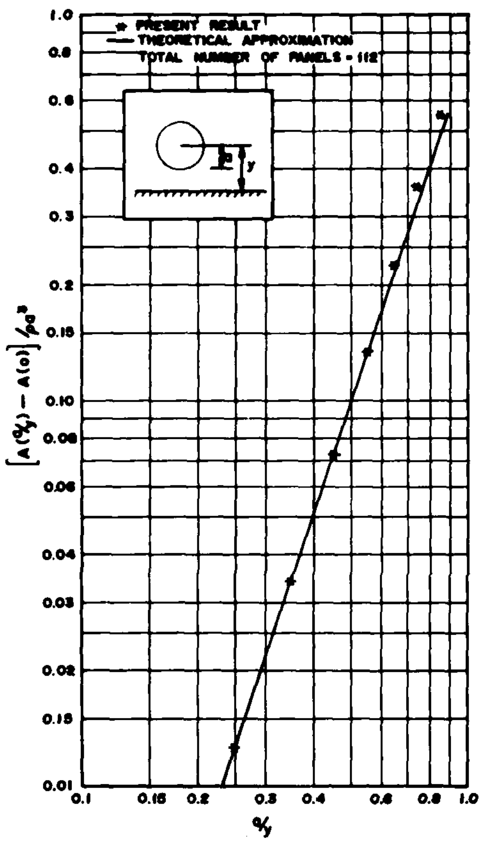

Figure 1 - Added Mass of a Sphere Moving in a Direction Perpendicular to a Wall

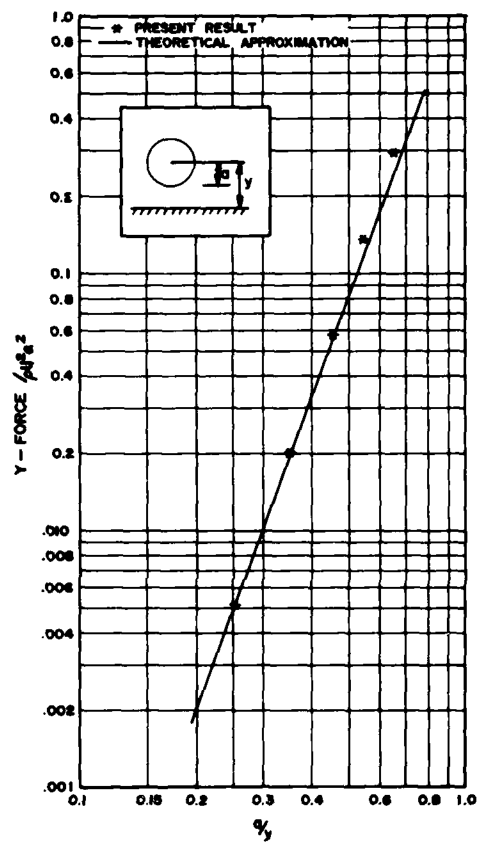

Figure 2 – Force on a Sphere Moving in a Circular Direction Perpendicular to a Wall

the first two terms in the right-hand side of Equation (17), but the third term involves not only a double integration but an oscillatory integrand. Nevertheless, the degree of difficulty can be reduced if one rewrites G in terms of the exponential function[11], E_1, and changes the order of integration so that one integrates Equation (17) first over the surface, ds, and then over the angle $d\theta$. Following Havelock[12], we rewrite Equation (7) in the form

$$\phi_i = -\frac{1}{4\pi}\left\{\iint_{S_B} D \frac{\partial}{\partial n}\left(\frac{1}{r} - \frac{1}{r^*} - \frac{1}{\pi}\int_{-\pi}^{\pi} K_o \sec^2\theta\, e^{-iK_o \sec^2 z}\int_{\infty}^{z} \frac{e^{iK_o \sec^2\theta u}}{u}\, du d\theta\right)\right\} dS$$

which in the two-dimensional case reduces to,

$$\phi_i = \frac{-1}{2\pi} \iint_{S_B} D \frac{\partial}{\partial n} \left(\ln r - \ln r^* - 2e^{-iK_oZ} \int_{\infty}^{Z} \frac{e^{iK_ou}}{u} du \right) dS \tag{18}$$

where $Z = -i(z + z_o - 2f) + \overline{\omega}$ and

$$e^{-iK_oZ} \int_{\infty}^{Z} \frac{e^{iK_ou}}{u} du = -PV \int_{o}^{\infty} \frac{e^{-iKZ}}{k - K_o} dk + e^{-iK_oZ} \tag{19}$$

For the two-dimensional case, it is seen that the integral term in Equation (18) can be calculated from (19) or its asymptotic expansion for large Z. For the three-dimensional case, evaluation of this integral term takes most of the computing time. The integral for the three-dimensional case can be considered as an integral of equivalent two-dimensional cases. The computer time required for calculation will depend on how many numerical integrations of equivalent two-dimensional cases are required to approximate the true integral. Our preliminary calculations have shown that fairly good accuracy can be achieved without dividing the angle into small intervals when one applies a Gaussian integration method to the surface integrations at given angles. A similar integral form has been evaluated by Huang and Wang[13] in a study of the wave resistance of a moving pressure on a free surface. They showed convergence of the integral even when singularities and field points are both located at an undisturbed free surface. The behavior of this integral with respect to integration over θ was also investigated by Yeung[14]. To evaluate the approach the present method has been applied to some simple bodies whose forces are known analytically. Figure 3 shows the wave resistance and lift for a submerged circular cylinder. The forces are plotted against submergence Froude number. The asterisk in Figure 3 indicates the present result, while the broken line and solid lines are the analytical results of first order and second order approximations of the body boundary conditions due to Havelock[12]. The present result agrees well with the second order approximation. This is not unexpected because Havelock[12] has shown, for this particular case, that the forces contributed from terms higher than the second order are indeed negligible. Giesing and Smith[15] have also obtained similar results from a sink-source singularity distribution method.

Figure 4 shows a comparison of the calculated wave resistance of a body of revolution (Series 58 Model 4164) with experimental data. Figure 5 compares the wave resistance of a submerged sphere with the approximate analytical results of Havelock[16] and Bessho[17]. While not very obvious, the agreement in Figure 5 is not as good as it is for the two-dimensional cases. Nevertheless, we consider that the present method has potential for general applications, because the number of panels used in the above calculations was only 60 and computing times between 5 to 15 minutes on a CDC 6700 computer, depending upon the

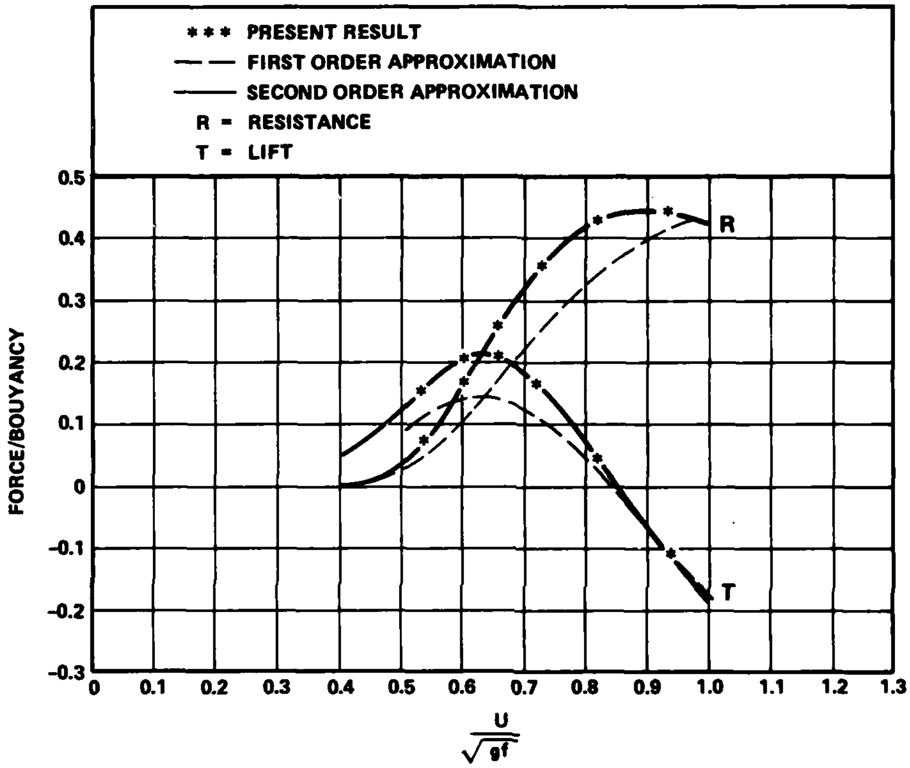

Figure 3 – Comparison of Wave Resistance and Lift on Circular Cylinder Calculated by Present Method and Theoretical Approximations

Froude number. If more panels are used and a more efficient program is written, we believe that more accurate computations can be achieved in reasonable times. Because the purpose of this paper is not to demonstrate a superior accuracy for the present approach, but is to evaluate the general applicaton of the approach, we will not discuss further the numerical scheme required for improved results.

5. Submerged Lifting Body

The system of equations developed earlier for bodies deeply-submerged or near a free surface can only be applied to potential flows without circulation. In problems associated with lifting bodies, Equations (7), (8) and (9) can only be used to obtain the part of the velocity potential which contributes no circulation; that is, if one writes ϕ_o as

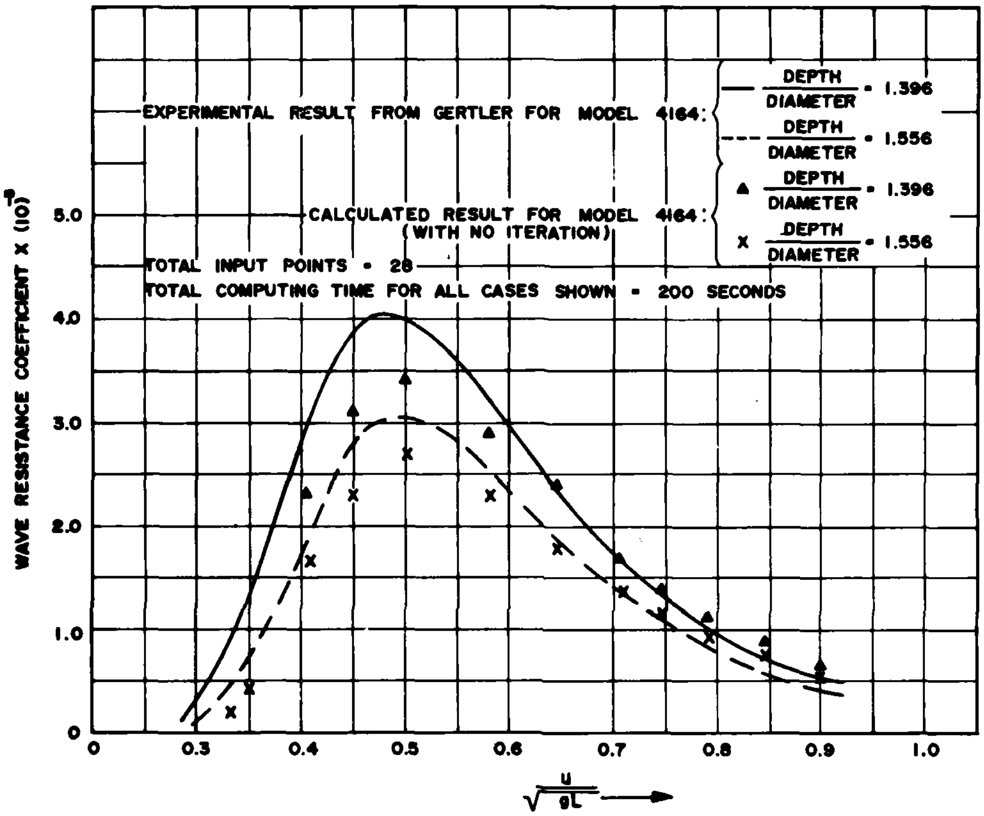

Figure 4 – Comparison of Calculated and Experimentally Determined Wave Resistances for Model 4646 of Series 58

$$\phi_o = \phi_{o1} + \phi_{o2} + \phi_{o3}, \tag{20}$$

where ϕ_{o1} is the only velocity potential when the body develops no lift and $(\phi_{o2} + \phi_{o3})$ are additional velocity potentials necessary to form a lifting body, with ϕ_{o2} contributing no circulation, then Equations (7), (8) and (9) are only applicable to ϕ_{o1} and ϕ_{o2}. The determination of ϕ_{o1} has been discussed and demonstrated in the previous sections; only the calculations of ϕ_{o2} and ϕ_{o3} will be discussed here.

To produce lift, a certain vorticity distribution is necessary. Let ϕ_{o3} be the velocity potential induced by a horseshoe vorticity distribution; from Equations (20) and (9) one has

$$\frac{\partial \phi_{o2}(P)}{\partial n_P} = - \frac{\partial \phi_{o3}(P)}{\partial n_P} \quad P \text{ on } S_B \tag{21}$$

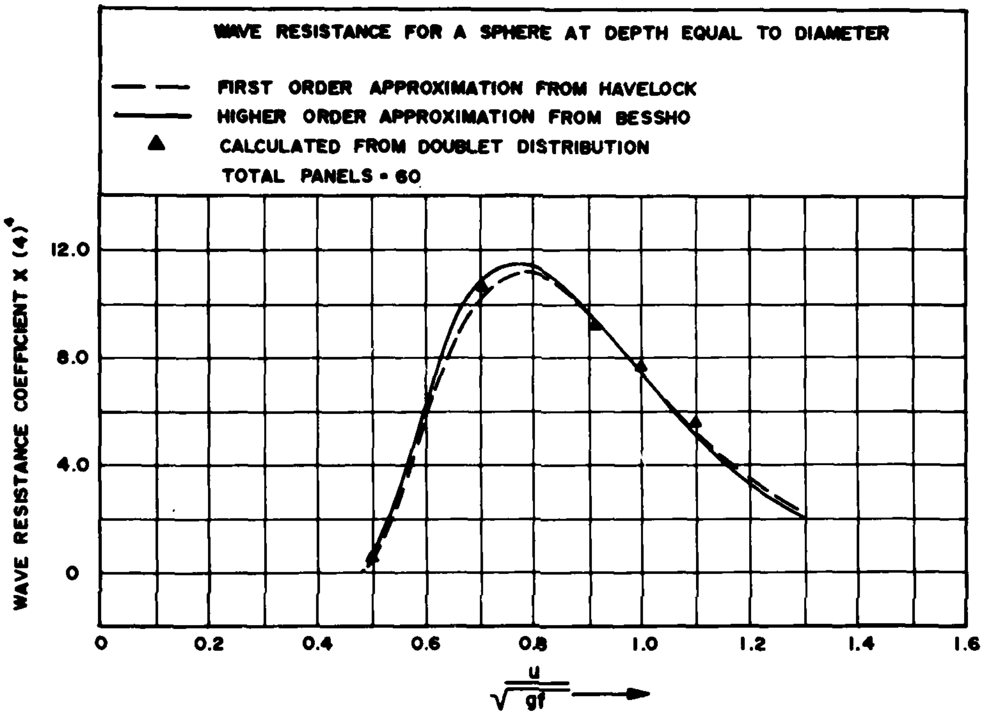

Figure 5 – Comparison of the Calculated Wave Resistance of a Sphere with Theoretical Approximations

and

$$\phi_{o2}(P) = \frac{1}{4\pi} \iint_{S_B} D_2(Q) \frac{\partial G(P,Q)}{\partial n_Q} dS, \quad P \epsilon R_o \tag{22}$$

Taking the normal derivative of (22), and evaluating this at $P \epsilon S_B$, we have

$$\frac{\partial \phi_{o2}(P)}{\partial n_P} = \frac{1}{4\pi} \iint_{S_B} D_2(Q) \frac{\partial}{\partial n_P} \frac{\partial}{\partial n_Q} G(P,Q)\, dS \quad P \text{ on } S_B \tag{23}$$

After the doublet distribution D_2 is determined from (23) for an assumed ϕ_{o3}, ϕ_{o2} can be calculated from (22). For each assumed ϕ_{o3}, one obtains a corresponding ϕ_{o2}; $\phi_{o2} + \phi_{o3}$ is not uniquely determined without further physical constraints on ϕ_{o3}. In a lifting body problem, one, in general, first assumes that the positions of the trailing free vortices are known. Second, one assumes that the Kutta condition is satisfied at the trailing edge. Then applying these

constraints to ϕ_{o3} for a known ϕ_{o1}, the total velocity potential $\phi_{o1} + \phi_{o2} + \phi_{o3}$ is obtained through (20), (22), and (23).

For lifting body problems, the present method adopts the same fundamental physics as is used in other methods. It differs from other methods only in the numerical approach. In satisfying the Kutta condition, velocities are not calculated through the singularity kernel for the velocity; instead velocities are calculated from the doublet distribution on the body surface by a finite difference scheme. It is known that velocities obtained from integration of the potentials due to singularities on the body surface are very sensitive to the distribution of singularities on each control panel. The present method avoids this difficulty.

The pressure distribution over two-dimensional foils has been calculated by the present method. The calculations were done with ϕ_{o3} representing the velocity potential generated by a two-dimensional vortex located in the center of the foil. The strength of the vortex was obtained from the Kutta condition, $\partial\phi_o/\partial S = 0$ on the trailing edge, by a finite difference scheme, where the derivative is taken on the body surface along the direction perpendicular to the trailing edge.

Figure 6 shows the computed pressure coefficients over some deeply submerged NACA foils[18]. Calculated results agree well with experimental results. Figure 7 shows the pressure distribution on the upper surface of a 12-percent thick-symmetric Joukowski hydrofoil at 5° angle of attack for three different submergence depths. The calculated results are in fair agreement with the experimental results of Parkin, etc. However at much shallower submergence, not shown here, the calculated results agreed poorly with the experimental results. This disagreement was also reported by Giesing and Smith[15]. The discrepancy between numerical calculation and experimental results is possibly due to the use of a linearized free surface condition.

6. Surface Piercing Body - Ship

In a previous section, we have shown that, with a linearized free-surface condition, a ship can be represented by a doublet distribution on the ship hull and a line of horizontal doublets and sources on the contour, C, which is the intersection of the ship hull and the undisturbed free surface. However, numerically, if one uses only singularity methods to calculate the doublet distribution from this representation, the calculation will be very complicated. This is not only because the singularities are not disturbed over a closed surface as in the submerged body cases, but also because the constraint between the strength of the sources and the velocity on the contour requires a tedious calculation of velocities from the singularity distribution. We have found that if velocity potentials are specified only on

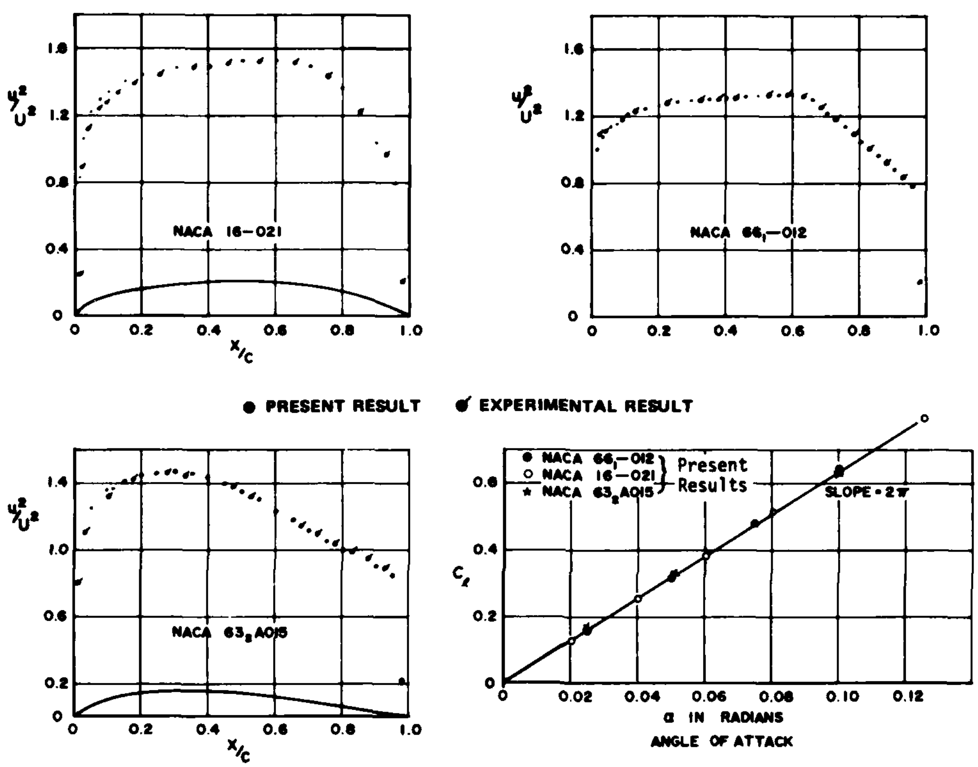

Figure 6 – Pressure Distribution and Lift Coefficients for Some of NACA Foils

the ship hull, the solution is unstable; the potential should be specified on both the ship hull and the portion of the free surface inside the ship hull. We have also found that the relationship between the doublet strength and the velocity potential enables one to express the velocities in terms of the doublet strength through a finite difference scheme which simplifies the calculation tremendously. The system of equations we used to calculate the velocity potential is

$$- Ux = \frac{-1}{4\pi}\left\{\iint_{S_B+S_2} D\,\frac{\partial G}{\partial n'}\,dS - \int_{C_a}\frac{1}{K_o}\left[\left(\frac{\partial\phi_o}{\partial x}\Big|_{C_a} - \frac{\partial\phi_o}{\partial x}\Big|_{C_f}\right)G - (D^+ - D^-)\,\frac{\partial G}{\partial x}\right]dy\right\}, \quad P\epsilon R_i \tag{24}$$

$$D = D(C_f) + \alpha x \quad \text{on } S_2$$

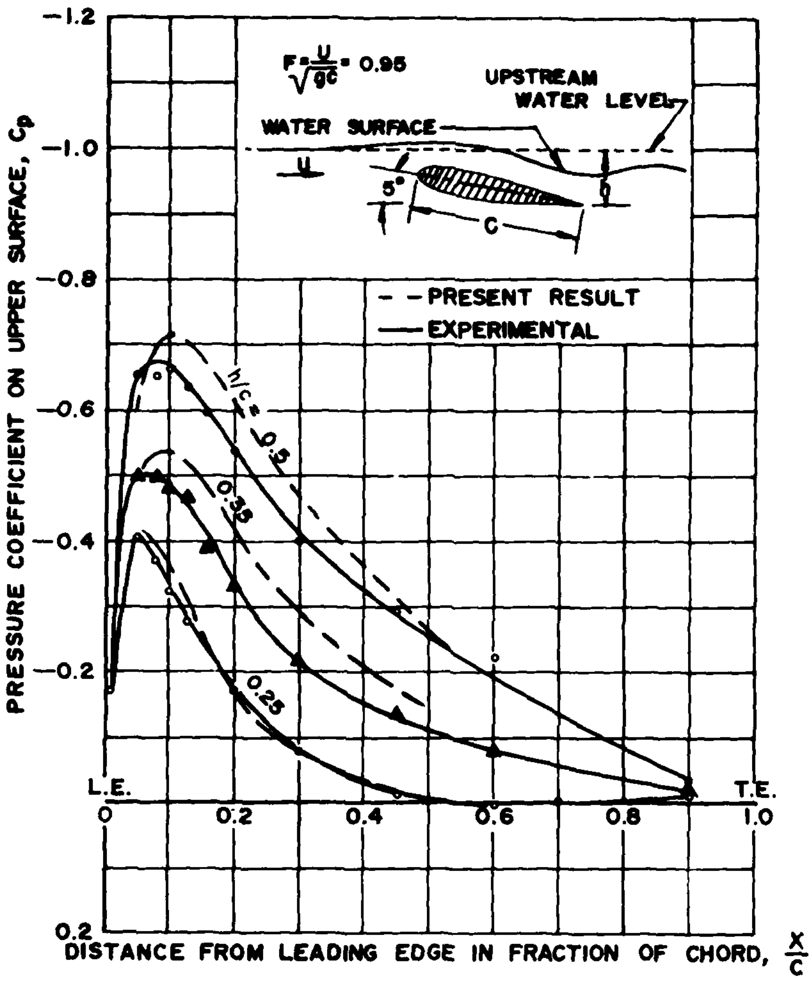

Figure 7 – Calculated and Experimental Pressure Distributions on a Joukowski Hydrofoil with Various Depth Submergences

and

$$\phi_o = D - Ux, \quad \frac{\partial \phi_o}{\partial n} = -U \frac{\partial x}{\partial n} \quad \text{on } S_B$$

where S_B and S_2 are the surface of the ship hull and the undisturbed free surface inside the hull, respectively, C_f and C_a are the forward and aft portions of the waterline contour, the difference $D^+ - D^-$ denotes the jump of D on C_a when approached from S_B and S_2, and a is a speed dependent constant.

Equation (24) can be derived as follows; since anywhere inside of the ship hull

$$- Ux + \phi_i^* = - \frac{1}{4\pi} \iint_{S_B+S_2} \left[G \frac{\partial(-Ux + \phi_i^*)}{\partial n'} - (-Ux + \phi_i^*) \frac{\partial G}{\partial n'} \right] dS \qquad (25)$$

and

$$o = \frac{1}{4\pi} \iint_{S_B+S_f} \left[G \frac{\partial \phi_o^{**}}{\partial n} - \phi_o^{**} \frac{\partial G}{\partial n} \right] dS$$

where ϕ_i^* and ϕ_o^{**} are single-valued potential-functions and S_f is the undisturbed free surface occupied by fluid. If ϕ_i^* and ϕ_o^{**} satisfy $\partial(-Ux + \phi_i^* - \phi_o^{**})/\partial n = 0$ on S_B, one has that

$$- Ux + \phi_i^* = \frac{-1}{4\pi} \left\{ \iint_{S_B} \left[G \frac{\partial(-Ux + \phi_i^* - \phi_o^{**})}{\partial n'} - (-Ux + \phi_i^* - \phi_o^{**}) \frac{\partial G}{\partial n'} \right] \right.$$

$$\left. + \iint_{S_2} \left[(-Ux + \phi_i^*) \frac{\partial G}{\partial z} - G \frac{\partial(-Ux + \phi_i^*)}{\partial z} \right] dS + \iint_{S_f} \left[\phi_o^{**} \frac{\partial G}{\partial z} - G \frac{\partial \phi_o^{**}}{\partial z} \right] dS \right\} \qquad (26)$$

or

$$- Ux = - \phi_i^* - \frac{1}{4\pi} \left\{ \iint_{S_B} D \frac{\partial G}{\partial x} dS + \frac{1}{K_o} \int_C \left[D \frac{\partial G}{\partial x} - G \frac{\partial(-Ux + \phi_i^* - \phi_o^{**})}{\partial x} \right] dy \right\} \qquad (27)$$

where $D = -(-Ux + \phi_i^* - \phi_o^{**})$. Note that, since $\partial(\phi_i^* - \phi_o^{**})/\partial n = U\, \partial x/\partial n$ the solution is $\phi_o^{**} - \phi_i^*$; i.e. $\phi_o = D - Ux$.

If ϕ_i^* is the velocity potential generated by a linear vertical doublet-distribution on the surface S_2, one obtains Equation (24) through the use of the free-surface condition for both $\phi_i^* - \phi_o^{**}$ and G.

It is seen in (24) that a ship may be represented by: (1) normal surface doublets on S_B and S_2 where the surface doublet distribution is continuous on the forward contour, C_f, and discontinuous on C_a; (2) horizontal doublets on the contour C_a, whose strengths are the jumps across the contour of the surface doublets divided by K_o; and (3) sources on C_a, whose strengths are proportional to the differences in the x-component velocities on the forward and aft portions of the hull. In the present method, the source strength on C_a can be expressed in terms of a doublet distribution over the contour C_a through a finite difference scheme. (For a two-dimensional body, the line-integral term is identically zero). Physically, one may interpret the above representation in terms of an equivalent submerged body with a flat top moving at an infinitesimal distance, $\epsilon \to o$, below the free surface. Since the ship hull and flat top have different slopes, no solution may be possible unless additional singularities are

distributed on the corner to make up for the velocity jumps there. In the present method these additional singularities are expressed in terms of local surface doublets. The determination of the strengths of the surface doublets does not require the calculation of a velocity kernel. Thus, a considerable amount of numerical calculation can be eliminated in comparison to other singularity methods. Table 2 gives the velocity potentials calculated for a two-dimensional surface-piercing ellipse. The dimensions of the ellipse are shown in Figure 8. The solutions were found to be stable with respect to the choice of control points. The speed dependent constant α increases with increasing speed. It is 0.85 and 0.93 for U^2/gL of 1.28 and 3.4, respectively. However, since the uniqueness of the solution for this problem has not yet been proved, the significance of the result is subject to further study.

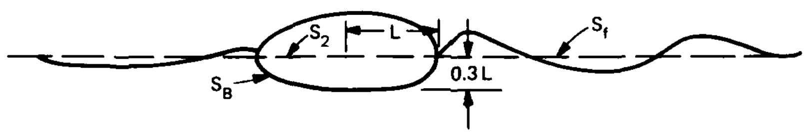

Figure 8 – Sketch of Elliptical Body in a Free Surface

7. Concluding Remarks

The numerical method developed by Pien and Chang[5] and Pien,[6] for calculating the potential field generated by a moving body has been shown to possess the virtues of singularity methods and finite difference schemes. The method differs from the usual finite difference schemes in that the velocity potential, ϕ_0, on the body surface is calculated from a singularity method through a kernel function. Unlike the finite difference scheme, this method satisfies the Laplace equation and the far-field boundary conditions automatically through the singularity function and thus many fewer control points are required than in a finite difference scheme. This method also differs from the customarily-used singularity method which calculates the velocities from singularities through the velocity kernel. As shown by Hess and Smith[3], the calculation of tangential velocities through a singularity kernel for velocity requires a good approximation of the singularity distribution over each panel. The present method allows one to evaluate the velocities from a finite difference scheme and eliminates the lengthy computation of the velocity kernel. Therefore, the present numerical scheme is more efficient than the earlier singularity methods. The approach of Pien and Chang incorporates the advantages of both a singularity method and a finite difference scheme. However, there are cases, where the fluid region is arbitrary and G is not known, then the method by Pien and Chang may not be applied whereas a finite difference scheme can still be used.

TABLE 2
Velocity Potential for a Surface-Piercing Ellipse

	Panel No.	Position of Center of Panel X/L	Y/L	(Potential + Ux)/L x U $\frac{gL}{U^2} = 0.78$	$\frac{gL}{U^2} = 0.3$
	1	0.99965	0.00000	1.10831	1.07484
	2	0.99687	0.00000	1.10595	1.07225
	3	0.98791	0.00000	1.09834	1.06390
	4	0.96894	0.00000	1.08218	1.04621
	5	0.93652	0.00000	1.05438	1.01579
	6	0.88772	0.00000	1.01269	0.97017
	7	0.82024	0.00000	0.95514	0.90723
	8	0.73272	0.00000	0.88036	0.82549
	9	0.62431	0.00000	0.78772	0.72428
	10	0.49524	0.00000	0.67731	0.60368
	11	0.34654	0.00000	0.55004	0.46474
	12	0.18008	0.00000	0.40740	0.30905
S_2	13	0.00000	0.00000	0.25302	0.14066
	14	-0.18008	0.00000	0.09865	-0.02773
	15	-0.34654	0.00000	-0.04404	-0.18345
	16	-0.49524	0.00000	-0.17131	-0.32240
	17	-0.62431	0.00000	-0.28176	-0.44302
	18	-0.73272	0.00000	-0.37439	-0.54423
	19	-0.82029	0.00000	-0.44920	-0.62600
	20	-0.88772	0.00000	-0.50672	-0.68892
	21	-0.93652	0.00000	-0.54838	-0.73464
	22	-0.96894	0.00000	-0.57609	-0.76492
	23	-0.98792	0.00000	-0.59223	-0.78261
	24	-0.99687	0.00000	-0.59983	-0.79096
	25	-0.99965	0.00000	-0.60218	-0.79355
	26	-0.99965	-0.00561	-0.61348	-0.80315
	27	-0.99687	-0.02142	-0.65595	-0.83427
	28	-0.98791	-0.04481	-0.70009	-0.86141
	29	-0.96894	-0.07256	-0.73388	-0.87481
	30	-0.93652	-0.10375	-0.75000	-0.86964
	31	-0.88772	-0.13681	-0.74285	-0.84159
	32	-0.82029	-0.17037	-0.70834	-0.78789
	33	-0.73272	-0.20301	-0.64473	-0.70667
	34	-0.62431	-0.23323	-0.54935	-0.59708
	35	-0.49524	-0.25951	-0.42351	-0.45944
	36	-0.34654	-0.28027	-0.26857	-0.29531
S_B	37	-0.18008	-0.29389	-0.08717	-0.10708
	38	0.00000	-0.29871	0.11458	0.09977
	39	0.18008	-0.29389	0.32024	0.30796
	40	0.34654	-0.28027	0.51060	0.49928
	41	0.49524	-0.25951	0.67973	0.66845
	42	0.62431	-0.23323	0.82474	0.81270
	43	0.73272	-0.20301	0.94352	0.93011
	44	0.82029	-0.17037	1.03538	1.02009
	45	0.88772	-0.13681	1.10061	1.08306
	46	0.93652	-0.10375	1.14074	1.12057
	47	0.96894	-0.07256	1.15708	1.13486
	48	0.98791	-0.04461	1.15558	1.12969
	49	0.99687	-0.02142	1.13946	1.10986
	50	0.99965	-0.00561	1.11619	1.08358

Acknowledgments

This work was performed under the Naval Sea Systems Command General Hydrodynamics Research Program, Task Area SR 023 0101, Program Element 61135N, Work Unit 1521-027.

References

1. Lamb, H., "**Hydrodynamics**", Dover publications, New York, 1945.

2. Brard, R., "**The Representation of a Given Ship Form by Singularity Distribution When the Boundary Condition on the Free Surface is Linearized**", J.S.R. Vol. 16, No. 1, pp. 79-92, 1972.

3. Hess, J.L. and A.M.O. Smith, "**Calculation of Non-lifting Potential Flow About Arbitrary Three-Dimensional Bodies**", Douglass Aircraft Co., Report E.S. 40622, 1962.

4. Dawson, C.W. and Dean, J.S., "**The XYZ Potential Flow Program**", Naval Ship Research and Development Center, Report 3892, 1972.

5. Pien, P.C. and Chang, M.S., "**Potential Flow About a General Three-Dimensional Body**", Naval Ship Research and Development Center, Report 3608, 1971.

6. Pien, P.C., "**Calculation of Non-Lifting Potential Flow About Arbitrary Three-Dimensional Bodies Based on Doublet Distributions**", Naval Ship Research and Development Center, Department Report SPD 601-01, 1975.

7. Lunde, J.K., "**On the Linearized Theory of Wave Resistance for Displacement Ships in Steady and Acceleration Motion**", Transactions of the Society of Naval Architects and Marine Engineers, Vol. 59, pp. 25-85, 1951.

8. Milne-Thomson, L.M., "**Theoretical Hydrodynamics**", The MacMillan Co., New York, N.Y., 1960.

9. Landweber, L. and Winzer, A., "**A Comparison of the Added Masses of Streamlined Bodies and Prolate Spheroids**", Davidson Lab Report 572, 1955.

10. Landweber, L., "**The Axially Symmetric Potential Flow About Elongated Bodies of Revolution**", David Taylor Model Basin Report No. 761, 1951.

11. Abromowitz, M. and Stegun, J.A., "**Handbook of Mathematical Functions with Formulas, Graphs, and Mathematical Tables**", National Bureau of Standards Applied Mathematics Series 55, 1964.

12. Havelock, T.H., "**The Forces on a Circular Cylinder Submerged in a Uniform Stream**", Proc. Roy. Soc. Lond., Ser. A 157, pp. 562-534, 1936.

13. Huang, T.T., and Wong, K.K., "**Disturbance Induced by a Pressure Distribution Moving Over a Free Surface**", J.S.R. Vol. 14, No. 3, pp. 195-203, 1970.

14. Yeung, R.W., "**Sinkage and Trim in First-Order Thin-Ship Theory**", J.S.R. Vol. 16, No. 1, pp. 47-59, 1972.

15. Giesing, T.P. and Smith, A.M.O., "**Potential Flow About Two-Dimensional Hydrofoils**", J.F.M., Vol. 28, No. 1, pp. 113-129, 1967.

16. Havelock, T.H., "**The Wave Resistance of a Spheroid**", Proc. Roy. Soc. Lond., Ser. A 131, pp. 275-285, 1931.

17. Bessho, M., 1957, "**On the Wave Resistance Theory of a Submerged Body**", The Society of Naval Architects of Japan, 60th Anniversary Series, Vol. 2, pp. 135-172, 1957.

18. Abbott, H.I. and Von Doenhoff, A.E., "**Theory of Wing Sections**", Dover Publication, New York, 1949.

19. Parkin, B.R., Perry, B. and Wu, T.Y., "**Pressure Distribution on a Hydrofoil Running Near the Water Surface**", California Institute of Technology, Hydrodynamics Lab. Report No. 47-2, 1955.

A NUMERICAL SOLUTION OF THE EXACT IRROTATIONAL GRAVITY-WAVE PROBLEM

J.W. Thomas

Department of Mathematics
Colorado State University
Fort Collins, Colorado 80523 U.S.A.

ABSTRACT

Consider the problem of calculating the free streamline of progressive waves in an inviscid, incompressible fluid. Assume that the motion is irrotational and two-dimensional and that the bottom is horizontal. The problem is reformulated in terms of Nekrasov's nonlinear integral equation which is solved by an iterative procedure developed by Bueckner. This technique is then used to obtain the form of the free streamline, the total flow field, the relationship between A / h and c^2/gh (the dimensionless parameters that describe the flow), and the form of the highest wave.

1. Introduction

The problem of finding free streamlines in hydrodynamics is an old and very difficult one. The apparent difficulty stems from the fact that the problem is a mixed Dirichlet-Neumman boundary value problem in which part of the boundary is unknown. Thus to solve this problem it is necessary to calculate the form of the free boundary under the condition that the pressure on it is constant. This constant pressure condition will be referred to as the free boundary condition.

In this paper we shall be concerned with steady progressive free-surface waves in an inviscid, incompressible fluid. We shall assume that the motion is irrotational and two-dimensional and that the bottom is horizontal. The results will include also the case of a fluid of infinite depth.

Much work has been done on this problem. The results begin with the work of Franz J. V. Gerstner, [1], (in which he showed that a properly chosen trochiodal profile satisfies the free boundary condition exactly) and extend to several of the papers being presented at this conference. For an excellent review article of work prior to 1960 we refer the reader to the paper of Wehausen and Laitone, [2]. We shall include here only the historical facts that are somewhat pertinent to this paper.

Stokes in 1849 and 1880, [3] and [4], solved the problem numerically by using a perturbation scheme, but calculated solutions using only the third order terms. He found that the scheme converged slowly for values of depth/wave length (h/λ) that were not small. It was at this time that Stokes also showed that the highest free-surface wave (assuming that such a wave exists) would include an angle of 120° at the crest. Several other people have extended Stokes' perturbation scheme. The most recent extension is that of L. W. Schwartz, [5], in which he calculates the expansion to a high order of accuracy with a computer.

Existence of periodic gravity waves was proved by Nekrasov, [6], [7] and [8], and Levi-Civita, [9], using perturbation techniques. Nekrasov's method involved reducing the problem to one of solving a nonlinear integral equation. Both of the results, however, were true in some neighborhood of the expansion parameter. Krasovskii, in [10] and [11], used topological techniques on Nekrasov's integral equation to prove existence of waves for all values of the Froude number in a given interval.

In this paper we use Nekrasov's integral equation to obtain numerical solutions to the free-surface wave problem. We solve the integral equation by a method of successive approximations that was developed by Hans F. Bueckner, [12], for the integral equation associated with the case of infinite depth. For certain initial guesses it can be proved that this iterative technique converges to nontrivial solutions. This method enables us to calculate, in addition to the form of the free streamline, the total flow field associated with the problem and the relationship between the Froude number (c^2/gh) and the amplitude of the wave/depth of the fluid (A/h). A review of several other problems that have been studied numerically by this same method appears in [13].

Section 2 gives a brief sketch of the derivation of Nekrasov's integral equation, repeated here because there are several intermediate equations that we shall need. Section 3 contains a description of the numerical technique and a brief discussion of how this technique was implemented. Section 4 is devoted to a discussion of our results, including a comparison of our results with those of Schwartz, [5], and Salvesen and von Kerczek, [14]. (The results of Salvesen and von Kerczek are obtained by solving the problem of the steady two-dimensional flow past a submerged line vortex by finite differences. The flow far downstream from the vortex becomes a train of periodic progressive waves.)

2. Derivation of Nekrasov's Integral Equation

As was pointed out in the Introduction, the numerical scheme that we discuss in this paper solves Nekrasov's integral equation. Since we need several of Nekrasov's intermediate equations in order to derive the method of calculating the total flow field and in order to calculate the c^2/gh versus A/h curves, we include here a brief derivation of Nekrasov's integral equation. For a more complete derivation see [8] or [15].

We are considering a periodic wave moving with constant velocity c from right to left on the surface of an inviscid, incompressible fluid that is at rest at infinity. We assume that the motion is irrotational. The bottom is horizontal, and the depth of the undisturbed fluid is h. If a constant velocity c from left to right is superimposed on the fluid, the wave form is reduced to rest in space, the motion becomes steady, and the velocity at infinity becomes c from left to right. The motion of the fluid contained in one wave length will now be studied.

The form of the free surface is unknown, but we can map the region occupied by the fluid onto a known region in the Z-plane ($Z = X+iY=re^{it}$). Determination of the mapping function will lead to the form of the free surface. Let the known region be $R = \{Z: \ r_o \leq r \leq 1 \text{ and } -\pi \leq t \leq \pi\}$, where r_o is between 0 and 1 and is yet to be determined. Denote the mapping by

$$z = F(Z) \tag{1}$$

and let corresponding points in the two planes be denoted by the same letter.

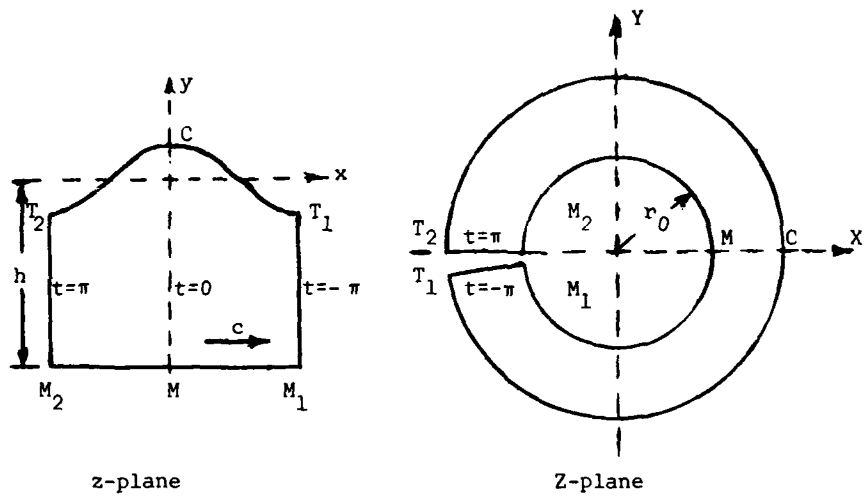

Figure 1.

We map the crest into the point (1, 0) in the Z-plane and the line CM into the line CM in the Z-plane, which we take to lie on the X-axis. This function will map M_2T_2 and M_1T_1 into $t = \pi$ and $t = -\pi$, respectively. See Figure 1.

We see that a jump discontinuity is required when going from T_2 to T_1. This jump can be provided by a term of the form $(\frac{i\lambda}{2\pi}) \log Z$. The remainder of the function can then be written as a Laurent expansion in R. Thus it is sufficient for F to be of the form

$$F(Z) = \frac{i\lambda}{2\pi} [\log Z + K_o - \sum_{n=2}^{\infty} \frac{a_{-n}}{n-1} Z^{1-n} + \sum_{n=0}^{\infty} \frac{a_n}{n+1} Z^{n+1}]. \tag{2}$$

Let

$$f(Z) = \sum_{n=-\infty}^{\infty} a_n Z^n \tag{3}$$

in R, where $a_{-1} = 0$. We then see that

$$\frac{dz}{dZ} = F'(Z) = \frac{i\lambda}{2\pi}\left[\frac{1}{Z} + f(Z)\right]. \tag{4}$$

The point $Z = r_o e^{it}$ must map onto a point on the bottom of the channel so $x - ih = F(r_o e^{it})$. We see that if we choose $K_o = 0$, $r_o = \exp(-2\pi h/\lambda)$ and write F as

$$F(Z) = \frac{i\lambda}{2\pi}\left[\log Z + \sum_{n=1}^{\infty} \frac{d_n}{n}\left(\frac{Z^n}{r_o^n} - \frac{r_o^n}{Z^n}\right)\right], \tag{5}$$

where the d_n are given in terms of the a_n and must be real, then the imaginary part of $F(r_o e^{it})$ will be $-h$.

We next consider the flow in the Z-plane. The boundary conditions for the problem are as follows:

$\psi = 0$ in the free streamline $(r = 1)$; (6)

$\psi = \psi_n$; a constant, on the bottom $(r = r_o)$; (7)

$\frac{1}{\lambda}\int_\Gamma (u - iv)dz = c$, where Γ is the line segment (8)

$x - ih$, $-\frac{\lambda}{2} \leq x \leq \frac{\lambda}{2}$. (Note that expression (8) is actually the definition of the wave speed c.) It is not hard to see that the complex potential

$$w = -\frac{ic\lambda}{2\pi} \log Z \tag{9}$$

satisfies the boundary conditions (6) - (8) for this flow in the Z-plane.

Let $Q(r, t)\exp[i\theta(r, t)]$ be the velocity at the point (r, t), where Q is a real function. Then

$$-\frac{dw}{dz} = Q(r, t)\exp[i\theta(r, t)] = -\frac{dw}{dZ}\frac{dZ}{dz} = c/(1 + Zf(Z)). \tag{10}$$

So if we let

$$1 + Zf(Z) = \exp[T(Z)], \tag{11}$$

T(Z) can be written as

$$T(Z) = s(r, t) + i\theta(r, t) \tag{12}$$

where

$$c \exp[-s(r, t)] = Q(r, t). \tag{13}$$

Solving (11) for T yields

$$T(Z) = \log\,[1 + Z\,f(Z)] = \sum_{n=-\infty}^{\infty} b_n Z^n \tag{14}$$

where the b_n are obtainable from the a_n in equation (3). Since Q and hence s must be real for $r = r_o$, $T(r_o e^{it})$ must be real. It is sufficient to express T as

$$T(Z) = c_o + \sum_{n=1}^{\infty} c_n(r_o^{-n} Z^n + r_n^{\,n} Z^{-n}), \tag{15}$$

where the c_n are real.

We are most interested in the flow on the free streamline. Hence we introduce the special notation that $\theta(t) = \theta(1, t)$ and $s(t) = s(1, t)$. Then θ will give the direction of the tangent along the free streamline and s along with equation (13) will give the fluid speed.

The purpose of the work done since equation (9) has been to express our problem in a convenient form for applying our last major piece of information, namely Bernoulli's equation. Theoretically, the plan at this time is to use the fact that since the surface is a streamline, Bernoulli's equation for constant pressure,

$$Q^2(1, t) + 2gy = \text{constant}, \tag{16}$$

must be satisfied in order to calculate one of the sets of coefficients d_n, a_n, b_n, or c_n, any of which would determine F. This method is, in fact, the one used by Stokes, [3], [4], and Schwartz, [5]. They let r=1 in equation (10) and substitute into Bernoulli's equation (16) to obtain a system of equations that determine the a_n. They then calculate the a_n by using various perturbation schemes. Our approach is somewhat different.

We use equation (16) to obtain eventually an integral equation for $\theta(t)$. Assuming that we solve for $\theta(t)$ we could then find the a_n. We shall see, however, we never have to use the a_n.

We proceed by differentiating (16) to get

$$\frac{d}{dt} Q^2 = -2g \frac{dy}{dt} . \tag{17}$$

Since $Z = e^{it}$ on the free streamline, (4), (11) and (12) give

$$\frac{dz}{dt} = - \frac{\lambda}{2\pi} \exp \left[s(t) + i\theta(t) \right]. \tag{18}$$

Equating the real and imaginary parts of equation (18) then yields

$$\frac{dx}{dt} = - \frac{\lambda}{2\pi} \exp[s(t)] \cos \theta(t) \tag{19}$$

$$\frac{dy}{dt} = - \frac{\lambda}{2\pi} \exp[s(t)] \sin \theta(t). \tag{20}$$

Then equations (13), (17) and (20) yield

$$e^{-3s(t)} = \frac{3g\lambda}{2\pi c^2} \left(\frac{1}{\mu} + \int_0^t \sin \theta(\tau)\, d\tau \right) \tag{21}$$

where $\frac{1}{\mu}$ is the arbitrary constant of integration.

Thus we have established a relationship between s and θ. The next step is to obtain another relationship between s and θ, which leads to an equation in θ alone. Since we have already obtained the auxiliary equations that we shall need, all we now desire is the integral equation. Thus we shall do the next part in a briefer fashion.

The next step is to calculate the coefficients in equation (15) in terms of s by considering T on the free surface, i.e. for $r = 1$. With a fair amount of manipulation we can write T as

$$T(e^{it}) = \frac{1}{2\pi} \int_{-\pi}^{\pi} s(x) \left[\frac{1 - e^{2it}}{1 - e^{it} \cos x + e^{2it}} - i \frac{\partial}{\partial x} \log \frac{\sin 1/2\ (t + x)}{\sin 1/2\ (t - x)} \right] dx$$
$$+ \frac{i}{2\pi} \int_{\pi}^{\pi} s(x) \frac{\partial}{\partial x} \log \frac{\operatorname{sn} \frac{K}{\pi}(t + x)}{\operatorname{sn} \frac{K}{\pi}(t - x)} dx, \tag{22}$$

where K is the half period of the Jacobi elliptic sine and the last integral is interpreted as a Cauchy principal value. It can easily be shown that the first integral in (22) is zero. Then integration by parts yields

$$T(e^{it}) = \frac{i}{2\pi}\left[s(x)\log\frac{\mathrm{sn}\frac{K}{\pi}(t+x)}{\mathrm{sn}\frac{K}{\pi}(t-x)}\right]_{x=-\pi}^{x=\pi} - \frac{i}{2\pi}\int_{-\pi}^{\pi} s'(x)\log\frac{\mathrm{sn}\frac{K}{\pi}(t+x)}{\mathrm{sn}\frac{K}{\pi}(t-x)}dx. \quad (23)$$

But the first term is just s(t) so equating the imaginary parts of equation (23) yields

$$\theta(t) = -\frac{1}{2\pi}\int_{-\pi}^{\pi} s'(x)\,K(x,t)\,dx, \quad (24)$$

where $K(x, t) = \log[\mathrm{sn}\frac{K}{\pi}(t + x)/\mathrm{sn}\frac{K}{\pi}(t - x)]$. This is the desired second relationship between s and θ. Substitution of the s function from equation (21) then yields

$$\theta(t) = \frac{\mu}{6\pi}\int_{-\pi}^{\pi} \frac{\sin\theta(x)}{1+\mu\int_0^x \sin\theta(u)\,du} K(x,t)dx.$$

The symmetry of our functions then allows us to write this as

$$\theta(t) = \frac{\mu}{3\pi}\int_{0}^{\pi} \frac{\sin\ (x)}{1+\mu\int_0^x \sin\theta(u)\,du} K(x,t)dx. \quad (25)$$

The above equation is the integral equation due to Nekrasov (in a class of integral equations that were called Milne-Thomson integral equations by the author and W. E. Conway in [13]) that will yield the form of the free streamline for the problem. We shall show in the next section how to solve equation (25). In the remainder of this section we show how to calculate the free streamline, the c^2/gh - A/h relationships, and the total flow field given that we know $\theta(t)$. Before proceeding, however, it is worthwhile to note the following facts about our problem and the integral equation. In deriving the equation, we have assumed that the wave length, λ, and the fluid depth, h, were known. Thus it is necessary to choose λ and h, both of which appear in equation (25) indirectly through K, the half period of the Jacobi elliptic sine. K can be found in a book of tables, [16] page 610, from the Nome $q = r_o^2 = \exp[-4\pi h/\lambda]$.

The Free Streamline. Once $\theta(t)$ and μ have been found it is fairly easy to calculate the form of the free streamline. We wish to use equation (19) and (20). From equation (21) we see that

$$e^{s(t)} = \left(\frac{3g\lambda}{2\pi c^2}\right)^{-1/3}\left(\frac{1}{\mu} + \int_o^t \sin\theta(\tau)\, d\tau\right)^{-1/3} \tag{26}$$

Thus we know $e^{s(t)}$ up to a multiplicative constant and can write

$$e^{s(t)} = e^{s(0)}\left(1 + \mu\int_o^t \sin\theta(\tau)\, d\tau\right)^{-1/3}. \tag{27}$$

Since we know that $x(0) = 0$ and $x(\pi) = -\lambda/2$, we can integrate equation (19) along with equation (27) to get $e^{s(0)}$. We then have

$$x(t) = -\frac{\lambda}{2\pi}\int_o^t e^{s(t)} \cos\theta(\tau) d\tau. \tag{28}$$

Equation (20) gives y up to an additive constant as

$$y(t) = y(0) - \frac{\lambda}{2\pi}\int_o^t e^{s(\tau)} \sin\theta(\tau) d\tau. \tag{29}$$

The constant $y(0)$ is calculated by equating the real and imaginary parts of equation (5) with $z = e^{it}$ to get

$$x(t) = -\frac{\lambda}{2\pi}\left[t + \sum_{n=1}^{\infty} \frac{d_n}{n}(r_o^{-n} + r_o^{n})\sin nt\right], \tag{30}$$

$$y(t) = \frac{\lambda}{2\pi}\sum_{n=1}^{\infty} \frac{d_n}{n}(r_o^{-n} - r_o^{n}) \cos nt. \tag{31}$$

Then solving equation (30) for d_n we get

$$d_n = \frac{-4nr_o^n}{\lambda(1 + r_o^{2n})}\int_o^{\pi} x^*(\tau) \sin n\tau\, d\tau,\ d_n = 1, 2, \ldots \tag{32}$$

where $x^*(\tau) = x(\tau) + \frac{\lambda}{2\pi}\tau$. If we then insert d_n into equation (31) and interchange the summation and integration, we get

$$y(t) = \frac{2}{\pi}\int_o^{\pi}\left[\sum_{n=1}^{\infty} \frac{1 - r_o^{2n}}{1 + r_o^{2n}} \sin n\tau \cos nt\right]x^*(\tau)d\tau.$$

Then

$$y(0) = \frac{2}{\pi}\int_0^\pi [\sum_{n=1}^{\infty} \frac{1 - r_o^{2n}}{1 + r_o^{2n}} \sin n\tau] x^*(\tau) d\tau. \tag{33}$$

Thus since x^* is known, we can calculate $y(0)$. We use the technique described above to circumvent the necessity of using finite Fourier series to calculate $y(0)$. It should be noted that all of the calculations in this paper are performed without ever calculating a Fourier series expansion, a fact which we feel is to our advantage.

The relationship between c^2/gh and A/h. In order to obtain the relationship between c^2/gh and A/h we must be able to calculate c. (We have g, h and $A = |y(\pi) - y(0)|$.) If we combine equations (26) and (28) with the fact that $x(\pi) = -\lambda/2$, we get

$$-\frac{\lambda}{2} = -\frac{\lambda}{2\pi}\int_0^\pi (\frac{3g\lambda}{2\pi c^2})^{-1/3}(\frac{1}{\mu} + \int_0^\tau \sin\theta(\xi)d\xi)^{-1/3}\cos\theta(\tau)d\tau$$

or

$$\frac{c^2}{gh} = \frac{3\lambda\pi^2}{2h}[\int_0^\pi (\frac{1}{\mu} + \int_0^\pi \sin\theta(\xi)d\xi)^{-1/3}\cos\theta(\tau)d\tau]^{-3}. \tag{34}$$

Thus for given values of θ, μ, λ and h we can calculate A/h and c^2/gh and represent them on a graph.

Total Flow Field. One method for calculating streamlines that are not free streamlines is to use equation (5). The d_n could be calculated from equation (3.2) so the method would be to fix r and vary t in equation (5). (We note that the streamlines in the Z-plane are r = constant and that streamlines will map onto streamlines.)

Our approach is essentially the same as the one described above except that we shall manipulate our equations so that we can integrate to find the x and y values rather than use the finite Fourier series. We shall do this in the same way we calculated $y(0)$.

We note that if we put $Z = re^{it}$ in equation (5) and equate real and imaginary parts we get

$$x(r, t) = -\frac{\lambda}{2\pi}\{t + \sum_{n=1}^{\infty} \frac{d_n}{n} [(\frac{r}{r_o})^n + (\frac{r_o}{r})^n] \sin nt\} \tag{35}$$

and

$$y(r, t) = \frac{\lambda}{2\pi} \{\log r + \sum_{n=1}^{\infty} \frac{d_n}{n} [(\frac{r}{r_o})^n - (\frac{r_o}{r})^n] \cos nt\}. \tag{36}$$

If we substitute the values for d_n given by equation (32) into equations (35) and (36) and interchange the order of summation and integration, we obtain the following:

$$x(r, t) = -\frac{\lambda}{2\pi} t + \frac{2}{\pi}\int_o^{\pi} L_1(r, r_o, t, \tau)x^*(\tau)d\tau \tag{37}$$

and

$$y(r, t) = \frac{\lambda}{2\pi} \log r + \frac{2}{\pi}\int_o^{\pi} L_2(r, r_o, t. \tau)x^*(\tau)d\tau \tag{38}$$

where

$$L_1(r, r_o, t, \tau) = \sum_{n=1}^{\infty} \frac{r^{2n} + r_o^{2n}}{r^n(1 + r_o^{2n})} \sin \tau \sin t$$

and

$$L_2(r, r_o, t, \tau) = \sum_{n=1}^{\infty} \frac{r^{2n} - r_o^{2n}}{r^n(1 + r_o^{2n})} \cos nt \sin n\tau.$$

These kernel functions would have to be tabulated - or hopefully written in closed form (which the author has not been able to do) - and then the values of x(r, t) and y(r, t) for fixed r and varying t can be found and plotted.

3. Numerical Technique

In [12] H. F. Bueckner developed an iterative technique for solving the integral equation associated with the problem handled in this paper in a fluid with infinite depth. The author in [17] showed that this method would apply also to equation (25). It is this technique that we shall discuss in this section.

We consider the Hilbert space X with inner product (,) and norm $\| \ \|$ and suppose that $T : X \to X$ is a compact operator. We wish to solve the eigenvalue problem

$$x = \mu T(x). \tag{39}$$

In order to express the problem considered in this paper in this form we rewrite integral equation (25) as

$$u(t) = \mu \sin \left[\frac{1}{3\pi} \int_0^\pi \frac{u(\tau)}{1 + \int_0^\tau u(\xi)d\xi} K(\tau, t)d\tau\right] \tag{40}$$

where $u(t) = \mu \sin \theta(t)$. The iterative procedure used is a common one. We suppose that we have an initial approximation to the solution, x_o, and the eigenvalue, μ_o, we then define

$$x_{n+1} = \mu_n T(x_n), \ \mu_n = \frac{(x_n, T(x_n))}{\|T(x_n)\|^2} \ \text{(for } x_n \neq \theta). \tag{41}$$

To obtain a result which ensures convergence of the sequence (x_n, μ_n) we assume the following additional conditions on T:

(C1) T is continuously differentiable on X. Let $T'(\theta) = L$.

(C2) The spectral radius of L, denoted by r, is nonzero; L has exactly one eigenvalue, λ, of absolute value r, and the invariant manifold associated with λ, X_1, is an eigenmanifold.

(C3) The dimension of X_1 is one.

We can then state the following theorem.

<u>THEOREM</u>. Suppose that x satisfies (i) $\|x\| = 1$ and (ii) $w(x) < w'$; and that $|\alpha|$ is sufficiently small. Then if we let $x_o = \alpha x$, the sequence $\{(x_n, \mu_n)\}$ *will converge to a nontrivial* solution of equation (39).

The function w and the constant w' are given in terms of constants that arise in the proof of the above theorem. We shall not prove the above theorem and hence shall not exhibit w and w'. The reason for this omission is that though the theorem does give sufficient conditions under which we are guaranteed a nontrivial solution, it is difficult to verify that these conditions are satisfied. Furthermore, the numerical results indicate that actually a much stronger theorem is available. Iteration

(41) has been run for approximately forty (x_o, μ_o) pairs and never once has convergence not occurred (obvious numerical convergence). Moreover, we have not chosen a "sufficiently small" coefficient on x_o. Also, as can be seen in [13], this iteration has been run on several integral equations that do not satisfy the hypothese and the technique still converges.

There are no theoretical results concerning the rate of convergence of this numerical technique. Bueckner states in [12] that the sequence seems to converge much like a geometric series with ratio 1/2. The author also observed this to be the case. At times the convergence seems even better than the 1/2 ratio.

In order to calculate the form of the free streamline of the highest wave, we use a variation of iteration (41). We rewrite equation (25) as

$$\theta(t) = \frac{1}{3\pi}\int_o^\pi \frac{\sin\theta(\tau)}{\frac{1}{\mu} + \int_o^\tau \sin\theta(\xi)d\xi} K(\tau, t)d\tau, \tag{42}$$

fix μ at some large value and let $u(t) = \sin\theta(t)$. Equation (42) can then be expressed as

$$u(t) = \frac{1}{3\pi}\int_o^\pi \frac{u(t)}{\frac{1}{\mu} + \int_o^\tau u(\xi)d\xi} K(\tau, t)d\tau = T(\mu, u). \tag{43}$$

We then choose an initial approximate solution, u_o, and use the iteration

$$u_{n+1} = T(\mu, u_n). \tag{44}$$

Bueckner in [12] stated that he found this technique to be unsatisfactory. We found that it did quite well for large values of μ. With large values of μ it did not perform as well as iteration (41) did for smaller values of μ, but this is to be expected. When μ gets large we are very near a solution that is difficult mathematically (in fact, its existence has still not been proved). The difference in our results in using iteration (44) and Bueckner's statement probably results from the fact that he indicated that he tried to use $u_{n+1} = \mu T(u_n)$ in place of iteration (41) for small values of μ. We fix μ in our iterative scheme in a much different way.

The iteration techniques were implemented in the most obvious way. We used the trapazoidal rule to integrate $T(u_{n-1})$ at each step. The problem

of getting the Jacobi elliptic sines into the machine was solved by using a technique due to H. E. Salzer, [18].

4. Numerical Results

The iterative techniques discussed in Section 3 have been applied by the author many times. References [15] and [17] give the form of several free streamlines in a fluid of infinite and finite depth. In [19] the author calculated 36 values of $(A/h, c^2/gh)$ and numerically drew the curves relating the parameters A/h and c^2/gh. This system of curves is given in Figure 2.

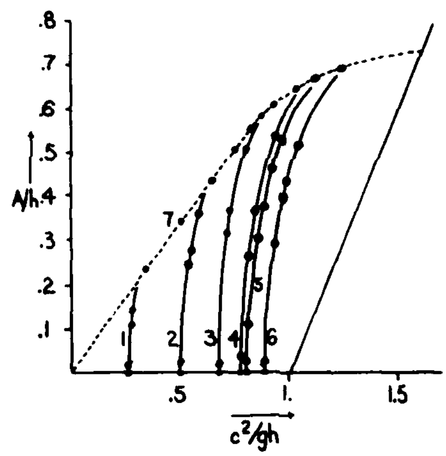

Figure 2

The curves (1) - (6) are the graphs of A/h versus c^2/gh for values of h/λ = 0.6, 0.3, 0.2, 0.15, 0.13655, and 0.10632, respectively. Curve (7) is the limiting case of A/h versus c^2/gh for the highest wave.

It should be noted that, besides the 36 points calculated numerically, there are six points plotted on the c^2/gh-axis that were found using the expression (see [2], page 660)

$$c^2/gh = \frac{1}{mh}\tanh(mh). \tag{45}$$

Also we note that there are two bounding curves in Figure 2. The curve bounding the system on the right is given by

$$c^2/gh = 1 + (A/h) - (1/10)(A/h)^2 - (3/20)(A/h)^3 + (9/400)(A/h)^4. \qquad (46)$$

This is a second order approximation to the relationship between A/h and c^2/gh for the solitary wave (see [2], page 711).

The curve that bounds from above, (7), is the relationship between A/h and c^2/gh for the highest wave. This curve is graphed using the numerical values calculated by the iterative technique (44) on equation (43). These values were calculated fixing μ at values between 3000 and 4000.

The majority of the new numerical results calculated were done in order to compare our results with those of Schwartz, [5], and Salvesen and von Kerczek, [14].

Schwartz in [5] used perturbation techniques to calculate the free streamlines and the A/h - c^2/gh relationship. Since we calculated (A/h, c^2/gh) points for different values of h/λ, it is difficult to compare the results. For this reason we have calculated several (A/h, c^2/gh) values for h/λ = .145, .256, and .366. (The value of .145 was used instead of .146 (as Schwartz used) so that we could also use these values to compare with Salvesen and von Kerczek.) The values calculated are given in Table 1.

$h/\lambda(q)$	.145(.161)	.256(.04)	.366(.01)
	(.133, .799)	(.230, .588)	(.260, .457)
(A/h, c^2/gh)	(.327, .822)	(.346, .617)	(.182, .436)
	(.626, .947)	(.473, .664)	(.355, .490)
	(.660, .957)	(.495, .668)	(.371, .493)

Table 1

To compare the above results with those of Schwartz we have drawn the part of Schwartz's system of curves that is applicable. (See Figure 3) On these curves we have plotted our values associated with these values

of h/λ. It should be noted that there is fair agreement between our results and those of Schwartz. The values are closer for smaller values of h/λ.

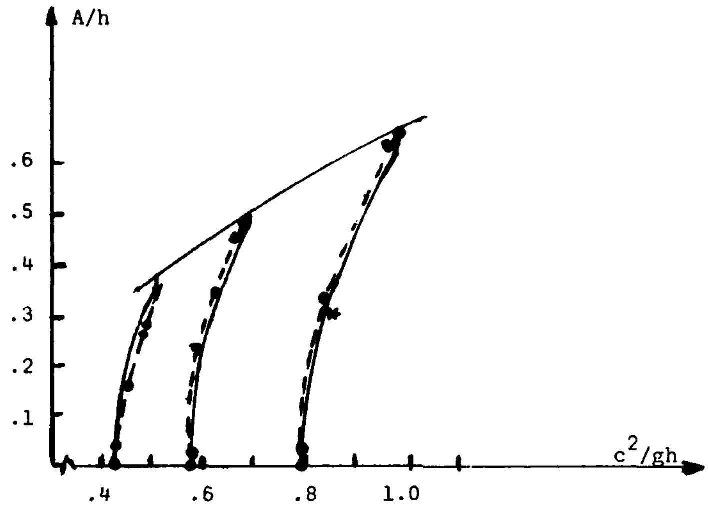

A/h versus c^2/gh: Schwartz's results ———; our results ------.

Figure 3

In [14] Salvesen and von Kerczek obtain results that for $h/\lambda = .145$, $A/h = .3$ and $c^2/gh = .841$. This point is plotted in Figure 3 as a star. As can be seen, the point fits fairly well on both Schwartz's and our curves.

Finally, since the main emphasis of the method discussed in this paper was on calculating free streamlines, in Figure 4 we give profiles of three surface waves.

We close this section and the paper with a brief discussion of the numerical integration that was used and the convergence criterion. The results given in [15], [17] and [19] were obtained from trapezoidal rule integration by breaking the interval $[0, \pi]$ into 400 pieces. The 400 figure was essentially arbitrary. A limitation of available computer time led the author to experiment with fewer partition points. Most of the new calculations given in this paper were done using 100 partition points in $[0, \pi]$. The scheme behaved nicely and understandably was much faster. Some calculations were done with fewer than 100 points and again conver-

gence was excellent. By convergence here and in all other numerical results we mean to require that the maximum of $|u_{n+1} - u_n|$ over the partition points be less than .0001 or better. When we used only 100 or fewer points, a smaller tolerance was required to get satisfactory results.

h = 18.85
μ = 4000

h = 7.98
μ = 375.15

h = 4.52
μ = 124.65

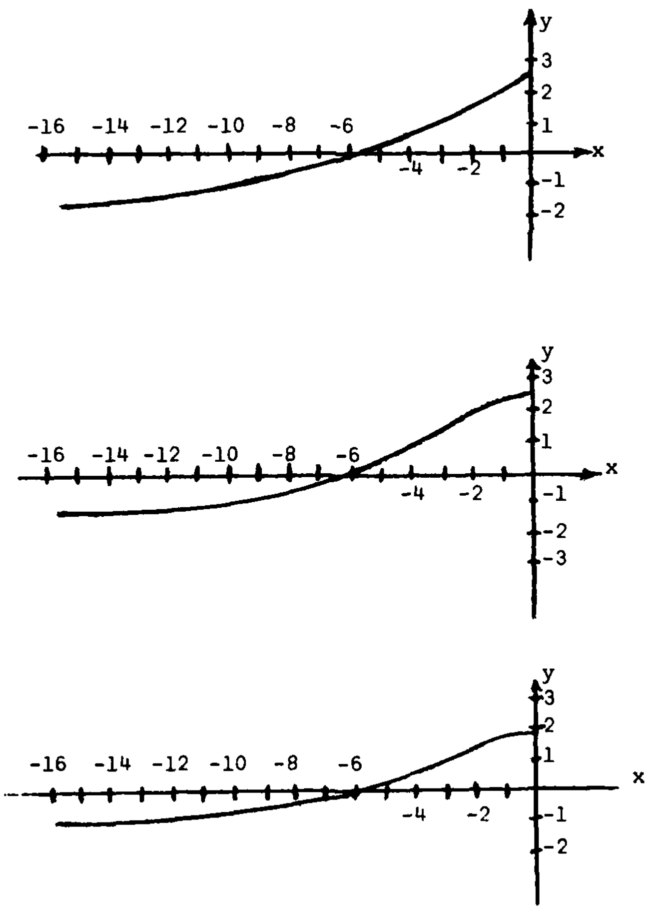

Free Streamlines
Figure 4

REFERENCES

[1] Gerstner, Franz J. V. Theorie der wellen sammt einer abgeleiteten Theorie der deich profile, Abh. Bohm. Ges Wiss. (3), 1, (1804).

[2] Wehausen, John V. and Edmund V. Laitone, Surface Waves, Encyclopedia of Physics, Vol. IX, 1960, 446-814.

[3] Stokes, G. G., On the theory of oscillatory waves, Trans. Cambridge Phil. Soc., 8, 1849, p. 441-455.

[4] _____, Mathematical and Physical Papers, vol. 1, Cambridge Univ. Press, 1880, p. 314-326.

[5] Schwartz, Leonard W., Computer extension and analytic continuation of Stokes' expansion for gravity waves, J. Fluid Mech., vol. 62, part 3, 1974, pp. 553-578.

[6] Nekrasov, A. I., On waves of permanent type on the surface of a heavy fluid, Trudy Vsiross. S'ezda Matematikov, Moskva, 1928, pp. 258-262.

[7] _____, The exact theory of waves of permanent type on the surface of heavy fluid, Moscow; Izdatel'stvo Akad. Nauk. SSSR, 1951.

[8] _____, The exact theory of steady state waves on the surface of a heavy liquid, Translated by D. V. Thampuran, Edited by C. W. Cryer, MRC Report #813, 1967.

[9] Levi-Civita, T., Determination Rigoureuse des Ondes permanentes d'ampleur Finie, Math. Ann., Vol. 93, 1925.

[10] Krasovskii, Yu. P., The existence of aperiodic flows with free boundaries, Doklady Akad. Nauk., Vol. 133, No. 4(1960).

[11] _____, The theory of steady-state waves of large amplitude, Sov. Phy.-Dokl., Vol. 5, (1960).

[12] Bueckner, Hans F., An iterative method for solving nonlinear integral equations, MRC Tech. Report #207, 1960.

[13] Conway, W. E. and J. W. Thomas, Free streamline problems and the Milne-Thomson integral equation, J. of Math and Phy. Sci., Vol. 8, 1(1974).

[14] Salvesen, N. and C. H. von Kerczek, Comparison of numerical and perturbation solutions of two-dimensional nonlinear water-wave problems, to be published in J. of Ship Research (1976).

[15] Thomas, J. W., Irrotational gravity waves of finite height: a numerical study, Mathematika 15(1968), pp. 139-148.

[16] Abramowitz, M. and I. A. Stegun (eds.), Handbook of Mathematical Functions with Formulas, Graphs, and Mathematical Tables, Nat. Bureau of Standards Applied Math. Series 55, 1964.

[17] Thomas, J. W., On the exact form of gravity waves on the surface of an inviscid liquid, dissertation, Univ. of Arizona, 1967.

[18] Salzer, Herbert E., Quick calculation of Jacobian elliptic functions, Comm. of the ACM, Vol. 5, 1962, p. 339.

[19] Thomas, J. W., A numerical study of the relationship between the dimensionless parameters in the problem of periodic waves of permanent type in a liquid of finite depth, Quart. of Applied Math., Jan., 1975.

A HYBRID INTEGRAL-EQUATION METHOD FOR TIME-HARMONIC FREE-SURFACE FLOW

Ronald W. Yeung

Massachusetts Institute of Technology
Cambridge, Massachusetts 02139 U.S.A.

ABSTRACT

The two-dimensional boundary-value problems for time-harmonic free-surface flow in water of arbitrary bottom topography are considered. A novel and versatile approach for the solution of these types of problems is presented in this paper. The inner region of changing topography is described by an integral relation while the outer regions of constant depths are characterized by eigenfunctions. Pressure and flux fields of the two representations are matched at the radiation boundaries. The resulting "hybrid" integral equation is solved numerically. The method is applied to a variety of radiation and scattering problems. Test computations agree well with existing results. New results for a number of realistic geometries are also given to illustrate the versatility of the method.

1. Introduction

Hydrodynamic-force coefficients for two-dimensional objects in or near a free surface are of particular relevance to ship-motion or platform-motion theory. The term radiation problem applies to situations where the body oscillates in otherwise calm water, while scattering problems usually refer to cases where the body is held fixed in a train of incident waves. The two types of problems are mathematically and physically related. The radiation and scattering properties

of an object depend not only on its own geometry, but also strongly on the physical features of the environment. The advent of supersize vessels and huge offshore structures has made the consideration of effects of restricted water important. This paper presents a new technique of solving the radiation and scattering problem in water of complicated boundary configuration, a subject which has not received much attention in the literature.

A brief review of existing solution methods for the type of problems being considered is in order. The classical work is due to Ursell (1948) who solved the heaving problem of a circular cylinder in an infinite fluid using a sequence of singularities located at the origin. A more versatile formulation for general-shaped bodies consists of distributing the so-called wave-sources on the body contour. The strength of these sources is obtained by solving a Fredholm integral equation of the second kind [Lebreton and Margnac (1966), Frank (1967)]. This approach is still applicable when the water depth is not constant, in which case the unknown strength in the integral equation will also include that part of the bottom boundary that is varying. If the depth changes from one limiting value to another, on the opposite side, the problem is considerably more complicated. A variety of approaches have been used by previous workers to tackle scattering problems associated with certain simple geometries. Bartholomeusz (1957) obtained a long-wave solution for propagation over a step of finite height by considering an integral equation which was arrived at by matching the potential above the step. Newman (1965) provided results for the transmission and reflection coefficients over an infinite step by matching wave-maker solutions for the two regions. Miles (1967) considered a more exact solution of the unequal-depths problem by using Schwinger's variational formulation. Hilaly (1967) treated the same problem by matching eigenfunction expansions. All these problems as well as the more general case of a non-

step- ke transition can be handled, in principle, by exploiting a Green function, if available, that satisfies the bottom conditions on both sides of the transition region. Evans (1972) in fact derived this function. The resulting expression is quite complex. To this author's knowledge, no application of it to practical problems has yet been made. Bai and Yeung (1974) investigated two new approaches for treating the problem of general bottom topography. One method utilizes a variational formulation with the fluid domain represented by finite elements; minimization of a certain functional then leads to the solution of the problem. The other approach consists of applying the simple source function for an infinite fluid to a finite fluid domain, resulting in an integral equation along the fluid boundary that has to be solved. Chan and Hirt (1974) used an initial-value problem formulation and a finite-difference mesh to tackle the problem.

The method described in this paper stems from the author's earlier work [Yeung (1973), also Bai and Yeung (1974)] in which case, the inner region where all the geometrical changes occur is described by Green's theorem using the source function for an infinite fluid. However, instead of applying a radiation condition at a large distance from the origin of disturbance, we now match the flux and pressure fields at the "radiation boundaries" with solutions in the outer fields represented by eigenfunction expansions. The location of the radiation boundary can now be chosen arbitrarily close to the body, thus shortening the length of the contour which bounds the inner field. The method is found to be highly efficient from the computation viewpoint.

2. The Boundary-Value Problems

Consider the two-dimensional motion of an inviscid fluid with a free surface, as shown in Figure 1. The bottom topography can be arbitrary, but must approach some asymptotic depths h^+, h^- which need not be equal. Fluid motion may be

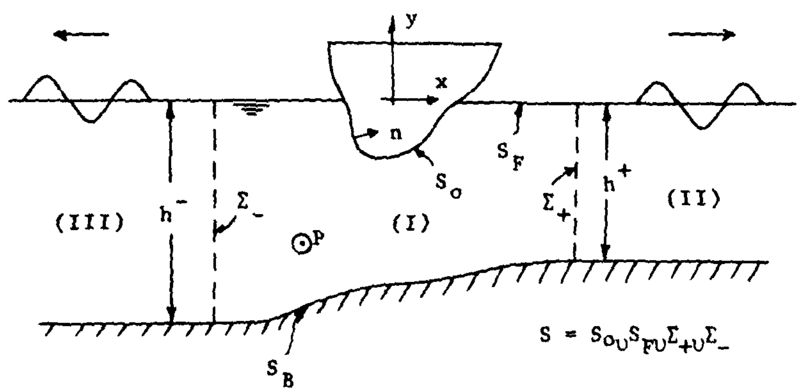

Figure 1. Coordinate System and Notation

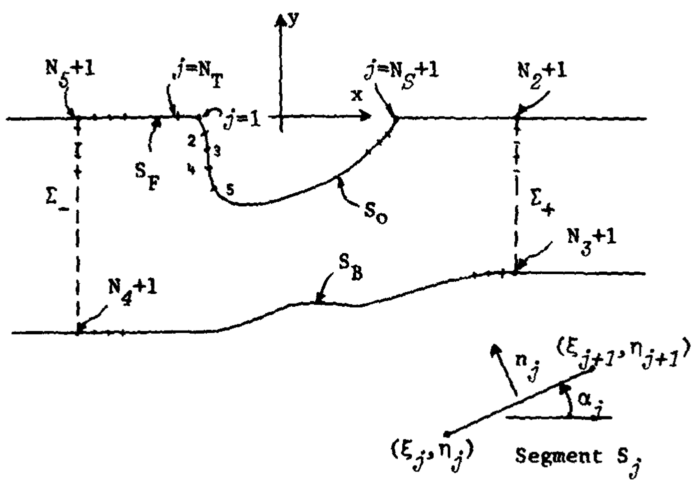

Figure 2. Subdivision of Boundary Contour

generated by the oscillation of the body or by an incident wave system impinging on the body. If the flow is assumed irrotational and time-harmonic of angular frequency σ , the fluid motion can be described by a velocity potential function,

$$\Phi(x,y,t) = \mathcal{R}e\left[\varphi(x,y)\,\alpha(t)\right], \quad \varphi = \varphi_1 + i\varphi_2 \tag{2.1a}$$

where

$$\alpha(t) = \mathcal{R}e\left[a(t)\right] \equiv \mathcal{R}e\left[(a_1 + i a_2)\, e^{-i\sigma t}\right], \quad i = \sqrt{-1} \tag{2.1b}$$

with $\alpha(t)$ being the amplitude of the body motion. $\varphi(x,y)$ is the unknown complex-valued spatial function which satisfies Laplace's equation in the fluid:

$$\nabla^2\varphi(x,y) = 0 \tag{2.2}$$

and the following linearized boundary conditions:

$$\varphi_y - \nu\varphi = 0 \qquad \text{on } S_F \tag{2.3a}$$

$$\varphi_n = 0 \qquad \text{on } S_B, \tag{2.3b}$$

$$\varphi_n = f(s) \qquad \text{on } S_o, \tag{2.3c}$$

where $\nu = \sigma^2/g$, g being the acceleration of gravity, S_F is the undisturbed free surface, S_B the bottom surface, and S_o the wetted portion of the body in its equilibrium position. If $\vec{n}$ is the unit inward normal of the body with components (n_x, n_y), the functions associated with the inhomogeneous boundary condition, $f(s)$, for sway, heave and roll motion of the body are n_x , n_y , and $(xn_y - yn_x)$ respectively. Aside from the conditions (2.3), a radiation condition must be imposed in order to render the problem unique. This may be stated as that all propagating waves must be outgoing.

Once φ is known, the linearized hydrodynamic force or moment (about 0) acting on the body can be obtained from the

time-dependent Bernoulli's equation and are usually written in terms of components in phase with the body acceleration and the body velocity. For instance, for the heave motion we have

$$F_y = -\mu_{yy}\ddot{\alpha}(t) - \lambda_{yy}\dot{\alpha}(t) , \tag{2.4}$$

where μ_{yy} and λ_{yy} are the added-mass and damping coefficients for heave and are defined in terms of the solution of $\varphi(x,y)$, corresponding to $f(s) = n_y$, by

$$\mu_{yy} + i\frac{\lambda_{yy}}{\sigma} = \rho\int_{S_0} \varphi \frac{\partial\varphi}{\partial n}\, ds \tag{2.5}$$

Coupling coefficients also exist if more than one degree of freedom of motion occurs.

If one is concerned with the diffraction problem, the definition used in (2.1) is still applicable provided we choose $a_1 = 0$ and $a_2 = 1/\sigma$. In this work, it will be more convenient to solve for the total potential known usually as the scattering potential defined by

$$\varphi = \varphi_I + \varphi_D \tag{2.6}$$

where φ_I is the incident-wave spatial potential, defined by

$$\varphi_I = \frac{gA}{\sigma}\ \frac{\cosh m_0^-(y+h^-)}{\cosh m_0^- h^-}\, e^{i m_0^- x} \ , \quad m_0^- \tanh m_0^- h^- = \sigma^2/g \tag{2.7}$$

and φ_D is the so-called diffraction potential. Hence, for the incident-wave problem, the scattering potential defined by (2.6) satisfies (2.2), (2.3a) and (2.3b) but

$$\varphi_n = 0 \qquad \text{on} \quad S_0 . \tag{2.8}$$

The inhomogeneity will come from the radiation boundaries as detailed in the next section.

The free-surface elevation $\zeta(x,y)$ for either type of problem can be obtained from the dynamic boundary condition on

AD-A119 315 DAVID W TAYLOR NAVAL SHIP RESEARCH AND DEVELOPMENT CE--ETC F/G 20/4
FIRST INTERNATIONAL CONFERENCE ON NUMERICAL SHIP HYDRODYNAMICS --ETC(U)
1975 J W SCHOT, N. SALVESEN

UNCLASSIFIED NL

AD A
119315

the free surface and is given by

$$\zeta(x,t) = \mathcal{R}_e \left[Y(x) e^{-i\sigma t} \right] \tag{2.9}$$

with

$$Y(x) = \nu \varphi(x,0) \left(a_1 + i a_2 \right). \tag{2.10}$$

Nothing has been said so far about how the two types of problems are related. Such relations can be most conveniently obtained by the application of Green's second formula. This was indicated in a recent work by Newman (1975) pertaining to the case of equal asymptotic-depths. The results can be generalized for the unequal-depths case. For this latter case, there exist two sets of transmission and reflection coefficients, corresponding to the two different directions of incidence of the propagating waves. The two sets are somewhat related as indicated by Kreisel (1949) and Newman (1965). If (R_1, T_1), (R_2, T_2) denote the reflection and transmission coefficients due to incident waves from the left and the right respectively, i.e.

$$\varphi_1 \sim \begin{cases} \left[e^{i m_0^- x} + R_1 e^{-i m_0^- x} \right] K^-(y), & x \to -\infty \\ T_1 e^{i m_0^+ x} K^+(y), & x \to \infty \end{cases} \tag{2.11a}$$

and

$$\varphi_2 \sim \begin{cases} \left[e^{-i m_0^+ x} + R_2 e^{i m_0^+ x} \right] K^+(y), & x \to \infty \\ T_2 e^{-i m_0^- x} K^-(y), & x \to -\infty \end{cases} \tag{2.11b}$$

where

$$K^\pm(y) = \cosh m_0^\pm (y + h^\pm) / \cosh m_0^\pm h^\pm , \tag{2.11c}$$

then

$$R_1 R_1^* + T_1 T_1^* (D^+/D^-) = 1 \tag{2.11}$$

$$R_2 R_2^* + T_2 T_2^* (D^-/D^+) = 1 \tag{2.12}$$

$$D^- T_2 = T_1 D^+ \tag{2.13}$$

$$|R_1| = |R_2| \tag{2.14}$$

$$T_1^*/T_1 = R_2^*/R_1 \tag{2.15}$$

where

$$D^{\pm} = 4 \frac{sh\, 2m_0^{\pm} h^{\pm} + 2m_0^{\pm} h^{\pm}}{ch\, 2m_0^{\pm} h^{\pm} + 1} \tag{2.16}$$

These are useful relations for checking consistency of the numerical solution. The well-known Haskind's relation remains basically the same:

$$F_j^{\pm} = -\frac{\rho g^2}{4\sigma} D^{\pm} Y_j^{\pm} \tag{2.17}$$

where $F_j^{\pm}$ is the exciting force or moment in the j-th direction due to a unit-amplitude incident wave and $Y_j^{\pm}$ is the complex wave-amplitudes due to the forced oscillation of the body or any part of the bottom contour (i.e., if we are interested in the force on that particular portion) in the j-th direction. Finally, if $A_{\pm}$, $B_{\pm}$ denote the radiation wave-amplitudes of two independent solutions (or experiments) of the radiation problem,

$$\begin{bmatrix} R_1 \\ T_1 \end{bmatrix} = \frac{1}{A_-^* B_+^* - A_+^* B_-^*} \begin{bmatrix} A_+^* B_- - A_- B_+^* \\ (A_- B_-^* - A_-^* B_-) D^-/D^+ \end{bmatrix} \tag{2.18}$$

which can be used to obtain the coefficients (R_1, T_1). (T_2 , R_2) then follow from (2.13), (2.14) and (2.15).

3. The Method of Solution

We illustrate the method of solution by applying it to the forced-motion or radiation problem. The treatment for the scattering problem requires only slight modification. First let Σ_+, Σ_-, be two artificially chosen vertical boundaries subdividing the fluid domain into an inner region of changing geometry and two outer regions of constant depths. These are denoted by regions I, II, and III as shown in Fig. 1. Let P be a field point in Region I, and Q be a variable point on the boundary of this region. Application of Green's second identity to φ and $\log \frac{1}{r}$, r being the distance between P and Q, then yields

$$2\pi \varphi(P) = \oint_{S} \frac{\partial \varphi(Q)}{\partial n} \log \frac{1}{r} \, ds(Q) - \oint_{S} \varphi \frac{\partial}{\partial n}\left[\log \frac{1}{r}\right] ds(Q) \qquad (3.1)$$

where

$$\frac{\partial}{\partial n} = \vec{n} \cdot \left(\frac{\partial}{\partial \xi}, \frac{\partial}{\partial \eta} \right)$$

ξ, η being variables of integration along S. Here ds denotes an infinitesimal arclength element along the boundary. On S_F, S_o, and S_B, the normal derivative of φ is either known or expressible in terms of φ itself. Hence

$$\begin{aligned} 2\pi \varphi(P) = & \int_{S_o} \varphi(Q) \frac{\partial}{\partial n} \log r \, ds(Q) + \int_{S_F} \varphi \left[\frac{\partial}{\partial n} \log r - \nu \log r \right] ds \\ & + \int_{S_B} \varphi \frac{\partial}{\partial n} \log r \, ds + \int_{\Sigma_+ \cup \Sigma_-} \left[\varphi \frac{\partial}{\partial n} \log r - \varphi_n \log r \right] ds \\ & - \int_{S_o} f(s) \frac{\partial}{\partial n} \log r \, ds \end{aligned} \qquad (3.2)$$

Consider now regions II and III. Since the fluid depth is constant, the solution in either one of these regions may be written in the form of eigenfunction expansions [Wehausen, 1969], viz.,

$$\varphi(x,y) = A_0^+ e^{-im_0^+ x} \frac{\cosh m_0^+(y+h^+)}{\cosh m_0^+ h^+} + \sum_{k=1}^{\infty} C_k^+ e^{-m_k^+ x} \frac{\cos m_k^+(y+h^+)}{\cos m_k^+ h^+}$$

for $x \geq X_R$ (3.3)

and

$$\varphi(x,y) = A_0^- e^{-im_0^- x} \frac{\cosh m_0^-(y+h^-)}{\cosh m_0^- h^-} + \sum_{k=1}^{\infty} C_k^- e^{m_k^- x} \frac{\cos m_k^-(y+h^-)}{\cos m_k^- h^-}$$

for $x \leq X_L$ (3.4)

with the coefficients $A_0^{\pm}$ and $C_k^{\pm}$ being unknown. The eigenvalues m_0, im_k, $k=1,2\ldots.$ are roots of the transcendental equation:

$$m \tanh mh = \sigma^2/g \tag{3.5}$$

where m represents either m_0 or im_K. The functional forms of (3.3) and (3.4) have been chosen so that φ represents outgoing waves to the right and left in Regions II and III, respectively. If we now make use of these representations of φ and substitute them into (3.2), i.e., if we match at Σ_+ and Σ_- the potential (which is proportional to the fluid pressure) and the normal velocity of the inner regions with those of the outer regions, we may rewrite (3.2) as:

$$2\pi\varphi(x,y) = \int_{S_U S_B} \varphi \frac{\partial}{\partial n} \log r \, ds + \int_{S_F} \varphi\left[\frac{\partial}{\partial n}\log r - \nu \log r\right] ds - \int_{S_0} f(s) \log r \, ds$$
$$+ A_0^+ e^{im_0^+ \xi_R}\left[\mathcal{F}_0^+ - i G_0^+\right] + \sum_{k=1}^{\infty} C_k^+ e^{-m_k^+ \xi_R}\left[\mathcal{F}_k^+ + G_k^+\right]$$

$$-A_0^- e^{-im_0^- \xi_L}\left[\mathcal{F}_0^- + i G_0^-\right] + \sum_{k=1}^{\infty} C_k^- e^{m_k^- \xi_L}\left[\mathcal{F}_k^- + G_k^-\right] \tag{3.6}$$

where the functions $\mathcal{F}_k(x-\xi, y)$ and $G_k(x-\xi, y)$ are defined by the following integrals:

$$\begin{matrix} \mathcal{F}_0(x-\xi, y) \\ G_0(x-\xi, y) \end{matrix} = \int_{-h}^{0} d\eta \, \frac{\cosh m_0(\eta+h)}{\cosh m_0 h} \begin{pmatrix} \frac{\partial}{\partial \xi} \log r \\ m_0 \log r \end{pmatrix} \tag{3.7}$$

$$\begin{matrix} \mathcal{F}_k(x-\xi, y) \\ G_k(x-\xi, y) \end{matrix} = \int_{-h}^{0} d\eta \, \frac{\cos m_k(\eta+h)}{\cos m_k h} \begin{pmatrix} \frac{\partial}{\partial \xi} \log r \\ m_k \log r \end{pmatrix} \tag{3.8}$$

The superscripts in (3.6) are used to designate the wave number m_0 and depth h on the appropriate side. Physically, one may think of the last four terms of (3.6) as a vertical distribution of sources and normal dipoles of certain assumed forms on the "radiation boundaries". The functional form of this distribution is chosen to satisfy Laplace's equation. This idea follows from one type of treatment used by Yeung (1973), in which case, an exponentially decaying distribution was used on the radiation boundary to represent the behavior of an outgoing wave in water of infinite depth. The present expansion is evidently a more complete treatment. In practice, only a finite number of terms in the series of (3.6) will be taken; we denote this by N_R and N_L.

Referring to (3.6) we see that the velocity potential, φ, will be known everywhere if φ is known on the boundary $S_0 \cup S_B \cup S_F$, *and* if the coefficients of the expansions are known. To obtain an equation for the $\varphi(Q)$, we simply let

the field point approach the aforementioned boundary. The following "hybrid" integral equation then results.

$$-\pi\Phi(P) + \int_{S_0 \cup S_B} \Phi \frac{\partial}{\partial n}\log r \, ds + \int_{S_F} \Phi\left[\frac{\partial}{\partial n}\log r - \nu \log r\right] ds$$

$$+ A_0^+ e^{i m_0^+ \xi_R}\left[\mathcal{F}_0^+ - i G_0^+\right] + \sum_{K=1}^{N_R} C_K^+ e^{-m_K^+ \xi_R}\left[\mathcal{F}_K^+ + G_K^+\right]$$

$$- A_0^- e^{-i m_0^- \xi_L}\left[\mathcal{F}_0^- + i G_0^-\right] + \sum_{K=1}^{N_L} C_K^- e^{+m_K^- \xi_L}\left[-\mathcal{F}_K^- + G_K^-\right]$$

$$= \int_{S_0} f(s) \log r \, ds \qquad \text{for } P \in S_0 \cup S_F \cup S_B \tag{3.9}$$

If we now place the point P at ($N_R + 1$) distinct locations on Σ_+, and ($N_L + 1$) distinct locations on Σ_-, we shall have enough equations to determine the unknown coefficients of the expansions. Whence, making use of (3.3) and (3.4) on the left-hand side of (3.6) and observing that the $\mathcal{F}_K$'s give a finite contribution when the limit of $r \to 0$ is taken, we get

$$\int_{S_0 \cup S_B} \Phi \frac{\partial}{\partial n}\log r \, ds + \int_{S_F} \Phi\left[\frac{\partial}{\partial n}\log r - \nu \log r\right] ds$$

$$+ A_0^+ e^{i m_0^+ \xi_R}\left[-\pi \frac{\cosh m_0^+(y+h^+)}{\cosh m_0^+ h^+} - i G_0^+(0,y)\right] + \sum_{K=1}^{N_R} C_K^+ e^{-m_K^+ \xi_R}\left[-\pi \frac{\cos m_K^+(y+h^+)}{\cos m_K^+ h^+} + G_K^+(0,y)\right]$$

$$- A_0^- e^{-i m_0^- \xi_L}\left[\mathcal{F}_0^-(\xi_R - \xi_L) + i G_0^-\right] + \sum_{K=1}^{N_L} C_K^- e^{+m_K^- \xi_L}\left[-\mathcal{F}_K^- + G_K^-\right]$$

$$= \int_{S_0} f(s) \log r \, ds \, ,$$

$$\text{for } P \in \Sigma_+ \tag{3.10}$$

with a similarly modified expression for $P \in \Sigma_-$. It was found that the choice of these so-called control-points on Σ_+ or Σ_-, with everything else held constant, have no effects on the numerical solution of the problem. Of course, one must not choose two points to be so close that they become numerically indistinctive. (3.9) and (3.10) thus are a rational system of equations for the solution of the problem under consideration. One caution however one should take in solving (3.9) and (3.10) is that it is more desirable to absorb the exponential factor following $C_K^{\pm}$ by defining new coefficients, say $\tilde{C}_K^{\pm}$, representing the product of the two. This will prevent certain column elements of the matrix of the linear equations representing equations (3.9) and (3.10), which will be discussed later, from becoming excessively small if X_R or X_L have a large value.

For the scattering problem, we observe that the representation of (3.3, and (3.4) is incomplete. If the right-moving incident wave is of amplitude A_I in Region III, the scattering potential is

$$\varphi(x,y) = \left\{A_I e^{im_0^- x} + A_0^- e^{-im_0^- x}\right\}\frac{\cosh m_0^-(y+h^-)}{\cosh m_0^- h^-} + \sum_{K=1}^{\infty} C_K^- e^{m_K^- x}\frac{\cos m_K^-(y+h^-)}{\cos m_K^- h^-} \quad (3.11)$$

The quantity A_0^+ in (3.3) is now proportional to the amplitude of the transmitted wave. By (2.8) the third integral of (3.2) now vanishes. Transposing all unknown quantities to the left-hand side of the equation, we obtain the following equation as the analog of (3.9)

$$-\pi\varphi(P) + \int_{S_0 \cup S_B} \varphi \frac{\partial}{\partial n}\log r\, ds + \int_{S_F} \varphi\left[\frac{\partial}{\partial n}\log r - \nu \log r\right] ds$$

$$+A_0^+ e^{im_0^+ \xi_R}\left[\mathcal{F}_0^+ - i G_0^+\right] + \sum_{K=1}^{N_R} C_K^+ e^{-m_K^+ \xi_R}\left[\mathcal{F}_K^+ + G_K^+\right]$$

$$-A_o^- e^{-im_o^- \xi_L} \left[\mathcal{F}_o^- + i G_o^- \right] + \sum_{K=1}^{N_L} C_K^- e^{m_K^- \xi_L} \left[-\mathcal{F}_K^- + G_K^- \right]$$

$$= - A_I e^{i m_o^- \xi_L} \left[-\mathcal{F}_o^- + i G_o^- \right] \tag{3.12}$$

The inhomogeneity now occurs on the left radiation boundary. The analog of (3.10) can also be obtained in a similar fashion. Once the system of equations is solved, the complex-valued transmission and reflection coefficients are simply given respectively by

$$\begin{aligned} T_1 &= A_o^+ / A_I \\ R_1 &= A_o^- / A_I \end{aligned} \tag{3.13}$$

It is worthwhile to note in passing that in classical elliptic boundary-value problems, one normally specifies either the potential or the normal derivative on the boundary. In our present approach, an *indirect* specification of both φ and φ_n on Σ_+ and Σ_- is accomplished by requiring them to be expandable in the y-direction as a sequence of orthogonal functions with unknown coefficients. Although such a type of "boundary condition" is hardly discussed in the theory of partial differential equations, we have experienced no difficulty in finding a stable numerical solution, which will be discussed next.

4. Solution by the Method of Discretization

By the method of discretization, the integral equations (3.10) and (3.11) for the unknown continuous function $\varphi(Q)$ can be reduced to a set of linear algebraic equations. First, a set of grid points is chosen along the contour S_o, S_F, and S_B in Region I. Let these be denoted by (ξ_j, η_j), as defined in Figure 2.* For a sufficiently fine grid, the unknown $\varphi(Q)$ between each pair of consecutive grid points may be

---

*See page 584.

approximated by a constant function Φ_j. If equation (3.10) is evaluated now at a set of control points denoted by (x_i, y_i) on the boundary, the following discretized representation is possible:

$$\sum_j \left[-\pi\delta_{ij} + C_{ij}\right]\Phi_j + A_o^+ S_{io}^+ + \sum_{K=1}^{N_R} C_K^+ S_{iK}^+$$

$$+ A_o^- S_{io}^- + \sum_{K=1}^{N_L} C_K^- S_{iK}^- = \sum_{j=1}^{N_2} P_{ij} f(x_j, y_j)$$

$$\text{for } i = 1, 2, \cdots, N_2 \qquad (4.1)$$
$$i = N_3+1, \cdots, N_4$$
$$i = N_5+1, \cdots, N_T$$

where δ_{ij} is the Kronecker delta and the values of j in the first sum are identical to those of i. The influence coefficients C_{ij} and S_{iK} are defined by integrals as follows:

$$C_{ij} = \begin{cases} Q_{ij} & \text{for } j = 1, \cdots\cdots, N_s; \\ & \quad\; j = N_3+1, \cdots\cdots, N_4; \\ Q_{ij} - \nu P_{ij} & \text{for } j = N_3+1, \cdots\cdots, N_2; \\ & \quad\; j = N_5+1, \cdots\cdots, N_T; \end{cases} \qquad (4.2)$$

with Q_{ij} and P_{ij} being line integrals over a small segment S_j:

$$P_{ij}(\xi_j, \eta_j; \xi_{j+1}, \eta_{j+1}) = \int_{S_j} \log\left[(x_i-\xi)^2 + (y_i-\eta)^2\right]^{1/2} dS \qquad (4.3)$$

$$Q_{ij}(\xi_j, \eta_j; \xi_{j+1}, \eta_{j+1}) = \int_{S_j} \frac{\partial}{\partial n_j} \log\left[(x_i-\xi)^2 + (y_i-\eta)^2\right]^{1/2} dS \qquad (4.4)$$

and

$$S_{io}^{\pm} = e^{\pm i m_o \xi}\left[\pm \mathcal{F}_o^{\pm}(x_i-\xi, y_i) - i\, G_o^{\pm}(x_i-\xi, y_i)\right]$$

$$S_{iK}^{\pm} = \left[\pm \mathcal{F}_K^{\pm}(x_i-\xi, y_i) + G_K^{\pm}(x_i-\xi, y_i)\right] \qquad (4.5)$$

with the $\mathcal{F}_K$ and G_K defined by (3.8) and (3.9). In Equation (4.5), the top and bottom signs are to be associated with the right and left radiation boundaries respectively.

If the control points are located on Σ_+, Equation (3.11) is to be used. The corresponding form for it is:

$$\sum_j C_{ij}\varphi_j + A_0^+ T_{i0}^+ + \sum_{K=1}^{N_R} C_K^+ T_{iK}^+ + A_0^- S_{i0}^- + \sum_{K=1}^{N_L} C_K^- S_{iK}^- = \sum_{j=1}^{N_B} P_{ij} f(x_j, y_j) \tag{4.6}$$

for $i = N_2+1, \cdots, N_3$

where for obvious reasons, $N_3 - N_2 = N_R$. The T_{iK}^+ are defined by:

$$T_{i0}^+ = e^{i m_0^+ \xi_R}\left[-\pi \frac{\cosh m_0^+(y+h^+)}{\cosh m_0^+ h^+} + i G_0^+(0,y)\right] \tag{4.7a}$$

$$T_{iK}^+ = \left[-\pi \frac{\cos m_K^+(y+h^+)}{\cos m_K^+ h^+} + G^+(0,y)\right], \quad K=1,2,\cdots. \tag{4.7b}$$

N_L+1 equations for (x_i, y_i) on Σ_- can also be written in a similar manner. Therefore combining these with (4.1) and (4.6) we have altogether N_T linear equations for N_T unknowns which can be solved simultaneously. Of course, much of the efficiency and feasibility of the method will obviously depend on our ability to handle integrals defined by (4.3), (4.4), (3.8), and (3.9). The integrals P_{ij} and Q_{ij} can be evaluated analytically in a rather straightforward manner, but the $\mathcal{F}$'s and G's have no simple closed-form solution. While (3.8) does not pose any problem for numerical quadrature, (3.9) requires more careful consideration because of the oscillatory behavior of its integrand, particularly when K is large. It can be shown that these source and normal derivative-integrals can be written in terms of standard exponential integrals with

complex arguments. Namely, define the complex numbers

$$\zeta_1 = m(a+iy), \quad \zeta_2 = m[a+i(y+h)], \quad y \leq 0 \tag{4.8}$$

then

$$\begin{aligned} F(a,y) &\equiv \int_{-h}^{0} \cos m(y+h) \frac{\partial}{\partial \xi}\left\{\log\left[a^2+(y-\eta)^2\right]^{\frac{1}{2}}\right\} d\eta \\ &= -\pi \operatorname{sign}(a)\, e^{-|a|m} \cos m(y+h) \\ &\quad + \frac{1}{2} \mathcal{I}m\left[e^{\zeta_2} E_1(\zeta_2) + e^{-\zeta_2} E_1(-\zeta_2)\right] \\ &\quad - \frac{1}{2} \mathcal{I}m\left[e^{imh} e^{\zeta_1} E_1(\zeta_1) + e^{-imh} e^{-\zeta_1} E_1(-\zeta_1)\right] \end{aligned} \tag{4.9}$$

$$\begin{aligned} G(a,y) &\equiv m\int_{-h}^{0} \cos m(y+h) \log\left[a^2+(y-\eta)^2\right]^{\frac{1}{2}} d\eta \\ &= \sin mh \log\left[a^2+y^2\right]^{\frac{1}{2}} - \pi \cos m(h+y)\, e^{-|a|m} \\ &\quad - \frac{1}{2} \mathcal{I}m\left[e^{\zeta_2} E_1(\zeta_2) - e^{-\zeta_2} E_1(-\zeta_2)\right] \\ &\quad + \frac{1}{2} \mathcal{I}m\left[e^{imh} e^{\zeta_1} E_1(\zeta_1) - e^{-imh} e^{-\zeta_1} E_1(-\zeta_1)\right] \end{aligned} \tag{4.10}$$

where the exponential-integral special function $E_1(\zeta)$ is defined to be

$$E_1(\zeta) = \int_{\zeta}^{\infty} \frac{e^{-t}}{t}\, dt \quad , \quad |\arg \zeta| < \pi \tag{4.11}$$

A preponderance of techniques is available in the literature for efficient evaluation of this special function.

5. Results and Discussions

The present method of solution has been applied to a number of radiation and scattering problems. In all cases where existing results are available and are known to be correct, the present computation yields very good agreement. As an example, the heave added-mass and damping coefficients (or wave amplitude ratio) for a circular cylinder as well as a rectangular cylinder in water of finite but constant depth are shown in Figures 3. For the rectangular case, these are compared with Lebreton and Margnac (1966) who used the Green-function integral-equation technique to solve the problem. For the circular case, results are compared with Bai and Yeung (1974) obtained by two different methods. The present calculations are consistent with the author's previous calculations using the fundamental-singularity distribution method. For a circular cylinder in water depth of h/a = 2.0, the current calculations yield a limiting value of added-mass coefficient equal to 0.500 as the frequency goes to zero. This value is found to be consistent with that obtained by an alternative approach of considering the limiting boundary-value problem (Newman and Yeung, 1975). The corresponding limiting value of the rectangular cylinder is 0.822. Yeung (1973) showed that for a fluid with different depths on each side, the damping coefficient is related to the asymptotic wave-amplitudes by

$$\frac{2\sigma^3}{\rho g^2}\lambda_{kk} \Big/ \left[\left|\frac{\Upsilon^+}{a}\right|^2 D^+ + \left|\frac{\Upsilon^-}{a}\right|^2 D^- \right] = 1. \tag{5.1}$$

This equation provides a consistency check of the integral of the potential on the body, Equation (2.5), and the asymptotic wave-amplitude defined by the first term of the eigenfunction expansion, Equations (3.3) and (3.4). In all results shown, Equation (5.1) is satisfied very accurately.

Figure 4 shows the hydrodynamic coefficients of a bulbous

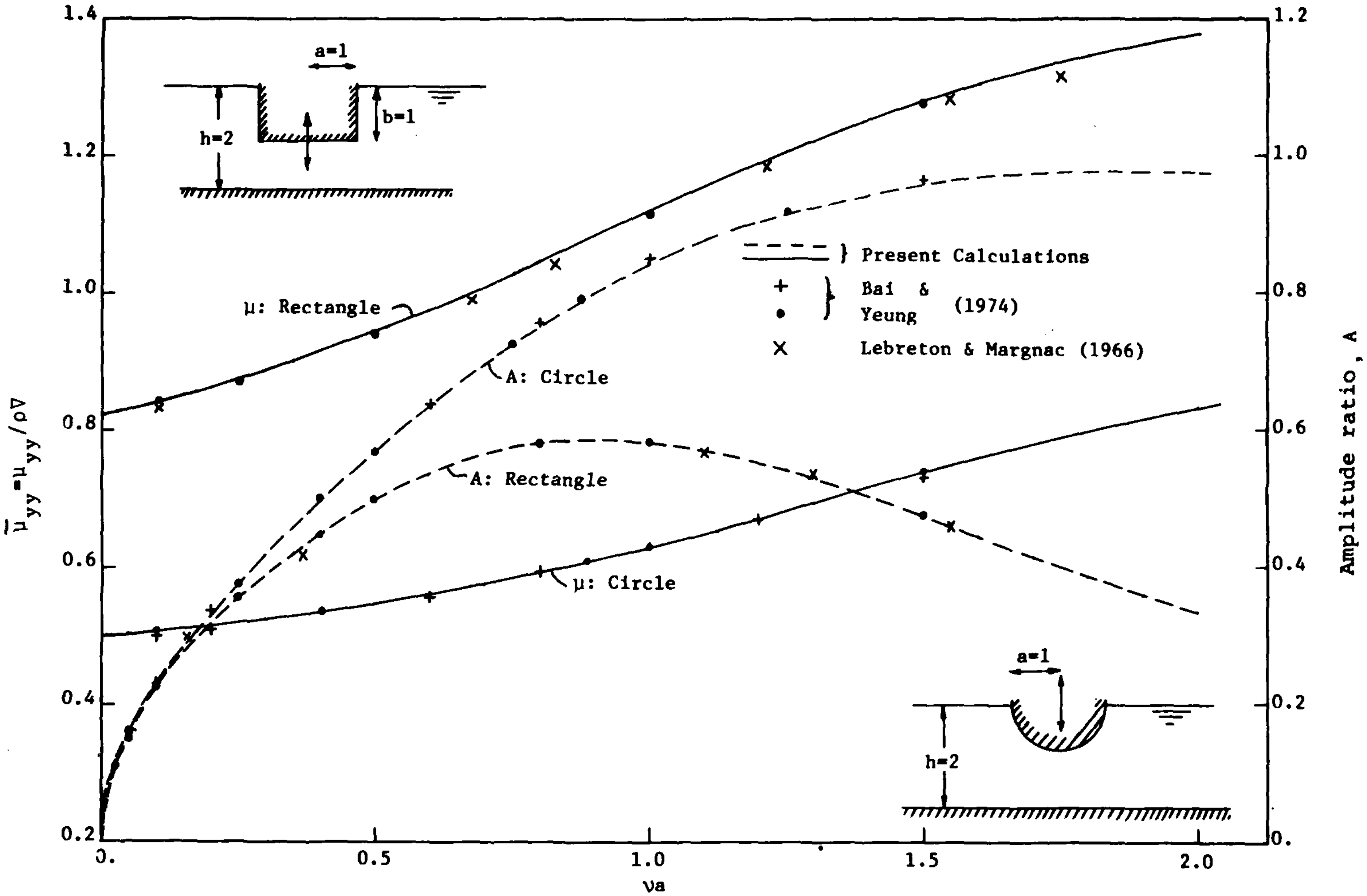

Fig. 3 Heave added-mass coefficients and wave-amplitude ratios of circular and rectangular cylinders

cylinder undergoing sway or heave motion in water of varying depth. A sinusoid is used to represent the transition region. Results for the constant depth case with the depth being the average of the two sides are also shown. For the particular configuration considered, forces associated with the heave mode are much less sensitive to the change in bottom topography as compared to those of the sway mode. Coefficients associated with the sway mode also become practically indistinguishable for the two cases when $\nu a \geqslant 0.2$. This corresponds to a mean depth/wave-length ratio of approximately 0.463. We observe that the phenomenon of radiationless frequency for heave occurs also in water of finite depth. Furthermore there exists a frequency range in which the sway added mass becomes vanishingly small and even slightly negative. Similar occurrences of negative added-mass coefficients were observed by Ogilvie (1963) when he considered the swaying force on a submerged circular cylinder near the free surface.

Turning our attention now to scattering problems, we show in Figure 5 the total wave amplitude function $Y_T(x)$ due to a right-moving wave propagating over a sinusoidal hump. The results obtained earlier by Bai and Yeung (1974) using a finite-element method have been incorrectly given. The complex wave function $Y_T(x)$ is defined as

$$Y_T(x) = i e^{i m_0 x} + Y_D(x) \equiv Y_1(x) + i Y_2(x) \tag{5.2}$$

where the first term after the first equality sign represents the incident wave and the second the diffracted waves.

The scattering characteristics of a finite-size step are given in Table 1 and are compared with Hilaly (1967). By Equation (2.11):

$$\gamma |Y^+|^2 + |Y^-|^2 = 1 \,, \qquad \gamma = D^+/D^- \tag{5.3}$$

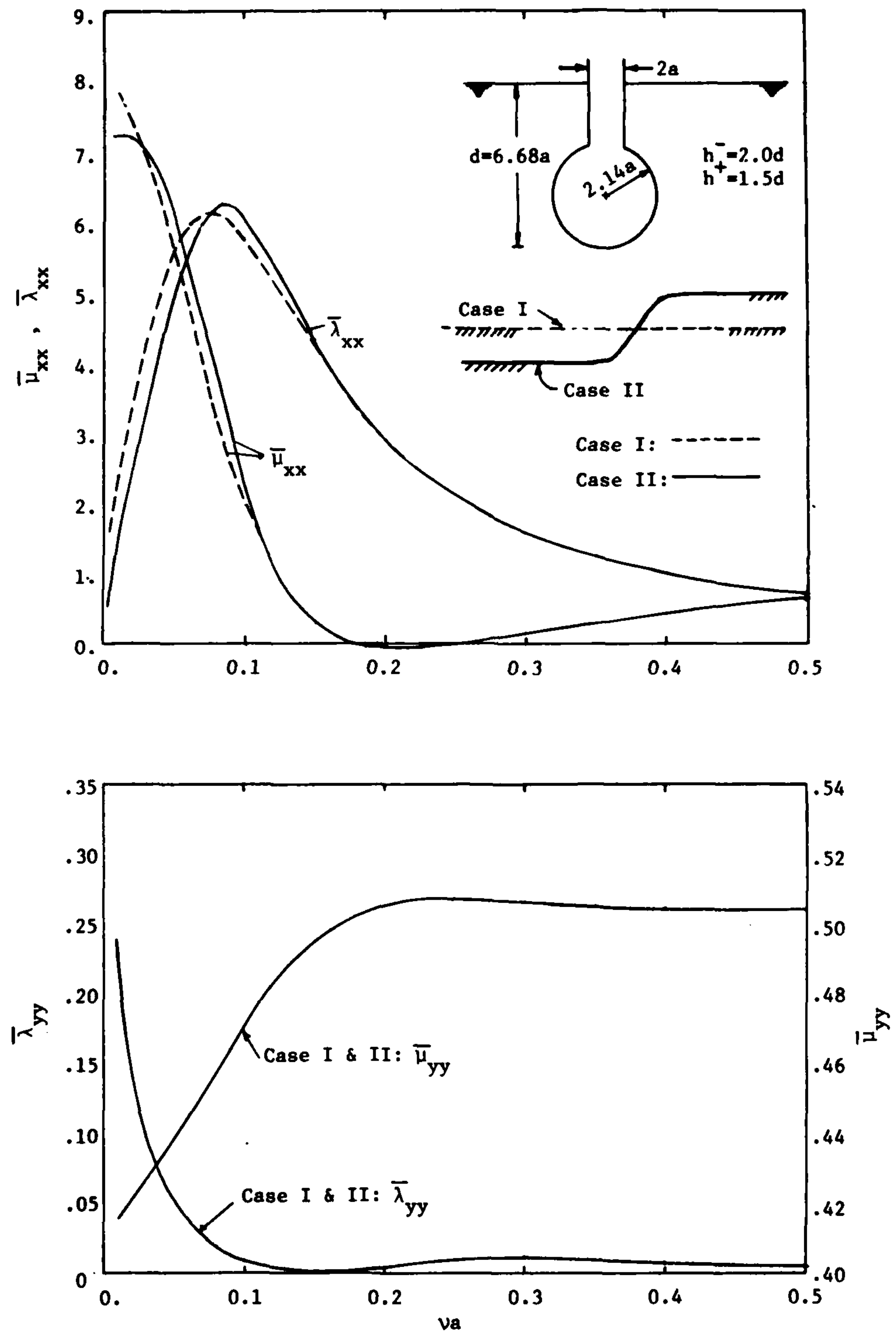

Fig. 4 Force coefficients for bulbous cylinder

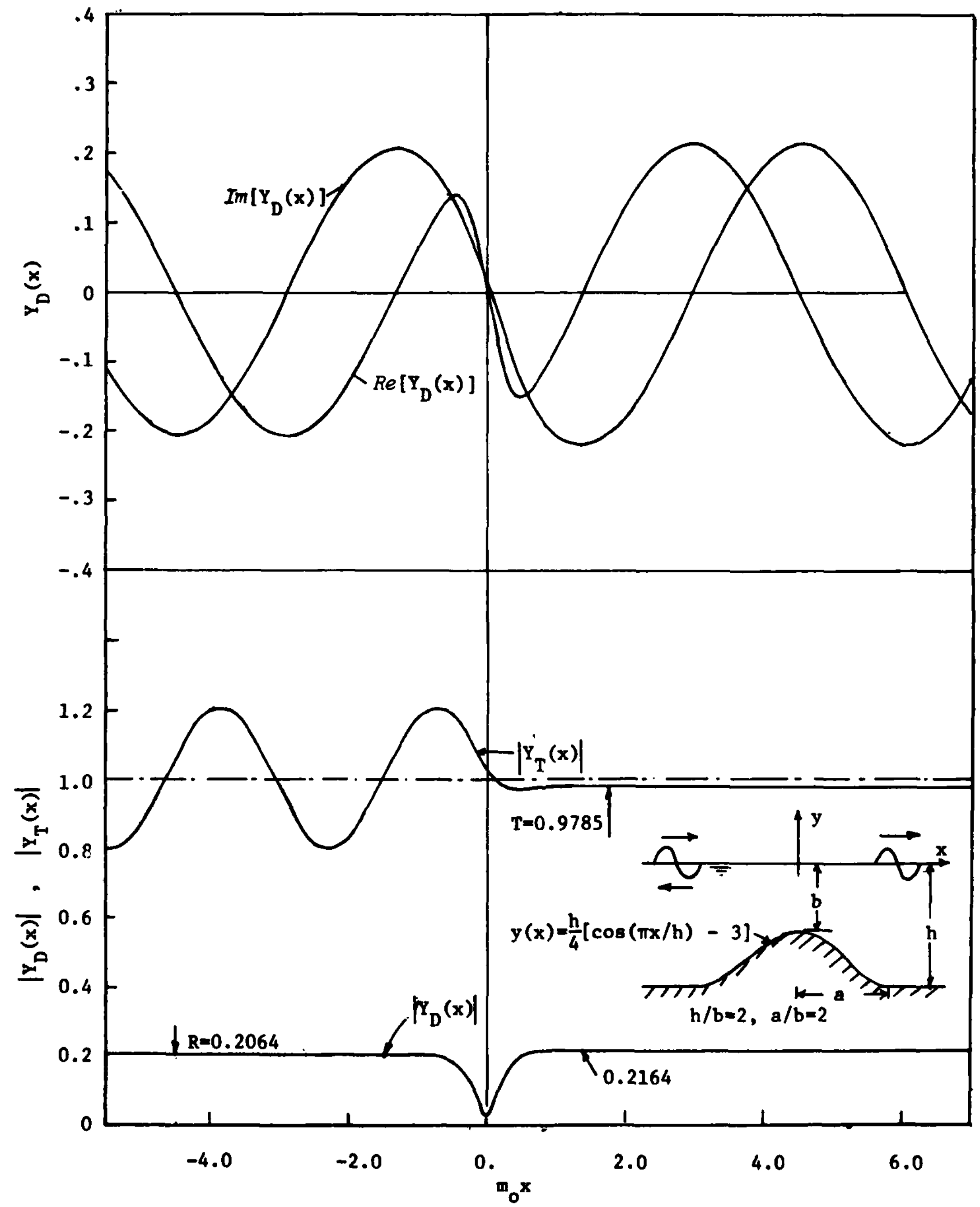

Fig. 5 Amplitudes of diffracted and total waves for a sinusoidal hump. ($m_o h=0.5$)

where Y^+ and Y^-, being the resulting wave amplitudes corresponding to unit-amplitude incoming wave, are essentially the transmission and reflection coefficients respectively. Here, γ evidently represents the group-velocity ratio. The agreement as can be seen is quite good

Our method is next applied to determine the reflection ability of a steep hump located in front of a step. The specific geometry of the hump is shown in Figure 6, with the results presented also therein. Transmission characteristics of a finite-size step without the hump are also plotted for the purpose of comparison. A considerable increase in the reflection coefficient occurs. However, one would still consider the performance of the hump as a submerged breakwater to be relatively poor.

6. Concluding Remarks

We have examined in this paper a very versatile method for solving the two-dimensional time-harmonic free-surface flow problem for a fluid of arbitrary bottom topography. The method is quite stable. Results obtained always satisfy consistency and energy checks very well. Generally speaking, the numerical accuracy is not as good for scattering problems when the reflection coefficient is vanishingly small. This corresponds to situations in which the wave frequency is fairly high. For low to moderately high frequency, the technique discussed here represents a simple yet potent tool for investigating the hydrodynamic interaction of bodies with their physical environment which can be made as realistic as possible.

Table 1. Reflection and Transmission Coefficients of a Finite-height Step

νh^-	R_1		T_1		Eqn (5.3),
	$\|R_1\|$	arg R_1(°)	$\|T_1\|$	arg T_1(°)	L.H.S.=
0.03395	.4269 .4273*	-163.14 -163.26*	.5799 .5797*	4.99 4.97*	1.00025 1.00001
0.04365	.4242 .4246	-160.86 -161.00	.5846 .5846	5.64 5.61	1.00016 1.00001
0.05813	.4201 .4205	-157.86 -158.02	.5918 .5917	6.46 6.44	1.00011 1.00005
0.06644	.4134 .4138	-153.73 -153.93	.6035 .6034	7.56 7.53	1.00002 1.00007
0.12115	.4016 .4021	-147.68 -147.94	.6244 .6244	9.04 9.02	.99980 1.00008
0.20031	.3774 .3777	-137.97 -138.32	.6679 .6681	11.07 11.04	.99938 1.00031
0.39260	.3158 .3162	-120.25 -120.83	.7803 .7810	13.05 13.03	.99851 1.00023
1.09093	.1458 .1470	-90.67 -91.99	1.0395 1.0407	7.61 7.69	.99760 1.00025

*Taken from Hilaly(1967). His phase angle α is related to the present notation by: $\alpha = -(\pi + \arg R)$.

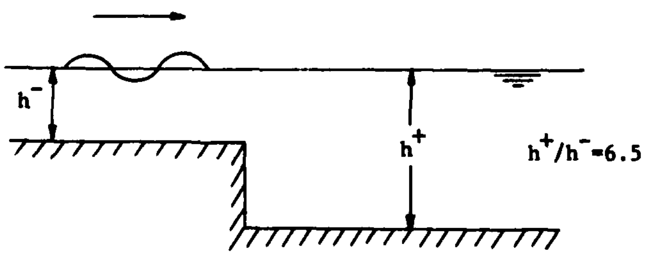

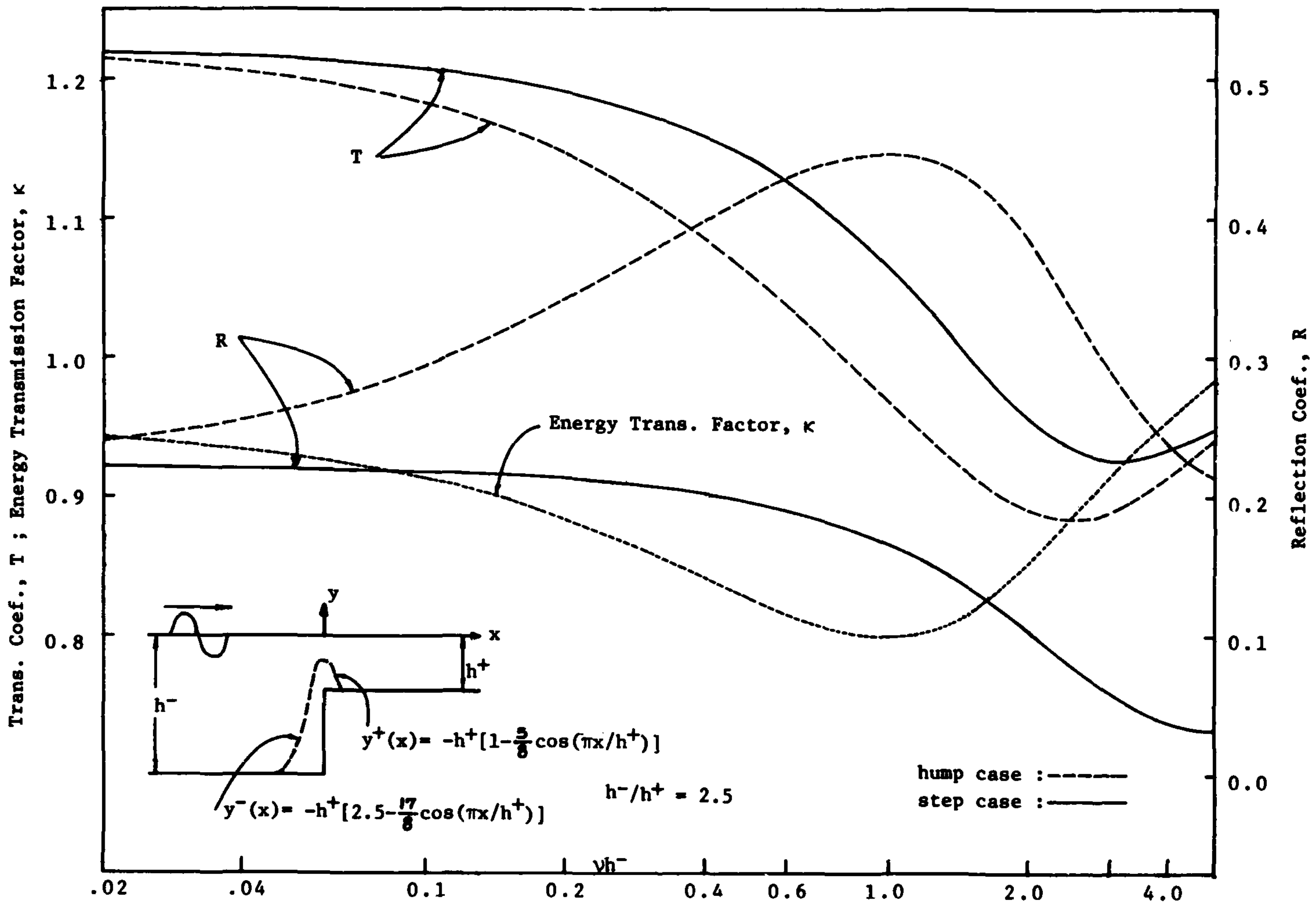

Fig. 6 Reflection and Transmission Coeffs. of a hump

Acknowledgement

This work was carried out under the Naval Ship Systems Command General Hydrodynamics Research Program administered by the Naval Ship Research and Development Center, Contract Number N00016-75-C-0236. The author is also grateful to partial support by the National Science Foundation, Grant Number GK-43886X. Acknowledgement is made for the valuable assistance of Mr. Y. H. Kim, Research Assistant in the Department of Ocean Engineering, MIT.

REFERENCES

1. Bai, K. J. and Yeung, R. W., "Numerical Solutions to Free-Surface Flow Problems," *10th Symp. on Naval Hydro.*, Cambridge, Mass., 1974.

2. Bartholomeusz, E. F., "The Reflexion of Long Waves at a Step," *Proc. Camb. Phil. Soc.*, vol. 54, 1958, pp. 106-118.

3. Chan, R. K. and Hirt, C. W., "Two-dimensional Calculations of the Motion of Floating Bodies," *10th Symp. on Naval Hydro.*, Cambridge, Mass., 1974.

4. Evans, D. V., "The Application of a New Source Potential to the Problem of the Transmission of Water Waves over a Shelf of Arbitrary Profile," *Proc. Camb. Phil. Soc.*, vol. 71, 1972, pp. 391-410.

5. Frank. W., "Oscillation of Cylinders in or Below the Free Surface of Deep Fluids," Naval Ship Research and Development Center, Report 2375, 1967, vi + 40 pp.

6. Hilaly, N., "Diffraction of Water Waves over Bottom Discontinuities," Univ. of Calif. Berkeley, Rept. HEL 1-7, Sept. 1967, 142 pp.

7. Kreisel, G., "Surface Waves," *Quart. Appl. Math.*, vol. 7, 1949, pp. 21-44.

8. Lebreton, J. C. and Margnac, M. A., "Traitement sur Ordinateur de Quelques Problems Concernant l'Action de là Houle sur Corps Flottants en Theorie Bidimensionelle," *Bulletin du Centre de Recherches et d'essais de Chatou*, No. 18, 1966.

9. Miles, J. W., "Surface-Wave Scattering Matrix for Shelf," *J. Fluid Mech.*, vol. 28, 1967, pp. 755-767.

10. Newman, J. N., "Propogation of Water Waves over an Infinite Step," *J. Fluid Mech.*, vol. 23, 1965, pp. 399-415.

11. Newman, J. N., "Interaction of Waves with Two-dimensional Obstacles: a Relation between the Radiation and Scattering Problems," to be published in *J. Fluid Mech.*, 1975.

12. Newman, J. N. and Yeung, R. W., "On the Low-frequency Limit of Added Mass of Cylinders," in preparation, 1975.

13. Ogilvie, T. F., "First- and Second-Order Forces on a Cylinder Submerged under a Free Surface," *J. Fluid Mech.*, vol. 16, 1963, pp. 451-472.

14. Ursell, F., "On the Heaving Motion of a Circular Cylinder in the Free Surface of a Fluid," *Quart. J. Mech. Appl. Math.*, vol. 2, 1949, pp. 218-231.

15. Wehausen, J. V. and Laitone, E. V., "Surface Waves," *Handbuch der Physik*, vol. 9, pp. 446-778, Springer-Verlag, Berlin, 1960.

16. Yeung, R. W., "A Singularity-Distribution Method for Free-Surface Flow Problems with an Oscillating Body," Univ. of Calif. Berkeley, College of Engineering, Report NA 73-6, Aug., 1973, vi + 124 pp.

A REVIEW OF NUMERICAL TECHNIQUES

Patrick J. Roache

Science Applications, Inc.
122 LaVeta, N.E.
Albuquerque, New Mexico 87108 U.S.A.

ABSTRACT

A review is presented of recently developed numerical techniques which have been successful in other areas of fluid dynamics but which, to the author's knowledge, have had little or no application to the challenging field of ship hydrodynamics. The topics have been selected to complement the topics covered in other papers of this conference, as judged from the preliminary program.

The principal topics covered are as follows: parabolic marching equations, which are intermediate to the full Navier-Stokes equations and the classical boundary layer equations; semi-analytic (or semi-discrete) methods; vortex filament methods; high-order finite difference and spline methods; analytical and numerical coordinate transformations; semi-direct methods, which use direct (non-iterative) linear equation solvers in a non-time-like iteration to solve nonlinear problems; and the adaptation of a pseudo-spectral method based on the Fast Fourier Transform to non-periodic problems.

Also presented is a cursory discussion of the cell Reynolds number limitations and some recent comprehensive contributions to the rapidly growing literature of computational fluid dynamics.

1. Introduction

The literature on numerical techniques applicable to fluid dynamics has become enormous. The writing of Ref. 1 was completed in mid-1972 and contains about 1250 references. It is not complete - I had accumulated

roughly another 400 references which I did not cite (or read) and I missed others. Since then, the number of publications has increased considerably. It was no trouble at all to come up with the additional 130 references (all appearing since mid-1972) cited in the review paper (Ref. 2) which was compiled in the fall of 1974. If Ref. 1 were being written today, it would probably need a 50% increase in the number of citations, these having been published in the roughly three-year intervening period.

I do not think that it is possible for anyone to keep up conscientiously with this literature, unless perhaps they are willing to make it a full time job and do no original work themselves. Survey papers and meetings such as this present conference, therefore, can be valuable in the cross-fertilizing of neighboring fields, e.g., advances by workers in aerodynamics and plasma physics may find applications in ship hydrodynamics.

It is in that spirit that this review is written. The citations used here are far from complete, and the entire field of numerical techniques has not been covered. Rather, the topics have been selected to complement those topics covered in other papers at this conference, as judged from the preliminary program. To my knowledge, these numerical techniques have had little or no application as yet to the challenging field of ship hydrodynamics.

2. Comprehensive Publications

Refs. 3-16 are comprehensive publications in computational fluid dynamics which have appeared since mid-1972. Of these, Refs. 3-7 are each the work of one or two authors, and Refs. 8-16 are proceedings from specialists meetings, like this one. I will offer some personal opinions on these latter published proceedings.

There is a growing trend towards rather uncritical publication in book form of the proceedings of specialists meetings. Contributed papers for these meetings are accepted usually on the basis of an abstract or extended summary, sometimes of unfinished work. The people who accept the papers are not selected by an editorial board of an established

archive journal (except perhaps for Refs. 9 and 10). The acceptance procedure does not involve any iterations, i.e., the abstract is read and either accepted or rejected, without the stately point-counterpoint of author submittal, referee criticism, author rebuttal, etc., etc., which often precedes publication in an archive journal. The invited papers are "accepted" by the organizing committee just on the basis of the author's past work, often before even a title is agreed upon. For both contributed and invited papers, the published work is sometimes frankly acknowledged to be incomplete.

It therefore is very interesting to me in my experience with these published proceedings, that (1) the usefulness of these papers, on the average, equals or surpasses that of papers in refereed archive journals, (2) the papers usually are more timely than journal papers, and (3) the usefulness of the contributed papers as a whole surpasses that of the invited papers.

The disadvantage of this trend is that no vehicle exists for the publication of criticism. This disadvantage is partially offset by the free exchange of healthy criticism and skepticism at the meetings themselves, all the more so when the discussion sessions are also published in the proceedings, as in Refs. 14 and 15. This disadvantage is further minimized by the clearly discernible trend away from published criticism or comments in the archive journals. However, it is still a disadvantage.

I propose to professional societies like the AIAA and APS, and to the editorial staff of journals such as the Journal of Ship Research and the Journal of Computational Physics, that they consider the advisability of opening their journals to technical comments and replies on papers which did not appear in their journals but which have been published and widely distributed in proceedings of specialists meetings.

3. Parabolic Marching Equations

The Parabolic Marching Equations are a system intermediate to the classical Prandtl (or higher-order) boundary layer equations and the full Navier-Stokes equations. Davis (Ref. 17) used this concept with great

success as early as 1968 in the calculation of the hypersonic viscous shock layer. One of the original contributions for incompressible flows was by Patankar and Spalding (Ref. 18) who solved 3D flow through a rectangular channel. The flow has a parabolic or initial-value character in the z-direction (primary flow direction) but an elliptic character in the x-y plane. There is no difficulty in neglecting the streamwise diffusion terms in the momenta equations, but ellipticity in z also occurs because of the pressure. The pressure can be specified as P(z), or can be iterated to allow for more rapid changes in channel geometry. Briley (Ref. 19) solved similar problems, but with some important differences in the detailed calculations.

Other related systems are the viscous shock-layer equations used by Eaton and Larson (Ref. 20) for symmetry-plane calculations of the blunt-body shock-layer; the "boundary region equations" or "parabolized Navier-Stokes equations" used by Lin and Rubin (Ref. 21) which include cross-flow diffusion and streamwise pressure gradients; and the "corner-layer equations" used by Ghia (Ref. 22) and others. Other references to earlier work may be found in Ref. 1 (p. 306).

The parabolic marching equation approach appears to be preferable in some respects to the 3D boundary layer equations. It does not require separate solutions and definitions of the inviscid and viscous flow regions, and requires no search for the "edge" of the boundary layer. Also, large separation of the cross flow velocity components (e.g., swirling flow in a duct) can be accommodated.

4. Semi-Discrete Methods

The basic idea in semi-discrete (or equivalently, semi-analytic) treatment of partial differential equations is to have one coordinate continuous, at least formally. The problem then becomes one of solving a coupled set of ordinary difference equations along the remaining coordinate line(s); hence, the name "method of lines" is often used. In the continuous coordinate, the solution may be expressed as a power series, as in the work of Underwood (Ref. 22). Usually, the idea is to apply the efficient and robust "canned" numerical solvers for ordinary differential

equations to the "continuous" coordinate. Actually, this procedure yields a discretized solution in this "continuous" coordinate also, but the technique appears to the user as though it were continuous, with essentially negligible error in that coordinate. (For example, the technique could be set up on a hybrid digital-analog computer with that coordinate represented by continuous real time on the analog components.) Earlier references on semi-analytical methods may be found in Ref. 1, pg. 312.

Jones et al. (Ref. 24) have reviewed the concepts of method of lines for elliptic equations, and have presented a fourth-order accurate method of lines which requires only the relatively simple tri-diagonal solutions. Madsen and Sincovec (Ref. 25) have also solved elliptic problems by leaving one spatial coordinate "continuous"; a disadvantage is that the resulting equations are "stiff" (even though fully discretized equations for the same problem are not) and, therefore, are demanding on the o.d.e solver used. (However, such "stiff equation solvers" are indeed available; probably the most well-known is the "Gear package"). Oberkampf and Goh (Ref. 26) have used the method of lines to solve time-dependent problems by leaving the time coordinate "continuous" and using Runge-Kutta solvers in time. This procedure does not introduce stiffness into the equations. They found the 4-th order Runge-Kutta time integration to be more stable than 2-nd order. They treated irregular boundaries by a simple mapping, and transformed infinity conditions by a tanh transformation, neither of which adversely affected the method of lines.

5. Vortex Filament Methods

Vortex filament methods (Refs. 27-37) are an interesting departure from classical finite-difference and finite-element methods. The basic idea is that the grid-free (Lagrangian) positions of a finite number of vortex filaments are calculated, with their subsequent motions being determined by free-stream advection and the mutual induction of the various vortex filaments. Some authors (Refs. 30, 31, 33) have included viscosity in an approximate way, but the primary development has been for inviscid vortical flows. Some applications to date include aircraft

trailing vortexes and other vortex ring interactions (Ref. 33), finite-amplitude Kelvin-Helmholtz instability (Ref. 36), and (of particular interest for this conference) free-surface flows (Refs. 34, 35, 37).

For free-surface calculations, the method is particularly powerful when the only vorticity present is that generated at the free surface. Since the free-surface contains the only active elements in the calculation, the vortex filament formulation of the problem effectively collapses a computational dimension out of the problem, as pointed out by Thompson and Meng (Ref. 35). That is, a planar flow problem which ordinarily would be expressed in two spatial coordinates (x,y) becomes a one-dimensional problem with vortex filament segments spaced along the free-surface coordinate, s.

The mutual inductions of discrete vortex segments are essentially calculated by the Biot-Savart Law, or Green's integral. When the non-zero vorticity is more distributed, as in viscous flow problems, this procedure is extremely inefficient (see our evaluation of the efficiency of the Integro-Differential system for viscous flows in Ref. 2, pp. 212-214). In the "vortex-in-cell" method of Thomson and Meng (Ref. 35) flexibility in this formulation is allowed. For a small number of vortex segments, a Biot-Savart evaluation is used. ("Small" is here judged in relation to the number of mesh points required for a two-dimensional discretization of the same problem by more conventional methods.) For a large number of vortex segments, a Poisson equation for stream function (with the vorticity of the distributed vortex segments as source terms) is solved efficiently by Fast Fourier Transform techniques.

6. Higher Order Methods

Some papers presented at this conference have used conventional higher-order equations; see the papers in these Proceedings by Haussling and Van Eseltine and by Ohring. We would like to bring attention to certain fourth-order difference schemes called "compact schemes" which have recently been used in viscous flow calculations.

Orszag and Israeli (Ref. 5) and Hirsh (Ref. 38) have credited this scheme to Kreiss and refer to it as "compact differencing," a term which

we will use here. But according to Rubin and Khosla (Ref. 39) the following methods are equivalent, i.e., any one can be derived from any other: Kreiss compact, Hermitian, Padé approximation, Mehrstelleng, and Rubin and Khosla's own 4th-order spline-on-spline. We will follow the notation used by Hirsh (Ref. 38).

Consider a discrete function g_i, for which we want to evaluate an approximation F_i to the first partial derivative, and an approximation S_i to the second partial derivative. To evaluate F_i, we first evaluate the usual second-order centered difference approximation for the first derivative and store it in an array called f_i; that is,

$$f_i = \frac{g_{i+1}-g_{i-1}}{2h}$$

where h is the mesh spacing. Then, a 4-th order approximation F_i is obtained by solving

$$\frac{1}{6}(F_{i+1} + 4F_i + F_{i-1}) = f_i$$

Conventional 4-th order approximations are explicit formulae involving 5 local points (i and its neighbors $i\pm1$, $i\pm2$). The compact scheme involves only three points (i and $i\pm1$) in the formula, but the formula is implicit, that is, non-local. The F_i are solved by a tridiagonal solution of the above equation, so that values of F at all i are dependent on one another, and thus on f_i and g_i, globally rather than locally. (In this global dependence, the compact scheme is like spectral and pseudo-spectral methods. See Refs. 4 and 5, for example.) Also, the compact scheme has a lower coefficient of the truncation error term of $O(h^4)$ than does the conventional 4-th order method.

In a similar way, the second-order approximation to the second derivative is calculated explicitly and stored in s_i; that is,

$$s_i = \frac{g_{i+1}-2g_i+g_{i-1}}{h^2}$$

Then a 4-th order S_i is obtained from the tridiagonal solution of

$$\frac{1}{12}(S_{i+1} + 10S_i + S_{i-1}) = s_i$$

By itself, the equation for the F_i's would require a boundary condition on the first derivative, and similarly for S_i's. This is a common difficulty with higher-order methods. However, Hirsh (Ref. 38) has shown that the boundary values for the coupled system can be obtained to 4-th order accuracy by using the second diagonal Padé approximant,

$$g_i - g_{i+1} + \frac{h}{2}(F_i+F_{i+1}) + \frac{h^2}{12}(S_i-S_{i+1}) = 0$$

This equation allows the coupled system for F_i and S_i to retain both its 4-th order accuracy and its tridiagonal form right up to the boundary. This form is thus simpler than conventional 5-point expressions, as well as more accurate.

Hirsh has solved two-dimensional low Reynolds number viscous steady flows using this compact scheme applied in an ADI manner (see Ref. 1). For roughly the same accuracy, the compact scheme showed a savings over a second-order scheme of a factor of 20 in computer time and a factor of 3 in storage. The boundary conditions on vorticity were lagged, as is commonly done when only the steady-state solution is of interest, so that temporal accuracy is lost.

The spline-on-spline formulation of Rubin and Khosla (Ref. 39) includes variable mesh spacing h, in which case the accuracy of F_i remains $O(h^4)$ but the accuracy of S_i deteriorates to $O(h^3)$.

7. Coordinate Transformations

There are basically three approaches of general applicability which one could try on the problem of treating irregular boundaries with finite difference methods, rather than finite element methods. The first approach, mentioned in all older books on numerical methods, is to use

partial-cell equations (non-centered finite differences) at nodes adjacent to boundaries. These equations are complicated, and become very inaccurate when the irregular boundary comes too close to a grid point. However, this approach has been made to work in some cases; see the application by Carlson to transonic flow (Ref. 40) and the paper on free surface waves by Salveson and von Kerczek in these Proceedings. (It appears that this approach is more likely to succeed for inviscid flows, with which these papers deal.)

The second approach of general applicability is to write finite difference equations over an irregular mesh. These superficially look like finite element methods, but are not; see Girault (Ref. 41) and Section 11 of Ref. 2. This approach is used in the YAQUI code, developed at Los Alamos (Ref. 42), which has the powerful capability of moving the irregular grid in a self-adaptive manner to follow the gradients of the developing flow solution. In fact, this flexible code allows for Eulerian or Lagrangian description or anything in between - that is, the mesh points can be given an arbitrary velocity relative to the fluid. It has been used with an Eulerian description in one direction and a Lagrangian description in another direction. A 3D version also exists (Ref. 43). In another paper at this conference, Boris has presented his work with a self-adaptive triangular mesh for Lagrangian calculations.

The third approach of general applicability, which appears to us to be the most accurate approach, is to transform the original coordinates to a new coordinate system in which the problem boundaries align conveniently with the transformed coordinates. This subject of coordinate transformations is extremely important, because it provides generality to finite difference methods, semi-analytic methods, and spectral and pseudospectral methods.

When only one coordinate has to be transformed, the approach is very easy. The transformation can be determined before the flow calculation by some analytical expression, or can be solved numerically. The numerical transformation is more general, and can be made self-adaptive to fit the developing solution. One-dimensional numerical coordinate transformations are used in Refs. 44-46.

In multidimensional problems, the coordinate transformation can be either analytical or numerical, and either orthogonal or non-orthogonal. Mehta and Lavan (Ref. 47) used an analytical and orthogonal Joukowski transformation. They calculated viscous stall and transients of airfoils, using Arakawa's method for advection terms and the DuFort-Frankel method for viscous terms. (Examples of their calculations and their grid can also be found in Ref. 2.)

Non-orthogonal transformations complicate the form of the flow equations, introducing cross-derivatives, but they do not affect the bandwidth of the equation matrix nor do they change the character of the equations. Some non-orthogonal transformations appropriate for particular problems are discussed in Section VI-B of Ref. 1 and Sections 3B, 3C, 3D of Ref. 2.

Thompson et al. (Ref. 48) have developed a very general technique for numerically solving a non-orthogonal transformation. Unlike orthogonal transformations (defined either analytically or numerically) this non-orthogonal transformation allows an arbitrary spacing of the body-fitted coordinate lines around the body. The (x,y) coordinates are transformed to (ξ,η) as shown in Figure 1. The entire body contour C_1 transforms to C_1' at a constant value of η. Likewise, the entire outer flow boundary C_3 transforms to C_3' at $\eta=0$. The cutting line between C_1 and C_3 transforms to C_2' and C_4' at constant ξ values. Periodic boundary conditions apply on C_2' and C_4', while the flow boundary conditions (transformed) apply along C_1' and C_3'. (For further flexibility, the corners of the transformed coordinate plane can be arbitrarily positioned in the physical plane, in which case the periodic boundary conditions might apply only on portions of C_2' and C_4'.) All calculations, including the transformation solution, are done on the regular rectangular mesh in (ξ,η). The transformation $\xi(x,y)$, $\eta(x,y)$ is determined by solving the following non-linear equations by iterative methods.

$$\alpha x_{\xi\xi} - 2\beta x_{\xi\eta} + \gamma x_{\eta\eta} = 0$$

$$\alpha y_{\xi\xi} - 2\beta y_{\xi\eta} + \gamma y_{\eta\eta} = 0$$

where

$$\alpha = x_\eta^2 + y_\eta^2$$

$$\beta = x_\xi x_\eta + y_\xi y_\eta$$

$$\gamma = x_\xi^2 + y_\xi^2$$

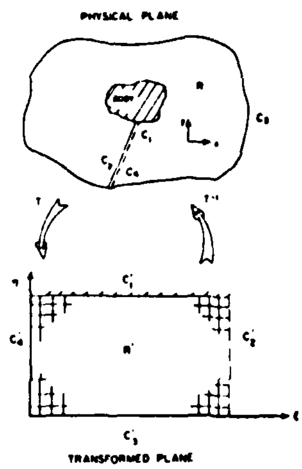

Figure 1. Field Transformation for a Single Body, using the Numerical Nonorthogonal Coordinate Transformation of Thompson et al. (1974).

The information on the boundary location gets into the (ξ,η) coordinates as boundary values of $x(\xi,\eta)$ and $y(\xi,\eta)$. We repeat: all calculations are performed in the regular (ξ,η) mesh; partial-cell differencing is never required. The transformation also allows the boundary position to be time-dependent.

Thompson et al. (Ref. 48) present their calculation of potential flow around an airfoil which agrees very closely with the analytical solution. To demonstrate the generality, they also calculate a coordinate system for a (two-dimensional) rock, and potential flow over the rock. (Some of these results are also presented in Ref. 2.) Finally, they present examples of multiple body calculations, and state that the concept can be extended to 3D. Other methods of numerically generating both orthogonal and nonorthogonal coordinate systems have been published, and all are useful, but the method of Thompson et al. is an improvement in that no folding of the transformed coordinates can occur. They also present some initial attempts at a self-adaptive 2D coordinate transformation. Of course, such coordinate transformations alone will not remove the multi-valued vorticity singularities at sharp corners on the body; if

locally accurate solutions are required, local treatment of the singularities is still required.

In Ref. 49, Thompson et al. have presented their initial applications of this body-fitted coordinate system to the problem of a viscous nonlinear water wave generated by a submerged hydrofoil.

A fourth method for treating a specific irregular boundary occuring in a steady free-surface problem is to transform the dependent variable (see next section of this paper). Although not as generally applicable as the first three approaches noted here, this is also a viable approach for an important class of problems.

Still another approach is, of course, the finite element method (or perhaps "methodology"). This approach is well represented by other papers in these Proceedings. I will not repeat here my criticisms of previous publications of finite element solutions of problems in fluid dynamics (see Ref. 2, pp. 230-236). Suffice it to say that my remarks therein were not so much criticisms of finite element methods per se as they were criticisms of the papers, with (what seemed to me) their often exaggerated and often unfounded claims of superiority.

I am not competent to claim some sweeping advantage of one approach over the other, especially since eminent mathematicians disagree on the very definition of a finite element method. Leaving the final comparison of the finite-difference and finite-element methods to braver souls, I will point out that the above examples, of four distinct and successful methods of treating irregular boundaries by finite difference methods, do indicate that statements on the necessity of the finite element approach for such problems are clearly in error.

8. Semi-Direct Methods

When only a steady-state solution (possibly in a moving coordinate system) is of interest, the time derivatives can be set to zero in the flow equations. However, when conventional iterative methods are then used to solve these steady-state equations, comparatively little gain is realized over using the actual time dependent equations, as noted in

Ref. 1. However, semi-direct methods which make use of fast direct solvers for linear equations can offer a very considerable advantage over time-like methods for steady-state problems.

In Refs. 50-53, we have presented four semi-direct methods for solving the steady-state Navier-Stokes equations in finite-difference forms. (The descriptive term "semi-direct" has been coined by Martin and Lomax and we adopt it here in preference to the term "steady-state methods" which we have used previously.) These methods are nonconventional, being neither time-dependent nor even time-like in their iterations. They are based on recent advances in solving linear equations by direct (non-iterative) methods.

The NOS method* for the vorticity transport equation is defined as

$$\nabla^2\zeta^k - Re\nabla \cdot (\vec{V}^{k-1}\zeta^k) = 0$$

The usual second-order centered differences are used throughout. The nonlinear velocities are lagged in the iteration, and the boundary values of ζ are under-relaxed by a factor r, in the usual way. This method requires a direct method for second-order linear equations which is general, i.e., it allows first-order terms. (See the EVP method,* pp. 124-131 of Ref. 1.) The LAD method* is defined by

$$\nabla^2\zeta^k = Re\nabla \cdot (\vec{V}^{k-1}\zeta^{k-1})$$

This method requires only the more generally available fast Poisson solvers. The NOS method converges much faster than LAD for flow-through problems typified by the developing channel-flow problem, but it unfortunately requires the reinitialization of the linear solver at each iteration, which is time-consuming.

The Split NOS method combines some virtues of both the LAD and NOS methods. Defining the initial guess at the velocity field as $\vec{V}^0$, we write the total velocity V as $\vec{V} = V^0 + \vec{V}'$. Then the Split NOS method is

*NOS refers to the numerical Oseen method, EVP to the error vector propagation method, and LAD to the Laplacian driver method.

$$\nabla^2\zeta^k - \mathrm{Re}\nabla \cdot (\vec{V}^0\zeta^k) = \mathrm{Re}\nabla \cdot (\vec{V}'^{k-1}\zeta^{k-1})$$

The linear operator need not be reinitialized at each iterative step, yet it has some of the advection information. The performance is equal to the NOS method at low Re, and is actually an improvement at high Re. The problem of developing channel flow was computed in as few as 11 iterations, each of which requires computer time comparable to a single time-step using an explicit method.

For this Split NOS method, the linear solver must be reinitialized only when Re is changed. It is also possible to improve the guess on $\vec{V}^0$ by reinitializing the linear solver, once or periodically; if done at each iteration, the Split NOS reverts to the simple NOS.

For recirculating flows as typified by the driven cavity problem, the convergence rates of the LAD, NOS and Split NOS are approximately the same; they are better than representative time-dependent methods, but are not as good as anticipated. Numerical experiments have demonstrated that the lagging boundary values of vorticity were responsible for this less-than-anticipated performance.

This difficulty is overcome by the biharmonic-driver method, or BID method. Combining the vorticity transport and Poisson equations gives

$$\frac{\partial}{\partial t}(\nabla^2\psi) = -\mathrm{Re}\nabla \cdot (\vec{V}\nabla^2\psi) + \nabla^2(\nabla^2\psi)$$

The BID method is then defined as

$$\nabla^4\psi^k = \mathrm{Re}\nabla \cdot (\vec{V}^{k-1}\nabla^2\psi^{k-1})$$

This method uses a second-order 13-point biharmonic operator at interior points. Near the moving "lid" of the cavity, an additional term containing the lid speed appears only in the right member of the above equation.

Since the steady-state boundary conditions on ψ are known and need not be iterated (or under-relaxed), the BID method converges rapidly. Unequivocal convergence is obtained in 8 iterations at Re = 20, and 6 iterations at Re = 10, for mesh sizes from Δ = 1/10 to 1/100. The steady-state solution for Re = 0 is attained at the first iteration (although a second iteration is required to mechanically verify the convergence criterion), demonstrating clearly that the method is not at all time-like.

The fourth-order method analogous to the (simple) NOS method would be the FOD (fourth-order driver) method

$$\nabla^4\psi^{k+1} - Re\nabla \cdot (\vec{V}^k\nabla^2\psi^{k+1}) = 0$$

Similarly, a method analogous to Split NOS would be the Split FOD method

$$\nabla^4\psi^{k+1} - Re\nabla \cdot (\vec{V}^0\nabla^2\psi^{k+1}) = Re\nabla \cdot (\vec{V}'^k\nabla^2\psi^k)$$

By analogy with the results for the LAD and NOS methods, we infer that these methods would probably converge in fewer iterations than BID, and would probably accomplish the high Re iterative convergence for flow-through problems. We hope to test these methods in the future.

The Split NOS approach appears to be adaptable to 3D, to the primitive (u-v-P) equations, to higher-order finite difference expressions, and also to compressible subsonic flows.

Morihara and Cheng (Ref. 54) have presented another semi-direct method for solving the steady-state Navier-Stokes equations. They use a form of the Navier-Stokes equations in which pressure has been eliminated and the velocity terms appear up to third-order partial derivatives. The iterative convergence is aided by a quasilinearization treatment of the advective terms. A discussion of this method is given in Ref. 2, pp 209-210, and some suggestions are given for combining the best features of their method and the Split NOS method. Also, Martin and Lomax (Ref. 55) have used the same concept for the solution of nonlinear inviscid

aerodynamics problems. Additional references to their work can be found in Refs. 2 and 6.

A possible application to an inviscid problem of naval interest is the steady (translating) water wave problem with a nonlinear free surface boundary condition. Dalrymple (Ref. 56) has used the Dubreil-Jacotin transformation to change the independent variables, going from stream function $\psi(x,y)$ to $y(\psi,x)$. The transformed interior equation is

$$y_\psi^2 y_{xx} - 2y_x y_\psi y_{x\psi} + (1 + y_x^2)y_{\psi\psi} = -y_\psi^3 f(\psi)$$

Although this transformed equation is nonlinear and contains cross-derivatives, the boundary position in (ψ,x) is known and is even rectangular. This problem, including the nonlinear boundary condition, would be amenable to a semi-direct solution using the EVP linear equation solver previously mentioned.

In the near future, we hope to apply semi-direct methods to a viscous problem of naval interest, that of the rapid design calculation of 3D turbulent flows in flush inlets, with possible strong separation.

9. Pseudo-Spectral Methods for Nonperiodic Problems

Spectral and pseudo-spectral methods for fluid dynamics have been pioneered by S. A. Orszag. The article by Orszag and Israeli (Ref. 5) provides references and an introduction to the subject. For periodic problems, the spatial derivatives are evaluated from the Discrete Fourier Transform using the well-known FFT (Fast Fourier Transform) algorithm. The pseudo-spectral methods are more general and simpler than the spectral methods for the variable coefficient problems of interest here.

The use of FFT over N node points corresponds to using N-th order trigonometric interpolation to evaluate derivatives. This procedure is of "infinite order" (Ref. 5) in the sense that it may be shown to converge (ultimately) faster than any finite-order finite difference expression when all derivatives are continuous. However, the FFT is limited to periodic (and similar) boundary conditions. For viscous problems

with no-slip walls, the boundary conditions are not so simple. Orszag uses Tchebychef polynomials (instead of the trigonometric polynomials of FFT) and fast transform techniques similar to FFT as the basis of the orthogonal expansion for these problems. Different problems in different coordinate systems require that new orthogonal expansions be found, and this is not a trivial task in general.

In order to use only the simpler FFT and still use pseudo-spectral methods for nonperiodic problems, some computational artifice must be used. For the computation of a pulse propagation in Burger's equation, with the pulse extending over $0 \leq x \leq D_1$, Gazdag (Ref. 57) added an artificial data set over $-D_0 \leq x \leq 0$. This data set over D_0 is chosen so as to give continuous functions and derivatives when the total function is extended periodically with period $D = D_0 + D_1$. Then the FFT is applied over D, but the results for spatial derivatives are computed only over D_1. Additional computational time is required for the FFT to apply over $D_0 + D_1$, and the form of the data added in D_0 is appropriate only for the particular problem.

As a more general artifice that involves no penalty of additional FFT time, we have developed the following technique which we call "reduction to periodicity." Consider an arbitrary distribution of the independent variable f_1 at some time. The f_1-distribution is decomposed, in one direction at a time, into the sum of a polynominal g and a residual function f_2. The n-th order polynomial is chosen so that the residual function, when extended as a periodic function of period D_1, is continuous in the n-th derivatives at the boundaries. The FFT is applied only to the residual function f_2 to obtain its derivatives, while the derivatives of the polynomial function g are obtained analytically.

For example, the derivatives of the original (total)function f_1 (x) at the boundaries can be evaluated by one-sided difference formulas, applied successively for higher-order derivatives. Then the reducing polynomial g(x) is solved so as to match these derivatives in the residual function $f_2(x)$ at the left and right boundaries (x=0 and x=1) as follows.

$$f_2(x) = f_1(x) - g(x)$$

$$g(x) = ax + bx^2 + cx^3 + \ldots + f_1(o)$$

Let $$D^0 = f(1) - f(o)$$

$$D^1 = f'(1) - f'(o),$$

$$D^2 = f''(1) - f''(o),$$

etc.

Then, for g a quintic,

$$e = \frac{1}{120} D^4$$

$$d = \frac{1}{24} D^3 - \frac{5}{2} e$$

$$c = \frac{1}{6} D^2 - 2d - \frac{10}{3} e$$

$$b = \frac{1}{2} D^1 - \frac{3}{2} c - 2d - \frac{5}{2} e$$

$$a = D^0 - b - c - d - e$$

The value of the derivatives D^n at the boundaries must either be given or must be evaluated by one-sided finite difference methods. Even when finite differences are used to evaluate derivatives at the boundaries, we have introduced no discretization error at this point. The decomposition is exact, even for arbitrary values of a, b, c, etc., since these only serve to define $g(x)$. But if values are good, then $f_2(x)$ will appear to the discrete FFT to be continuous with continuous n-th derivatives at the

quasi-periodic boundaries. Even with $g(x) = 0$, the process is convergent, but the discontinuities in $f_1(x)$ and its derivatives, when extended periodically, give rise to a "ringing" or Gibbs phenomena in the FFT representation which slows the convergence. The only purpose of the polynomial evaluation is to reduce the "ringing" in the FFT representation of $f_2(x)$. Although the convergence rate may ultimately (i.e., as $\Delta x \to o$) be limited by the truncation order of the finite difference method used to evaluate $g(x)$, for a practical range (up to $\Delta x=1/128$) it is not. The order of the reducing polynomial is important, however.

From tests on nonperiodic trigonometric and algebraic test functions and on the solution for Burgers equation, we have found that $n=3$ (i.e., g a cubic polynomial) is required to give acceptable results in the evaluation of $f_1'(x)$ and $n=5$ is required for $f_1''(x)$. Using only $O(\Delta x^2)$ methods for D^n and $n=5$, the maximum error (which occurs near boundaries) in the evaluation of $f_1'(x)$ is between those of conventional $O(\Delta x^4)$ and $O(\Delta x^6)$ finite difference methods, and the maximum error for $f_1''(x)$ is between those of $O(\Delta x^2)$ and $O(\Delta x^4)$ methods. (This ranking applies for $\Delta x=1/128$; for larger Δx, the present technique gives more favorable comparisons.) However, when the exact values of D^n are used, this reduction-to-periodicity technique gives a maximum error better than that of $O(\Delta x^6)$ methods for $f_1'(x)$, and a maximum error between those of $O(\Delta x^4)$ and $O(\Delta x^6)$ methoas for $f_1''(x)$. Thus, it appears that it will be advantageous to use higher truncation-order methods for D^n, and also perhaps higher order polynomials for g, although it is expected that machine round-off error will soon limit these.

We have solved time-dependent problems in Burgers equation for various Reynolds numbers using this technique. We used the 3-level, $O(\Delta t^2)$ Adams-Bashforth method (Ref. 1) as suggested by Orszag (Ref. 5) and started it with a two-level, $O(\Delta t^2)$ iterative approximation to a Crank-Nicholson method. The spatial and temporal accuracies were roughly equivalent to Gazdag's results (Ref. 57). The present technique appears to be more generally applicable and to have a substantially lower operation count compared to Gazdag's artifice and time differencing. However, we gladly acknowledge that Gazdag's work was the first to demonstrate that

pseudo-spectral FFT methods could be adapted to non-periodic problems, and in fact provided the motivation for this present work.

10. High Reynolds Number Calculations

The problem of obtaining accurate computations of the Navier-Stokes equations at high Re is a perplexing computational problem. The difficulties which we will discuss (in only a cursory manner) are purely computational, having nothing to do with turbulence modeling or transition physics.

Consider the one-dimensional model equation,

$$\frac{\partial \zeta}{\partial t} = -u \text{ Re } \frac{\partial \zeta}{\partial x} + \frac{\partial^2 \zeta}{\partial x^2} \qquad (*)$$

The first problem that arises for Re>>1 is that second-order differences do not yield a "balanced" method. If second-order difference methods are used for both first and second derivatives in Eqn. (*), then the truncation error from the advection term is $O(u\text{Re}\Delta x^2)$, while the truncation error from the diffusion term is $O(\Delta x^2)$. For Re sufficiently large, for $u=O(1)$, and for achievable Δx, the truncation error of $O(u\text{Re}\Delta x^2)$ will be greater than the entire diffusion term, so that the actual contribution of the (viscous) diffusion term is lost in the truncation error of the advection term. In multidimensional flow problems, accurate solutions can still be obtained in certain cases, for example, boundary layer flows. In the streamwise direction, the diffusion term does not appreciably affect the solution; in the transverse direction, diffusion is important but the transverse velocity, corresponding to u in the one-dimensional model equation, is small so that the truncation error of the advection term can still be acceptable, i.e., $u\text{Re}\Delta x^2 < O(1)$. In some instances, even more complicated flow fields can be calculated with sufficient accuracy, as further discussed in Ref. 1, pp. 64-73, 161-165, 364-365, but generally, we cannot *a priori* have confidence in the solutions for high Re. One plausible criterion to use is that the method be "balanced" in

truncation error, with the size of the truncation error from the advection term being approximately equal to that from the diffusion term. To achieve this, one can use high-order methods for the advection term. For $\Delta x = 1/100$, it may readily be verified that an $O(\Delta x^4)$ method indicates balance up to Re $\simeq 10^4$, and an $O(\Delta x^6)$ method indicates balance up to Re $\simeq 10^8$. Practically, the Re may even go higher, since the u-coefficients will be <1 near the separation and reattachment points where the full Navier-Stokes equations are important. Similar considerations should be given to the evaluation of the nonlinear advection coefficients and the boundary conditions.

The second problem that arises for Re>>1 is that the discretized solution using centered differences can be oscillatory. Figure 2 is a reproduction of Figure 3-27, pg. 164 of Ref. 1. Part (a) shows continuous steady-state solutions to Eqn. (*) for various constant values of u and $\alpha = 1/\text{Re}$. Part (b) shows discrete solutions using $O(\Delta x^2)$ centered differences for parameters up to the condition $R_c = 2$, where R_c is the cell Re, defined as $R_c = u\text{Re}\Delta x$. It is the local Reynolds number based on Δx as a characteristic length. For $R_c \leq 2$, the discrete solutions are at least qualitatively similar to the continuum solutions of part (a). Part (c) shows the solutions for $R_c > 2$. Unlike the continuum solutions, these discrete solutions are oscillatory and even violate the boundedness restriction, i.e., $\zeta(10) < 0$.

These oscillatory solutions are not the result of any temporal instability (they are obtained by a non-iterative tridiagonal solution) although they can manifest themselves as temporal oscillations in a multidimensional problem. Neither are they the result of nonlinearities. They simply are the exact, steady-state, $O(\Delta x^2)$ finite difference solution to Eqn. (*) with linear, constant coefficients.

For a discussion of this phenomenon, and how it may be alleviated by outflow boundary conditions and/or the use of upwind differences, see Ref. 1, pp. 161-165. Suffice it to say at this point that the oscillations can be cured by the use of $O(\Delta x)$ upwind differences, but at the expense of the aggravation of the first problem of high Re flows, i.e.,

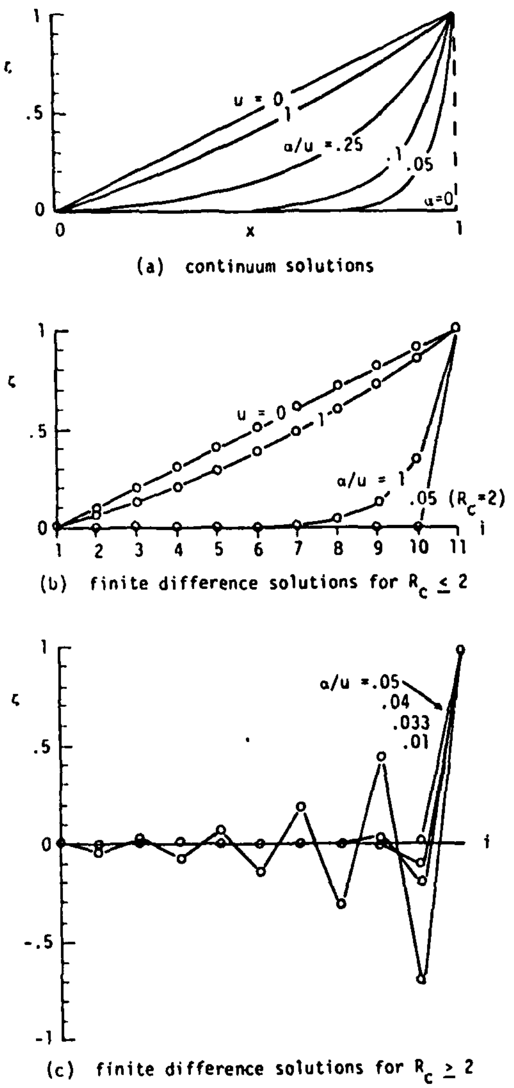

Figure 2. Continuum and Finite Difference Solutions to the Steady-State Linear Model Advection-Diffusion Equation: $0 = -u(\partial\zeta/\partial x) + \alpha(\partial^2\zeta/\partial x^2)$, $\zeta(0) = 0$, $\zeta(1) = 1$, Constant u. Centered Differences, $\Delta x = 1/10$. The cell Reynolds number $R_c = u\Delta x/\alpha$.(Ref. 1, pg. 164)

obtaining a "balanced" method. The utility of the upwind difference method here might be interpreted as due to its directionality, which models the directionality of the continuum advection term, in contrast to the $O(\Delta x^2)$ centered differences which do not preserve the unidirectional flow of information (see Ref. 1, pp. 64-74). It might also be interpreted simply as a manifestation of the artificial viscosity of the upwind difference method, which artificially thickens the boundary region near the right boundary so that the last interior node is inside the boundary region. However, for this simple model problem, a second-order accurate upwind difference scheme (Ref. 58) will eliminate the wiggles. It is not clear that it will eliminate them for more general problems; Atias et al. (Ref. 59) have recently applied it to 2D viscous problems and have pointed out that it is non-conservative. Other devices are available to achieve monotonicity; see the paper by Rubin and Khosla (Ref. 60) and the FCT algorithm of Boris (Ref. 61). Although the development of the FCT algorithm was motivated primarily by the quest for monotonicity in shock-smearing methods, it is also applicable to viscous problems.

The most fundamental aspect of the high Re problem is the Nyquist frequency limitation. It is fundamental to information theory that the highest-frequency component which can be represented by discrete sampling is that with wavelength $\lambda = 2\Delta x$. When a traveling wave in the Burgers equations is solved numerically, the following becomes evident. At a cell Reynolds number $R_c = 2$, the numerical solution (if it is free of artificial viscosity) becomes a three-point ramp function. That is, the width of the wave becomes equal to $2\Delta x$, with one node point precisely in the middle of the wave. The continuum wave structure (a tanh function) is then minimally represented by a single Fourier component at the Nyquist frequency. If the Re is further increased, the continuum wave width further decreases, requiring a higher-frequency Fourier component even for a minimal qualitative representation. Since this frequency is not available within the mesh spacing Δx, oscillations develop from the resulting aliasing error.

If we use a flux-limiter like FCT, or some other device, to achieve monotonicity, we of course are not solving for the wave structure itself.

In shock problems, it is usually the case that the global solution is not sensitive to this fine structure solution, provided that conservation laws prevail in the discrete representation (see, e.g., Ref. 1, pp. 28-33, Ch. V, and pp. 230-232). In viscous problems, this insensitivity may or may not be the case.

Note that very high Re solutions are attainable for certain flows, notably for boundary-layer flows, even though these may be solved by the full Navier-Stokes equations. The reason is that the viscous shearing stress is not the term that causes the difficulties discussed here; rather it is the viscous <u>normal</u> stress. Ordinarily this is regarded as a shock problem (indeed the traveling wave solution to Burgers equation is used as a prototype of shock problems) but it also arises in purely subsonic viscous flows. Thus, for a boundary-layer flow, the troublesome cell Reynolds numbers is not $Rc_x = uRe\Delta x$, but rather $Rc_y = vRe\Delta y$. In fact, it can readily be seen from the Blasius solution that this computational difficulty for a flat plate boundary layer is no problem, provided, of course, that Δy is scaled with the boundary layer thickness δ. Even one mesh point in the boundary layer will assure that the local cell Re at that point gives $Rc_y < 2$. However, a blowing wall boundary layer can develop $Re_y > 2$, and the computational difficulties described above then occur even for the boundary layer equations.

The scaling of the fine structure with Re is not always linear, as it is for the Burgers equation. It is problem-dependent, and different regions of the flow may scale differently (see the paper in this proceedings by Davis). The elementary estimate of dissipation rate for the Navier-Stokes equations indicates $E = O(1/R_e)$ (Ref. 62, pg. 239) which would imply a length scaling $\propto 1/Re$ as in the Burgers equation. Usually, the scaling for Navier-Stokes solutions (see Ref. 63, Ch. 5) is not as severe as this 1/Re linear scaling, but it has been experimentally observed by many authors that the condition $R_c < 2$ is very often the correct practical limitation, in the absence of artificial viscosity. On the slightly more optimistic side, we note that the calculation of turbulent flows using eddy viscosity methods or similar concepts has an easier computational restriction than laminar flows, since the eddy viscosity is

always much greater than the molecular viscosity and the corresponding turbulence cell Re is lower. (This, of course, says nothing about the accuracy of these models.) Furthermore, estimates of the scaling for homogenous isotropic turbulence indicate (Ref. 62, pg. 240) that the size of viscous regions $\delta \propto Re^{-3/4}$, which is less troublesome than the linear scaling used here.

The question is, how important is this irresolvable fine structure to the global solution? The answer cannot be given confidently, and considerable disagreement exists over the practical Reynolds number limitations for Navier-Stokes solutions. It is clear that the answer is highly problem-dependent. Certainly for attached well-behaved boundary layers, it is not a big problem, as we have already seen. Also, flows which approach Re-independence (e.g., flows near to Couette flow or Poiseuille flow) will obviously not be a problem. Flows with massive separation clearly require the full Navier-Stokes equations and are therefore candidates for trouble; yet if the separation point is strongly determined by the geometry (e.g., a sharp-corner backstep) it is known that overall flow properties can often be characterized to an accuracy sufficient for some engineering applications. The structure of turbulence becomes finer as Re increases, yet Orszag (e.g., Ref. 5) has shown that the tendency for homogeneous isotropic turbulence to become Re-independent may make possible high Re calculations for this case; more general non-homogeneous turbulence can be treated with sub-grid modeling (which essentially builds in a fine structure below the $\lambda = 2\Delta x$ component). On the other hand, if the fine structure is globally significant, the limit of $R_c = 2$ may not be adequate for accuracy using second-order methods; it may suffice for spectral methods (since the $\lambda = 2\Delta x$ component is still represented exactly) but the rule-of-thumb given in Ref. 5 states that about 20 grid points per wavelength are required for a 5% accuracy. This would indicate a very restrictive condition, like $R_c \leq 0.2$, to accurately resolve fine structure viscous normal stresses with $O(\Delta x^2)$ methods, if the size of the viscous regions δ scales as 1/Re as does the Burgers solution. In addition to the effect of the physical problem on this question, computational boundary conditions (particularly at outflow boundaries) are

also known to have a strong influence (see Ref. 1, pp. 154-165, 364-365). Most importantly, the coordinate system can be the major factor in success or failure - see the discussion of "optimal coordinates" given by R. T. Davis in his paper in these Proceedings, and his references therein.

Since this question of Re limitations on accuracy is so problem-dependent, little can be said with certainty. I tend (now) to be more cautious and pessimistic than some other workers in this area when approaching a high Re problem, yet I generally feel that such a computation (even using first-order methods, if necessary) can be of value in an engineering problem, provided that the results are viewed with suspicion. (This is not a bad attitude to have with experimental or analytical results, either.)

However, this discussion does lead me to some conclusions about computers. For a particular family of flow problems, assuming conservatively that $\delta \propto 1/Re$, we may require from experience that $R_c \leq 0(1)$ for qualitative representation of the fine structure, or perhaps $R_c \leq 0.2$ for a 5% accuracy of the fine structure, or perhaps $R_c \leq 10$ for a benign problem that is not globally sensitive to the fine structure. In any case, we have a requirement that $R_c \leq K$, which implies an Re limitation that is <u>linear with $1/\Delta x$</u>. Suppose that we have an adequately accurate solution to some flow problem at Re_1. We presume that the mesh spacing in all directions is just fine enough to give our desired accuracy, without unnecessarily fine resolution in any direction. Suppose now that we wish to raise our Re to $2Re_1$. If the viscous effects are confined to small regions, we may accomplish this by local mesh refinement, but if not, we must uniformly halve the mesh spacing in each direction to consistently maintain the same limitation on $R_c \leq K$. To maintain consistent accuracy in a time-dependent calculation, we must also halve Δt in accordance with the Courant number restriction. (We are not concerned here with stability, but accuracy, and we are presuming an intelligent treatment of viscous terms by implicit or other methods which remove the diffusion stability limitation on Δt. Otherwise, we would have $\Delta t \propto \Delta x^2$, which would add another factor of 2 to the table below.) Thus, regardless of the value of K in the limitation $R_c \leq K$, we can calculate the increase in computing time

required to double our maximum Re. The computer time per time step is proportional to the number of mesh points, which has doubled in each direction, and the number of required time steps to reach the same problem time (either a transient time of interest or the approximation of a steady-state) has also doubled. For semi-direct methods, the number of iterations required to reach steady-state does not change with Δx, but may change with Re; this possible effect is not included. The results are presented in Table 1.

Table 1

Increase in Computing Time to Double (p=2) Max Re for a Cell Reynolds Number Limitation of the Form $R_c<K$

Factor of Computing Time	$p^2 = 4$	$p^3 = 8$	$p^3 = 8$	$p^4 = 16$
	2D, semi-direct	2D, time-like	3D, semi-direct	3D, time-like

Clearly, the computing time required to maintain accuracy is a strong function of Re. Turning it around, this indicates that the maximum Re attainable with any fixed limitations on computer time is only weakly improved by gains in computing efficiency. For example, an imaginary machine with 10^4 times the speed and 10^3 times the storage of the ILLIAC IV would give only a factor of 10 increase in maximum Re for 3D problems using time-like methods.

This estimate is pessimistic because (1) many flow problems of practical interest are not viscous-dominated in all directions, and (2) because scaling of $\delta \propto 1/Re$ has been assumed. If $\delta \propto 1/\sqrt{Re}$ as in boundary layer and other problems (see Ch. 5 of Ref. 63) then p in Table 1 is replaced by $\sqrt{p}$, or the estimates of computing time increase now apply to a four-folded increase of Re_1 . Orszag's estimates (Ref. 62, pp. 234-242) for turbulence simulation indicate computing time $\propto Re^3$, or a factor of 8 increase in computer time to double Re_1. Even though the estimates in Table 1 may be conservative, my principal conclusion from this exercise is that improvements in computational algorithms (including coordinate transformations and results from singular perturbation analyses) offer more hope for the high Re problem than do improvements in computers.

ACKNOWLEDGMENT

This work was partially supported by the Office of Naval Research under Contract N00014-75-C-0068 (NR 061-224/8-1-74 438).

REFERENCES

1. Roache, P. J. (1972), Computational Fluid Dynamics, Hermosa Publishers, P. O. Box 8172, Albuquerque, New Mexico.

2. Roache, P. J. (1975), "Recent Developments and Problem Areas in Computational Fluid Dynamics", in Computational Mechanics, J. T. Oden, Ed., "Lecture Notes in Mathematics", Vol. 461, Springer-Verlag, Berlin, pp. 195-256.

3. Taylor, T. D. (1973), Numerical Methods for Predicting Subsonic, Transonic and Supersonic Flow, AGARDograph No. 187. Available from NASA-Langley, Report Distribution and Storage Unit, Langley Field, Va. 23365.

4. Kreiss, H. and Oliger, J. (1973), Methods for the Approximate Solution of Time Dependent Problems, GARP Publication Series No. 10, World Meteorological Organization, Feb. 1973. *Available from* UNIPUB, Inc., P.O. Box 433, New York, N.Y. 10016.

5. Orszag, S. A. and Israeli, M. (1974), "Numerical Simulation of Viscous Incompressible Flows", in Annual Review of Fluid Mechanics, Vol. 6, pp. 281-318, Annual Review, Inc., Palo Alto, Ca.

6. Lomax, H. and Steger, J. L. (1975), "Relaxation Methods in Fluid Mechanics", in Annual Review of Fluid Mechanics, Vol. 7, pp. 63-88, Annual Reviews, Inc., Palo Alto, Ca.

7. Peyret, R. and Viviand, H. (1975), Computation of Viscous Compressible Flows Based on the Navier-Stokes Equations, AGARDograph No. 212. Available from NASA-Langley, Report Distribution and Storage Unit, Langley Field, Va. 23365.

8. AIAA (1973), Proceedings of the AIAA Computational Fluid Dynamics Conference, Palm Springs, Ca., July 19-20, 1973.

9. AIAA (1975), Proceedings of the Second AIAA Computational Fluid Dynamics Conference, Hartford, Conn., June 19-20, 1975.

10. Cabannes, H. and Temam, R. (1973), eds., Proceedings of the Third International Conference on Numerical Methods in Fluid Mechanics, Paris, France, July 3-7, 1972, Volumes I and II, in "Lecture Notes in Physics", Volumes 18 and 19, Springer-Verlag, Berlin.

11. Richtmyer, R. D. (1975), ed., Proceedings of the Fourth International Conference on Numerical Methods in Fluid Mechanics, University of Colorado, June 24-28, 1974, in "Lecture Notes in Physics", Vol. 35, Springer-Verlag, Berlin.

12. Oden, J. T. (1974), ed., Computational Methods in Nonlinear Mechanics, Texas Institute for Computational Mechanics, University of Texas at Austin, Texas.

13. Oden, J. T. (1975), ed., Computational Mechanics, in "Lecture Notes in Mathematics", Vol. 461, Springer-Verlag, Berlin.

14. Anon. (1975), Proceedings of the Workshop on Numerical Hydrodynamics, May 20-21, 1974, National Academy of Sciences, Washington, D. C.

15. Anon. (1975), Numerical Models of Ocean Circulation, Proceedings of a Symposium held at Durham, N. H. on October 17-20, 1972, National Academy of Sciences, Washington, D. C.

16. Kinney, R. B. (1975), ed., Unsteady Aerodynamics, Vol. I and II, Proceedings of a Symposium held at University of Arizona, March 18-2C, 1975, The University of Arizona, Tucson, Arizona.

17. Davis, R. T. (1970), "Numerical Solution of the Hypersonic Viscous Shock-Layer Equations", AIAA Journal, Vol. 8, No. 5, May 1970, pp. 843-851.

18. Patankar, S. V. and Spalding, D. B. (1972), "A Calculation Procedure for Three-Dimensional Parabolic Flows", Intl. J. Heat and Mass Transfer, Vol. 15, pg. 1787.

19. Briley, W. R. (1975), "Numerical Method for Predicting Three-Dimensional Steady Viscous Flow in Ducts", J. Computational Physics, Vol. 14, No. 1, Jan. 1974, pp. 8-28.

20. Eaton, R. P. and Larson, D. E., (1974), "Laminar and Turbulent Viscous Shock-Layer Flow in the Symmetry Plane of Bodies at Angle of Attack", AIAA Paper No. 74-599.

21. Lin, T. C. and Rubin, S. G. (1973), "Viscous Flow Over Spinning Cones at Angle of Attack", see Ref. 8, pp. 51-62. Also, AIAA Journal, Vol. 12, No. 7, July 1974, pp. 975-984.

22. Ghia, K. N. and Davis, R. T. (1974), "Corner Layer Flow: Optimization of Numerical Method of Solution", Computers and Fluids, Vol. 2 No. 1, March 1974, pp. 17-34.

23. Underwood, R. L. (1969), "Calculation of Incompressible Flow Past a Circular Cylinder at Moderate Reynolds Numbers", J. Fluid Mechanics, Vol. 37, Part 1, pp. 95-114.

24. Jones, D. J., South, J. C., Jr., and Klunker, E. B. (1972), "On the Numerical Solution of Elliptic Partial Differential Equations by the Method of Lines", J. Computational Physics, Vol. 9, No. 3, June 1972, pp. 496-527.

25. Madsen, N. K. and Sincovec, R. F. (1974) "The Numerical Solution of Nonlinear Partial Differential Equations", pp. 371-380 of Ref. 13.

26. Oberkampf, W. L and Goh, S. C. (1974) "Numerical Solutions of Incompressible Viscous Flow In Irregular Tubes", pp. 569-580 of Ref. 13.

27. Buneman, O. (1970), "Vortices, the 'Particles' of Fluid and Gas Dynamics", in Proc. Fourth Conference on Numerical Simulation of Plasmas, N.R.L., Nov. 2-3, 1970. J. P. Boris and R. A. Shanny, U.S. Government Printing Office, Stock No. 0851-00059.

28. Buneman, O. (1973), "Subgrid Resolution of Flow and Force Fields", J. Computational Physics, Vol. 11, pp. 250-568.

29. Buneman, O. (1974), "Variationally Optimized, Grid-Insensitive Vortex Tracing", see pp. 111-116 of Ref. 11.

30. Chorin, A. J. (1972), "A Vortex Method for the Study of Rapid Flow", see pp. 100-103 of Ref. 10.

31. Chorin, A. J. (1973), "Numerical Study of Slightly Viscous Flow", J. Fluid Mechanics, Vol. 57, Part 4, pp. 785-796.

32. Chorin, A. J. and Bernard, P. S. (1973), "Discretization of a Vortex Sheet, with an Example of Roll-Up", J. Computational Physics, Vol. 13, pp. 423-429.

33. Leonard, A. (1974), "Numerical Simulation of Interacting, Three-Dimensional Vortex Filaments", see pp. 245-250 of Ref. 11.

34. Thomson, J. A. L. and Meng, J. C. S. (1974), "Studies of Free Buoyant and Shear Flows by the Vortex-in-Cell Method", see pp. 403-416 of Ref. 11.

35. Thomson, J. A. and Meng, J. C. S (1973), "Atmospheric Modeling: Development of Vortex Structures in Buóyant and Shear Flows", RADC-TR-74-117, Rome Air Development Center, AFSC, Griffiss AFB, N. Y..

36. Zalosh, R. G. (1975), "A Discrete Vortex Simulation of Finite Amplitude Kelvin-Helmholtz Instability", pp. 205-219 of Ref. 9.

37. Zaroodny, S. J. and Greenberg, M. D. (1973), "On a Vortex Sheet Approach to the Numerical Calculation of Water Waves", J. Computational Physics, Vol. 11, pp. 440-446.

38. Hirsh, R. S. (1975), "Higher Order Accurate Difference Solutions of Fluid Mechanics Problems by a Compact Differencing Scheme", J. Computational Physics, Vol. 19, pp. 90-109.

39. Rubin, S. G. and Khosla, P. K. (1975), "Higher-Order Numerical Solutions Using Cubic Splines", see pp. 55-66 of Ref. 9.

40. Carlson, L. A. (1975), "Transonic Airfoil Analysis and Design Using Cartesian Coordinates", see pp. 175-183 of Ref. 9.

41. Girault, V. (1974), "Theory of a Finite Difference Method on Irregular Networks", SIAM J. Numerical Analysis, Vol. 11, No. 2, April 1974, pp. 260-282.

42. Hirt, C. W., Amsden, A. A., and Cook, J. L. (1974), "An Arbitrary Lagrangian-Eulerian Computing Method for All Flow Speeds", J. Computational Physics, Vol. 14, pp. 227-253.

43. Pracht, W. E. (1975), "Calculating Three-Dimensional Fluid Flows at all Speeds with an Eulerian-Lagrangian Computing Mesh", J. Computational Physics, Vol. 17, pp. 132-159.

44. Briley, W. R. and McDonald, H. (1974), "Numerical Prediction of Incompressible Separation Bubbles", UARL Report N110887-3. United Aircraft Research Laboratories, East Hartford, Conn., June 1974. See also pp. 105-110 of Ref. 11.

45. Blottner, F. G. (1974), "Variable Grid Scheme Applied to Turbulent Boundary Layers", SLA-74-5009, Sandia Laboratories, Albuquerque, N.M. See also pp. 91-97 of Ref. 11.

46. Gough, D. O., Spiegel, E. A., and Toomre, J. (1974), "Highly Stretched Meshes as Functionals of Solutions", see pp. 191-196 of Ref. 11.

47. Mehta, U. B. and Lavan, Z. (1975), "Starting Vortex, Separation Bubbles, and Stall: A Numerical Study of Laminar Unsteady Flow Around an Airfoil", J. Fluid Mechanics, Vol. 67, part 2, pp. 227-256.

48. Thompson, J. F., Thames, F. C., and Mastin, C. W. (1974), "Automatic Numerical Generation of Body-Fitted Curvilinear Coordinate System for Field Containing Any Number of Arbitrary Two-Dimensional Bodies", J. Computational Physics, Vol. 15, No. 3, July 1974, pp. 299-319.

49. Thompson, J. F., Thames, F. C., Mastin, C. W. and Shanks, S. P. (1975), "Use of Numerically Generated Body-Fitted Coordinate Systems for Solution of the Navier-Stokes Equations", see pp. 68-80 of Ref. 9.

50. Roache, P. J. (1972), "Finite Difference Methods for the Steady-State Navier-Stokes Equations", see pp. 138-145 of Ref. 10.

51. Roache, P. J. (1974), "The Split NOS and BID Methods for the Steady State Navier-Stokes Equations", see pp. 347-352 of Ref. 11.

52. Roache, P. J. (1975), "The LAD, NOS and Split NOS Methods for the Steady-State Navier-Stokes Equations", Computers and Fluids, Vol. 3, pp. 179-195.

53. Roache, P. J. and Ellis, M. A. (1975), "The BID Method for the Steady-State Navier-Stokes Equations", accepted for publication in Computers and Fluids.

54. Morihara, H. and Cheng, R. T. (1973), "Numerical Solution of the Viscous Flow in the Entrance Region of Parallel Plates", J. Computational Physics, Vol. 11, pp. 550-572.

55. Lomax, H. and Martin, E. D. (1974), Fast Direct Numerical Solution of the Nonhomogeneous Cauchy-Riemann Equations", J. Computational Physics, Vol. 15, No. 1, May 1974, pp. 55-80.

56. Dalrymple, R. A. (1973), "Water Wave Models and Wave Forces with Shear Currents", TR No. 20, College of Engineering, Univ. of Florida, Gainesville, Fla., August 1973.

57. Gazdag, J. (1973), "Numerical Convective Schemes Based on Accurate Computation of Space Derivatives", J. Computational Physics, Vol. 13, No. 1, Sept. 1973, pp. 100-113.

58. Price, H. S., Varga, R. S., and Warren, J. E. (1966), "Application of Oscillation Matrices to Diffusion-Convection Equations," J. Mathematics and Physics, Vol. 45, pp. 301-311.

59. Atias, M., Wolfshtein, M., and Israeli, M. (1975), "A Study of the Efficiency of Various Navier-Stokes Solvers," see pp. 81-90 of Ref. 9.

60. Khosla, P. K. and Rubin, S. G. (1974), "A Diagonally Dominant Second-Order Accurate Implicit Scheme," Computers and Fluids, Vol. 2. pp. 207-209.

61. Book, D. L., Boris, J. P., and Hain, K. (1975), "Flux-Corrected Transport II: Generalizations of the Method," J. Computational Physics, Vol. 18, pp. 248-283.

62. Orszag, S. A. (1975), "Numerical Simulation of Turbulent Flow," see pp. 231-279 of Ref. 14.

63. Schlichting, H. (1968), Boundary Layer Theory, 6th edition, McGraw-Hill Book Co., Inc., New York, N. Y.

A FAST FOURTH-ORDER LAPLACE SOLVER FOR APPLICATION TO NUMERICAL THREE-DIMENSIONAL WATER WAVE PROBLEMS

Samuel Ohring

David W. Taylor Naval Ship Research and Development Center
Bethesda, Maryland 20084 U.S.A.

ABSTRACT

A fast direct method for the numerical solution of the Laplace equation in three dimensions is described for application in constructing solutions to water wave problems. The method directly solves the system of linear algebraic equations that arises from the 27-point, fourth-order, finite difference approximation to the Laplace equation used at each point on a box grid. The method is a modified diagonal decomposition technique which relies heavily on the fast Fourier transform and computes values of the solution for only small regions of the total domain. Applications of the method to three-dimensional thin-ship and moving-pressure-distribution problems are described. In addition, suggestions are offered for applying the method to nonlinear water wave problems. Results are presented.

1. Introduction

This paper describes a numerical method which greatly facilitates velocity potential formulations for use in numerical water wave problems. Such formulations ordinarily depend upon the use of finite difference or finite element techniques in the solution of Laplace's equation as part of the overall numerical scheme--a very time consuming process, particularly when three dimensions are involved. The practice of solving the Laplace equation over the entire region, usually with an iterative method, accounts for the extensive amount of computer time required. However, for calculations of the vertical velocity of the free surface or the wave resistance of a thin ship, for instance, it is sufficient to solve the Laplace equation directly over only part of the total region defined. This paper describes a powerful, direct method known as diagonal decomposition [1,2] which is

extended to three dimensions and fourth-order accuracy and modified to numerically integrate the Laplace equation over such partial domains, the solution obtained being part of the solution over the entire region. The method described can be used effectively both in numerical schemes for three-dimensional linear, transient or steady-state water wave problems involving box regions and in numerical perturbation schemes. Test results from the application of this efficient and accurate method to three-dimensional, linear, transient, thin-ship and moving-pressure-distribution problems are presented. Suggestions based on a Taylor series approach described by Chan [3] are offered for applying this method to nonlinear problems. Preliminary test results are given. A brief review of direct methods for numerically solving elliptic partial differential equations is provided in the following paragraph.

The past decade has seen the emergence of so-called direct methods for numerically solving certain elliptic partial differential equations. These direct methods are noniterative in that they directly solve large systems of linear algebraic equations which when expressed in coefficient matrix notation have sparse tridiagonal block matrix structure, each block being tridiagonal. Such sparse regular block structures of the coefficient matrix occur from finite differencing certain separable elliptic partial differential equations over a rectangular region with Dirichlet, Neumann, or periodic boundary conditions. Several direct methods for solving the Poisson equation are described in Buzbee [1]. These direct methods are much more efficient and accurate than iterative methods since in theory they yield the exact solution to the difference equation. A comparison between several direct and iterative methods with regard to efficiency and accuracy is given in Buzbee [4]. Extensions of direct methods to nonrectangular regions are described in Buzbee [5] and George [6]. Most direct methods require that the number of grid points in either coordinate direction be a power of two for greatest efficiency since they usually employ cyclic reduction on blocks [1] or scalars and/or the fast Fourier transform [7]. Recently cyclic block reduction has been generalized, with less efficiency, to numbers other than a power of two [8]. Also, a semidirect method, which uses a direct method as its basic component, has been developed for solving nonseparable elliptic equations [9]. Direct methods have been successfully

applied to viscous fluid-flow problems [10], [11], [12].

2. The Numerical Method

In a Cartesian coordinate reference frame moving with a thin ship, the boundary conditions for Region D for the Laplace equation

$$\phi_{xx} + \phi_{yy} + \phi_{zz} = 0 \tag{1}$$

are

$$\phi_x = 0 \qquad \text{at } x = 0, L_1 \tag{2}$$

$$\phi_y = 0 \qquad \text{at } y = -h \tag{3}$$

$$\phi_z = 0 \qquad \text{at } z = L_2 \tag{4}$$

$$\phi_z = h_x \qquad \text{at } z = 0 \text{ on the thin ship} \tag{5}$$

$$\phi_z = 0 \qquad \text{at } z = 0 \text{ off the thin ship} \tag{6}$$

$$\phi = g \qquad \text{at } y = 0 \tag{7}$$

where ϕ is the disturbance velocity potential, $h = h(x,y)$ is the hull shape of the thin ship, g is the numerical velocity potential at $y = 0$, and D is the numerical computational region (Figure 1). If $h_x = 0$ in Equation (5), the model represented by Equations (1)-(7) could be interpreted as that for the moving pressure distribution problem [13], for example.

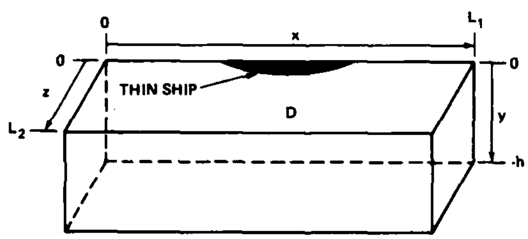

Figure 1. The Numerical Computational Region D

The goal of the numerical method is to calculate in a most efficient and accurate manner the fourth-order numerical derivative for $\phi_y(y=0)$, using the Equations (1) through (7), and to insert the result in the linear free

surface equations. Higher derivatives such as $\phi_{yy}(y=0)$, $\phi_{yyy}(y=0)$, $\phi_{yyyy}(y=0)$ will also be calculated numerically by this method, their use in a nonlinear scheme described in a later section of this report.

The following numerical grid D_h is introduced into the region D subject to the restriction

$$\Delta x = \Delta y = \Delta z = \delta \tag{8}$$

$[x_j = j\Delta x,\ y_i = i(-\Delta y),\ z_k = k\Delta z]$ with $j=0,1,\ldots,\ell-1$; $i=0,1,\ldots,m=1$; $k=0,1,\ldots,n-1$ where $(\ell-1)\Delta x = L_1$, $(m-1)(-\Delta y) = -h$, $(n-1)\Delta z = L_2$. Then $\phi_{j,i,k} = \phi(x_j,y_i,z_k)$.

Let $\ell-1 = 2^{p_\ell}$, $m-1 = 2^{p_m}$, $n-1 = 2^{p_n}$, where p_ℓ,p_m,p_n are integers. The 27-point operator represented schematically by the stencil shown in Figure 2a is introduced to approximate the Laplacian at an interior grid point (x_j,y_i,z_k) of D_h. The stencil can be interpreted as a sum of 27 products, each product being a velocity potential value at a grid point multiplied by the corresponding constant of the stencil. This stencil approximates the Laplacian to fourth-order accuracy subject to the restriction of Equation (8) and with the Laplacian equal to zero; thus

$$\text{27-point stencil} = \phi_{xx} + \phi_{yy} + \phi_{zz} + O(\delta^4) \tag{9}$$

This 27-point stencil is compared with the standard second-order stencil (Figure 2b).

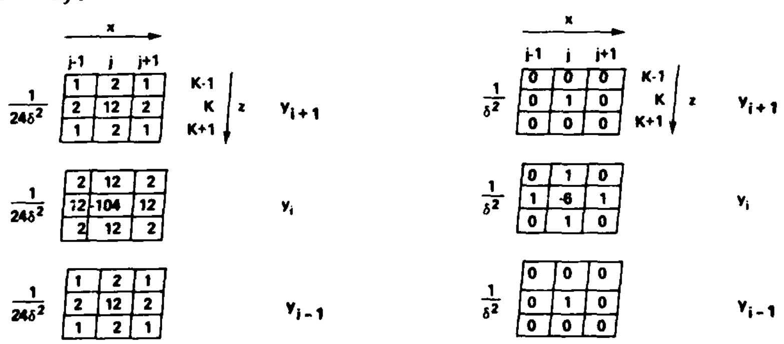

Figure 2a. 27-Point Stencil

Figure 2b. Standard Second-Order Stencil

Figure 2. Comparison of Finite Difference Operators

The 27-point approximation for Equation (1), taken at each point of D_h yields a linear equation, the system of linear equations being expressed as the following tridiagonal block matrix system:

$$\begin{bmatrix} B & C & & & \\ C & B & C & & \\ & \ddots & \ddots & \ddots & \\ & & C & B & C \\ & & & 2C & B \end{bmatrix} \begin{bmatrix} \vec{X}_1 \\ \vec{X}_2 \\ \vdots \\ \vec{X}_{m-2} \\ \vec{X}_{m-1} \end{bmatrix} = \begin{bmatrix} \vec{S}_1 \\ \vec{S}_2 \\ \vdots \\ \vec{S}_{m-2} \\ \vec{S}_{m-1} \end{bmatrix} \tag{10}$$

WHERE

$$B = \begin{bmatrix} A & 2T & & & \\ T & A & T & & \\ & \ddots & \ddots & \ddots & \\ & & T & A & T \\ & & & 2T & A \end{bmatrix}_{n\times n}, \quad C = \begin{bmatrix} T & 2E & & & \\ E & T & E & & \\ & \ddots & \ddots & \ddots & \\ & & E & T & E \\ & & & 2E & T \end{bmatrix}_{n\times n}$$

WITH

$$A = \begin{bmatrix} -104 & 24 & & & \\ 12 & -104 & 12 & & \\ & \ddots & \ddots & \ddots & \\ & & 12 & -104 & 12 \\ & & & 24 & -104 \end{bmatrix}_{\ell\times\ell}, \quad T = \begin{bmatrix} 12 & 4 & & & \\ 2 & 12 & 2 & & \\ & \ddots & \ddots & \ddots & \\ & & 2 & 12 & 2 \\ & & & 4 & 12 \end{bmatrix}_{\ell\times\ell}, \quad E = \begin{bmatrix} 2 & 2 & & & \\ 1 & 2 & 1 & & \\ & \ddots & \ddots & \ddots & \\ & & 1 & 2 & 1 \\ & & & 2 & 2 \end{bmatrix}_{\ell\times\ell}$$

Each vector $\vec{X}_i$ is given by

$$\underset{(i=1,\ldots,m-1)}{\vec{X}_i} = \begin{bmatrix} \vec{\Phi}_{i0} \\ \vec{\Phi}_{i1} \\ \vdots \\ \vec{\Phi}_{i,n-1} \end{bmatrix} \quad \text{WHERE } \underset{(k=0,1,\ldots,n-1)}{\vec{\Phi}_{ik}} = \begin{bmatrix} \phi_{0,i,k} \\ \phi_{1,i,k} \\ \phi_{2,i,k} \\ \vdots \\ \phi_{\ell-1,i,k} \end{bmatrix}$$

Each vector $\vec{S}_i$ is correspondingly given by

$$\underset{(i=1,\ldots,m-1)}{\vec{S}_i} = \begin{bmatrix} \vec{S}_{i0} \\ \vec{S}_{i1} \\ \cdot \\ \cdot \\ \cdot \\ \cdot \\ \vec{S}_{i,n-1} \end{bmatrix} \qquad \underset{(k=0,1,\ldots,n-1)}{\text{WHERE } \vec{S}_{ik}} = \begin{bmatrix} S_{0,i,k} \\ S_{1,i,k} \\ S_{2,i,k} \\ \cdot \\ \cdot \\ \cdot \\ S_{\ell-1,i,k} \end{bmatrix}$$

For purposes of explanation assume that the thin ship occupies an entire face of D_h at z=0 (Figure 1). Significant additional computational economy is gained when the thin ship is represented as shown in Figure 1, as will be obvious from the numerical procedure. We have

$$\vec{S}_{ik} = 0 \quad \text{for } i=2,\ldots,m-1;\ k=1,\ldots,n-1 \tag{11}$$

and

$$S_{j,i,0} = 48\delta\ \phi_z(x_j,y_i,z_0) \text{ for } i=2,\ldots,m-1;\ j=0,\ldots,\ell-1 \tag{12}$$

where $S_{j,i,0}$ are the elements of the vector $\vec{S}_{i0}$, i=2,...,m-1. The vector $\vec{S}_1$ primarily results from the shifting of the remainder of the 27-point operator to the right-hand side of the linear system of Equations (10) due to the condition expressed in Equation (7). For instance

$$\begin{aligned} S_{j,1,k} = -[12\phi_{j,0,k} &+ 2(\phi_{j+1,0,k}+\phi_{j-1,0,k}+\phi_{j,0,k-1}+\phi_{j,0,k+1}) \\ &+\phi_{j+1,0,k-1}+\phi_{j+1,0,k+1}+\phi_{j-1,0,k-1}+\phi_{j-1,0,k+1}] \end{aligned} \tag{13}$$

$$\text{for } j=1,\ldots,\ell-2;\ k=1,\ldots,n-2$$

The remaining elements of $\vec{S}_1$ result from truncations of the 27-point operator at boundary points of D_h and the boundary conditions expressed in Equation (2) and Equations (4) through (7). For example, the elements of $\vec{S}_{10}$ are

$$S_{0,1,0} = -(12\phi_{0,0,0}+4(\phi_{1,0,0}+\phi_{0,0,1}+\phi_{1,0,1}))+48\delta\ \phi_z(x_0,y_1,z_0) \tag{14}$$

$$S_{j,1,0} = -(12\phi_{j,0,0}+4\phi_{j,0,1}+2(\phi_{j-1,0,0}+\phi_{j-1,0,1}+\phi_{j+1,0,0}+\phi_{j+1,0,1}))+48\delta\ \phi_z(x_j,y_1,z_0) \quad \text{for } j=1,\ldots,\ell-2 \tag{15}$$

$$S_{\ell-1,1,0} = -(12\phi_{\ell-1,0,0}+4(\phi_{\ell-2,0,0}+\phi_{\ell-2,0,1}+\phi_{\ell-1,0,1}))+48\delta\ \phi_z(x_{\ell-1},y_1,z_0) \tag{16}$$

The block matrices A,T,E commute, and thus have the same set of linearly independent eigenvectors which are the column vectors of R_ℓ.

$$R_\ell = \sqrt{\frac{2}{\ell-1}} \begin{bmatrix} 1 & 1 & 1 & \cdots\cdots & 1 \\ 1 & \cos\frac{\pi}{\ell-1} & \cos\frac{2\pi}{\ell-1} & \cdots\cdots & \cos\pi \\ 1 & \cos\frac{2\pi}{\ell-1} & \cos\frac{2\cdot2\pi}{\ell-1} & \cdots\cdots & \cos2\pi \\ \vdots & \vdots & \vdots & & \vdots \\ 1 & \cos\pi & \cos2\pi & \cdots\cdots & \cos(\ell-1)\pi \end{bmatrix}_{\ell\times\ell} \tag{17}$$

The inverse of R_ℓ is

$$R_\ell^{-1} = \frac{1}{(2^{3/2})\sqrt{\ell-1}} \begin{bmatrix} 1 & 2 & \cdots\cdots & 2 & 1 \\ 2 & 4\cos\frac{\pi}{\ell-1} & \cdots\cdots & 4\cos\frac{(\ell-2)\pi}{\ell-1} & 2\cos\pi \\ 2 & 4\cos\frac{2\pi}{\ell-1} & & 4\cos\frac{2(\ell-2)\pi}{\ell-1} & 2\cos2\pi \\ \vdots & \vdots & & \vdots & \vdots \\ 2 & 4\cos\frac{(\ell-3)\pi}{\ell-1} & \cdots\cdots & 4\cos\frac{(\ell-3)(\ell-2)\pi}{\ell-1} & 2\cos(\ell-3)\pi \\ 2 & 4\cos\frac{(\ell-2)\pi}{\ell-1} & \cdots\cdots & 4\cos\frac{(\ell-2)(\ell-2)\pi}{\ell-1} & 2\cos(\ell-2)\pi \\ 1 & 2\cos\pi & \cdots\cdots & 2\cos(\ell-2)\pi & \cos(\ell-1)\pi \end{bmatrix}_{\ell\times\ell} \tag{18}$$

The eigenvalues of A,T,E are given by λ_j, ω_j, η_j respectively, where

$$\left.\begin{aligned} \lambda_j &= -104 + 24 \cos \frac{j\pi}{\ell-1} \\ \omega_j &= 12 + 4 \cos \frac{j\pi}{\ell-1} \\ \eta_j &= 2 + 2 \cos \frac{j\pi}{\ell-1} \end{aligned}\right\} \quad j=0,1,\ldots,\ell-1$$

Each block line of the system given in Equation (10) (which involves A,T,E) can then be multiplied on the left by R_ℓ^{-1}, resulting in

$$\begin{bmatrix} \tilde{B} & \tilde{C} & & & \\ \tilde{C} & \tilde{B} & \tilde{C} & & \\ & \ddots & \ddots & \ddots & \\ & & \tilde{C} & \tilde{B} & \tilde{C} \\ & & & 2\tilde{C} & \tilde{B} \end{bmatrix} \begin{bmatrix} \vec{\tilde{X}}_1 \\ \vec{\tilde{X}}_2 \\ \vdots \\ \vec{\tilde{X}}_{m-2} \\ \vec{\tilde{X}}_{m-1} \end{bmatrix} = \begin{bmatrix} \vec{\tilde{S}}_1 \\ \vec{\tilde{S}}_2 \\ \vdots \\ \vec{\tilde{S}}_{m-2} \\ \vec{\tilde{S}}_{m-1} \end{bmatrix} \text{ WITH } \underset{(i=1,\ldots,m-1)}{\vec{\tilde{X}}_i =} \begin{bmatrix} \vec{\tilde{\Phi}}_{i0} \\ \vec{\tilde{\Phi}}_{i1} \\ \vdots \\ \vec{\tilde{\Phi}}_{in-1} \end{bmatrix} = \begin{bmatrix} R_\ell^{-1}\vec{\Phi}_{i0} \\ R_\ell^{-1}\vec{\Phi}_{i1} \\ \vdots \\ R_\ell^{-1}\vec{\Phi}_{in-1} \end{bmatrix} ; \underset{(i=1,\ldots,m-1)}{\vec{\tilde{S}}_i =} \begin{bmatrix} \vec{\tilde{S}}_{i0} \\ \vec{\tilde{S}}_{i1} \\ \vdots \\ \vec{\tilde{S}}_{in-1} \end{bmatrix} = \begin{bmatrix} R_\ell^{-1}\vec{S}_{i0} \\ R_\ell^{-1}\vec{S}_{i1} \\ \vdots \\ R_\ell^{-1}\vec{S}_{in-1} \end{bmatrix} \quad (19)$$

where

$$\tilde{B} = \begin{bmatrix} \Lambda & 2\Omega & & & \\ \Omega & \Lambda & \Omega & & \\ & \ddots & \ddots & \ddots & \\ & & \Omega & \Lambda & \Omega \\ & & & 2\Omega & \Lambda \end{bmatrix}_{n \times n}, \quad \tilde{C} = \begin{bmatrix} \Omega & 2H & & & \\ H & \Omega & H & & \\ & \ddots & \ddots & \ddots & \\ & & H & \Omega & H \\ & & & 2H & \Omega \end{bmatrix}_{n \times n}$$

with

$$\Lambda = \begin{bmatrix} \lambda_0 & & \\ & \ddots & \\ & & \lambda_{\ell-1} \end{bmatrix}, \quad \Omega = \begin{bmatrix} \omega_0 & & \\ & \ddots & \\ & & \omega_{\ell-1} \end{bmatrix}, \quad H = \begin{bmatrix} \eta_0 & & \\ & \ddots & \\ & & \eta_{\ell-1} \end{bmatrix}$$

Note that $\vec{\tilde{S}}_{i1}, \vec{\tilde{S}}_{i2}, \ldots, \vec{\tilde{S}}_{in-1}$ are zero vectors for $i=2,3,\ldots,m-1$. From this diagonalized block system represented by Equation (19) select the j^{th} equation from each block line (involving Λ, Ω, H) and regroup to form the following two-dimensional problem with x held fixed at subscript j

$(j = 0,1,\ldots,\ell-1)$

$$\begin{bmatrix} P_j & Q_j & & & \\ Q_j & P_j & Q_j & & \\ & \ddots & \ddots & \ddots & \\ & & Q_j & P_j & Q_j \\ & & & 2Q_j & P_j \end{bmatrix} \begin{bmatrix} \vec{\tilde{X}}_{1j} \\ \vec{\tilde{X}}_{2j} \\ \vdots \\ \vec{\tilde{X}}_{m-2j} \\ \vec{\tilde{X}}_{m-1j} \end{bmatrix} = \begin{bmatrix} \vec{\tilde{S}}_{1j} \\ \vec{\tilde{S}}_{2j} \\ \vdots \\ \vec{\tilde{S}}_{m-2j} \\ \vec{\tilde{S}}_{m-1j} \end{bmatrix} \tag{20}$$

where

$$P_j = \begin{bmatrix} \lambda_j & 2\omega_j & & & \\ \omega_j & \lambda_j & \omega_j & & \\ & \ddots & \ddots & \ddots & \\ & & \omega_j & \lambda_j & \omega_j \\ & & & 2\omega_j & \lambda_j \end{bmatrix}_{n\times n}, \quad Q_j = \begin{bmatrix} \omega_j & 2\eta_j & & & \\ \eta_j & \omega_j & \eta_j & & \\ & \ddots & \ddots & \ddots & \\ & & \eta_j & \omega_j & \eta_j \\ & & & 2\eta_j & \omega_j \end{bmatrix}_{n\times n}$$

with

$$\underset{(i=1,\ldots,m-1)}{\vec{\tilde{X}}_{ij}} = \begin{bmatrix} \tilde{\phi}_{j,i,0} \\ \tilde{\phi}_{j,i,1} \\ \vdots \\ \vdots \\ \tilde{\phi}_{j,i,n-1} \end{bmatrix}, \quad \vec{\tilde{S}}_{1j} = \begin{bmatrix} \tilde{S}_{j,1,0} \\ \tilde{S}_{j,1,1} \\ \vdots \\ \vdots \\ \tilde{S}_{j,1,n-1} \end{bmatrix}, \quad \vec{\tilde{S}}_{ij} = \begin{bmatrix} \tilde{S}_{j,i,0} \\ 0 \\ \vdots \\ \vdots \\ 0 \end{bmatrix} \quad (i=2,\ldots m-1)$$

The elements $\tilde{\phi}_{j,i,k}$, $\tilde{S}_{j,i,k}$ are elements of the vectors $\vec{\tilde{\phi}}_{ik}$, $\vec{\tilde{S}}_{ik}$, respectively, ordered in the same way as elements of $\vec{\phi}_{ik}$, $\vec{S}_{ik}$. The matrices P_j, Q_j commute and thus have the same eigenvectors which are given by the column vectors of R_ℓ (Equation (17)) with ℓ replaced by n. Also the eigenvalues of P_j, Q_j are given by $\tilde{\lambda}_{j,k}$, $\tilde{\omega}_{j,k}$, respectively:

$$\left.\begin{aligned} \tilde{\lambda}_{j,k} &= \lambda_j + 2\omega_j \cos\frac{k\pi}{n-1} \\ \tilde{\omega}_{j,k} &= \omega_j + 2\eta_j \cos\frac{k\pi}{n-1} \end{aligned}\right\} \quad k=0,1,\ldots,n-1 \tag{21}$$

Each block line of Equation (20) can then be multiplied on the left by R_n^{-1}. This results in

$$\begin{bmatrix} \tilde\Lambda_j & \tilde\Omega_j & & & \\ \tilde\Omega_j & \tilde\Lambda_j & \tilde\Omega_j & & \\ & \ddots & \ddots & \ddots & \\ & & \tilde\Omega_j & \tilde\Lambda_j & \tilde\Omega_j \\ & & & 2\tilde\Omega_j & \tilde\Lambda_j \end{bmatrix} \begin{bmatrix} \tilde{\vec{X}}_{1j} \\ \tilde{\vec{X}}_{2j} \\ \vdots \\ \tilde{\vec{X}}_{m-2,j} \\ \tilde{\vec{X}}_{m-1,j} \end{bmatrix} = \begin{bmatrix} \tilde{\vec{S}}_{1j} \\ \tilde{\vec{S}}_{2j} \\ \vdots \\ \tilde{\vec{S}}_{m-2,j} \\ \tilde{\vec{S}}_{m-1,j} \end{bmatrix} \text{WHERE } \tilde\Lambda_j = \begin{bmatrix} \tilde\lambda_{j,0} & & \\ & \ddots & \\ & & \tilde\lambda_{j,n-1} \end{bmatrix}_{n \times n}, \tilde\Omega_j = \begin{bmatrix} \tilde\omega_{j,0} & & \\ & \ddots & \\ & & \tilde\omega_{j,n-1} \end{bmatrix}_{n \times n} \qquad (22)$$

with

$$\tilde{\vec{X}}_{ij} = R_n^{-1}\vec{X}_{ij} = \begin{bmatrix} \tilde\phi_{j,i,0} \\ \tilde\phi_{j,i,1} \\ \vdots \\ \tilde\phi_{j,i,n-1} \end{bmatrix} \; (i=1,\ldots,m-1), \quad \tilde{\vec{S}}_{ij} = R_n^{-1}\vec{S}_{ij} = \begin{bmatrix} \tilde S_{j,i,0} \\ \tilde S_{j,i,1} \\ \vdots \\ \tilde S_{j,i,n-1} \end{bmatrix} \; (i=1,\ldots,m-1), \quad \tilde{\vec{S}}_{ij} = \frac{\tilde S_{j,i,0}}{(2^{3/2})\sqrt{n-1}} \begin{bmatrix} 1 \\ 2 \\ 2 \\ \vdots \\ 2 \\ 2 \\ 1 \end{bmatrix} \; (i=2,\ldots,m-1) \qquad (23)$$

with j fixed. From this diagonalized block system given in Equation (22), the k^{th} equation from each block line is selected and regrouped to form the following one-dimensional problem with z fixed at subscript k and x fixed at subscript j, $(j=0,1,\ldots,\ell-1;\ k=0,1,\ldots,n-1)$

$$\begin{bmatrix} \tilde\lambda_{j,k} & \tilde\omega_{j,k} & & & \\ \tilde\omega_{j,k} & \tilde\lambda_{j,k} & \tilde\omega_{j,k} & & \\ & \ddots & \ddots & \ddots & \\ & & \tilde\omega_{j,k} & \tilde\lambda_{j,k} & \tilde\omega_{j,k} \\ & & & 2\tilde\omega_{j,k} & \tilde\lambda_{j,k} \end{bmatrix} \begin{bmatrix} \tilde\phi_{j,1,k} \\ \tilde\phi_{j,2,k} \\ \vdots \\ \tilde\phi_{j,m-2,k} \\ \tilde\phi_{j,m-1,k} \end{bmatrix} = \begin{bmatrix} \tilde S_{j,1,k} \\ \tilde S_{j,2,k} \\ \vdots \\ \tilde S_{j,m-2,k} \\ \tilde S_{j,m-1,k} \end{bmatrix} \qquad (24)$$

Note that if Equation (5) holds in D_h for $1 \leq i \leq M$, $(M \leq m-1)$, then $\tilde{S}_{j,i,k} = 0$ in Equation (24) for i>M. To calculate the numerical derivative $\phi_y(y=0)$ to

fourth-order accuracy for all x_j, z_k, only $\tilde{\tilde{\phi}}_{j,1,k}$, $\tilde{\tilde{\phi}}_{j,2,k}$, $\tilde{\tilde{\phi}}_{j,3,k}$, $\tilde{\tilde{\phi}}_{j,4,k}$ (all j,k) need be solved. To accomplish this, scalar cyclic reduction [7] is used, as will be described shortly. Finally, the velocity potential $\phi_{j,i,k}$ (for $i=1,2,3,4$; $j=0,1,\ldots,\ell-1$; $k=0,1,\ldots,n-1$) is calculated in a reverse process via the following transforms:

$$
\underset{\begin{pmatrix} i=1,2,3,4 \\ \text{ALL } j \end{pmatrix}}{R_n \tilde{\tilde{\vec{X}}}_{ij} = \tilde{\vec{X}}_{ij}} \Longrightarrow \underset{(i=1 \to 4)}{\tilde{\vec{X}}_i =} \begin{bmatrix} R_\ell^{-1}\vec{\Phi}_{i0} \\ R_\ell^{-1}\vec{\Phi}_{i1} \\ \vdots \\ R_\ell^{-1}\vec{\Phi}_{in-1} \end{bmatrix} \tag{25}
$$

$$
\underset{\begin{pmatrix} i=1 \to 4 \\ k=0,1,\ldots,n-1 \end{pmatrix}}{R_\ell\,[R_\ell^{-1}\vec{\Phi}_{i,k}] = \vec{\Phi}_{ik}} \Longrightarrow \underset{(i=1 \to 4)}{\vec{X}_i} \text{ (THE SOLUTION)} \tag{26}
$$

To briefly illustrate scalar cyclic reduction, rewrite Equation (24) dropping all superscripts and subscripts, and replace $\tilde{\tilde{\phi}}$'s with v's and $\tilde{\tilde{S}}$'s with r's, so that the following system of equations is obtained:

$$
\begin{array}{ll} & \omega \\ & -\lambda \\ \omega & \omega \\ -\lambda & \\ \omega & \vdots \\ & \\ & 2\omega \\ & -\lambda \end{array}
\begin{bmatrix} \lambda & \omega & & & & & \\ \omega & \lambda & \omega & & & & \\ & \omega & \lambda & \omega & & & \\ & & \omega & \lambda & \omega & & \\ & & & \omega & \lambda & \omega & \\ & & & & \ddots & \ddots & \ddots \\ & & & & \omega & \lambda & \omega \\ & & & & & 2\omega & \lambda \end{bmatrix}
\begin{bmatrix} v_1 \\ v_2 \\ v_3 \\ v_4 \\ v_5 \\ \vdots \\ v_{m-2} \\ v_{m-1} \end{bmatrix} =
\begin{bmatrix} r_1 \\ r_2 \\ r_3 \\ r_4 \\ r_5 \\ \vdots \\ r_{m-2} \\ r_{m-1} \end{bmatrix} \tag{27}
$$

The first equation in System (27) is multiplied by ω, the second by $-\lambda$, and the third by ω, and then the three equations are added. The third, fourth, and fifth equations, and then the fifth, sixth, and seventh equations, and so on, are then operated on in a similar manner, as indicated by the left

multipliers in System (27). This process produces a first reduced system for the even-numbered unknowns, in the same form as that used in System (27). This reduction process is repeated until p_m reduced systems have been obtained. Note that only the first equation of each reduced system is considered in a back-solving process, first for $v_{2^{p_m}}$, then for $v_{2^{p_m}-1},\ldots,v_2,v_1$. This set of equations (with $m-1 = 2^{p_m}$) is

$$\left.\begin{array}{lll}
\lambda^{(p_m)} v_{2^{p_m}} & & = r^{(p_m)}_{2^{p_m}} \\
\lambda^{(p_m-1)} v_{2^{p_m}-1} & + \omega^{(p_m-1)} v_{2^{p_m}} & = r^{(p_m-1)}_{2^{p_m}-1} \\
\vdots & \vdots & \vdots \\
\lambda^{(t)} v_{2^t} & + \omega^{(t)} v_{2\cdot 2^t} & = r^{(t)}_{2^t} \\
\vdots & \vdots & \vdots \\
\lambda v_1 & + \omega v_2 & = r_1
\end{array}\right\} \quad (28)$$

where

$$\left.\begin{array}{ll}
\omega^{(t)} = (\omega^{(t-1)})^2 & t=1,\ldots,p_{m-1} \\
\lambda^{(t)} = 2(\omega^{(t-1)})^2 - (\lambda^{(t-1)})^2 & t=1,\ldots,p_m \\
r^{(t)}_{2^t} = \omega^{(t-1)}(r^{(t-1)}_{2^t-2^{t-1}}+r^{(t-1)}_{2^t+2^{t-1}})-\lambda^{(t-1)}r^{(t-1)}_{2^t} & t=1,\ldots,p_{m-1} \\
r^{(p_m)}_{2^{p_m}} = 2\omega^{(p_{m-1})} r^{(p_{m-1})}_{2^{p_m}-1} - \lambda^{(p_{m-1})} r^{(p_{m-1})}_{2^{p_m}} &
\end{array}\right\} \quad (29)$$

with

$$\omega^{(0)} = \omega, \quad \lambda^{(0)} = \lambda, \quad r_i^{(0)} = r_i \qquad (i=1,\ldots,m-1)$$

The following algorithm summarizes all the computational steps of the numerical method:

1) Precompute the coefficients of cyclic reduction ($\lambda^{(t)}$, $\omega^{(t)}$ in Equation (28)).
2) Compute source vector $\vec{S}_1$ of the block matrix system represented in Equation (10) from Equations (13) through (16) and similar relations.
3) Compute $\tilde{\vec{S}}_i$ (i=1,...,m-1) of the diagonalized block system represented by Equation (19) via the fast Fourier transform [14], [15] while observing that $\tilde{\vec{S}}_{i1}$, $\tilde{\vec{S}}_{i2}, \ldots, \tilde{\vec{S}}_{in-1}$ are zero vectors for i=2,3,...,m-1.
4) Compute $\tilde{\tilde{\vec{S}}}_{1j}$ in Equation (23) for all j by the fast Fourier transform; compute $\tilde{\tilde{\vec{S}}}_{ij}$ (i=2,...,m-1; all j) by the relation of Equation (23).
5) Solve Equation (24) for $\tilde{\tilde{\phi}}_{j,1,k}$, $\tilde{\tilde{\phi}}_{j,2,k}$, $\tilde{\tilde{\phi}}_{j,3,k}$, $\tilde{\tilde{\phi}}_{j,4,k}$ (all j,k) using the scalar cyclic reduction procedure described in Equations (27), (28), and (29).
6) Compute vectors $\tilde{\vec{X}}_i$ of Equation (25) for i=1,2,3,4 via the fast Fourier transform.
7) Compute the solution vectors $\vec{X}_i$ of Equation (26) for i=1,2,3,4 via the fast Fourier transform.
8) Calculate numerically $\phi_y(y=0)$, $\phi_{yy}(y=0)$, $\phi_{yyy}(y=0)$, $\phi_{yyyy}(y=0)$ from the solution $\phi_{j,i,k}$ (i=1,2,3,4; all j,k).

If $\phi_z = 0$ in Equation (5), as occurs in the case of a moving pressure distribution model, then $\tilde{\tilde{S}}_{j,2,k} \to \tilde{\tilde{S}}_{j,m-1,k}$ will be zero in Equation (24) and significant additional computation efficiency in steps 3, 4, and 5 of the computational algorithm will result.

3. Numerical Results

The numerical method was used to perform calculations for thin-ship boundary conditions satisfied by the test analytic solution given for

Table 1, and for moving-pressure-distribution boundary conditions satisfied by the test analytic solution given for Table 2. Results of the calculations are given in Tables 1 and 2. In the three test cases of Table 1, the hull condition ($\phi_z(0)\neq 0$) occupies an entire face of D_h and is "wavy" in x, providing a difficult test of the numerical method. In both tables, higher numerical derivatives have been considered, since little additional computation time was required and they have possible application in nonlinear numerical schemes mentioned briefly at the end of this section. The notation "% error" refers to the following:

$$\left\{\frac{[\phi_y]_{\text{analytic}} - [\phi_y]_{\text{numerical}}}{[\phi_y]_{\text{analytic}}}\right\}_{y=0} = \phi_y(y=0)\ \%\ \text{error}$$

The notation "four-point derivatives" denotes numerical derivatives that were computed from $\phi_{j,i,k}$ ($i=0,1,\ldots,4$; all j,k) where $\phi_{j,0,k}$ represents the Dirichlet condition; "five-point derivatives" denotes derivatives that were computed from $\phi_{j,i,k}$ ($i=0,1,\ldots,5$; all j,k) necessitating that i have a range of 5 in steps 5, 6, and 7 of the computational algorithm. Parameters for both tables were:

$$L_1 = L_2 = \pi$$

$$h = \pi/4$$

$$\Delta x = \Delta y = \Delta z = \delta = \pi/64$$

$$\ell(\text{no. of x pts.}) = n(\text{no. of z pts.}) = 65$$

$$m(\text{no. of y pts.}) = 17$$

As a further test, the fourth-order Laplace solver was used in an implicit numerical scheme for the linear three-dimensional moving-pressure-distribution problem described by Haussling and VanEseltine [13]. Figure 3 shows the impulsively started pressure distribution (the square) having traveled 2.16 of its length upstream to the left (i.e., t=2.16), with Froude number = Fr = $(2\pi)^{-1/2} \doteq 0.4$ based on length and $\delta = 0.01$ representing the strength of the pressure distribution [13]. The pressure distribution is set equal to $(\sin^2 x)(\sin^2 z)$ in a small domain (the square), chosen such that the pressure and its first derivatives are continuous everywhere. Surface elevation contours represented by the constant values

TABLE 1 - FOURTH-ORDER LAPLACE SOLVER CALCULATION RESULTS FOR THIN-SHIP BOUNDARY CONDITIONS

	CASE I	CASE II	CASE III
λ	3	5	7
GRID PTS/WAVE LENGTH (X-DIR)	43	26	18
GRID PTS/WAVE LENGTH (Z-DIR)	85	51	37
FOUR POINT DERIVATIVES			
ϕ_y (y=0) % ERROR	0.011	0.073	0.237
ϕ_{yy} (y=0) % ERROR	0.284	1.129	2.637
ϕ_{yyy} (y=0) % ERROR	3.759	9.039	15.370
ϕ_{yyyy} (y=0) % ERROR	27.390	41.490	52.470
TIME (SECONDS) CDC-6400	9.43	SAME	SAME
FIVE POINT DERIVATIVES			
ϕ_y (y=0) % ERROR	0.001	0.015	0.065
ϕ_{yy} (y=0) % ERROR	0.040	0.249	0.773
ϕ_{yyy} (y=0) % ERROR	0.619	2.301	5.175
ϕ_{yyyy} (y=0) % ERROR	5.813	13.440	22.150
TIME (SECONDS) CDC-6400	10.84	SAME	SAME

The test analytic solution

$$\phi(x,y,z) = \cosh((h+y)\lambda\sqrt{5/4})(\cos \lambda x)(\cos[\lambda(z+\pi)/2])$$

satisfies the boundary conditions for Table 1:

$$\nabla^2\phi = 0 \quad \text{in } D$$

$$\phi_x(0) = \phi_x(L_1) = 0$$

$$\phi_z(0) = -(\lambda/2)\cosh((h+y)\lambda\sqrt{5/4})\cos \lambda x \sin \lambda\pi/2$$

$$\phi_z(L_2) = 0$$

$$\phi_y(-h) = 0$$

TABLE 2 - FOURTH-ORDER LAPLACE SOLVER CALCULATION RESULTS FOR MOVING-PRESSURE-DISTRIBUTION BOUNDARY CONDITIONS

	CASE I	CASE II	CASE III
λ	3	4	6
GRID PTS/WAVE LENGTH	43	32	21
FOUR POINT DERIVATIVES			
ϕ_y (y=0) % ERROR	0.027	0.076	0.312
ϕ_{yy} (y=0) % ERROR	0.543	1.165	3.210
ϕ_{yyy} (y=0) % ERROR	5.681	9.217	17.340
ϕ_{yyyy} (y=0) % ERROR	33.480	41.860	55.260
TIME (SECONDS) CDC-6400	4.80	SAME	SAME
FIVE POINT DERIVATIVES			
ϕ_y (y=0) % ERROR	0.004	0.016	0.092
ϕ_{yy} (y=0) % ERROR	0.094	0.260	1.006
ϕ_{yyy} (y=0) % ERROR	1.141	2.371	6.231
ϕ_{yyyy} (y=0) % ERROR	8.629	13.690	24.780
TIME (SECONDS) CDC-6400	5.51	SAME	SAME

The test analytic solution

$$\phi(x,y,z) = \cosh((h+y)\lambda\sqrt{2})(\cos \lambda x)(\cos \lambda z)$$

satisifes the boundary conditions for Table 2:

$$\nabla^2\phi = 0 \quad \text{in } D$$

$$\phi_x(0) = \phi_x(L_1) = 0$$

$$\varphi_z(0) = \phi_z(L_2) = 0$$

$$\phi_y(-h) = 0$$

±0.02, ±0.015, ±0.01, ±0.0075, ±0.005, and ±0.0025 have been plotted by computer, with solid line contours indicating wave crests and dotted line contours indicating wave troughs. The grid used contained 65x65x17 points, 11 of them used for the length of the pressure distribution. The numerical scheme conserved energy. Only 110 seconds of CDC 6600 computing time was needed to calculate half of the solution shown in Figure 3 from an impulsive start. Because of symmetry, only half the solution need be calculated.

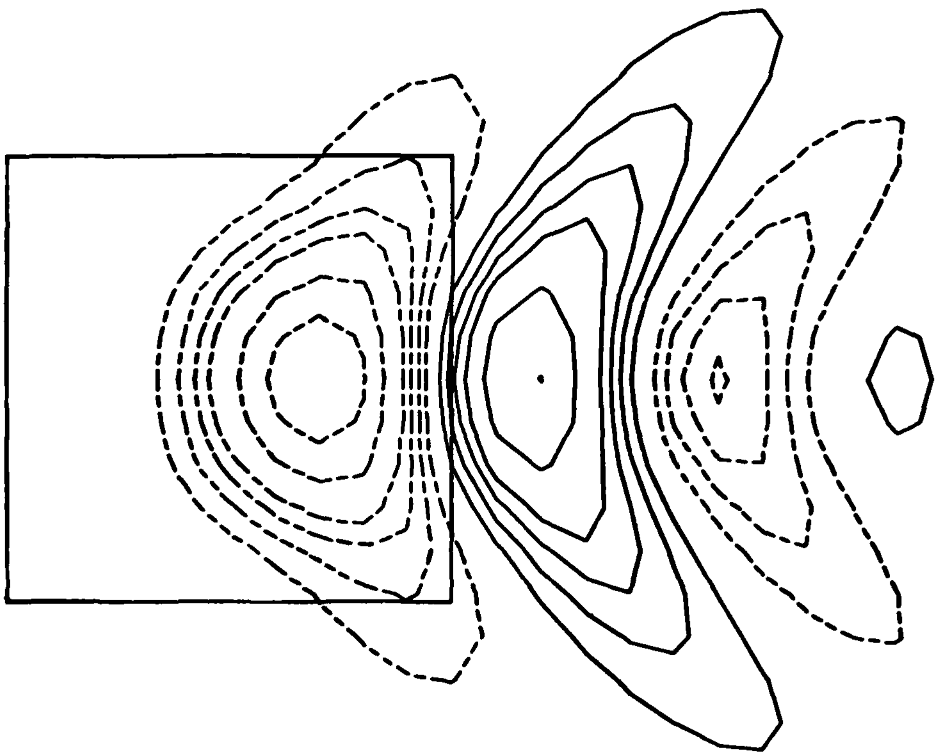

Figure 3. Surface Elevation Contours Generated by an Abruptly Started Moving Pressure Distribution for $Fr=(2\pi)^{-1/2}$, $\delta=0.01$, at $t=2.16$.

The fourth-order method was also tested in a numerical, linear, transient, thin-ship model, with $\ell=n=65$ grid points and $m=17$ grid points. This

grid system was chosen for convenience, although a grid system consisting of ℓ=129 grid points, n=33 grid points, and m=17 grid points, for example, would be more appropriate and would require the same computational time. The model is represented by the Laplace Equation (1) and the boundary conditions expressed by Equations (2) through (7) and the free surface equations

$$\eta_t = -\eta_x + \phi_y \tag{30}$$

$$\phi_t = -\phi_x - \frac{1}{Fr^2}\eta \tag{31}$$

where η is the free surface elevation, lengths are scaled by L_s (the ship length), and velocities are scaled by the free stream velocity U. The Froude number is $U/\sqrt{gL_s}$ where g is the gravitational acceleration constant and t is nondimensional time. An impulsive start is chosen so that $\eta=\phi=0$ at t=0. The hull condition (Equation (5)) was approximated in a test case by $h_x = \tan 15°$ for x_j, y_i (with $j=18 \rightarrow 25$, $i=1 \rightarrow 4$); $h_x = -\tan 15°$ for x_j, y_i (with $j=34 \rightarrow 41$, $i=1 \rightarrow 4$); $h_x = 0$ elsewhere. For this test case, Fr = 0.2. The ship occupied a length of 24 grid points in the relatively small numerical region. Fourth-order line inversions of the Equations (30) and (31) were used, in conjunction with the fourth-order Laplace solver, in an implicit numerical scheme to advance the solution in time. Figure 4 shows contours of surface elevation plotted by computer for waves generated when the ship has moved 0.32 of its length upstream to the left (i.e., t=0.32). Solid line contours represented by the constants 0.013, 0.011,...,0.003 indicate wave crests and dotted line contours represented by constants -0.013, -0.011,...,-0.003 indicate wave troughs. Approximately 2.5 minutes of CDC 6600 computing time were used to calculate the solution in Figure 4 from the impulsive start.

A Taylor series approach was suggested in Chan [3] for numerically solving nonlinear problems. Thus, in a two-dimensional, transient, nonlinear problem, for example, the velocity potential ϕ would be expressed as a truncated Taylor series about the undisturbed mean level y=0, as shown in Figure 5.

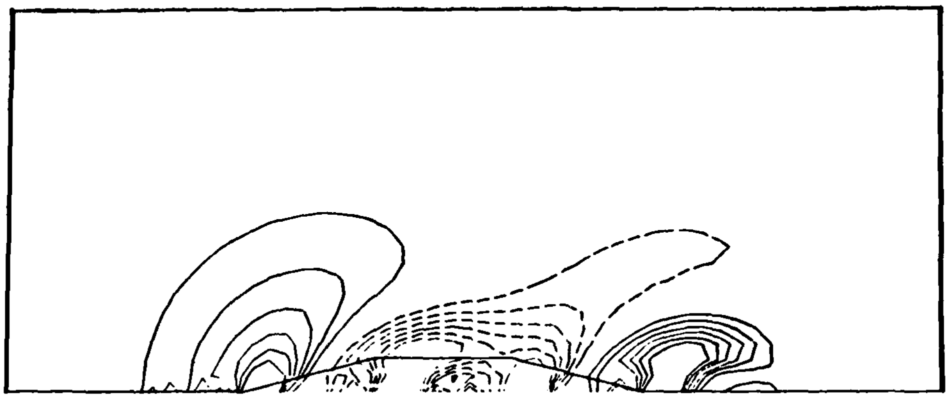

Figure 4. Surface Elevation Contours Generated by an Abruptly Started Thin Ship for Fr = 0.2 at t = 0.32.

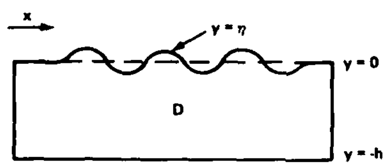

Figure 5. The Region D.

For example,

$$\phi(x,y,t) = \phi(x,0,t) + y\phi_y(x,0,t) + \frac{y^2}{2}\phi_{yy}(x,0,t) + \frac{y^3}{3!}\phi_{yyy}(x,0,t) + \frac{y^4}{4!}\phi_{yyyy}(x,0,t) \tag{32}$$

In particular, if $\eta = \eta(x,t)$ is the free surface elevation, then

$$\phi(x,\eta,t) = \phi(x,0,t) + \eta\phi_y(x,0,t) + \frac{\eta^2}{2}\phi_{yy}(x,0,t) + \frac{\eta^3}{3!}\phi_{yyy}(x,0,t) + \frac{\eta^4}{4!}\phi_{yyyy}(x,0,t) \tag{33}$$

It can be seen from the following typical nonlinear free surface equations (Stoker [16]),

$$\left.\begin{aligned} &\phi_x \eta_x - \phi_y + \eta_t = 0 && \text{at } y=\eta \\ &g\eta + \phi_t + \frac{1}{2}(\phi_x^2 + \phi_y^2) + \frac{p}{\rho} = 0 && \text{at } y=\eta \end{aligned}\right\} \quad (34)$$

where g, p, ρ are gravitational acceleration, surface pressure, and fluid density, respectively, that numerical schemes can be constructed using Taylor expansions such as those of Equation (33) in Equation (34). Such a scheme assumes ϕ is harmonic in the rectangular region D.

A numerical scheme has been constructed which uses an analogous fourth-order Laplace solver in two dimensions, involving a nine-point finite-difference operator. This scheme computes ϕ_y, ϕ_{yy}, ϕ_{yyy}, ϕ_{yyyy} at y=0, quickly and accurately. Derivatives of the Taylor coefficients with respect to x are necessary. A preliminary test was made on the transient, two-dimensional moving-pressure-distribution model described by Haussling and VanEseltine [13] for $Fr = (2\pi)^{-1/2}$, $\delta = 0.01$. Again Fr is based on length, and δ is a measure of the strength of the pressure distribution. The pressure is set equal to $\sin^2 x$ in a small domain (the bracketed area in Figure 6), chosen so that the pressure and its first derivatives are continuous everywhere. Figure 6 shows the surface elevation computed from this Taylor series scheme (including terms up to η^2 only) at an early nondimensional time t = 2.16, using a time step $\Delta t \approx 0.03$; that is, the impulsively started pressure distribution has moved 2.16 of its length upstream to the left. Nonlinear effects are evident in the sharp peak and the broad trough. In this scheme, 129 points were used in x, 16 per wavelength of the pressure distribution. The scheme conserves energy, and the surface elevation and wave resistance calculations agree well with results reported by Haussling and VanEseltine [13] through t = 2.16.

Taylor series schemes which use the fast fourth-order Laplace solver described appear promising, especially for three-dimensional water wave problems.

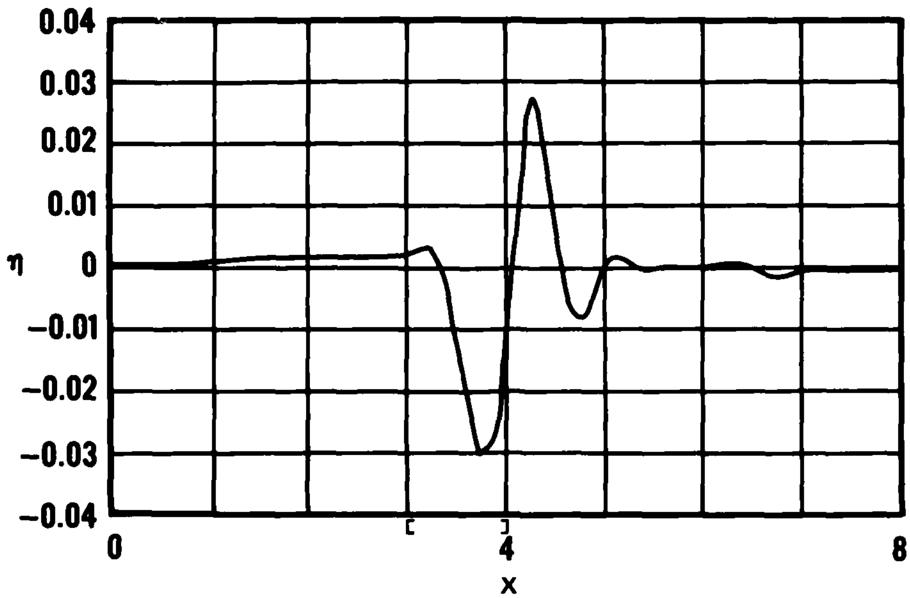

Figure 6. Nonlinear Surface Elevation Computed from the Taylor Series Method for an Abruptly Started Moving Pressure Distribution with Fr = 0.4, δ = 0.01 at t = 2.16.

4. Conclusions

The fast fourth-order Laplace solver described in this paper can be beneficially applied to linear three-dimensional numerical water wave problems, both transient and steady state, that involve box regions. It can also be beneficially applied in numerical perturbation schemes. Its use in nonlinear problems, especially in three dimensions, appears promising.

Acknowledgments

The author is indebted to Dr. H.J. Haussling and Mr. C.W. Dawson for valuable discussions and assistance. The author also wishes to thank Mr. John Telste for his assistance in coding the Taylor series scheme. This work has been supported by the Numerical Naval Hydrodynamics Program at the David W. Taylor Naval Ship Research and Development Center. This program is

jointly sponsored by the Office of Naval Research, the Naval Sea Systems Command, and DTNSRDC.

References

1. Buzbee, B.L., et.al., "On Direct Methods for Solving Poisson's Equations," Journ. SIAM 7, p. 627 (1970).
2. Buzbee, B.L., "A Fast Poisson Solver Amenable to Parallel Computation," I.E.E.E. Transactions on Computers, Vol. C22, No. 8, p. 793 (1973).
3. Chan, R.K.-C. and C.W. Hirt, "Two-Dimensional Calculations of the Motion of Floating Bodies," Proceedings of the Tenth Symposium on Naval Hydrodynamics, MIT (Jun 1974).
4. Buzbee, B.L., et.al., "The Method of Odd/Even Reduction and Factorization with Application to Poisson's Equation, Part II," Los Alamos Report LA-4288 (May 1970).
5. Buzbee, B.L., et.al., "The Direct Solution of the Discrete Poisson Equation on Irregular Regions," Journ. SIAM 8, p. 722 (1971).
6. George, J.A., "The Use of Direct Methods for the Solution of the Discrete Poisson Equation on Non-Rectangular Regions," Stanford University Report Stan-CS-70-159 (Jun 1970).
7. Hockney, R.W., "The Potential Calculation and Some Applications," Methods in Computational Physics, Vol. 9, p. 135 (1970).
8. Sweet, R.A., "A Generalized Cyclic Reduction Algorithm," Journ. SIAM 11, p. 506 (1974).
9. Concus, P. and G.H. Golub, "Use of Fast Direct Methods for the Efficient Numerical Solution of Nonseparable Elliptic Equations," Journ. SIAM 10, p. 1103 (1973).
10. Lugt, H.J. and S. Ohring, "Efficiency of Numerical Methods in Solving the Time-Dependent Two-Dimensional Navier-Stokes Equations," Proceedings of the International Conference on Numerical Methods in Fluid Dynamics, University of Southampton, England (Sep 1973). Published in Numerical Methods in Fluid Dynamics, Pentech Press, London.
11. Lugt, H.J. and S. Ohring, "Laminar Flow Behavior Under Slip-Boundary Conditions," Physics of Fluids 18 (Jan 1975).

12. Lugt, H.J. and S. Ohring, "Rotating Thin Elliptic Cylinder in a Parallel Viscous Fluid Flow," Proceedings of the Fourth International Conference on Numerical Methods in Fluid Dynamics, Univ. of Colorado (Jun 1974). Published in Lecture Notes in Physics (35), Springer-Verlag.
13. Haussling, H.J. and R.T. VanEseltine, "Finite-Difference Methods for Transient Potential Flows with Free Surfaces," Proceedings of First International Conference on Numerical Ship Hydrodynamics (Oct 1975).
14. Cooley, J.W. and J.W. Tukey, "An Algorithm for the Machine Calculation of Complex Fourier Series," Math. Comp. 19, 90, p. 297-301 (Apr 1965).
15. Whittaker and Robinson, Calculus of Observations, Blackie and Son, London (1944) p. 260.
16. Stoker, J.J., Water Waves, Interscience Publishers, Inc., New York (1957).

ACCURATE PARAMETRIC REPRESENTATION OF SHIP SECTIONS BY CONFORMAL MAPPING

L. Landweber and M. Macagno

Iowa Institute of Hydraulic Research
Iowa City, Iowa 52242 U.S.A.

Introduction

When problems of ship vibration or ship motions are treated by means of "strip" theory, it may be convenient to solve the associated two-dimensional formulation by means of complex variables and the transformation of each double ship section into a circle. Such an application has been presented by the present authors for a ship-vibration problem [1], but for reasons discussed in a subsequent paper [2], the Bieberbach method used in [1] could not be expected to be applicable to all ship sections.

An alternative conformal-mapping procedure of wider applicability is that employing the Gershgorin integral equation, which has been thoroughly treated by Gaier [3]. Numerical experience with the method [2,4,5,6] has indicated that, for roughly circular sections (for which the ratio of the maximum to minimum distances from an interior origin does not exceed an order of 2), the integral equation yields accurate solutions after a few iterations. For elongated or odd-shaped sections, however, results have been less accurate, even after many more iterations. Consequently, preliminary mappings, to eliminate corner points (common in double ship sections with flat bottoms and oblique intersections at the free surface) and to transform the section into a more nearly circular one, were introduced in ref. [2].

A principal cause of the slow convergence of the iterations for solving the Gershgorin integral equation is that the usual first approximation, which yields the Neumann series solution for a Fredholm integral equation of the second kind, is a poor one for an elongated body. Furthermore, by modifying the integrand of the integral equation so that it becomes cyclic, one can then apply the "best possible" quadrature formula, as defined and applied in [4], to reduce numerical errors. Thirdly, the

numerical accuracy can be improved by eliminating the need to compute the curvatures of the profile, which occur in the expressions for the diagonal elements of the matrix of the discretized kernel, a significant source of error when a profile is defined either numerically or graphically. An important by-product of this last modification of the integral equation is that the resulting form is valid at both smooth and corner points of a profile, so that a preliminary transformation to eliminate corner points, as was used in [2], becomes unnecessary.

A procedure for solving the Gershgorin integral equation, which incorporates the aforementioned improvements, is described in the present work. It will be shown that the parametric mathematical representation of a ship section, derived by this method, accurately reproduces the given profile.

Statement of Problem

Let us suppose that a simple closed curve C, such as a double ship section, is defined in the complex plane $z = x + iy$ by

$$z = r(\phi)e^{i\phi} \tag{1}$$

where (r,ϕ) are polar coordinates in the z-plane relative to an origin centrally located within the profile. Let $z = f(\zeta)$ be a function of the complex variable $\zeta = \rho e^{i\theta}$ which maps the exterior of the given curve (1) one-to-one into the exterior of the unit circle about the origin in the ζ-plane, such that a point $\zeta(\phi)$ of the curve corresponds to the point $\zeta = e^{i\theta}$ of the unit circle. See Fig. 1.

The mapping function may be expressed as the Laurent series

$$z = A\zeta + \frac{a_1}{\zeta} + \frac{a_2}{\zeta^2} + \ldots \tag{2}$$

where, in general, the coefficients are complex numbers. For a double ship section with two planes of symmetry, the a_i are also real and $a_2 = a_4 = \ldots = 0$. For the latter case, when $\zeta = e^{i\theta}$, the real and imaginary parts of (2) yield

$$x = (A + a_1)\cos\theta + a_3 \cos 3\theta + a_5 \cos 5\theta + \ldots \tag{3}$$

$$y = (A - a_1)\sin\theta - a_3 \sin 3\theta - a_5 \sin 5\theta - \ldots \tag{4}$$

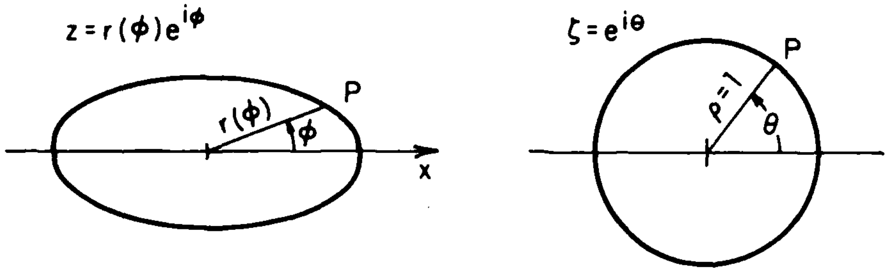

Figure 1

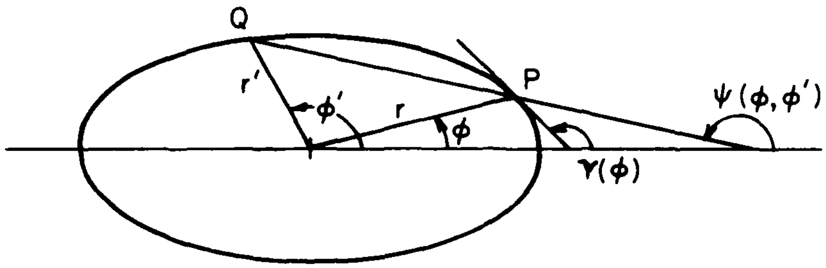

Figure 2

Once the coefficients A, a_1, a_3, ... have been determined, equations (3) and (4) may be interpreted as parametric equations of the given curve, a point of view employed by von Kerczek and Tuck [7] to obtain a mathematical representation of an entire ship form.

The solution of the conformal mapping problem will give a relation $\theta = \theta(\phi)$ between the polar angles in the z- and ζ-planes. This relation, together with equations (1) and (2), immediately yields the expressions for the Fourier coefficients

$$A = \frac{1}{2\pi}\int_0^{2\pi} r(\phi)e^{i(\phi-\theta)}d\theta \tag{5}$$

$$a_n = \frac{1}{2\pi}\int_0^{2\pi} r(\phi)e^{i(\phi+n\theta)}d\theta,\ n = 1,2,3,... \tag{6}$$

The required function $\theta(\phi)$ will be derived from the Gershgorin integral equation [3]

$$\theta(\phi) = -\frac{1}{\pi}\int_0^{2\pi} \frac{\partial\psi(\phi,\phi')}{\partial\phi'}\ \theta(\phi')d\phi' + 2\psi(0,\phi) \tag{7}$$

where, as indicated in Fig. 2, $\psi(\phi,\phi')$ denotes the polar angle of the position vector $z(\phi') - z(\phi)$,

$$\psi(\phi,\phi') = \arctan\frac{y(\phi') - y(\phi)}{x(\phi') - x(\phi)} \tag{8}$$

When ϕ' approaches ϕ, this vector approaches the tangent to the given curve, and we have

$$\lim_{\phi'\to\phi} \psi(\phi,\phi') = \begin{cases}\gamma(\phi), & \phi' = \phi+\\ \gamma(\phi) + \pi, & \phi' = \phi-\end{cases} \tag{9}$$

where $\gamma(\phi)$ denotes the azimuthal angle of the tangent vector in the sense of increasing values of ϕ. Thus $\psi(\phi,\phi')$ varies continuously from $\gamma(\phi)$ to $\gamma(\phi) + \pi$ as ϕ' increases from ϕ to $\phi + 2\pi$. In the range $0 \leq \phi \leq 2\pi$, however, $\psi(\phi,\phi')$ is a discontinuous function, as indicated by (9). It will be convenient to define the associated continuous function

$$\omega(\phi,\phi') = \begin{cases}\psi(\phi,\phi') - \pi, & 0 < \phi' < \phi\\ \psi(\phi,\phi') & , \phi < \phi' < 2\pi\end{cases} \tag{10}$$

We note that $\partial\omega/\partial\phi' = \partial\psi/\partial\phi'$,

$$\psi(\phi',\phi) - \psi(\phi,\phi') = \pi,\ \phi' < \phi \tag{11}$$

and that

$$\frac{1}{\pi}\int_0^{2\pi} \frac{\partial\psi(\phi,\phi')}{\partial\phi'}\, d\phi' = 1 \tag{12}$$

since, by (10),

$$\int_0^{2\pi} \frac{\partial\psi}{\partial\phi'}\, d\phi' = \int_0^{2\pi} \frac{\partial\omega}{\partial\phi'}\, d\phi' = \omega(\phi,2\pi) - \omega(\phi,o) = \psi(\phi,o) - [\psi(\phi,o) - \pi] = \pi$$

In polar coordinates, the kernel becomes

$$\frac{1}{\pi}\frac{\partial\psi(\phi,\phi')}{\partial\phi'} = \frac{1}{\pi}\,\frac{r'^2 - rr'\cos(\phi-\phi') + r\left(\frac{dr'}{d\phi'}\right)\sin(\phi-\phi')}{r^2 + r'^2 - 2rr'\cos(\phi-\phi')} \tag{13}$$

where $r' = r(\phi')$, and the quantity $\psi(o,\phi)$ in (7) is given by

$$\psi(o,\phi) = \arctan\frac{r(\phi)\sin\phi}{r(\phi)\cos\phi - r(o)} \tag{14}$$

The kernel is indeterminate at $\phi' = \phi$, but one can readily show [3] that it is given by

$$\lim_{\phi'\to\phi} \frac{\partial\psi(\phi,\phi')}{\partial\phi'} = \frac{k}{2}\frac{ds}{d\phi} \tag{15}$$

where s denotes arc length and $k(\phi)$ the curvature.

Treatment of Corner Points

If z is a corner point of the curve C with interior angle $\alpha\pi$, the Gershgorin integral equation becomes [3]

$$(2-\alpha)\,\theta(\phi) = -\frac{1}{\pi}\int_0^{2\pi} \frac{\partial\psi(\phi,\phi')}{\partial\phi'}\,\theta(\phi')\, d\phi' + 2\psi(o,\phi) \tag{16}$$

At this point, the discontinuity in ψ at $\phi = \phi'$ becomes

$$\pi + \gamma_-(\phi) - \gamma_+(\phi) = \pi\alpha$$

instead of that given by (9); and, instead of (12), we obtain

$$\frac{1}{\pi}\int_0^{2\pi} \frac{\partial\psi(\phi,\phi')}{\partial\phi'}\, d\phi' = \alpha \tag{17}$$

Elimination of α between (16) and (17) then yields the alternative form of the integral equation,

$$\theta(\phi) = -\frac{1}{2\pi}\int_0^{2\pi} \frac{\partial\psi(\phi,\phi')}{\partial\phi'}\,[\theta(\phi') - \theta(\phi)]\,d\phi' + \psi(o,\phi) \tag{18}$$

This latter form has two important advantages over the original one (7). Since α does not appear in (17), the latter equation is applicable

at both smooth and corner points. Secondly, the integrand of this equation becomes zero at $\phi = \phi'$. With the original form, according to (15), it would be necessary to calculate the curvature at various points of C, with a consequent loss of accuracy if C is defined numerically or graphically.

Selection of a First Approximation

For solving (7) by iteration, the usual first approximation of the theory of Fredholm integral equations of the second kind, $\theta_1 = 2\psi(o,\phi)$, is a poor one, as is seen by applying it to the simplest case, that of a circular section. Then θ can differ from ϕ by only a constant,

$$\theta = \phi + C$$

and we have

$$\frac{\partial\psi}{\partial\phi'} = \frac{1}{2}, \quad 2\psi(o,\phi) = \phi + \pi$$

Then (7) gives

$$\phi + C = -\frac{1}{2\pi}\int_o^{2\pi} \theta d\theta + \phi + \pi = \phi$$

Thus the approximation $\theta_1 = \phi + \pi$ is inconsistent with the exact solution $\theta = \phi$. If, however, (7) is written in the form

$$\theta - \pi = -\frac{1}{\pi}\int_o^{2\pi} \frac{\partial\psi}{\partial\phi'} (\theta' - \pi)d\phi' + 2\psi(o,\phi) - 2\pi$$

in which the unknown function is $\theta - \pi$, the usual first approximation would give

$$\theta_1 = 2\psi(o,\phi) - \pi \tag{19}$$

which yields the exact solution $\theta = \phi$ for the sphere.

A family of possible first approximations is suggested by expressing the integral equation (16) in the form

$$(2-\alpha)[\theta - f(\phi)] = -\frac{1}{\pi}\int_o^{2\pi} \frac{\partial\psi}{\partial\phi'} (\theta' - f')d\phi' - \frac{1}{\pi}\int_o^{2\pi} \frac{\partial\psi}{\partial\phi'} f'd\phi' + 2\psi(o,\phi) - (2-\alpha)f(\phi) \tag{20}$$

where $f' = f(\phi')$ and $\theta - f(\phi)$ is treated as the unknown function. This suggests, for the first approximation θ_1,

$$\theta_1 = \frac{1}{2-\alpha}\left[-\frac{1}{\pi}\int_o^{2\pi} \frac{\partial\psi}{\partial\phi'} f'd\phi' + 2\psi(o,\phi)\right] \tag{21}$$

of which (19) is the special case for $f(\phi) = \pi$ and $\alpha = 1$. Comparison of (21) with (16) indicates that θ_1 may also be considered as a second approximation derived from the first approximation, $f(\phi)$.

A disadvantage of the approximation (19) is that, for a doubly symmetric form, it does not satisfy the relation

$$\theta_1(\pi - \phi) = \pi - \theta(\phi) \tag{22}$$

Alternative approximations which have the foregoing property are $\theta_1 = \phi$ and $\theta_1 = \gamma(\phi) - \frac{\pi}{2}$. These are good first approximations for nearly circular sections, but are very poor near the nose and tail of an elongated body. The mean of these two approximations gave a good first approximation for an elongated ellipse, but was discarded because, for an irregularly-shaped section, the slopes may vary widely and may not be monotonic.

In order to find an acceptable first approximation, let us consider the exact solution for the ellipse,

$$\theta = \arctan\left(\frac{a}{b} \tan \phi\right) \tag{23}$$

where 2a and 2b are the length and thickness of the ellipse

$$x = a \cos \theta, \quad y = b \sin \theta \tag{24}$$

Then we have

$$r^2(\phi) = a^2 \cos^2 \theta + b^2 \sin^2 \theta \tag{25}$$

and

$$\frac{d\theta}{d\phi} = \frac{ab}{a^2 + b^2 - r^2(\phi)} \tag{26}$$

This suggests, for an arbitrary profile of length l and thickness d, the approximation

$$\theta_1 = \frac{1}{I} \int_o^\phi \frac{d\phi}{l^2 + d^2 - 4r^2(\phi)}, \quad I = \frac{1}{2\pi} \int_o^{2\pi} \frac{d\phi}{l^2 + d^2 - 4r^2(\phi)} \tag{27}$$

The "Best Possible" Quadrature Formula

As shown in [4], for a continuous, cyclic integrand, the "best possible" quadrature formula is proportional to a simple sum of the ordinates for uniformly-spaced abscissae. For profiles without corner points, this formula can be applied in the present case since the integrand in (18) can be made cyclic by writing the integral in the form

$$\frac{1}{\pi}\int_o^{2\pi} \frac{\partial\psi}{\partial\phi'}\,\theta' d\phi' = \frac{1}{\pi}\int_o^{2\pi} \frac{\partial\psi}{\partial\phi'}\,(\theta' - 2\omega)d\phi' + \frac{1}{\pi}[\omega^2(\phi,2\pi) - \omega^2(\phi,o)]$$

$$= \frac{1}{\pi}\int_o^{2\pi} \frac{\partial\psi}{\partial\phi'}\,(\theta' - 2\omega)d\phi' + \pi + 2\psi(o,\phi) \tag{28}$$

since $\omega(\phi,2\pi) = \pi + \omega(\phi,o) = \pi + \psi(o,\phi)$. The integral equation (18) then becomes

$$\theta(\phi) = -\frac{1}{2\pi}\int_o^{2\pi} \frac{\partial\psi}{\partial\phi'}\,(\theta' - \theta - 2\omega + 2\gamma)d\phi' + \gamma(\phi) - \frac{\pi}{2} \tag{29}$$

Here the integrand has again been adjusted so as to vanish at $\phi' = \phi$, thus avoiding the necessity of calculating the curvature of the profile. Form (29), however, requires the calculation of an additional matrix, the values of $\omega(\phi,\phi')$. Only numerical experimentation can determine whether the increased accuracy of the quadrature formula justifies the greater complexity.

Solution by Iteration and Discretization

a) Smooth Sections.

For sections without corner points, numerical solutions of (29) can be obtained from the iteration formulae

$$\theta_2(\phi) = -\frac{1}{2\pi}\int_o^{2\pi} \frac{\partial\psi}{\partial\phi'}\,(\theta_1' - \theta_1 - 2\omega + 2\gamma)d\phi' + \gamma(\phi) - \frac{\pi}{2} \tag{30}$$

$$\bar{\theta}_2 = \frac{1}{2}(\theta_1 + \theta_2) \tag{31}$$

$$\bar{\theta}_{n+1} = -\frac{1}{2\pi}\int_o^{2\pi} \frac{\partial\psi}{\partial\phi'}\,(\bar{\theta}_n' - \bar{\theta}_n - 2\omega + 2\gamma)d\phi' + \gamma - \frac{\pi}{2},\ n = 2,3,\ldots \tag{32}$$

where θ_1 is given by (27). The slight modification (31) of the iteration formula after the second approximation is a consequence of the fact that the first eigenvalue of the kernel lies on the circle of convergence of the Neumann series equivalent to the unmodified iteration formula. As is shown in [7], the above modification assures convergence of the iteration formula, and, in practice, effectively accelerates its convergence.

With the integrals in (30) and (32) represented by the "best possible" quadrature formula, these become iteration formulae for solving the set of linear equations

$$\bar{\theta}_{n+1,i} = -\frac{1}{N}\sum_{j=0}^{N-1} [(\frac{\partial\psi}{\partial\phi'})_{ij}(\bar{\theta}_{ni} - \bar{\theta}_{ni} - 2\omega_{ij} + 2\gamma_i)] + \gamma_i - \frac{\pi}{2} \tag{33}$$

with a similar expression for (30). Here $\bar{\theta}_{ni} = \bar{\theta}_n(\phi_i)$, $\omega_{ij} = \omega(\phi_i,\phi_j)$, etc., and $\phi_{i+1} - \phi_i = \Delta\phi$, a constant interval. The term in brackets is set equal to zero when $i = j$. Since θ and γ change rapidly with ϕ near the extremities of an elongated profile, a small interval $\Delta\phi$, such as one degree, should be selected. Here $j = 0$ corresponds to $\phi = 0$ and $j = 1$ to $\phi = \Delta\phi$.

For sections symmetrical about the x-axis, it suffices to calculate the θ_i corresponding to values of ϕ_i in the range $0 \le \phi \le \pi$; for double ship sections with two planes of symmetry, only the values of ϕ_i in the range $0 \le \phi \le \pi/2$ need be considered. Thus for the case of one plane of symmetry, with N an even integer, $N = 2p$, we have $\theta_{N-i} = 2\pi - \theta_i$, and (33) becomes

$$\bar{\theta}_{n+1,i} = -\frac{1}{N}\Big[\sum_{j=1}^{p-1}(K_{ij} - K_{i,N-j})\bar{\theta}_{nj} + 2\pi\sum_{j=1}^{p-1}K_{i,N-j}$$

$$+ \sum_{j=0}^{N-1}K_{ij}(2\gamma_i - 2\omega_{ij} - \bar{\theta}_{ni}) + \pi K_{ip}\Big] + \gamma_i - \frac{\pi}{2} \tag{34}$$

where $K_{ij} \equiv (\partial\psi/\partial\phi')_{ij}$.

If the section is symmetrical about the x- and y-axes, we take $N = 4q$, q an integer, and note that

$$\theta_i = \pi - \theta_{2q-i} = \theta_{2q+i} - \pi = 2\pi - \theta_{N-i}$$

Hence (33) becomes

$$\bar{\theta}_{n+1,i} = -\frac{1}{N}\Big[\sum_{j=1}^{q-1}C_{ij}\bar{\theta}_{nj} + \frac{\pi}{2}H_i + \pi L_i + (2\gamma_i - \bar{\theta}_{ni})M_i - N_i\Big] + \gamma_i - \frac{\pi}{2} \tag{35}$$

where

$$C_{ij} = K_{ij} - K_{i,2q-j} + K_{i,2q+j} - K_{i,N-j}$$

$$\left.\begin{aligned} H_i &= K_{iq} + 2K_{i,2q} + 3K_{i,3q} \\ L_i &= \sum_{j=1}^{q-1}(K_{i,2q-j} + K_{i,2q+j} + 2K_{i,N-j}) \\ M_i &= \sum_{j=0}^{N-1}K_{ij}, \quad N_i = 2\sum_{j=0}^{N-1}K_{ij}\omega_{ij} \end{aligned}\right\} \tag{36}$$

In computing C_{ij}, H_i, L_i and M_i, we should set $K_{ii} = 0$ in the computer program, since this element occurs with a zero factor.

For starting the iteration, the first approximation (27) will be

assumed. This gives the discretized forms

$$\theta_{1i} = \frac{\Delta\phi}{I} \sum_{j=0}^{i} \frac{R_i}{1^2 + d^2 - 4r_j^2}, \; R_0 = R_i = \frac{1}{2}, \quad R_1 = R_2 = \dots = R_{i-1} = 1 \quad (37)$$

$$I = \frac{1}{N} \sum_{j=0}^{N-1} \frac{1}{1^2 + d^2 - 4r_j^2}$$

b. Sections with Corner Points.

When corner points are present, the "best possible" quadradure formula cannot be used, although (18) remains applicable. For doubly symmetric sections, this may be written in the form

$$\theta(\phi) = -\frac{1}{2\pi}\{\int_0^{\pi/2} [K(\phi,\phi')\theta' + K(\phi,\pi-\phi')(\pi-\theta') + K(\phi,\pi+\phi')(\pi+\theta')$$

$$+ K(\phi,2\pi-\phi')(2\pi-\theta')]d\phi' - \theta\int_0^{\pi/2} K(\phi,\phi')d\phi' - \theta\int_{\pi/2}^{2\pi} \frac{\partial\psi}{\partial\phi'} d\phi'\} + \psi(o,\phi)$$

$$= -\frac{1}{2\pi}\{\int_0^{\frac{\pi}{2}} [G(\phi,\phi')\theta' - K(\phi,\phi')\theta]d\phi' + \theta[\psi(\phi,\tfrac{\pi}{2}) - \psi(\phi,2\pi)]$$

$$+ \pi[2\psi(\phi,2\pi) - \psi(\phi,\tfrac{3\pi}{2}) - \psi(\phi,\tfrac{\pi}{2})]\} + \psi(o,\phi) \quad (38)$$

where

$$G(\phi,\phi') = K(\phi,\phi') - K(\phi,\pi-\phi') + K(\phi,\pi+\phi') - K(\phi,2\pi-\phi')]$$

But

$$\psi(\phi,2\pi) = \psi(\phi,o) = \pi + \psi(o,\phi)$$

Also

$$\int_0^{\frac{\pi}{2}} K(\phi,2\pi-\phi')\theta' d\phi' = \int_0^{\frac{\pi}{2}} K(\phi,2\pi-\phi')(\theta'-\theta)d\phi' + \theta[\psi(\phi,2\pi) - \psi(\phi,\tfrac{3\pi}{2})]$$

will be used to improve the accuracy of the quadrature formula for the left member when $K(\phi,2\pi-\phi)$ is large, as is usually the case near the free surface $(\phi = o)$ of a double ship section. Then (38) becomes

$$\theta(\phi) = -\frac{1}{2\pi}\{\int_0^{\frac{\pi}{2}} [G(\phi,\phi')\theta' + (K(\phi,2\pi-\phi') - K(\phi,\phi'))\theta]d\phi' + \theta[\psi(\phi,\tfrac{\pi}{2})$$

$$+ \psi(\phi,\tfrac{3\pi}{2}) - 2\psi(\phi,o)] - \pi[\psi(\phi,\tfrac{\pi}{2}) + \psi(\phi,\tfrac{3\pi}{2})]\} - \pi \quad (39)$$

or, discretized,

$$\theta_{n+1,i} = -\frac{1}{2\pi}\{\sum_{j=1}^{q} R_j G_{ij}\theta_{nj} + \theta_{ni}[\sum_{j=1}^{q} R_j(K_{i,N-j} - K_{ij}) + \psi_{iq} + \psi_{i,3q} - 2\psi_{io}] - \pi(\psi_{iq} + \psi_{i,3q})\} - \pi \tag{40}$$

Here also we should set $K_{ii} = 0$ in the computer program, and use (27) as the first approximation for starting the iteration.

The forms of the integral equation in (39) and (40) are suitable for ship sections with smooth bottoms, which intersect the free surface obliquely. If the keel is V-shaped, or is flat for a small interval about the centerline, the kernel $K(\phi,\pi-\phi)$ will become large near $\phi = \pi/2$. In order to improve the accuracy of the quadrature formula, we should then also put

$$\int_0^{\frac{\pi}{2}} K(\phi,\pi-\phi')\theta' d\phi' = \int_0^{\frac{\pi}{2}} K(\phi,\pi-\phi')(\theta'-\theta)d\phi' + \theta[\psi(\phi,\pi) - \psi(\phi,\tfrac{\pi}{2})]$$

with which (39) and (40) become

$$\theta(\phi) = -\frac{1}{2\pi}\{\int_0^{\frac{\pi}{2}}[G(\phi,\phi')\theta' + (K(\phi,2\pi-\phi') + K(\phi,\pi-\phi') - K(\phi,\phi'))\theta]d\phi' + \theta[2\psi(\phi,\tfrac{\pi}{2}) - \psi(\phi,\pi) + \psi(\phi,\tfrac{3\pi}{2}) - 2\psi(\phi,0)] - \pi[\psi(\phi,\tfrac{\pi}{2}) + \psi(\phi,\tfrac{3\pi}{2})]\} - \pi \tag{39a}$$

and

$$\theta_{n+1,i} = -\frac{1}{2\pi}\{\sum_{j=1}^{q} R_j G_{ij}\theta_{nj} + \theta_{ni}[\sum_{j=1}^{q} R_j(K_{i,N-j} + K_{i,2q-j} - K_{ij}) + 2\psi_{iq} - \psi_{i,2q} + \psi_{i,3q} - 2\psi_{io}] - \pi(\psi_{iq} + \psi_{i,3q})\} - \pi \tag{40a}$$

Finally, after the θ_i have been obtained, the coefficients of the parametric equations can be calculated from (5) and (6), employing the same quadrature formula as was used in discretizing the integral equation. For this purpose, the coefficients are rewritten in the form

$$A = \frac{1}{2\pi}\int_0^{2\pi} r(\phi)e^{i(\theta-\phi)}\frac{d\theta}{d\phi}d\phi, \quad a_n = \frac{1}{2\pi}\int_0^{2\pi} r(\phi)e^{i(\phi+n\theta)}\frac{d\theta}{d\phi}d\phi \tag{41}$$

For a double ship section, these yield

$$A = \frac{2}{\pi}\int_0^{\pi/2} r(\phi)\cos(\theta-\phi)\frac{d\theta}{d\phi}d\phi, \quad a_n = \frac{2}{\pi}\int_0^{\pi/2} r(\phi)\cos(\phi+n\theta)\frac{d\theta}{d\phi}d\phi \tag{42}$$

$n = 1, 3, 5, \ldots$; or discretized,

$$A = \frac{2}{\pi} \sum_{i=0}^{q} R_i r_i \cos(\theta_i - \phi_i)\left(\frac{d\theta}{d\phi}\right)_i, \quad a_n = \frac{2}{\pi} \sum_{i=0}^{q} R_i r_i \cos(\phi_i + n\theta_i)\left(\frac{d\theta}{d\phi}\right)_i \tag{43}$$

If the section has no corner points, (41), evaluated by means of the "best possible" quadrature formula, yields

$$\left.\begin{aligned} A &= \frac{4}{N}\left[\sum_{i=1}^{q-1} r_i \cos(\theta_i - \phi_i)\left(\frac{d\theta}{d\phi}\right)_i + \frac{r_o}{2}\left(\frac{d\theta}{d\phi}\right)_o + \frac{r_q}{2}\left(\frac{d\theta}{d\phi}\right)_q\right] \\ a_n &= \frac{4}{N}\left[\sum_{i=1}^{q-1} r_i \cos(\phi_i + n\theta_i)\left(\frac{d\theta}{d\phi}\right)_i + \frac{r_o}{2}\left(\frac{d\theta}{d\phi}\right)_o + (-1)^{\frac{n+1}{2}} \tfrac{1}{2} r_q \left(\frac{d\theta}{d\phi}\right)_q\right] \end{aligned}\right\} \tag{44}$$

Applications

Two applications will be presented, one for an ellipse of length-thickness ratio 5, the other for a Lewis form of draft-beam ratio 0.9 and section-area coefficient 0.925. The shape of this Lewis form is shown in Reference [2].

For the ellipse, eq. (2) is

$$z = 0.6\zeta + \frac{0.4}{\zeta} \tag{45}$$

and the parametric equations are

$$x = \cos\theta, \quad y = 0.2 \sin\theta \tag{46}$$

The input data for the computer program, $r(\phi)$ and $dr/d\phi$, are then given by

$$\left.\begin{aligned} \theta &= \arctan(5 \tan\phi) \\ r &= \sqrt{\cos^2\theta + 0.2 \sin^2\theta} \\ \frac{dr}{d\phi} &= -\,2.4r \sin 2\theta \end{aligned}\right\} \tag{47}$$

The first approximation (27) could not be used in this case since this gives, immediately, the exact solution. Consequently, the value $d = 0.5$, instead of 0.4, was used in (27). In Table 1, the values of θ_{1i}, θ_{2i}, $\theta_{21,i}$, and $\theta_{41,i}$, are compared with the exact solution θ_i. The coefficients A and a_i, derived from $\theta_{41,i}$, are compared with the exact values from (45) in Table 2. In Table 3, some original and recovered values of x and y are also compared. The agreement between the exact and computed values is seen to be excellent.

For the selected Lewis form, eq. (2) is

$$z = \zeta - \frac{2}{5\zeta} - \frac{1}{15\zeta^3} \tag{48}$$

TABLE 1 Comparison of Successive Approximations with Exact Solution for a 5:1 Ellipse

ϕ (deg.)	θ (rad.)	θ_1	θ_2	θ_{21}	θ_{41}
0	0	0	0	0	0
10	0.7225755	0.67032	0.67858	0.72242	0.7225753
20	1.0683405	0.82904	0.91112	1.06820	1.0683403
30	1.2373232	0.94840	1.05746	1.23722	1.2373230
40	1.3368114	1.05759	1.16850	1.33673	1.3368113
50	1.4045258	1.16271	1.26173	1.40447	1.4045257
60	1.4558354	1.26585	1.34512	1.45580	1.4558354
70	1.4981305	1.36796	1.42289	1.49811	1.4981304
80	1.5355455	1.46950	1.49755	1.53553	1.5355455
90	$\pi/2$	$\pi/2$	$\pi/2$	$\pi/2$	$\pi/2$

TABLE 2 Coefficients of Parametric Equations for a 5:1 Ellipse

			$a_n \times 10^6$								
	A	a_1	n=3	5	7	9	11	13	15	17	19
Exact	0.600	0.400	0	0	0	0	0	0	0	0	0
Computed	0.599997	.399997	-8	-10	-6	-3	-2	-2	-3	-3	-4

TABLE 3 Comparison between Exact and Recovered Coordinates of Ellipse

ϕ (deg.)	x	y	x_{41}	y_{41}
0	1.0	0	1.0	0
10	.750105	.132264	.750107	.132263
20	.481579	.175281	.481577	.175280
30	.327327	.188982	.327327	.188978
40	.231856	.194550	.231853	.194548
50	.165505	.197242	.165505	.197242
60	.114708	.198680	.114710	.198679
70	.072602	.199472	.072604	.199470
80	.035243	.199876	.035245	.199872
90	0	0.20	0	.199996

TABLE 4 Comparison of Successive Approximations with Exact Solution for a Lewis Form

ϕ (deg.)	θ	θ_1	θ_2	θ_{21}	θ_{41}
0	0	0	0	0	0
10	.058840	.101114	.080073	.058843	.058843
20	.121924	.182075	.152187	.121916	.121916
30	.194790	.265015	.230207	.194785	.194785
40	.286696	.351924	.319809	.286692	.286692
50	.415928	.447235	.432630	.415927	.415927
60	.621030	.563942	.595502	.621030	.621030
70	..936864	.748728	.849362	.936864	.936864
80	1.272154	1.093232	1.187846	1.272153	1.272153
90	1.570796	1.570796	1.570796	1.570796	1.570796

which gives the parametric equations

$$x = \frac{3}{5} \cos \theta - \frac{1}{15} \cos 3\theta, \qquad y = \frac{7}{5} \sin \theta + \frac{1}{15} \sin 3\theta \tag{49}$$

The input data for the computer program are then given by

$$\tan \phi = \frac{21 \sin \theta + \sin 3\theta}{9 \cos \theta - \cos 3\theta} = \tan \theta \, \frac{6 - \sin^2 \theta}{3 - \cos^2 \theta} \tag{50}$$

$$r = \sqrt{x^2 + y^2}$$

$$\frac{dr}{d\phi} = -2r \, \frac{a_1(1+a_3)\sin 2\theta + 2a_3 \sin 4\theta}{1 - a_1^2 - 3a_3^2 - 4a_1a_3 \cos 2\theta - 2a_3 \cos 4\theta} \tag{51}$$

Values of θ corresponding to given values of ϕ can be obtained by solving eq. (46) by means of the iteration formula

$$\tan \theta^{(n+1)} = \tan \phi \, \frac{3 - \cos^2 \theta^{(n)}}{6 - \sin^2 \theta^{(n)}} \tag{52}$$

with $\theta^{(1)} = \frac{1}{3} \phi^{(1)}$ when $\phi = 1°, 2°, \ldots 15°$, and

$$\tan \theta_{i+1}^{(1)} = \tan \phi_{i+1} \, \frac{3 - \cos^2 \theta_i}{6 - \sin^2 \theta_i}, \qquad 16° \leq \phi \leq 89° \tag{53}$$

A comparison of the values of θ_{1i}, θ_{2i}, $\theta_{21,i}$, and $\theta_{41,i}$, derived from the integral equation, with the exact values defined by (46), is shown in Table 4. The coefficients A and a_i, derived from $\theta_{41,i}$, their exact values, and some original and recovered values of x and y, are shown in Tables 5 and 6. The agreement between the exact and computed values is again seen to be excellent.

Discussion and Conslusions

Double ship sections without corner points can be accurately mapped into a unit circle by a procedure which employs the Gershgorin integral equation, with various refinements. These consist of the selection of a good first approximation, elimination of the need to compute the curvatures of the given section at the diagonal elements of the equivalent matrix, and the transformation of integrands into cyclic form so that the "best possible" quadrature formula may be used. This mapping then yields an accurate parametric representation of the ship section.

For sections with corner points, it has been shown that the modified form of the integral equation used for "smooth" sections remains valid at

TABLE 5 Coefficients of Parametric Equations for a Lewis Form

	A	a_1	a_3	$a_n \times 10^{-5}$							
				n=5	7	9	11	13	15	17	19
Exact	1.00	-2/5	-1/15	0	0	0	0	0	0	0	0
Computed	1.00002	-.39978	-.06648	17	12	10	5	1	-6	-10	-17

TABLE 6 Comparison between Exact and Recovered Coordinates of the Lewis Form

ϕ(deg.)	x	y	x_{41}	y_{41}
0	.5333	.0	.5341	.0
10	.5333	.0940	.5342	.0941
20	.5333	.1941	.5344	.1940
30	.5331	.3078	.5340	.3071
40	.5320	.4464	.5323	.4457
50	.5277	.6289	.5277	.6289
60	.5072	.8785	.5064	.8782
70	.4184	1.1497	.4186	1.1496
80	.2286	1.2964	.2286	1.2964
90	.0	1.3333	.0	1.3333

the corners. The pre. :e of the corners, however, introduces additional errors in the quadrature formulas, and the resulting conformal mapping and parametric representation, derived by a procedure similar to that for the smooth case, was not considered sufficiently accurate. The difficulty is due to the very rapid variation of the kernel of the integral equation in the neighborhood of a corner point. The present procedures are being modified to take this effect properly into account, but, because of time limitations, results for ship sections cannot be included in this contribution.

Acknowledgment

This work was supported by the Office of Naval Research under Contract N00014-68-A-0196-0011.

References

1. L. Landweber and M. Macagno, "Added Masses of Two-Dimensional Forms by Conformal Mapping," Journal of Ship Research, Vol. 11, No. 2, June 1967.

2. L. Landweber, "Parametric Equations of Ship Forms by Conformal Mapping of Ship Sections," Seventh Symposium on Naval Hydrodynamics, p. 1619, Rome, Italy, 1968.

3. D. Gaier, Konstructive Methoden der Konformen Abbildung, Springer Tracts in Natural Philosophy, Vol. 3, Springer-Verlag, Berlin, 1964.

4. G. Birkhoff, D.M. Young, and E.H. Zarantonello, "Numerical Methods in Conformal Mapping," Proceedings of the Fourth Symposium in Applied Mathematics of the American Mathematical Society, Univ. of Maryland, June 1951.

5. J. Todd and S.E. Warschawski, "On the solution of the Lichtenstein-Gershgorin integral equation in conformal mapping; II. Computational experiments," Experiments in the Computation of Conformal Maps, National Bureau of Standards, Applied Mathematics Series. 42, 1955.

6. E.B. Becker, H.B. Wilson, and C.H. Parr, "Further Development of Conformal Mapping Techniques," Rohm & Haas Co., Redstone Arsenal, Report No. S-46, 1964.

7. C.V. Kerczek and E.O. Tuck, "The Representation of Ship Hulls by Conformal Mapping Functions," Journal of Ship Research, Vol. 13, No. 4, December 1969.

8. L. Landweber and M. Macagno, "Irrotational Flow about Ship Forms," IIHR Report 123, December 1969.

FREE SURFACE HYDRODYNAMICS USING A LAGRANGIAN TRIANGULAR MESH

J.P. Boris and K.L. Hain

U.S. Naval Research Laboratory
Washington, D.C. 20375 U.S.A.

and

M.J. Fritts

Science Applications, Inc.
McLean, Virginia 22101 U.S.A.

ABSTRACT

This paper presents and discusses algorithms to implement a Lagrangian treatment of incompressible hydrodynamics coupled to a triangular representation of the finite-difference mesh. The added complexity of a general connectivity triangular mesh pays great dividends in permitting longtime solutions of complicated flows with shear, wave breaking in free-surface problems, and flow along and around complicated structures. Many of the techniques discussed here have ' een tested but many are new, and the optimum algorithms in some cases have yet to be determined.

1. Introduction

This paper describes numerical techniques and models for the Lagrangian integration of transient free-surface problems in hydrodynamics. The techniques described here involve the use of a Lagrangian, finite-difference mesh of connected triangles to represent the fluid motion and the various interfaces and free surfaces. This approach is a fruition of efforts carried out at NRL and elsewhere during the past few years. Many of the basic concepts were developed by Crowley[1] using a code called FLAG. Our NRL work has concentrated on the free-surface and magneto-hydrodynamic aspects of the problem. The major efforts centered on LINUS2[2-4], a 2D MHD code with axial symmetry. Attention recently turned

toward solving free-surface problems in naval hydrodynamics, problems which are now soluble numerically using these new methods and capitalizing on recent advances in computer technology. These problems include:

- the generation and breaking of gravity waves,
- the nonlinear interaction of large amplitude gravity waves and internal waves,
- the rise and bursting of bubbles,
- the transient and steady-state flows past immersed structures, and
- the self-consistent forces, moments, and motions induced in immersed bodies and surfaces.

Clearly a general free-surface capability, first in two and later in three dimensions, will allow an almost inexhaustible list of important hydrodynamics problems to be solved.

A good example of the type of problem in which we need improved numerical techniques is the problem of a large amplitude breaking wave. When the wave top separates from the wave due to bottom shallowing, nonlinear wave interaction, or strong surface winds, it falls back into the wave trough in a complicated flow which the usual techniques cannot handle. It is the goal of this paper to define Lagrangian triangular mesh methods in which the crest of the numerical wave can separate accurately from the body of the wave, can fall under the influence of gravity and any strong winds back into the trough of the wave, and become reabsorbed smoothly without invalidating the numerical representation of the fluid at the surface. Thus, this paper proposes methods in which the topology of the problem can change self-consistently with the evolution of the system. Figure 1 illustrates the use of a Lagrangian triangular mesh to facilitate the solution of this problem. Clearly, any representation of the problem, to be adequate, must be capable of drastic local changes to reflect complicated motions such as the breaking of a large amplitude wave.

Previous Lagrangian treatments[5,6] have been restricted to simple flows or small amplitude motions because of the use of a topologically rectangular finite-difference mesh. The major practical problem with these methods arises out of the inflexible connectivity of the various mesh points. In complicated and strongly sheared flows, where one

element of fluid may become widely separated in space from a nearby element, the usual Lagrangian treatments break down because the advantages of a simply structured rectangular mesh are nullified as the mesh becomes too severely distorted to allow adequate accuracy in the representation of the fluid flow. Another main drawback of such approaches is a difficulty in representing complicated boundaries and structures because of the limited topology of the mesh. Further, when the mesh becomes sufficiently distorted that no greater Lagrangian distortion can be permitted, the usually-applied process of continually rezoning amounts to a form of numerical diffusion. Thus, the usual Lagrangian treatments are capable of extending linear models significantly into the nonlinear regime but are not capable of providing a satisfactorily accurate long-time representation of highly complicated flows bordering on turbulent phenomena.

Rectangular mesh approaches also appear to suffer a serious "even-odd" or computational-mode instability which must be overcome by some form of added numerical damping. This damping destroys the reversibility of the algorithm and limits its usefulness for high Reynolds-number flows even though some care has been given to developing damping algorithms which minimize this nonphysical diffusion.

Two-dimensional Cartesian geometry is fully adequate to develop the necessary techniques for fluid zones to disconnect and reconnect freely in following complicated motions. Furthermore, the methods given here generalize easily. Regular and irregular tessellations of the x-y plane are possible with triangles. Complicated boundaries, complicated interfaces, and complicated structures can all be represented smoothly and uniformly with grids composed of triangles. Figure 2 shows examples of such tessellations in the hydrofoil/free-surface problem.

A triangular-element mesh has several advantages. The grid can be restructured. The number of triangles meeting at a vertex is variable, and therefore, increased accuracy in one region of the flow does not force unnecessary resolution in other areas of the flow. Individual triangles and sides can also be bisected or rearranged to give new grid structures which better represent changing fluid flows. The triangle is a much less ambiguous structure than a rectangle or higher-order

AD-A119 315 DAVID W TAYLOR NAVAL SHIP RESEARCH AND DEVELOPMENT CE--ETC F/G 20/4
FIRST INTERNATIONAL CONFERENCE ON NUMERICAL SHIP HYDRODYNAMICS --ETC(U)
1975 J W SCHOT, N SALVESEN

UNCLASSIFIED NL

8 of 8

AD A
119315

END
DATE
FILMED
10-82
DTIC

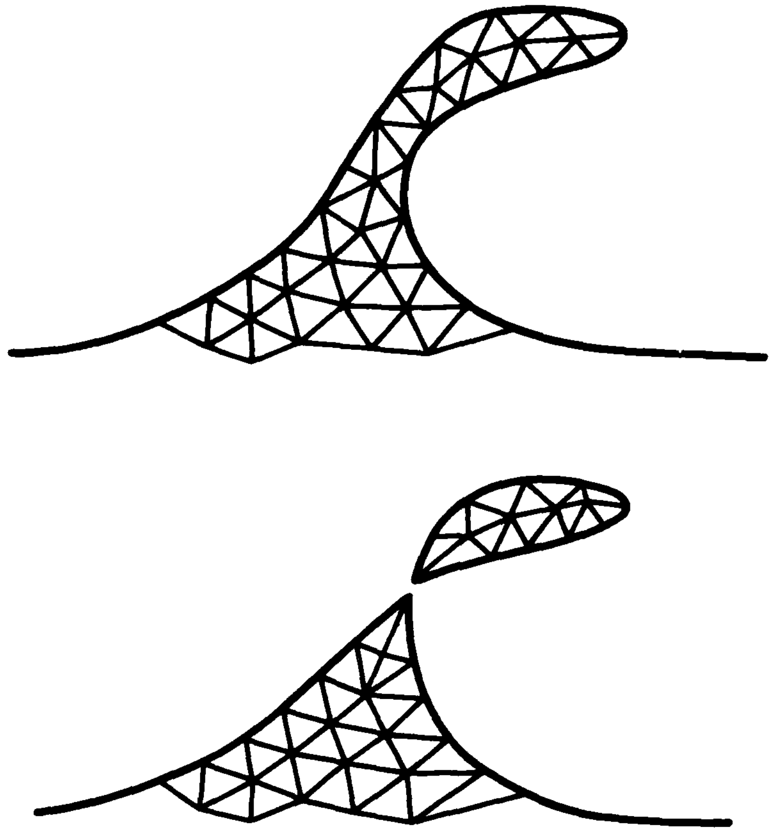

Figure 1. The use of a Lagrangian triangular mesh to facilitate the nonlinear hydrodynamics of separating free-surface flows.

polygon and hence interpolations and integrals are usually simpler to perform. Moreover, the even-odd problems of rectangular schemes appear to be absent, or at least greatly subdued, in the triangular representation. Because of the three-sided figures (rather than four-sided), there is no ambiguous labelling of grid points as even and odd. A vertex, which is one point removed from its neighbor along a particular path, will be two points removed by another. This does not mean that an even-odd problem cannot occur, only that it is not a topologically natural mode of instability and hence should be considerably slower

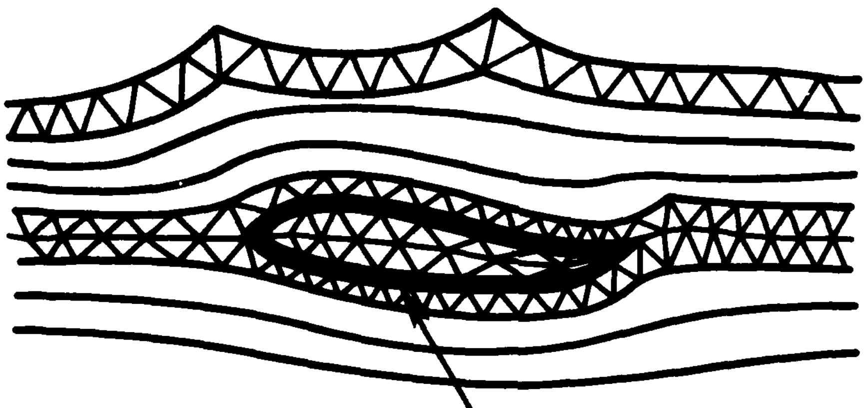

Figure 2. Use of a triangular mesh to represent a submerged body near the free surface.

growing than its rectangular-mesh counterpart. Experience with the SPLISH and SPLASH codes supports this; a reversible algorithm, or at least a very weakly damped one, is feasible using the Lagrangian triangular mesh approach.

Of course there are also some problems with the triangles. A general connectivity triangular mesh has cumbersome bookkeeping problems associated with the connections, with the grid, the sides of the triangles, and the basic cells of the fluid dynamic system. Numerical experience with triangles is much more limited than experience with rectangular meshes and the statement of the hydrodynamic equations in triangular systems requires that especially good attention be paid to the spatial derivative terms which are needed. There are, as well, some intrinsic numerical complications in triangular systems. The major one, discussed in detail in Section 3, is the counting of equations and free unknowns. This difficulty can be argued to be the price we pay for the relative suppression of the "even-odd" or "computational" modes observed in more standard rectangular approaches.

In this paper, we will restrict ourselves to the study of systems in which the fluid is inviscid and incompressible but has variable density.

We also restrict consideration to problems in which the gravity is constant and directed in the negative $\hat{y}$ direction. These are not necessary restrictions but simplify the analysis and allow the full spectrum of problems of current interest to be solved. The basic equations of the system are:

$$\rho \frac{d\underline{V}}{dt} = - \underline{\nabla}P - \rho g \hat{y} \quad \text{and} \tag{1}$$

$$\underline{\nabla} \cdot \underline{V} = 0, \tag{2}$$

where the fluid density ρ, pressure P, and velocity $\underline{V}$, are assumed to vary only with x and y. Equation (2), incompressibility, removes the sound waves. We will assume that P = constant along free surfaces and hence the free-surface boundary condition can be deduced from the component of Eq. (1) resolved parallel to the free surface. If we use $\hat{\tau}$ to denote the unit tangent vector to the free surface, the free-surface condition becomes

$$\frac{d\, V_\tau}{dt} = - \; g\, \hat{y} \cdot \hat{\tau} . \tag{3}$$

The basic discussion of triangular grids and connection of grid vertices, triangle sides and triangle volumes is found in Section 2. Tessellation of the plane is considered and the representation of complicated surfaces and interfaces by a triangular mesh is described. Concepts and a notation for this triangular mesh representation are developed and the vector aspects which can be utilized numerically are given.

Section 3 is devoted to describing methods for solving the equations of incompressible hydrodynamics. A counting problem encountered in some schemes is described and the motion of the mesh is discussed. We have found several approaches to overcome this counting problem where it occurs but, as in other treatments of incompressible flow, we arrive at iterative algorithms for solving the equations. We also discuss briefly questions of mass, momentum and energy conservation.

Section 4 is devoted to the numerical aspects of integrating the equations of motion. Two essentially reversible algorithms are possible,

leap-frog and centered implicit. Each can be coupled to any of the several possible spatial treatments. Reversibility is desired because it reflects a property of the inviscid physical equations. Major emphasis is concentrated on the choice of algorithms actually implemented in the Cartesian SPLISH code.

Section 5 treats the important aspects of adjusting and restructuring the mesh. It describes methods of setting up the grid structure initially and the various techniques which can be used to modify the grid to better follow the Lagrangian motion of the fluid. One of the most important aspects of this restructuring is that strong shear flows can be followed for long times with minimal numerical diffusion.

A short summary with examples using the original ψ-ζ formalism are contained in Section 6. More extensive reports are planned for the near future including the details of test calculations and alternate algorithms which have not yet been tested.

2. Triangular Mesh Logic

In this section, we will describe and illustrate some of the features of triangular meshes and the representation of the vertex interconnections. The techniques for adjusting and restructuring the mesh during the actual course of a calculation will be attacked later in Section 5. Figure 3 shows a section of a triangular mesh representation with an interface of a fluid of type I connected to a fluid of type II. The basic elements involved in the construction of a triangular mesh are shown. A particular triangle j, is shown in heavy lines and the various elements of that triangle are labelled. Three vertices, V_1, V_2, and V_3, are connected consecutively by sides S_1, S_2, and S_3. Clearly, triangle j shares these vertices and sides with other triangles. The direction of labelling around each triangle is taken to be counter-clockwise and the z direction is taken to be out of the page. Since the mesh can be irregularly connected, an arbitrary number of triangles can meet at each vertex. For example, five triangles and sides meet at vertex 1. The number of triangles and sides meeting at a vertex is equal except near free-surfaces where there may be no grid above the surface. Each side is bounded by two triangles (in general) and each triangle shares sides with

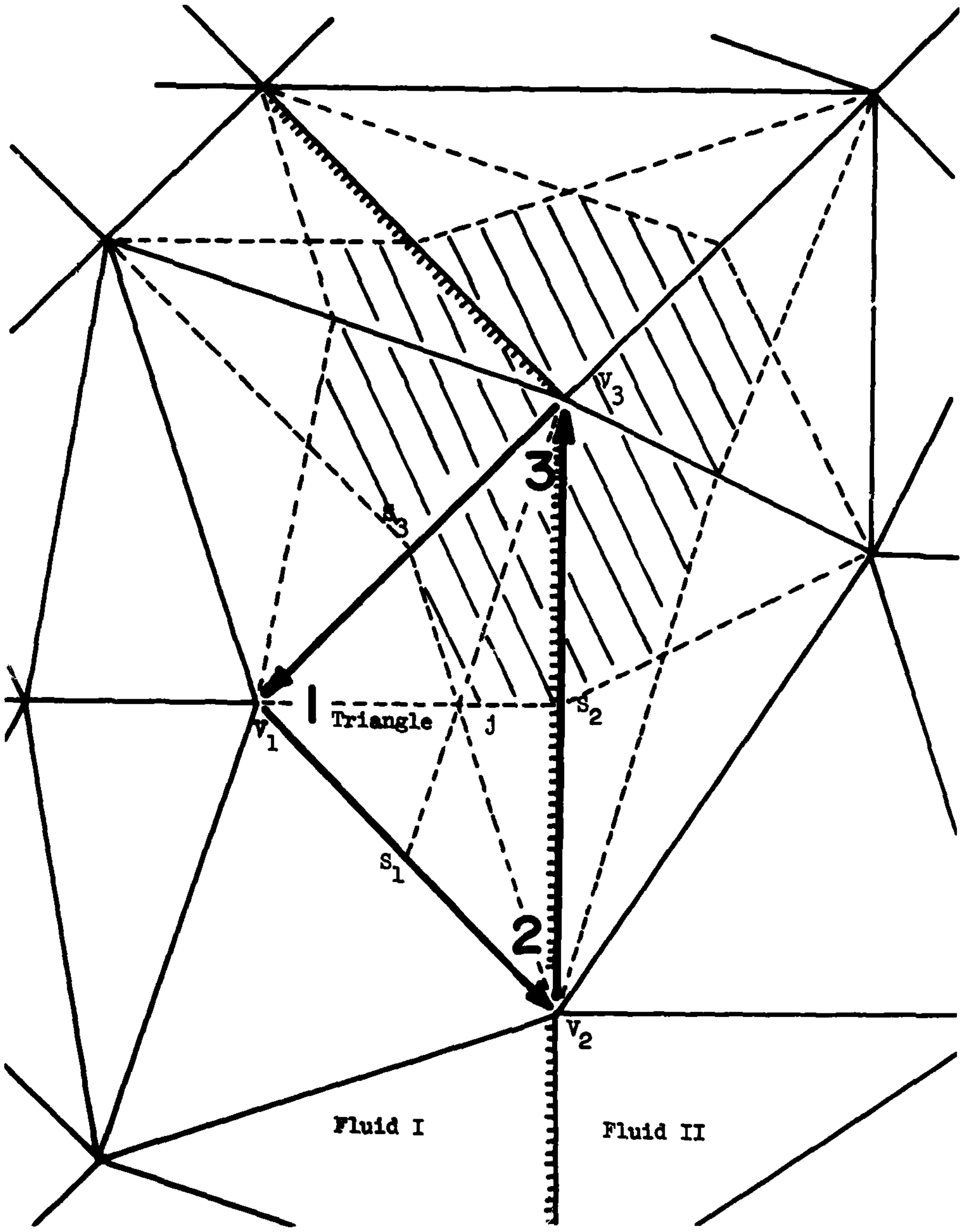

Figure 3. A section of a triangular mesh including an interface and showing a vertex cell.

three other triangles.

Figure 3 also illustrates several important features of triangles which are used throughout the remainder of this paper. It is convenient to define a cell surrounding a vertex as shown by the shaded region surrounding vertex 3. The borders of such vertex-centered cells are determined by constructing all of the side bisectors for each triangle. Since the three side bisectors all intersect at a point, as shown for triangle j, there is no ambiguity in constructing the vertex cells as indicated. The point of intersection of the side bisectors, known as the centroid of the triangle, is the center of gravity for the figure and this is true in r-z as well as Cartesian (x-y) coordinates. The three side bisectors of any triangle divide the triangle into six subtriangles. These six subtriangles all have the same area and, therefore, the quadrilaterals associated with each of the three vertex cells and into which the triangle is decomposed all have the same area. When the density is constant over a triangle, the mass contributions from a triangle to each of the three vertex cells are equal. These features of side bisectors make the calculation of cell volumes and cell areas particularly simple.

For a complete tessellation no fewer than three non-degenerate triangles can meet at any one vertex. Since a structure with three triangles meeting at an interior vertex must have a larger triangle surrounding the three, the central vertex is redundant and can be eliminated. Thus we can assume that at least four triangles meet at a vertex. Since there are more triangles than vertices, care must be taken when solving vertex equations using triangle constraints. Only when three triangles meet at each vertex do we have as many vertices as triangles. In a hexagonal tessellation of the plane, each interior vertex has six triangles and there are, therefore, two triangles per vertex. One, therefore, must expect to fix roughly two vertex quantities for each triangle constraint.

Any computational representation of such a triangular mesh must record all important aspects of the mesh interconnection. Therefore, the following lists are essential:

1. For each vertex a list must be kept of the following items: (A) the vertices to which the given vertex is connected; (B) the sides to which it is connected; and (C) the triangles which meet at that vertex. If each vertex is numbered, each side is numbered and each triangle is numbered, these lists could simply take the form of an ordered series of integers and could be stored quite compactly in a computer.
2. For each side, lists must be kept recording: (A) the starting and the finishing vertex of that side, and (B) the triangle to the right and the left of that side considered as a directed vector from the starting vertex to the finishing vertex.
3. For each triangle the following lists must be recorded: (A) the three vertices of the triangle ordered in a counterclockwise direction, (B) the three sides of the triangle again ordered in a counterclockwise direction between the listed corresponding vertices.

Since these lists are not all independent, they are not all needed. Knowing only the vertices to which a given vertex is connected, for example, still permits all of the other quantities to be determined. If vertex 2 is connected to vertex 7, a search of the side lists can be performed to determine which side connects vertex 7 and vertex 2 and, thus, the various sides connected to a given vertex can be determined.

Given the mesh and all its interconnections it is appropriate to assume that various physical quantities of interest can be associated with the vertices, the sides, or the triangles. An array of triangle areas, for example, is a meaningful quantity to store and an array of side lengths is equally useful. Since it is the mesh of vertices which determines the structure of the grid, it is natural to assume that an array of positions is recorded for the sequence of vertices in the problem. To update these positions, it is necessary to know the Lagrangian velocity of the vertices. Therefore, we will also assume that the velocities of the vertices can be found in such a way that integration of the equations of motion for the vertex position is possible using these velocities. Since the velocities are assumed known at the vertices,

a velocity field can be constructed by linear interpolation within a triangle which is then piecewise linear throughout the entire mesh. This velocity field is continuous, single-valued and easily determined at any point in space. Since linear interpolation is used, the velocities at the center of the sides are simply the average of the velocities at the starting and finishing vertex of that side.

Unfortunately, the first derivatives of this representation are discontinuous and the linear representation ensures that the incompressible equations of motion cannot be satisfied identically within a single triangle except for a few simple cases such as solid body translation. In fact, a real fluid element which is initially triangular would be very shortly transported in a real fluid to a figure with non-straight sides. These deformations of the triangle sides are a measure of the error in the numerical methods we are proposing and are fully equivalent to the errors made in neglecting the deformation of rectangle sides in a topologically rectangular representation.

It should be clear that the arrays of quantities used to define the grid and its motion involve the storage of only local information about a vertex. The connection path between two vertices can be determined only by searching sequentially through neighboring vertices along triangle sides. There is no global representation of the mesh in general, although for some specific geometries, such a global representation may be possible. The lack of a global representation in which the vertex numbering denotes a corresponding relative spatial position greatly complicates any implicit calculations. Poisson's Equation, for example, has to be solved by iteration and explicit time and space derivatives are the best that one has any right to hope for. Nevertheless, using the incompressible formulation ensures that timestep limitations due to acoustic transit times are not a problem.

We will use the following notations and conventions. The subscript i will generally be used to label vertices and the subscript j will generally be used to label triangles. Thus $\sum_i$ denotes a sum over all vertices and $\sum_j$ is a sum over triangles. The sum over all three vertices of triangle j is denoted by $\sum_{i(j)}$ where the symbol is read "the sum over

vertices i around triangle j". Similarly a sum over triangles around a central vertex c would be denoted by $\sum_{j\copyright}$. The notation $\sum_{i\copyright}$ is the sum over vertices i around a central vertex c. In such sums the sequence of vertices is assumed to be counter-clockwise around the central vertex. Thus the quantity $A_{i+\frac{1}{2}}$ can be used to represent the triangle area of the triangle with vertices (c, i, i+1). Similarly $L_{j+\frac{1}{2}}$ appearing in $\sum_{j\copyright}$ would be the length of the side radiating from vertex c and separating triangle j from triangle $j+1$.

In Figure 3 the area of triangle j is given by

$$2A_j = (\underline{r}_3 - \underline{r}_2) \times (\underline{r}_1 - \underline{r}_3) \cdot \hat{z} \qquad (4)$$

and thus h_1, the height of vertex 1 above the opposite side (S_2), is simply

$$h_1^{-1} = |(\underline{r}_3 - \underline{r}_2)|/(2A_j). \qquad (5)$$

Notice that the area is a signed quantity and will be positive when the vertices are sequenced in counterclockwise order around the triangle. In fact, it is often convenient to use the sign of the area to test whether or not a triangle has inverted during the flow, i.e., whether vertex 1, for instance, has passed through side 2.

As illustrations of these formulae and notations, the area of the cell centered on vertex i is

$$A_i = \sum_{j①} \tfrac{1}{3} A_j \qquad (6)$$

and the area-weighted average cell velocity $\underline{V}_i$ is given by

$$\underline{V}_i = (\sum_{j①} \tfrac{1}{3} A_j \, \underline{V}_j)/\, A_i. \qquad (7)$$

Of course all the sums have to be modified near a wall, an interface, or a free surface but the way to do this in any particular case is usually obvious.

If the pressure $\{P_i\}$ is specified at each vertex and is assumed to be piecewise linear everywhere between the vertices, the vector gradient of P (constant throughout the triangle and discontinuous at the triangle sides) is given by

$$(\underline{\nabla}P)_j = P_1 \frac{\hat{z}\times(\underline{r}_3-\underline{r}_2)}{2A_j} + P_2 \frac{\hat{z}\times(\underline{r}_1-\underline{r}_3)}{2A_j} + P_3 \frac{\hat{z}\times(\underline{r}_2-\underline{r}_1)}{2A_j} \tag{8}$$

$$= \sum_{i(j)} P_i \frac{\hat{z}\times(\underline{r}_{i-1}-\underline{r}_{i+1})}{2A_j} .$$

Similarly, the triangle velocity $\underline{V}_j$ (constant throughout the triangle and discontinuous at the triangle sides) is given by

$$\underline{V}_j \equiv (\underline{\nabla}\times\psi)_j = \sum_{i(j)} \psi_i \frac{(\underline{r}_{i-1}-\underline{r}_{i+1})}{2A_j} \tag{9}$$

where $\{\psi_i\}$ is the vertex-defined velocity stream function (only a single z component in 2D) and the notation i-1 and i+1 denote clockwise and counter-clockwise vertices from vertex i around triangle j.

For a vector field $\{\underline{V}_i\}$ defined at all the vertices the z component of the curl and the divergence of the vector are also defined for the triangles.

$$A_j\zeta_j = \int_j (\underline{\nabla}\times\underline{V})_j^z \cdot d\underline{A} = \tfrac{1}{2} \sum_{i(j)} (\underline{V}_{i+1}+\underline{V}_i) \cdot (\underline{r}_{i+1}-\underline{r}_i), \tag{10}$$

$$A_j \langle\underline{\nabla}\cdot\underline{V}\rangle_j = \int_j (\underline{\nabla}\cdot\underline{V})_j \, dA = \tfrac{1}{2} \sum_{i(j)} (\underline{V}_{i+1}+\underline{V}_i) \times (\underline{r}_{i+1}-\underline{r}_i)\cdot\hat{z} . \tag{11}$$

Equations (8-11) define various physical quantities at triangle centroids. The corresponding quantities can usually be defined at the vertices of the finite-difference mesh by area weighting the triangle quantities as in Eq. (7). For example, the pressure gradient at vertex cell c is just

$$(\underline{\nabla}P)_c \equiv \Big[\sum_{j(c)} \sum_{i(j)} \frac{P_i}{6} \hat{z} \times (\underline{r}_{i-1}-\underline{r}_{i+1})\Big] / A_c \tag{12}$$

where the factors A_j in numerator and denominator cancel. Equation (12)

is a linear combination of all the nearest neighbor pressures to vertex c which gives exactly the correct value when the pressure is constant or linear. It is important to note that the coefficient of P_c in Eq. (12) is identically zero since $\sum_{i©} (\underline{r}_{i-1}-\underline{r}_{i+1})$ is a telescoping sum when vertex c is an interior vertex.

The representation detailed above is appropriately unique and orthogonal. By orthogonal we mean that the numerical finite difference operators satisfy the continuum orthogonality conditions

$$\underline{\nabla} \times \underline{\nabla}\phi = 0, \quad \underline{\nabla} \cdot (\underline{\nabla} \times \psi_z) = 0. \tag{13}$$

The preceding curl and divergence operators in Eqs. (13) of course act on triangle quantities since ϕ and ψ are assumed to be vertex quantities as above (but are otherwise arbitrary scalar fields). The second of Eqs. (13), for example, can be written in our finite-difference notation as

$$\begin{aligned} A_c\langle \underline{\nabla} \cdot (\underline{\nabla} \times \psi_z)\rangle_c &= \int_{\text{cell } c} \underline{\nabla} \cdot (\underline{\nabla} \times \psi) dA = \\ &= \sum_{i©} \frac{(\underline{r}_{i+1}-\underline{r}_i)}{4A_{i+\frac{1}{2}}} \times \left[\psi_i(\underline{r}_i-\underline{r}_{i+1}) + \psi_{i+1}(\underline{r}_i-\underline{r}_c) + \psi_c(\underline{r}_{i+1}-\underline{r}_i)\right] \end{aligned} \tag{14}$$

This is just the flux of $\underline{\nabla} \times \psi$ (constant over triangles) out of cell c. Clearly the ψ_c coefficient is zero term by term because of the cross product. The ψ_i and ψ_{i+1} terms have as coefficients $+\frac{1}{2}$ and $-\frac{1}{2}$, respectively, because $(\underline{r}_i-\underline{r}_c) \times (\underline{r}_{i+1}-\underline{r}_i) = 2A_{i+\frac{1}{2}}$. Thus Eq. (14) is identically zero when summed around an interior vertex. By a virtually identical argument the first of Eqs. (13) can be demonstrated to be identically zero.

By uniqueness we merely mean here that the triangle vector equation

$$\underline{V} = \underline{\nabla}\phi + \underline{\nabla} \times \psi_z \tag{15}$$

uniquely relates $\underline{V}$ and (ϕ, ψ_z) (assuming well posed conditions on ϕ and ψ_z at the system boundaries where the derivatives are not defined). Given ϕ and ψ_z on vertices, Eqs. (8) and (9) allow an unambiguous

determination of $\underline{V}$ at the triangle centroids. Going the other way we use orthogonality. The divergence of a known $\underline{V}$ expunges the ψ_z term. Thus

$$A_c \langle \underline{\nabla} \cdot \underline{V} \rangle_c = \sum_{i©} \underline{V}_{i+\frac{1}{2}} \times \frac{(\underline{r}_{i+1}-\underline{r}_i)}{2} = \underline{\nabla} \cdot \underline{\nabla}\phi = \tag{16}$$

$$= \sum_{i©} \left[\phi_i \frac{\hat{z}\times(\underline{r}_c-\underline{r}_{i+1})}{2A_{i+\frac{1}{2}}} + \phi_{i+1} \frac{\hat{z}\times(\underline{r}_i-\underline{r}_c)}{2A_{i+\frac{1}{2}}} + \phi_c \frac{\hat{z}\times(\underline{r}_{i+1}-\underline{r}_i)}{2A_{i+\frac{1}{2}}} \right] \times \frac{(\underline{r}_{i+1}-\underline{r}_i)}{2} \cdot z.$$

The second line of Eq. (16) is the finite-difference form of the ∇^2 operator and Eq. (16) is a triangular-grid Poisson Equation. Notice that the coefficient of the ϕ_c term is $-\sum_{i\,c} |\underline{r}_{i+1}-\underline{r}_i|^2/4A_{i+\frac{1}{2}}$ and is always negative. The matrix is diagonally dominant and hence normal iterative procedures for finding ϕ by inverting Eq. (16) work well.

An equation similar to (16) can be constructed, except for sign, by taking the curl of Eq. (15). Then

$$A_c \langle \underline{\nabla} \times \underline{V} \rangle = \underline{\nabla} \times (\underline{\nabla} \times \psi_z) \tag{17}$$

allows the determination of ψ_z from $\underline{V}$.

3. Finite-Difference Approaches

The preceding sections prepared the ground work for our discussion of alternate algorithms to solve the equations of incompressible hydrodynamics. The incompressibility inherent in Eq. (2) can be interpreted in many ways. One would like, for example, to conserve the triangle areas but this is essentially impossible except for the simplest types of flows. There are roughly twice as many triangles as there are vertices. When there are more than six triangles on the average at each vertex, the previously mentioned "counting problem" comes into play. The x and y values of the vertex positions, the variables available to ensure conservation of triangle area, are fewer in number than the constraints. Even when there are fewer than six triangles per vertex on the average, the number of variables left free after all of the constraints have been satisfied are extremely few in number and cannot be used to represent the flow vorticity (or lack thereof) with acceptable accuracy.

Once the idea of conserving triangle areas has been abandoned, the next logical attempt is to conserve vertex-centered cell areas. This is attractive since the cell area ($\underline{\nabla} \cdot \underline{V}$) and the cell rotation ($\underline{\nabla} \times \underline{V}$) are both known for each vertex and there are correspondingly two variables for each vertex, V_x and V_y, which are free to satisfy these constraints. A great deal of effort has been invested in this approach with mixed results. The cell area must at all times have the value it started with initially. The cell vorticity integral is likewise known. When the curl of Eq. (1) is integrated over a cell we obtain

$$\frac{d}{dt} \int_{cell} \underline{\nabla} \times \underline{V} \cdot d\underline{A} = - \int_{cell} \underline{\nabla} \times \left(\frac{\underline{\underline{\nabla P}}}{\rho}\right) \cdot d\underline{A} \qquad (18)$$

where the term on the right hand side can be evaluated explicitly. The left hand side, the time derivative of the average vorticity times the cell area, can thus be used to advance the cell vorticity in time. Knowing the desired cell vorticity and cell area, the new vertex velocities can be iterated (ensuring momentum conservation via the equations of motion) until the actual cell areas and vorticities are correct.

Unfortunately the effective Poisson-like equations which result are non-local and convergence of the iterations are correspondingly slow. While there is no counting problem with this approach, an allied topological constraint crops up when more than six triangles meet at a vertex. We have been able to show that a purely local rotation conserving all cell areas is not generally possible when seven or more triangles meet at that vertex. In other words, more than just the nearest neighbor vertices must have non-zero velocities to conserve all cell areas; purely local vortices are not generally possible and this gets reflected in the convergence rate of the iterated solution. Similarly, a purely vorticity-free local expansion is not generally possible when more than six triangles meet at a vertex. This constraint is not entirely prohibitive, but the cost of exact area and vorticity conservation <u>with</u> momentum conservation is high in terms of computer time so faster, less demanding algorithms were sought.

There is no strict requirement to maintain physically conserved quantities any more accurately than the truncation error levels implicit

in the finite-difference algorithms--even though such strict conservation is esthetically attractive. With this in mind we investigated algorithms which minimized a positive definite error functional over the whole mesh. Since the desired curl $\{C_i^*\}$ and divergence $\{D_i^*\}$ are known, and since Eqs. (7), (10) and (11) allow us to define at any instant the actual values $\{C_i\}$ and $\{D_i\}$, we chose as our error functional

$$E = \sum_i \left[\omega_i (C_i - C_i^*)^2 + W_i (D_i - D_i^*)^2\right] . \tag{19}$$

The weights $\{\omega_i\}$ and $\{W_i\}$ are free to emphasize small or large triangles, fast or slow flow regions, etc. Taking the partial derivatives $\partial E / \partial \underline{V}_i = 0$ gives as many equations as one needs to advance the fluid velocities. We never actually coded up this method, however, because the programming complication is prohibitive and the application of boundary conditions and momentum conservation is obscure.

The method we have adopted as most useful and esthetically pleasing is to rely on the orthogonality of curl and gradient operators discussed in the previous section. We force the velocity, now defined on the triangles, to arise from a stream function according to Eq. (9). Such a flow is divergence free by construction as described earlier; the flux into or out of each vertex cell is identically zero. In fact, such a flow, as shown in Figure 4 for one vertex and its nearest neighbors, is also divergence free on each triangle. Since $\underline{V}_j$ is constant throughout a triangle and since the normal component of $\underline{V}$ is continuous across all triangle sides, the flow field described by $\underline{V} = \underline{\nabla} \times \psi_z$ allows no accumulation of fluid in a triangle or loss of material from a triangle. Figure 4 shows how this can be by displaying actual stream lines from such a flow. These stream lines are closer together where the flow is faster and are continuous crossing triangle sides even though their direction changes.

A flow which is divergence free on triangles would seem to contradict our counting problem described earlier. Although the triangle velocities are divergence free, the area-weighted vertex velocities are not. Thus, when the appropriate averages are taken to move the vertices, the triangle areas change necessarily and even the cell areas change slightly. If an

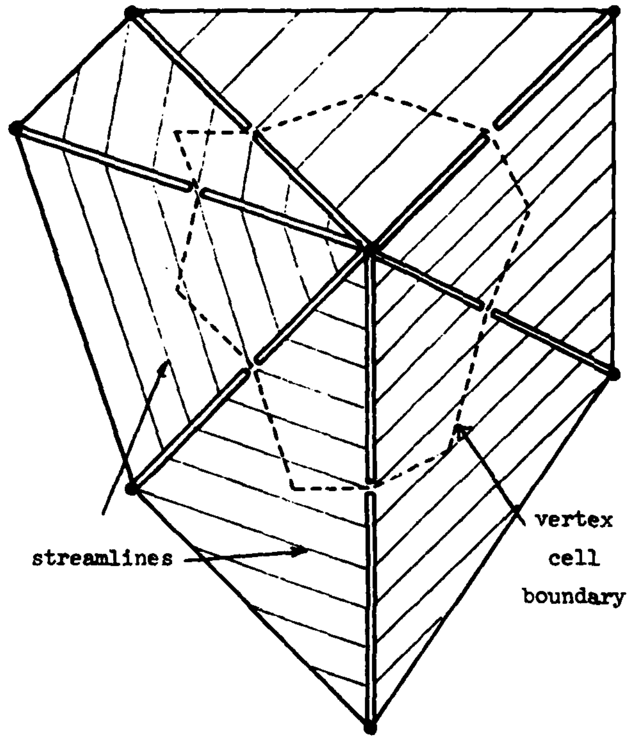

Figure 4. Streamlines of a flow field calculated from a vertex-centered stream function. $\underline{V}$ is constant throughout each triangle.

array of marker particles is followed in the instantaneous flow field while the grid is held fixed, the density of markers is locally constant moving with the fluid. This is a meaningful expression of the incompressibility we wish to obtain. The current SPLISH (x-y) and SPLASH (r-z) codes incorporate these latter algorithms where the triangle velocities are the basic physical quantities. The implementations of the ψ-ζ and the P-$\underline{V}$ formulations of this approach are discussed in the next section.

In any formulation the incompressibility assumption forces a physically nonlocal character on the flow and this gets reflected in the numerical necessity of iterating a Poisson-like equation with appropriate boundary conditions. In ψ-ζ forms, the vorticity ζ is advanced at each cell during each timestep and then $\underline{\nabla} \times (\underline{\nabla} \times \psi) = \zeta$ must be solved for the velocity stream function ψ. The velocity divergence is zero by construction. In the primitive P-$\underline{V}$ formulations, the divergence of velocity is forced to zero by choosing P to satisfy $\underline{\nabla} \cdot (\underline{V} \cdot \underline{\nabla} \underline{V}) = - \underline{\nabla} \cdot \frac{1}{\rho} \underline{\nabla} P$. In this latter case the vorticity must fend for itself via the equations of motion used to advance $\underline{V}$. In either case the complicated grid connections virtually preclude a fast direct solution or even a globally implicit iteration. In solving these equations we have been using a simple point-relaxation technique with a home-grown acceleration formula. We have found, however, that simple extrapolation using the two previous values of the quantity being iterated (P or ψ) makes the biggest impact. Extrapolation reduces the residual by one to two orders of magnitude before iteration even begins. What is even more important, however, is the fact that extrapolation is most accurate for the long wavelength components of the solution desired. This is extremely helpful because the long wavelength components of the residual are the slowest to converge under iteration. Therefore, using extrapolation not only reduces the initial residual appreciably, it effectively increases the rate of convergence of the iteration itself.

4. The Incompressible Flow Algorithms

The actual temporal integration scheme chosen should be reversible, because the physical equations being solved are reversible.[7] In addition, reversibility usually means that artificial numerical damping is absent and that higher Reynold's number flows can be treated accurately. Conversely, the total absence of numerical damping is often accompanied by an even-odd or computational mode of numerical instability in which the total lack of diffusive interaction allows decoupling of the finite-difference mesh or variables in one obnoxious manner or another. Previously we have argued that our triangular grid algorithms minimize the virulence of this problem and in Section 6 we will show several completely undamped

reversible calculations. For now we concentrate on defining reversible algorithms since damping can also be added where and when needed.

There are two easy ways to achieve the desired reversibility--using a leapfrog $\underline{x}$-$\underline{v}$ integration in time and using a centered implicit $\underline{x}$-$\underline{v}$ integration. Either approach can be applied with either the ψ-ζ formulation or the P-$\underline{V}$ formulation of the basic equations. The choice appears to be a matter of convenience although we have not tried all combinations.

Since the flow is Lagrangian, we can use the following time-integration template

$$\begin{aligned} \underline{V}_i(t+\delta t/2) &= \underline{V}_i(t-\delta t/2) + \delta t\, \underline{a}_i(t, \{\underline{X}\}, \text{etc}), \\ \underline{X}_i(t+\delta t) &= \underline{X}_i(t) + \delta t\ \underline{V}_i(t+\delta t/2). \end{aligned} \qquad (20)$$

The subscript i labels the vertices (or the triangle centroids). The important points are that the acceleration terms $\{\underline{a}_i\}$ can be calculated at time t using positions and other quantities whose values are already known at time t and that this "leapfrog" integration is explicit as expressed above. Alternately the centered implicit formulation can be used.

$$\begin{aligned} \underline{V}_i(t+\delta t) &= \underline{V}_i(t) + \delta t\ \underline{a}_i(t+\delta t/2), \\ \underline{X}_i(t+\delta t) &= \underline{X}_i(t) + \frac{\delta t}{2}\,[\underline{V}_i(t) + \underline{V}_i(t+\delta t)] \end{aligned} \qquad (21)$$

where the accelerations $\underline{a}_i(t+\delta t/2)$ are calculated either as the outer average $\frac{1}{2}[\underline{a}_i(t) + \underline{a}_i(t+\delta t)]$ or the inner average $a_i(t+\delta t/2, \frac{1}{2}\{X_i(t) + X_i(t+\delta t)\}, \text{etc.})$. The formulation of Eqs. (21) is clearly reversible and, insofar as the velocities $\underline{V}_i(t+\delta t)$ are not known a priori, the formulation is implicit and must be iterated. Since we are iterating the acoustic waves (incompressibility) anyway, this extra iteration imposes no great hardship. Furthermore, the implicit nature sometimes means that longer timesteps can be taken stably.

The easiest algorithm will be considered first, the leapfrog ψ-ζ formulation. We start knowing the positions of the vertices $\underline{X}_i$ at time t and the vorticity at these same vertices at time $t-\delta t/2$. We also know the parallel velocity of any free surface vertices $\underline{V}_i$ at time $t-\delta t/2$. Using Eq. (3) the free-surface velocities have a new parallel component which is

$$V_{\tau i}(t+\delta t/2) = V_{\tau i}(t-\delta t/2) - \delta t\, g\,\hat{y} \cdot \hat{\tau}(t). \qquad (22)$$

This is reversible and the vorticity can likewise be advanced to $\zeta_i(t+\delta t/2)$ reversibly using Eq. (18). Of course the vorticity is conserved in the Lagrangian frame unless $\underline{\nabla}\, \rho \neq 0$. When $\underline{\nabla}\, \rho \neq 0$, the pressure field has to be determined, a point we return to shortly.

The next step is to calculate ψ from the usual equation $\underline{\nabla} \times (\underline{\nabla}\times\psi) = \zeta$. Here we encounter our only snag, a spatial grid at time $t+\delta t/2$ is required if $\psi_i(t+\delta t/2)$ is to be found. We do this in SPLISH, our Cartesian code, by calculating $\underline{X}_i(t+\delta t/2)$ as the average of the new and the old grid positions. Of course this is reversible provided we iterate exactly as in the implicit formulation. Once $\{\psi_i\}$ has been found, the triangle velocities at time $t+\delta t/2$ can be calculated using Eq. (9). Forming the vertex area-weighted averages of $\underline{V}_i$ from Eq. (7) gives $\{\underline{V}_i(t+\delta t/2)\}$ which can be used to advance the vertex positions $\underline{X}_i$ from t to $t+\delta t$.

The boundary conditions in the Poisson Equation are simple on a solid wall; ψ = constant. On the bottom of a fluid layer periodic in X, we set $\psi = 0$. If a lid were placed on the top of the fluid, the constant value of ψ at the top could be different from the value on the bottom. The difference in the two constants would be the rate of flow across a vertical surface from the top to the bottom. This rate is independent of the X position of the vertical surface because the fluid is incompressible.

The boundary condition at the free surface is merely that the component of velocity of a free-surface vertex parallel to the surface is known. The normal gradient of ψ, area weighted to the free-surface vertices, must give the known values. Since the point by point iteration of the interior ψ points can be performed, the normal gradient can be

adjusted by appropriately choosing the free-surface ψ values. An explicit evaluation of these values is possible, just as with the interior points, but we have chosen an implicit formulation of this boundary condition which couples all of the surface ψ values in a tridiagonal system. In addition to taking the interaction with neighboring surface vertices into account, this method speeds convergence over the whole mesh because two widely separated vertices can "communicate numerically" very quickly if they are reasonably close to the surface.

When an internal cavity is present in the fluid due to the existence of a bubble or to cavitation, the ψ-ζ boundary conditions are greatly complicated. For example, the formation of a bubble has to move the free surface upward to conserve area. Since $\partial\psi/\partial\tau$ along the surface is the velocity normal to the surface, the net upward velocity, $\int_0^L \frac{\partial\psi}{\partial\tau}\,d\ell$, must be non-zero. In a periodic system the formation of a bubble or cavity thus requires ψ to be non-periodic even though the derivative must be. In other words, ψ must have a branch cut whose jump varies with the rate of expansion or contraction of the bubble. While this nasty complication is not insurmountable, it certainly requires the calculation of a self-consistent pressure field. Since the fully nonlinear source term for internal waves, as mentioned earlier, also requires this pressure, a primitive solution method using P and $\underline{V}$ has definite advantages over the ψ-ζ formulation, even though it is intrinsically a little more complicated in 2D. A further argument in favor of the P-$\underline{V}$ formulation arises when we consider the eventual generalization to three dimensions. Then $\underline{\psi}$ is a true vector having three components, and three Poisson equations must be solved. In the P-$\underline{V}$ formulation P would still be a scalar so only one Poisson equation needs to be solved.

Our P-$\underline{V}$ formulation has $\underline{P}_i$, $\underline{V}_j$, and $\underline{X}_i$, all specified at times t, $t+\delta t$, $t+2\delta t$, $\cdots$. Using a split step algorithm[7] we integrate the velocities forward half a timestep, advance the grid one full timestep, and then advance the velocities forward the other half timestep.

$$\underline{V}_j^{\frac{1}{2}} = \underline{V}_j^o - \frac{\delta t}{2\rho_j} (\underline{\nabla}P)_j^o - \frac{\delta t}{2} g\,\hat{y}\,, \tag{23}$$

$$\underline{V}_i^{\frac{1}{2}} = \tfrac{1}{2}(\underline{V}_i^o + \underline{V}_i^n), \tag{24}$$

$$\underline{X}_i^n = \underline{X}_i^o + \delta t\, \underline{V}_i^{\frac{1}{2}}, \tag{25}$$

$$\underline{\tilde{V}}_j^{\frac{1}{2}} = \underline{\underline{R}}\,(\{\underline{X}_i^o\},\ \{\underline{X}_i^n\}) \cdot \underline{V}_j^{\frac{1}{2}}, \tag{26}$$

$$\underline{V}_j^n = \underline{\tilde{V}}_j^{\frac{1}{2}} - \frac{\delta t}{2\rho_j} (\underline{\nabla}P)_j^n - \frac{\delta t}{2} g\,\hat{y}\,. \tag{27}$$

The velocity $\underline{V}_i^n$ appearing in Eq. (24) is area weighted from $\{\underline{V}_j^n\}$ from Eq. (27) as calculated at the previous iteration. Eqs. (23) and (27) contain the evolution of $\{\underline{V}_j\}$ according to the Lagrangian equation of motion. Eq. (26) is the numerical reflection of the fact that velocities must rotate and stretch as the grid rotates and stretches. The transformation $\underline{\underline{R}}$ is linear and given by the following three scalar equations:

$$\begin{aligned}
\tilde{V}_j^{\frac{1}{2}} \cdot (\underline{X}_2^n - \underline{X}_1^n) &= \underline{V}_j^{\frac{1}{2}} \cdot (\underline{X}_2^o - \underline{X}_1^o), \\
\tilde{V}_j^{\frac{1}{2}} \cdot (\underline{X}_3^n - \underline{X}_2^n) &= \underline{V}_j^{\frac{1}{2}} \cdot (\underline{X}_3^o - \underline{X}_2^o), \\
\tilde{V}_j^{\frac{1}{2}} \cdot (\underline{X}_1^n - \underline{X}_3^n) &= \underline{V}_j^{\frac{1}{2}} \cdot (\underline{X}_1^o - \underline{X}_3^o).
\end{aligned} \tag{28}$$

This transformation ensures that the vorticity integral, calculated about <u>any</u> interior vertex, is invariant during the displacement of the grid. Clearly Eqs. (28), and hence Eq. (26), are fully reversible. It is gratifying, furthermore, that the three equations are not linearly independent since only two components of $\underline{\tilde{V}}_j^{\frac{1}{2}}$ need to be determined.

As has been established previously the $\underline{\nabla}P$ and gravity terms cannot alter the vorticity either, since $\underline{\nabla} \times \underline{\nabla}P \equiv 0$ and gravity is a constant. Only the physically correct variations of $\frac{1}{\rho_j}$ can cause changes in vorticity, exactly as they should. Thus the entire algorithm advances the positions of the vertices and the triangle velocities reversibly while evolving the correct vorticity about every interior vertex. The pressures $\{P_i^n\}$ at $t+\delta t$ are derived from the condition that the new velocities $\{\underline{V}_j^n\}$ should

be divergence free at time $t+\delta t$. Thus, from Eq. (27) we derive the pressure Poisson Equation by setting $(\underline{\nabla} \cdot \underline{V}_j^n)_i = 0$. We obtain

$$\frac{\delta t}{2}(\underline{\nabla} \cdot \frac{1}{\rho_j} \underline{\nabla} P_i^n)_i = (\underline{\nabla} \cdot \tilde{\underline{V}}_j^{\frac{1}{2}})_i. \tag{29}$$

The right hand side, which can be evaluated at each iteration explicitly, is the exact numerical analogue of the $\underline{\nabla} \cdot (\underline{V} \cdot \underline{\nabla}\, \underline{V})$ term which arises when the divergence of Eq. (1) is taken.

Solving Eq. (29) iteratively for $\{P_i^n\}$ completes the calculation of the timestep. The boundary conditions on P for Eq. (29) are very similar to those described for the ψ-ζ formulation earlier. At a free-surface P = constant (P = 0 at the top and the constant value within a bubble is determined by the bubble volume, surface tension, etc.). At the bottom or on a wall $\partial P/\partial n$ must be chosen so that the velocity normal to the wall is zero. Thus an implicit tridiagonal system can be developed linking all pressures on the wall (or bottom) to the nearest neighbor interior values.

5. Adjusting and Restructuring the Mesh

The major advantage of using a general connectivity triangular mesh is the flexibility which it permits to follow complicated flows with a Lagrangian grid over long times. To make full use of this flexibility requires that we provide for several types of adjustment and local mesh restructuring to maintain the uniformity and accuracy of the discrete mesh representation. A mesh adjustment is a nonphysical movement or adjustment of the position of one or more vertices which is accomplished without changing the connectivity of the mesh vertices. These adjustments are designed to simplify and regularize the mesh and result in the effective transfer of fluid across triangle boundaries.

A restructuring of the mesh, on the other hand, does not generally involve movement of any of the vertices but does include many sorts of triangle and side additions, reconnections, and subtractions. In a sense, adjustment and restructuring are orthogonal procedures--one leaving the vertex positions unchanged, the other leaving the mesh connectivity or topology unchanged. Since restructuring involves the changed position

of a side, it also can involve the nonphysical flow of fluid across triangle boundaries.

Both adjustment and restructuring represent departures from a purely Lagrangian description and hence threaten the reintroduction of unwanted numerical diffusion back into the system. To minimize the diffusive and other errors, it is necessary to pay strict attention to mass and momentum conservation and to leave undisturbed the vertices and triangle sides lying along boundaries, surfaces, and interfaces. There are a number of different types of mesh adjustment and restructuring which are possible, too many to cover in depth here. Therefore we will merely list the simplest techniques which have been considered with a brief description of each technique.

A. Mesh Adjustment - Local Relocation

In some situations it is quite likely that several very small or narrow triangles will border on much larger ones. This disparity in size could cause errors or problems of several types including:

1. Derivatives become more and more difficult to evaluate accurately.
2. Timestep limitations become severe, because of short sides.
3. Triangle inversion becomes increasingly likely.
4. Resolution can become uncomfortably nonuniform.

Clearly this disparity cannot be allowed to increase indefinitely although, in principle, the Lagrangian motion of the vertices could bring the situation about naturally. In practice it may become necessary to move one or more vertices nonphysically. In the course of such a local relocation in the fluid the total mass and momentum of the triangles or cells affected should of course be conserved. Many possible formulae for the new position have been tried in LINUS2. One of the simplest has also proven to be one of the most useful--the new vertex position is taken to be the average of the surrounding positions.

B. Mesh Adjustment - Side Equalization

Sometimes along a surface in the fluid the vertices may accumulate in some areas and separate in others. This would happen if an incompressible upwelling at a free surface were occurring. This accumulation and stretching of vertices at separatrices can be easily handled by the various restructuring techniques discussed later in this section or it

could be handled by letting the flow slip through the grid locally.

This local Eulerian behavior is similar to the rezone procedure employed by Chan [6] in a topologically rectangular mesh code. Of course one would like to eliminate these numerically diffusive Eulerian adjustments within the fluid region so the numerical model of the fluid mirrors the usual reversibility characteristic of an inviscid fluid as nearly as possible. To this end the various restructuring operations described in the remainder of this section are useful. When Eulerian slippage is necessary, however, the recently developed Flux-Corrected Transport algorithms [8] can be adapted to minimize the diffusion and dispersive phase errors associated with the flow across the cell boundaries.

C. Mesh Restructuring - Reconnection

When a triangle becomes too small or narrow, as has triangle o-a-c in Figure 5, the diagonal of the quadrilateral (a-b-o-c) which extends from a to o can be removed and the other diagonal (b-c) can be constructed in its place as indicated by the solid line.

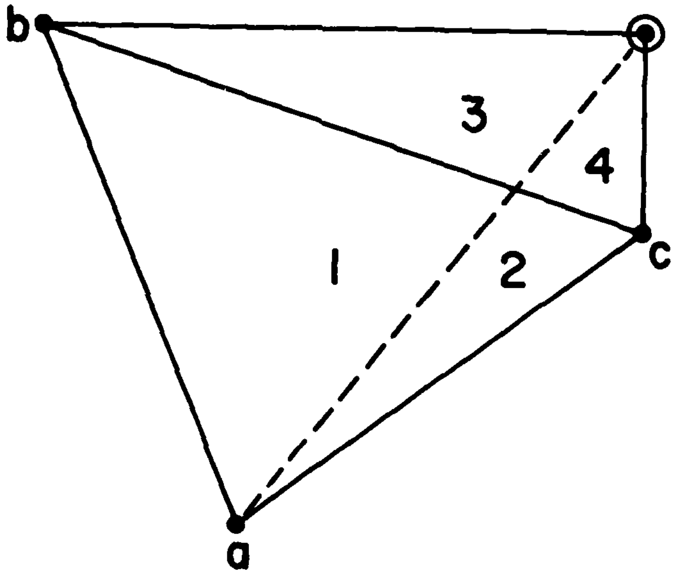

Figure 5. Mesh restructuring by reconnection of vertices across the quadrilateral diagonal.

Clearly this procedure does not involve the nonphysical motion of any of the vertices so non-reversible changes of the vertex positions are not required. Care should be taken to ensure that momentum and mass are conserved when the reconnection is performed in fluids and no reconnections can be performed which involve the erasure of a side which is a material interface. The reconnection can be triggered in two ways: when the area disparity becomes too large or when the difference in the two diagonal lengths becomes appreciable. In general nearly equal areas and short diagonals are to be preferred. Sometimes these two desirables are mutually exclusive. In all cases triangle inversion cannot be permitted. This means that a diagonal passing outside the quadrilateral cannot be formed.

This reconnection procedure allows one row of triangles to slip smoothly by another row without having to adjust the Lagrangian vertex positions or velocities. In the corresponding fixed grid system, the triangles or rectangles bordering either side of the shear interface would soon become stretched unacceptably and a diffusive rezone procedure would have to be applied. The mesh reconnection described here is a much less drastic change since the vertex positions and momenta can be left alone.

D. Mesh Restructuring - Adding Vertices

The adjustments considered above all kept the number of vertices and the number of triangles and the number of sides fixed. Often, however, it may be necessary to increase resolution in some region where the flow is not naturally accumulating vertices. Such a situation occurs in cylindrical coordinates when the fluid flow is converging on the axis somewhere. Then the triangular zones become larger and larger in cross-sectional area, but the radius of curvature becomes smaller and smaller. Better resolution is clearly required.

A similar situation occurs near the leading edge of a foil travelling into relatively undisturbed water (or air). The resolution required to represent accurately the flow separation of a fluid element at the leading edge is intrinsically much finer than the resolution needed in the same undisturbed fluid element just a short time earlier.

There are at least two ways of adding triangles to improve the

resolution, triangle trisection and side bisection. In side bisection a new vertex is inserted somewhere on side (b-c) of Fig. 5 (for want of another position we can assume the side is bisected). The lines from vertex o and a to the new vertex are added, resulting finally in two new triangles, three new sides, and a new vertex. The bisection of side (b-c) results in two pairs of triangles of equal area.

The values of physical variables at the new vertex must be determined by interpolation, and hence some numerical smoothing is implied. The improvement in resolution arises because the bisected side becomes two sides and is no longer required to be straight. Thus decreasing radius of curvature can be met by increased resolution. Furthermore, there is no restriction implied by material interfaces. If any of the sides is an interface, the bisection can still be performed.

A new vertex can also be added within a triangle--not on any triangle side--in a restructuring we call trisection. Trisection alone is irrelevant because the three new smaller triangles are surrounded by a single large triangle whose behavior is constrained just as if the new vertex were not there. To be effective, trisection must be followed immediately by at least a single side reconnection. The result then is two new triangles, three new sides, and a new vertex which does not lie on the original quadrilateral diagonal. Physical variables at the new vertex are determined by interpolation just as in the case of side bisection.

E. Mesh Restructuring - Subtracting Vertices

After a fluid element has moved out of a region where high resolution is required, it is efficient to remove vertices and hence reduce the computational cost in that fluid region. Subtracting vertices can be done simply as the inverse of the two processes, triangle trisection and side bisection, described above. For triangle "untrisection" a side is reconnected so that the resulting configuration has a single triangle which surrounds a vertex and three subtriangles. The interior vertex is then erased and two triangles and three sides disappear.

Similarly, a vertex can be relocated until two of the sides emanating from it form a straight line. If these two sides belong to triangles which share common sides, the two interior sides which do not form a straight line can be erased and the two straight lines combined

into a single line. Here again the starting configuration for side "unbisection" must be a quadrilateral with four triangles inside. If such a configuration does not exist, it can be forced by local reconnections.

In subtracting triangles care should again be taken to ensure conservation of the appropriate quantities on the new reduced mesh; this means careful monitoring of the interpolation formulae.

F. Initialization

We conclude this section with a brief description of a generalized mesh initialization procedure. Clearly one could specify by hand all the vertex positions, all the sides, all the triangles, etc. This is both laborious and apt to be repeated time and again as the physical problem is changed. The process can be automated provided that several general utility routines are written to connect vertices (and store the appropriate information in the mesh index lists), to set up a triangle given three ordered vertices, to bisect sides, to reconnect quadrilateral diagonals, and to adjust interior vertex locations.

The programmer specifies an ordered set of boundary points surrounding a region as in Figure 6a and specifies how many interior vertices in the region he would like. The initialization program can then proceed around the circumference of the region as in Figure 6b, forming triangles until the region is completely tessellated. To add the interior vertices the longest remaining interior side is bisected repeatedly until all the required vertices have been injected as in Figure 6c. The reconnection and vertex adjustment routines are then used iteratively in conjunction until the final relaxed mesh is determined as in Figure 6d.

Clearly the procedure can be repeated until each separate region has been filled with the desired number of vertices and the grid smoothed. Equally obvious should be the fact that a great deal of careful programming will be required to implement this rather simple procedure.

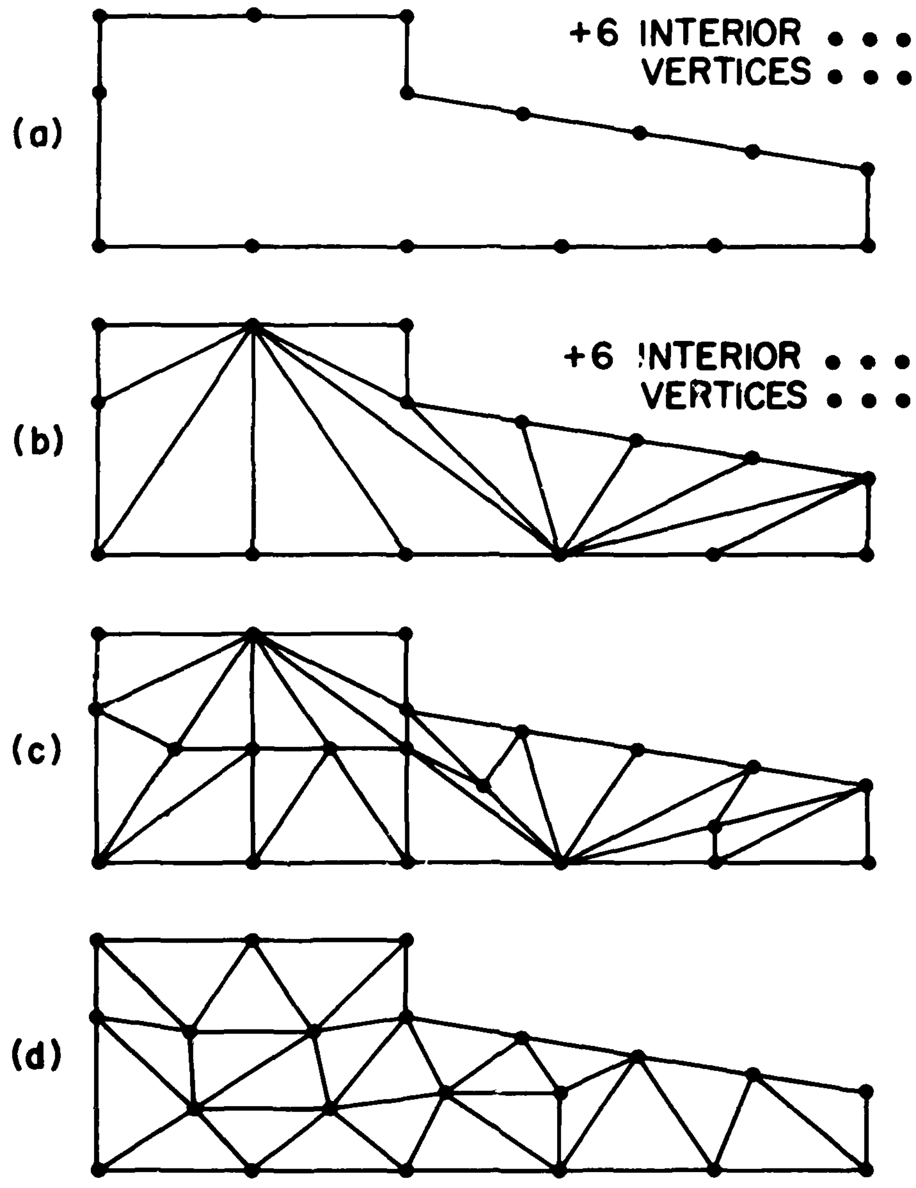

Figure 6. The four stages of automatic initialization for a triangular mesh region with irregular boundaries.

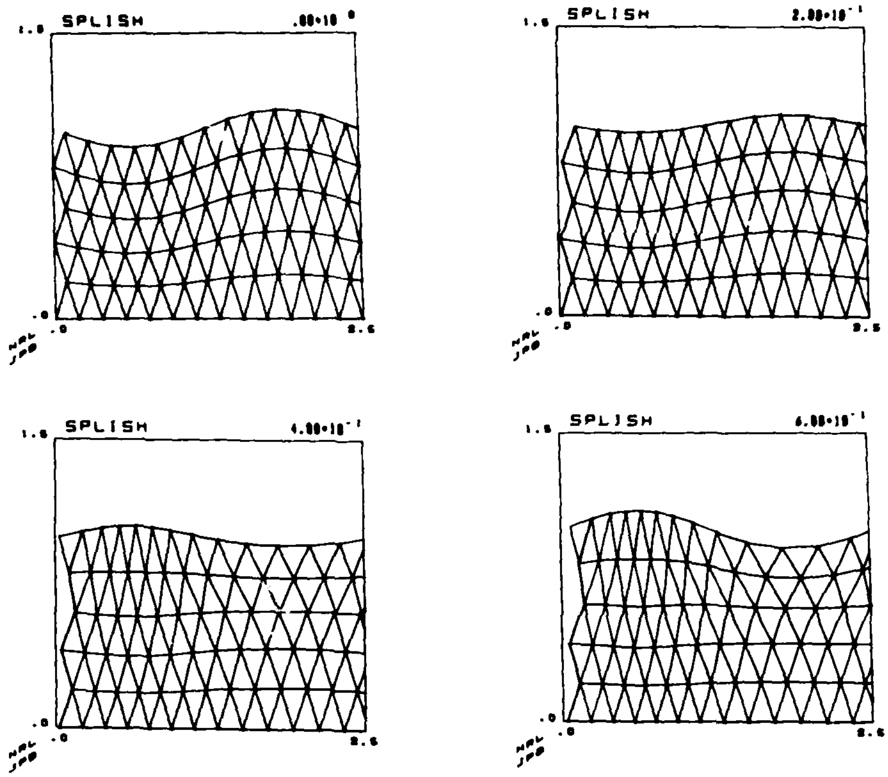

Figure 7. A gravity wave of large amplitude in shallow water without density stratification.

6. Summary and Examples

In this paper we have described an entire series of techniques and algorithms for using a Lagrangian 2D mesh of triangles to represent and solve free surface problems in incompressible hydrodynamics. The results of our research in this area are two free-surface hydrodynamics codes, SPLISH (x-y) and SPLASH (r-z), an r-z MHD code called LINUS2 for electromagnetically imploded liquid metal rings, and TORUS2, an r-z quasi-static MHD code for calculating the evolution of Tokamak cross-sections. Our experience with these codes is by no means extensive, however, and much work remains in all these areas before the understanding of hydrodynamics using Lagrangian triangular meshes is complete.

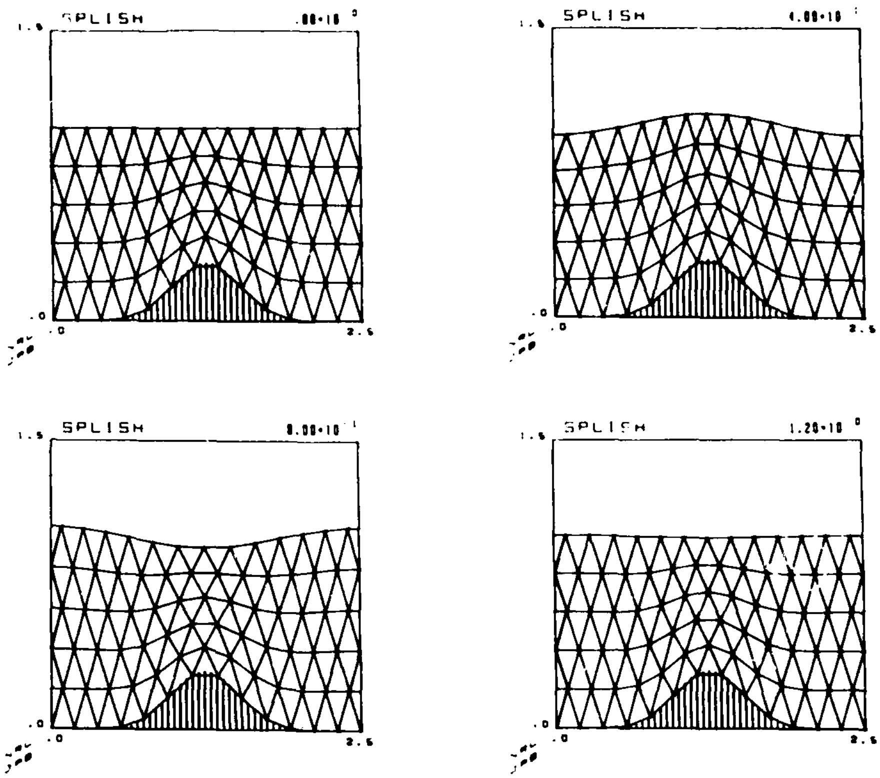

Figure 8. Gravity wave over an undersea obstacle with weak density stratification to generate internal waves.

Following are results from several test calculations performed with the recently constructed x-y code. Figure 7 shows several time steps from a run with a flat bottom and zero density stratification. The finite depth dispersion relation for these gravity waves is $\omega^2 = gk \cdot \tanh kh$ where $g = 980$ cm/sec^2, $h = 1$ cm and $k = 2\pi/2.5$ cm^{-1}. The period is theoretically 0.1274 sec for small amplitude waves. The initial wave amplitude, 0.2 cm, is small but not totally negligible, so some nonlinear effects are clearly taking place. The numerical period measured is between .112 sec and .128 sec (nearer to the latter probably) and appears to be slightly shorter than the linear 0.1274 sec predicted. Since

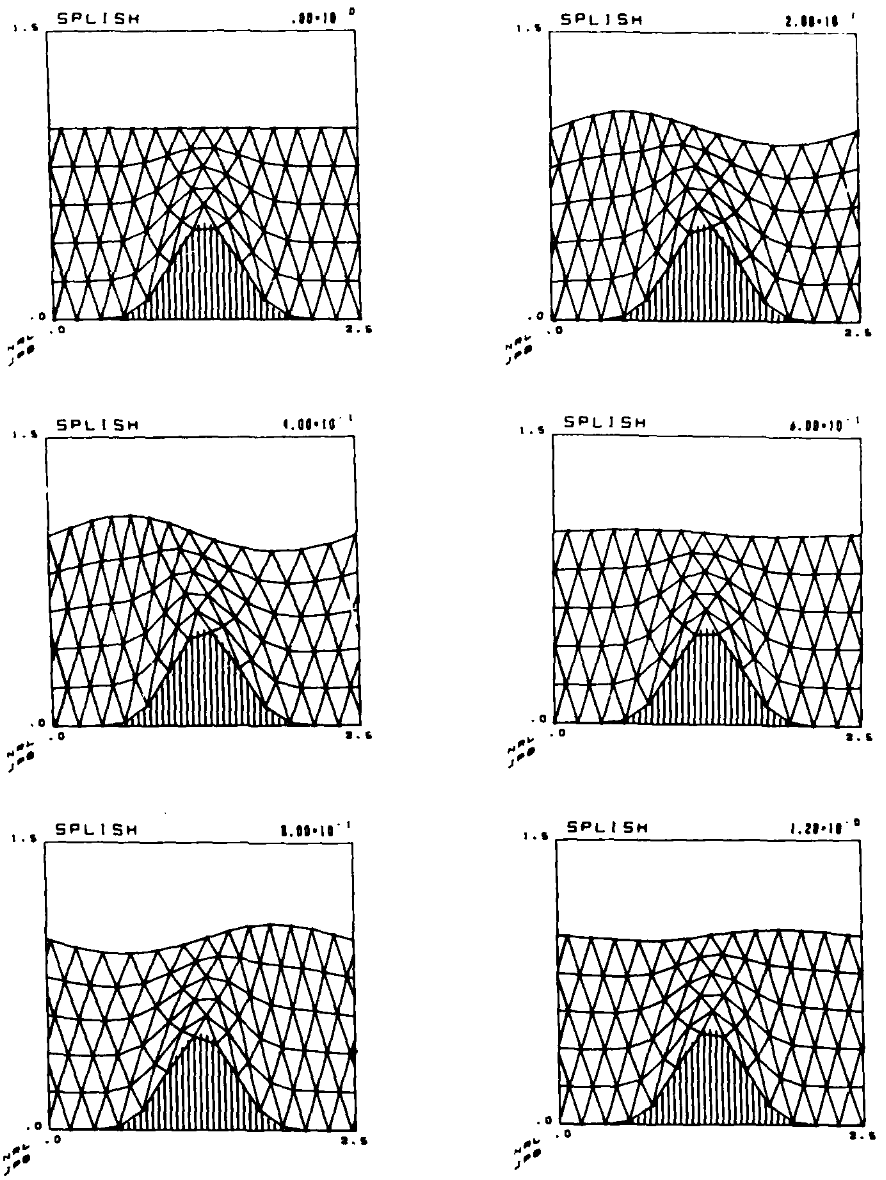

Figure 9. A larger amplitude bottom obstacle (0.5 cm) and an antisymmetric perturbation with a 1.0 - 1.2 gm/cc density stratification.

gravity waves run faster in shallow water when $kh > 1$, the nonlinear change in depth should cause a net reduction in the period as observed.

Figure 8 shows several frames from a run which was initialized symmetrically to test the program coding. Any error in the initialization, the physics, or the boundary conditions would lead almost immediately to an asymmetry in the computed solutions which could be used to debug the code. The test showed complete symmetry and thus precluded a large class of possible coding errors. The density was stratified linearly from 1.0 gm/cc at the top to 1.2 gm/cc at the bottom (depth 1 cm). The height of the obstacle was 0.3 cm. The surface gravity wave has a period of between .120 and .124 sec, somewhat shorter than the .127 sec predicted by linear theory for constant density and a depth of 1 cm. Because of the bottom topology, the average depth is less than 1 cm and hence the period is shortened slightly.

Figure 9 shows an asymmetric calculation with an even larger obstacle of 0.5 cm height. A lot of grid distortion is expected and seen. Still the calculation gave perfectly well-behaved waves.

References

1. W. P. Crowley, Proceedings of the Second International Conference on Numerical Methods in Fluid Dynamics, (Springer-Verlag, New York, 1971).

2. J. Boris and K. Hain, Bull. Am. Phys. Soc., paper 6G1, p 1299, October 1973.

3. P. C. Liewer and J. P. Boris, Bull. Am. Phys. Soc., paper DK12, p483, April 1974.

4. Barcilon, Book, Boris, Cooper, Hain, Liewer, Robson, Shanny, Turchi, and Winsor, Plasma Physics and Controlled Nuclear Fusion Research, 1974, IAEA-CN-33, p567.

5. C. Brennen and A. K. Whitney, "Unsteady, Free Surface Flows; Solutions Employing the Lagrangian Description of the Motion", 8th Symposium on Naval Hydrodynamics, Pasadena, August 1970.

6. R. K-C. Chan, "A Generalized Arbitrary Lagrangian-Eulerian (GALE) Method for Incompressible Flows with Sharp Interfaces," Science Applications, Inc. Report 73-575-LJ, November 1973.

7. J. P. Boris, Proceedings of the Fourth Conference on the Numerical Simulation of Plasma, Nav. Res. Lab., Wash., D. C. 2-3 November 1970.

8. J. P. Boris and D. L. Book, Chapter 11, Vol. 16, Methods in Computational Physics

AN EFFICIENT DIFFERENTIO-INTEGRAL EQUATION TECHNIQUE FOR TIME-DEPENDENT POTENTIAL FLOWS WITH A FREE SURFACE

Amiram Harten

Courant Institute of Mathematical Sciences
New York University, New York, N.Y. 10012 U.S.A.

ABSTRACT

Time-dependent potential flows with free surface have been treated before by integral equation techniques based on time-dependent kernels. Because these kernels are rather complicated, this approach led to inefficient numerical implementations.

In the present approach a time-independent kernel, i.e. the fundamental solution of the Laplacian operator, is used, leading to a very efficient numerical method, which we call TDIET (Time-dependent Differentio-Integral Equation Technique). TDIET assumes that the normal derivative of the potential is a given function of time along the boundary, except on that part of the boundary which is the free surface; there the normal derivative is a function of the time derivatives of the potential.

The potential on the boundary is given by the appropriate Green's integral equation. This equation is discretized by a cubic spline approximation of the potential, resulting in a linear system. After certain algebraic manipulations and the use of our assumptions, a system of ordinary differential equations for the values of the potential at the nodal points on the free surface obtains. This system of ordinary differential equations represents the time evolution of the potential and can be easily solved by a standard method.

Numerical tests demonstrate the accuracy and the efficiency of TDIET.

1. Introduction

In this paper we consider the following two-dimensional potential flow problem: One or several bodies are floating in a channel; the floating bodies and the channel are assumed to be infinitely long in the y-direction and to have a uniform and bounded x-z cross-section $\mathcal{D}$. The fluid and the floating bodies are initially at rest and their motion, which we assume to be small, is generated by the excitation of the confining boundary or the floating bodies.

The motion of the fluid is described by means of a velocity potential $\phi(\underline{x},t)$, $\underline{x} = (x,z)$, satisfying Laplace's equation

$$(1.1) \qquad \Delta\phi = \phi_{xx} + \phi_{zz} = 0 \qquad \underline{x} \in \mathcal{D}, \ t > 0$$

and the linearized free surface condition on the undisturbed water surface Γ_F (see Figure 1)

$$(1.2) \qquad \phi_{tt} + g\phi_z = 0 \qquad \underline{x} \in \Gamma_F, \ t > 0$$

where g is the gravitation acceleration. If the free surface is described by $z = \eta(x,t)$, then

$$(1.3) \qquad \eta(x,t) = -\frac{1}{g}\,\phi_t(\underline{x},t) \qquad \underline{x} \in \Gamma_F, \ t \geq 0$$

On $\Gamma_R = \Gamma - \Gamma_F$, which is a rigid boundary, we require the normal velocity of the fluid to coincide with the normal velocity of the boundary. On the boundary of the floating bodies Γ_B

$$(1.4a) \qquad \phi_n(\underline{x},t) = -n_x\dot{X}(t) - n_z\dot{Z}(t) + [(x-x_G)n_x - (z-z_G)n_z]\dot{\Lambda}(t)$$
$$\equiv \sum_{j=1}^{3} b_j(\underline{x})\, V_j(t) \qquad \underline{x} \in \Gamma_B, \ t \geq 0$$

Here $\underline{n} = (n_x, n_z)$ is the unit normal pointing into the domain $\mathcal{D}$; (x_G, z_G) is the center of giration of the body and (X,Z) is its displacement from the rest position; Λ is the angle of the floating body measured from a vertical line.

The confining wall $\Gamma_W = \Gamma_R - \Gamma_B$ is excited externally

$$(1.4b) \qquad \phi_n(\underline{x},t) = a_n(\underline{x})\, T(t) \qquad \underline{x} \in \Gamma_W, \ t \geq 0$$

and the fluid itself is initially at rest.

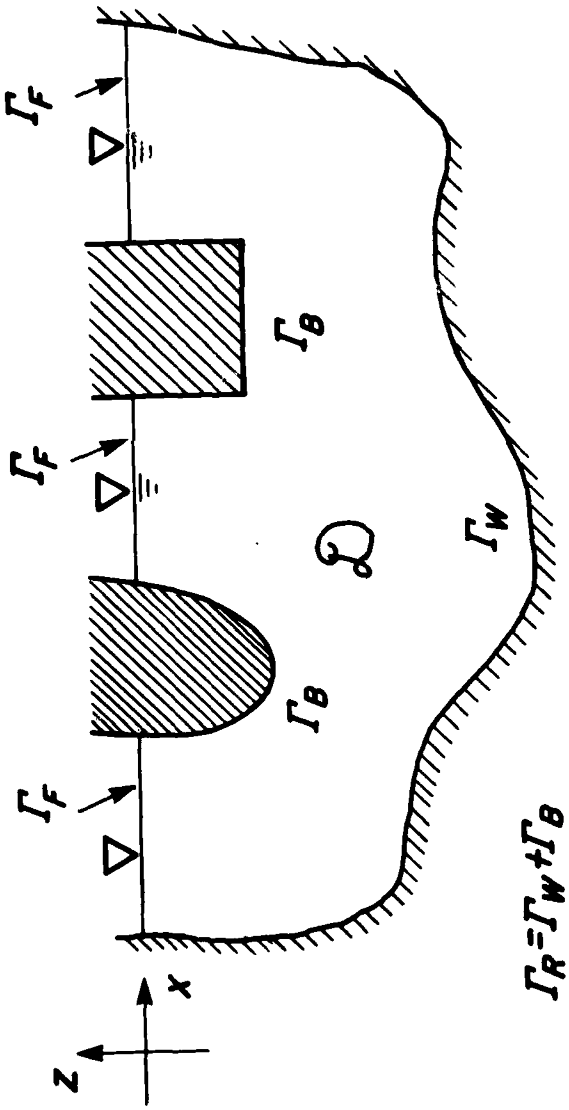

$$\Gamma_R = \Gamma_W + \Gamma_B$$

$$\Gamma = \Gamma_R + \Gamma_F$$

FIGURE I

(1.5) $\quad \phi(\underline{x},0) = \phi_t(\underline{x},0) = 0 \qquad \underline{x} \in \Gamma_F$

The pressure $P(\underline{x},t)$ is determined by Euler's integral

(1.6) $\quad P + \rho\phi_t + \rho g z = 0 \qquad \underline{x} \in \mathcal{D} + \Gamma, \quad t \geq 0$

with the term $\frac{1}{2}\rho|\nabla\phi|^2$ suppressed as being of higher order; ρ is the density of the fluid.

The problem (1.1) - (1.6) can be solved directly by using a finite-difference approximation to the Laplacian operator and the boundary conditions (see [1]). However, in many engineering problems only the solution on the boundary, i.e. the wave height (1.3) and the pressure on the floating bodies and the confining walls, is of interest. Hence it might be advantageous to use methods based on Green's identity in order to solve only for the boundary potential. One usually starts by applying the Green's identity to the acceleration potential $\psi = \phi_t$.

(1.7a) $\quad \lambda(\underline{x})\psi(\underline{x},\tau) = \int_{\Gamma} [G(\underline{x},\underline{\xi};t-\tau)\psi_n(\underline{\xi},\tau) - G_n(\underline{x},\underline{\xi},t-\tau)\psi(\underline{\xi},\tau)]ds_{\xi}$

where

(1.7b) $$\lambda(\underline{x}) = \begin{cases} 2\pi & \underline{x} \in \mathcal{D} \\ \pi & \underline{x} \in \Gamma, \ \Gamma \text{ smooth at } \underline{x} \\ \text{angle between tangents} & \underline{x} \in \Gamma, \ \Gamma \text{ has discontinuous first derivatives at } \underline{x} \end{cases}$$

and

(1.7c) $\quad G(x,z;\xi,\zeta;t) \equiv G(\underline{x},\underline{\xi},t) = \log R + W(\underline{x},\underline{\xi},t)$

Here $R^2 = (x-\xi)^2 + (z-\zeta)^2$ and W is an arbitrary function which is harmonic in $\mathcal{D}$.

One can choose $G(\underline{x},\underline{\xi},t)$ which satisfies the following condition (see [4]).

(1.8a) $\quad G(\underline{x},\underline{\xi}_o,o) = 0$

(1.8b) $\quad G_{tt}(\underline{x},\underline{\xi}_o,t) + gG_z(\underline{x},\underline{\xi}_o,t) = 0$

for $\underline{\xi}_o \in \Gamma_F$. In addition G satisfies

(1.9) $\quad G(\underline{x},\underline{\xi}, -t) = G(\underline{x},\underline{\xi},t) \qquad \underline{\xi} \in \Gamma + \mathcal{D}, \ t > 0$

Typically such a choice of a time-dependent Green's function leads to the following integral equation

$$(1.10) \qquad L\,\phi = \lambda(\underline{x})\phi(\underline{x},t) + \int_{\Gamma_R} \phi(\underline{\xi},t)G_n(\underline{x},\underline{\xi},o)ds_\xi$$
$$+ \int_0^t d\tau \int_{\Gamma_R} \phi(\underline{\xi},t)G_{nt}(\underline{x},\underline{\xi},t-\tau)ds_\xi = F(t)$$

where $F(t)$ is a function of known quantities. L contains a convolution with respect to time; consequently it becomes increasingly expensive to compute as t increases.

In the next section we shall describe TDIET which is an efficient numerical technique based on a choice of a time-independent Green's function ($W \equiv 0$ in (1.7c))

2. TDIET

Let $G(\underline{x},\underline{\xi})$ be the following time-independent Green's function

$$(2.1) \qquad G(\underline{x},\underline{\xi}) = \log R + W(\underline{x},\underline{\xi})$$

where W is harmonic in $\mathcal{D}$. Substituting this G and the boundary conditions (1.2) and (1.4) in (1.7) results in the following integro-differential equation

$$(2.2) \quad \lambda(\underline{x})\phi(\underline{x},t) + \oint_\Gamma \phi(\underline{\xi},t)G_n(\underline{x},\underline{\xi})ds_\xi + \frac{1}{g}\int_{\Gamma_F} G(\underline{x},\underline{\xi})\phi_{tt}(\underline{\xi},t)ds_\xi$$
$$= T(t)\int_{\Gamma_W} G(\underline{x},\underline{\xi})\, a_n(\underline{\xi})ds_\xi + \sum_{j=1}^{3} V_j(t)\int_{\Gamma_B} G(\underline{x},\underline{\xi})b_j(\underline{\xi})ds_\xi \equiv F(t)$$

A convenient choice for a Green's function is one which satisfies

$$(2.3) \qquad G_n(\underline{x},\underline{\xi}) = 0 \qquad\qquad \underline{\xi} \in \Gamma_R$$

In this case, the first integral on the left hand side of (2.2) is taken along Γ_F only and a discretization leads to a linear system of ordinary differential equations

$$(2.4) \qquad A\,\frac{d^2}{dt^2}\,\underline{\phi}_F(t) + B\,\underline{\phi}_F(t) = \underline{\alpha}(t)$$

for $\underline{\phi}_F$, the N_F discrete values of the potential along the free surface Γ_F; A and B are $N_F \times N_F$ constant matrices. First we solve (2.4) as an initial value problem, thus obtaining an approximation $\tilde{\phi}_F(\underline{x},t)$ to the free surface potential in the time interval of interest. Now we can compute $\tilde{\phi}_R$, which is some discrete polynomial approximation to the potential on Γ_R, by solving (2.2) with $G(\underline{x},\underline{\xi}) = \log R$

$$\text{(2.5)} \quad \lambda(\underline{x})\tilde{\phi}_R(\underline{x},t) + \int_{\Gamma_R} \tilde{\phi}_R(\underline{\xi},t) \frac{\partial}{\partial n} \log R \, ds_\xi = F(t)$$

$$- \int_{\Gamma_F} [\tilde{\phi}_F(\underline{\xi},t) \frac{\partial}{\partial n} \log R + \frac{1}{g} \log R \cdot \frac{d^2}{dt^2} \tilde{\phi}_F(\underline{\xi},t)] ds_\xi$$

The right hand side of (2.5) is known in the time interval of interest and therefore the discretization of (2.5) leads to a simple system of linear equations

$$\text{(2.6)} \qquad C \, \underline{\phi}_R(t) = \underline{\beta}(t)$$

for the N_R discrete values of the potential along Γ_R; the $N_R \times N_R$ matrix C is independent of time.

This approach cannot be implemented directly in a numerical code since an explicit expression for $G(\underline{x},\underline{\xi})$ such that $G_n(\underline{x},\underline{\xi}) = 0$ for $\underline{\xi} \in \Gamma_R$, is not always available. In the following we shall present a technique to arrive at (2.4) and (2.6) without using an explicit form of such a Green's function. The main idea in TDIET is to first discretize (2.2) with $G = \log R$ and then to obtain the desired decomposition by an ordered elimination procedure.

(i) <u>Discretization</u>: Let $\underline{x}_j$, $1 \leq j \leq N$, be a partition of the boundary Γ, and let $\phi_j(t) = \phi(\underline{x}_j,t)$. It is convenient to order the partition points so that $\underline{x}_j$, $1 \leq j \leq N_R$, are the points along Γ_R and $\underline{x}_j$, $N_R + 1 \leq j \leq N$, are the partition points along the free surface Γ_F; $N = N_R + N_F$ (see Figure 1).

The integrands in (2.2) are products of a smooth function (ϕ or ϕ_{tt}) multiplied by a singular function (G or G_n).

Therefore we discretize (2.2) by approximating only the potential, using an accurate enough polynomial approximation, e.g. B - splines or cubic splines. In the following we shall use cubic spline approximation. The integrals of the products of the polynomials multiplied by G or G_n, can be computed analytically due to the simplicity of the Green's function. This should be done at least in the vicinity of the singularity at $\underline{x}_i = \underline{\xi}$ (see [3]).

We denote by $S_j(\underline{x})$ the unit cubic spline such that

$$S_j(\underline{x}_i) = \delta_{ij} \quad (\delta_{ij} \text{ is the Kronicker } \delta) \tag{2.7}$$

In case the boundary has corners, we construct $S_j(\underline{x})$ so that it will be continuous up to the second derivative in a smooth segment which contains $\underline{x}_j$, and to be identically zero in all other segments. This way, the approximation

$$\phi(\underline{x},t) \sim \sum_{j=1}^{N} S_j(\underline{x})\phi_j(t) \tag{2.8a}$$

$$\phi_{tt}(\underline{x},t) \sim \sum_{j=1}^{N} S_j(\underline{x})\ddot{\phi}_j(t)$$

is continuous up to the second derivative, except at corners where it is only continuous. Because of the singular nature of the corners, the partition points are distributed more densely around the corners.

Next, equation (2.2) is discretized by using the cubic spline approximation (2.8) and $G = \log R$

$$\begin{aligned}(2.9)\quad & \lambda(\underline{x}_i)\phi_i(t) + \sum_{j=1}^{N} \phi_j(t) \oint_\Gamma S_j(\underline{\xi})G_n(\underline{x}_i,\underline{\xi})ds \\ & + \frac{1}{g}\sum_{j=N_R+1}^{N} \ddot{\phi}_j(t)\int_{\Gamma_F} S_j(\underline{\xi})G(\underline{x}_i,\underline{\xi})ds = T(t)\int_{\Gamma_W} G(\underline{x}_i,\underline{\xi})\ a_n(\underline{\xi})ds \\ & + \sum_{k=1}^{3} V_k(t)\int_{\Gamma_B} G(\underline{x}_i,\underline{\xi})b_k(\underline{\xi})ds \qquad\qquad 1 \le i \le N\end{aligned}$$

The N equations (2.9) can be written in the following matrix form

$$E \cdot \underline{\mu}(t) = \underline{\gamma}(t) \tag{2.10}$$

where $\underline{\mu}(t)$ is an $N + N_F$ vector whose components are

$$\mu_i = \begin{cases} \phi_R(\underline{x}_i, t) & 1 \le i \le N_R \\ \dfrac{\partial^2}{\partial t^2} \phi_F(\underline{x}_i, t) & N_R + 1 \le i \le N \\ \phi_F(\underline{x}_{i-N_F}, t) & N + 1 \le i \le N + N_F \end{cases} \tag{2.11}$$

$\underline{\gamma}(t)$ is an N vector

$$\underline{\gamma}(t) = T(t)\underline{\alpha} + \sum_{k=1}^{3} V_k(t)\underline{\beta}_k \tag{2.12a}$$

where

$$\alpha_i = \int_{\Gamma_W} G(\underline{x}_i, \underline{\xi})\, a_n(\underline{\xi}) ds \qquad 1 \le i \le N \tag{2.12b}$$

$$\beta_{i,k} = \int_{\Gamma_B} G(\underline{x}_i, \underline{\xi}) b_k(\underline{\xi}) ds \quad , \qquad k = 1,2,3 \; ; \quad 1 \le i \le N \tag{2.12c}$$

E is an $N \times (N+N_F)$ matrix, the entries of which are

$$E_{ij} = \lambda(\underline{x}_i)\delta_{ij} + \int_{\Gamma} S_j(\underline{\xi}) G_n(\underline{x}_i, \underline{\xi}) ds \qquad 1 \le i \le N,\ 1 \le j \le N_R \tag{2.13a}$$

$$E_{ij} = \frac{1}{g} \int_{\Gamma_F} S_j(\underline{\xi}) G(\underline{x}_i, \underline{\xi}) ds \qquad 1 \le i \le N,\ N_R+1 \le j \le N \tag{2.13b}$$

$$E_{ij} = \lambda(\underline{x}_i)\delta_{i,j-N_F} + \int_{\Gamma} S_{j-N_F}(\underline{\xi}) G_n(\underline{x}_i, \underline{\xi})\, ds \qquad 1 \le i \le N\ ,\ N+1 \le j \le N+N_F \tag{2.13c}$$

We observe that the entries E_{ij} as well as the coefficients α_i and $\beta_{i,k}$ depend only on the geometry of the boundary and do not depend on time.

(ii) Solution of the discrete problem

In order to obtain an analog to the equations (2.4) and (2.6), a Gaussian elimination procedure (with row pivoting) is applied to the matrix equation (2.10). The unknowns

$\mu_1, \ldots, \mu_{j-1}$ are eliminated from the j-th equation, $2 \leq j \leq N$. The resulting matrix equation is of the following form

(2.14)

$$\begin{array}{cc} & \begin{array}{ccc} N_R & N_F & N_F \end{array} \\ \begin{array}{c} N_R \\ N_F \end{array} & \left[\begin{array}{c:c:c} U_R & Q & R \\ \hdashline \underline{0} \quad 0 & U_F \;\; 0 & M \end{array}\right] \end{array} \begin{bmatrix} \underline{\phi}_R(t) \\ \hline \ddot{\underline{\phi}}_F(t) \\ \hline \underline{\phi}_F(t) \end{bmatrix} = T(t) \begin{bmatrix} \tilde{\underline{\alpha}}_R \\ \hline \tilde{\underline{\alpha}}_F \end{bmatrix} + \sum_{k=1}^{3} V_k(t) \begin{bmatrix} \tilde{\underline{\beta}}_R^{(k)} \\ \hline \tilde{\underline{\beta}}_F^{(k)} \end{bmatrix}$$

The last N_F equations

(2.15) $$U_F \ddot{\underline{\phi}}_F(t) + M \underline{\phi}_F(t) = T(t)\, \tilde{\underline{\alpha}}_F + \sum_{k=1}^{3} V_k(t) \underline{\beta}_F^{(k)}$$

constitutes a system of linear ordinary differential equations similar to (2.4); U_F is a constant upper triangular matrix. This sub-problem for the free surface potential is now solved independently as an initial value problem with the initial conditions (1.5)

(2.16) $$\underline{\phi}_F(0) = \dot{\underline{\phi}}_F(0) = 0$$

The computation of the initial value problem (2.15) - (2.16) can be accomplished by any standard method; our computer code uses a fourth order accurate Runge-Kutta method.

Once the free surface potential $\underline{\phi}_F(t)$ has been computed in the time interval of interest, $\underline{\phi}_R(t)$ can be computed at the desired time-levels by solving the system of linear

equations composed of the first N_R equations in (2.14).

$$U_R \underline{\phi}_R(t) = T(t)\underline{\tilde{\alpha}}_R + \sum_{k=1}^{3} V_k(t)\underline{\beta}_R^{(k)} - Q\underline{\dot{\phi}}_F(t) - R\underline{\phi}_F(t) \tag{2.17}$$

We observe that U_R is an upper triangular matrix. Hence, once the right hand side of (2.17) has been computed, the solution $\underline{\phi}_R(t)$ is computed inexpensively by back substitution.

3. Discussion

In many engineering applications it is the acceleration potential $\psi = \phi_t$, rather than the velocity potential ϕ, which is of interest since the acceleration potential is proportional to the hydrodynamic pressure and the linearized elevation of the free surface. Equations for approximation of the acceleration potential are obtained simply by differentiating (2.14) with respect to time. The initial conditions are obtained from (2.15) and (2.16)

$$\underline{\psi}_F(0) = 0 \tag{3.1a}$$

$$\dot{\psi}_F(0) = U_F^{-1}[\dot{T}(0)\underline{\tilde{\alpha}}_F + \sum_{k=1}^{3} \dot{V}_k(0)\underline{\beta}_F^{(k)}] \tag{3.1b}$$

In Section 2 we have considered $(V_1,V_2,V_3) = (X,Z,\Lambda)$ as given functions of time. When computing the motion of freely floating bodies these quantities are unknowns, and the equations (1.1) - (1.6) for the fluid motion are supplemented by equations for the body motion of the form

$$\begin{aligned} \ddot{X} &= f_1(X,Z,\Lambda,\psi_B) \\ \ddot{Z} &= f_2(X,Z,\Lambda,\psi_B) \\ \ddot{\Lambda} &= f_3(X,Z,\Lambda,\psi_B) \end{aligned} \tag{3.2}$$

(see [4]). One can solve simultaneously the system (2.15), (2.16) and (3.2) in a straightforward manner by using only the information at time t to compute the solution at the time $(t + \Delta t)$. This approach leads to a first order

accurate method. Furthermore, ψ_B has to be computed at each time step, even if not needed for engineering purposes. It is possible to eliminate ψ_B from (3.2) by using the corresponding equations in (2.17) and to arrive at a system of ordinary differential equation involving only the free surface potential and the displacement of the floating body. The details will be given elsewhere.

In its present form, TDIET is applicable for problems in a bounded domain where only the boundary potential is needed. In case the potential is needed in the domain $\mathcal{D}$, but only at few time levels, it still is efficient to use TDIET to compute the boundary potential at the desired time levels and then to solve a Dirichlet problem.

We have described TDIET for two dimensional computations. For the formulation in three dimensional case one only has to change the Green's function and the notations; unfortunately, computerwise, it is much more difficult.

TDIET is relatively very fast. We found in [2] that it is about 600 times faster than QUAKE, which is a Green's function technique of the type (1.8) - (1.10). The test case considered corresponds to an excitation due to an earthquake with a duration of 50 seconds. A comparison with the finite difference method of [1] shows that TDIET is about 70 times faster.

Acknowledgement

The author thanks Professor O. Widlund and Professor E. Turkel for critically reading this manuscript. This research was partially sponsored by Frederic R. Harris, Inc. Many helpful discussions with Mr. H. Bomze and Dr. Y. K. Chung, concerning engineering applications of this method, are gratefully acknowledged.

References

[1] R. K. Chan and C. W. Hirt, "Two-dimensional Calculations of the Motion of Floating Bodies", Proceedings of the 10th Hydrodynamic Symposium, MIT, June 1974.

[2] A. Harten and Y. K. Chung, "Green's Function Techniques for the Solution of Time-dependent Potential Flows with a Free Surface in a Bounded Domain (A Preliminary Report)", ERDA Report Courant Institute of Mathematical Sciences, N.Y.U. (October 1975).

[3] R. T. Ho and A. Harten, "On Green's Function Techniques for Solutions of Floating Body Problems", Proceedings of Ocean Engineering III, University of Delaware, June 1975.

[4] J. V. Wehausen, "The Motion of Floating Bodies", Annual Review of Fluid Mechanics, Vol. 3, 1971, pp. 237-268.

LIST OF PARTICIPANTS

Adee, Bruce H. University of Washington, U.S.A.
Ankudinov, V. Hydronautics, Inc., Laurel, Md, U.S.A.
Bai, K.J. DTNSRDC, Bethesda, Md, U.S.A.
Baker, Elwyn S. DTNSRDC, Bethesda, Md, U.S.A.
Bales, Susan L. DTNSRDC, Bethesda, Md, U.S.A.
Barr, Roderick Hydronautics, Inc., Laurel, Md, U.S.A.
Birkhoff, Garrett Harvard University, U.S.A.
Blake, William K. DTNSRDC, Bethesda, Md, U.S.A.
Boichot, Lance Sun Shipbuilding, Chester, Pa., U.S.A.
Bomze, Herman Frederic R. Harris, Inc., Great Neck, N.Y., U.S.A.
Boris, Jay P. Naval Research Lab, Washington, D.C., U.S.A.
Bourianoff, George I. Austin Research Associates, Austin, Texas, U.S.A.
Bowers, Brian E. DTNSRDC, Bethesda, Md, U.S.A.
Briggs, David G. Rutgers University, U.S.A.
Brodsky, Stuart L. Office of Naval Research, Arlington, Va., U.S.A.
Brown, Samuel H. DTNSRDC, Annapolis, Md, U.S.A.
Breslin, John P. Stevens Institute of Technology, U.S.A.
Casarella, Mario J. Catholic University, U.S.A.
Cebeci, Tuncer Douglas Aircraft Co., Long Beach, Ca., U.S.A.
Chan, R.K.-C. JAYCOR, Del Mar, Ca., U.S.A.
Chang, Ming S. DTNSRDC, Bethesda, Md, U.S.A.
Chapman, Richard B. DTNSRDC, Bethesda, Md, U.S.A.
Cheng, S.I. Princeton University, U.S.A.
Coder, David W. DTNSRDC, Bethesda, Md, U.S.A.
Coleman, Roderick DTNSRDC, Bethesda, Md, U.S.A.
Comstock, Edward N. Naval Ship Engineering Center, Hyattsville, Md, U.S.A.
Cooper, Morton Office of Naval Research, Arlington, Va., U.S.A.
Cooper, Ralph Office of Naval Research, Arlington, Va., U.S.A.
Cox, Bruce D. DTNSRDC, Bethesda, Md, U.S.A.
Cross, Raymond DTNSRDC, Bethesda, Md, U.S.A.
Crump, Stuart F. DTNSRDC, Bethesda, Md, U.S.A.
Curphey, Richard M. DTNSRDC, Bethesda, Md, U.S.A.
Cuthill, Elizabeth H. DTNSRDC, Bethesda, Md, U.S.A.
Davis, Ronald W. National Bureau of Standards, Gaithersburg, Md, U.S.A.
Dawson, Charles DTNSRDC, Bethesda, Md, U.S.A.
Dean, Janet DTNSRDC, Bethesda, Md, U.S.A.
Dhir, Surendra K. DTNSRDC, Bethesda, Md, U.S.A.
Diskin, Jack DTNSRDC, Bethesda, Md, U.S.A.
Dobay, Gabor F. DTNSRDC, Bethesda, Md, U.S.A.
Doctors, L.J. University of New South Wales, Australia
Doroff, Stanley W. Office of Naval Research, Arlington, Va., U.S.A.
Dougalis, V.A. Harvard University, U.S.A

Eddy, Robert P. DTNSRDC, Bethesda, Md, U.S.A.
Eggers, Klaus Institut fur Schiffbau, Hamburg, W. Germany
Eisenhuth, Joseph J. Pennsylvania State University, U.S.A.
Everstine, Gordon DTNSRDC, Bethesda, Md, U.S.A.
Falls, Robert Maritime Administration, Washington, D.C., U.S.A.
Feifel, Winfried M. Boeing Aerospace, Seattle, Wash., U.S.A.
Fein, James A. DTNSRDC, Bethesda, Md, U.S.A.
Franz, Gerald J. DTNSRDC, Bethesda, Md, U.S.A.
Frenkiel, Francois N. DTNSRDC, Bethesda, Md, U.S.A.
Fritts, Martin Science Applications, Inc., McLean, Va., U.S.A.
Fuller, Nathan R., Jr. Naval Ship Engineering Center, Hyattsville, Md, U.S.A.
Furuya, Okitsugu Tetra Tech, Inc., Pasadena, Ca., U.S.A.
Gleissner, Gene DTNSRDC, Bethesda, Md, U.S.A.
Gospodnetic, Drasvo National Research Council of Canada, Ottawa, Canada
Grafton, Robert B. Office of Naval Research, New York, N.Y., U.S.A.
Granville, Paul S. DTNSRDC, Bethesda, Md, U.S.A.
Groves, Nancy C. DTNSRDC, Bethesda, Md, U.S.A.
Hain, K. U.S. Naval Research Lab, Washington, D.C., U.S.A.
Harten, Amiram Courant Institute, New York, N.Y., U.S.A.
Haussling, Henry J. *DTNSRDC, Bethesda,* Md, U.S.A.
Hess, John L. Douglas Aircraft Co., Long Beach, Ca., U.S.A.
Hershey, Allen V. Naval Surface Weapons Centers, Dahlgren, Va., U.S.A.
Higgins, Laurie DTNSRDC, Bethesda, Md, U.S.A.
Hirt, C.W. Los Alamos Scientific Lab, Los Alamos, N.M., U.S.A.
Hsiung, Chi-Chao U.S. Merchant Marine Academy, Kings Point, N.Y., U.S.A.
Hsu, Chun-Che Hydronautics, Inc., Laurel, Md, U.S.A.
Huang, Thomas T. DTNSRDC, Bethesda, Md, U.S.A.
Jacobsen, Bent Kofoed Skibstenknisk Lab, Lyngby, Denmark
Karafiath, Gabor DTNSRDC, Bethesda, Md, U.S.A.
Kerney, Keith P. DTNSRDC, Bethesda, Md, U.S.A.
Keane, Robert G., Jr. Naval Ship Engineering Center, Hyattsville, Md, U.S.A.
Kennell, Colen Naval Ship Engineering Center, Hyattsville, Md, U.S.A.
Kim, Michael W.D. Ocean Engineering & Const. Project Office, Washington, D.C., U.S.A.
Kuiper, G. Netherlands Ship Model Basin, Wageningen, The Netherlands
Landweber, Louis University of Iowa, U.S.A.
Langan, Thomas J. DTNSRDC, Bethesda, Md, U.S.A.
Larsson, Lars Swedish State Shipbuilding Experimental Tank, Gothenburg, Sweden
Lau, Richard Office of Naval Research, Pasadena, California, U.S.A.
Lea, George K. National Science Foundation, U.S.A.
Lee, Choung DTNSRDC, Bethesda, Md, U.S.A.
Leehey, Patrick Massachusetts Institute of Technology, U.S.A.
Lin, W.C. DTNSRDC, Bethesda, Md, U.S.A.

Liu, Chen-Ya Battelle Memorial Institute, Columbus, Ohio, U.S.A.
Lugt, Hans J. DTNSRDC, Bethesda, Md, U.S.A.
Magnuson, Allen H. DTNSRDC, Bethesda, Md, U.S.A.
Matula, Petro DTNSRDC, Bethesda, Md, U.S.A.
McCarthy, Justin H. DTNSRDC, Bethesda, Md, U.S.A.
McCreight, Kathryn K. DTNSRDC, Bethesda, Md, U.S.A.
McCreight, William R. DTNSRDC, Bethesda, Md, U.S.A.
McDonald, William W. Naval Surface Weapons Center, White Oak, Md, U.S.A.
McKee, James M. DTNSRDC, Bethesda, Md, U.S.A.
Mei, Chiang C. Massachusetts Institute of Technology, U.S.A.
Meng, James C.-S. Science Applications, Inc., La Jolla, Ca., U.S.A.
Mercer, John Flow Research, Inc., Kent, Wash., U.S.A.
Miles, Michael National Research Council of Canada, Ottawa, Canada
Mindak, Robert J. Office of Naval Research, Arlington, Va., U.S.A.
Moran, David D. DTNSRDC, Bethesda, Md, U.S.A.
Morgan, William B. DTNSRDC, Bethesda, Md, U.S.A.
Morawitz, Cathleen S. Courant Institute, New York University, U.S.A.
Murman, Earll M. Flow Research, Inc., Kent, Wash., U.S.A.
Murthy, T.K.S. Portsmouth Polytechnic, Portsmouth, England
Nath, John H. Oregon State University, U.S.A.
Neal, Eddie DTNSRDC, Bethesda, Md, U.S.A.
Newman, J. Nicholas Massachusetts Institute of Technology, U.S.A.
Nichols, B.D. Los Alamos Scientific Lab, Los Alamos, N.M., U.S.A.
Niedzwecki, John M. Catholic University, U.S.A. (Student)
Nielson, Finn Gunnar Ship Research Institute of Norway, Trondheim, Norway
Noblesse, Francis Stanford University, U.S.A.
Noordzij, L. Netherlands Ship Model Basin, Wageningen, The Netherlands
O'Brien, Vivian Johns Hopkins Applied Physics Lab, Laurel, Md, U.S.A.
Ogilvie, T. Francis University of Michigan, U.S.A.
Ohring, Samuel DTNSRDC, Bethesda, Md, U.S.A.
Oser, Hans J. National Bureau of Standards, Gaithersburg, Md, U.S.A.
Pien, Pao C. DTNSRDC, Bethesda, Md, U.S.A.
Powell, Alan DTNSRDC, Bethesda, Md, U.S.A.
Potash, Roger L. Lockheed Ocean Systems, Sunnyvale, Ca., U.S.A.
Reed, Arthur DTNSRDC, Bethesda, Md, U.S.A.
Rehm, Ronald National Bureau of Standards, Gaithersburg, Md, U.S.A.
Rispin, Paul P. DTNSRDC, Bethesda, Md, U.S.A.
Roache, Patrick J. Science Applications, Inc., Albuquerque, N.M., U.S.A.
Roberts, Glyn O. University of Colorado, U.S.A.
Rogers, Joel C.W. Naval Surface Weapons Center, White Oak, Md, U.S.A.
Rood, Edwin P. DTNSRDC, Bethesda, Md, U.S.A.
Salvesen, Nils DTNSRDC, Bethesda, Md, U.S.A.

Sambuco, Edmund Hydronautics, Inc., Laurel, Md, U.S.A.
Sasajima, Takao Mitsubishi Heavy Industries, Hiroshima, Japan
Schmid, Lawrence A. NASA, Goddard Space Flight Center, Greenbelt, Md, U.S.A.
Schot, Joanna Wood DTNSRDC, Bethesda, Md, U.S.A.
Schot, Steven H. American University, U.S.A.
Schroeder, Erwin A. DTNSRDC, Bethesda, Md, U.S.A.
Seto, Hideyuki Mitsubishi Heavy Industries, Hiroshima, Japan
Shanks, Daniel DTNSRDC, Bethesda, Md, U.S.A.
Shen, Y.T. DTNSRDC, Bethesda, Md, U.S.A.
Sigillito, Vincent John Hopkins Applied Physics Lab, Laurel, Md, U.S.A.
Smith, Neill S. Naval Coastal Systems Lab, Panama City, Fla., U.S.A.
Tanaka, Hiraku Ship Research Institute of Tokyo, Japan
Theilheimer, Feodor DTNSRDC, Bethesda, Md, U.S.A.
Thomas, James W. Colorado State University, U.S.A.
Thompson, Joe F. Mississippi State University, U.S.A.
Timman, R. Delft Technische Hogeschool, Delft, The Netherlands
Tolefson, D.C. Deepsea Ventures, Inc., Gloucester Point, Va., U.S.A.
Troesch, Armin University of Michigan, U.S.A.
Tzou, Kent T.S. Westinghouse Oceanic Division, Annapolis, Md, U.S.A.
Vander Vorst, Michael J. Naval Surface Weapons Center, White Oak, Md, U.S.A.
Van Eseltine, Richard DTNSRDC, Bethesda, Md, U.S.A.
Van Tuyl, Andrew H. Naval Surface Weapons Center, White Oak, Md, U.S.A.
Vinje, Tor University of Trondheim, Norway
Von Kerczek, Christian H. DTNSRDC, Bethesda, Md, U.S.A.
Wang, C.G. I.B.M. Research Center, Millwood, N.Y., U.S.A.
Ward, Lawrence W. Webb Institute of Naval Architecture, U.S.A.
Wehausen, John V. University of California Berkeley, Ca., U.S.A.
Whalen, Joseph E. Operations Research, Inc., Silver Spring, Md, U.S.A.
Whitehead, Robert E. DTNSRDC, Bethesda, Md, U.S.A.
Wilkins, Capt. James R., Jr., USN Naval Ship Engineering Center, Hyattsville, Md, U.S.A.
Wilkins, Mark L. Lawrence Livermore Lab, Livermore, Ca., U.S.A.
Wilkins, Paul Mare Island Naval Shipyard, Vallejo, Ca., U.S.A.
Wilson, Michael DTNSRDC, Bethesda, Md, U.S.A.
Wu, Theodore Y. California Institute of Technology, U.S.A.
Yen, Shee-Mee University of Illinois, U.S.A.
Yeung, Ronald W. Massachusetts Institute of Technology, U.S.A.
Yim, Bohyun DTNSRDC, Bethesda, Md, U.S.A.
Zarda, Richard DTNSRDC, Bethesda, Md, U.S.A.
Zarnick, Ernest E. DTNSRDC, Bethesda, Md, U.S.A.

AUTHOR INDEX

☆ U. S. GOVERNMENT PRINTING OFFICE : 1976 O - 215-752